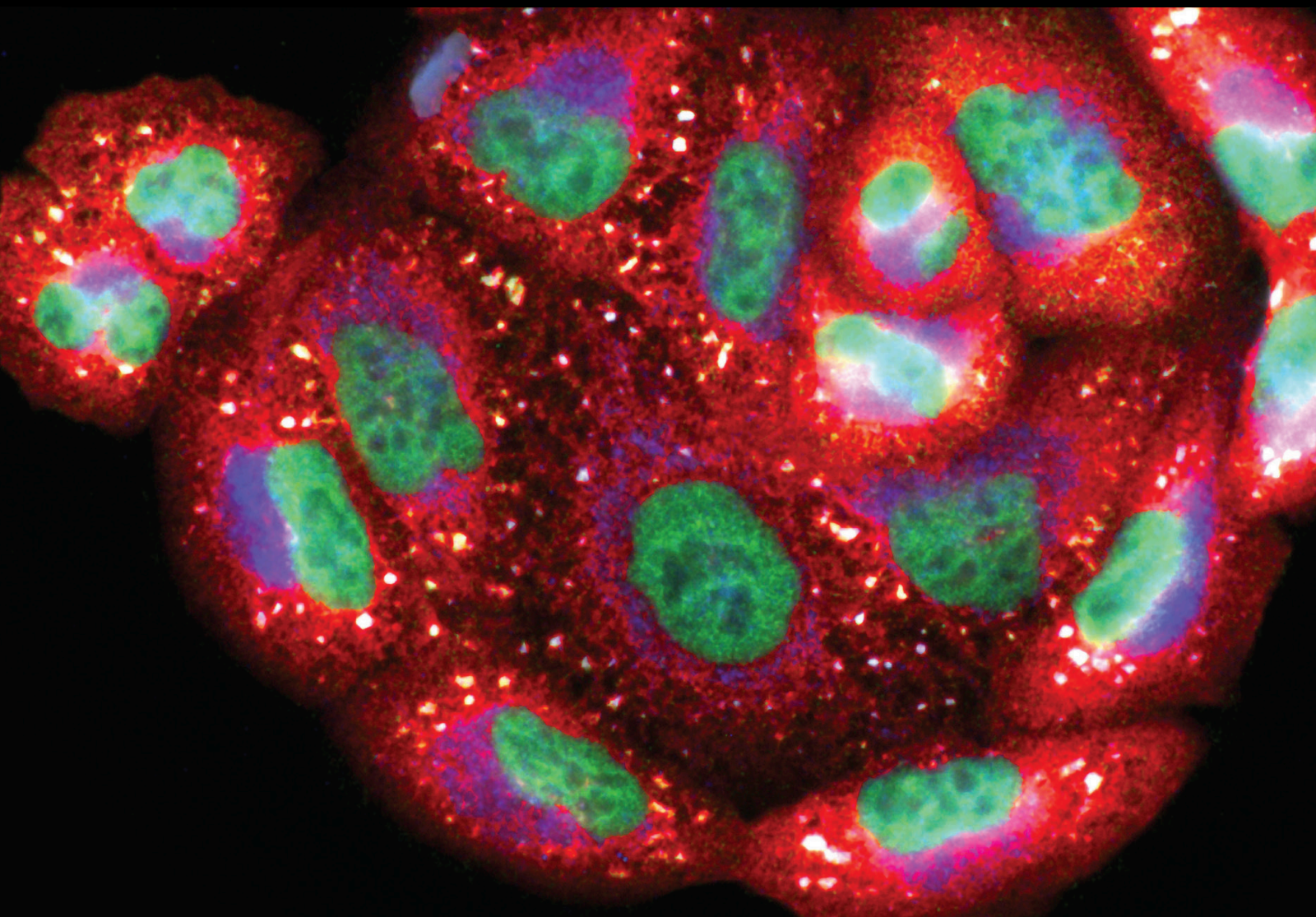# The Role of Natural and Synthetic Antioxidants in Modulating Oxidative Stress in Drug-induced Injury and Metabolic Disorders 2020

Lead Guest Editor: Ayman M. Mahmoud
Guest Editors: Fiona L. Wilkinson, Adam P. Lightfoot, Julia M. Dos Santos, and Mansur A. Sandhu

The Role of Natural and Synthetic Antioxidants in Modulating Oxidative Stress in Drug-induced Injury and Metabolic Disorders 2020

The Role of Natural and Synthetic Antioxidants in Modulating Oxidative Stress in Drug-induced Injury and Metabolic Disorders 2020

Lead Guest Editor: Ayman M. Mahmoud
Guest Editors: Fiona L. Wilkinson, Adam P. Lightfoot, Julia M. Dos Santos, and Mansur A. Sandhu

Contents

Editorial

The Role of Natural and Synthetic Antioxidants in Modulating Oxidative Stress in Drug-Induced Injury and Metabolic Disorders 2020

Ayman M. Mahmoud [iD],[1] **Fiona L. Wilkinson** [iD],[2] **Adam P. Lightfoot** [iD],[2] **Julia M. Dos Santos** [iD],[3] **and Mansur A. Sandhu** [iD][4]

[1]*Physiology Division, Zoology Department, Faculty of Science, Beni-Suef University, Egypt*
[2]*Department of Life Sciences, Faculty of Science and Engineering, Manchester Metropolitan University, UK*
[3]*College of Education, Health & Human Performance, Fairmont State University, Fairmont, USA*
[4]*Department of Biomedical Sciences, Faculty of Veterinary & Animal Sciences, PMAS, Arid Agriculture University, Pakistan*

Correspondence should be addressed to Ayman M. Mahmoud; ayman.mahmoud@science.bsu.edu.eg

Received 13 October 2021; Accepted 13 October 2021; Published 18 October 2021

Oxidative stress is an imbalance in cellular redox reactions that plays a key role in the pathogenesis of metabolic disorders and drug-induced injury. Oxidative stress is the result of reactive oxygen species (ROS) overproduction or a decline in antioxidant defense mechanisms. Although ROS production can be beneficial in some instances as they are used by the immune system, in general, excessive generation of ROS results in deleterious effects causing damage to DNA, proteins, and lipids, ultimately leading to cell death. Several diseases, including cancer, neurodegeneration, obesity, metabolic syndrome, diabetes mellitus, liver disease, and others, are well-known to be associated with excessive ROS production. Therefore, agents counteracting excess ROS and/or boosting the antioxidant defenses represent an appealing strategy for the treatment of multiple diseases.

Antioxidant substances could be natural or synthetic. Natural antioxidants are obtained entirely from natural sources and have been used in food, cosmetics, and pharmaceutical industries for some time. On the other hand, synthetic antioxidants are substances created from chemical processes. The current understanding of the complex role of ROS in physiological and pathological processes points to the necessity of developing multifunctional antioxidants, which can maintain oxidative homeostasis, both in health and in disease. In this context, numerous research groups focus on the characterization and application of natural antioxidant agents in different diseases. In addition, a great deal of effort is being conducted to design and synthesize free radical scavenging and antioxidant substances that can diminish excessive ROS production and improve the endogenous antioxidant defenses. Understanding and validating the biological activities of natural and synthetic antioxidant compounds and their molecular mechanisms in counteracting ROS and oxidative stress will provide a solid scientific foundation to the application of antioxidants in the prevention and treatment of multiple diseases.

This special issue encompasses 12 research articles focusing on the usefulness of antioxidants as novel therapeutic approaches to prevent and fight different disease conditions, including phototoxicity, drug-induced liver injury, autoimmune encephalomyelitis, nonalcoholic fatty liver disease, and hypoxia-induced cardiomyocyte injury. The guest editors are pleased to present a compendium of these cutting-edge original research articles as follows:

Research article: "Gender difference on the effect of omega-3 polyunsaturated fatty acids on acetaminophen-induced acute liver failure". In this article, Y. Liu et al. investigated the effect of n-3 polyunsaturated fatty acids (PUFAs) on acetaminophen- (APAP-) induced liver damage in male and female *fat-1* mice. The results revealed the sex-differential effect of n-3 PUFA on APAP-induced liver injury in mice. β-Catenin-mediated

regulation of autophagy represented the essential event for the n-3 PUFA-modulated APAP hepatotoxicity.

Research article: "Metabolomic analysis of the ameliorative effect of enhanced proline metabolism on hypoxia-induced injury in cardiomyocytes". Based on previous cardiovascular metabolomics studies showing severe altered proline metabolism after cardiomyocyte hypoxia, J. Wang et al. investigated the ameliorative effect of enhancing proline metabolism by overexpressing proline dehydrogenase (PRODH) on hypoxia-induced injury in cardiomyocytes. The results demonstrated that PRODH was downregulated after myocardial infarction and hypoxia and overexpression of this enzyme reduced ROS and apoptosis levels, an effect that was associated with significant changes in sphingolipid signaling pathways, glutathione disulfide, unsaturated fatty acid biosynthesis, phosphocreatine, aminoacyl-tRNA biosynthesis, and ABC transporters.

Research article: "Phloroglucinol strengthens the antioxidant barrier and reduces oxidative/nitrosative stress in nonalcoholic fatty liver disease (NAFLD)". K. Drygalski et al. reported that NAFLD and hydrogen peroxide models are comparable and suitable for assessing hepatic oxidative/nitrosative stress. The results showed that phloroglucinol is an effective nutraceutical in counteracting NAFLD, and its effectiveness is comparable with α-lipoic acid and N-acetylcysteine.

Research article: "Ascorbic acid: a new player of epigenetic regulation in LPS-gingivalis treated human periodontal ligament stem cells". Periodontal disease is an infectious disease that can lead to the progressive destruction of the periodontal ligament tissue as well as bone and tooth loss. In this study, G. Marconi et al. investigated the effects of ascorbic acid in primary culture of human periodontal ligament stem cells (hPDLSCs) exposed to Porphyromonas gingivalis lipopolysaccharide (LPS-G). Ascorbic acid exerted a protective effect against oxidative stress and inflammation and modulated miR-210 in an in vitro periodontitis model.

Research article: "Preclinical evaluation of safety, pharmacokinetics, efficacy, and mechanism of radioprotective agent HL-003". In this study, Y. Liu et al. evaluated the antioxidant and radioprotective properties of the small molecule amifostine derivative HL-003. This compound showed a radical-scavenging activity in vitro and exerted protective effect against radiation-induced intestinal injury by promoting the proliferation, differentiation, and regeneration of the intestinal epithelium, protecting DNA from radiation damage, and inhibiting apoptosis in mice.

Research article: "Inhibition of calcium oxalate formation and antioxidant activity of carboxymethylated Poria cocos polysaccharides". C. Li et al. obtained three carboxymethylated Poria cocos polysaccharides through carboxymethylation of the original polysaccharide and studied their antioxidant activity in vitro. The carboxymethylated polysaccharides prevented oxalate-induced oxidative damage in human kidney proximal tubular epithelial cells by inhibiting excessive generation of ROS and DNA damage.

Research article: "Bu Shen Yi Sui capsule alleviates neuroinflammation and demyelination by promoting microglia toward M2 polarization, which correlates with changes in miR-124 and miR-155 in experimental autoimmune encephalomyelitis". Z. Zha et al. examined the effects of Bu Shen Yi Sui (BSYS) on microglial polarization in mice with experimental autoimmune encephalomyelitis (EAE). The results revealed that BSYS regulated the inflammatory factors, ameliorated neurological function, and suppressed demyelination by promoting M2 polarization of microglia, effects that were correlated with the changes of miR-124 and miR-155 in vivo.

Research article: "Melatonin alleviates the toxicity of high nicotinamide concentrations in oocytes: potential interaction with nicotinamide methylation signaling". In this study, M. El-Sheikh et al. reported that the administration of melatonin during in vitro maturation can protect bovine oocytes against high nicotinamide-induced excess ROS production, DNA damage, and mitochondrial dysfunction. These findings might be attributed to a potential involvement of melatonin in regulating nicotinamide hypermethylation signaling.

Research article: "Pharmacological activation of Nrf2 by rosolic acid attenuates endoplasmic reticulum stress in endothelial cells". K. Amin et al. contributed a research article showing that rosolic acid treatment dose-dependently activates Nrf2 and attenuates endoplasmic reticulum stress in endothelial cells stimulated with thapsigargin.

Research article: "Comparative studies on the hepatoprotective effect of white and coloured rice bran oil against acetaminophen-induced oxidative stress in mice through antioxidant- and xenobiotic-metabolizing systems". In this study, W. Phannasorn et al. compared the phytoconstituents and antioxidant properties of white rice bran oil (WRBO) and coloured rice bran oil (CRBO) and tested their hepatoprotective effect in APAP-treated mice. CRBO exhibited greater antioxidant potential and attenuated APAP hepatotoxicity induced through enhancement of antioxidants and modulation of APAP metabolism.

Research article: "Maternal probiotic or synbiotic supplementation modulates jejunal and colonic antioxidant capacity, mitochondrial function, and microbial abundance in Bama mini-piglets". K. Wang et al. investigated the role of maternal probiotic or symbiotic, supplemented during gestation and lactation, on redox homeostasis, mitochondrial function, and intestinal microbiota in offspring weaned piglets. The study concluded that maternal probiotic or synbiotic supplementation improves the antioxidant capacity and mitochondrial function of weaned piglets by altering the intestinal microbiota.

Research article: "Red ginseng oil attenuates oxidative stress and offers protection against ultraviolet-induced photo toxicity". Owing to the beneficial therapeutic effects of ginseng, H.M. Arif Ullah et al. investigated the protective effect of red ginseng extract (RGE) and red ginseng oil (RGO) against APAP hepatotoxicity in mice. Besides, their in vitro radical-scavenging efficacies, RGE, and RGO ameliorated liver function markers and DNA oxidative damage in APAP-intoxicated mice. RGO protected 3T3 cells against UV irradiation-induced injury.

The editors anticipate this special issue to be of interest to the readers and expect researchers to benefit in making

further progress in understanding the mechanisms underlying the therapeutic potential of natural and synthetic antioxidants in different diseases.

Conflicts of Interest

The editors declare that they have no conflicts of interest regarding the publication of this special issue.

Acknowledgments

Ayman M. Mahmoud
Fiona L. Wilkinson
Adam P. Lightfoot
Julia M. Dos Santos
Mansur A. Sandhu

Research Article

Red Ginseng Oil Attenuates Oxidative Stress and Offers Protection against Ultraviolet-Induced Photo Toxicity

H. M. Arif Ullah [ID],[1] **Yuan Yee Lee** [ID],[1] **Minki Kim** [ID],[1] **Tae-Wan Kim** [ID],[1] **Evelyn Saba** [ID],[2] **Yi-Seong Kwak** [ID],[3] **Mansur Abdullah Sandhu** [ID],[2] **and Man Hee Rhee** [ID][1]

[1]*Laboratory of Physiology and Cell Signaling, College of Veterinary Medicine, Kyungpook National University, Daegu 41566, Republic of Korea*
[2]*Department of Veterinary Biomedical Sciences, Faculty of Veterinary and Animal Sciences, Pir Mehr Ali Shah-Arid Agriculture University, Rawalpindi, Pakistan*
[3]*R&D Headquarters, Korea Ginseng Cooperation, Daejeon 34520, Republic of Korea*

Correspondence should be addressed to Man Hee Rhee; rheemh@knu.ac.kr

Ginseng (*Panax ginseng* Meyer) is a well-known herbal medicine that has been used for a long time in Korea to treat various diseases. This study investigated the *in vitro* and *in vivo* protective effects of red ginseng extract (RGE) and red ginseng oil (RGO). Liver injury was produced in BALB/c mice by 400 mg/kg of acetaminophen intraperitoneal injection. The antioxidant effects of RGE and RGO on the free radicals 2,2-diphenyl-1-picryl-hydrazyl-hydrate (DPPH) and $2,2'$-azino-bis-3-ethylbenzothiazoline-6-sulfonic acid (ABTS) were measured. In addition, the hepatoprotective activities of RGE and RGO on liver markers, including alanine aminotransferase (ALT), aspartate aminotransferase (AST), and oxidative stress markers, including superoxide dismutase (SOD), catalase (CAT) enzyme activity, and 8-hydroxy-2-deoxyguanosine (8-OHdG) in serum and histopathological analysis, were evaluated. The protective effect of RGO on UV-induced phototoxicity was also evaluated in Balb/c 3T3 mouse fibroblast cell line. RGE and RGO effectively inhibited the radicals DPPH and ABTS compared with ascorbic acid and trolox, respectively. Moreover, RGE and RGO significantly decreased the liver enzyme (ALT and AST) levels, increased the antioxidant enzyme (SOD and CAT) levels, and decreased the DNA oxidation product (8-OHdG) content in mice serum. RGO also exhibited protective effect against UV irradiation compared with chlorpromazine hydrochloride, a known phototoxic drug, in Balb/c 3T3 cell line. RGE and RGO possess antioxidant and hepatoprotective properties in mice, and RGO exerts nonphototoxic activity in Balb/c 3T3 cells.

1. Introduction

Ginseng has been used as an herbal medicine and a functional food in Asia for more than 200 years due to its beneficial effects [1–3]. Approximately 12 species of ginseng have been recognized, among which *Panax ginseng* Meyer (Korean ginseng) is well-known and widely consumed. Red ginseng is the most widely used ginseng product in Asia, especially Korea, due to its various pharmacological activities, including antidiabetic, anticancer, antiplatelet, antioxidant, and antiobesity effects [4–7]. The major chemical compounds in red ginseng are the key sources for its

medicinal activities [1]. Red ginseng is produced from fresh ginseng using a repeated process of steaming and followed by drying process [3, 8]. Ginseng is commonly consumed in the various forms including tablets, capsules, candies, jellies, and various types of fermented products [1].

Ginsenosides are the bioactive constituents of red ginseng and having biological properties. Various ginsenosides have been discovered in red ginseng extract (RGE) and used widely due to their specific pharmacological effects [9]. Studies reported that the major ginsenoside profiles of the RGE are Rg1, Re Rf, Rh1, Rg2, Rb1, Rc, Rb2, Rb3, Rd, and Rg3 [1, 10]. In addition, based on gas chromatography analysis,

it has been shown that the major constituents of red ginseng oil (RGO) are unsaturated fatty acid (linoleic acid), saturated fatty acid (palmitic acid), phytosterins (alpha-tocopherol, Beta-sitosterol, gamma-sitosterol, Stigmasterol), and hydrocarbon (bicyclo) [11, 12]. It has been reported that red ginseng essential oil has antioxidant and hepatoprotective effects in hydrogen peroxide- (H_2O_2-) treated HepG2 cells and carbon tetrachloride- (CCl_4-) treated mice [8]. Moreover, a recent study demonstrated the antimelanogenic activities of Korean red ginseng oil (RGO) in a UV-B-induced hairless mouse [13].

Oxidative stress is the result of the production of reactive oxygen species (ROS) and reactive nitrogen species generated by the normal metabolic process and by exogenous stimuli in the body. These free radicals can damage the structure and function of cells, and increased concentrations of free radicals in metabolism are responsible for the development of various diseases [14, 15]. Antioxidant enzymes and antioxidant molecules can prevent or reduce the generation of these free radicals through the antioxidative defense system, which neutralizes ROS or scavenges free radicals [14, 16]. Several previous studies have demonstrated that an overdose of acetaminophen (APAP) can increase ROS production, and as a result, the oxidative stress causes severe liver injury [17–19]. APAP induces oxidative stress that can attack cell organelles, damage the cell membrane, induce lipid peroxidation, and ultimately result in liver injury [20]. Furthermore, high-energy visible and ultraviolet (UVA specifically) light have high energy and cause strong phototoxic reaction [21, 22]. The phototoxic reaction is primarily induced by exposure of photoreactive chemicals to UV light, and these chemically activated compounds are responsible for the formation of ROS/free radicals [23]. Hence, UV can damage the skin cells, which may lead to aging and cause itchiness, wrinkles, pigmentation, erythema, and eschar formation [21, 22].

This study was conducted to determine antioxidant and hepatoprotective potential of red ginseng extract (RGE) and red ginseng oil (RGO) in mice and the nonphototoxic activity of RGO using the Balb/c 3T3 mouse cell line. Here, we demonstrated that RGE and RGO have potential scavenging effects on free radicals, thus suggesting an important role in oxidative stress.

2. Materials and Methods

2.1. Chemicals and Reagents. The following materials were used in this study: RGE and RGO (Korea Ginseng Corporation, Daejeon, Republic of Korea), chlorpromazine hydrochloride (CPZ; Sigma, #MKBT6268V), Balb/c 3T3 cells, clone A31 (ATCC), DMEM (Gibco, #2041847), newborn calf serum (Gibco, #1749272), penicillin/streptomycin (Gibco, #2019314), neutral red (NR) solution (Sigma, #RNBG6531), and UV lamp (BIO-SUN, Serial number, 15-101159). All other chemicals and reagents were of the highest grade.

2.2. Sample Preparation of RGE and RGO. Red ginseng powder was obtained from Korea Ginseng Corporation (Daejeon, Republic of Korea). RGE was prepared using water as described in a previously reported procedure with slight modification [24]. Briefly, in hot water, red ginseng was extracted and heated at 90°C for 1 h. After cooling, the supernatant was collected and centrifuged at 3000 rpm for 5 min and evaporated. After evaporation, the samples were stored at 4°C until use. RGO was prepared as described previously with modification [8]. Briefly, red ginseng powder was extracted with the CO_2 extraction system at a pressure of 450 bar and a temperature of 65°C. The oil extract of red ginseng was preserved in a vial and stored at 4°C until use.

2.3. Cell Culture. Balb/c 3T3 mouse cells were cultured in DMEM supplemented with 10% newborn calf serum and 1% 100 IU/mL penicillin and 100 μg/mL streptomycin. Cells were seeded in a 96-well plate at different densities for the measurement of cell viability. RGO concentrations of 7.81, 15.63, 31.25, 62.5, 125, 500, and 1000 μg/mL were used. For positive control, CPZ concentrations of 0.04, 0.08, 0.16, 0.31, 0.63, 1.25, 2.5, and 5 μg/mL and 1.56, 3.13, 6.25, 12.5, 25, 50, 100, and 200 μg/mL were used with UV and without UV, respectively.

2.4. Irradiation Condition. A UV irradiation device (BIO-SUN, Serial number, 15-101159) was used for UV light source. The amount of UV light was 5 J/cm² with emitting wavelengths of 315–400 nm. For this amount of UV light (5 J/cm²), the exposure time was calculated by applying the light intensity measured 1 min after the starting of UV irradiation.

2.5. Animal Treatment. The animals were housed in pathogen-free facility at 21 ± 2°C with a humidity of 60 ± 10% under a 12-h light and dark cycle and feed and water were supplied ad libitum. Animal care and experimental procedure were conducted with the Institutional Animal Care and Use Committee (IACUC) guidelines, and the animal protocols were approved by the Animal Care Committee of the College of Veterinary Medicine, Kyungpook National University, Daegu, South Korea (approval number: 2019-0046). Male Balb/c mice aged 6 weeks were treated with 100 mg/kg and 300 mg/kg of RGE and RGO for 2 weeks orally every day. As a positive control, 75 mg/kg N-acetyl cysteine (NAC) was used. After 2 weeks, the mice were injected with 400 mg/kg of APAP through the intraperitoneal route, and after 2 h, the mice were anesthetized, and blood was collected by cardiac puncture. The blood was left to settle for 2 h in a blood collection tube (BD, Plymouth, UK). The tubes were then centrifuged at 3000 rpm for 15 min to separate the serum, which was collected and stored at −70°C until assay. Liver sample was collected for histopathological examination.

2.6. Measurement of Antioxidant Activity. The DPPH free-radical scavenging activity and 2, 2′-azino-bis-3-ethylbenzothiazoline-6-sulfonic acid (ABTS) radical-scavenging activity of RGE and RGO were evaluated using the method described by Kandi Sridhar and Albert Linton Charles with modification [14]. Briefly, RGE and RGO sample extract or positive control (ascorbic acid) with various concentrations were added to the same volume of DPPH (100 μM). The mixtures were vortexed and incubated at room temperature for 20 min

in the dark. Finally, the absorbance was determined using a spectrophotometer at 515 nm. For the ABTS assay, the ABTS method was produced with reacting the aqueous solution of ABTS with potassium persulfate in the same volume and allowed to react for 24 h at room temperature in the dark. The ABTS radical cation (1 mL) solution was mixed with 0.1 mL of extract or positive control (trolox) at different concentrations. The mixtures were incubated at room temperature for 10 min in the dark. Finally, the absorbance was measured at 734 nm with spectrophotometer.

2.7. Measurement of Serum Markers for Oxidative Stress Alanine Aminotransferase and Aspartate Aminotransferase Activity in Serum. Mice were sacrificed 2 h after the last administration from each group. Blood samples were collected and centrifuged. The levels of alanine aminotransferase (ALT), aspartate aminotransferase (AST), superoxide dismutase (SOD), catalase (CAT), and 8-hydroxy-2-deoxy-guanosine (8-OHdG) were measured according to kit instructions.

2.8. Histological Analysis. For evaluating the histopathological changes, the liver tissues were fixed in 10% formalin and routinely processed in a graded ethanol series and toluene, as described previously [25]. The tissues were then embedded in paraffin and sectioned into 5-μm-thick slices. The sections were stained with hematoxylin and eosin (H&E) as previously described, and the pathological changes were observed under a light microscope.

2.9. Determination of Phototoxicity. Phototoxicity was evaluated using RGO and CPZ on the mouse fibroblast cell line Balb/c 3T3 using a previously described method [21]. Cells were seeded in two 96-well plates with (+UV) and without (−UV) UV light for RGO and CPZ at a density of 1×10^4 cells/well. DMSO in cell media was used as a negative control. After dispensing 100 μL of cell suspension (1×10^4 cells/well) in the culture medium, the plates were incubated for 24 h at 37°C and 5% CO$_2$. After 24 h, the medium was removed, cells were washed with PBS, and 100 μL of the test materials, positive control, and negative control were added to the wells ($n = 3$). The plates were incubated at 37°C and 5% CO$_2$ for 1 h, after which the irradiated plate was exposed to UV light (5 J/cm^2), and the nonirradiated plate was shielded with an aluminum foil. After UV exposure, the medium was decanted, and 100 μL of the medium was added. The cells were incubated at 37°C and 5% CO$_2$ for 24 h. The medium was removed and washed with PBS. Then, 100 μL of NR solution (50 μg/mL) was added to each well and incubated at 37°C and 5% CO$_2$ for 3 h. After removing the NR medium, it was washed with PBS. Next, 150 μL of NR extractant solution was added to each well, and the plates were shaken on a plate shaker for 30 min in a light-shielded state. Finally, the absorbance was measured at a wavelength of 540 nm using a multichannel microplate reader. The absorbance data were used in the phototox software (Phototox 2.0, ZEBET at the BFR, Berlin Germany) to obtain cell viability data at different concentrations.

2.10. Statistical Analysis. The experimental data were expressed as mean ± the standard deviation (SD). Statistical significance was determined using ANOVA. The statistical significance of data is denoted on the graphs by asterisks (*), with the significance values as $^*P < 0.05$, $^{**}P < 0.01$, and $^{***}P < 0.001$.

3. Results

3.1. Effects of RGE and RGO on DPPH and ABTS Free Radicals. The antioxidant activities of RGE and RGO were determined using the DPPH and ABTS assay. The results showed that RGE effectively scavenged the radicals of DPPH at 60 mg/mL to the extent of the positive control, which was 10 mg/mL of ascorbic acid (Figure 1(a)). On the other hand, RGO scavenged the radicals of DPPH from concentrations of 125 to 500 mg/mL (Figure 1(b)). Regarding the ABTS assay results, it was found that RGE effectively reduced the radicals completely at 5 mg/mL concentration, similar to the level of trolox, a water-soluble conjugate of vitamin E that was used as a positive control in this assay (Figure 1(c)). The concentration of trolox used in this study was 10 μM. In the case of RGO, a concentration of 30 mg/mL showed an efficacy of approximately 80% in inhibiting ABTS radicals (Figure 1(d)).

3.2. Effects of RGE and RGO on ALT and AST Activity in Serum. APAP treatment resulted in extremely elevated levels of ALT in the serum of mice compared to the control group. However, this increase was significantly reduced by NAC treatment. Treatment with RGE and RGO also reduced the levels of ALT in a dose-dependent manner (Figure 2(a)). NAC treatment reduced the levels of AST in serum induced by APAP. Treatment with 100 mg/kg RGE did not significantly reduce the levels of AST. However, treatment with 300 mg/kg RGE significantly reduced the levels of AST (Figure 2(b)). Comparatively, both concentrations of RGE and RGO led to a significant reduce in ALT and AST levels comparable to the levels observed with NAC treatment.

3.3. Effects of RGE and RGO on Oxidative Stress in Serum. SOD is an enzyme known to catalyze dismutation of the superoxide (O$_2^-$) radical into oxygen and hydrogen peroxide, which comprises an extremely important defense against oxidative stress in the body. Our results showed that APAP considerably reduced the levels of SOD in the serum. This reduction was recovered by NAC treatment. Treatment with 100 mg/kg of both RGO and RGE showed no significant increase in SOD levels. However, high doses of both RGO and RGE led to recovery of SOD levels (Figure 2(c)). CAT is an enzyme that is detected in all organisms when exposed to oxygen as it catalyzes the decomposition of hydrogen peroxide to water and oxygen. Therefore, it is an important enzyme against oxidative stress. Our study results showed that APAP reduced the activity of CAT compared to that in the control group. NAC treatment improved CAT levels in the serum to even higher levels than those in the control group. Both RGO and RGE increased the CAT activity in a dose-dependent manner (Figure 2(d)). 8-OHdG is the major
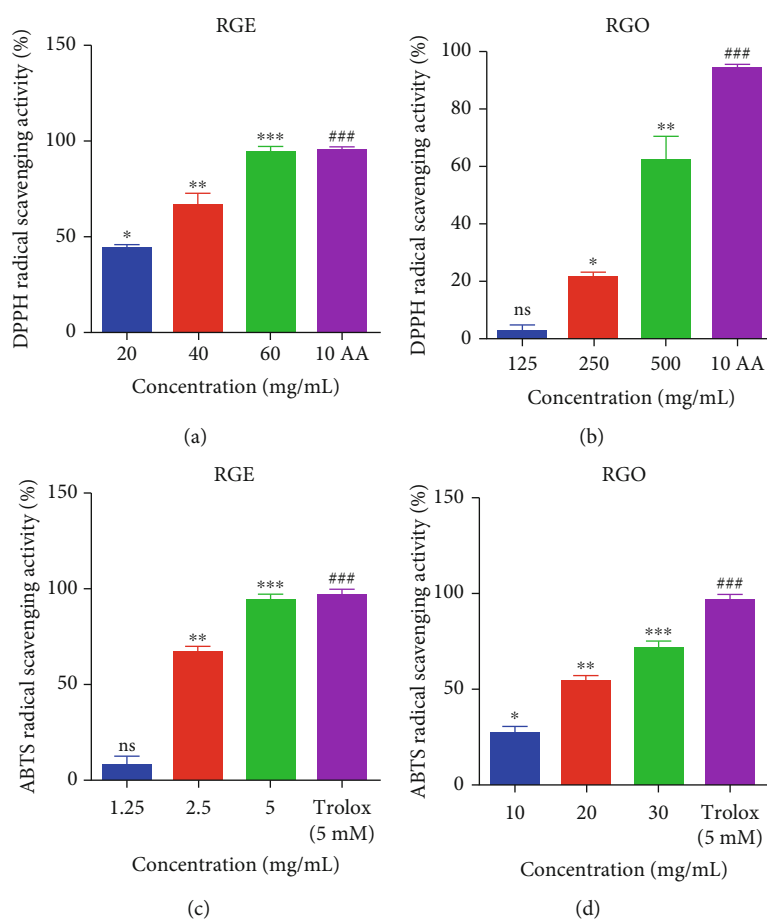
FIGURE 1: Determination of in vitro antioxidant activities of red ginseng extract (RGE) and red ginseng oil (RGO). (a, b) DPPH and (c, d) ABTS assays for RGE and RGO, respectively. In DPPH and ABTS methods, the standards were ascorbic acid (AA) in DPPH and trolox in ABTS, respectively. Radical-scavenging capacities were dose-dependent upon treatment with RGE and RGO. Data are presented as mean $\pm$ standard deviation (SD) ($n = 3$). $^{###}P < 0.001$ for standard, $^*P < 0.05$, $^{**}P < 0.01$, and $^{***}P < 0.001$ compared with standard.

product of DNA oxidation and is a marker of DNA damage. Our results demonstrated that in mice treated with APAP, 8-OHdG activity was increased and improved with NAC treatment. Treatment with RGE and RGO also improved the activity of 8-OHdG in a dose-dependent manner, where treatment with 300 mg/kg of both samples recovered the DNA oxidative damage to the levels of the control group (Figure 2(e)). These results may be due to the presence of the major ginsenosides in red ginseng determined by ultra-performance liquid chromatography (UPLC) (Table 1).

3.4. Effects of RGE and RGO on Pathological Changes in the Liver. Hepatocyte cells showed normal morphology, the hepatic lobules and sinusoids were intact, and the central veins were normal in the control group. However, in the APAP-treated group, the central veins were congestive and dilated, and degeneration of hepatocytes, infiltration of inflammatory cells, vacuolation of hepatocytes, and necrosis of hepatocytes were observed. In the NAC-treated group, there were no histopathological changes. In addition, treatment with 100 mg/kg of RGE and RGO significantly recovered the tissue damages compared to the APAP-treated group. Moreover, groups treated with 300 mg/kg of

RGE and RGO showed normal arrangement of hepatocytes with no significant damage and infiltration of inflammatory cells and hepatocytes, similar to that in the control group (Figure 3). This result indicated that RGE and RGO have significant protective effects against APAP-induced hepatic injury.

3.5. Effects of RGO on Phototoxicity. Phototoxicity was evaluated using RGO and CPZ in Balb/c 3T3 mouse cell line. Cell viability was measured at various concentrations of RGO and CPZ in the presence (exposure) or absence (no exposure) of UV light (Figures 4(a)–4(d)). RGO was found to be nonphototoxic and displayed insensitivity to phototoxic reaction (Figure 5(a)), whereas CPZ demonstrated toxicity potential in the presence of UV light (Figure 5(b)). Earlier, Peters and Holzhutter (2002) reported that sample is considered to be nonphototoxic if it has a photoirritation factor (PIF) < 2 or a mean photo effect (MPE) < 0.1; probably phototoxic if PIF is >2 and <5 or MPE is >0.1 and <0.15; and phototoxic if PIF is >5 or MPE is >0.15. In the case of CPZ, the PIF and MPE values were 25.721 and 0.236, respectively. Based on the assessment of parameters, RGO was found to be completely nonphototoxic, with the MPE being 0.006 (MPE < 0.1,
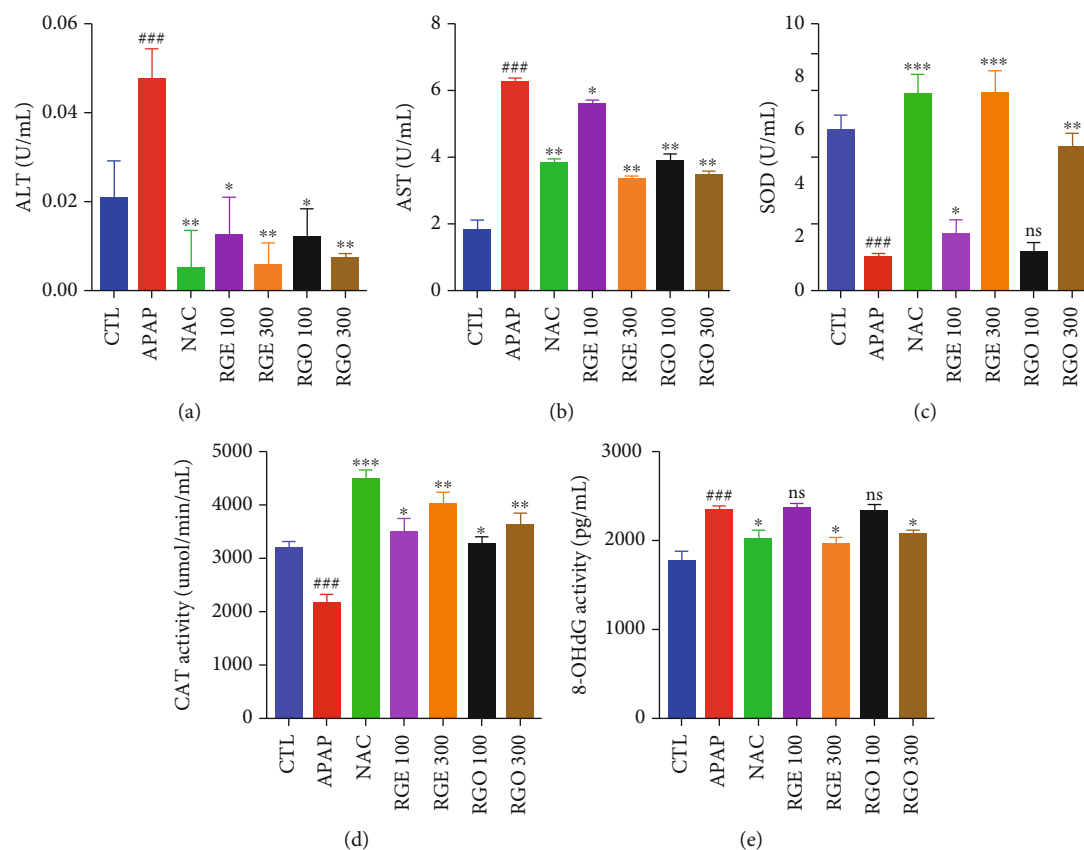
Figure 2: Effects of RGE and RGO in serum markers on APAP-induced liver injury in mice. (a) Effects of RGE and RGO on the ALT level in the serum. (b) Effects of RGE and RGO on the AST level in the serum. (c) Effects of RGE and RGO on the SOD activity in the serum. (d) Effects of RGE and RGO on the CAT activity in the serum. (e) Effects of RGE and RGO on the 8-OHdG content in the serum. Data are presented as mean $\pm$ standard deviation (SD) ($n = 5$). Significant difference at $^{\#\#\#}P < 0.001$ compared with control (CTL) group and $^{*}P < 0.05$, $^{**}P < 0.01$, and $^{***}P < 0.001$ compared with the APAP-treated group.

nonphototoxic) [26]. In contrast, CPZ exhibited phototoxic activity, with the MPE being 0.236 (MPE > 0.15, phototoxic), in the presence of UV light (Table 2).

4. Discussion

The liver is the major organ that metabolizes the majority of drugs. APAP is one of the most widely used drugs to reduce fever and pain. However, an overdose of APAP induces oxidative stress and production of ROS, which causes metabolic dysfunction, damage to the antioxidant defense system, and other tissue and hepatic injuries [20, 27]. Similarly, when cells are continuously exposed to sunlight, free radicals such as superoxide anion and hydroxyl radical and nonradical intermediates, including hydrogen peroxide and singlet oxygen, are generated [21]. These ROS can be produced by several sources, such as water, molecular oxygen, and enzymes. However, cells react to these ROS using nonenzymatic antioxidants such as vitamin C, vitamin E, and enzymatic antioxidants such as CAT and SOD [28]. Imbalance between these systems can modulate protein function, causing destructive action on DNA, which has been implicated in mutagenesis, carcinogenesis, and aging [21, 29]. Therefore, the inhibition of oxidative stress is a promising therapeutic strategy for liver damage and phototoxicity.

Table 1: Determination of ginsenosides in red ginseng [1]. Data are presented as mean $\pm$ standard deviation (SD) ($n = 3$).

Classification	Ginsenoside	Composition (mg/g)
Panaxatriol	Rg1	3.00 ± 0.033
	Rg2	3.26 ± 0.085
	Rg3	4.04 ± 0.049
Panaxadiol	Rb1	10.51 ± 0.048
	Rb2	4.51 ± 0.053
	Rb3	0.32 ± 0.067
	Rc	5.37 ± 0.074
	Rd	3.47 ± 0.111
	Rk1	4.04 ± 0.051

Several studies have demonstrated that natural antioxidants have potential pharmacological activities to protect organs from toxic substances, including the adverse effects of APAP and sunlight. The major active components in the RGE are the ginsenosides which play key role for the various beneficial effects [1]. Previous study demonstrated that sitosterol was influenced the cellular protective systems via
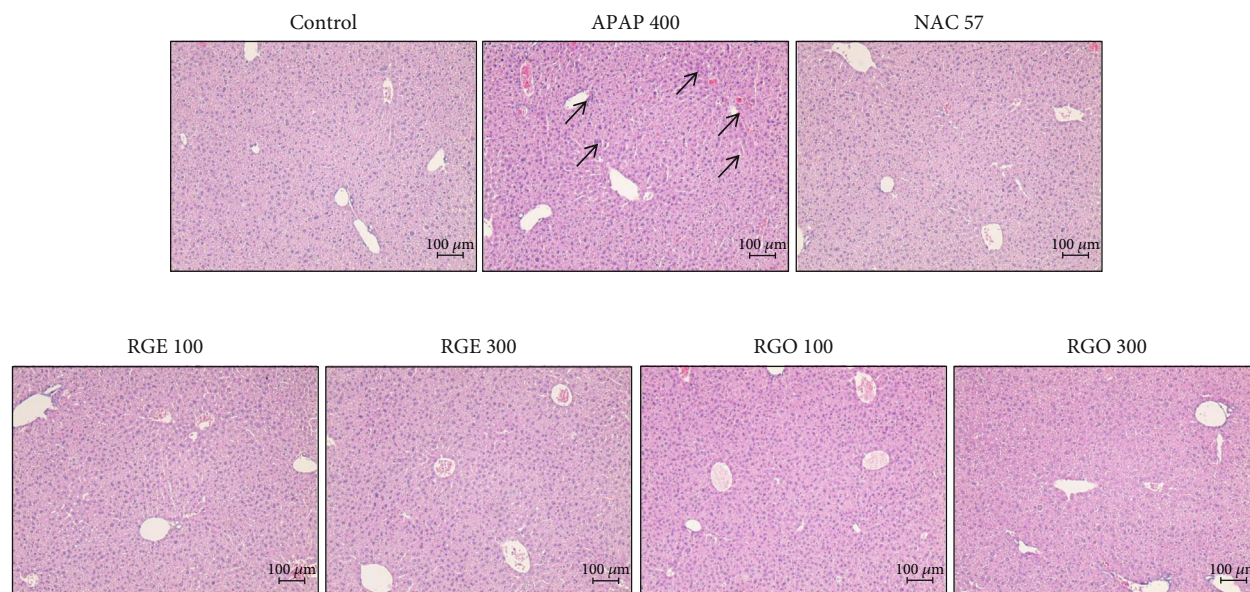
FIGURE 3: Histopathological changes by RGE and RGO on APAP-induced liver injury in mice. Mice were treated with APAP (400 mg/kg) to induce hepatotoxicity. In the APAP-treated group, there were degeneration of hepatocytes, congestive and dilated central veins, infiltration of inflammatory cells, vacuolation of hepatocytes, and necrosis of hepatocytes (arrows). N-acetyl cysteine (75 mg/kg) was used as a positive control. The concentrations of 100 and 300 mg/mL were used for RGE and RGO, respectively. Original magnification ×100.
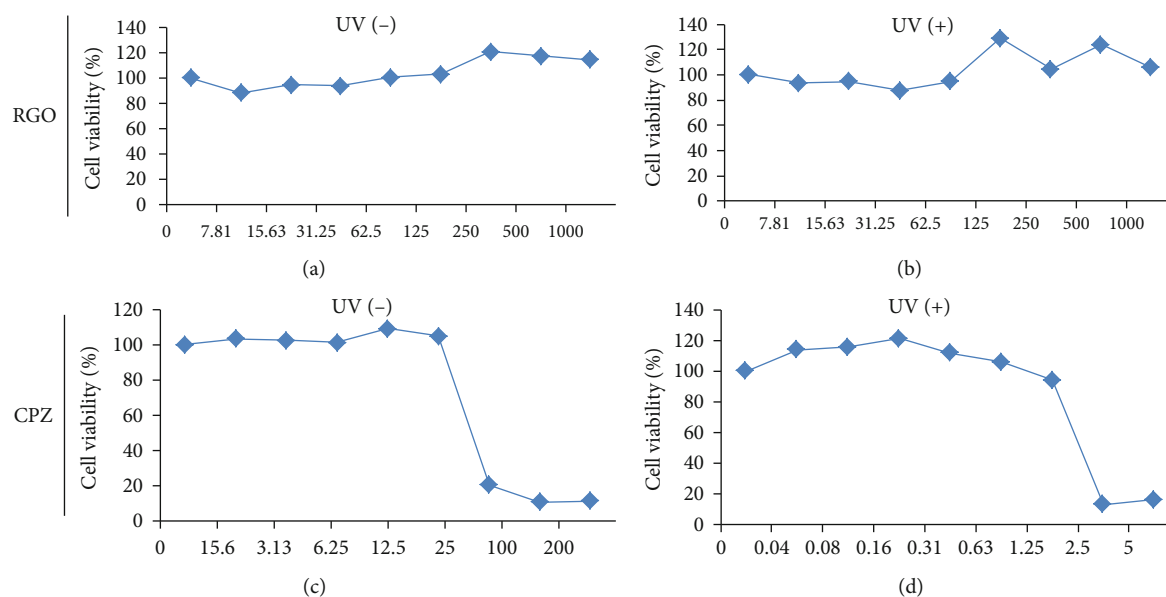
FIGURE 4: Effects of RGO and CPZ on cell viability with UV (-) and UV (+) light exposure in Balb/c 3T3 cells. (a, b) Cell viability was evaluated at different concentrations of RGO in the absence or presence of UV light. (c, d) Cell viability was evaluated at different concentrations of chlorpromazine (CPZ) in the absence or presence of UV light.

enhancement of nuclear factor erythroid-2 related factor-2 (Nfr2) pathway in HepG2 cells [30]. Moreover, beta-sitosterol and stigmasterol were protected oxidative stress induced by nitrophenol through activation of Nrf2-mediated antioxidant enzymes in rat, reported by Zhang et al. [31].

In this study, the antioxidant properties of RGE and RGO were investigated using the commonly used antioxidant methods, including DPPH and ABTS assays. The results clearly demonstrated that both RGE and RGO significantly inhibited the production of free radicals based on the concentration obtained by DPPH and ABTS methods (Figures 1(a)–1(d)). The scavenging capacity of DPPH increased in a dose-dependent manner (20, 40, and 60 mg/mL and 125, 150, and 500 mg/mL for RGE and RGO, respectively). Ascorbic acid was used as a standard solution (10 mg/mL) that exhibited the highest inhibition (95.25%) by the DPPH method, whereas the highest inhibition value was 94.13% for RGE at the concentration 60 mg/mL. Similarly, with RGO treatment,
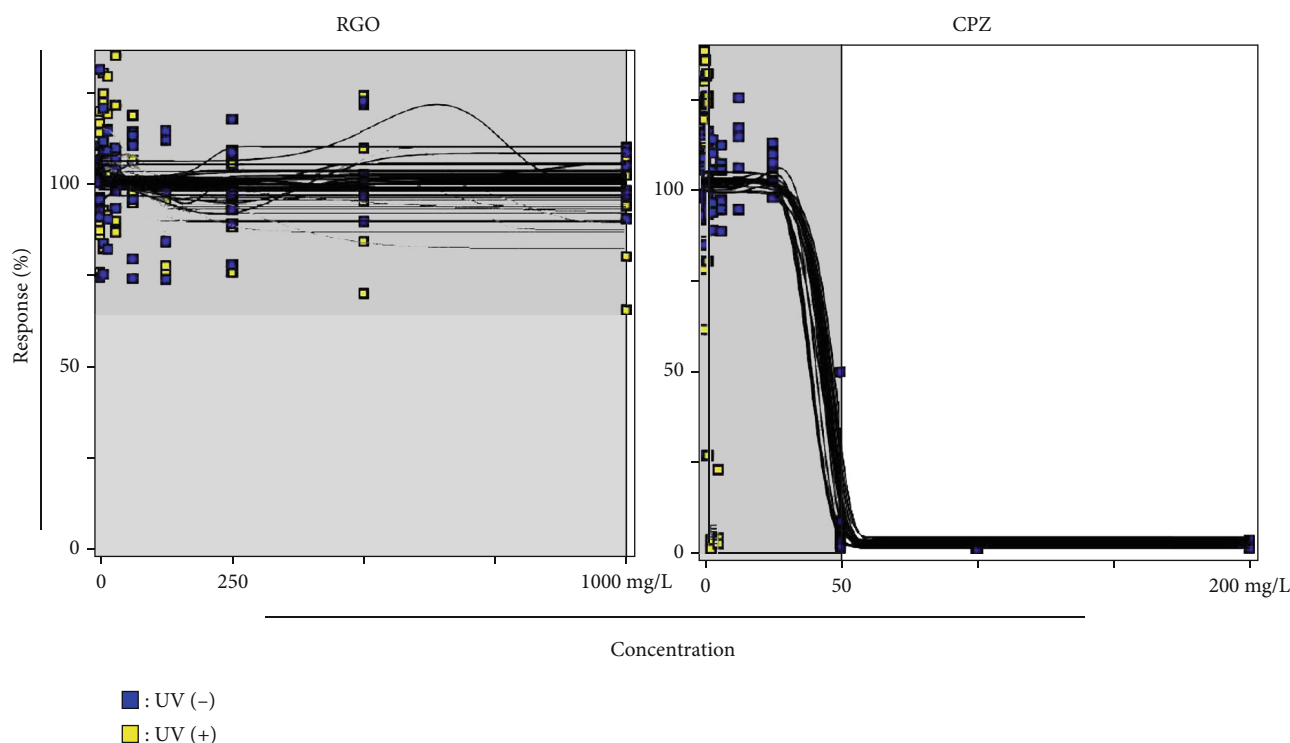
FIGURE 5: Effects of concentrations in RGO and CPZ with UV (-) and UV (+) light exposure in Balb/c 3T3 cells. (a) Effect of increasing concentrations with UV (-) and UV (+) of RGO on percentage response of Balb/c 3T3 cells. (b) Effect of increasing concentrations with UV (-) and UV (+) of CPZ on percentage response of Balb/c 3T3 cells. No exposure of UV light (blue) and exposure to UV light (yellow).

TABLE 2: Using the software (Phototox 2.0, at the BFR, Berlin Germany), photo irritation factor (PIF), and mean photo effect (MPE) values were generated for RGO and CPZ in Balb/c 3T3 cells.

Group	PIF	MPE	Phototoxicity	Phototoxic parameter
RGO	0	0.006	Nonphototoxic	PIF < 2 or MPE < 0.1 = nonphototoxic
CPZ	25.721	0.236	Phototoxic	PIF > 2 and <5 or MPE > 0.1 and <0.15 = probably phototoxic
				PIF > 5 or MPE > 0.15 = phototoxic

the maximum inhibition was 62.64% at the highest concentration of 500 mg/mL. The DPPH scavenging capacity results showed that RGE and RGO exhibited high antioxidant effects compared with ascorbic acid. Ryu et al. reported about the free radical-scavenging capacity of Korean red ginseng for erectile dysfunction in rats with noninsulin-dependent diabetes mellitus [5].

On the other hand, a similar trend was observed by the ABTS method, wherein the scavenging activity of ABTS was increased in a dose-dependent manner (1.25, 2.5, and 5 mg/mL and 10, 20, and 30 mg/mL for RGE and RGO, respectively). This result was compared with the standard solution trolox (5 mM), a vitamin E conjugate, which showed the highest inhibition (97.25%). RGE treatment resulted in the highest inhibition value (95.14%) at the highest concentration (5 mg/mL), whereas RGO treatment also exhibited the same trend of the highest inhibition (72.7%) at the highest concentration (30 mg/mL). This result indicated that both RGE and RGO possess potent antioxidant capacity as evaluated by the ABTS assay. Earlier report demonstrated that

ethanolic extracts of red ginseng and puffed red ginseng significantly showed radical scavenging ability by DPPH and ABTS assays [3].

Liver enzymes, primarily ALT and AST, in the blood are the major indicators to evaluate liver function [32]. Increasing levels of serum liver enzymes indicate hepatic injury because these enzymes are normally located in the cytoplasm, but after hepatic dysfunction, the enzymes are released into the circulation. An overdose of APAP increases the levels of liver enzymes, indicating liver damage. Kim et al., reported that pretreatment with Korean red ginseng reduced the expression of ALT and AST levels on aflatoxin B1-induced liver toxicity in rat model [33]. Our results demonstrated that serum ALT and AST levels were significantly reduced by RGE and RGO treatment (Figures 2(a) and 2(b)), suggesting that both RGE and RGO have protective activity against the APAP-induced liver injury.

SOD and CAT are the most important antioxidant enzymes against ROS. Under the normal physiological condition, SOD and CAT counteract with free radicals, but these
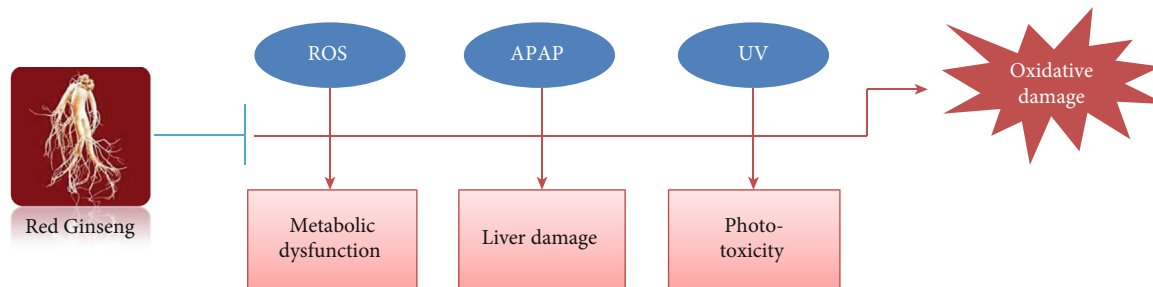
FIGURE 6: Schematic model showing the role of red ginseng in oxidative damage. Free radicals, overdose of acetaminophen (APAP), and UV radiation lead to metabolic dysfunction, liver toxicity, and phototoxicity, causing damage to the antioxidant defense system. Red ginseng extract (RGE) and red ginseng oil (RGO) protect against reactive oxygen species (ROS) and APAP- and UV-induced oxidative damage.

enzymes are reduced when there is overproduction of ROS [34–36]. In the past, it was reported that saponin fraction of red ginseng supplementation was markedly increased SOD and catalase levels in hepatic tissue in mice [37]. In this study, the levels of SOD and CAT were significantly reduced after APAP administration; meanwhile, RGE and RGO treatment significantly elevated their activities (Figures 2(c) and 2(d)). These results indicated that both RGE and RGO significantly elevated the levels of SOD and CAT in mice serum. Our results supported the previous report which stated that RGE significantly upregulated the SOD activity in healthy subjects (age 20-65 years) [38].

8-OHdG is the major product of DNA oxidation, and its elevation in the serum indicates excessive oxidative stress [34, 39]. An overdose of APAP increased the DNA oxidation and reduced the activity of antioxidant enzymes. Our results demonstrated that the levels of 8-OHdG were significantly reduced in the RGE- and RGO-treated groups (Figure 2(e)), suggesting that both RGE and RGO could protect DNA oxidation and improve the DNA damage induced by APAP. Red ginseng extract showed potential antioxidant activity in oxidative stress-mediated DNA damage, various studies previously reported [33, 40].

Liver histological pathology is another indicator to evaluate hepatic injury [32, 41]. Observation of the hepatic tissue histopathology confirmed the inhibitory effects of RGE and RGO in APAP-treated liver damage. According to the H&E staining result, the RGE- and RGO-treated groups showed reduced hepatocyte degeneration and decreased infiltration of inflammatory cells compared to the APAP-treated group (Figure 3). Moreover, significantly reduced hepatic necrosis and dilated sinusoids were observed in the RGE- and RGO-treated groups. This protective activity was dose-dependent, although there was no high difference between two doses (100 and 300 mg/mL) in these groups. Based on histopathological findings, there was no significant difference between NAC treatment at 75 mg/mL and the control group. Pretreated with Korean red ginseng were significantly suppressed hepatic lesions such as necrosis of hepatocytes, hemorrhage, and loss of hepatic cords according to previous report [33]. Our results demonstrated that both RGE and RGO have significant protective capacity against APAP-induced hepatic damage.

In this study, we demonstrated RGO provides protection against UV light in Balb/c 3T3 cells (Figure 5(a)), suggesting

that RGO has nonphototoxic capacity. It is assumed that the nonphototoxic activity could be caused because of antioxidant properties. CPZ was used as a positive control due to the phototoxic activity (Figure 5(b)) and caused damage to the DNA by direct and indirect mechanisms [21, 42]. However, further studies are required to confirm the degree of nonphototoxic activity of RGO.

5. Conclusions

In summary, RGE and RGO exhibited antioxidant and radical-scavenging properties, suggesting that both RGE and RGO possessing antioxidant activities can prevent the cell or tissue from oxidative damage induced by toxic chemicals or radiation (Figure 6). Our study indicated that Korean red ginseng may be potential substance in skin care and sunscreen formulations. To the best of our knowledge, this is the first report to demonstrate the effects of RGE and RGO on oxidative stress and attenuated activity of RGO on ultraviolet-induced photo toxicity. Further study in large scale is mandatory to determine the exact mechanism underlying the protective effects of red ginseng.

Data Availability

Data analyzed or generated during this study are included in this manuscript.

Conflicts of Interest

The authors declare that they have no competing interest.

Authors' Contributions

H M Arif Ullah, Yuan Yee Lee, and Mansour Abdullah Sandhu contributed equally to this work.

Acknowledgments

References

[1] E. Saba, Y. Y. Lee, M. Kim et al., "A novel herbal formulation consisting of red ginseng extract and *Epimedium koreanum*

Nakai-attenuated dextran sulfate sodium-induced colitis in mice," *Journal of Ginseng Research*, vol. 44, no. 6, pp. 833–842, 2020.

[2] S. Lee, K. Youn, W.-S. Jeong, C.-T. Ho, and M. Jun, "Protective effects of red ginseng oil against $A\beta_{25-35}$–induced neuronal apoptosis and inflammation in PC12 cells," *International Journal of Molecular Sciences*, vol. 18, no. 10, p. 2218, 2017.

[3] S.-J. Lee, S. Oh, M.-J. Kim, G.-S. Sim, T. W. Moon, and J. Lee, "Oxidative stability of extracts from red ginseng and puffed red ginseng in bulk oil or oil-in-water emulsion matrix," *Journal of ginseng research*, vol. 42, no. 3, pp. 320–326, 2018.

[4] H. Liu, J. Wang, M. Liu et al., "Antiobesity effects of ginsenoside Rg1 on 3T3-L1 preadipocytes and high fat diet-induced obese mice mediated by AMPK," *Nutrients*, vol. 10, no. 7, p. 830, 2018.

[5] J.-K. Ryu, T. Lee, D.-J. Kim et al., "Free radical-scavenging activity of Korean red ginseng for erectile dysfunction in non-insulin-dependent diabetes mellitus rats," *Urology*, vol. 65, no. 3, pp. 611–615, 2005.

[6] J. Kim, "Protective effects of Asian dietary items on cancers-soy and ginseng," *Asian Pacific Journal of Cancer Prevention*, vol. 9, no. 4, pp. 543–548, 2008.

[7] M. Irfan, M. Kim, and M. H. Rhee, "Anti-platelet role of Korean ginseng and ginsenosides in cardiovascular diseases," *Journal of ginseng research*, vol. 44, no. 1, pp. 24–32, 2020.

[8] M.-J. Bak, M. Jun, and W.-S. Jeong, "Antioxidant and hepatoprotective effects of the red ginseng essential oil in H_2O_2-treated HepG2 cells and CCl_4-treated mice," *International Journal of Molecular Sciences*, vol. 13, no. 2, pp. 2314–2330, 2012.

[9] J.-M. Lu, Q. Yao, and C. Chen, "Ginseng compounds: an update on their molecular mechanisms and medical applications," *Current Vascular Pharmacology*, vol. 7, no. 3, pp. 293–302, 2009.

[10] S. M. Lee, B.-S. Bae, H.-W. Park et al., "Characterization of Korean Red Ginseng (Panax ginseng Meyer): history, preparation method, and chemical composition," *Journal of ginseng research*, vol. 39, no. 4, pp. 384–391, 2015.

[11] A. W. B. Reyes, H. T. Hop, L. T. Arayan et al., "The host immune enhancing agent Korean red ginseng oil successfully attenuates Brucella abortus infection in a murine model," *Journal of Ethnopharmacology*, vol. 198, pp. 5–14, 2017.

[12] M. J. Bak, V.-L. Truong, S.-Y. Ko et al., "Induction of Nrf2/ARE-mediated cytoprotective genes by red ginseng oil through ASK1–MKK4/7–JNK and p38 MAPK signaling pathways in HepG2 cells," *Journal of ginseng research*, vol. 40, no. 4, pp. 423–430, 2016.

[13] E. Saba, S.-H. Kim, Y. Y. Lee et al., "Anti-melanogenic effects of Korean red ginseng oil in an ultraviolet B-induced hairless mouse model," *Molecules*, vol. 25, no. 20, p. 4755, 2020.

[14] K. Sridhar and A. L. Charles, "*In vitro* antioxidant activity of Kyoho grape extracts in DPPH and ABTS assays: estimation methods for EC_{50} using advanced statistical programs," *Food Chemistry*, vol. 275, pp. 41–49, 2019.

[15] R. F. de Araújo, D. B. G. Martins, and M. A. C. Borba, "Oxidative stress and disease," in *A master regulator of oxidative stress-the transcription factor nrf2*, IntechOpen, 2016.

[16] P. Sharma, A. B. Jha, R. S. Dubey, and M. Pessarakli, "Reactive oxygen species, oxidative damage, and antioxidative defense mechanism in plants under stressful conditions," *Journal of botany*, vol. 2012, Article ID 217037, 26 pages, 2012.

[17] A. J. Makin and R. Williams, "Acetaminophen-induced hepatotoxicity: predisposing factors and treatments," *Advances in Internal Medicine*, vol. 42, pp. 453–483, 1997.

[18] W. M. Lee, "Drug-induced hepatotoxicity," *The New England Journal of Medicine*, vol. 349, no. 5, pp. 474–485, 2003.

[19] M. R. McGill, C. D. Williams, Y. Xie, A. Ramachandran, and H. Jaeschke, "Acetaminophen-induced liver injury in rats and mice: comparison of protein adducts, mitochondrial dysfunction, and oxidative stress in the mechanism of toxicity," *Toxicology and Applied Pharmacology*, vol. 264, no. 3, pp. 387–394, 2012.

[20] H. Nikravesh, M. J. Khodayar, M. Mahdavinia, E. Mansouri, L. Zeidooni, and F. Dehbashi, "Protective effect of gemfibrozil on hepatotoxicity induced by acetaminophen in mice: the importance of oxidative stress suppression," *Advanced pharmaceutical bulletin*, vol. 8, no. 2, pp. 331–339, 2018.

[21] V. Rai, N. Dayan, and B. Michniak-Kohn, "A comparative evaluation of photo-toxic effect of fractionated melanin and chlorpromazine hydrochloride on human (dermal fibroblasts and epidermal keratinocytes) and mouse cell line/s (fibroblast Balb/c 3T3)," *Toxicology In Vitro*, vol. 25, no. 2, pp. 538–544, 2011.

[22] N. H. Youn, E. J. Kim, J.-S. Yi et al., "Evaluation of skin phototoxicity of transdermally administered pharmaceuticals in Sprague-Dawley rats," *Laboratory Animal Research*, vol. 36, no. 1, pp. 42–47, 2020.

[23] Y. Yonezawa, T. Ohsumi, T. Miyashita et al., "Evaluation of skin phototoxicity study using SD rats by transdermal and oral administration," *The Journal of toxicological sciences*, vol. 40, no. 6, pp. 667–683, 2015.

[24] T. Ramesh, S.-W. Kim, S.-Y. Hwang, S.-H. Sohn, S.-K. Yoo, and S.-K. Kim, "Panax ginseng reduces oxidative stress and restores antioxidant capacity in aged rats," *Nutrition Research*, vol. 32, no. 9, pp. 718–726, 2012.

[25] Y.-S. Son, H. M. A. Ullah, A. K. Elfadl et al., "Preventive effects of vitamin C on diethylnitrosamine-induced hepatotoxicity in Smp 30 knockout mice," *In Vivo*, vol. 32, no. 1, pp. 93–99, 2018.

[26] B. Peters and H.-G. Holzhütter, "In vitro phototoxicity testing: development and validation of a new concentration response analysis software and biostatistical analyses related to the use of various prediction models," *Alternatives to Laboratory Animals*, vol. 30, no. 4, pp. 415–432, 2002.

[27] M. Y. Yoon, S. J. Kim, B.-H. Lee, J.-H. Chung, and Y. C. Kim, "Effects of dimethylsulfoxide on metabolism and toxicity of acetaminophen in mice," *Biological & Pharmaceutical Bulletin*, vol. 29, no. 8, pp. 1618–1624, 2006.

[28] K. Brawn and I. Fridovich, "Superoxide radical and superoxide dismutases: threat and defense," in *Autoxidation in food and biological systems*, pp. 429–446, Springer, 1980.

[29] P. Fu, S.-H. Cheng, L. Coop et al., "Photoreaction, phototoxicity, and photocarcinogenicity of retinoids," *Journal of Environmental Science and Health, Part C*, vol. 21, no. 2, pp. 165–197, 2003.

[30] H. S. Kang, M. J. Park, K. S. Jin et al., "Regulatory roles of Chrysanthemum zawadskii roots in nuclear factor E2-related factor 2/antioxidant response element pathway," *Food Science and Biotechnology*, vol. 17, no. 2, pp. 367–372, 2008.

[31] Y. Zhang, M. Song, X. Rui, S. Pu, Y. Li, and C. Li, "Supplemental dietary phytosterin protects against 4-nitrophenol-induced oxidative stress and apoptosis in rat testes," *Toxicology reports*, vol. 2, pp. 664–676, 2015.

[32] Y. Zhuang, Q. Ma, Y. Guo, and L. Sun, "Protective effects of rambutan (Nephelium lappaceum) peel phenolics on H_2O_2-induced oxidative damages in HepG2 cells and d-galactose-induced aging mice," *Food and Chemical Toxicology*, vol. 108, no. Part B, pp. 554–562, 2017.

[33] Y.-S. Kim, Y.-H. Kim, J.-R. Noh, E.-S. Cho, J.-H. Park, and H.-Y. Son, "Protective effect of Korean red ginseng against aflatoxin B1-induced hepatotoxicity in rat," *Journal of ginseng research*, vol. 35, no. 2, pp. 243–249, 2011.

[34] J. Gao, Z. Yu, S. Jing et al., "Protective effect of Anwulignan against D-galactose-induced hepatic injury through activating p38 MAPK–Nrf2–HO-1 pathway in mice," *Clinical Interventions in Aging*, vol. 13, pp. 1859–1869, 2018.

[35] O. Bayrak, N. Bavbek, Karatas OF et al., "Nigella sativa protects against ischaemia/reperfusion injury in rat kidneys," *Nephrology Dialysis Transplantation*, vol. 23, no. 7, pp. 2206–2212, 2008.

[36] F. Dong, S. Wang, Y. Wang et al., "Quercetin ameliorates learning and memory via the Nrf2-ARE signaling pathway in d-galactose-induced neurotoxicity in mice," *Biochemical and Biophysical Research Communications*, vol. 491, no. 3, pp. 636–641, 2017.

[37] D.-J. Kim, K.-S. Seong, D.-W. Kim, S.-R. Kim, and C.-C. Chang, "Antioxidative effects of red ginseng saponins on paraquat-induced oxidative stress," *Journal of Ginseng Research*, vol. 28, no. 1, pp. 5–10, 2004.

[38] J. Y. Kim, J. Y. Park, H. J. Kang, O. Y. Kim, and J. H. Lee, "Beneficial effects of Korean red ginseng on lymphocyte DNA damage, antioxidant enzyme activity, and LDL oxidation in healthy participants: a randomized, double-blind, placebo-controlled trial," *Nutrition Journal*, vol. 11, no. 1, pp. 1–9, 2012.

[39] A. Valavanidis, T. Vlachogianni, and C. Fiotakis, "8-Hydroxy-2′-deoxyguanosine (8-OHdG): a critical biomarker of oxidative stress and carcinogenesis," *Journal of environmental science and health Part C*, vol. 27, no. 2, pp. 120–139, 2009.

[40] H. J. Choi, H. S. Han, J. H. Park et al., "Antioxidantive, phospholipase A2 inhibiting, and anticancer effect of polyphenol rich fractions from Panax ginseng CA Meyer," *Journal of the korean Society of Agricultural and Biotechnology*, vol. 46, no. 3, pp. 251–256, 2003.

[41] L.-Q. Xu, Y.-L. Xie, S.-H. Gui et al., "Polydatin attenuates d-galactose-induced liver and brain damage through its anti-oxidative, anti-inflammatory and anti-apoptotic effects in mice," *Food & Function*, vol. 7, no. 11, pp. 4545–4555, 2016.

[42] I. E. Kochevar, "Phototoxicity mechanisms: chlorpromazine photosensitized damage to DNA and cell membranes," *The Journal of Investigative Dermatology*, vol. 77, no. 1, pp. 59–64, 1981.

Research Article

Maternal Probiotic or Synbiotic Supplementation Modulates Jejunal and Colonic Antioxidant Capacity, Mitochondrial Function, and Microbial Abundance in Bama Mini-piglets

Kai Wang [1,2,3,4] **Xiangfeng Kong** [2] **Md. Abul Kalam Azad** [2] **Qian Zhu,**[2] **Liang Xiong,**[2] **Yuzhong Zheng** [4] **Zhangli Hu,**[1,3] **Yulong Yin,**[2] **and Qinghua He** [1]

^{1}*Department of Food Science and Engineering, College of Chemistry and Environmental Engineering, Shenzhen University, Shenzhen 518000, China*
^{2}*CAS Key Laboratory of Agro-Ecological Processes in Subtropical Regions, Hunan Provincial Key Laboratory of Animal Nutritional Physiology and Metabolic Process, National Engineering Laboratory for Pollution Control and Waste Utilization in Livestock and Poultry Production, Institute of Subtropical Agriculture, Chinese Academy of Sciences, Changsha 410125, China*
^{3}*Key Laboratory of Optoelectronic Devices and Systems of Ministry of Education and Guangdong Province, College of Optoelectronic Engineering, Shenzhen University, Shenzhen 518000, China*
^{4}*School of Food Engineering and Biotechnology, Hanshan Normal University, Chaozhou 521041, China*

Correspondence should be addressed to Xiangfeng Kong; nnkxf@isa.ac.cn and Qinghua He; qinghua.he@szu.edu.cn

The present study was conducted to investigate the effects of maternal probiotic or synbiotic supplementation during gestation and lactation on antioxidant capacity, mitochondrial function, and intestinal microbiota abundance in offspring weaned piglets. A total of 64 pregnant Bama mini-sows were randomly allocated into the control group (basal diet), antibiotic group (basal diet + 50 g/t virginiamycin), probiotic group (basal diet + 200 mL/d probiotics per pig), or synbiotic group (basal diet + 200 mL/d probiotics per pig + 500 g/t xylo-oligosaccharides). On day 30 of post-weaning, eight piglets per group with average body weight were selected for sample collection. The results showed that maternal probiotic supplementation increased the catalase (CAT) activity in plasma and glutathione peroxidase (GSH-Px) and superoxide dismutase (SOD) activities in plasma, jejunum, and colon of piglets while decreased the malondialdehyde (MDA) and H_2O_2 concentrations in plasma compared with the control group ($P < 0.05$). Moreover, maternal synbiotic supplementation increased the plasma CAT activity, jejunal glutathione and GSH-Px activities, jejunal and colonic total antioxidant capacity activity, and plasma and colonic SOD activity while decreased the colonic MDA concentration of offspring piglets compared with the control group ($P < 0.05$). The mRNA levels of antioxidant enzyme-related genes (copper- and zinc-containing superoxide dismutase, nuclear factor erythroid 2-related factor 1, and nuclear factor erythroid 2-related factor 2) and mitochondrial-related genes (adenosine triphosphate synthase alpha subunit, adenosine triphosphate synthase β, and mitochondrial transcription factor A) in the jejunal mucosa were significantly upregulated, while the level of colonic peroxisome proliferator-activated receptor γ coactivator-1α was downregulated by maternal synbiotic supplementation ($P < 0.05$). Maternal probiotic supplementation increased ($P < 0.05$) the *Bacteroidetes* abundance in the jejunum and *Bifidobacterium* abundance in the jejunum and colon, and synbiotic supplementation increased ($P < 0.05$) the abundances of Firmicutes, *Bacteroidetes*, *Bifidobacterium*, and *Lactobacillus* in the jejunum of piglets. Furthermore, correlation analysis revealed that intestinal microbiota abundances were significantly correlated with antioxidant enzyme activities and mitochondrial-related indexes. These findings indicated that maternal probiotic or synbiotic supplementation might be a promising strategy to improve the antioxidant capacity and mitochondrial function of offspring weaned piglets by altering the intestinal microbiota.

1. Introduction

The gastrointestinal tract (GIT) of mammalian animals has been known as a harbor of microbes [1]. The gut microbes play crucial roles in nutrients metabolism, intestinal barrier function, and immune function [2, 3]. Accumulating evidence showed that healthy maternal gut microbes are essential for the growth and health of their offspring. Microbes can be transmitted to the offspring through direct contact with the birth canal during parturition and colostrum or milk during lactation, which contributes to long-term health benefits in offspring [4–6]. However, maternal gut microbes and milk or colostrum quality are influenced by maternal diet compositions, and thus, maternal dietary intervention may be an effective way to improve offspring's overall health.

Piglets are highly susceptible to intestinal structural abnormalities and functional disorders due to their immature immune system and lack of diverse intestinal microbiota, resulting in increased incidence of diarrhea, growth retardation, and even death. Oxidative stress occurs under a condition when the production of reactive oxygen (ROS) and their elimination by the antioxidant mechanism is imbalanced. The sows undergo systematic oxidative stress during late pregnancy and lactation, which does not fully recover until weaned and could affect their offspring's health [7]. Furthermore, there is also a high correlation between maternal and fetal (cord blood) plasma antioxidant markers, suggesting that maternal oxidative stress status can transfer to the fetus [8]. Therefore, late gestation and early postnatal periods are the critical window periods for oxidative stress regulation [9].

Probiotics are defined as "live microorganisms which when administered in adequate amounts confer a health benefit on the host" [10]; prebiotics are defined as a "nonviable food component that confers a health benefit on the host associated with modulation of the microbiota"; Gibson and Roberfroid introduced the term "synbiotic" to describe a combination of synergistically acting probiotics and prebiotics [11, 12]. Currently, increasing evidence has indicated that probiotic/synbiotic supplementation could improve antioxidant capacity and reduce oxidative stress [13]. *Lactobacillus acidophilus* and *Lactobacillus bulgaricus*, as the lactic acid bacteria, have been reported to exhibit antioxidant capacity by chelating metal ions and scavenging ROS [14]. Nie et al. reported that *Lactobacillus frumenti* improved antioxidant capacity via nitric oxide production mediated by nitric oxide synthase 1 activation in intestinal epithelial cells [15]. As a probiotic yeast, *Saccharomyces cerevisiae* (*S. cerevisiae*) showed strong antioxidant activity, reducing nitric oxide and hydroxyl radical scavenging activity [16]. Several studies have reported that the administration of probiotics or synbiotics during gestation and lactation have been considered as a potential strategy to improve the growth performance and modulate intestinal microbiota of offspring piglets [17–19]. Furthermore, maternal dietary fiber supplementation during gestation has an important role in improving the antioxidative capacity of their offspring through modulating the composition of the gut microbiota [20]. However, whether maternal probiotic or synbiotic supplementation during gestation and lactation can change the intestinal antioxidant capacity and mitochondrial function of offspring by altering the gut microbiota remains unclear.

Our previous study has found that dietary synbiotic supplementation to sows during pregnancy and lactation can improve piglet's survival and lipid metabolism by altering gut microbiota diversity and composition [21]. Therefore, we hypothesized that maternal probiotic or synbiotic supplementation could improve the antioxidant capacity and mitochondrial function by altering the gut microbiota of offspring weaned piglets. Considering that Bama mini–pigs' anatomy and physiology are similar to humans' [22, 23], Bama mini–pigs were chosen as a research model in this study. Our findings may, in turn, have important implications for understanding the link between maternal diets and infant intestinal health.

2. Materials and Methods

2.1. Experimental Design and Animal Management. The animal use and animal trials in this study have been approved by the Animal Care and Use Committee of the Institute of Subtropical Agriculture, Chinese Academy of Sciences.

A total of 64 pregnant Bama mini–sows with similar physical conditions with 3-5 parities were randomly assigned to the control group (sows fed a basal diet), antibiotic group (sows fed a basal diet supplemented with 50 g/t virginiamycin), probiotic group (sows fed a basal diet supplemented with 200 mL/d probiotic fermentation broth per pig), or synbiotic group (sows fed a basal diet supplemented with 200 mL/d probiotic fermentation broth per pig and 500 g/t xylo-oligosaccharides). From mating (day 0) to day 104 of pregnancy, the sows were individually housed in gestation crates (2.2 m × 0.6 m). On day 105, the sows were transferred to individual farrowing units (2.2 m × 1.8 m).

After weaning on day 28, two piglets per litter close to the average body weight were selected for the remaining of the trial, and four piglets from the same group were fed in one pen, and each group consisted of eight pens (replicates). Basal diets for the sows and piglets designed according to (NY/T65-2004), the Chinese nutrient requirements of swine in china (Supplementary Table 1 and Table 2) [24]. Sows were fed twice daily (at 8:00 and 17:00) according to their body conditions. Sows and piglets had available *ad libitum* access to water during the trial period. Hunan Lifeng Biotechnology Co., Ltd. (Changsha, China) provided the viable probiotic fermentation broth (*Lactobacillus plantarum* B90 (CGMCC1.12934) $\geq 1.0 \times 10^8$ CFU/g; *S.cerevisiae* P11 (CGMCC2.3854) $\geq 0.2 \times 10^8$ CFU/g). Shandong Longlive Biotechnology Co., Ltd. (Dezhou, China) afforded the xylo-oligosaccharides (XOS), which contained the xylobiose, xylotriose, and xylotetraose (≥35%).

2.2. Sampling. On day 30 of post–weaning, eight piglets (one piglet per replicate) from each group were selected and weighed at 12 h after the last feeding. Blood samples (10 mL) were collected from the precaval vein into heparin-treated tubes, and the plasma was obtained by centrifuging at 3,500 g for 10 min at 4°C and then stored at −20°C for further analysis. The piglets were then sacrificed using electrical

stunning (120 V, 200 Hz), and the contents of the jejunum (10 cm below the flexure of duodenum-jejunum) and colon (middle position) were collected, immediately frozen in liquid nitrogen, and stored at −80°C for bacterial DNA extraction. In addition, the intestinal tissues of the jejunum and the colon were excised and rinsed with ice-cold physiological saline. The mucosa scrapings were collected, immediately frozen in liquid nitrogen, and stored at −80°C for further analyses.

2.3. *Determination of Plasma and Intestinal Mucosa Antioxidant Capacity.* Approximately 100 mg of frozen jejunum and colon tissues was removed quickly and homogenized with ice-cold physiologic saline (1 : 9, w/v) and then centrifuged at 2,000 g for 20 min at 4°C. The intestinal supernatants were used for further analysis. Plasma and intestinal antioxidant indicators, including catalase (CAT), superoxide dismutase (SOD), glutathione (GSH), and glutathione peroxidase (GSH-Px), as well as malondialdehyde (MDA) were analyzed by ELISA assay kits from Jiangsu Meimian Institute (Mei mian, Yancheng, China). The total antioxidant capacity (T-AOC) and H_2O_2 assay kits were purchased from Nanjing Jiancheng Bioengineering Institute (Nanjing, China). The test for each index was carried out according to the instructions of the kits. The absorbance values were read on a Multiscan Spectrum Spectrophotometer (Tecan, Infinite M200 Pro, Switzerland). The jejunal and colonic mucous antioxidant parameters were normalized to the total protein concentration (mg/L) quantified by the Pierce BCA Protein Assay Kit (CoWin Biosciences, Suzhou, China).

2.4. *Determination of Intestinal Mucosa ATP Concentration.* The ATP concentration of the jejunal and colonic mucosa was determined using the ATP assay kit (Mei mian, Yancheng, China) based on firefly luciferase by a Multiscan Spectrum Spectrophotometer (Tecan, Infinite M200 Pro, Switzerland). The methods for intestinal tissue homogenization and total protein quantification were the same as mentioned above.

2.5. *Determination of Mitochondrial Complex I and III Activities.* The NADH ubiquinone oxidoreductase complex I and III activities in the jejunal and colonic mucosa were assessed using commercially available kits (Comin bio. Co., Suzhou, China), according to the manufacturer's instructions. The methods for intestinal tissue homogenization and total protein quantification were the same as mentioned above. The complex I and III activities were normalized to the total protein.

2.6. *Real-Time Quantitative PCR Analysis of Intestinal Mucosa Antioxidant-Related Genes and Mitochondrial-Related Genes.* Total RNA was extracted from the frozen jejunal and colonic mucosa using a Trizol Reagent (Magen, Guangzhou, China) according to the manufacturers' protocol. The total RNA (1,000 ng) was used as a template for the cDNA reaction, which was synthesized using a Prime-Script RT reagent kit with gDNA Eraser (TaKaRa, Dalian, China). Real-time PCR analysis was performed on the Light-Cycler® 480 II Real-Time PCR System (Roche, Basel, Swiss) (384-cell standard block). Pig-specific primers were designed and synthesized by Sangon Biotech (Shanghai, China) Co., Ltd (Table 1). The specificity of the primers was examined by the Primer-BLAST tool (https://www.ncbi.nlm.nih.gov/tools/primer-blast) and confirmed by single peaks in the melting curves. The reaction mixture (10 μL) consisted of 5.0 μL SYBR Premix Ex TaqTM (AG11701; Accurate Biotechnology, Changsha, China), 2.0 μL of template DNA, 0.25 μL of each primer, and 2.5 μL of double-distilled water. The PCR amplification conditions were followed according to the instructions of SYBR Green Premix. The relative levels of the gene expression were analyzed using $2^{-\Delta\Delta Ct}$ value, and the reference gene β-actin was used as an internal control.

2.7. *Quantification of the Intestinal Mucosa Mitochondrial DNA Content.* Total DNA was extracted from the jejunal and colonic mucosa of each piglet using a DNAiso Reagent according to the manufacturer's protocol (Accurate Biotechnology, Changsha, China). The concentration of extracted DNA was measured at 260 nm with a NanoDrop One Microvolume UV-Vis Spectrophotometer (Thermo Scientific, Waltham, USA), and the extracted DNA was stored at −20°C until further use. The content of mitochondrial DNA (mtDNA) relative to the nuclear genomic DNA was measured by amplifying the mt D-loop and nuclear-encoded β-actin gene using a real-time PCR assay as described above. The primer sequences for mt D-loop and G6PC are presented in Table 2. The mtDNA expression $2^{-\Delta\Delta Ct}$ value was calculated, and the reference gene G6PC was used as an internal control.

2.8. *Real-Time Quantitative PCR Analysis for Jejunal and Colonic Microbiota Abundances.* The total bacterial genomic DNA was extracted from 300 mg of jejunal and colonic luminal contents using a Mag-Bind® Stool DNA Kit (Omega, Guangzhou, China) according to the manufacturer's protocol. The primers of the selected genes are listed in Table 3. The reaction mixture (10 μL) consisted of 5.0 μL SYBR Premix Ex Taq TM (AG11701; Accurate Biotechnology, Changsha, China), 2.0 μL of template DNA, 0.25 μL of each primer, and 2.5 μL of double-distilled water. The standard curves of each gene were generated with 10-fold serial dilutions of the respective 16S rRNA genes [25]. The qPCR amplification was carried out according to the instructions of SYBR green premix (Takara Biotechnology, Dalian, China). Melting curves were checked for each gene after amplification. The results are expressed as Lg16S ribosomal DNA gene copies/g intestine contents.

2.9. *Statistical Analysis.* Statistical analyses were performed using the SPSS 22.0 statistical software (SPSS Inc., Chicago, IL). Data were analyzed by one-way ANOVA, and comparative analyses were conducted using the Tukey post hoc test. Statistical results are presented as means ± standard error of the mean (SEM). Differences were considered significant if $P < 0.05$, and $0.05 \leq P < 0.10$ was considered a trend. The R package of "Hmisc" was used for calculating Spearman's correlation coefficient.

TABLE 1: Primer sequences used for intestinal mucosa antioxidant-related genes and mitochondrial-related genes.

Genes[a]	Primers (5′-3′)	Size (bp)	Accession NO.
β-Actin	F: GATCTGGCACCACACCTTCTACAAC R: TCATCTTCTCACGGTTGGCTTTGG	107	XM_021086047.1
CAT	F: AGCCTACGTCCTGAGTCTCTGC R: TCCATATCCGTTCATGTGCCTGTG	90	NM_214301.2
GPx1	F: TGCTCATTGAGAACGTAGCGT R: CAGGATCTCCCCATTCTTGGC	161	NM_214201.1
GPx4	F: GATTCTGGCCTTCCCTTGC R: TCCCCTTGGGCTGGACTTT	173	NM_214407.1
Keap1	F: CGCCTCATCGAGTTCGCTTACAC R: GCACGGACCACACTGTCAATCTG	107	NM_001114671.1
CuZnSOD	F: CCAGTGCAGGTCCTCACTTCAATC R: CGGCCAATGATGGAATGGTCTCC	172	NM_001190422.1
MnSOD	F: GGACAAATCTGAGCCCTAACG R: CCTTGTTGAAACCGAGCC	159	NM_214127.2
NQO1	F: GTGGAAGCCGCAGACCTTGTG R: CGTTCAAACCAGCCTTTCAGAATAGC	83	NM_001159613.1
Nrf1	F: CGATGCTTCAGAATTGCCAACTACAG R: GCGTTGTCTGGATGGTCATCTCAC	125	XM_021078993.1
Nrf2	F: CCAATTCAGCCAGCACAACACATC R: GACTGAGCCTGGTTAGGAGCAATG	149	XM_003133500
ATP5A1	F: ACGCCATTGATGGAAAGGGT R: TGGTTCCCGCACAGAGATTC	98	NM_001185142.1
ATP5B	F: CATGTTGGGCTTTGTGGGTC R: ATAGTCTCTGGCAGGCTGGA	139	XM_001929410.4
PGC1α	F: ATGGAGCAATAAAGCGAAGAGCATTTG R: GAGGAGGGTCATCATTTGTGGTCAG	101	NM_213963.2
TFAM	F: AAATTGCTGAGCTGTGGAGGGAAC R: TACACCTGCCAGTCTGCCCTATAAG	82	NM_001130211.1

[a]CAT: catalase; GPx1: glutathione peroxidase 1; GPx4: glutathione peroxidase 4; Keap1: kelch-like ECH-associated protein 1; CuZnSOD: copper- and zinc-containing superoxide dismutase; MnSOD: manganese-containing superoxide dismutase; NQO1: nicotinamide adenine dinucleotide (phosphate) dependency quinone oxidoreductase 1; Nrf1: nuclear factor erythroid 2-related factor 1; Nrf2: nuclear factor erythroid 2-related factor 2; mtDNA: mitochondrial DNA; ATP5A1: adenosine triphosphate synthase alpha subunit; ATP5B: adenosine triphosphate synthase β; PGC-1α: peroxisome proliferator-activated receptor γ coactivator-1α; TFAM: mitochondrial transcription factor A.

TABLE 2: Primer sequences used for intestinal mucosa mtDNA copy number analysis.

Gene[a]	Primers (5′-3′)	Size (bp)	Accession NO.
mt D-loop	F: GATCGTACATAGCACATATCATGTC R: GGTCCTGAAGTAAGAACCAGATG	198	AF276923
G6PC	F: AAGCCAAGCGAAGGTGTGAGC R: GGAACGGGAACCACTTGCTGAG	165	NM_001113445.1

[a]mt D-loop: mitochondria DNA loop; G6PC: glucose-6-phosphatase.

3. Results

3.1. Effect of Maternal Probiotic or Synbiotic Supplementation on Piglets' Plasma Redox Status.

To explore whether maternal probiotic or synbiotic supplementation contributes to the systemic redox status, we determined the antioxidant and oxidative parameters in plasma. As shown in Figure 1, in comparison with the control group, the activities of CAT, GSH-Px, and SOD were higher, whereas the concentrations of MDA and H_2O_2 were lower in the probiotic group ($P < 0.05$). Synbiotic supplementation increased ($P < 0.05$) plasma CAT, GSH-Px, and SOD activities compared with the control group. Meanwhile, plasma GSH-Px, SOD, and T-AOC activities in the probiotic and synbiotic groups were elevated ($P < 0.05$) compared with the antibiotic group. These findings suggest that maternal probiotic or synbiotic

TABLE 3: Primer sequences used for bacteria 16S rRNA.

Bacteria	Sequence 5′-3′	Length (bp)	Reference	Annealing temp, ℃
Total bacteria	F: GTGSTGCAYGGYYGTCGTCA R: ACGTCRTCCMCNCCTTCCTC	123	[26]	60
Bacteroidetes	F: GGARCATGTGGTTTAATTCGATGAT R: AGCTGACGACAACCATGCAG	126	[27]	60
Firmicutes	F: GGAGYATGTGGTTTAATTCGAAGCA R: AGCTGACGACAACCATGCAC	126	[27]	60
Bifidobacterium	F: TCGCGTCYGGTGTGAAAG R: GGTGTTCTTCCCGATATCTACA	128	[28]	62
Clostridium cluster IV	F: GCACAAGCAGTGGAGT R: CTTCCTCCGTTTTGTCAA	240	[29]	54
Escherichia coli	F: CATGCCGCGTGTATGAAGAA R: CGGGTAACGTCAATGAGCAAA	95	[30]	62
Lactobacillus	F: AGCAGTAGGGAATCTTCCA R: ATTCCACCGCTACACATG	345	[31]	62
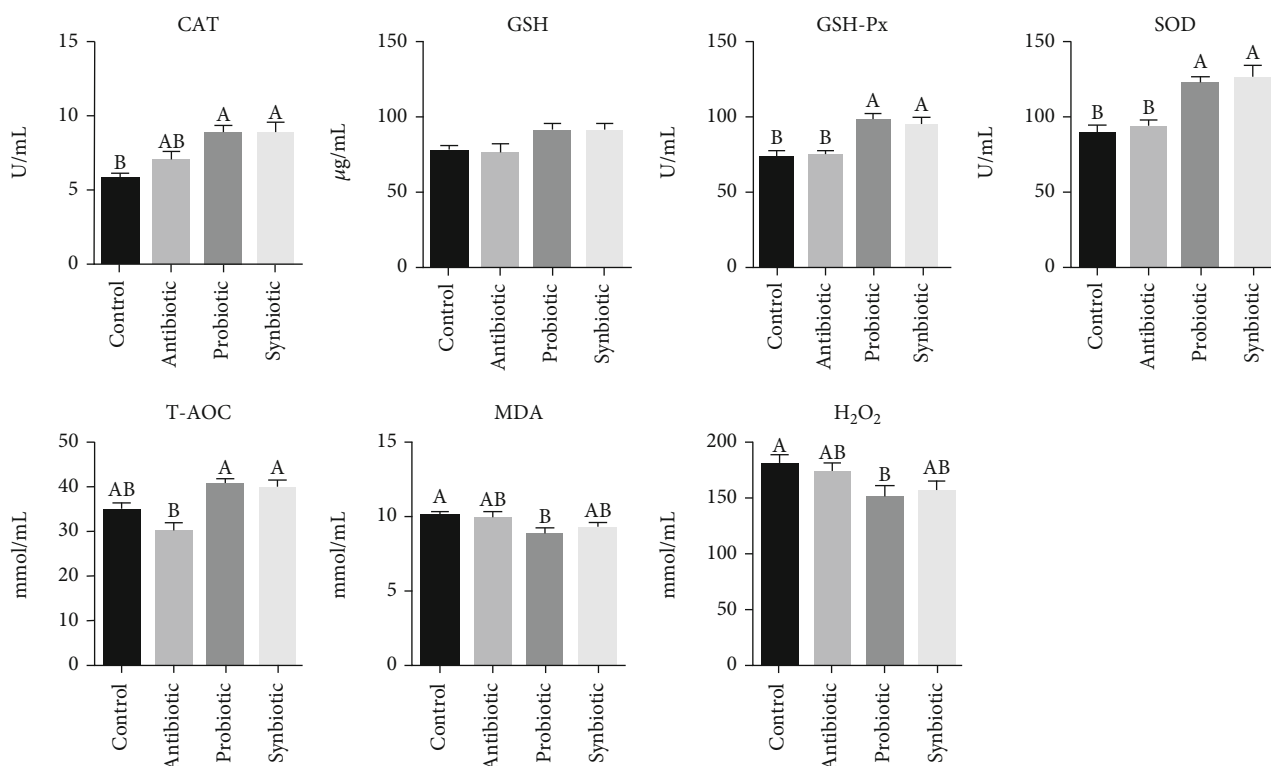
FIGURE 1: Effect of maternal probiotic or synbiotic supplementation during gestation and lactation on piglets' plasma redox status. Data are expressed as means ± SEM ($n = 8$). Values with different letters mean statistically significant differences ($P < 0.05$). Values with no letters mean no statistically significant differences among the groups ($P > 0.05$). CAT: catalase; GSH: glutathione; GSH-Px: glutathione peroxidase; SOD: superoxide dismutase; T-AOC: total antioxidant capacity; MDA: malondialdehyde.

supplementation could improve the systemic antioxidant capacity of offspring piglets.

3.2. Effect of Maternal Probiotic or Synbiotic Supplementation on Piglets' Intestinal Antioxidant Capacity. We further investigated the role of probiotic or synbiotic on jejunal and colonic antioxidant capacity. As shown in Figure 2, in the jejunum, the activities of GSH-Px and SOD were increased in the probiotic group ($P < 0.05$), and the GSH, GSH-Px, and T-AOC activities were increased in the synbiotic group ($P < 0.05$) when compared with the control group. In addition, maternal probiotic supplementation increased ($P < 0.05$) the GSH-Px and SOD activities, while maternal synbiotic supplementation increased ($P < 0.05$) the GSH-Px

FIGURE 2: Effect of maternal probiotic or synbiotic supplementation during gestation and lactation on piglets' oxidant/antioxidant status in the jejunum and colon. Data are expressed as means ± SEM ($n = 8$). Values with different letters mean statistically significant differences ($P < 0.05$). Values with no letters mean no statistically significant differences among the groups ($P > 0.05$). GSH: glutathione; GSH-Px: glutathione peroxidase; SOD: superoxide dismutase; T-AOC: total antioxidant capacity; MDA: malondialdehyde.

activity compared with the antibiotic group. In the colon, compared with the control group, the GSH-Px and SOD activities were higher ($P < 0.05$) in the probiotic group, as well as the SOD and T-AOC activities in the synbiotic group, while the MDA concentration was lower ($P < 0.05$) in the synbiotic group. In addition, the GSH-Px and SOD activities in the probiotic group and the SOD activity in the synbiotic group were increased ($P < 0.05$) in comparison to the antibiotic group. Therefore, these results indicate that maternal probiotic or synbiotic supplementation facilitates improving the intestinal antioxidant capacity in offspring piglets.

3.3. Effect of Maternal Probiotic or Synbiotic Supplementation on Piglets' Intestinal Antioxidant Enzyme-Related Genes. To investigate the molecular mechanism by which maternal probiotic or synbiotic supplementation may influence the intestinal antioxidant function, the expression of genes related to the antioxidant capacity was determined. Maternal synbiotic supplementation upregulated ($P < 0.05$) the relative mRNA expressions of CuZnSOD, Nrf1, and Nrf2 in the jejunum compared with the control and antibiotic groups. The mRNA expression of GPx1 was tended to upregulate in the probiotic ($P = 0.090$) and synbiotic ($P = 0.068$) groups compared with the control group. Interestingly, the mRNA expressions of GPx4, Nrf1, and Nrf2 in the colon were lower ($P < 0.05$) in the antibiotic group than those in the control group. Meanwhile, the mRNA expression of colonic Nrf2 in the probiotic

($P = 0.095$) and synbiotic ($P = 0.087$) groups was tended to increase compared with the antibiotic group (Table 4). Our data indicated that maternal probiotic or synbiotic supplementation could improve the jejunal antioxidant enzyme-related genes to some extent, while had no significant effect on the colon.

3.4. Effect of Maternal Probiotic or Synbiotic Supplementation on Piglets' Intestinal ATP Concentrations, Mitochondrial Complex I and III Activities. As enterocytes have high energy demands to maintain renewal and the transport of nutrients, the effect of maternal probiotic or synbiotic supplementation on the mitochondrial oxidative metabolism and the jejunal and colonic mucosal ATP production were measured. Although there were no significant differences in the jejunal ATP concentration among the four groups, the concentration of jejunal ATP was higher by 9.1% and 18.7% in the probiotic and synbiotic groups, respectively, than the control group (Figure S1). The jejunal mitochondrial complex I activity in the antibiotic group was higher compared with the other three groups. Compared to the control group, the activity of colonic mitochondrial complex I was higher by 20.16% and 44.82% in the antibiotic and probiotic groups, while tended to decreased ($P = 0.086$) in the synbiotic group (Figure S2A). However, there were no significant differences in the mitochondrial complex III activity in the jejunum and colon among the four groups (Figure S2B).

Table 4: Effect of maternal probiotic or synbiotic supplementation during gestation and lactation on piglets' antioxidant-related gene expressions in the jejunum and colon.

Items[a]	Dietary treatment				SEM	P values
	Control	Antibiotic	Probiotic	Synbiotic		
Jejunum						
CAT	1.12	0.89	1.66	1.61	0.143	0.181
GPx1	1.05	1.38	1.62	1.67	0.093	0.049
GPx4	1.11	1.26	1.49	1.35	0.090	0.482
Keap1	1.02	0.93	1.09	1.12	0.036	0.305
CuZnSOD	1.09[b]	1.01[b]	1.26[ab]	1.82[a]	0.102	0.020
MnSOD	1.05	1.22	1.25	1.52	0.077	0.188
NQO1	1.18	1.49	1.18	1.29	0.142	0.875
Nrf1	1.02[b]	0.95[b]	1.06[ab]	1.31[a]	0.038	0.002
Nrf2	1.11[b]	1.12[b]	1.33[ab]	1.63[a]	0.072	0.032
Colon						
CAT	1.05	0.74	0.82	0.78	0.049	0.076
GPx1	1.03	0.71	0.90	1.00	0.053	0.146
GPx4	1.08[a]	0.38[b]	0.90[ab]	0.95[ab]	0.087	0.020
Keap1	1.00	0.96	1.04	0.94	0.028	0.618
CuZnSOD	0.95	0.57	0.86	0.88	0.059	0.117
MnSOD	1.06	0.95	1.25	1.13	0.070	0.516
NQO1	1.15	0.64	0.87	1.20	0.109	0.269
Nrf1	1.02[a]	0.77[b]	0.93[ab]	1.03[a]	0.033	0.018
Nrf2	1.07[a]	0.64[b]	0.75[ab]	0.73[ab]	0.056	0.014

Data are expressed as means with SEM ($n = 8$). Means with different superscript letters in the same row were significantly different ($P < 0.05$). Values with no letters mean no statistically significant differences among the groups ($P > 0.05$). [a]CAT: catalase; GPx1: glutathione peroxidase 1; GPx4: glutathione peroxidase 4; Keap1: kelch-like ECH-associated protein 1; CuZnSOD: copper- and zinc-containing superoxide dismutase; MnSOD: manganese-containing superoxide dismutase; NQO1: nicotinamide adenine dinucleotide (phosphate) dependency quinone oxidoreductase 1; Nrf1: nuclear factor erythroid 2-related factor 1; Nrf2: nuclear factor erythroid 2-related factor 2.

These findings suggest that maternal probiotic or synbiotic supplementation tends to improve jejunal mitochondrial function.

3.5. Effect of Maternal Probiotic or Synbiotic Supplementation on Piglets' Mitochondrial Biogenesis-Related Genes in the Jejunum and Colon. Subsequently, mitochondrial biogenesis-related genes in the intestinal mucosa were measured to understand further protective effects of maternal probiotic or synbiotic on mitochondria. As shown in Table 5, in the jejunal mucosa, maternal synbiotic supplementation increased ($P < 0.05$) the mRNA expressions of ATP5A1, ATP5B, and TFAM compared to the control group, as well as the mRNA expressions of ATP5A1 and ATP5B compared with the antibiotic group. In comparison with the probiotic group, maternal synbiotic supplementation increased ($P < 0.05$) the mRNA expression of ATP5B in piglets' jejunum. However, in the colonic mucosa, the PGC1α mRNA expression level was decreased ($P < 0.05$) in the synbiotic group compared with the control group. The results demonstrated that maternal synbiotic supplementation could improve the jejunal mitochondrial biogenesis-related genes.

3.6. Effect of Maternal Probiotic or Synbiotic Supplementation on Piglets' Microbial Abundances in the Jejunum and Colon. We further investigated the effects of maternal probiotic or synbiotic supplementation on the selected intestinal microbiota abundances in offspring piglets. As shown in Figure 3, in the jejunum, maternal probiotic supplementation increased ($P < 0.05$) the relative abundances of Bacteroidetes and Bifidobacterium, and synbiotic supplementation increased ($P < 0.05$) the relative abundances of Firmicutes, Bacteroidetes, Bifidobacterium, and Lactobacillus when compared with the control group. Similarly, maternal antibiotic supplementation also increased the relative abundances of total bacteria ($P = 0.066$), Bifidobacterium ($P < 0.05$), and Lactobacillus ($P < 0.05$) compared with the control group. In the colon, the relative abundance of Bifidobacterium in the probiotic group was higher ($P < 0.05$) compared with the control and antibiotic groups. However, there were no significant differences in the abundances of total bacteria, Bacteroides, Clostridium cluster IV, and Lactobacillus among the four groups. These results indicated that maternal probiotic or synbiotic significantly changed particular bacteria abundances in offspring piglets, with an increase in the counts of beneficial bacteria in the jejunum.

3.7. Correlation Analysis of Antioxidant Index, Mitochondrial Index, and Intestinal Bacteria Abundance in the Jejunum and Colon. The correlation analysis of all measured bacterial abundance, antioxidant index, and mitochondrial function parameters is shown in Figure 4. The correlation analysis

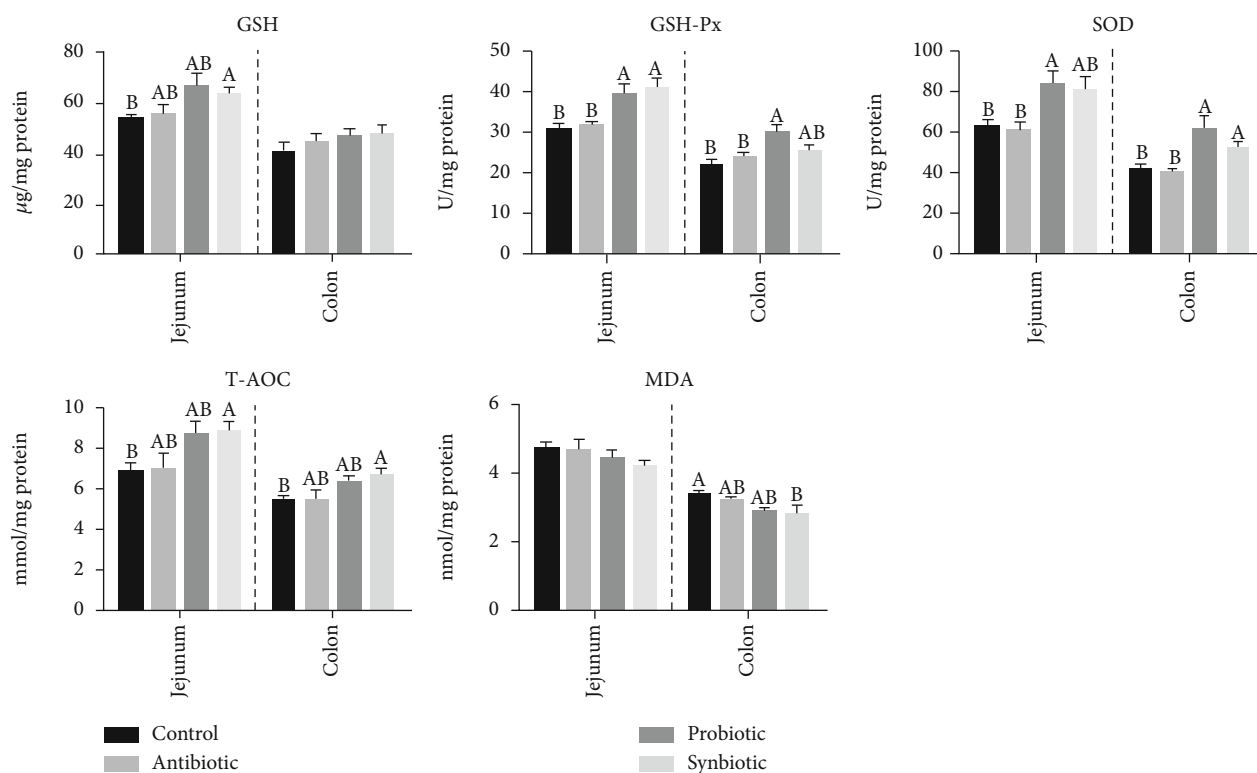TABLE 5: Effect of maternal probiotic or synbiotic supplementation during gestation and lactation on mitochondrial-related gene expression in the jejunum and colon of piglets.

Items[a]	Dietary treatment				SEM	P values
	Control	Antibiotic	Probiotic	Synbiotic		
Jejunum						
mtDNA	1.02	0.997	1.08	0.936	0.0381	0.661
ATP5A1	1.02[b]	0.95[b]	1.17[ab]	1.43[a]	0.057	0.014
ATP5B	1.03[b]	1.07[b]	1.20[b]	1.64[a]	0.066	0.001
PGC1α	1.04	0.80	1.18	1.14	0.058	0.110
TFAM	1.05[b]	1.21[ab]	1.28[ab]	1.51[a]	0.055	0.016
Colon						
mtDNA	1.06	1.09	0.98	0.80	0.051	0.192
ATP5A1	1.03	0.75	0.89	0.98	0.042	0.100
ATP5B	1.02	0.93	1.08	1.06	0.041	0.629
PGC1α	1.11[a]	0.65[ab]	1.16[ab]	0.60[b]	0.076	0.008
TFAM	1.03[a]	0.71[b]	0.89[ab]	0.86[ab]	0.047	0.106

Data are expressed as means with their SEM ($n = 8$). Values with different letters in the same row were significantly different ($P < 0.05$). Values with no letters mean no statistically significant differences among the groups ($P > 0.05$). [a]mtDNA: mitochondrial DNA; ATP5A1: adenosine triphosphate synthase alpha subunit; ATP5B: adenosine triphosphate synthase β, polypeptide; PGC-1α: peroxisome proliferator-activated receptor γ coactivator-1α; TFAM: mitochondrial transcription factor A.
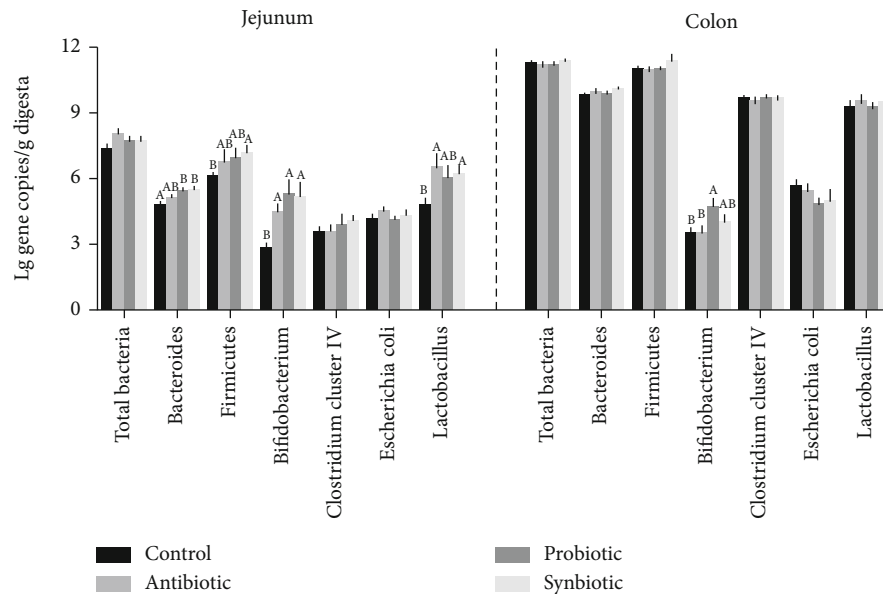
FIGURE 3: Effect of maternal probiotic or synbiotic supplementation during gestation and lactation on the copy numbers (Lg (copies/g)) of bacterial abundance in offspring piglets. Data are expressed as means ± SEM ($n = 8$). Values with different letters mean statistically significant differences ($P < 0.05$). Values with no letters mean no statistically significant differences among the groups ($P > 0.05$).

revealed that jejunal *Bifidobacterium* abundance was positively correlated ($P < 0.05$) with the jejunal CAT expression and colonic GSH-Px activity but negatively correlated ($P < 0.05$) with the colonic MDA concentration. The jejunal *Escherichia coli* abundance was positively correlated ($P < 0.05$) with jejunal MDA concentration, while negatively correlated ($P < 0.05$) with the jejunal MnSOD expression and colonic mtDNA expression. The jejunal *Lactobacillus* abundance was positively correlated ($P < 0.05$) with the jejunal CAT and NQO1 expression. The jejunal *Bacteroidetes*

was positively correlated ($P < 0.05$) with plasma CAT and GSH-Px activities, jejunal T-AOC activity and mtDNA expression, and colonic T-AOC activity. The jejunal Firmicutes abundance was positively correlated ($P < 0.05$) with colonic GSH-Px activity and jejunal CAT and NQO1 expression. The jejunal GSH-Px activity showed positive correlations ($P < 0.05$) with plasma CAT, GSH-Px, SOD, and T-AOC activities; colonic T-AOC activity; and jejunal GPx1, GPx4, Nrf1, ATP5A1, ATP5B, and TFAM mRNA levels, while showed negative correlations ($P < 0.05$) with MDA concentration in
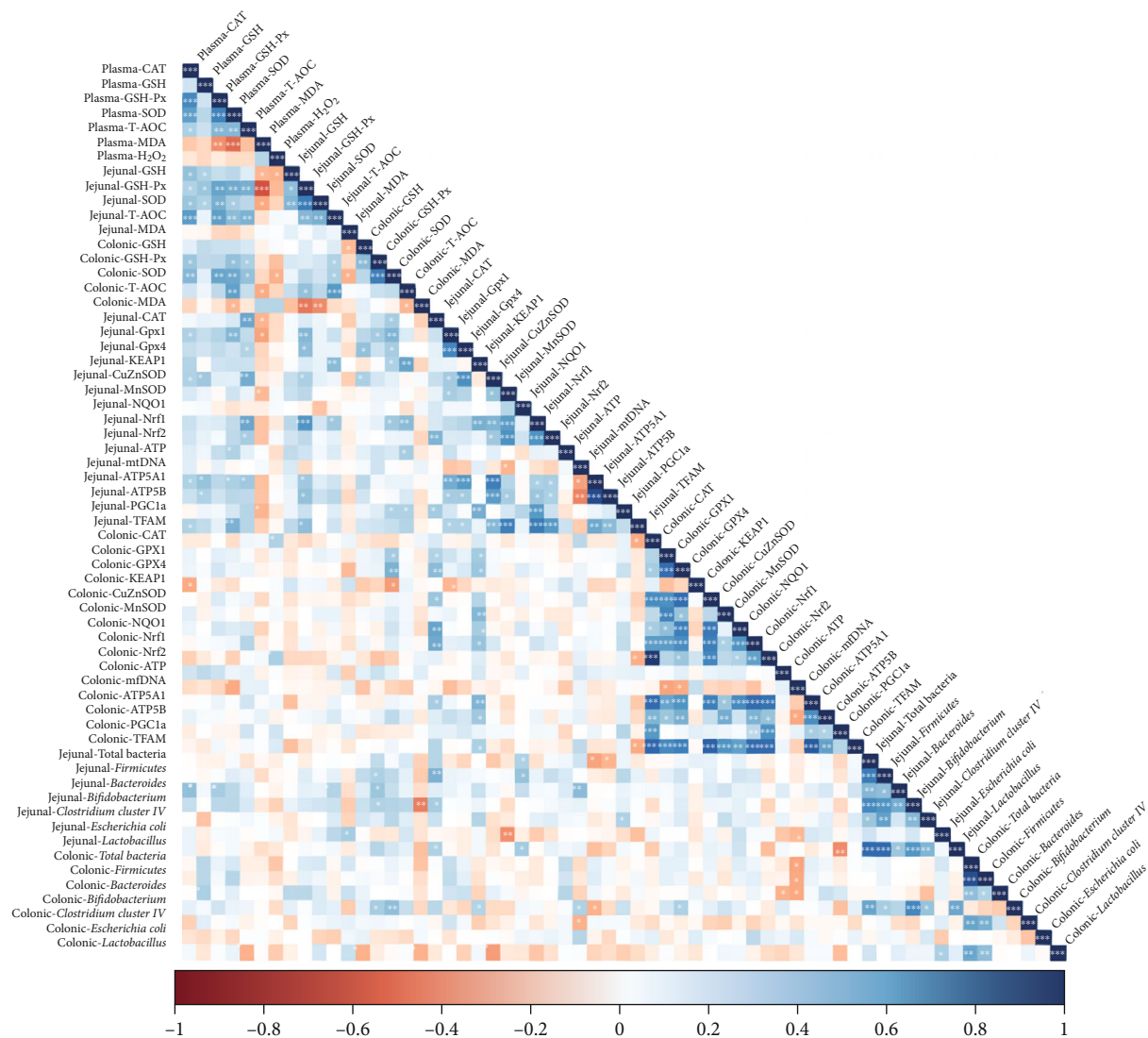
FIGURE 4: Correlation of antioxidant indexes, mitochondrial function indexes, and bacteria abundances. The R package of "corroplot" was used for generating the heat maps. The blue color represents a significant positive correlation, and red color represents a significant negative correlation. Asterisks indicate statistically significant difference: $*P < 0.05$; $**P < 0.01$; $***P < 0.001$. CAT: catalase; GSH: glutathione; GSH-Px: glutathione peroxidase; SOD: superoxide dismutase; T-AOC: total antioxidant capacity; MDA: malondialdehyde; GPx1: glutathione peroxidase 1; GPx4: glutathione peroxidase 4; Keap1: kelch-like ECH-associated protein 1; CuZnSOD: copper- and zinc-containing superoxide dismutase; MnSOD: manganese-containing superoxide dismutase; NQO1: nicotinamide adenine dinucleotide (phosphate) dependency quinone oxidoreductase 1; Nrf1: nuclear factor erythroid 2-related factor 1; Nrf2: nuclear factor erythroid 2-related factor 2; mtDNA: mitochondrial DNA; ATP5A1: adenosine triphosphate synthase alpha subunit; ATP5B: adenosine triphosphate synthase β, polypeptide; PGC-1α: peroxisome proliferator-activated receptor γ coactivator-1α; TFAM: mitochondrial transcription factor A.

the plasma and colon. The jejunal T-AOC activity showed positive correlations ($P < 0.05$) with plasma CAT, GSH-Px, SOD, and T-AOC activities; colonic GSH-Px and SOD activities; and jejunal Keap1 and Nrf1 expressions. In the colon, *Bifidobacterium* abundance was positively correlated ($P < 0.05$) with colonic GSH-Px and SOD activities, and GPx4 expression. Besides, colonic *Lactobacillus* abundance was negatively correlated with colonic GSH activity and MDA concentration.

4. Discussion

In humans, maternal nutritional strategies during gestation and lactation have been investigated due to their potential impact on fetal growth and development, as well as the beneficial effects on offspring's health [32]. Moreover, maternal adverse nutritional conditions may alter the structure and function of particular organs of offspring and lead to many complications later in life [33]. Previous studies have found that the administration of probiotics and prebiotics during gestation and lactation is a possible dietary strategy to benefit infant health [34]. Probiotics present many beneficial effects, and strain-specific probiotics can exhibit antioxidant activity and reduce the intestinal damage caused by oxidation [35]. The present study investigates whether dietary probiotic or synbiotic supplementation to sows during gestation and lactation affects the antioxidant capacity and mitochondrial

function in offspring piglets and further explored whether it is associated with intestinal bacteria. We found that maternal probiotic or synbiotic supplementation during gestation and lactation significantly enhanced systemic and intestinal antioxidant capacity, improved mitochondrial biogenesis, and altered the jejunal and colonic bacteria communities in offspring piglets. Furthermore, correlation analysis revealed that jejunal and colonic microbiota abundances were significantly correlated with antioxidant enzyme activities and mitochondrial biogenesis-related indexes.

The antioxidant capacity in plasma reflects the host's systemic capacity to respond to oxidative damage. H_2O_2, as a major type of ROS, is involved in lipoperoxidation [36]. The MDA is a decomposition product of lipoperoxidation, is the important marker of oxidative stress [37]. By lowering the MDA level in plasma, it is possible to lower the degree of lipid destruction and enhance the ability of ROS scavenging. In the present study, dietary probiotic supplementation to sows decreased plasma MDA and H_2O_2 concentrations of offspring piglets. The major GSH-dependent enzymatic antioxidants are SOD, GSH-Px, and CAT, which play a vital role in scavenging ROS [38]. The GSH serves as the major endogenous antioxidant, acting as a free radical scavenger in the cell. GSH-px is a key enzyme to catalyze GSH into GSSG. Our results showed that the activity of GSH-Px in the plasma of probiotic- or synbiotic-treated piglets was significantly higher than those in the control group. However, the GSH content in the plasma of probiotic- or synbiotic-treated piglets was increased numerically but not significantly. Based on these results, we speculated that maternal probiotic or synbiotic supplementation may contribute slightly to regulate the oxidation and reduction reactions of GSH; however, the exact mechanism remained unknown. The redox status of GSH can be expressed by its half-cell redox potential (GSH/GSSG Eh) [39]. Further studies are needed to explore the effect of maternal probiotic or synbiotic supplementation on the GSSG and GSH/GSSG Eh levels to fully understand the GSH redox status.

The intestinal mucosa, the front-line barrier to food antigens, pathogens, and commensal organisms, plays a crucial role in sustaining intestinal epithelial homeostasis [40]. However, many stimuli factors (i.e., infection and inflammation) can induce the overproduction of proinflammatory cytokines and ROS to damage intestinal barrier function [41]. In the present study, consistent with the findings in plasma, the MDA content in the colonic mucosa of maternal synbiotic-treated piglets was significantly decreased. Furthermore, maternal probiotic or synbiotic supplementation can partially increase the antioxidant enzyme activities in the jejunum and colon of offspring piglets. Gu et al. reported that isomalto-oligosaccharide and *Bacillus* supplementation to sows during late gestation could improve the placental antioxidant capacity and the piglets' birth weight [42]. In a human study, it was found that plasma and erythrocyte MDA levels were significantly higher, and the erythrocyte GSH level was lower in the pregnant women than in the nonpregnant women, and there was a significant positive correlation in MDA, GSH-R, and GSH-P levels between maternal and cord blood erythrocyte. These results indicated that the fetus may affect by the oxidant status of pregnant women [8]. Synbiotic supplementation could improve the T-AOC level and slightly reduce MDA level in human breastmilk [43]. However, the effect of dietary probiotic or synbiotic supplementation on the antioxidant enzymes in sows' breastmilk or placenta is unclear. Further studies are necessary to explore the effect of probiotic or synbiotic on the transmission of antioxidant capacity from sows to their offspring.

The Nrf2 pathway plays an important role in the regulation of intracellular redox status [44]. We further confirmed that the relative expression of Nrf2 mRNA was increased in the jejunum of the synbiotic group. In addition, dietary synbiotic treatment upregulated the Nrf2-regulated genes, including CuZnSOD (SOD1) and GPx1. These findings indicated that maternal synbiotic supplementation could enhance the antioxidant capacity of offspring piglets by upregulating the Nrf2 pathway. The ATP production and utilization are very active in the intestinal epithelial cells [45], due to the intestinal epithelial cells maintain cell turnover every 3-5 days [46]. Therefore, energy deficits can easily lead to impaired intestinal barrier function. Mitochondria is one of the key sources of oxidative stress, as it utilizes oxygen for cellular ATP production. Oxidative stress in cells can lead to impaired mitochondrial function, including the content of mtDNA and the expression of mitochondrial genes [47]. In the present study, the jejunal ATP concentration in piglets tended to increase after the addition of probiotic or synbiotic in the sows' diets. Furthermore, maternal synbiotic supplementation significantly upregulated the mRNA expression of jejunal ATP5A1 and ATP5B, which might be responsible for the increased ATP level in the synbiotic-treated piglets. An increase in TFAM expression was observed in the jejunal mucosa of maternal synbiotic-treated piglets. It has been reported that TFAM plays a critical role in mitochondrial biogenesis and regulates the mtDNA copy number [48]. Collectively, these findings indicated that maternal probiotic or synbiotic supplementation might improve the processes of jejunum energy metabolism in offspring piglets. Moreover, in the present study, antibiotic and probiotic treatment increased the activity of colonic mitochondrial complex I, which could result in a boost of mitochondrial energy generation. Similar findings were observed in cardiac mitochondrial dysfunction of insulin-resistant rats treated with prebiotics, probiotics, and synbiotics which showed improved cardiac mitochondrial function and reduced oxidative stress [49].

Intestinal microbiota plays a crucial role in maintaining health and regulating pathogenesis in the host. Probiotics can stimulate the colonization of the piglet's gut with beneficial bacteria, enriches the gut microbiota diversity, and prevents the intestinal infection of neonatal piglets [50]. Moreover, probiotics could also exert antioxidant effects by modulating the composition of intestinal microbiota [35]. In humans, supplementing probiotic to the pregnant mother during late pregnancy could promote the colonization of the infant's gut with beneficial bacteria such as *L. rhamnosus GG* or *Bifidobacteria* [51, 52]. Our study in pigs showed that maternal probiotic supplementation significantly increased
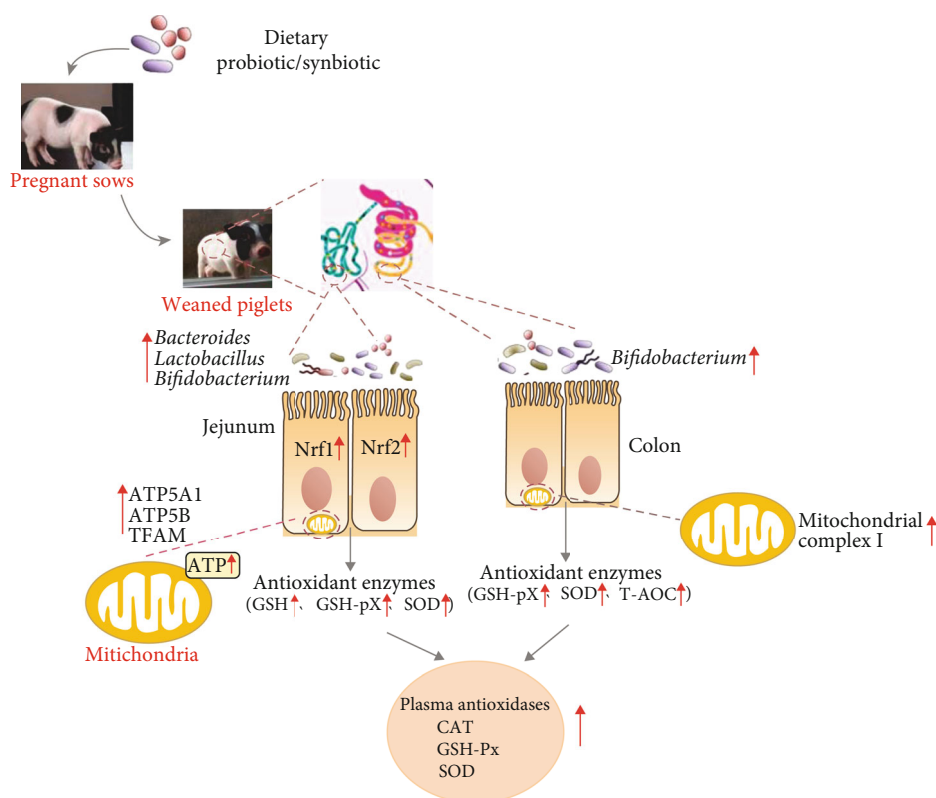
FIGURE 5: Schematic demonstrated the hypothesized mechanism of maternal probiotic or synbiotic effects on antioxidant capacity of offspring piglets. CAT: catalase; GSH: glutathione; GSH-Px: glutathione peroxidase; SOD: superoxide dismutase; T-AOC: total antioxidant capacity; Nrf1: nuclear factor erythroid 2-related factor 1; Nrf2: nuclear factor erythroid 2-related factor 2; ATP5A1: adenosine triphosphate synthase alpha subunit; ATP5B: adenosine triphosphate synthase β, polypeptide; TFAM: mitochondrial transcription factor A.

the *Bacteroidetes* and *Bifidobacterium* abundances in the jejunum and *Bifidobacterium* in the colon of offspring piglets. *Bacteroidetes* are known as short-chain fatty acids producing bacteria, which protects the mocusa of the host from damage by pathogens, provides nutrition for colonic epithelial cells, and reduces inflammation. In addition, *Bacteroidetes* can supply energy to the host via carbohydrate degradation and associated with the immune response of the host [53]. The present study also found that maternal synbiotic supplementation during gestation and lactation increased the relative abundances of Firmicutes, *Bacteroidetes*, *Bifidobacterium*, and *Lactobacillus* in the jejunum of piglets. Firmicutes were found associated with the degradation of different carbon sources, oligosaccharides, proteins, and amino acids and their fermentative metabolisms to provide energy to the host [54]. Furthermore, *Lactobacillus* and *Bifidobacterium*, as the most common probiotic species, could inhibit the growth of pathogenic bacteria to maintain the balance of the intestinal microbiota and thus alleviate the intestinal oxidative stress [55, 56]. Previous studies research also reported that changes in the intestinal microbiota were strongly associated with oxidative stress in high-fat diet-fed mice [57]. Consistent with these findings, the correlation analysis in the present study showed that the antioxidant enzyme activities exhibited a positive correlation with the abundances of Firmicutes, *Bacteroidetes*, *Bifidobacterium*, and *Lactobacillus* while MDA level was negatively correlated with the abundances of jejunal

Bifidobacterium and colonic *Lactobacillus*. Collectively, these findings indicated that maternal probiotic or synbiotic supplementation alleviated the intestinal oxidative stress in offspring piglets, which might be attributed to the increase in the abundances of beneficial bacteria, such as *Bifidobacterium*.

5. Conclusions

The present study showed a beneficial effect of maternal probiotic (*Lactobacillus Plantarum* and *Saccharomyces cerevisiae*) or synbiotic (probiotic + xylo-oligosaccharides) supplementation during gestation and lactation on antioxidant capacity and mitochondrial biogenesis, which may partly be attributed to altered intestinal microbiota in offspring weaned piglets. However, maternal synbiotic supplementation did not show any enhanced effects compared to probiotic in offspring weaned piglets (Figure 5). These findings implicated that probiotic or synbiotic would be potential maternal dietary additives to improve offspring's intestinal health.

Data Availability

The data used to support the findings of this study are included in the article and the supplementary information files.

Conflicts of Interest

The authors declare that there is no conflict of interest.

Authors' Contributions

KXF, YYL, and HQH designed the experiment. WK, AMAK, ZQ, XL, ZYZ, and HZL carried out the animal experience, sample collection, and sample analysis. WK performed the statistical analyses. WK, HQH, and KXF wrote the manuscript. All authors read and approved the final manuscript.

Acknowledgments

Supplementary Materials

Table S1: composition and nutrient levels of the sows' basal diets (air-dry basis; %). Table S2: composition and nutrient levels of the basal diet for weaned piglets. Figure S1: effect of maternal probiotic or synbiotic supplementation during gestation and lactation on ATP concentrations in the jejunum and colon of piglets. Figure S2: effect of maternal probiotic or synbiotic supplementation during gestation and lactation on mitochondrial complex I and III activities in the jejunum and colon of piglets. (*Supplementary materials*)

References

[1] M. G. Rooks and W. S. Garrett, "Gut microbiota, metabolites and host immunity," *Nature Reviews. Immunology*, vol. 16, no. 6, pp. 341–352, 2016.

[2] T. C. Fung, C. A. Olson, and E. Y. Hsiao, "Interactions between the microbiota, immune and nervous systems in health and disease," *Nature Neuroscience*, vol. 20, no. 2, pp. 145–155, 2017.

[3] Y. Belkaid and O. J. Harrison, "Homeostatic immunity and the microbiota," *Immunity*, vol. 46, no. 4, pp. 562–576, 2017.

[4] S. Wang, C. A. Ryan, P. Boyaval, E. M. Dempsey, R. P. Ross, and C. Stanton, "Maternal vertical transmission affecting early-life microbiota development," *Trends in Microbiology*, vol. 28, no. 1, pp. 28–45, 2020.

[5] Q. Shang, H. Liu, S. Liu, T. He, and X. Piao, "Effects of dietary fiber sources during late gestation and lactation on sow performance, milk quality, and intestinal health in piglets1," *Journal of Animal Science*, vol. 97, no. 12, pp. 4922–4933, 2019.

[6] M. Gomez de Aguero, S. C. Ganal-Vonarburg, T. Fuhrer et al., "The maternal microbiota drives early postnatal innate immune development," *Science*, vol. 351, no. 6279, pp. 1296–1302, 2016.

[7] C. B. Berchieri-Ronchi, S. W. Kim, Y. Zhao, C. R. Correa, K. J. Yeum, and A. L. Ferreira, "Oxidative stress status of highly prolific sows during gestation and lactation," *Animal*, vol. 5, no. 11, pp. 1774–1779, 2011.

[8] S. Arikan, D. Konukoğlu, C. Arikan, T. Akçay, and I. Davas, "Lipid peroxidation and antioxidant status in maternal and cord blood," *Gynecologic and Obstetric Investigation*, vol. 51, no. 3, pp. 145–149, 2001.

[9] Z. C. Luo, W. D. Fraser, P. Julien et al., "Tracing the origins of "fetal origins" of adult diseases: programming by oxidative stress?," *Medical Hypotheses*, vol. 66, no. 1, pp. 38–44, 2006.

[10] N. T. Williams, "Probiotics," *American Journal of Health-System Pharmacy*, vol. 67, no. 6, pp. 449–458, 2010.

[11] K. R. Pandey, S. R. Naik, and B. V. Vakil, "Probiotics, prebiotics and synbiotics- a review," *Journal of Food Science and Technology*, vol. 52, no. 12, pp. 7577–7587, 2015.

[12] G. R. Gibson and M. B. Roberfroid, "Dietary modulation of the human colonic microbiota: introducing the concept of prebiotics," *The Journal of Nutrition*, vol. 125, no. 6, pp. 1401–1412, 1995.

[13] B. Pourrajab, S. Fatahi, M. H. Sohouli, M. A. Gaman, and F. Shidfar, "The effects of probiotic/synbiotic supplementation compared to placebo on biomarkers of oxidative stress in adults: a systematic review and meta-analysis of randomized controlled trials," *Critical Reviews in Food Science and Nutrition*, vol. 12, no. 1, pp. 1–18, 2020.

[14] M. Y. Lin and C. L. Yen, "Antioxidative ability of lactic acid bacteria," *Journal of Agricultural and Food Chemistry*, vol. 47, no. 4, pp. 1460–1466, 1999.

[15] Y. Nie, J. Hu, Q. Hou et al., "Lactobacillus frumenti improves antioxidant capacity via nitric oxide synthase 1 in intestinal epithelial cells," *The FASEB Journal*, vol. 33, no. 10, pp. 10705–10716, 2019.

[16] M. Fakruddin, M. N. Hossain, and M. M. Ahmed, "Antimicrobial and antioxidant activities of Saccharomyces cerevisiae IFST062013, a potential probiotic," *BMC Complementary and Alternative Medicine*, vol. 17, no. 1, p. 64, 2017.

[17] A. A. Baker, E. Davis, J. D. Spencer, R. Moser, and T. Rehberger, "The effect of a Bacillus-based direct-fed microbial supplemented to sows on the gastrointestinal microbiota of their neonatal piglets," *Journal of Animal Science*, vol. 91, no. 7, pp. 3390–3399, 2013.

[18] D. Song, X. Li, Y. Cheng et al., "Effects of supplementing sow diets with Saccharomyces cerevisiae refermented sorghum dried distiller's grains with solubles from late gestation to weaning on the performance of sows and progeny," *Journal of Animal Science*, vol. 95, no. 5, pp. 2025–2031, 2017.

[19] R. Lan and I. Kim, "Enterococcus faecium supplementation in sows during gestation and lactation improves the performance of sucking piglets," *Veterinary Medicine and Science*, vol. 6, no. 1, pp. 92–99, 2020.

[20] Y. Li, H. Liu, L. Zhang et al., "Maternal dietary fiber composition during gestation induces changes in offspring antioxidative capacity, inflammatory response, and gut microbiota in a sow model," *International Journal of Molecular Sciences*, vol. 21, no. 1, p. 31, 2020.

[21] C. Ma, W. Zhang, Q. Gao et al., "Dietary synbiotic alters plasma biochemical parameters and fecal microbiota and metabolites in sows," *Journal of Functional Foods*, vol. 75, article 104221, 2020.

[22] S. J. Koopmans and T. Schuurman, "Considerations on pig models for appetite, metabolic syndrome and obese type 2 diabetes: from food intake to metabolic disease," *European Journal of Pharmacology*, vol. 759, pp. 231–239, 2015.

[23] J. Yang, L. Dai, Q. Yu, and Q. Yang, "Histological and anatomical structure of the nasal cavity of Bama minipigs," *PLoS One*, vol. 12, no. 3, article e0173902, 2017.

[24] K. Wang, Q. Zhu, X. Kong et al., "Dietary probiotics or synbiotics supplementation during gestation, lactation, and nursery periods modifies colonic microbiota, antioxidant capacity, and immune function in weaned piglets," *Frontiers in Veterinary Science*, vol. 7, p. 597832, 2020.

[25] M. Yu, C. Zhang, Y. Yang et al., "Long-term effects of early antibiotic intervention on blood parameters, apparent nutrient digestibility, and fecal microbial fermentation profile in pigs with different dietary protein levels," *Journal of Animal Science and Biotechnology*, vol. 9, no. 1, pp. 175–186, 2018.

[26] H. Maeda, C. Fujimoto, Y. Haruki et al., "Quantitative real-time PCR using TaqMan and SYBR green for *Actinobacillus actinomycetemcomitans*, *Porphyromonas gingivalis*, *Prevotella intermedia*, tetQ gene and total bacteria," *FEMS Immunology and Medical Microbiology*, vol. 39, no. 1, pp. 81–86, 2003.

[27] X. Guo, X. Xia, R. Tang, J. Zhou, H. Zhao, and K. Wang, "Development of a real-time PCR method for Firmicutes and Bacteroidetes in faeces and its application to quantify intestinal population of obese and lean pigs," *Letters in Applied Microbiology*, vol. 47, no. 5, pp. 367–373, 2008.

[28] T. Matsuki, K. Watanabe, J. Fujimoto, T. Takada, and R. Tanaka, "Use of 16S rRNA gene-targeted group-specific primers for real-time PCR analysis of predominant bacteria in human feces," *Applied and Environmental Microbiology*, vol. 70, no. 12, pp. 7220–7228, 2004.

[29] X. W. Huijsdens, R. K. Linskens, M. Mak, S. G. Meuwissen, C. M. Vandenbroucke-Grauls, and P. H. Savelkoul, "Quantification of bacteria adherent to gastrointestinal mucosa by real-time PCR," *Journal of Clinical Microbiology*, vol. 40, no. 12, pp. 4423–4427, 2002.

[30] E. Khafipour, S. Li, J. C. Plaizier, and D. O. Krause, "Rumen microbiome composition determined using two nutritional models of subacute ruminal acidosis," *Applied and Environmental Microbiology*, vol. 75, no. 22, pp. 7115–7124, 2009.

[31] A. W. Walker, J. Ince, S. H. Duncan et al., "Dominant and diet-responsive groups of bacteria within the human colonic microbiota," *The ISME Journal*, vol. 5, no. 2, pp. 220–230, 2011.

[32] M. A. K. Azad, G. Liu, P. Bin et al., "Sulfur-containing amino acid supplementation to gilts from late pregnancy to lactation altered offspring's intestinal microbiota and plasma metabolites," *Applied Microbiology and Biotechnology*, vol. 104, no. 3, pp. 1227–1242, 2020.

[33] C. N. Hsu and Y. L. Tain, "The good, the bad, and the ugly of pregnancy nutrients and developmental programming of adult disease," *Nutrients*, vol. 11, no. 4, p. 894, 2019.

[34] Y. Sanz, "Gut microbiota and probiotics in maternal and infant health," *The American Journal of Clinical Nutrition*, vol. 94, 6 Suppl, pp. 2000S–2005S, 2011.

[35] Y. Wang, Y. Wu, Y. Wang et al., "Antioxidant properties of probiotic bacteria," *Nutrients*, vol. 9, no. 5, p. 521, 2017.

[36] R. Mittler, S. Vanderauwera, N. Suzuki et al., "ROS signaling: the new wave?," *Trends in Plant Science*, vol. 16, no. 6, pp. 300–309, 2011.

[37] A. G. Pirinccioglu, D. Gokalp, M. Pirinccioglu, G. Kizil, and M. Kizil, "Malondialdehyde (MDA) and protein carbonyl (PCO) levels as biomarkers of oxidative stress in subjects with familial hypercholesterolemia," *Clinical Biochemistry*, vol. 43, no. 15, pp. 1220–1224, 2010.

[38] O. M. Ighodaro and O. A. Akinloye, "First line defence antioxidants-superoxide dismutase (SOD), catalase (CAT) and glutathione peroxidase (GPX): their fundamental role in

[39] the entire antioxidant defence grid," *Alexandria Journal of Medicine*, vol. 54, pp. 287–293, 2019.

[39] J. Degroote, W. Wang, H. Vergauwen, S. De Smet, C. Van Ginneken, and J. Michiels, "Impact of a dietary challenge with peroxidized oil on the glutathione redox status and integrity of the small intestine in weaned piglets," *Animal*, vol. 13, no. 8, pp. 1641–1650, 2019.

[40] J. M. Allaire, S. M. Crowley, H. T. Law, S. Y. Chang, H. J. Ko, and B. A. Vallance, "The intestinal epithelium: central coordinator of mucosal immunity," *Trends in Immunology*, vol. 39, no. 9, pp. 677–696, 2018.

[41] Y. Liu, F. Chen, J. Odle et al., "Fish oil enhances intestinal integrity and inhibits TLR4 and NOD2 signaling pathways in weaned pigs after LPS challenge," *The Journal of Nutrition*, vol. 142, no. 11, pp. 2017–2024, 2012.

[42] X. L. Gu, H. Li, Z. H. Song, Y. N. Ding, X. He, and Z. Y. Fan, "Effects of isomaltooligosaccharide and Bacillus supplementation on sow performance, serum metabolites, and serum and placental oxidative status," *Animal Reproduction Science*, vol. 207, pp. 52–60, 2019.

[43] L. Nikniaz, R. Mahdavi, A. Ostadrahimi, M. A. Hejazi, and A. M. Vatankhah, "Effects of synbiotic supplementation on total antioxidant capacity of human breastmilk," *Breastfeeding Medicine*, vol. 8, no. 2, pp. 217–222, 2013.

[44] X. L. Chen, G. Dodd, S. Thomas et al., "Activation of Nrf2/ARE pathway protects endothelial cells from oxidant injury and inhibits inflammatory gene expression," *American Journal of Physiology. Heart and Circulatory Physiology*, vol. 290, no. 5, pp. H1862–H1870, 2006.

[45] M. Watford, P. Lund, and H. A. Krebs, "Isolation and metabolic characteristics of rat and chicken enterocytes," *The Biochemical Journal*, vol. 178, no. 3, pp. 589–596, 1979.

[46] K. A. Moore and I. R. Lemischka, "Stem cells and their niches," *Science*, vol. 311, no. 5769, pp. 1880–1885, 2006.

[47] A. H. Bhat, K. B. Dar, S. Anees et al., "Oxidative stress, mitochondrial dysfunction and neurodegenerative diseases; a mechanistic insight," *Biomedicine & Pharmacotherapy*, vol. 74, pp. 101–110, 2015.

[48] M. I. Ekstrand, M. Falkenberg, A. Rantanen et al., "Mitochondrial transcription factor A regulates mtDNA copy number in mammals," *Human Molecular Genetics*, vol. 13, no. 9, pp. 935–944, 2004.

[49] W. Tunapong, N. Apaijai, S. Yasom et al., "Chronic treatment with prebiotics, probiotics and synbiotics attenuated cardiac dysfunction by improving cardiac mitochondrial dysfunction in male obese insulin-resistant rats," *European Journal of Nutrition*, vol. 57, no. 6, pp. 2091–2104, 2018.

[50] K. Veljović, M. Dinić, J. Lukić et al., "Promotion of early gut colonization by probiotic intervention on microbiota diversity in pregnant sows," *Frontiers in Microbiology*, vol. 8, p. 2028, 2017.

[51] S. Michael, G. Claudia, J. Y. Rose, I. Peter, and A. V. Jon, "Administration of oral probiotic bacteria to pregnant women causes temporary infantile colonization," *Journal of Pediatric Gastroenterology and Nutrition*, vol. 38, pp. 293–297, 2004.

[52] N. F. Krebs, J. E. Westcott, N. Butler, C. Robinson, and K. M. Hambidge, "Meat as a first complementary food for breastfed infants: feasibility and impact on zinc intake and status," *Journal of Pediatric Gastroenterology and Nutrition*, vol. 42, no. 2, pp. 207–214, 2006.

[53] L. V. Hooper, T. Midtvedt, and J. I. Gordon, "How host-microbial interactions shape the nutrient environment of the

mammalian intestine," *Annual Review of Nutrition*, vol. 22, no. 1, pp. 283–307, 2002.

[54] H. Ye, J. Liu, P. Feng, W. Zhu, and S. Mao, "Grain-rich diets altered the colonic fermentation and mucosa-associated bacterial communities and induced mucosal injuries in goats," *Scientific Reports*, vol. 6, no. 1, p. 20329, 2016.

[55] S. Doron and S. L. Gorbach, "Probiotics: their role in the treatment and prevention of disease," *Expert Review of Anti-Infective Therapy*, vol. 4, no. 2, pp. 261–275, 2006.

[56] M. I. Alvarez-Olmos and R. A. Oberhelman, "Probiotic agents and infectious diseases: a modern perspective on a traditional therapy," *Clinical Infectious Diseases*, vol. 32, no. 11, pp. 1567–1576, 2001.

[57] Y. Qiao, J. Sun, Y. Ding, G. Le, and Y. Shi, "Alterations of the gut microbiota in high-fat diet mice is strongly linked to oxidative stress," *Applied Microbiology and Biotechnology*, vol. 97, no. 4, pp. 1689–1697, 2013.

Research Article

Comparative Studies on the Hepatoprotective Effect of White and Coloured Rice Bran Oil against Acetaminophen-Induced Oxidative Stress in Mice through Antioxidant- and Xenobiotic-Metabolizing Systems

Warunyoo Phannasorn [1] **Arpamas Chariyakornkul,** [1,2] **Phumon Sookwong,** [3] **and Rawiwan Wongpoomchai** [1]

[1]*Department of Biochemistry, Faculty of Medicine, Chiang Mai University, Chiang Mai 50200, Thailand*
[2]*Functional Food Research Unit, Science and Technology Research Institute, Chiang Mai University, Chiang Mai 50200, Thailand*
[3]*Rice and Cereal Chemistry Research Laboratory, Department of Chemistry, Faculty of Science, Chiang Mai University, Chiang Mai 50200, Thailand*

Correspondence should be addressed to Rawiwan Wongpoomchai; rawiwan.wong@cmu.ac.th

Rice bran oil (RBO) comprises various nutrients and phytochemicals which exhibit several health benefits. There are no studies regarding the functional effects of different colours of RBO. This study was aimed to compare the constituents and antioxidant activities of white rice bran oil (WRBO) and coloured rice bran oil (CRBO). Each RBO showed similar free fatty acid profiles. However, greater amounts of vitamin E, phytosterols, carotenoids, and chlorophylls were found in CRBO, which had lower γ-oryzanol content than WRBO. Oxidative stress was induced in male mice by an overdose of acetaminophen (APAP) at 300 mg/kg body weight. The mice were then fed with RBO at the equivalent dose to 100 mg/kg body weight of γ-oryzanol three hours later and sacrificed six hours after APAP treatment. The administration of 100 mg γ-oryzanol equivalent in CRBO ameliorated APAP-induced hepatotoxicity in mice more strongly than 100 mg γ-oryzanol equivalent in WRBO, as evidenced by the significant reduction of serum ALT, hepatocellular necrosis, and hepatic lipid peroxidation. CRBO could improve xenobiotic-metabolizing and antioxidant enzyme activities, including glutathione S-transferase, superoxide dismutase, glutathione peroxidase, and glutathione reductase, and also increase mRNA expression of various antioxidant-responsive genes. Vitamin E, phytosterols, carotenoids, and chlorophyll might be the protective compounds in CRBO that alleviate APAP-induced hepatotoxicity through the interruption of APAP metabolism and the activation of antioxidant systems at both transcriptional and enzymatic levels. These findings might provide a protective role of CRBO on oxidative stress associated with several degenerative diseases.

1. Introduction

Oxidative stress results from an imbalance between the accumulation of free radicals and their elimination by antioxidant systems and causes damage to biomolecules such as lipids, DNA, and proteins [1]. Oxidative stress can accelerate the development of several degenerative diseases, such as diabetes mellitus, arthritis, cardiovascular diseases, neurodegener- ative diseases, multiorgan failure, and cancer, and also plays a role in the aging process [2]. Several studies have shown that these diseases are associated with a decline of antioxidant potential resulting from an increase of free radical production along with a decrease of the concentrations of antioxidant enzymes and, also induction of an inflammatory state [3]. Antioxidants are a defence mechanism that protects biological systems from reactive oxygen and nitrogen species

(RONS) produced by several processes [3]. Endogenous antioxidants include enzymatic and nonenzymatic pathways. Superoxide dismutase (SOD) converts the superoxide anion ($O_2^{\bullet-}$) to hydrogen peroxide (H_2O_2) and oxygen. H_2O_2 is further catalyzed to water and molecular oxygen by catalase (CAT). Glutathione peroxidase (GPx) also catalyzes the breakdown of hydrogen peroxide and lipid hydroperoxides in the reaction with reduced glutathione (GSH) to form oxidized glutathione (GSSG). Glutathione reductase (GR) then reduces GSSG to regenerate GSH [4]. Additionally, nonenzymatic antioxidants including bilirubin, vitamin E, β-carotene, albumin, and uric acid are molecules that interact with free radicals and terminate the chain reactions [5]. Interestingly, exogenous antioxidants also neutralize RONS. They prevent lipid peroxidation of cell membranes such as vitamin C, vitamin E, phenolic compounds, acetylcysteine, and oil lecithin and so suppress pathological conditions [6]. Therefore, prevention strategies, particularly the consumption of dietary antioxidants in daily life, are recommended to reduce oxidative stress and its potential impact on disease.

Vegetable oil has been recommended for daily cooking due to its high monounsaturated and ω-6 polyunsaturated fatty acid contents and its positive health benefit on heart disease and cancer in clinical studies [7, 8]. Previous works have reported the health benefits of edible oils. Olive oil containing β-carotene, lutein, tocopherols, squalene, and phenolic compounds exhibited antioxidant, anti-inflammatory, antimicrobial, anti-atherogenic, and anti-carcinogenic characteristics [9]. Sesame oil and its components showed antioxidant and anti-inflammatory effects, which alleviate cardiovascular diseases [10]. Safflower oil, extracted from seeds by screw pressing, demonstrated potent antioxidant effects and antimicrobial activity against skin pathogens [11].

Rice bran oil (RBO) is extracted from the cuticle between the husk and the grain obtained from the rice milling process. The global market of RBO was US$ 4.04 billion in 2018 and will increase to US$ 5.12 billion by 2025. Although it is not widely used as cooking oil, its demand as a healthy oil in applications and functional foods has been steadily increasing [12]. RBO contains a great source of phytochemicals such as tocopherols and tocotrienols, γ-oryzanols, and phytosterols [13] providing health advantages including antioxidation, anti-inflammation, anticancer, and hypolipidemic properties [14, 15]. In Thailand, Jasmine rice is primarily grown and is the most widely exported white rice product while Riceberry, a newly registered organic purple rice variety obtained from crossbreeding, has become the most popular rice known for its health benefits. Several studies have reported antioxidant activities of white rice bran oil (WRBO), but few have studied coloured rice bran oil (CRBO), especially in *in vivo* experiments. Therefore, the present study was aimed to compare the contents of phytonutrients and phytochemicals between WRBO and CRBO and their antioxidant properties using acetaminophen (APAP)-induced oxidative stress and hepatotoxicity in a mouse model. This classical model has been used to investigate the hepatoprotective effect of therapeutic compounds [16].

2. Materials and Methods

2.1. Chemicals. APAP, *N*-acetylcysteine (NAC), thiobarbituric acid (TBA), 5,5′-dithiobis-2-nitrobenzoic acid (DTNB), xanthine, xanthine oxidase, nitroblue tetrazolium, GR, reduced GSH, phenylmethylsulfonyl fluoride (PMSF), *p*-nitrophenol (*p*-NP), *p*-nitrocatechol, and tert-butyl hydroperoxide (t-BHP) were purchased from Sigma Aldrich Corp. (St. Louis, MO, USA). Bovine serum albumin (BSA) and 1-chloro-2,4-dinitrobenzene (CDNB) were obtained from Thermo Fisher Scientific Inc. (Waltham, MA, USA). Trichloroacetic acid (TCA) and H_2O_2 were bought from Merck Millipore (Burlington, MA, USA). UDP-glucuronic acid was provided by the United States Biological (Salem, MA, USA). β-NADPH was obtained from Nacalai Tesque (Kyoto, Japan). Potassium chloride, magnesium chloride, sodium carbonate, and glycerol were purchased from VWR Corp. (Radnor, PA, USA). Ethylenediaminetetraacetic acid (EDTA) was obtained from Vivantis Technologies (Selangor Darul Ehsan, Malaysia). HPLC grade butanol, hexane, isopropanol, ethyl acetate, acetic acid, methanol, and acetonitrile were obtained from RCI Labscan Ltd. (Bangkok, Thailand).

2.2. RBO Preparation. White and coloured rice (*Oryza sativa* L.) obtained from Kurk Rice Mill (Chiang Rai, Thailand) were planted from October to December 2018 in Wiang Chai District, Chiang Rai, Thailand. White and coloured rice varieties used in this study were Khao Dawk Mali 105 and Riceberry, respectively. WRBO and CRBO were extracted using a mechanical screw press machine and then filtered by paper to remove precipitate. After that, RBO was further purified by press filtration. RBO was collected into a glass bottle with light protection and kept at room temperature until investigation.

2.3. Analysis of Phytonutrients and Phytochemicals. The free fatty acid profile was analysed by the Institute of Food Research and Product Development, Kasetsart University, Bangkok, Thailand, using a gas chromatography-mass spectrometry technique according to an in-house method based on the Compendium of Methods for Food Analysis Thailand, 1st edition, 2003.

The assessment of γ-oryzanols was performed according to the method of Pintha et al. [17]. The HPLC system consisted of an Agilent HPLC 1260 connected to a diode array detector (Model G1311 C; Agilent Technologies, Santa Clara, CA, USA). RBO dissolved in ethanol was analysed using reversed-phased HPLC with a C18 column (Inertsil ODS-3 250×4.6 mm, $5\,\mu$m; GL Sciences Inc., Tokyo, Japan). The mobile phase included methanol and acetonitrile (65 : 35) with isocratic elution and a flow rate of $1.0\,\text{ml min}^{-1}$. A wavelength of 325 nm was used to monitor γ-oryzanols.

The determination of total vitamin E or tocols was performed by HPLC using a modified method of Huang et al. [18]. The system consisted of an Agilent HPLC 1100 connected to a fluorescence detector (Model 1046A; Hewlett Packard, Palo Alto, CA, USA). Twenty microliters of sample were injected into a normal-phase silica column (Verti-SepTM UPS 4.6 mm × 250 mm, $5\,\mu$m; Vertical

Chromatography Co., Ltd., Nonthaburi, Thailand). The mobile phase was an isocratic gradient of hexane: isopropanol: ethyl acetate: acetic acid (97.6 : 0.8 : 0.8 : 0.8, $v/v/v/v$) with a flow rate 1 ml min^{-1}, at room temperature. Tocols were fluorescently detected with the excitation at 294 nm and emission at 326 nm.

Phytosterols were analysed following the method of Pokkanta et al. [13]. The HPLC system consisted of an Agilent HPLC 1100 connected to a diode array detector (Model G1315 A; Agilent Technologies, Santa Clara, CA, USA). Each sample (5 μL) was injected into a Kinetex PFP column (4.6 × 250 mm, 5 μm, Phenomenex, Inc., Torrance, CA, USA) and gradually eluted by a mixed methanol and water solution with a flow rate of 1.0 ml min^{-1} for 30 min. Each form of phytosterols was detected at the wavelength of 210 nm.

Carotenoids and chlorophyll contents were determined using spectrophotometry. RBO was dissolved in 10% hexane (w/v). Carotenoid content was determined using the absorbance at 446 nm, while chlorophyll content was measured using the absorbance at wavelengths of 630, 670, and 710 nm and computed using the equations described by Pohndorf et al. [19].

2.4. Animals and Experimental Protocol.
Ten-week-old male Mlac: ICR mice, weighing approximately 40–50 g, were purchased from the National Laboratory Animal Center, Mahidol University, Nakhon Pathom, Thailand. All mice were kept in cages following standard conditions including temperature at 25°C under a dark-light cycle and were fed ad libitum with basal diet and drinking water. An experimental protocol was approved by The Animal Ethics Committee of the Faculty of Medicine, Chiang Mai University (07/2561). Forty-two mice were randomly divided into seven groups, six mice per group. All mice were fasted overnight for 12–15 hours prior to APAP treatment. Groups 1–3 were orally administrated with 0.9% warmed saline (a vehicle), while groups 4–7 were orally fed with 300 mg kg^{-1} body weight (BW) of APAP. After APAP induction for three hours, groups 1 and 4 were then fed with 15 ml kg^{-1} BW of distilled water. Groups 2 and 5 were orally administrated with WRBO, while groups 3 and 6 were treated with CRBO at the equivalent dose to 100 mg kg^{-1} BW of γ-oryzanols. Group 7 was fed with 1200 mg kg^{-1} BW of NAC as a positive drug control (Figure 1(a)). After that, mice were euthanized six hours after APAP treatment under anaesthesia by intraperitoneal injection of 200 mg kg^{-1} BW of sodium pentothiol. Blood was collected from the hepatic portal vein and then centrifuged at 3500 g and 4°C to obtain serum for alanine aminotransferase (ALT) analysis using an automated analyser by the Small Animal Hospital, Faculty of Veterinary Medicine, Chiang Mai University. After liver tissues were excised and weighed, the cut portions were stored at –80°C until further biochemical evaluation or fixed in 10% phosphate-buffered formalin for histopathological analysis by haematoxylin and eosin (H&E) staining.

2.5. Preparation of Liver Homogenate, Cytosol, and Microsome.
The liver tissue was homogenized in an ice-cold homogenizing buffer containing 1.15% w/v KCl and 0.25 mM PMSF. The homogenate was centrifuged at 10,000 rpm for 20 min at 4°C. The supernatant was collected and then centrifuged at 100,000 g at 4°C for 60 min to obtain a cytosolic supernatant and a microsomal pellet. The microsomal fraction was washed in homogenizing buffer and resuspended in microsomal suspension buffer pH 7.4, containing 30% (v/v) glycerol and 1 mM dithiothreitol. The cytosol and microsomal fractions were kept at –80°C until analysis. The protein content was measured by the Lowry method using BSA as a standard.

2.6. Liver Thiobarbituric Acid Reactive Substance Level.
Lipid peroxidation in the liver was measured using a thiobarbituric acid reactive substance (TBARS) assay as previously described by Noeman et al. [20]. Liver homogenate was pre-incubated with TCA for 5 min and then centrifuged at 6,000 g, 4°C for 20 min. The supernatant was incubated with TBA in boiling water for 10 min. The resulting pink chromogen was extracted in butanol. The mixture was centrifuged at 3000 g for 10 min, and the supernatant was monitored using the optimal density at a wavelength of 532 nm.

2.7. Glutathione Content.
Total GSH was determined using a GSH recycling system [21]. Liver homogenate was centrifuged at 14,000 rpm, 4°C for 20 min. The resulting upper part was mixed with the reaction mixture consisting of 6 unit ml^{-1} of GR and 1.5 mg ml^{-1} of DTNB at 25°C for 5 min and then 40 mg ml^{-1} of β-NADPH was added. The yellow colour was developed, and the absorbance was measured kinetically at 405 nm for 5 min. Total GSH was calculated using a calibration curve and expressed as nmol mg^{-1} protein. For GSSG measurement, the liver cytosol was treated with 4-vinylpyridine for 1 h before adding the reaction mixture. The GSSG content was calculated from the standard curve and expressed as nmol mg^{-1} protein. Reduced GSH content was obtained by subtracting the levels of GSSG from total GSH.

2.8. Activities of Xenobiotic-Metabolizing Enzymes.
Cytochrome P450 2E1 (CYP2E1) activity was determined by measurement of p-nitrocatechol formation from p-NP. The liver microsome was added to the reaction mixture containing assay buffer, p-NP, NADP$^+$, D-glucose-6 phosphate, MgCl$_2$•6H$_2$O, and glucose-6 phosphate dehydrogenase and then incubated for 30 min at 37°C. The reaction was halted with 10% TCA and was centrifuged at 10,000 g for 5 min. The supernatant was neutralized with NaOH. The end product, 4-nitrocatechol, was monitored at a wavelength of 535 nm [22].

UDP-glucuronosyl transferase (UGT) activity was determined using a modified method of Chariyakornkul et al. [23]. The reaction mixture containing p-NP, Tris–HCl buffer at pH 8.5, and MgCl$_2$ was preincubated with microsomal fraction at 37°C for 5 min. UDP-glucuronic acid was added to the reaction mixture, and then, this was incubated for 20 min at 37°C. After stopping the reaction with 10% TCA, the mixture was then centrifuged at 10,000 g for 5 min. The supernatant was alkalinized with 0.5 M NaOH. The

(a)

(b)
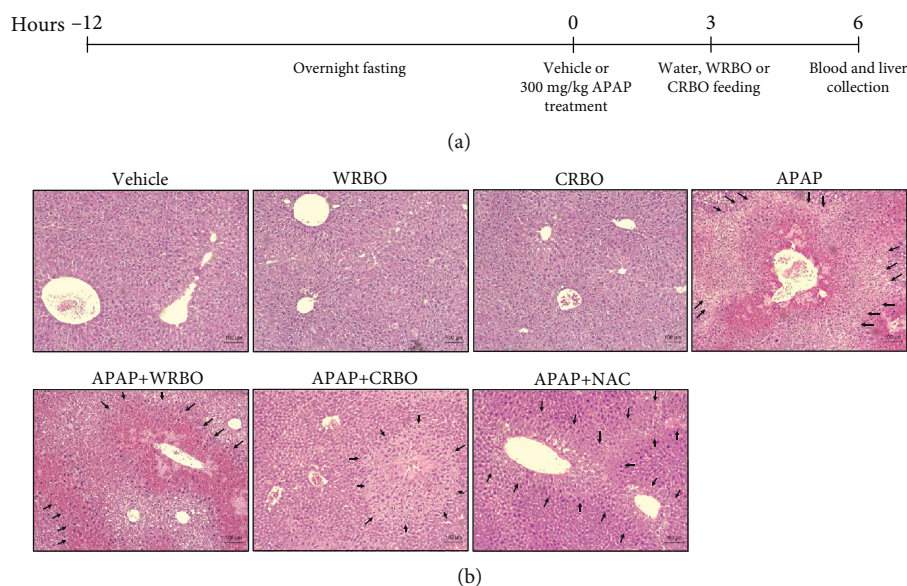
FIGURE 1: (a) The experimental protocol of RBO treatment in APAP-induced mice. Fasted male mice were orally administered with vehicle or 300 mg kg−1 BW of APAP. Three hours later, mice were administered with distilled water, WRBO, CRBO, or NAC and then euthanized six hours after APAP treatment. (b) Hepatic histomorphological changes in APAP-treated mice after RBO treatment by H&E staining under light microscopy. Micrographs are shown at 100x magnification. Arrows indicate necrotic areas. APAP: acetaminophen; WRBO: white rice bran oil 105; CRBO: coloured rice bran oil; NAC: *N*-acetylcysteine.

conjugated p-NP was quantified at 405 nm. UGT activity was expressed as pmol p-NP conjugate formed min^{-1} mg^{-1} protein.

Glutathione S-transferase (GST) activity was analysed using the method of Chariyakornkul et al. [23]. The reaction mixture contained potassium phosphate buffer at pH 6.5, GSH, CDNB, and the cytosolic fraction. The reaction was performed at 37°C for 90 s. Then, the absorbance at 340 nm was recorded and calculated using an extinction coefficient of 9.6 M^{-1} cm^{-1}.

2.9. Antioxidant Enzyme Activities.
To determine SOD activity [24], the cytosol was preincubated with a reaction mixture containing xanthine, nitroblue tetrazolium, EDTA, sodium carbonate, and BSA at 25°C for 30 min. The reaction was stopped using $CuCl_2$ after adding xanthine oxidase and further incubated at 25°C for 20 min. The production of formazan was determined at a wavelength of 560 nm. The SOD activity was expressed as unit mg^{-1} protein.

To determine CAT activity [25], the reaction mixture consisting of H_2O_2 and phosphate buffer (pH 7.0) was mixed with the cytosolic sample. CAT activity was determined by the decrease in the absorbance of H_2O_2 at a wavelength of 240 nm and expressed as nmol of H_2O_2 min^{-1} mg^{-1} protein.

To determine GPx activity [26], the reaction mixture containing Tris–EDTA buffer (pH 8), GSH, β-NADPH, t-BHP, and GR was mixed with the cytosolic fraction. The decrease of β-NADPH was proportional to GPx activity at an absorbance 340 nm. The GPx activity was expressed as unit mg^{-1} protein.

To determine GR activity [27], the reaction mixture contained liver cytosol, GSSG, β-NADPH, and potassium phosphate buffer at pH 7.0. The decrease in absorbance of β-NADPH at 340 nm was determined spectrophotometrically at 37°C. Specific activity was expressed as unit mg^{-1} of protein.

2.10. Determination of Hepatic Antioxidant and Xenobiotic-Metabolizing Enzymes and Transcription Factor Involving APAP Metabolism in mRNA Levels.
Frozen liver tissue was thawed, and mRNA was extracted using Purezol reagent (Bio-rad, Hercules, CA, USA). Extracted mRNA was reverse transcribed to cDNA using a high-capacity cDNA reverse transcription kit (Applied Biosystems, Foster City, CA, USA). The RNA levels of antioxidant and xenobiotic-metabolizing genes including SOD1, CAT, GCLC, GSTA, GPX1, and also GSR and nuclear factor erythroid-derived 2-like2 (NFE2L2) were evaluated by quantitative reverse transcription polymerase chain reaction (qRT-PCR) using specific primers with a SensiFAST™ SYBR® Lo-ROX Kit reagent (Bioline, London, UK) in the QuantStudio™ 6 Flex System (Thermo Fisher Scientific, Waltham, MA, USA). Table 1 demonstrates the primer sequences for each target gene. The amplification procedure was run at 95°C for 2 min, followed by 40 cycles at 95°C for 5 s and 60°C for 35 s. RNA expression levels of target genes were normalized with β-actin mRNA and then presented as fold induction using the $\Delta\Delta^{Ct}$ method [28].

2.11. Statistical Analysis.
All data are represented as mean ± SEM. Statistical analysis was performed using Statistical Package for the Social Sciences (SPSS) version 17.0 software (SPSS Inc., Chicago, IL, USA). The significant difference between groups in each experiment was analysed using one-way analysis of variance (ANOVA) followed by least

TABLE 1: Primer sequences of qRT-PCR.

Genes	Forward primer	Reverse primer
NFE2L2	CGAGATATACGCAGGAGAGGTAAGA	GCTCGACAATGTTCTCCAGCTT
SOD1	GTGATTGGGATTGCGCAGTA	TGGTTTGAGGGTAGCAGATGAGT
CAT	GCAGATACCTGTGAACTGTC	GTAGAATGTCCGCACCTGAG
GCLC	GCACGGCATCCTCCAGTTCCT	TCGGATGGTTGGGGTTTGTCC
GSTA	CGTCCACCTGCTGGAACTTC	GCCTTCAGCAGCGGGAAAGG
GPX1	CTCACCCGCTCTTTACCTTC	CACACCGGAGACCAAATGATG
GSR	GCTATGCAACATTCGCAGATG	AGCGGTAAACTTTTTCCCATTG
β-Actin	GTATGACTCCACTCACGGCAAA	GGTCTCGCTCCTGGAAGATG
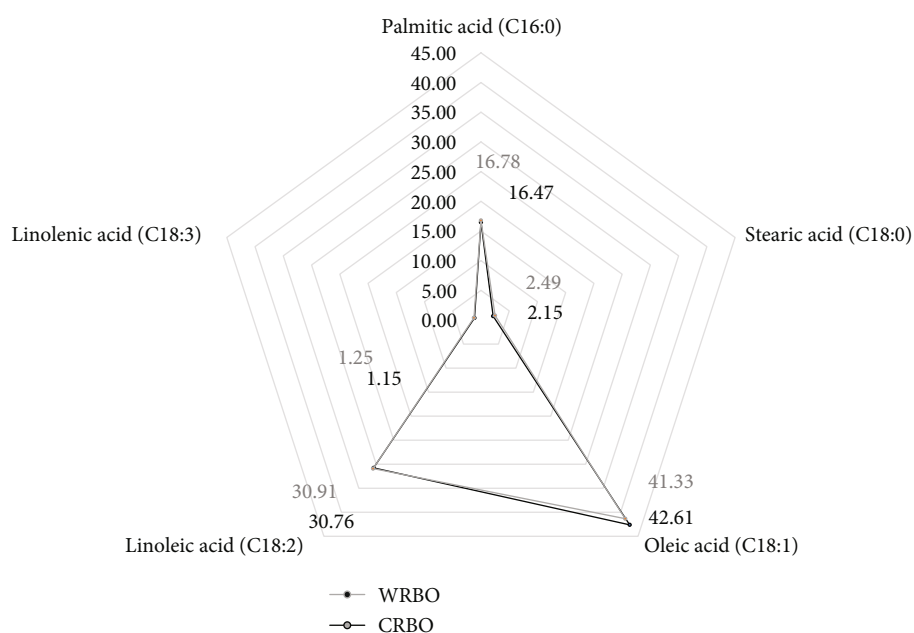
FIGURE 2: Composition of main free fatty acids in RBO analysed by gas chromatography-mass spectrometry (percentage of oil content).

significant difference (LSD) tests. Values of $p < 0.05$ were considered to be statistically significant.

3. Results

3.1. Phytonutrient and Phytochemical Composition in RBO.
First, we compared the main components in WRBO and CRBO. As summarized in Figure 2, free fatty acid profiles of WRBO and CRBO were very similar in the amounts of saturated fatty acids, monounsaturated fatty acids, and polyunsaturated fatty acids. The main free fatty acids were oleic acid, followed by linoleic acid (ω-3) and palmitic acid, respectively. Phytochemicals commonly found in RBO are shown in Table 2. With the exception of γ-oryzanols, the amounts of total vitamin E, phytosterols, carotenoids, and chlorophylls in CRBO were greater than in WRBO. The total γ-oryzanol content in WRBO (66.50 mg g^{-1} RBO) was higher than in CRBO (56.74 mg g^{-1} RBO), with β-sitosteryl ferulate being a major γ-oryzanol. While CRBO contained higher total amounts of vitamin E (1,467.24 μg g^{-1} RBO) than WRBO (1,151.41 μg g^{-1} RBO), γ-tocotrienol is a prominent vitamin E isoform in both RBOs. All isoforms of vitamin E were higher in CRBO than WRBO, with the exception of α-tocopherol and α-tocotrienol. Moreover, phytosterols, carotenoids, and chlorophylls, mainly found in edible oils, were found in large amounts in CRBO.

3.2. Hepatoprotective Effect of RBO on APAP-Induced Hepatotoxicity in Mice.
As APAP overdose causes liver damage, the changes in parameters of liver function after APAP induction were examined. APAP overdose significantly increased the levels of serum ALT in the APAP-treated group by 677-fold when compared to the control (Table 3). WRBO treatment slightly decreased serum ALT level ($p > 0.05$). While treatment with CRBO and NAC in mice three hours after APAP administration significantly decreased ALT level when compared to the APAP-treated alone group. The administration of RBO alone had no significant effect. The effect of various RBOs on the oxidative stress markers consisting of malondialdehyde (MDA), total GSH content, and GSSG/GSH ratio are also shown in Table 3. An increased MDA level and decreased total GSH content in the livers of APAP-fed mice were observed. RBO treatment alone did not affect MDA levels. However, the administration of

TABLE 2: Vitamin E, γ-oryzanol, phytosterols, carotenoids, and chlorophylls in RBO.

Compounds (μg/g rice bran oil)	WRBO	CRBO
Vitamin E		
α-Tocopherol	260.2 ± 2.7	$196.9 \pm 2.2^*$
β-Tocopherol	28.4 ± 0.1	$42.7 \pm 0.2^*$
γ-Tocopherol	77.7 ± 1.9	$251.7 \pm 1.7^*$
δ-Tocopherol	Nondetectable	14.4 ± 0.3
α-Tocotrienol	119.6 ± 1.7	$110.1 \pm 1.0^*$
γ-Tocotrienol	590 ± 3.9	$797.5 \pm 7.8^*$
δ-Tocotrienol	40.0 ± 0.1	$54.0 \pm 0.2^*$
Total	$1,151.4 \pm 10.0$	$1,467.2 \pm 12.6^*$
γ-Oryzanols		
Cycloartanyl ferulate	$12,094 \pm 40$	$8,312 \pm 6^*$
24-Methylene Cycloartanyl ferulate	$12,043 \pm 24$	$12,372 \pm 11^*$
Campesteryl ferulate	$18,726 \pm 97$	$17,709 \pm 2^*$
β-Sitosteryl ferulate	$23,636 \pm 318$	$18,074 \pm 64^*$
Total	$66,498 \pm 398$	$56,467 \pm 57^*$
Phytosterols		
Stigmasterol+campesterol	458 ± 2	$812 \pm 1^*$
β-Sitosterol	$1,152 \pm 6$	$5,196 \pm 9^*$
Total	$1,610 \pm 8$	$6,008 \pm 8^*$
Carotenoids	6.48 ± 0.99	$9.82 \pm 0.50^*$
Chlorophylls	9.53 ± 1.67	$32.58 \pm 1.24^*$

Values are shown as mean $\pm$ SEM of three independent experiments. *Significantly different from WRBO group ($p < 0.05$).

TABLE 3: The alteration of some liver injury and oxidative stress markers in APAP-induced mice after administration of various RBOs.

Treatment	Serum ALT ($U L^{-1}$)	Hepatic MDA (nmol mg^{-1} protein)	Hepatic total GSH (nmol mg^{-1} protein)	GSSG/GSH ratio
Vehicle	28 ± 9	0.326 ± 0.114	42.09 ± 3.75	0.31 ± 0.01
WRBO	$61 \pm 10^{\#}$	$0.306 \pm 0.033^{\#}$	$40.25 \pm 2.16^{\#}$	0.30 ± 0.04
CRBO	$52 \pm 7^{\#}$	$0.291 \pm 0.025^{\#}$	$42.43 \pm 1.07^{\#}$	0.30 ± 0.05
APAP	$16,625 \pm 5,419^*$	$0.556 \pm 0.182^*$	$14.66 \pm 5.17^*$	0.27 ± 0.01
APAP+WRBO	$14,082 \pm 4,907^*$	$0.520 \pm 0.063^*$	$11.64 \pm 1.95^{*,\$}$	0.31 ± 0.02
APAP+CRBO	$1,743 \pm 617^{\#}$	$0.187 \pm 0.064^{*,\#}$	$29.26 \pm 5.00^{\#,\$}$	0.29 ± 0.03
APAP+NAC	$6,764 \pm 1,634^{\#}$	$0.217 \pm 0.096^{\#}$	$69.78 \pm 8.24^{*,\#}$	0.28 ± 0.01

Values are represented as mean $\pm$ SEM ($n = 6$). *Significantly different from a vehicle group ($p < 0.05$). $^{\#}$Significantly different from APAP group ($p < 0.05$). $^{\$}$Significantly different from APAP+NAC group ($p < 0.05$). ALT: alanine aminotransferase; MDA: malondialdehyde; APAP: acetaminophen; WRBO: white rice bran oil; CRBO: coloured rice bran oil; NAC: N-acetylcysteine.

APAP, followed by CRBO or NAC feeding, could attenuate the increase of MDA levels observed in the APAP group ($p < 0.05$). The administration of CRBO and NAC restored liver total GSH levels in the APAP-treated group, which NAC is the most effective in GSH regeneration. Unexpectedly, the ratio of GSSG/GSH was not significantly different in all groups. These results show the hepatoprotective properties of CRBO in APAP-induced liver damage.

3.3. Effect of RBO on Mice Hepatic Histomorphological Changes in APAP-Induced Mice. Representative images of

the H&E-stained liver sections are shown in Figure 1(b). The livers of the control group showed the normal appearance of hepatic structure with normal central vein and hepatic lobule. The central vein was surrounded by normal hepatic cords and sinusoids. Similarly, the sections of liver tissue from mice treated with RBO alone had similar hepatic histomorphological patterns. In contrast, the livers of the APAP-treated alone group presented a large area of hepatocellular necrosis and inflammation. The congested central vein was filled with red blood cells and enclosed by hepatic cords with sinusoidal dilatation. Pyknosis and
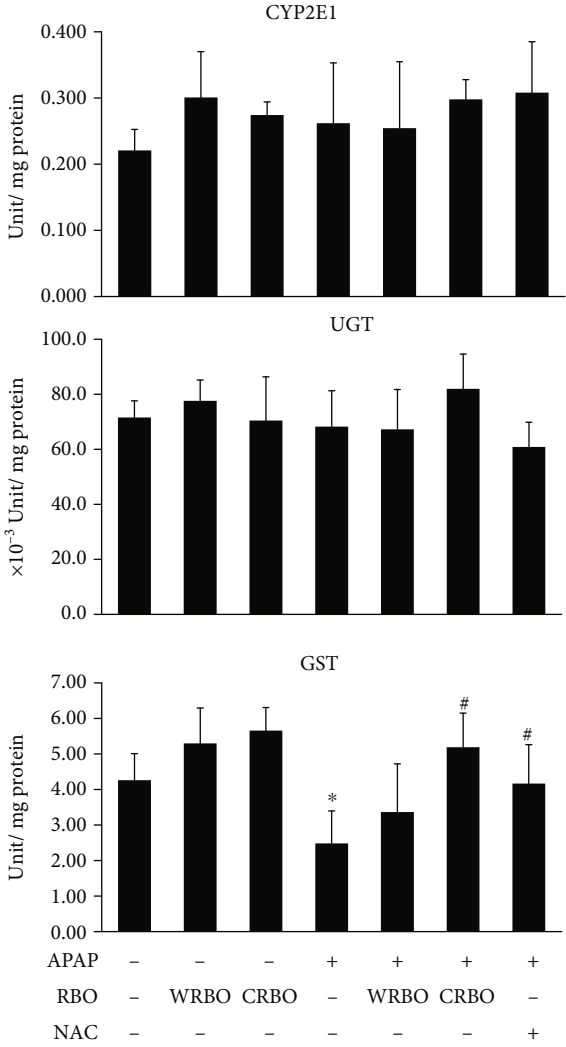
(a)

FIGURE 3: Continued.
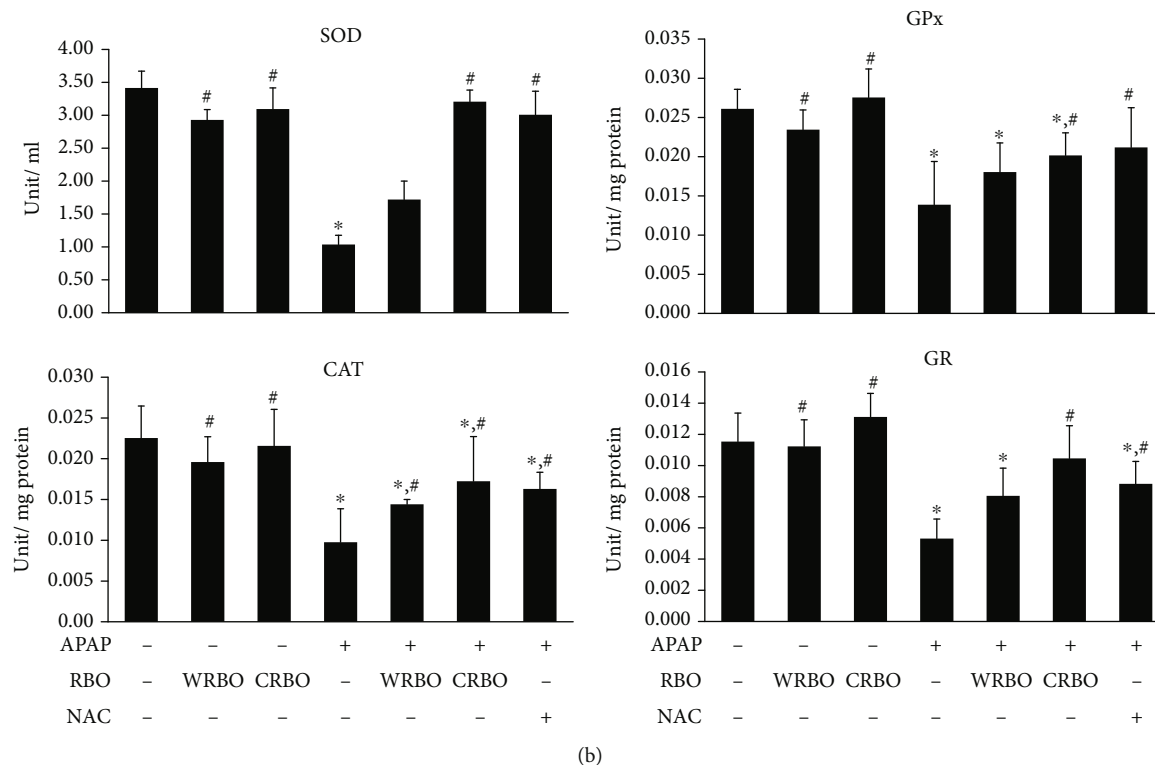
FIGURE 3: Effect of RBO administration on the activities of hepatic xenobiotic-metabolizing and antioxidant enzymes in mice. (a) APAP-metabolizing enzyme activities including CYP2E1, UGT, and GST. (b) Antioxidant enzyme activities including SOD, CAT, GPx, and GR. Results are expressed as mean ± SEM ($n = 6$). $^*p < 0.05$ significantly different from vehicle. $^\#p < 0.05$ indicates significant difference from APAP. CYP2E1: cytochrome P450 2E1; UGT: UDP-glucuronosyltransferase; GST: glutathione S-transferase; SOD: superoxide dismutase; CAT: catalase; GPx: glutathione peroxidase; GR: glutathione reductase; APAP: acetaminophen; RBO: rice bran oil; WRBO: white rice bran oil; CRBO: coloured rice bran oil; NAC: N-acetylcysteine.

neutrophilic and lymphocytic infiltration were also markedly detected. Interestingly, administration of CRBO or NAC after APAP treatment showed an amelioration of APAP hepatotoxicity with the presence of a mild necrotic area with the recovery of liver architecture.

3.4. APAP-Metabolizing and Antioxidant Enzyme Activities in the Liver. The beneficial effects of RBO on detoxifying and antioxidant systems are shown in Figure 3. The changes of APAP-metabolizing enzyme activity including CYP2E1 and UGT could not be observed in all treatments. However, the activity of GST was significantly ($p < 0.05$) decreased in APAP-treated mice compared to the control. After CRBO or NAC administration, the activity of this enzyme was increased significantly ($p < 0.05$) three hours later compared to the APAP-treated alone group (Figure 3(a)). As can be seen in Figure 3(b), the data demonstrated that treatment with APAP caused a significant decrease in the activities of hepatic antioxidant enzymes including SOD, CAT, GPx, and GR compared with those of the control mice. Administration of RBO alone caused insignificant increase of the activity of each enzyme in the liver compared to the control mice. In addition, the administration of CRBO or NAC significantly increased SOD, CAT, GPx, and GR activity in the liver compared with the APAP-treated alone group.

3.5. Expression of APAP-Metabolizing and Antioxidant Response Genes in the Liver. Treatment with CRBO or NAC improved GST, SOD, CAT, GPx, and GR activities in the livers of APAP-treated mice. Thus, qRT-PCR analysis for gene expression of these antioxidant enzymes and transcription factors was performed and the results are shown in Figure 4. The expression of transcription factor NFE2L2 and antioxidant responsive genes including GSTA1, GCLC, SOD1, CAT, GPX1, and GSR were increased in mice fed with APAP ($p < 0.05$). The administration of WRBO, CRBO, or NAC in APAP-treated mice did not affect the expression of SOD1, CAT, GPX1, and GSR genes when compared to APAP-administered alone group. Treatment with WRBO, CRBO, and NAC after APAP induction showed the increased mRNA levels of GSTA when compared to APAP-treated alone group. GSTA mRNA was highly expressed in the APAP with CRBO-fed group. Furthermore, the mRNA level GCLC (catalytic unit of glutathione biosynthesis enzyme) was significantly increased in the mice treated with APAP together with CRBO or NAC compared to the group treated with APAP alone. Interestingly, CRBO treatment enhanced the NFE2L2 gene for the oxidative response-transcription factor ($p < 0.05$) at the mRNA level in APAP-induced mice. These results show that CRBO improved the antioxidant properties not only at the level of enzyme activities, but also in transcriptional level.
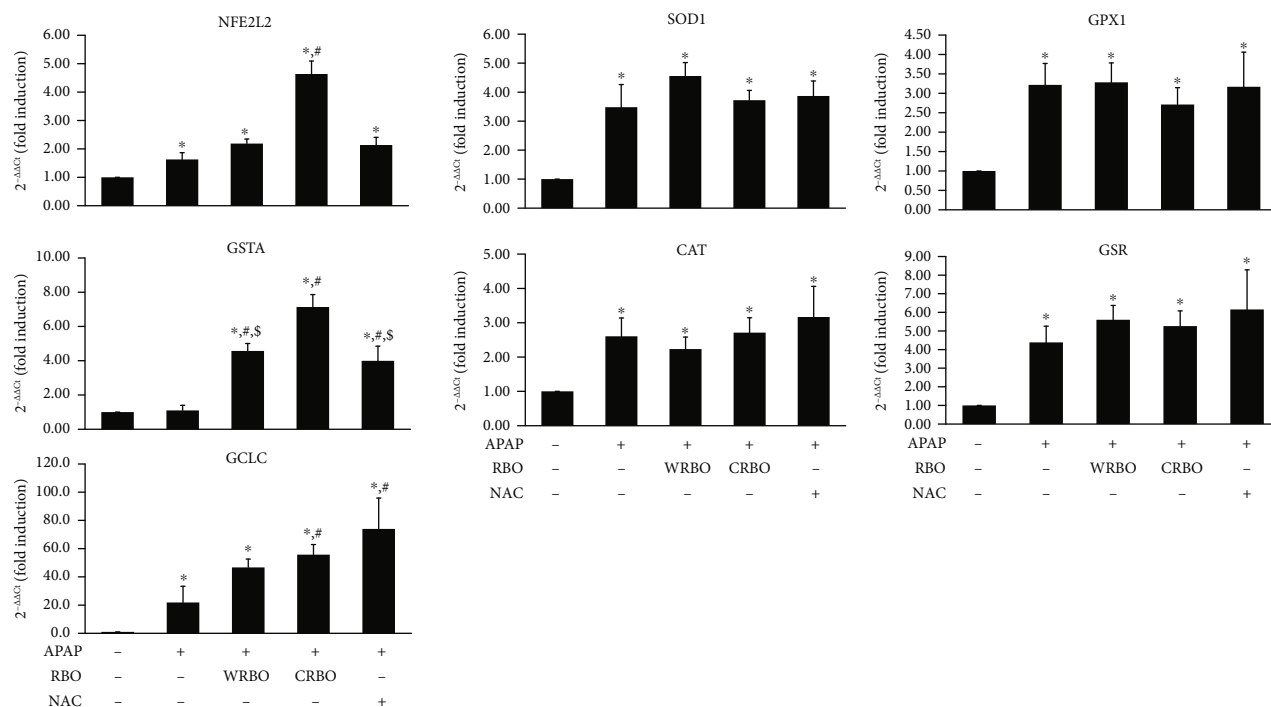
Figure 4: Effect of RBO administration on mRNA levels of antioxidant responsive genes in the livers of APAP-treated mice. Results are expressed as mean $\pm$ SD ($n = 6$). $^*p < 0.05$ significantly different from vehicle. $^\#p < 0.05$ indicates significantly different from APAP. $^\$p < 0.05$ significantly different from APAP+CRBO. NFE2L2: nuclear factor erythroid-derived 2-like2; GSTA: glutathione S-transferase A1; GCLC: glutamate-cysteine ligase catalytic subunit; SOD1: superoxide dismutase 1; CAT: catalase; GPX1: glutathione peroxidase 1; GSR, glutathione reductase; APAP: acetaminophen; RBO: rice bran oil; WRBO: white rice bran oil; CRBO: coloured rice bran oil; NAC: N-acetylcysteine.

4. Discussion

Under abnormal environmental stress, the overproduction of RONS causes significant damage to important biomolecules. This damage may occur to cell structures and functions and has a potential impact on several pathological effects. Natural and synthetic antioxidants could reduce the incidence of oxidative stress-mediated diseases. The study of the antioxidant activities from various bioactive compounds such as dietary fiber, phenolic compounds, tocols, phytic acid, and phytosterols is of growing interest in clinical trials [29]. Comparative studies showed that coloured rice bran contained higher amounts of phytochemicals such as γ-oryzanols and vitamin E than white rice bran and also showed higher antioxidant activities [30, 31]. Coloured rice bran extract showed greater antiproliferative activity than brown rice bran extract against MCF-7 and MDA-MB-231 breast cancer cell lines [32]. In addition, defatted sticky purple rice bran extract could inhibit preneoplastic lesion formation of carcinogen-induced hepatocarcinogenesis in rats with five weeks of treatment compared with white rice bran extract by attenuation of inflammation and cell proliferation [33]. Even though rice bran has been reported, studies comparing RBOs are few. Sengupta et al. [34] reported an antioxidative effect of RBO in arsenite-induced oxidative stress in rats by improvement of CAT, SOD, GPx, and GR activity and the inhibition of lipid peroxidation. The present study shows that RBO

obtained from coloured rice (Riceberry) also reduced hepatotoxicity and exhibited antioxidant activities in mice given an overdose of APAP.

APAP or N-acetyl-p-aminophenol is commonly used to treat pain and fever [35]. APAP usage at recommended therapeutic concentrations is important because an overdose of APAP can cause oxidative stress and then severe liver damage, resulting in acute liver failure. APAP overdose-induced liver hepatotoxicity is a well-known drug-induced liver injury. It is the most common cause of acute liver failure in several countries, replacing viral hepatitis [36]. Extensive oxidative stress is a characteristic of APAP hepatotoxicity during APAP metabolism. Detoxification of APAP is mainly catalyzed in the liver by UGT and sulfotransferases (SULT) at therapeutic doses. However, APAP overdose is metabolized by CYP2E1 to the active metabolite N-acetyl-p-benzoquinone imine (NAPQI) and excreted as the glutathione conjugated form by GST. Excess NAPQI can deplete hepatic GSH stores and adduct target proteins through binding their cysteine groups, especially mitochondrial proteins. Impairment of the mitochondrial electron transport system causes ROS formation, mitochondrial permeability transition (MPT), oxidative stress, and finally oncotic necrosis [16].

The classical mechanism of liver tissue damage by hepatotoxins such as APAP is hepatocellular enzyme leakage as diagnosed by increased serum ALT [37]. An abnormal ALT

was observed in APAP-treated mice in this study. CRBO reduced the increased ALT activities from an overdose of APAP. The hepatoprotective effect of CRBO was similar to NAC treatment, which is widely used as a therapeutic drug for liver failure from APAP poisoning [38]. Furthermore, liver necrosis and failure from APAP overdose could be observed by histopathological alteration. Consistent with the ALT level result, administration of 300 mg kg^{-1} BW of APAP caused markedly developed hepatocellular necrosis in cross sections of liver tissue, similar to those observed previously in mice [39]. Administration of CRBO gave liver sections with nearly normal architectures and normal hepatocytes in APAP-induced mice. Lipid peroxidation is one consequence of oxidative stress promoted by high intracellular concentrations of ROS. MDA is a well-known biomarker of oxidative stress produced by the reaction of polyunsaturated fatty acid peroxidation [40]. Overproduction of MDA is correlated with APAP-induced tissue damage. The results showed that a significantly increased MDA level in the livers of APAP-treated mice was decreased by administration of CRBO or NAC, indicating their properties to inhibit lipid peroxidation. These findings suggested the possibility of using the hepatoprotective effect of CRBO as shown by the significant recovery from hepatic necrosis, concurrently with decreased serum ALT levels.

At therapeutic doses, APAP is mostly converted to inactive glucuronide and sulfated conjugates by UGT and SULT, respectively. APAP also is marginally metabolized by cytochrome P450 to form the highly reactive species NAPQI, which is readily detoxified with GSH conjugation by glutathione S-transferase under normal conditions. However, saturation of detoxification pathways by APAP overdose causes the depletion of GSH and overproduction of NAPQI, mostly metabolized by CYP2E1 which directly binds to cellular biomolecules. The binding on cysteine residues of protein in mitochondria can cause mitochondria dysfunction including electron transport inhibition, mitochondrial oxidative stress, and onset mitochondrial permeability transition. This results in decreased energy production and finally cellular necrosis [41]. The results show that the activity of UGT and CYP2E1 did not alter in both APAP-treated alone and APAP treated with RBO groups when compared to the control group. Glucuronidation causes saturation at highly toxic doses, while CYP2E1 activity was raised 1 hour after APAP administration [41, 42]. Our data indicate UGT and CYP2E1 might not be involved in the hepatoprotective effect of RBO. However, GST could increase the activity in APAP-treated mice after the administration of CRBO or NAC 3 hours later. GST expressed higher activity than the other xenobiotic-metabolizing and antioxidant enzymes due to the lower K_m for NAPQI (15 μM), which suggested a critical role of GST in NAPQI detoxification by GSH to form APAP–GSH adducts [43]. This was also related to total GSH contents. GSH is a crucial cellular antioxidant which is maintained at a certain level in cells [44]. The quantity of total GSH in mice livers was decreased after 1 hour of overdose of APAP at 300 mg/kg bw until 6 hours and was then steadily regenerated [39]. Our results confirmed that hepatic GSH levels

had significantly decreased after 6 hours of APAP administration when compared to the vehicle group. Treatment with CRBO or NAC increased GSH levels 3 hours after APAP treatment. As expected, NAC, a precursor for GSH biosynthesis, might allow more GSH for detoxification of NAPQI. In addition, the hepatic GSSG/GSH ratio in mice increased significantly after 6 hours, which might be attributed to oxidative stress in mouse livers [39]. Unfortunately, the ratio of GSSG : GSH in this study did not show any substantial changes in each group. Glutathione might be destroyed by acetaminophen rather than oxidized by free radicals. Interestingly, the results suggest that CRBO treatment could accelerate GSH recovery and then promote GST activity in APAP-treated mice to play a critical role in NAPQI detoxification by GSH to form APAP–GSH adducts. Therefore, one mechanism of hepatoprotection from CRBO could involve APAP metabolism by conjugation with GSH, leading to reduction of oxidative stress.

SOD, CAT, GPx, and GR are the main endogenous enzymatic defence systems for preventing damage by oxidative stress of aerobic cells [4]. The results show that each antioxidant enzyme had decreased activity in the APAP-treated mice group due to excessive production of ROS. This suggested they had a critical role in the prevention of APAP hepatotoxicity. Treatment with CRBO and NAC could recover levels of SOD, CAT, GPx, and GR activities in APAP-induced mice when compared to the APAP-treated alone group. SOD had the highest activity compared with the activities of the other antioxidant enzymes. The reaction of superoxide with SOD is first order and has the greatest k_{cat}/K_m with respect to superoxide concentration for the defence of living cells exposed to oxygen [45]. The results show that CRBO has antioxidant properties leading to lowering the oxidative stress induced by APAP.

Nuclear factor erythroid 2-related factor 2 (Nrf2) is a key transcription factor encoded by the NFE2L2 gene that controls the expression of antioxidants and phase II of xenobiotic-metabolizing genes to regulate both normal and oxidative stress conditions. ROS activate the dissociation of Nrf2 from Keap1 and consequently translocate and bind to the antioxidant response element (ARE) in the nucleus, inducing the expression of ARE-responsive genes such as GSR, GCLM, GCLC, GPX, HMOX, G6PD1 [46]. CRBO administration significantly increased mRNA levels of NFE2L2, GSTA, and GCLC in the hepatocytes of APAP-treated mice. These results suggest that CRBO not only exhibited antioxidant properties in the activity levels, but this was also induced in gene expression levels. Therefore, CRBO is a promising target as an antioxidative agent.

RBO contains not only an abundance of polyunsaturated fatty acids but also a great source of phytochemicals including γ-oryzanols, tocotrienols, tocopherols, and phytosterols providing balancing oxidation-reduction properties with health benefits [47]. Despite having similar fatty acid profiles, WRBO contained a higher amount of γ-oryzanols, while levels of tocopherols, tocotrienols, phytosterols, carotenoids, and chlorophylls were higher in CRBO. According to the equal concentration of γ-oryzanols in the RBOs in this study,

CRBO showed effective antioxidant properties. This might be due to higher levels of vitamin E, phytosterols, and plant pigments in CRBO compared with WRBO. Previous reports have shown that oral supplementation of 200 mg/kg BW of tocotrienol rich fraction (one gram contains 41.02, 6.58, 9.96, and 23.8 mg of α-tocotrienol, β-tocotrienol, γ-tocotrienol, and δ-tocotrienol, respectively) caused increased gene and protein expression of hepatic GST isoenzymes in mice [48]. Oral administration of δ-tocotrienol at 300 mg twice daily for 12 weeks showed greater efficacy than a placebo by decreasing oxidative stress markers including serum ALT, high-sensitivity C-reactive protein, and MDA in patients with nonalcoholic fatty liver disease [49]. Furthermore, oral feeding at 25 mg/kg BW of β-sitosterol modulated liver function enzymes, lipid peroxidation, and increased intracellular SOD and CAT activities in carbon tetrachloride-induced oxidative stress and liver toxicity in rats [50]. Carotenoids have also shown hepatoprotective effects by restoring the antioxidant enzymes levels in the livers of APAP-treated mice after they received 10 mg/kg BW of β-carotene [51]. Other plant pigments, such as 13.54 mg/kg BW of chlorophyll in 50 mg/kg BW of pigment–protein complex, could reduce the carbon tetrachloride-induced elevation of MDA, serum ALT, and AST activities and also restored suppressed hepatic SOD, CAT, and GPx activities in mice [52]. From the administration of γ-oryzanols at 100 mg/kg BW in each of the RBO treatment groups, CRBO-treated mice obtained higher amounts of total tocotrienol, δ-tocotrienol, β-sitosterol, carotenoids, and chlorophyll (1,702, 95.58, 9,197, 17.38, and 57.67 μg/kg BW, respectively) than WRBO-treated mice (1,127, 60.16, 1,732, 9.74, and 14.33 μg/kg BW, respectively). These concentrations of each compound might not be the effective doses as shown in the above reports but could synergize activity of CRBO on the amelioration of APAP toxicity. Our work suggests that CRBO could be a promising product as it is a proven antioxidant.

5. Conclusion

CRBO exhibited greater antioxidant potential than WRBO. The administration of CRBO attenuated hepatotoxicity induced by APAP overdose in mice through the activation of antioxidant systems and the interruption of APAP metabolism by restoring GSH and also increasing GST activity in NAPQI detoxification in the liver. The antioxidant phytonutrients and phytochemicals in CRBO included tocotrienols, phytosterols, carotenoids, and chlorophyll.

Data Availability

No data were used to support this study.

Conflicts of Interest

The authors declare that there is no conflict of interest regarding the publication of this paper.

References

[1] S. Reuter, S. C. Gupta, M. M. Chaturvedi, and B. B. Aggarwal, "Oxidative stress, inflammation, and cancer: how are they linked?," *Free Radical Biology & Medicine*, vol. 49, no. 11, pp. 1603–1616, 2010.

[2] A. Phaniendra, D. B. Jestadi, and L. Periyasamy, "Free radicals: properties, sources, targets, and their implication in various diseases," *Indian Journal of Clinical Biochemistry*, vol. 30, no. 1, pp. 11–26, 2015.

[3] I. Liguori, G. Russo, F. Curcio et al., "Oxidative stress, aging, and diseases," *Clinical Interventions in Aging*, vol. Volume 13, pp. 757–772, 2018.

[4] E. Birben, U. M. Sahiner, C. Sackesen, S. Erzurum, and O. Kalayci, "Oxidative stress and antioxidant defense," *World Allergy Organization Journal*, vol. 5, no. 1, pp. 9–19, 2012.

[5] J. Q. Wu, T. R. Kosten, and X. Y. Zhang, "Free radicals, antioxidant defense systems, and schizophrenia," *Progress in Neuro-Psychopharmacology & Biological Psychiatry*, vol. 46, pp. 200–206, 2013.

[6] A. M. Pisoschi and A. Pop, "The role of antioxidants in the chemistry of oxidative stress: a review," *European Journal of Medicinal Chemistry*, vol. 97, pp. 55–74, 2015.

[7] M. Futakuchi, J. L. Cheng, M. Hirose et al., "Inhibition of conjugated fatty acids derived from safflower or perilla oil of induction and development of mammary tumors in rats induced by 2-amino-1-methyl-6-phenylimidazo[4,5- _b_]pyridine (PhIP)," *Cancer Letters*, vol. 178, no. 2, pp. 131–139, 2002.

[8] M. Vafa, N. Haghighat, N. Moslehi, S. Eghtesadi, and I. Heydari, "Effect of tocotrienols enriched canola oil on glycemic control and oxidative status in patients with type 2 diabetes mellitus: a randomized double-blind placebo-controlled clinical trial," *Journal of Research in Medical Sciences*, vol. 20, no. 6, pp. 540–547, 2015.

[9] M. Gorzynik-Debicka, P. Przychodzen, F. Cappello et al., "Potential health benefits of olive oil and plant polyphenols," *International Journal of Molecular Sciences*, vol. 19, no. 3, p. 686, 2018.

[10] E. Hsu and S. Parthasarathy, "Anti-inflammatory and antioxidant effects of sesame oil on atherosclerosis: a descriptive literature review," *Cureus*, vol. 9, no. 7, 2017.

[11] I. Khémiri, B. Essghaier, N. Sadfi-Zouaoui, and L. Bitri, "Antioxidant and antimicrobial potentials of seed oil from Carthamus tinctorius L. in the management of skin injuries," *Oxidative Medicine and Cellular Longevity*, vol. 2020, Article ID 4103418, 12 pages, 2020.

[12] O.-M. Lai, J. J. Jacoby, W.-F. Leong, and W.-T. Lai, *Chapter 2-nutritional studies of rice bran oil*, L.-Z. Cheong and X. Xu, Eds., in Rice Bran and Rice Bran Oil, AOCS Press, 2019.

[13] P. Pokkanta, P. Sookwong, M. Tanang, S. Setchaiyan, P. Boontakham, and S. Mahatheeranont, "Simultaneous determination of tocols, γ-oryzanols, phytosterols, squalene, cholecalciferol and phylloquinone in rice bran and vegetable oil samples," *Food Chemistry*, vol. 271, pp. 630–638, 2019.

[14] E. Kobayashi, J. Ito, N. Shimizu et al., "Evaluation of γ-oryzanol accumulation and lipid metabolism in the body of mice following long-term administration of γ-oryzanol," *Nutrients*, vol. 11, no. 1, p. 104, 2019.

[15] Z. Xu, N. Hua, and J. S. Godber, "Antioxidant activity of tocopherols, tocotrienols, and γ-oryzanol components from rice bran against cholesterol oxidation accelerated by 2, 2′-azobis (2-methylpropionamidine) dihydrochloride," *Journal of Agricultural and Food Chemistry*, vol. 49, no. 4, pp. 2077–2081, 2001.

[16] H. Jaeschke, M. R. McGill, and A. Ramachandran, "Oxidant stress, mitochondria, and cell death mechanisms in drug-induced liver injury: lessons learned from acetaminophen hepatotoxicity," *Drug Metabolism Reviews*, vol. 44, no. 1, pp. 88–106, 2012.

[17] K. Pintha, S. Yodkeeree, P. Pitchakarn, and P. Limtrakul, "Anti-invasive activity against cancer cells of phytochemicals in red jasmine rice (Oryza sativa L.)," *Asian Pacific Journal of Cancer Prevention*, vol. 15, no. 11, pp. 4601–4607, 2014.

[18] S. H. Huang and L. T. Ng, "Quantification of tocopherols, tocotrienols, and γ-Oryzanol contents and their distribution in some commercial rice varieties in Taiwan," *Journal of Agricultural and Food Chemistry*, vol. 59, no. 20, pp. 11150–11159, 2011.

[19] R. S. Pohndorf, T. R. S. Cadaval, and L. A. A. Pinto, "Kinetics and thermodynamics adsorption of carotenoids and chlorophylls in rice bran oil bleaching," *Journal of Food Engineering*, vol. 185, pp. 9–16, 2016.

[20] S. A. Noeman, H. E. Hamooda, and A. A. Baalash, "Biochemical study of oxidative stress markers in the liver, kidney and heart of high fat diet induced obesity in rats," *Diabetology & Metabolic Syndrome*, vol. 3, no. 1, 2011.

[21] I. H. Shaik and R. Mehvar, "Rapid determination of reduced and oxidized glutathione levels using a new thiol-masking reagent and the enzymatic recycling method: application to the rat liver and bile samples," *Analytical and Bioanalytical Chemistry*, vol. 385, no. 1, pp. 105–113, 2006.

[22] T. K. Chang, C. L. Crespi, and D. J. Waxman, "Spectrophotometric analysis of human CYP2E1-catalyzed p-nitrophenol hydroxylation," *Methods in Molecular Biology*, vol. 320, pp. 127–131, 2006.

[23] A. Chariyakornkul, C. Punvittayagul, S. Taya, and R. Wongpoomchai, "Inhibitory effect of purple rice husk extract on AFB1-induced micronucleus formation in rat liver through modulation of xenobiotic metabolizing enzymes," *BMC Complementary Medicine and Therapies*, vol. 19, no. 1, 2019.

[24] Y. Sun, L. W. Oberley, and Y. Li, "A simple method for clinical assay of superoxide dismutase," *Clinical Chemistry*, vol. 34, no. 3, pp. 497–500, 1988.

[25] H. Aebi, "[13] Catalase _in vitro_," *Methods in Enzymology*, vol. 105, pp. 121–126, 1984.

[26] N. Nagalakshmi and M. N. Prasad, "Responses of glutathione cycle enzymes and glutathione metabolism to copper stress in _Scenedesmus bijugatus_," *Plant Science*, vol. 160, no. 2, pp. 291–299, 2001.

[27] I. Carlberg and B. Mannervik, "[59] Glutathione reductase," *Methods in Enzymology*, vol. 113, pp. 484–490, 1985.

[28] S. Y. Hung, H. H. Lin, K. T. Yeh, and J. G. Chang, "Histone-modifying genes as biomarkers in hepatocellular carcinoma," *International Journal of Experimental Pathology*, vol. 7, no. 5, pp. 2496–2507, 2014.

[29] P. Suttiarporn, W. Chumpolsri, S. Mahatheeranont, S. Luangkamin, S. Teepsawang, and V. Leardkamolkarn, "Structures of phytosterols and triterpenoids with potential anti-cancer activity in bran of black non-glutinous rice," *Nutrients*, vol. 7, no. 3, pp. 1672–1687, 2015.

[30] A. Ghasemzadeh, A. Baghdadi, H. Z. E. Jaafar, M. Swamy, and P. M. Wahab, "Optimization of flavonoid extraction from red and brown rice bran and evaluation of the antioxidant properties," *Molecules*, vol. 23, no. 8, p. 1863, 2018.

[31] S. Mingyai, A. Kettawan, K. Srikaeo, and R. Singanusong, "Physicochemical and antioxidant properties of rice bran oils produced from colored rice using different extraction methods," *Journal of Oleo Science*, vol. 66, no. 6, pp. 565–572, 2017.

[32] A. Ghasemzadeh, M. T. Karbalaii, H. Z. E. Jaafar, and A. Rahmat, "Phytochemical constituents, antioxidant activity, and antiproliferative properties of black, red, and brown rice bran," *Chemistry Central journal*, vol. 12, no. 1, p. 17, 2018.

[33] A. Dokkaew, C. Punvittayagul, O. Insuan, P. Limtrakul Dejkriengkraikul, and R. Wongpoomchai, "Protective effects of defatted sticky rice bran extracts on the early stages of hepatocarcinogenesis in rats," *Molecules*, vol. 24, no. 11, p. 2142, 2019.

[34] A. Sengupta, M. Ghosh, and D. K. Bhattacharyya, "Antioxidative effect of rice bran oil and medium chain fatty acid rich rice bran oil in arsenite induced oxidative stress in rats," *Journal of Oleo Science*, vol. 63, no. 11, pp. 1117–1124, 2014.

[35] G. G. Graham and K. F. Scott, "Mechanism of action of paracetamol," *American Journal of Therapeutics*, vol. 12, no. 1, pp. 46–55, 2005.

[36] Z. Wang, W. Hao, J. Hu et al., "Maltol improves APAP-induced hepatotoxicity by inhibiting oxidative stress and inflammation response via NF-κB and PI3K/Akt signal pathways," *Antioxidants*, vol. 8, no. 9, p. 395, 2019.

[37] L. J. Chun, M. J. Tong, R. W. Busuttil, and J. R. Hiatt, "Acetaminophen hepatotoxicity and acute liver failure," *Journal of Clinical Gastroenterology*, vol. 43, no. 4, pp. 342–349, 2009.

[38] T. N. Athuraliya and A. L. Jones, "Prolonged N-acetylcysteine therapy in late acetaminophen poisoning associated with acute liver failure–a need to be more cautious?," *Critical Care*, vol. 13, no. 3, p. 144, 2009.

[39] M. R. McGill, C. D. Williams, Y. Xie, A. Ramachandran, and H. Jaeschke, "Acetaminophen-induced liver injury in rats and mice: comparison of protein adducts, mitochondrial dysfunction, and oxidative stress in the mechanism of toxicity," *Toxicology and Applied Pharmacology*, vol. 264, no. 3, pp. 387–394, 2012.

[40] D. Grotto, L. S. Maria, J. Valentini et al., "Importance of the lipid peroxidation biomarkers and methodological aspects for malondialdehyde quantification," *Química Nova*, vol. 32, no. 1, pp. 169–174, 2009.

[41] L. L. Mazaleuskaya, K. Sangkuhl, C. F. Thorn, G. A. Fitz Gerald, R. B. Altman, and T. E. Klein, "PharmGKB summary," *Pharmacogenetics and Genomics*, vol. 25, no. 8, pp. 416–426, 2015.

[42] M. R. McGill, M. R. Sharpe, C. D. Williams, M. Taha, S. C. Curry, and H. Jaeschke, "The mechanism underlying

acetaminophen-induced hepatotoxicity in humans and mice involves mitochondrial damage and nuclear DNA fragmentation," *Journal of Clinical Investigation*, vol. 122, no. 4, pp. 1574–1583, 2012.

[43] R. Ben-Shachar, Y. Chen, S. Luo, C. Hartman, M. Reed, and H. F. Nijhout, "The biochemistry of acetaminophen hepatotoxicity and rescue: a mathematical model," *Theoretical Biology and Medical Modelling*, vol. 9, no. 1, p. 55, 2012.

[44] H. J. Forman, H. Zhang, and A. Rinna, "Glutathione: overview of its protective roles, measurement, and biosynthesis," *Molecular Aspects of Medicine*, vol. 30, no. 1-2, pp. 1–12, 2009.

[45] T. Fukai and M. Ushio-Fukai, "Superoxide dismutases: role in redox signaling, vascular function, and diseases," *Antioxidants & Redox Signaling*, vol. 15, no. 6, pp. 1583–1606, 2011.

[46] E. Kansanen, S. M. Kuosmanen, H. Leinonen, and A.-L. Levonen, "The Keap1-Nrf2 pathway: Mechanisms of activation and dysregulation in cancer," *Redox Biology*, vol. 1, no. 1, pp. 45–49, 2013.

[47] M. Sohail, A. Rakha, M. S. Butt, M. J. Iqbal, and S. Rashid, "Rice bran nutraceutics: a comprehensive review," *Critical Reviews in Food Science and Nutrition*, vol. 57, no. 17, pp. 3771–3780, 2017.

[48] A. Atia, N. Alrawaiq, and A. Abdullah, "The effect of tocotrienol-rich fraction on the expression of glutathione S-transferase isoenzymes in mice liver," *Sains Malaysiana*, vol. 47, no. 11, pp. 2799–2809, 2018.

[49] M. A. Pervez, D. A. Khan, A. Ijaz, and S. Khan, "Effects of delta-tocotrienol supplementation on liver enzymes, inflammation, oxidative stress and hepatic steatosis in patients with nonalcoholic fatty liver disease," *Turkish Journal of Gastroenterology*, vol. 29, no. 2, pp. 170–176, 2018.

[50] E. Devaraj, A. Roy, G. Royapuram Veeraragavan et al., "β-Sitosterol attenuates carbon tetrachloride-induced oxidative stress and chronic liver injury in rats," *Naunyn-Schmiedeberg's Archives of Pharmacology*, vol. 393, no. 6, pp. 1067–1075, 2020.

[51] F. Morakinyo, I. Bolanle, O. Oyelowo, and J. Nnaji, "Anti-oxidative and hepatoprotective effect of beta-carotene on acetaminophen-induced liver damage in rats," *Biology and Medicine*, vol. 4, no. 3, pp. 134–140, 2012.

[52] X. Cai, Q. Yang, and S. Wang, "Antioxidant and hepatoprotective effects of a pigment-protein complex from Chlorella vulgaris on carbon tetrachloride-induced liver damage in vivo," *RSC Advances*, vol. 5, no. 116, pp. 96097–96104, 2015.

Research Article

Pharmacological Activation of Nrf2 by Rosolic Acid Attenuates Endoplasmic Reticulum Stress in Endothelial Cells

Karan Naresh Amin,[1] Palanisamy Rajagru,[2] Koustav Sarkar,[1] M. R. Ganesh,[3] Takayoshi Suzuki,[4] Daoud Ali,[5] and Ramkumar Kunka Mohanram [ID][1]

[1]SRM Research Institute and Department of Biotechnology, School of Bioengineering, SRM Institute of Science and Technology, Kattankulathur, 603 203 Tamilnadu, India
[2]Department of Life Sciences, Central University of Tamil Nadu, Tiruvarur 610005, India
[3]Interdisciplinary Institute of Indian System of Medicine, SRM Institute of Science and Technology, Kattankulathur, 603 203 Tamilnadu, India
[4]Division Cellular and Gene Therapy Products, National Institute of Health Sciences, Setagaya-Ku, Tokyo, Japan
[5]Department of Zoology, College of Science King Saud University, P.O. Box 2455, Riyadh 11451, Saudi Arabia

Correspondence should be addressed to Ramkumar Kunka Mohanram; ramkumak@srmist.edu.in

Endoplasmic reticulum (ER) plays a key role in the folding, modification, and trafficking of proteins. When the homeostasis of the ER is disturbed, un/misfolded proteins accumulate in the ER which leads to ER stress. Sustained ER stress results in apoptosis, which is associated with various diseases. Nuclear factor erythroid 2-related factor 2 (Nrf2) is a major transcription factor in redox homeostasis by regulating various genes associated with detoxification and cell-protective mechanisms. We found that Rosolic acid (RA) treatment dose-dependently activates Nrf2 in endothelial cells using the enzyme fragment complementation assay. The cytoprotective role of RA against ER stress-induced endothelial apoptosis and its molecular mechanism was explored in the present study. The Nrf2 and its target genes, as well as ER stress marker expressions, were measured by qPCR in ER stress-exposed endothelial cells. The contribution of Nrf2 in RA-mediated defense mechanism in endothelial cells was established by knockout studies using Nrf2-CRISPR/Cas9. The treatment with RA to ER stress-induced endothelial cells exhibited activation of Nrf2, as demonstrated by Nrf2 translocation and reduction of ER stress markers. We found that the Nrf2 knockout sensitized the endothelial cells against ER stress, and further, RA failed to mediate its cytoprotective effect. Proteomic studies using LC-MS/MS revealed that among the 1370 proteins detected, we found 296 differentially regulated proteins in ER stress-induced endothelial cells, and RA administration ameliorated 71 proteins towards the control levels. Of note, the ER stress in endothelial cells was attenuated by the treatment with the RA, suggesting the role of the Nrf2 activator in the pathological conditions of ER stress-associated diseases.

1. Introduction

The endothelium is the main component of the barricade for transporting many important biological compounds from the blood to the inner layer of cells. It is responsible for maintaining the vasculature by releasing various vasodilatory or vasoconstrictive factors like NO, endothelin-1, endothelium-derived hyperpolarizing factor, prostacyclin, and thromboxane [1]. Endothelial cells form a key compo-

nent of the inflammatory and immune response and are the first cells to be activated during inflammation [2]. Endothelial apoptosis is a causative factor for diabetes and its vascular complications [3]. Understanding the transitions in apoptotic pathways may allow an improved understanding of the pathogenesis of disease and in the development of novel therapies [4, 5]. The currently available research highlights endothelial apoptosis as an initial event in the progression of certain diseases, including diabetes [6, 7].

The perturbations to the endothelial cell metabolic pathways lead to oxidative stress, endoplasmic reticulum (ER) stress, and inflammatory processes, which are the important contributors to endothelial apoptosis. ER stress has increased more attention as a crucial factor connecting and congregating molecular relationships among oxidative stress, endothelial cell dysfunction, and insulin resistance and, therefore, is considered an auspicious drug target for controlling diabetes and cardiovascular problems. Increasing evidence identifies the cross talk between oxidative stress and ER stress in the pathogenesis of diabetes and its complications [8, 9].

Numerous therapeutic strategies have been developed to combat ER stress-induced endothelial cell dysfunction [10–12]. Nrf2 is a major transcription factor in cellular defense, which acts as the chief watchdog of reduction-oxidation status and detoxification. Nrf2 is generally found in the cytoplasm under physiological conditions and connected with its negative regulator, Kelch-like ECH-associated protein1 (Keap1) [13, 14]. When the cells encounter oxidative stress or electrophiles, Nrf2 detaches from the Nrf2-Keap1 complex and translocates to the nucleus that activates the gene expression of antioxidant responsive element (ARE) to sustain cellular redox homeostasis [15]. In recent years, activation of Nrf2 by small molecules have been demonstrated as a new promising therapeutic approach for counteracting endothelial apoptosis [16–19]. It is interesting to note that Nrf2 is reported to associate with the UPR sensor called pancreatic endoplasmic reticulum kinase [20].

We have developed a high-throughput screening system based on luciferase complementation to screen Nrf2 activators and demonstrated its role against oxidative and cytokine stress in pancreatic beta cells through Nrf2 activation [21–25]. Few Nrf2 activators showed promising results against hyperglycemia-induced endothelial dysfunction (ED) [16]. Earlier, we reported quercetin, a potent Nrf2 activator that showed a cytoprotective effect on endothelial cells against ER stress-induced ED [26]. We have established a co-culture system to examine the cross talk between pancreatic beta cells and endothelial cells under ER stress and validated with a recognized ER stress regulator, quercetin [27].

Rosolic acid (RA), an important polyphenol extracted from *Plantago asiatica* L., has been demonstrated to increase the levels of Heme oxygenase-1 (HO-1) in endothelial cells [28]. The role of RA on ER stress-induced ED and its effect as a therapeutic agent are yet to be revealed. Hence, this study investigated the effects of RA against ER stress-induced toxicity in endothelial cells. Further, the role of Nrf2 on RA-mediated cytoprotection was also investigated using Nrf2 knockout endothelial cells by CRISPR/Cas9. To offer better understanding of the underlying molecular mechanism, we have carried out a proteomic study on the RA-treated ER stress-induced endothelial cells using electrospray ionization tandem mass spectrometry (LC-MS/MS).

2. Materials and Methods

2.1. Cell Culture.
The immortalized human umbilical vein endothelial hybrid cell line, EA.hy926 cells, was maintained in DMEM medium (Clonetics; Lonza Ltd, Basel, Switzerland) along with Fetal bovine serum (FBS, 10%) (v/v) (HyClone, Logan, UT, USA), penicillin (100 U/ml), and streptomycin (100 μg/ml). The cells were kept in a humidified 5% CO_2 atmosphere at 37°C. Immortalized cell lines offer significant logistical advantages over primary cells when used for *in vitro* studies.

2.2. ER Stress Induction.
ER stress was induced in the EA.hy926 cells by exposing the cells to thapsigargin (TPG) (Sigma-Aldrich, USA) at a dose of 2 μM for two hours [29]. TPG inhibits sarcoplasmic/endoplasmic reticulum Ca^{2+}-ATPase, leading to a depletion of ER calcium storage, resulting in the accumulation of unfolded proteins and inducer of cell death [30].

2.3. Assay of Cell Viability.
The cell viability was measured using the MTT assay [31]. In brief, EA.hy926 cells (1×10^4 cells/well) were cultured in a 96-well plate for 24 h at 37°C and then pretreated with RA (0-100 μM) for the next 24 h. After incubation, the medium was replaced by MTT solution (5 mg/ml) and kept in a humidified 5% CO_2 atmosphere for 4 h at 37°C. 100 μl of DMSO was added to all the wells and mixed thoroughly and read at 570 nm by a microplate reader (TECAN, Switzerland).

To study the effect of RA on ER stress-induced cell death, the cells were pretreated with RA (0-100 μM) for at least 24 h trailed by TPG (2 μM) for 2 h. The assay of MTT was then carried out as described above.

2.4. Quantitative Real-Time PCR (qRT-PCR).
The molecular ER stress marker profiles, protein kinase R- (PKR-) like endoplasmic reticulum kinase (PERK), glucose-regulated protein (GRP) 78, C/ERB homologous protein (CHOP), activating transcription factor- (ATF-) 6, and Nrf2-regulated genes, including NAD(P)H quinone-oxidoreductase-1 (NQO1), heme oxygenase-1 (HO-1), catalase (CAT), and glutathione peroxidase (GPx), were performed using qRT-PCR (Bio-Rad, USA). The primers for the targeted genes were obtained from the genome DNA sequence database and NCBI human mRNA, and primers were designed using the primer3 plus, a free online bioinformatics tool, which is enumerated in Table 1. The cells were treated with different concentrations of RA for 24 h followed by thapsigargin (2 μM) for 2 h. The mRNA isolation was performed using the mRNA isolation kit (Qiagen, Germany), followed by the cDNA conversion using a commercially available kit (Qiagen, Germany) as per instructions provided by the manufacturer. The qRT-PCR was achieved using SYBR® Premix Ex Taq™ II (TaKaRa, Japan) as per the instructions provided by the manufacturer. The housekeeping gene Glyceraldehyde-3-phosphate dehydrogenase (GAPDH) was used as the internal control for normalization, and the results are represented as relative fold change.

2.5. ARE-Luciferase Reporter Gene Assay.
To confirm the Nrf2 activation potential, ARE promoter Responsive Luciferase Reporters such as GST-ARE-Luc and hNQO1-ARE-Luc reporter gene constructs were used in endothelial cells. Briefly, EA.hy926 cells were seeded and transfected with an ARE-Luc construct (500 ng/well) with the help of

TABLE 1: List of primers and its sequences used for the study.

S. No.	Gene	Forward	Reverse
1	NRF2	TGTAGATGACAATGAGGTTTC	ACTGAGCCTGATTAGTAGCAA
2	GPx	TTCCCGTGCAACCAGTTTG	TTCACCTCGCACTTCTCGAA
3	SOD	GAAGGTGTGGGGAAGCATTA	ACATTGCCCAAGTCTCCAAC
4	NQO1	AGGATGGAAGAAACGCCTGG	TCAGTTGGGATGGACTTGCC
5	HO1	GGGAATTCTCTTGGCTGGCT	AACTGAGGATGCTGAAGGGC
6	GRP78	GCGTCGGCGTGTTCAAGA	CAGACGGGTCATTCCACGTG
7	PERK	GAACCAGACGATGAGACA GAG	GGATGACACCAAGGAACCG
8	CHOP	GTACCTATGTTTCACCTCCTG G	TGGAATCTGGAGAGTGAGGG
9	ATF 6	CGGAGCCACTGAAGGAAG ATA	TTGAGTCTTGGGTGCTGCTG
10	GAPDH	AAGAAGGTGGTGAAGCAGGC	GTCAAAGGTGGAGGAGTGGG

Lipofectamine 2000. After 24 h, the transfected cells were administered with different amounts of RA (0-20 μM) and kept incubated for 8 h, and then the cells were assayed for luciferase activity by a luminometer (Promega, Madison, WI, USA). The luciferase activity was expressed in terms of relative fold variation compared to control cells.

2.6. Measurement of Intracellular Reactive Oxygen Species (ROS) Formation. 2′,7′-Dichlorofluorescin diacetate (DCFDA) (Sigma-Aldrich, USA) was used to measure the intracellular peroxides to assess the protective effect of RA against ROS formation in ER stress-induced endothelial cells. In brief, the endothelial cells were pretreated with RA (5 and 10 μM) for 24 h followed by exposure with 2 μM TPG for 2 h. Then, the cells were treated with DCFDA solution (25 μM) for 15 min, and the fluorescence was measured using flow cytometer (BD Biosciences, CA, USA) at 502 nm excitation and 550 nm emission wavelength.

2.7. Apoptosis Detection Using Annexin-V Labeling Assay by Flow Cytometry. Annexin-V-FITC was used to measure the apoptotic population percentage to evaluate the protective effect of RA against ER stress-induced endothelial cells. Briefly, the cells were harvested and centrifuged for 3 minutes at 1500 rpm. The cells were then stained with Annexin-V-FITC and determined using flow cytometer (BD Biosciences, CA, USA).

2.8. CRISPR/Cas9-Mediated Knockout of Nrf2 in Human Endothelial Cells. To confirm the role of RA on Nrf2-mediated protection, Nrf2-KO endothelial cells were generated using the CRISPR/Cas9 gene-editing tool. EA.hy926 cells were transfected with Nrf2-CRISPR/Cas9-GFP plasmid (sc-400017, Santa Cruz, USA). GFP$^+$ cell expression was screened using FACS. Western blot analysis for Nrf2-expression was performed to confirm successful Nrf2-depletion. Further, the Nrf2 role in RA which facilitated the protection of endothelial cells against ER stress was assessed using Nrf2 KO cells by assessing the expression of ER stress markers and cell viability.

2.9. Immunoblot Analysis. The cytosolic and nuclear extracts were prepared by using the NE-PER™ Nuclear and Cytoplasmic Extraction kit (Thermo Scientific, USA). Further, the whole-cell protein lysate from the cells was prepared using RIPA buffer, and the concentration of protein was measured using Bradford reagent (Bio-Rad, PA, USA). Equal quantities of proteins were used in SDS-PAGE and transferred to a nitrocellulose membrane. Then, they subjected to blocking with BSA (5%), followed by immunoblotting using respective primary antibodies, β-actin (Abcam, USA), Nrf2 (Santa Cruz, USA), GRP78 (Santa Cruz, USA), Lamin B1 (Santa Cruz, USA), CHOP (Santa Cruz, USA), and corresponding secondary antibody, anti-rabbit IgG, and HRP-linked antibody. The expression levels were detected by the enhanced chemiluminescence using (ECL) kit (Bio-Rad, PA, USA) and the ECL western blotting detection reagent, and the protein bands were captured using the ChemiDoc system (GBOX, Syngene, UK).

2.10. Enzyme Activities. The superoxide dismutase (SOD) activity was measured based on the nitro blue tetrazolium (NBT) reduction assay [32]. Catalase (CAT), and glutathione peroxidase (GPx) activities were determined by measuring the amount of the substrate consumed by colorimetrically [33].

2.11. Proteomic Investigations Performed by Nano LC-MS/MS Analysis. The molecular mechanism of RA-mediated protection in ER stress-induced endothelial cells was studied by the LC-MS/MS analysis. The protein digests were determined by nanoflow HPLC–electrospray tandem mass spectrometry (LC-MS/MS). The comprehensive methodology is provided in the supplementary material (available here).

2.12. Statistical Analysis. All experimental studies were completely achieved in a randomized design. One-way ANOVA followed by Tukey's post hoc test was subjected using the SPSS version 17.0 software (SPSS Inc., Chicago, IL, USA). All outcomes were reported as mean ± SD of at least independent tests of triplicates and $P \leq 0.05$ was measured as statistically significant.

3. Results

3.1. Cytoprotective Effect of RA on TPG-Stimulated ER Stress in Endothelial Cells. To evaluate the cytotoxic activity of RA in endothelial cells, cells were exposed to different

(a)

(b)
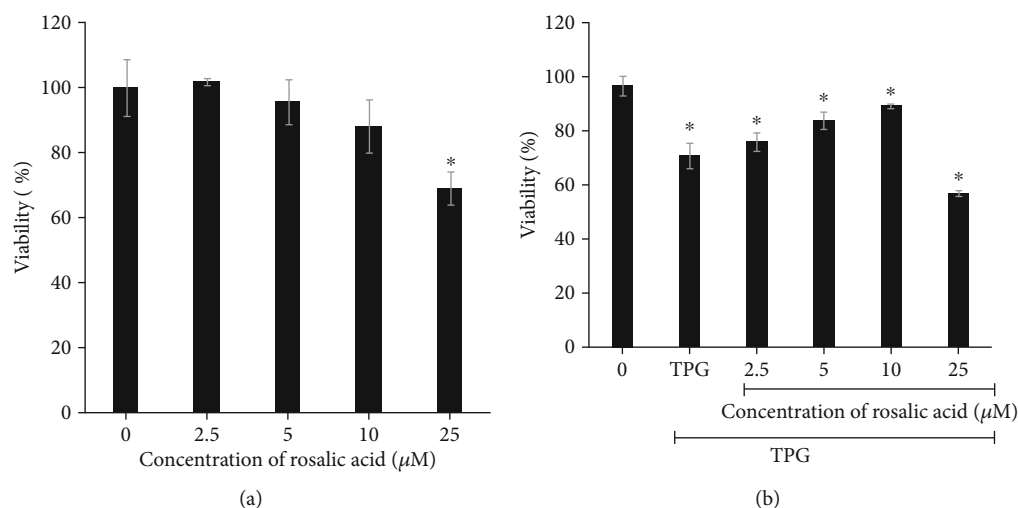
Figure 1: Effect of Rosolic acid on ER stress-induced toxicity in EA.hy926 cells. (a) Cytotoxicity of Rosolic acid on EA.hy926 cells as assessed by MTT assay. (b) Cytoprotective effect of Rosolic acid on EA.hy926 cells against thapsigargin-induced toxicity as assessed by MTT assay. Data are represented as mean ± SD of three independent experiments. ∗Significant compared with the control group; $P < 0.05$ determined by one-way ANOVA followed by Tukey's post hoc test (0, control; TPG, thapsigargin; 2.5, 5, 10, and 25, concentrations of Rosolic acid in μM).

(a)

(b)
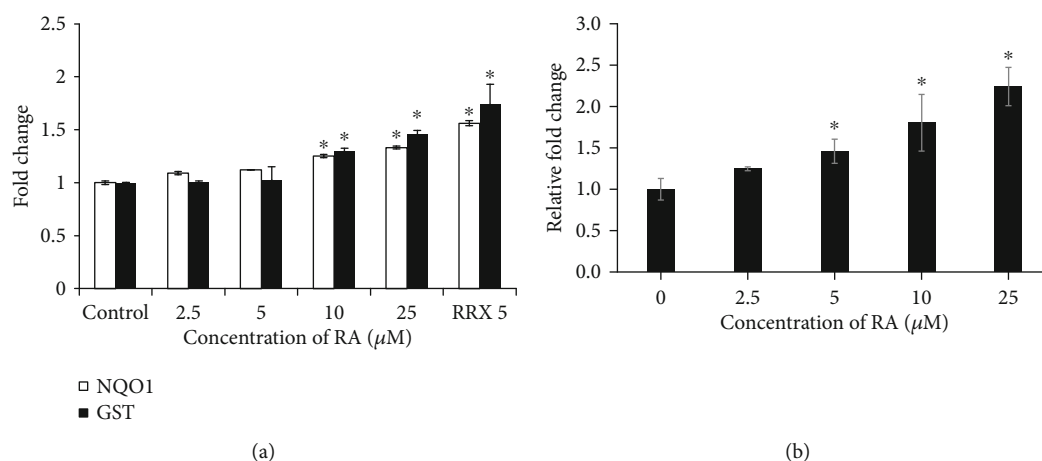
Figure 2: Nrf2 activation potential of Rosolic acid as assessed by ARE-Luciferase Reporter Assay. (a) HEK293T cells were transfected with either ARE-hNQO1/ARE-GST luciferase vector. Transfected cells were treated with Rosolic acid (0, 2, 5, 10, and 20 μM) for 8 h. A known Nrf2 activator, RRx, was used as a reference control. Luciferase activity was measured as described in methods and expressed as fold induction relative to values obtained from control cells. Photon flux data were normalized to total protein. Effect of Rosolic acid on Nrf2 expression in EA.hy926 cells (b). Data are represented as mean ± SD of three independent experiments. ∗Significant compared with the control group; $P < 0.05$ determined by one-way ANOVA followed by Tukey's post hoc test.

concentrations of RA for 24 h, and viable cells were determined by the MTT assay. The outcomes are presented in Figure 1(a). The cytoprotective effect of RA against TPG-induced apoptosis in endothelial cells was accessed using the MTT assay. Endothelial cells treated with TPG at 2 μM for 2 h showed a 35% reduction in cell viability. However, the cells pretreated with different concentrations of RA (2.5-25 μM) showed a dose-dependent increase in cell viability, and the protective effect was found to be maximum at 5 and 10 μM RA concentrations (Figure 1(b)), and at 25 μM, it was toxic to the cells.

3.2. Nrf2 Activation Potential of RA in Endothelial Cells. To determine the Nrf2 activation by RA, its binding potential to nuclear ARE and activation of its downstream regulatory

genes, reporter gene constructs, and their cell-based assays, GST-ARE-Luc and hNQO1-ARE-Luc were employed. Various concentrations of RA treated on endothelial cells, which were later harvested and measured the luciferase activity. A dose-dependent elevated reporter luciferase signals of GST and NQO1 were observed in RA-treated cells, presented in Figure 2(a). Furthermore, dose-dependent elevated levels of Nrf2 in RA-treated endothelial cells are also noticed in Figure 2(b). Based on the outcome, the study confirms the potential role of RA on the activation of Nrf2 in endothelial cells.

3.3. Efficacy of RA on Nrf2 Activation and Translocation in ER Stress-Stimulated Endothelial Cells. To study the role of RA on Nrf2-mediated protection of endothelial cells against

ER stress, we evaluated the impact of RA on the Nrf2 expression and its downstream target genes in endothelial cells. RA treatment resulted in increased levels of Nrf2 in ER stress-induced endothelial cells as assessed by qPCR and western blotting (Figures 3(a) and 3(b)). Further, RA-mediated Nrf2 activation was confirmed by Nrf2 translocation from cytosol to the nucleus. The RA-treated cells showed decreased levels of Nrf2 in cytosol fraction meanwhile increased levels in the nuclear fraction as demonstrated by western blotting. Further, the accumulation of cytosolic Nrf2 with a concomitant decrease in nuclear Nrf2 was observed in the TPG-treated endothelial cells was reversed upon RA pretreatment (Figure 3(c)). This confirms the role of RA-mediated Nrf2 activation against ER stress-induced ED.

3.4. Efficacy of RA on Nrf2 Activation and Its Downstream Regulation in ER Stress-Stimulated Endothelial Cells.

To study the effects of RA on Nrf2 downstream target genes, GPx, CAT, HO-1, and NQO1 expressions were studied. Upon treatment with TPG, the expressions of GPx, CAT, and NQO1 were downregulated, and HO-1 was marginally upregulated. Pretreatment with RA (5 and $10\,\mu M$) effectively upregulated the expression of all the above-mentioned Nrf2 downstream genes in a dose-respective manner (Figures 4(a)–4(d)). RA treatment alone increased the expression of antioxidant genes, showing its potential antioxidant property.

Further, to validate the potential of RA on reducing the oxidative stress via Nrf2 signaling, we have determined the enzyme activities of SOD, CAT, and GPx in endothelial cells. The activity of SOD in endothelial cells with TPG-induced ER stress was found to be significantly decreased (0.71 units/mg protein), which was restored upon pretreatment with $10\,\mu M$ RA (1.12 units/mg protein) to near-normal levels (1.21 units/mg protein). A similar pattern of results was observed for both CAT and GPx activities with a significant reduction of enzyme activity in the TPG-treated endothelial cells with enzyme activity $30.19\,\mu mol/min/mg$ protein and $123.11\,\mu mol/min/mg$ protein, respectively. RA pretreatment dose-dependently showed improvement in CAT and GPx activities in endothelial cells. The quantitative results proved that RA also protected ER stress-induced endothelial cells against oxidative damage (Table 2).

3.5. Efficacy of RA against ER Stress in Endothelial Cells Assessed by ER Stress Markers.

The protective effect of RA against TPG-induced ER stress in endothelial cells was evaluated by studying the expression of ER stress markers PERK, ATF-6, GRP78, and CHOP. All the tested ER stress gene expression was upregulated in TPG-treated cells, which confirm the stimulation of ER stress. Interestingly, pretreatment with RA (5 and $10\,\mu M$) exhibited a dose-respective reduction in the PERK, ATF-6, and GRP78 expression but not CHOP expression (Figures 5(a)–5(d)). RA treatment alone did not show any significant variation in the level of ER stress gene expressions even after 24 h exposure in endothelial cells. Further, RA-mediated protection against ER stress was confirmed by the levels of the decreased ER chaperone GRP-78 by western blotting (Figure 5(e)).

3.6. Effect of RA against ROS Formation against ER Stress in Endothelial Cells as Assessed by DCFDA Assay Using Flow Cytometry.

Intracellular ROS sensitive fluorescent probe DCFDA was used to evaluate whether RA could inhibit TPG-induced intracellular ROS generation in endothelial cells. As seen in Figure 6, there was a right shift in DCF peak in TPG- (Figure 6(c)) treated endothelial cells compared to control (Figure 6(a)), which confirm the increased free radical generation. Interestingly, a dose-dependent shift towards left was observed in the group pretreated with 5 (Figure 6(d)) and 10 (Figure 6(e)) μM RA, respectively, proving the effect of RA in reducing intracellular ROS generation and thus protecting the endothelial cells against oxidative stress.

3.7. Antiapoptotic Efficacy of RA against ER Stress-Stimulated Endothelial Apoptosis.

Annexin-V-FITC labeling assay by flow cytometry were implemented to examine the antiapoptotic property of RA against TPG-induced ER stress in endothelial cells. The apoptotic cell population was elevated by 43.87% (Figure 7) in TPG-treated cells. A dose-dependent reduction by 34.28% and 17.49% was observed in 5 and $10\,\mu M$ on RA pretreatment, respectively. There was no significant change seen in the cell population treated with RA alone compared with untreated EA.hy926 cells. This shows that the RA protects endothelial cells against apoptosis induced by ER stress.

3.8. Development of Nrf2-Knockout Endothelial Cells Using CRISPR/Cas9.

To determine whether the protective efficacy of RA was facilitated via activation of Nrf2, we have developed Nrf2-knockout endothelial cells using CRISPR/Cas9. The knockout cells were subjected to flow cytometry analysis, and a comparable level of GFP expression was recorded in both control and Nrf2 KO EA.hy926 cells, which shows equal transfection efficiency of both the plasmids. However, Nrf2 expression was completely lost in Nrf2 KO plasmid-transfected EA.hy926 cells when compared to the scrambled transfected control cells, as seen in Figure 8. Further, this result was validated using western blot analysis, where a complete reduction in the Nrf2 level was recorded in KO cells, and those cells were used for the further mechanistic study.

3.9. Efficacy of RA on TPG-Stimulated ER Stress in Nrf2 KO Endothelial Cells.

MTT assay was performed to check the modulation in the cytoprotective effect of RA on TPG-induced ER stress in Nrf2 KO cells. Increased sensitivity to apoptosis upon ER stress was observed in Nrf2 KO cells, which was confirmed by a 59.2% reduction in the cell viability upon exposure to TPG. Further pretreatment with different concentrations of RA (2.5–25 μM) for 24 h failed to protect the cells against ER stress (Figure 9(a)). This confirms that RA protects the endothelial cells against ER stress through the stimulation of the Nrf2 signaling pathway.

3.10. Effect of RA on ER Stress Markers in Nrf2-Knockout Endothelial Cells.

Further, we compared the effect of RA on the ER stress marker expressions, PERK, ATF-6, GRP-78,

(a)

(b)

(c)
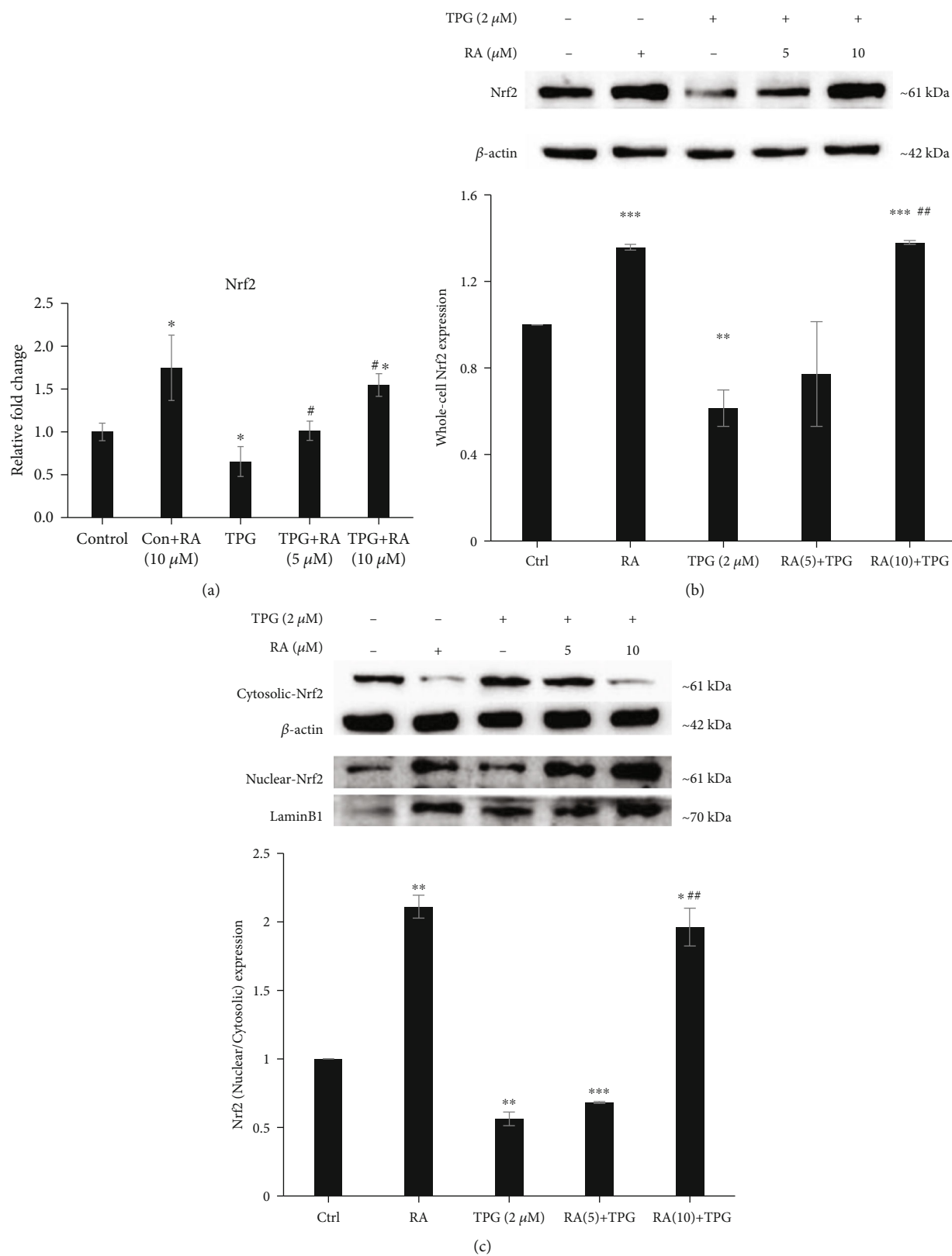
Figure 3: Effect of Rosolic acid on level of Nrf2 gene expression (a) by qRT-PCR analysis and protein level (b) by western blotting in ER stress-induced EA.hy926 cells. (c) The effect of Rosolic acid on Nrf2 translocation from cytosol to the nucleus by western blotting in EA.hy926 cells under ER stress. Data are represented as mean ± SD of three independent experiments. ∗Significant compared with the control group. #Significant compared with TPG group; $P < 0.05$ determined by one-way ANOVA followed by Tukey's post hoc test (0, control; TPG, thapsigargin; 2.5, 5, 10, and 25, concentrations of Rosolic acid in μM).

(a)

(b)

(c)

(d)
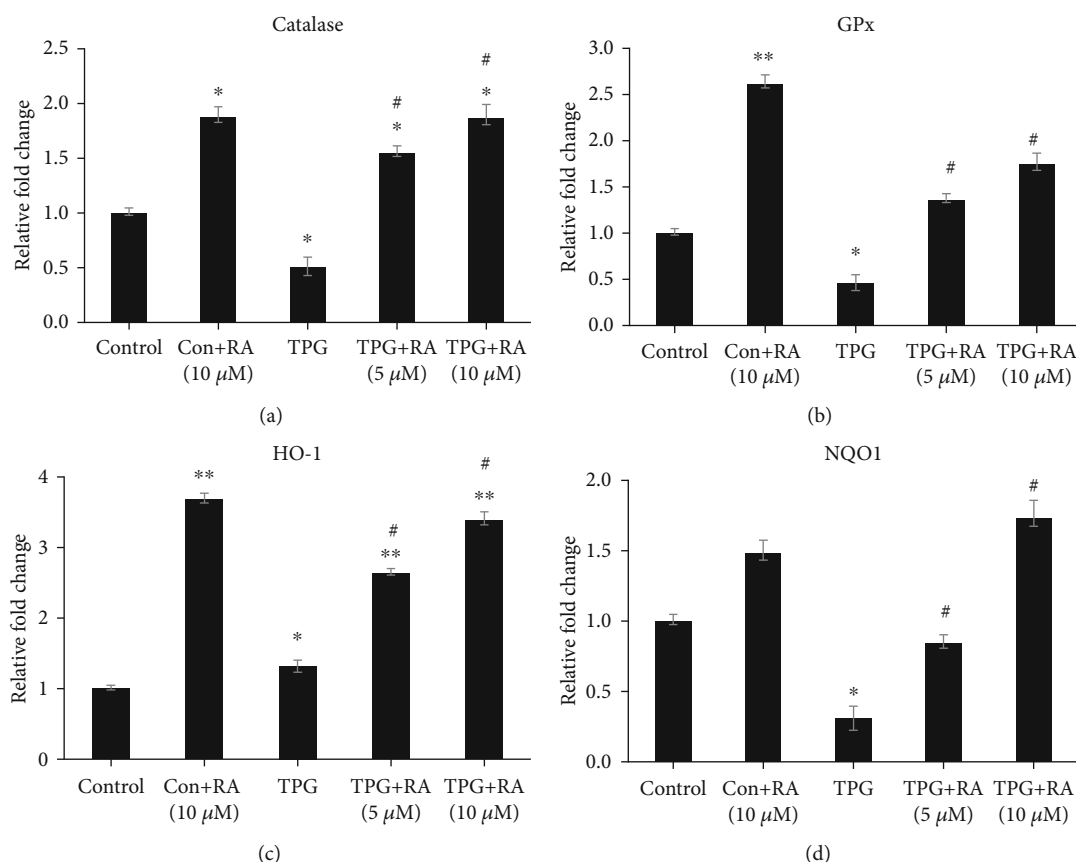
Figure 4: Effect of Rosolic acid on Nrf2 downstream targets such as (a) catalase (CAT), (b) glutathione peroxidase (GPx), (c) heme oxygenase-1 (HO-1), and (d) NAD(P)H: quinone-oxidoreductase-1 (NQO-1) expression in ER stress-induced EA.hy926 cells by qRT-PCR analysis. Data are represented as mean ± SD of three independent experiments. ∗Significant compared with Control group. #Significant compared with TPG group; $P < 0.05$ determined by one-way ANOVA followed by Tukey's post hoc test (0, control; TPG, thapsigargin; 2.5, 5, 10, and 25, concentrations of Rosolic acid in μM).

Table 2: Effect of Rosolic acid on activities of enzymatic antioxidants in ER stress-induced EA.hy926 cells.

Groups	SOD (units/mg protein)	CAT (μmol/min/mg protein)	GPx (μmol/min/mg protein)
Control	1.21 ± 0.04	39.62 ± 0.8	150.51 ± 9.61
RA (10 μM)	1.43 ± 0.09 ∗∗	42.21 ± 4.4	192.04 ± 13.72 ∗∗∗
TPG (2 μM)	0.71 ± 0.21 ∗∗	30.19 ± 1.1 ∗∗∗	123.11 ± 5.69 ∗∗∗
RA (5 μM)+TPG (2 μM)	0.81 ± 0.12 ∗∗∗	31.62 ± 2.7 ∗∗∗	118.06 ± 7.78 ∗∗∗###
RA (10 μM)+TPG (2 μM)	1.12 ± 0.16##	33.41 ± 0.2 ∗∗∗###	135.59 ± 9.89 ∗∗###

Data are represented as mean ± SD of three independent experiments. ∗Significant compared with the control group. #Significant compared with TPG group; $P < 0.05$ determined by one-way ANOVA followed by Tukey's post hoc test.

and CHOP in both Nrf2 wild-type and Nrf2 KO cells subjected to ER stress. RA-pretreated cells exhibited augmented ER stress marker expressions when compared to control cells. RA-mediated protection against ER stress was not observed in Nrf2 KO cells unlike in wild-type EA.hy926 cells where the protection was evident (Figure 9(b)).

3.11. Molecular Mechanism of RA-Mediated Protection against ER Stress through Proteomic Analysis. To study the molecular mechanism using proteomic analysis using LC-MS/MS on a Q Exactive mass spectrometer, we have taken

three groups, including control (Cont), TPG-treated endothelial cells (TPG), and RA-treated TPG-induced endothelial cells (TPG+RA). The results revealed that among the identified 1370 proteins, 35.03% of the proteins were known with one peptide, 18.61% with two peptides, 10.58% with three peptides, 6.27% with four peptides, and 27% of proteins with more than five peptides. The proteins with two or more peptides were considered for further analysis. We found 296 proteins were differentially expressed with twofold or more change and two or more peptides in TPG-treated cells when compared to the control in which 143 downregulated

(a)

(b)

(c)

(d)

(e)
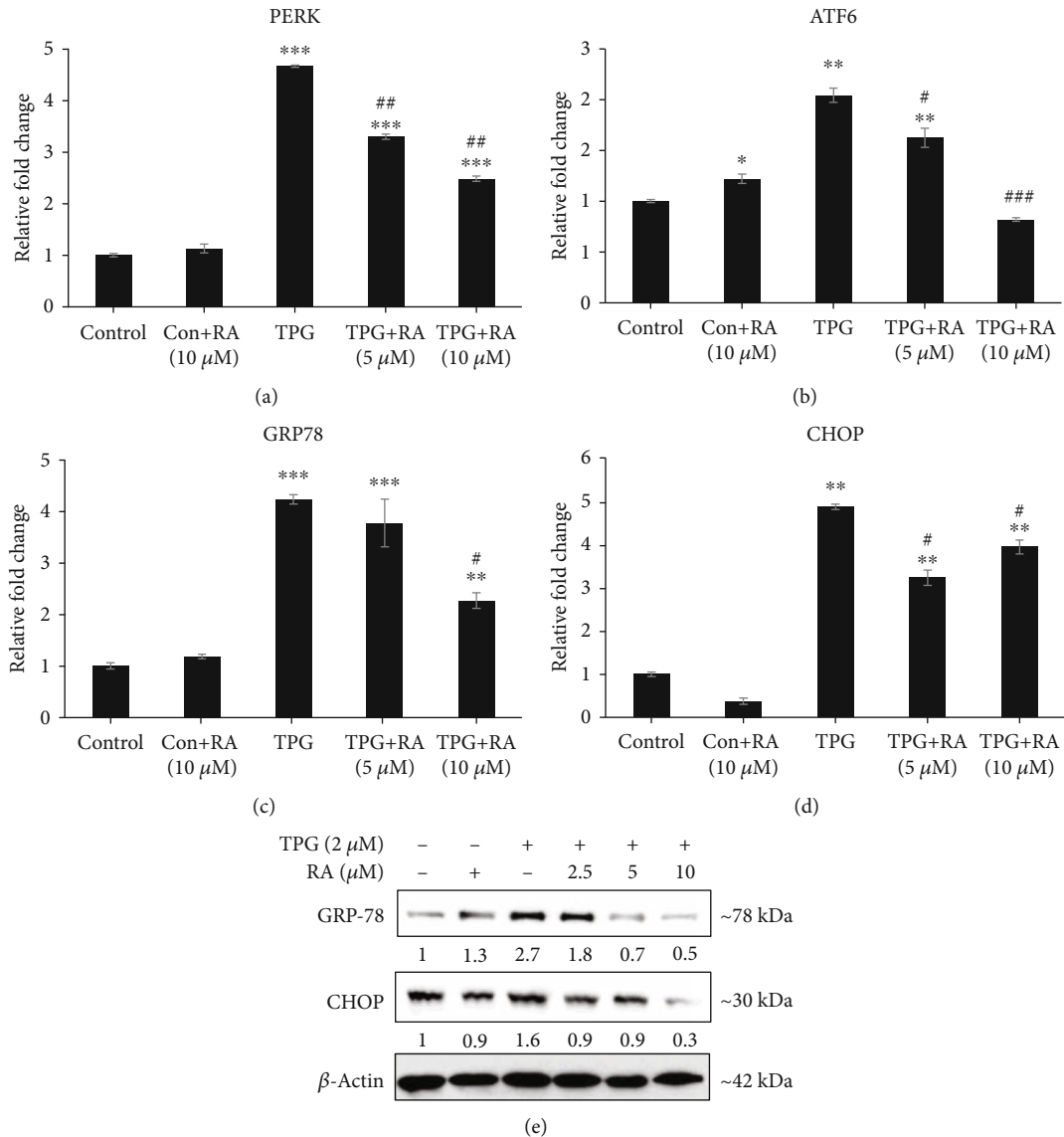
Figure 5: Effect of Rosolic acid against ER stress as assessed by ER stress markers such as (a) protein kinase R- (PKR-) like endoplasmic reticulum kinase (PERK), (b) activating transcription factor- (ATF-) 6, (c) glucose-regulated protein (GRP) 78, and (d) C/ERB homologous protein (CHOP) expression in ER stress-induced EA.hy926 cells qRT-PCR analysis. (e) The effect of Rosolic acid on GRP-78 and CHOP by western blotting in EA.hy926 cells under ER stress. Data are represented as mean ± SD of three independent experiments. * Significant compared with the control group. #Significant compared with TPG group; $P < 0.05$ determined by one-way ANOVA followed by Tukey's post hoc test.

and 153 upregulated. The STRING 11 online web tool was used to generate protein-protein interaction networks of differentially regulated proteins, with the settings of "MCL inflation parameter (3.0) and medium confidence (0.4)" (Figure 10(a)). We have identified eight major protein interaction network clusters, which are mainly involved in protein synthesis machinery, protein transport, stress response proteins, protein-folding proteins, and ER proteins.

The cellular organelle localization of the differentially regulated proteins was identified as 39.3% from the nucleus, 13.1% from the endoplasmic reticulum, 6.6% from the mitochondria, 8.2% from the Golgi apparatus, and 30.3% from the vacuoles using PANTHER. Further, the class of differentially regulated proteins was found that 16.9% proteins were asso-

ciated with cytoskeletal proteins, 15.1% with translational proteins, 9.6% with membrane traffic proteins, 8.4% with chaperones, and 14.5% in protein modifying enzymes (Figure 10(b)).

Further, the differentially regulated proteins were subjected to DAVID for their annotation. We found a total of 17 clusters with an enrichment score of more than 3. We have considered the clusters with an enrichment score of more than 10. The top three cellular components are occupied by "cell-cell adhesion proteins" with an enrichment score of 17.2. "Cell Chaperone" has an enrichment score of 13.35, and "GTP-binding" has an enrichment score of 10.88 (Table 3).

The list of DAVID–KEGG pathways of differentially regulated proteins are depicted in Table 4. 10.6% of the
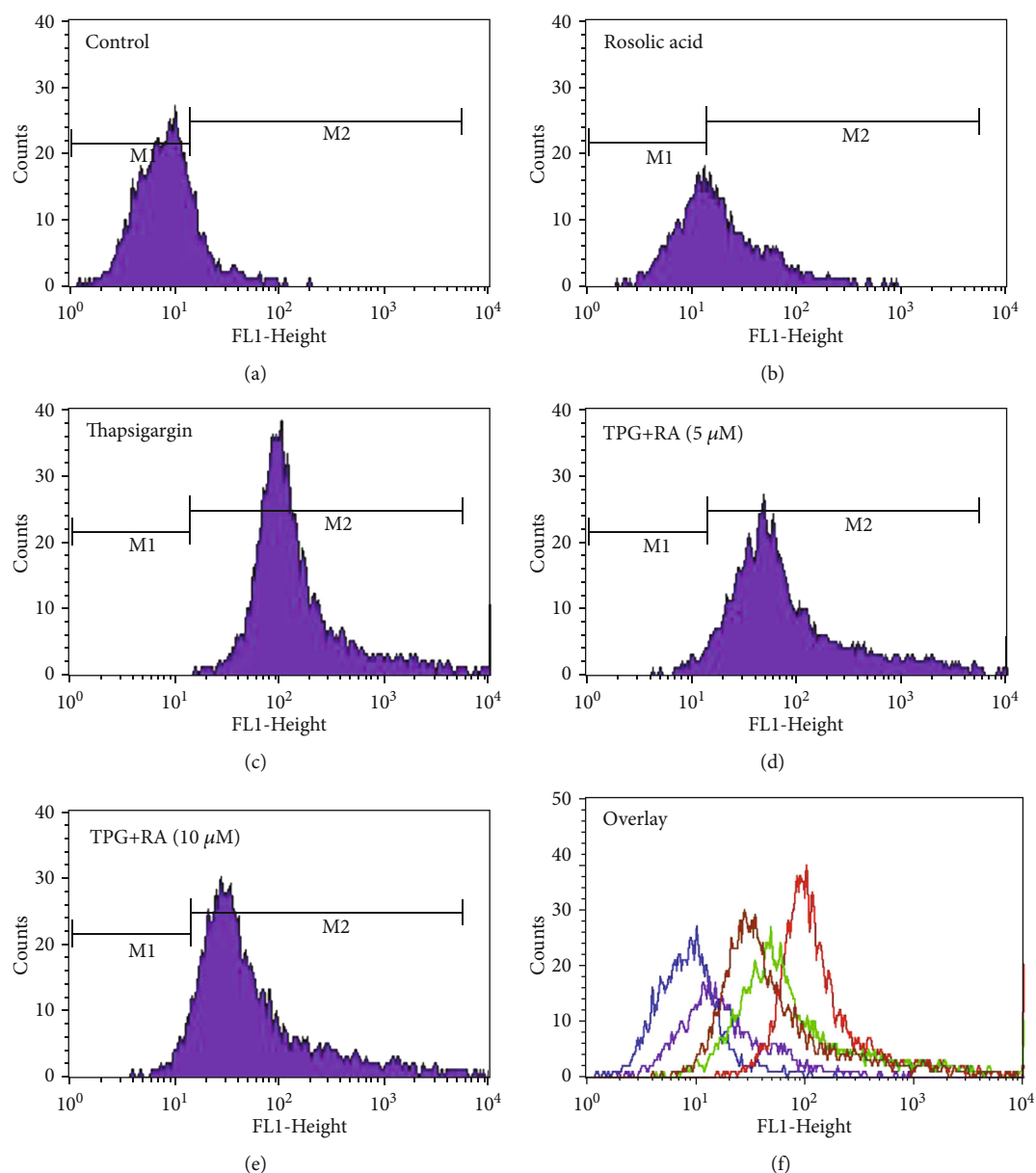
FIGURE 6: Analysis of reactive oxygen species formation in ER stress-induced EA.hy926 cells measured by flow cytometry using H2-DCFDA assay. Cells were pretreated with 5 and 10 μg for 24 hours and then treated with thapsigargin for 2 hours, and then the cells were incubated with 25 μM of DCFDA solution for 15 min and then harvested. After washing, the cells were subjected to flow cytometric analysis.

proteins belong to protein processing in the endoplasmic reticulum. The other classes of proteins include RNA transport, proteasome, antigen processing and presentation, phagosome, estrogen signaling pathway, leukocyte transendothelial migration, adherent junction, and AMPK signaling pathway.

4. Discussion

Though several approaches have been established to improve the endothelial functions, drugs that can effectively treat microvascular complications are limited. This study was performed to determine RA, a polyphenol isolated from the rhizome of *Plantago asiatica* L. which can be used as a therapeutic agent to treat hyperglycemia-induced ER stress and endothelial dysfunction. We provided the first line of evidence that RA attenuates ER stress-induced endothelial apoptosis. Further, we also provide evidence that attenuation of ER stress and apoptosis is a result of the activation of Nrf2 and its signaling network.

Generally, endothelial cells are metabolically dynamic, contributing to various physiological mechanisms, including
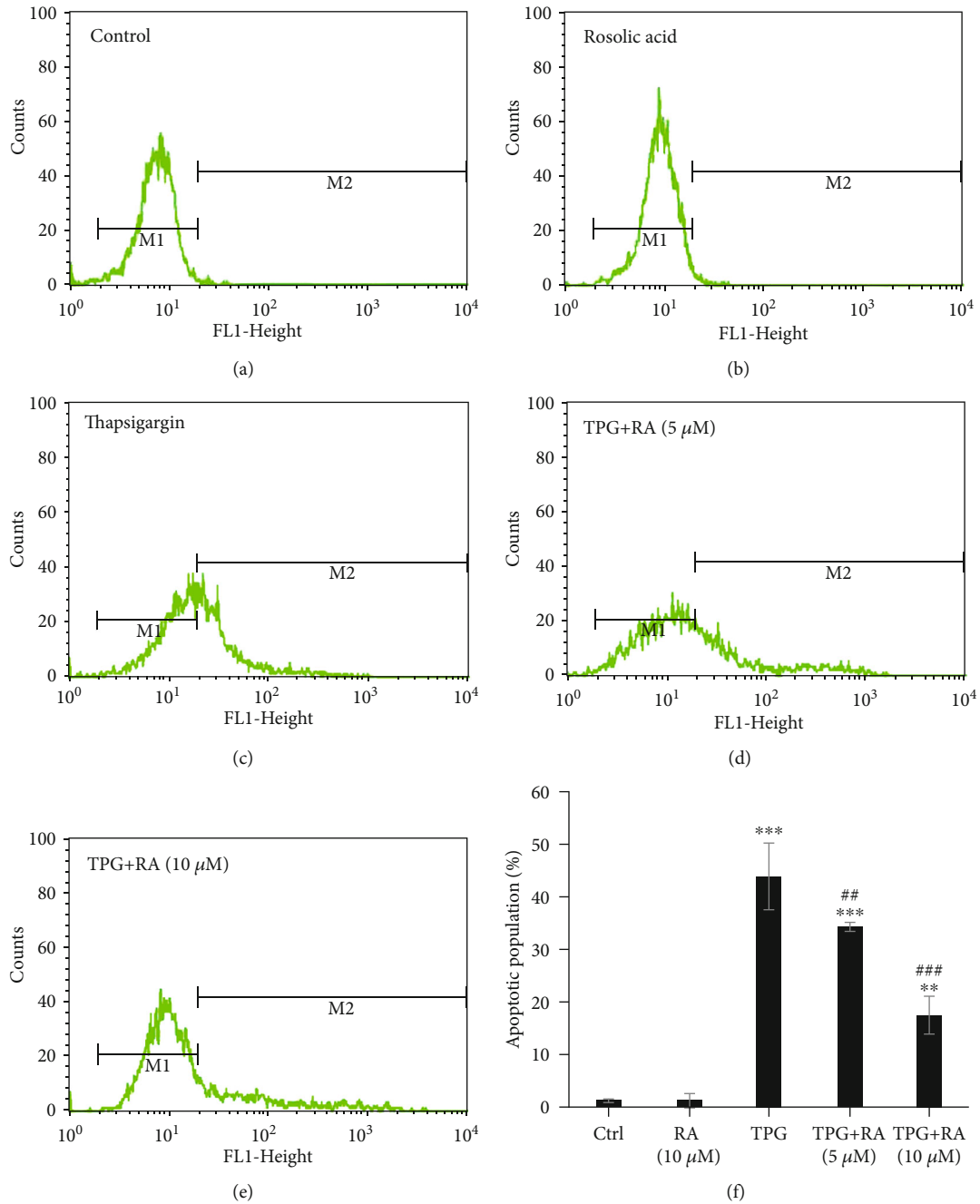
Figure 7: Analysis of apoptotic frequencies. Rosolic acid-treated EA.hy926 cells under ER stress was measured by flow cytometry using the Annexin-V labelling assay. Cells were pretreated with 5 and 10 μg for 24 hours and then treated with Thapsigargin for 2 hours and then incubated with FITC-labelled Annexin-V. After washing, the cells were subjected to flow cytometric analysis. The intensity of the Annexin-V-Fluos signal is represented on the *x*-axis. A significant peak shift towards right was observed in the endothelial cells exposed to TPG (c) in comparison with the untreated cells (a) whereas a dose-dependent shift was observed towards the control level in the RA-pretreated endothelial cells (d, e). No peak shift was observed in the cells exposed only RA (b). The apoptotic population (%) against the effect of Rosolic acid against the TPG-induced ER stress in EA.hy926 cells (f).

maintenance of blood fluidity, permeability, angiogenesis, and the control of vasomotor tone [34]. Oxidative stress, cytokines, and ER stress often cause endothelial cell injury, which disrupts ER homeostasis ensuing the accretion of unfolded or misfolded proteins, and thus activation of an adaptive response called UPR. The main function of UPR is

to decrease ER stress and prolong cell endurance. If ER stress is extended, the signaling shifts from prosurvival to prodeath, which leads to ER stress-stimulated apoptosis [35, 36]. The ER function disruption has often been connected to the progression of numerous illnesses, including diabetes [37–39]. Although the causative role is yet to be established, the

(a)

(b)

(c)
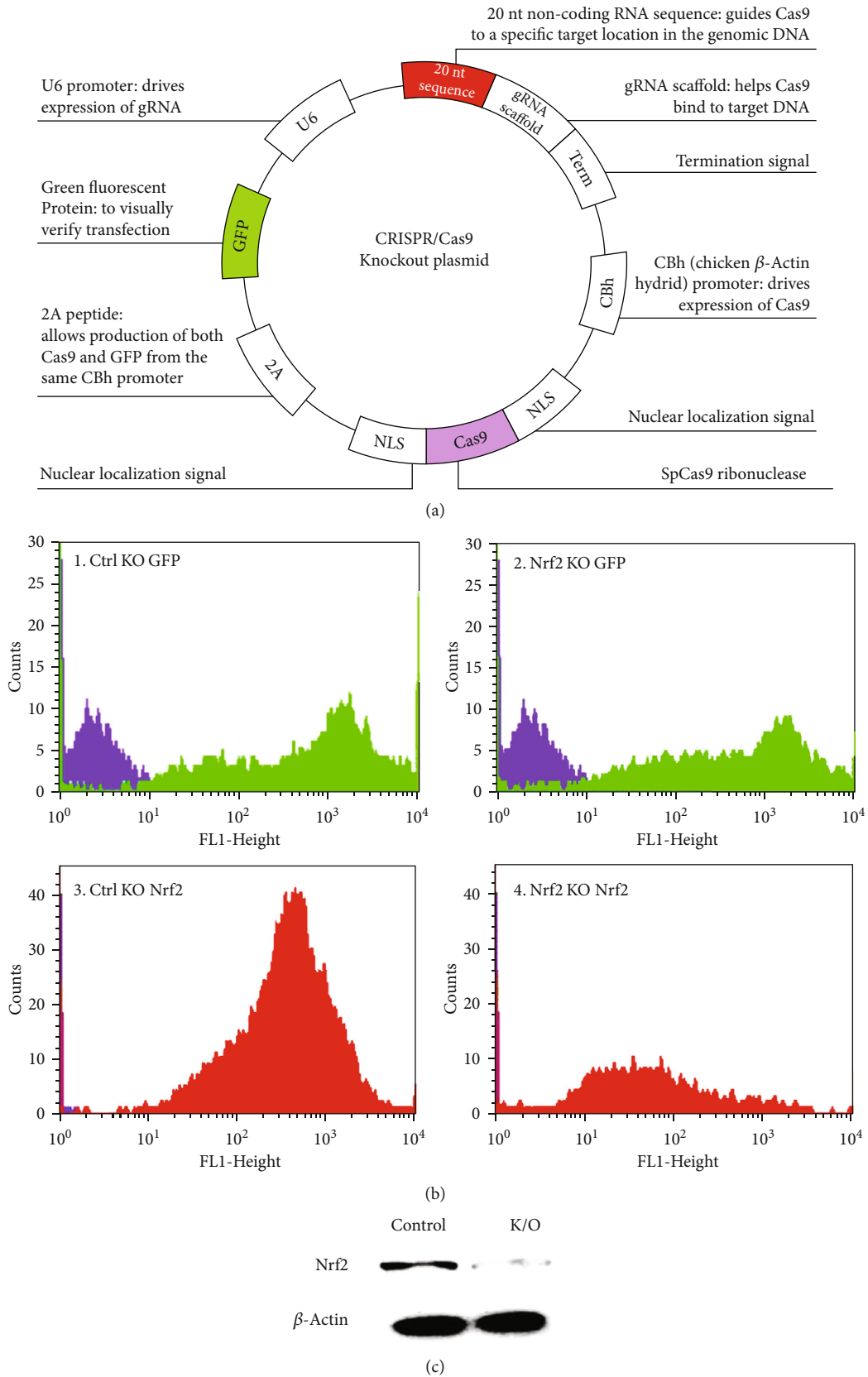
FIGURE 8: CRISPR/Cas9-mediated knockout of Nrf2 expression in EA.hy926 cells. The endothelial cells were transfected with Nrf2-CRISPR (a). CAS9-GFP plasmid and GFP+ cells expression were screened using FACS (b). Western blot analysis for Nrf2-expression was performed to confirm successful Nrf2-depletion (c).

(a)

(b)

(c)

(d)

(e)
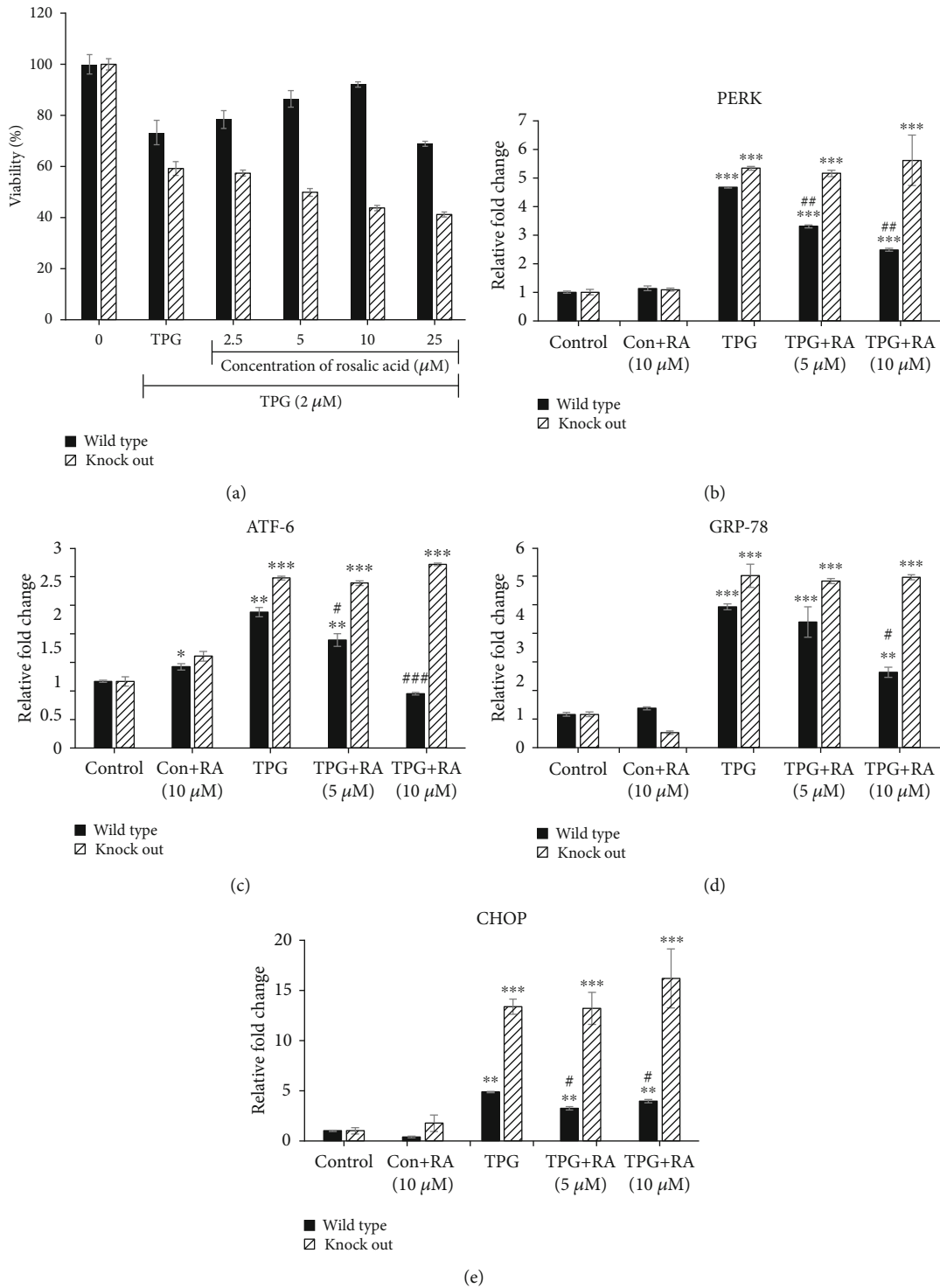
Figure 9: Effect of Rosolic acid on ER stress-induced toxicity in Nrf2 KO and wild-type EA.hy926 cells. (a) Cytoprotective effect of Rosolic acid in wild-type and Nrf2 KO EA.hy926 cells against thapsigargin-induced toxicity as assessed by MTT assay. (b) Effect of Rosolic acid on ER stress-induced toxicity in Nrf2 KO and wild-type cells as assessed by ER stress markers, (b) protein kinase R- (PKR-) like endoplasmic reticulum kinase (PERK), (c) activating transcription factor- (ATF-) 6, (d) glucose-regulated protein (GRP) 78, and (e) C/ERB homologous protein (CHOP) gene expression levels in ER stress-induced in wild-type and Nrf2 KO EA.hy926 cells using thapsigargin by qRT-PCR analysis. Data are represented as mean ± SD of three independent experiments. ∗Significant compared with the control group. #Significant compared with TPG group; $P < 0.05$ determined by one-way ANOVA followed by Tukey's post hoc test.

Protein synthesis machinery

Protein transport

Stress response proteins

Protein folding proteins

ER proteins

(a)
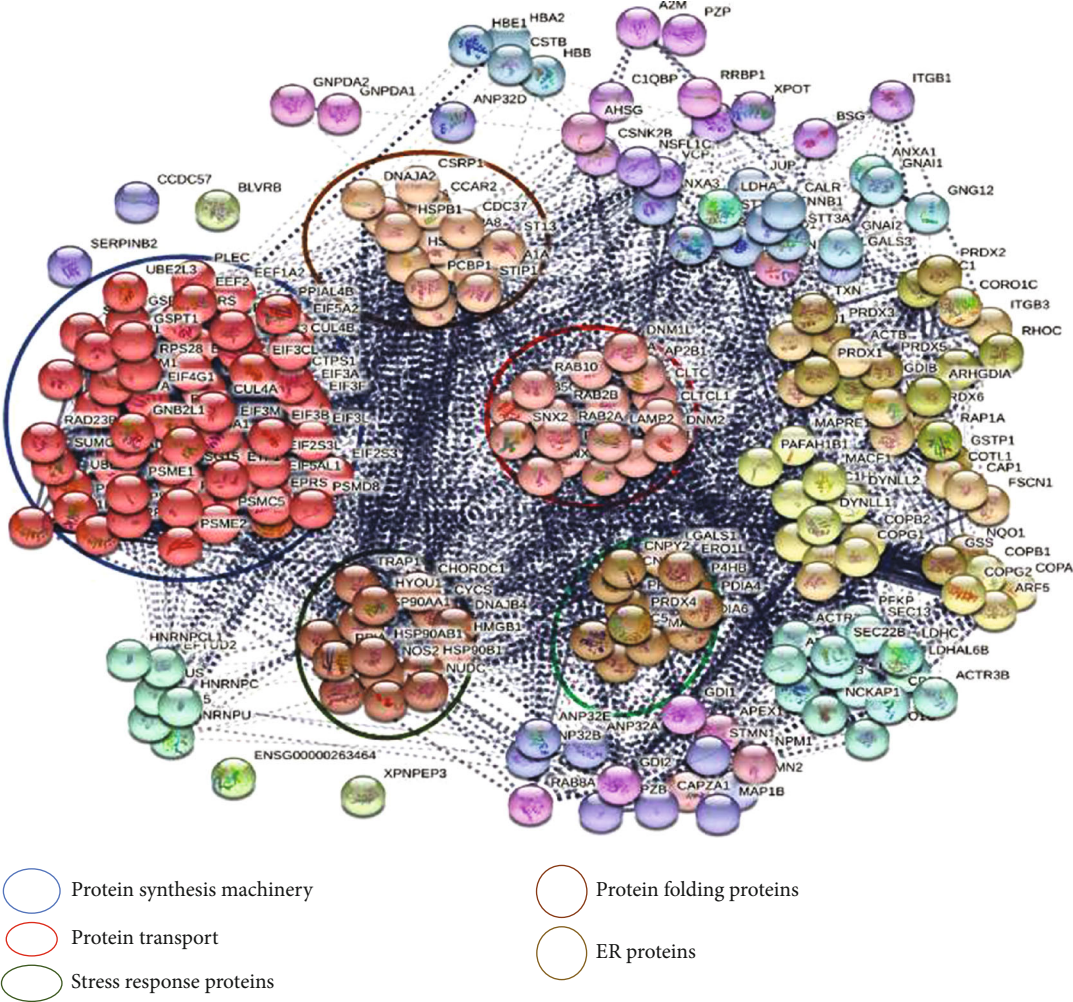
Figure 10: Continued.

(b)
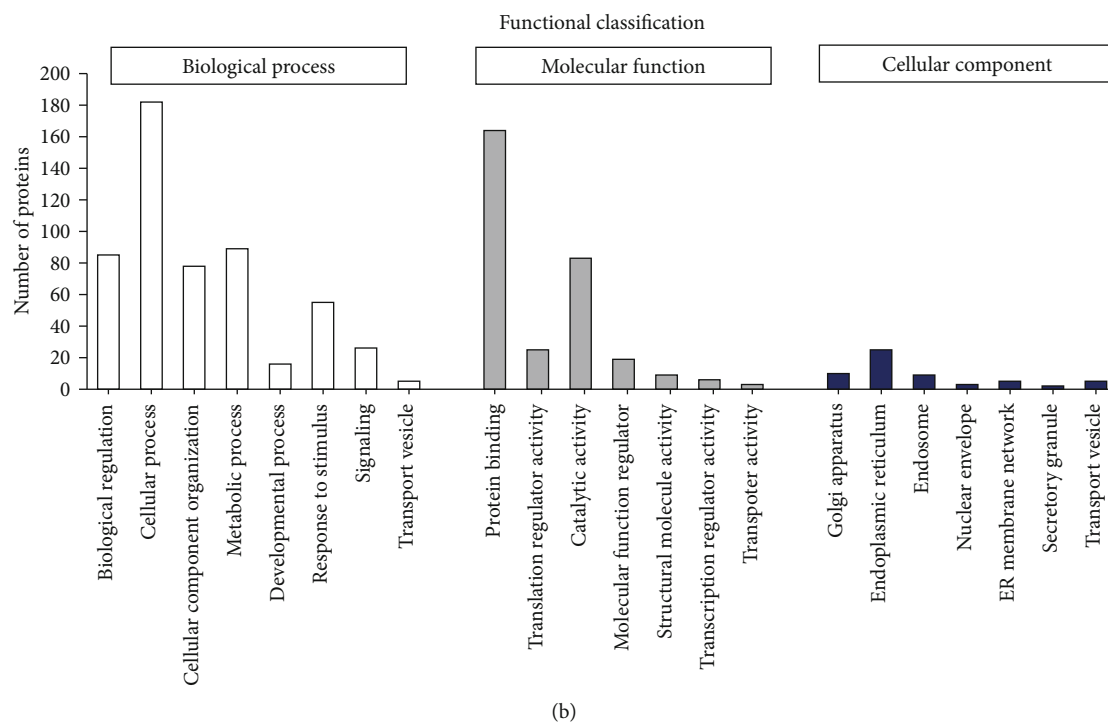
Figure 10: (a) Visualization of protein–protein interaction network of differentially regulated proteins using STRING 10.5 web tool with "MCL inflation parameter (3.0) and medium confidence (0.4)." The colour of nodes corresponds to a cluster, and intercluster edges are represented by dashed lines. MCL, Markov clustering algorithm; STRING, Search Tool for the Retrieval of Interacting Genes. (b) Bar chart showing biological process, molecular function and cellular localization of differentially regulated proteins using the PANTHER software. The total number of proteins in each division is shown on the y-axis.

underlying mechanisms by which ER dysfunction can recruit or stimulate a disease state have been suggested [40]. Few investigations have established that ER stress promotes apoptosis through the caspase activation in endothelial cells [41, 42]. Earlier investigations have also revealed that endothelial cells are highly susceptible to ER and oxidative stress, a pathological cause of endothelial injury [43]. Besides, a rate-limiting enzyme of the hexosamine pathway, fructose-6 phosphate amidotransferase, is overexpressed in diabetic settings, which contributes ER stress through inducing UPR-related gene expressions that eventually recruit proinflammatory and apoptosis mechanisms [44]. Also, increased levels of ER stress markers, CHOP, GRP-78, PERK, and ATF-6 are seen in cells under ER stress [45]. Mozzini et al. revealed high levels of GRP-78 and CHOP in the PBMCs of chronic T2DM patients to be linked to the loss of Nrf2/ARE defense [46]. The ER and oxidative stress responses were correlated to PERK-mediated activation of ATF4 and Nrf2 [47]. Yang et al. demonstrated the effects of palmitic acid toxicity on apoptosis of H9c2 cardiomyocytes, uncovered the corelation between ER and oxidative stress apoptotic signaling pathways, and further showed the ameliorative effect of N-acetylcysteine against oxidative and ER stress-induced cell apoptosis [48]. Recently, ER stress has been shown to have a direct link with the inflammatory response pathway. Lei et al. showed that the administration of lipopolysaccharide results in the activation of ER stress as assessed by marker protein expression GRP78 and CHOP along with the increased levels of proinflammatory cytokines

such as IL-1β, IL-6, IL-8, and TNF-α in mouse granulosa cells. Also, inhibition of ER stress by 4-phenylbutyrate (4-PBA) reduced the expression of proinflammatory cytokines and ER stress markers, CHOP and GRP78 [49].

A well-known ER stress inducer, thapsigargin, is an appropriate irreversible inhibitor of sarco/endoplasmic reticulum Ca^{2+}-ATPase (SERCA) which induces an elevation of calcium levels and causes fragmentation of DNA, resulting in cell demise by triggering apoptotic mechanisms or alteration in architecture of the cell [50]. In the current investigation, the two ER stress markers CHOP and GRP78 were induced in thapsigargin-exposed endothelial cells.

Rosolic acid is known for its beneficial effects on the cardiovascular system [28]. RA-induced HO-1 in endothelial cells thereby showed antioxidant, anti-inflammatory, and antiapoptotic effects in several pathophysiological mechanisms stimulated cardiac damage [28]. In the current study, we indicated that RA defends endothelial cells against apoptosis and ER stress, ensuring a favorable effect on the vascular system. The underlying mechanisms explaining the function of RA in endothelial cells and their regulation of physiological processes have not been explored yet. This is the opening line of proof highlighting the role of RA-mediated Nrf2 activation in endothelial cells. Nrf2 is a chief regulator of the cellular stress response, and the activation of Nrf2 by small molecules has shown protective effects against the development of ED both *in vitro* and *in vivo* studies [16]. In the present study, RA activated Nrf2, thereby triggering its downstream regulations, including HO-1,

TABLE 3: List of DAVID annotation clusters with enrichment score above 10.

Category	Term	Count	P value	Fold enrichment	Bonferroni	Benjamini	FDR
		Enrichment score: 17.2					
Annotation cluster 1							
GOTERM_MF_DIRECT	Cadherin binding involved in cell-cell adhesion	33	2.1E-19	7.9	9.1E-17	3.0E-17	3.0E-16
GOTERM_CC_DIRECT	Cell-cell adherens junction	33	5.3E-19	7.7	2.1E-16	3.0E-17	7.4E-16
GOTERM_BP_DIRECT	Cell-cell adhesion	28	2.2E-15	7.2	3.5E-12	1.8E-12	3.7E-12
		Enrichment score: 13.35					
Annotation cluster 2							
UP_KEYWORDS	Chaperone	32	1.4E-25	13.3	3.6E-23	1.2E-23	1.8E-22
GOTERM_MF_DIRECT	Unfolded protein binding	26	3.1E-23	16.4	1.3E-20	6.5E-21	4.3E-20
GOTERM_BP_DIRECT	Protein folding	30	2.4E-22	11.6	3.8E-19	3.8E-19	4.0E-19
UP_KEYWORDS	Stress response	22	1.4E-20	18.4	3.6E-18	6.0E-19	1.8E-17
INTERPRO	Heat shock protein Hsp90	10	5.4E-16	68.9	2.7E-13	2.7E-13	8.0E-13
INTERPRO	Heat shock protein Hsp90, N-terminal	8	2.2E-12	67.3	1.1E-9	5.3E-10	3.1E-9
INTERPRO	Ribosomal protein S5 domain 2-type fold	12	8.5E-12	20.7	4.1E-9	6.8E-10	1.2E-8
GOTERM_BP_DIRECT	Response to stress	12	9.4E-10	13.7	1.5E-6	1.4E-7	1.6E-6
INTERPRO	Histidine kinase-like ATPase, ATP-binding domain	9	8.3E-9	20.7	4.0E-6	3.3E-7	1.2E-5
SMART	HATPase_c	6	8.9E-8	46.1	8.5E-6	8.5E-6	9.8E-5
INTERPRO	Heat shock protein Hsp90, conserved site	4	8.9E-6	75.8	4.3E-3	2.2E-4	1.3E-2
PIR_SUPERFAMILY	Heat shock protein, HSP90/HTPG types	4	7.9E-5	35.2	2.4E-3	2.4E-3	6.7E-2
		Enrichment score: 10.88					
Annotation cluster 3							
UP_KEYWORDS	GTP-binding	30	1.1E-16	7.3	2.9E-14	4.1E-15	1.4E-13
UP_SEQ_FEATURE	Nucleotide phosphate-binding region: GTP	28	1.1E-15	7.4	8.7E-13	8.7E-13	1.7E-12
UP_KEYWORDS	Nucleotide-binding	64	2.0E-15	3.0	5.1E-13	6.4E-14	2.6E-12
GOTERM_MF_DIRECT	GTPase activity	26	5.4E-15	7.7	2.3E-12	4.5E-13	7.5E-12
GOTERM_MF_DIRECT	GTP binding	32	6.5E-15	5.8	2.7E-12	4.6E-13	9.1E-12
INTERPRO	Small GTP-binding protein domain	19	8.0E-12	8.6	3.8E-9	7.6E-10	1.1E-8
UP_KEYWORDS	Prenylation	18	1.9E-11	9.0	4.8E-9	4.3E-10	2.4E-8
UP_SEQ_FEATURE	Lipid moiety-binding region: S-geranylgeranyl cysteine	15	5.1E-11	11.4	4.0E-8	2.0E-8	7.8E-8
UP_SEQ_FEATURE	Short sequence motif: effector region	14	2.8E-10	11.4	2.2E-7	7.3E-8	4.3E-7
INTERPRO	P-loop containing nucleoside triphosphate hydrolase	38	3.5E-10	3.3	1.7E-7	2.1E-8	5.0E-7
INTERPRO	Small GTPase superfamily	15	4.3E-9	8.2	2.1E-6	1.9E-7	6.2E-6
GOTERM_BP_DIRECT	Small GTPase-mediated signal transduction	19	1.7E-8	5.4	2.8E-5	1.7E-6	2.9E-5
GOTERM_MF_DIRECT	GDP binding	9	9.7E-7	11.5	4.1E-4	3.4E-5	1.4E-3
UP_KEYWORDS	Lipoprotein	27	1.1E-5	2.7	2.9E-3	1.1E-4	1.5E-2

TABLE 4: List of DAVID–KEGG pathways of differentially regulated proteins.

Term	Count	%	P value	Fold enrichment	Bonferroni	Benjamini	FDR
Protein processing in endoplasmic reticulum	26	10.6	3.6E-14	6.7	6.0E-12	6.0E-12	4.3E-11
Endocytosis	20	8.1	1.8E-6	3.6	3.1E-4	7.8E-5	2.2E-3
RNA transport	17	6.9	1.5E-6	4.3	2.5E-4	8.3E-5	1.8E-3
Proteasome	9	3.7	5.2E-6	9.0	8.7E-4	1.8E-4	6.3E-3
Antigen processing and presentation	9	3.7	3.0E-4	5.2	4.9E-2	8.4E-3	3.6E-1
Phagosome	12	4.9	5.7E-4	3.5	9.1E-2	1.1E-2	6.9E-1
Estrogen signaling pathway	9	3.7	1.7E-3	4.0	2.6E-1	2.9E-2	2.1E0
Leukocyte transendothelial migration	9	3.7	4.4E-3	3.4	5.3E-1	6.6E-2	5.3E0
Adherent junction	6	2.4	2.2E-2	3.7	9.8E-1	1.9E-1	2.4E1
AMPK signaling pathway	8	3.3	2.1E-2	2.8	9.7E-1	1.9E-1	2.3E1
Rap1 signaling pathway	11	4.5	2.1E-2	2.3	9.7E-1	2.0E-1	2.3E1
Regulation of actin cytoskeleton	10	4.1	4.9E-2	2.1	1.0E0	3.5E-1	4.6E1
Pathways in cancer	15	6.1	6.2E-2	1.7	1.0E0	3.5E-1	5.4E1
Sphingolipid signaling pathway	7	2.8	5.5E-2	2.6	1.0E0	3.5E-1	5.0E1
Pyruvate metabolism	4	1.6	6.1E-2	4.4	1.0E0	3.6E-1	5.4E1
Cysteine and methionine metabolism	4	1.6	5.4E-2	4.6	1.0E0	3.6E-1	4.9E1
Platelet activation	7	2.8	7.5E-2	2.4	1.0E0	3.8E-1	6.1E1
Endocrine and other factor-regulated calcium reabsorption	4	1.6	8.1E-2	3.9	1.0E0	3.9E-1	6.4E1
Nucleotide excision repair	4	1.6	9.0E-2	3.7	1.0E0	4.0E-1	6.8E1

NQO1, GPx, and CAT. Further, we have used GST-ARE-Luc and hNQO1-ARE-Luc reporter gene constructs to confirm the RA-mediated Nrf2 activation potential of RA in EA.hy926 cells and recorded a dose-dependent increase in the Nrf2 expression levels. In agreement with the report published by Foresti et al., RA dose-dependently increased the expression of HO-1 [28]. The Nrf2 translocation from cytosol to nucleus further conformed the Nrf2 activation potential of RA as demonstrated by western blot.

Our data demonstrated TPG exposure decreased expression of HO-1, NQO1, GPx, and CAT, and a dose-dependent increase was observed in the RA pretreatment. Also, the activities of SOD, CAT, and GPx have further confirmed the role of RA in Nrf2 mediated cytoprotective action against oxidative stress in endothelial cells. It is well known that Nrf2 is a master regulator of detoxifying enzymes exerting the effect through its different downstream pathways targeting HO-1, NQO1, GPx, and CAT. Maamoun et al. have already proved that HO-1 independently shows a protective effect in HUVECs against ER stress-mediated endothelial apoptosis and also impaired angiogenesis in a high-lucose environment [51]. Along with HO-1, Chen et al. reported that Nrf2 downstream targets like GPx and glutathione (GSH) showed protection of endothelial cells against H_2O_2-induced cytotoxicity [52]. It was evidenced that under persistent high glucose and more prominently in oscillating high glucose conditions, there was a high increase in the apoptotic population of Primary Human Coronary Artery Endothelial Cells (HCAEC) accompanied by the suppressed expression of Nrf2 and HO-1 [53]. NQO1 and HO-1 have also been implicated in promoting angiogenesis which are reported in diabetic wound healing in various *in vitro* and *in vivo* models [54]. The role of SOD, CAT, and GPx against oxidative stress

has been demonstrated in many vascular complications [55, 56]. Many studies have reported the association of reduced SOD activity and increased vascular oxidative stress and also has been implicated in the vascular disorders with ED as the underlying cause [57–60]. Our earlier studies confirmed that pterostilbene, an Nrf2 activator, conferred protection against oxidative stress by elevating the levels of Nrf2 and its downstream genes and against cytokine stress [22, 24]. Further, the proteomic profiling of pancreatic tissue isolated from pterostilbene treated mice demonstrated that the majority of differentially regulated proteins were associated with oxidative and ER stress pathways [61].

In the current study, we observed a greater Nrf2 expression and downstream targets and significant inhibition in the expression of PERK, CHOP, and GRP78 in RA-treated endothelial cells. Our outcomes show that the cytoprotective effect of RA on endothelial apoptosis was mediated by the activation of Nrf2.

To determine whether the protective efficacy of RA was facilitated via activation of Nrf2, we have developed Nrf2 knockout endothelial cells using CRISPR/Cas9. We found a very minimal expression of Nrf2 in knockout cells. The probable reason could be the biological plasticity which rescues target Nrf2 activity in CRISPR knockouts. This concept has been observed in three truncated targets, BRD4, DNMT1, and NGLY1, which revealed partial preservation of protein function even after knock out by CRISPR/Cas9{Smits, 2019 #2260}. The Nrf2 cytoprotective adaptive response has evolved to be a powerful protective strategy for organisms against exposure to various insults. This Nrf2 signaling can provide plasticity in the cellular response to a wide array of chemical agents.

Since RA failed to show the protective effect against ER stress in Nrf2 KO by CRISPR/Cas9 in this study, it cannot be ruled out that the increased expression of Nrf2 caused inhibition of ER stress markers such as GRP78 and CHOP, thus restoring ER homeostasis. Additional investigations are needed to extrapolate the function of RA in ER stress-stimulated apoptosis in animal models.

There are many studies that have linked decreased Nrf2 activity leads to increased oxidative damage, leading to many pathophysiological disorders, including obesity, diabetes mellitus, and atherosclerosis which are the major contributors of cardiovascular disorders [62]. Few other Nrf2 activators have also shown promising therapeutics against hyperglycemia and ED as demonstrated by Wang et al. Cinnamaldehyde, an Nrf2 activator, preserved nitric oxide (NO) levels and upregulated Nrf2 levels and its downstream regulations in the HUVEC cells and mouse aortas in the hyperglycaemic environment [63]. Another major Nrf2 activator, dh404, upregulated Nrf2 in Akita mice and diabetic human aortic endothelial cells (HAECs) and proved to be a potential therapeutic agent against diabetes-induced ED [17]. The Nrf2 activators such as curcumin, resveratrol, and sulforaphane have also been explored as adjuvants against diabetic complications [64–66]. Ding proved that the dietary ellagic acid showed a protective effect against oxidative stress developed ED and atherosclerosis through the Nrf2 activation pathway in human umbilical vein endothelial cells and diabetic mice [67].

In our results, we found that RA has a protective effect against ER stress and that there are concentration-dependent effects. Furthermore, we used LC-MS/MS to evaluate the molecular mechanism of endothelial cells. By analyzing the differentially regulated proteins in RA-pretreated endothelial cells exposed to ER stress, we found that the differentially regulated proteins were mainly enriched for proteins from the protein-folding machinery and cell-cell adhesion proteins. It has been reported that under pathophysiological stimuli, the ER homeostasis has been disrupted and leads to the accumulation of misfolded and or unfolded proteins in the ER until correctly folded or demolished [68]. Sustained ER stress has been associated with ED. In the present study, treatment of endothelial cells with RA improved its function by inhibiting ER stress through the regulation of protein-folding machinery.

The adenosine monophosphate-activated protein kinase (AMPK) is a central protein kinase that has been reported to enhance the various protecting cells under different stress stimuli such as hypoxia [69], glucose deprivation [70], and hypertrophy [71] and act as a potential target for resisting atherosclerosis. It has been reported that the key target cells in cardiovascular endothelial cells or smooth muscle cells are directly or indirectly controlled by AMPK [72]. Few reports demonstrated that activation of AMPK is connected with protein synthesis inhibition through elongation factor 2 (eEF2) phosphorylation in heart muscles [73, 74]. Terai et al. reported that AMPK possibly inhibits the signaling of ER-linked apoptosis in heart muscles [73]. Zimmermann et al. demonstrated AMPK employs a positive effect in mouse embryonic fibroblast-associated signaling of Nrf2/heme oxy-genase- (HO-) 1 [75]. Numerous studies suggested that the collaboration of Nrf2 and AMPK contributes to the progressive signaling networks [76, 77]. The AMPK activation has been found to stimulate the unfolded protein response and reduce ER stress in many stressors [78]. Metformin, a known stimulator of AMPK inhibits GRP78 and phosphorylates eukaryotic initiation factor-2α resulting in a reduction of THP-induced ER stress [78]. The silencing of NRF2 during oxidative stress ensuing a constant activation of AMPK contributes to hyperactivation of autophagy [79]. Our results revealed that the RA-facilitated defense against ER stress might be through the amelioration of the AMPK pathway. In addition to these pathways, other significantly changed pathways were cell-cell adhesion proteins, GTP-binding proteins, stress response proteins, proteasomal pathway, RNA transport, etc. To our understanding, this is the preliminary pilot study that validates that RA exerts a direct impact on alleviating ER stress-mediated alterations in defending endothelial cells.

5. Conclusions

In conclusion, Rosolic acid is a potent Nrf2 activator and is protective against ER stress-induced endothelial apoptosis. This protective effect of Rosolic acid is attributed to the induction of Nrf2 and can be developed into a possible therapeutic intervention against ED in diabetes and related cardiovascular diseases. Further *in vivo* studies are essential to confirm the effect of Rosolic acid in diabetes.

Data Availability

The complete data of the findings of this study are available in "Results" and also from the corresponding author.

Conflicts of Interest

We declare that we have no competing financial interests and personal relationships with other people or organizations that can inappropriately influence our work. There is no professional or other personal interests of any nature or kind in any product, service, and/or company that could be construed as influencing the position presented in, or the review of, the manuscript.

Authors' Contributions

Karan Naresh Amin (KNA), Palanisamy Rajaguru (PR), Koustav Sarkar (KS), MR.Ganesh (MRG), Ramkumar Kunka Mohanram (RKM), Daoud Ali (DA), and Takayoshi Suzuki (TS) conceived the study. KNA, PR, KS, MRG, RKM, DA, and TS are responsible for methodology. RKM, DA, PR, and TS are responsible for Software. KNA, PR, KS, MRG, and RKM validated the study. RKM and DA are responsible for formal analysis. KNA, PR, KS, MRG, and RKM acquired resources. DA and RKM are responsible for data curation. KNA, RKM, and DA are responsible for writing—original draft preparation. DA, PR, KS, MRG, and RKM are responsible for writing—review and editing. PR and RKM visualized

Supplementary Materials

Figure S1: description of detailed methodology of proteomics. (Supplementary Materials)

References

[1] A. Sandoo, J. J. C. S. Veldhuijzen van Zanten, G. S. Metsios, D. Carroll, and G. D. Kitas, "The endothelium and its role in regulating vascular tone," *Open Cardiovascular Medicine Journal*, vol. 4, no. 1, pp. 302–312, 2010.

[2] J. S. Pober and W. C. Sessa, "Evolving functions of endothelial cells in inflammation," *Nature Reviews. Immunology*, vol. 7, no. 10, pp. 803–815, 2007.

[3] R. E. Gilbert, "Endothelial loss and repair in the vascular complications of diabetes: pathogenetic mechanisms and therapeutic implications," *Circulation Journal*, vol. 77, no. 4, pp. 849–856, 2013.

[4] J. C. Choy, D. J. Granville, D. W. Hunt, and B. M. McManus, "Endothelial cell apoptosis: biochemical characteristics and potential implications for atherosclerosis," *Journal of Molecular and Cellular Cardiology*, vol. 33, no. 9, pp. 1673–1690, 2001.

[5] Z. Mallat and A. Tedgui, "Apoptosis in the vasculature: mechanisms and functional importance," *British Journal of Pharmacology*, vol. 130, no. 5, pp. 947–962, 2000.

[6] A. Avogaro, M. Albiero, L. Menegazzo, S. de Kreutzenberg, and G. P. Fadini, "Endothelial dysfunction in diabetes: the role of reparatory mechanisms," *Diabetes Care*, vol. 34, Supplement 2, pp. S285–S290, 2011.

[7] A. Avogaro, G. P. Fadini, A. Gallo, E. Pagnin, and S. de Kreutzenberg, "Endothelial dysfunction in type 2 diabetes mellitus," *Nutrition, Metabolism, and Cardiovascular Diseases*, vol. 16, Suppl 1, pp. S39–S45, 2006.

[8] S. Z. Hasnain, "Endoplasmic reticulum and oxidative stress in immunopathology: understanding the crosstalk between cellular stress and inflammation," *Clinical & Translational Immunology*, vol. 7, no. 7, article e1035, 2018.

[9] H. Maamoun, T. Benameur, G. Pintus, S. Munusamy, and A. Agouni, "Crosstalk between oxidative stress and endoplasmic reticulum (er) stress in endothelial dysfunction and aberrant angiogenesis associated with diabetes: a focus on the protective roles of heme oxygenase (ho)-1," *Frontiers in Physiology*, vol. 10, 2019.

[10] G. Amodio, O. Moltedo, R. Faraonio, and P. Remondelli, "Targeting the endoplasmic reticulum unfolded protein response to counteract the oxidative stress-induced endothelial dysfunction," *Oxidative Medicine and Cellular Longevity*, vol. 2018, Article ID 4946289, 13 pages, 2018.

[11] Y. Dong, C. Fernandes, Y. Liu et al., "Role of endoplasmic reticulum stress signalling in diabetic endothelial dysfunction and atherosclerosis," *Diabetes & Vascular Disease Research*, vol. 14, no. 1, pp. 14–23, 2016.

[12] M. Toral, R. Jimenez, M. Romero et al., "Role of endoplasmic reticulum stress in the protective effects of pparbeta/delta activation on endothelial dysfunction induced by plasma from patients with lupus," *Arthritis Research & Therapy*, vol. 19, no. 1, 2017.

[13] J. A. David, W. J. Rifkin, P. S. Rabbani, and D. J. Ceradini, "The nrf2/keap1/are pathway and oxidative stress as a therapeutic target in type ii diabetes mellitus," *Journal Diabetes Research*, vol. 2017, article 4826724, pp. 1–15, 2017.

[14] E. Bhakkiyalakshmi, D. Sireesh, P. Rajaguru, R. Paulmurugan, and K. M. Ramkumar, "The emerging role of redox-sensitive nrf2-keap1 pathway in diabetes," *Pharmacological Research*, vol. 91, pp. 104–114, 2015.

[15] R. Li, Z. Jia, and H. Zhu, "Regulation of nrf2 signaling," *Reactive Oxygen Species (Apex)*, vol. 8, no. 24, pp. 312–322, 2019.

[16] A. Karan, E. Bhakkiyalakshmi, R. Jayasuriya, D. V. L. Sarada, and K. M. Ramkumar, "The pivotal role of nuclear factor erythroid 2-related factor 2 in diabetes- induced endothelial dysfunction," *Pharmacological Research*, vol. 153, article 104601, 2020.

[17] A. Sharma, L. Rizky, N. Stefanovic et al., "The nuclear factor (erythroid-derived 2)-like 2 (nrf2) activator dh404 protects against diabetes-induced endothelial dysfunction," *Cardiovascular Diabetology*, vol. 16, no. 1, 2017.

[18] Z. Ungvari, Z. Bagi, A. Feher et al., "Resveratrol confers endothelial protection via activation of the antioxidant transcription factor nrf2," *American Journal of Physiology. Heart and Circulatory Physiology*, vol. 299, no. 1, pp. H18–H24, 2010.

[19] H. Mao, T. Tao, X. Wang et al., "Zedoarondiol attenuates endothelial cells injury induced by oxidized low-density lipoprotein via nrf2 activation," *Cellular Physiology and Biochemistry*, vol. 48, no. 4, pp. 1468–1479, 2018.

[20] L. Cominacini, C. Mozzini, U. Garbin et al., "Endoplasmic reticulum stress and nrf2 signaling in cardiovascular diseases," *Free Radical Biology & Medicine*, vol. 88, no. Part B, pp. 233–242, 2015.

[21] K. M. Ramkumar, T. V. Sekar, K. Foygel, B. Elango, and R. Paulmurugan, "Reporter protein complementation imaging assay to screen and study nrf2 activators in cells and living animals," *Analytical Chemistry*, vol. 85, no. 15, pp. 7542–7549, 2013.

[22] E. Bhakkiyalakshmi, D. Shalini, T. V. Sekar, P. Rajaguru, R. Paulmurugan, and K. M. Ramkumar, "Therapeutic potential of pterostilbene against pancreatic beta-cell apoptosis mediated through nrf2," *British Journal of Pharmacology*, vol. 171, no. 7, pp. 1747–1757, 2014.

[23] B. Elango, S. Dornadula, R. Paulmurugan, and K. M. Ramkumar, "Pterostilbene ameliorates streptozotocin-induced diabetes through enhancing antioxidant signaling pathways mediated by nrf2," *Chemical Research in Toxicology*, vol. 29, no. 1, pp. 47–57, 2016.

[24] D. Sireesh, M. R. Ganesh, U. Dhamodharan et al., "Role of pterostilbene in attenuating immune mediated devastation of pancreatic beta cells via nrf2 signaling cascade," *The Journal of Nutritional Biochemistry*, vol. 44, pp. 11–21, 2017.

[25] P. Vanitha, S. Senthilkumar, S. Dornadula, S. Anandhakumar, P. Rajaguru, and K. M. Ramkumar, "Morin activates the nrf2-are pathway and reduces oxidative stress-induced DNA damage in pancreatic beta cells," *European Journal of Pharmacology*, vol. 801, pp. 9–18, 2017.

[26] N. Suganya, E. Bhakkiyalakshmi, S. Suriyanarayanan, R. Paulmurugan, and K. M. Ramkumar, "Quercetin ameliorates tunicamycin-induced endoplasmic reticulum stress in endothelial cells," *Cell Proliferation*, vol. 47, no. 3, pp. 231–240, 2014.

[27] N. Suganya, K. P. Mani, D. Sireesh et al., "Establishment of pancreatic microenvironment model of er stress: Quercetin attenuates β-cell apoptosis by invoking nitric oxide-cgmp signaling in endothelial cells," *The Journal of Nutritional Biochemistry*, vol. 55, pp. 142–156, 2018.

[28] R. Foresti, M. Hoque, D. Monti, C. J. Green, and R. Motterlini, "Differential activation of heme oxygenase-1 by chalcones and Rosolic acid in endothelial cells," *The Journal of Pharmacology and Experimental Therapeutics*, vol. 312, no. 2, pp. 686–693, 2005.

[29] C. M. Oslowski and F. Urano, "Measuring ER stress and the unfolded protein response using mammalian tissue culture system," *Methods in Enzymology*, vol. 490, pp. 71–92, 2011.

[30] P. Sehgal, P. Szalai, C. Olesen et al., "Inhibition of the sarco/endoplasmic reticulum (ER) Ca^{2+}-ATPase by thapsigargin analogs induces cell death via ER Ca^{2+} depletion and the unfolded protein response," *The Journal of Biological Chemistry*, vol. 292, no. 48, pp. 19656–19673, 2017.

[31] L. Tolosa, M. T. Donato, and M. J. Gomez-Lechon, "General cytotoxicity assessment by means of the MTT assay," *Methods in Molecular Biology*, vol. 1250, pp. 333–348, 2015.

[32] H. Sim Choi, J. Woo Kim, Y. N. Cha, and C. Kim, "A quantitative nitroblue tetrazolium assay for determining intracellular superoxide anion production in phagocytic cells," *Journal of Immunoassay & Immunochemistry*, vol. 27, no. 1, pp. 31–44, 2006.

[33] C. J. Weydert and J. J. Cullen, "Measurement of superoxide dismutase, catalase and glutathione peroxidase in cultured cells and tissue," *Nature Protocols*, vol. 5, no. 1, pp. 51–66, 2010.

[34] P. Rajendran, T. Rengarajan, J. Thangavel et al., "The vascular endothelium and human diseases," *International Journal of Biological Sciences*, vol. 9, no. 10, pp. 1057–1069, 2013.

[35] C. M. Scull and I. Tabas, "Mechanisms of er stress-induced apoptosis in atherosclerosis," *Arteriosclerosis, Thrombosis, and Vascular Biology*, vol. 31, no. 12, pp. 2792–2797, 2011.

[36] E. Szegezdi, S. E. Logue, A. M. Gorman, and A. Samali, "Mediators of endoplasmic reticulum stress-induced apoptosis," *EMBO Reports*, vol. 7, no. 9, pp. 880–885, 2006.

[37] L. Ozcan and I. Tabas, "Role of endoplasmic reticulum stress in metabolic disease and other disorders," *Annual Review of Medicine*, vol. 63, no. 1, pp. 317–328, 2012.

[38] H. P. Harding and D. Ron, "Endoplasmic reticulum stress and the development of diabetes: a review," *Diabetes*, vol. 51, Supplement 3, pp. S455–S461, 2002.

[39] X. Lei, S. Zhang, S. E. Barbour et al., "Spontaneous development of endoplasmic reticulum stress that can lead to diabetes mellitus is associated with higher calcium-independent phospholipase a2 expression: a role for regulation by srebp-1," *The Journal of Biological Chemistry*, vol. 285, no. 9, pp. 6693–6705, 2010.

[40] J. H. Lin, P. Walter, and T. S. Yen, "Endoplasmic reticulum stress in disease pathogenesis," *Annual Review of Pathology*, vol. 3, no. 1, pp. 399–425, 2008.

[41] R. Sano and J. C. Reed, "ER stress-induced cell death mechanisms," *Biochimica et Biophysica Acta*, vol. 1833, no. 12, pp. 3460–3470, 2013.

[42] N. Sovolyova, S. Healy, A. Samali, and S. E. Logue, "Stressed to death - mechanisms of ER stress-induced cell death," *Biological Chemistry*, vol. 395, no. 1, pp. 1–13, 2014.

[43] S. Lenna, R. Han, and M. Trojanowska, "Endoplasmic reticulum stress and endothelial dysfunction," *IUBMB Life*, vol. 66, no. 8, pp. 530–537, 2014.

[44] A. T. Sage, L. A. Walter, Y. Shi et al., "Hexosamine biosynthesis pathway flux promotes endoplasmic reticulum stress, lipid accumulation, and inflammatory gene expression in hepatic cells," *American Journal of Physiology. Endocrinology and Metabolism*, vol. 298, no. 3, pp. E499–E511, 2010.

[45] A. Samali, U. Fitzgerald, S. Deegan, and S. Gupta, "Methods for monitoring endoplasmic reticulum stress and the unfolded protein response," *International Journal of Cell Biology*, vol. 2010, Article ID 830307, 11 pages, 2010.

[46] C. Mozzini, U. Garbin, C. Stranieri et al., "Endoplasmic reticulum stress and nrf2 repression in circulating cells of type 2 diabetic patients without the recommended glycemic goals," *Free Radical Research*, vol. 49, no. 3, pp. 244–252, 2015.

[47] S. B. Cullinan and J. A. Diehl, "Coordination of ER and oxidative stress signaling: the perk/nrf2 signaling pathway," *The International Journal of Biochemistry & Cell Biology*, vol. 38, no. 3, pp. 317–332, 2006.

[48] L. Yang, G. Guan, L. Lei, J. Liu, L. Cao, and X. Wang, "Oxidative and endoplasmic reticulum stresses are involved in palmitic acid-induced h9c2 cell apoptosis," *Bioscience Reports*, vol. 39, no. 5, 2019.

[49] L. Lei, J. Ge, H. Zhao, X. Wang, and L. Yang, "Role of endoplasmic reticulum stress in lipopolysaccharide-inhibited mouse granulosa cell estradiol production," *The Journal of Reproduction and Development*, vol. 65, no. 5, pp. 459–465, 2019.

[50] Y. Kaneko and A. Tsukamoto, "Thapsigargin-induced persistent intracellular calcium pool depletion and apoptosis in human hepatoma cells," *Cancer Letters*, vol. 79, no. 2, pp. 147–155, 1994.

[51] H. Maamoun, M. Zachariah, J. H. McVey, F. R. Green, and A. Agouni, "Heme oxygenase (ho)-1 induction prevents endoplasmic reticulum stress-mediated endothelial cell death and impaired angiogenic capacity," *Biochemical Pharmacology*, vol. 127, pp. 46–59, 2017.

[52] J. S. Chen, P. H. Huang, C. H. Wang et al., "Nrf-2 mediated heme oxygenase-1 expression, an antioxidant-independent mechanism, contributes to anti-atherogenesis and vascular protective effects of ginkgo biloba extract," *Atherosclerosis*, vol. 214, no. 2, pp. 301–309, 2011.

[53] Z. Ungvari, L. Bailey-Downs, T. Gautam et al., "Adaptive induction of nf-e2-related factor-2-driven antioxidant genes in endothelial cells in response to hyperglycemia," *American Journal of Physiology. Heart and Circulatory Physiology*, vol. 300, no. 4, pp. H1133–H1140, 2011.

[54] A. Jindam, V. G. Yerra, and A. Kumar, "Nrf2: a promising trove for diabetic wound healing," *Annals of Translational Medicine*, vol. 5, no. 23, 2017.

[55] J. A. Leopold and J. Loscalzo, "Oxidative enzymopathies and vascular disease," *Arteriosclerosis, Thrombosis, and Vascular Biology*, vol. 25, no. 7, pp. 1332–1340, 2005.

[56] J. M. Li and A. M. Shah, "Endothelial cell superoxide generation: regulation and relevance for cardiovascular pathophysiology," *American Journal of Physiology. Regulatory, Integrative and Comparative Physiology*, vol. 287, no. 5, pp. R1014–R1030, 2004.

[57] U. Landmesser, R. Merten, S. Spiekermann, K. Buttner, H. Drexler, and B. Hornig, "Vascular extracellular superoxide dismutase activity in patients with coronary artery disease: relation to endothelium-dependent vasodilation," *Circulation*, vol. 101, no. 19, pp. 2264–2270, 2000.

[58] S. Hamed, B. Brenner, A. Aharon, D. Daoud, and A. Roguin, "Nitric oxide and superoxide dismutase modulate endothelial progenitor cell function in type 2 diabetes mellitus," *Cardiovascular Diabetology*, vol. 8, no. 1, 2009.

[59] D. D. Lund, Y. Chu, J. D. Miller, and D. D. Heistad, "Protective effect of extracellular superoxide dismutase on endothelial function during aging," *American Journal of Physiology. Heart and Circulatory Physiology*, vol. 296, no. 6, pp. H1920–H1925, 2009.

[60] D. D. Gutterman, H. Miura, and Y. Liu, "Redox modulation of vascular tone: focus of potassium channel mechanisms of dilation," *Arteriosclerosis, Thrombosis, and Vascular Biology*, vol. 25, no. 4, pp. 671–678, 2005.

[61] S. Dornadula, S. Thiruppathi, R. Palanisamy, D. Umapathy, T. Suzuki, and R. K. Mohanram, "Differential proteomic profiling identifies novel molecular targets of pterostilbene against experimental diabetes," *Journal of Cellular Physiology*, vol. 234, no. 3, pp. 1996–2012, 2018.

[62] R. M. da Costa, D. Rodrigues, C. A. Pereira et al., "Nrf2 as a potential mediator of cardiovascular risk in metabolic diseases," *Frontiers in Pharmacology*, vol. 10, 2019.

[63] F. Wang, C. Pu, P. Zhou et al., "Cinnamaldehyde prevents endothelial dysfunction induced by high glucose by activating nrf2," *Cellular Physiology and Biochemistry*, vol. 36, no. 1, pp. 315–324, 2015.

[64] N. Parsamanesh, M. Moossavi, A. Bahrami, A. E. Butler, and A. Sahebkar, "Therapeutic potential of curcumin in diabetic complications," *Pharmacological Research*, vol. 136, pp. 181–193, 2018.

[65] V. Ciddi and D. Dodda, "Therapeutic potential of resveratrol in diabetic complications: *in vitro* and *in vivo* studies," *Pharmacological Reports*, vol. 66, no. 5, pp. 799–803, 2014.

[66] S. Yamagishi and T. Matsui, "Protective role of sulphoraphane against vascular complications in diabetes," *Pharmaceutical Biology*, vol. 54, no. 10, pp. 2329–2339, 2016.

[67] Y. Ding, B. Zhang, K. Zhou et al., "Dietary ellagic acid improves oxidant-induced endothelial dysfunction and atherosclerosis: role of nrf2 activation," *International Journal of Cardiology*, vol. 175, no. 3, pp. 508–514, 2014.

[68] M. Wang and R. J. Kaufman, "Protein misfolding in the endoplasmic reticulum as a conduit to human disease," *Nature*, vol. 529, no. 7586, pp. 326–335, 2016.

[69] P. T. Mungai, G. B. Waypa, A. Jairaman et al., "Hypoxia triggers AMPK activation through reactive oxygen species-mediated activation of calcium release-activated calcium channels," *Molecular and Cellular Biology*, vol. 31, no. 17, pp. 3531–3545, 2011.

[70] Y. Ren and H. M. Shen, "Critical role of AMPK in redox regulation under glucose starvation," *Redox Biology*, vol. 25, article 101154, 2019.

[71] F. Mailleux, C. Beauloye, J. L. Balligand, S. Horman, and L. Bertrand, "Studying the role of AMPK in cardiac hypertrophy and protein synthesis," *Methods in Molecular Biology*, vol. 1732, pp. 321–342, 2018.

[72] Q. Xu and L. Y. Si, "Protective effects of AMP-activated protein kinase in the cardiovascular system," *Journal of Cellular and Molecular Medicine*, vol. 14, no. 11, pp. 2604–2613, 2010.

[73] K. Terai, Y. Hiramoto, M. Masaki et al., "AMP-activated protein kinase protects cardiomyocytes against hypoxic injury through attenuation of endoplasmic reticulum stress," *Molecular and Cellular Biology*, vol. 25, no. 21, pp. 9554–9575, 2005.

[74] G. J. Browne, S. G. Finn, and C. G. Proud, "Stimulation of the amp-activated protein kinase leads to activation of eukaryotic elongation factor 2 kinase and to its phosphorylation at a novel site, serine 398," *The Journal of Biological Chemistry*, vol. 279, no. 13, pp. 12220–12231, 2004.

[75] K. Zimmermann, J. Baldinger, B. Mayerhofer, A. G. Atanasov, V. M. Dirsch, and E. H. Heiss, "Activated ampk boosts the nrf2/ho-1 signaling axis–a role for the unfolded protein response," *Free Radical Biology & Medicine*, vol. 88, no. Part B, pp. 417–426, 2015.

[76] X. L. Chen, G. Dodd, S. Thomas et al., "Activation of nrf2/are pathway protects endothelial cells from oxidant injury and inhibits inflammatory gene expression," *American Journal of Physiology. Heart and Circulatory Physiology*, vol. 290, no. 5, pp. H1862–H1870, 2006.

[77] E. H. Heiss, D. Schachner, E. R. Werner, and V. M. Dirsch, "Active nf-e2-related factor (nrf2) contributes to keep endothelial no synthase (enos) in the coupled state: role of reactive oxygen species (ros), enos, and heme oxygenase (ho-1) levels," *The Journal of Biological Chemistry*, vol. 284, no. 46, pp. 31579–31586, 2009.

[78] H. Kim, S. Y. Moon, J. S. Kim et al., "Activation of amp-activated protein kinase inhibits er stress and renal fibrosis," *American Journal of Physiology. Renal Physiology*, vol. 308, no. 3, pp. F226–F236, 2015.

[79] M. Kosztelnik, A. Kurucz, D. Papp et al., "Suppression of AMPK/aak-2 by NRF2/SKN-1 down-regulates autophagy during prolonged oxidative stress," *The FASEB Journal*, vol. 33, no. 2, pp. 2372–2387, 2019.

Research Article

Melatonin Alleviates the Toxicity of High Nicotinamide Concentrations in Oocytes: Potential Interaction with Nicotinamide Methylation Signaling

Marwa El-Sheikh [ID],[1,2] **Ahmed Atef Mesalam** [ID],[1,3] **Seok-Hwan Song,**[4] **Jonghyeok Ko,**[4] **and Il-Keun Kong** [ID][1,4,5]

[1]*Division of Applied Life Science (BK21 Four), Gyeongsang National University, Jinju 52828, Republic of Korea*
[2]*Department of Microbial Biotechnology, Genetic Engineering and Biotechnology Division, National Research Centre (NRC), Dokki, Cairo 12622, Egypt*
[3]*Department of Therapeutic Chemistry, Division of Pharmaceutical and Drug Industries Research, National Research Centre (NRC), Dokki, Cairo 12622, Egypt*
[4]*The King Kong Corp. Ltd., Gyeongsang National University, Jinju 52828, Republic of Korea*
[5]*Institute of Agriculture and Life Science, Gyeongsang National University, Jinju 52828, Republic of Korea*

Correspondence should be addressed to Il-Keun Kong; ikong7900@gmail.com

Despite the numerous studies on melatonin and nicotinamide (NAM, the active form of vitamin B3), the linkage between these two biomolecules in the context of signaling pathways regulating preimplantation embryo development has not yet been investigated. In this study, we used bovine oocyte model to elucidate the effect of melatonin on the developmental competence of oocytes under the stress of high NAM concentrations. Results showed that NAM (20 mM) administration during in vitro maturation (IVM) significantly reduced oocyte maturation and actin distribution, while induced reactive oxygen species (ROS) accumulation and mitochondrial dysfunction, the multiple deleterious effects that were alleviated by melatonin (10^{-7} M). The RT-qPCR and/or immunofluorescence showed upregulation of the apoptosis (Caspase-3, Caspase-9, and BAX), autophagy (Beclin-1, LC3A, LC3B, ATG7, LAMP1, and LAMP2), cell cycle (P21, P27, and P53), and DNA damage (COX2 and 8-OxoG) specific markers in oocytes matured under NAM treatment, compared to NAM-melatonin dual-treated and the untreated ones. In addition, the total cleavage and blastocyst development rate, as well as the total number of cells and the inner cell mass (ICM) per blastocyst, were reduced, while DNA fragmentation was induced, in the group of NAM sole treatment than NAM-melatonin cotreatment and control. Inspecting the underlying mechanisms behind NAM-associated toxicity revealed an increase in transcription pattern of NAM methylation (NNMT and AHCY) genes in NAM-treated oocytes while the opposite profile was observed upon melatonin supplementation. In conclusion, to our knowledge, this is the first study reporting that melatonin can protect oocytes and embryos from NAM-induced injury through its ROS-scavenging activity together with potential interaction with NAM methylation signaling.

1. Introduction

The oxidative stress, due to reactive oxygen species (ROS) accumulation, is a key factor that can limit the structural and functional integrity of oocytes, leading to poor developmental competence. Melatonin (N-acetyl-5-methoxytrypta-

mine), a hormone mainly secreted by the pineal gland, has been shown to maintain oocyte quality and embryonic development through the direct protection against oxidative stress [1–3]. It can also trigger the activation of different antioxidant enzymes, such as superoxide dismutase (SOD) and glutathione (GSH) in oocytes [4, 5], and enhance the quality of

embryos through upregulating the genes essential for development and cryotolerance [6]. Under heat shock, prolonged culturing, vitrification, low quality of oocytes, the presence of toxic and antidevelopmental compounds, and other stress conditions, melatonin showed beneficial roles in maintaining oocyte maturation and embryo development [4, 7–11].

On the other hand, nicotinamide (NAM), a water soluble form of niacin (vitamin B3), is a dietary supplement that controls several conditions and diseases including cell survival, inflammations, cancer, and metabolic disorders [12]. Supplementation of NAM at low concentrations during in vitro maturation (IVM) significantly improved the developmental competence of oocytes and embryos [13]. However, exposure to high NAM concentrations has shown many adverse effects comprising obesity, liver toxicity, growth inhibition, DNA damage, risk of thrombocytopenia, epigenetic modifications, and cancer progression [14–17]. Moreover, it induced apoptosis, spindle defects, and mitochondrial dysfunction that significantly interfered with the developmental competence of oocytes and embryos, albeit the cellular signaling pathways regulating these adverse effects have not been entirely elucidated [13, 18, 19]. According to the global NAM market report in 2017, the consumption rate of NAM has increased by 30% [17]. Although this might reflect the public awareness of the beneficial role of NAM, the potential adverse effects of high doses of such dietary vitamin should be also considered.

Inside the cells, NAM is generally metabolized to NAM mononucleotide (NMN), by NAM phosphoribosyltransferase (NAMPT), which is converted to NAM adenine dinucleotide (NAD^+) by NAM mononucleotide adenylyltransferases 1-3 (NMNAT1-3) [20]. The vital role of NAD^+, generated via NAM-mediated metabolism, in regulating metabolic homeostasis and activating the key enzymes responsible for cellular survival and longevity highlights the therapeutic potential of NAM [21]. However, under excessive NAM accumulation, the methylation pathway modulated by NAM-N-methyltransferase (NNMT) to generate methylated NAM (N-methyl-nicotinamide, metNAM) [22] and the direct oxidation of NAM to form NAM-N-oxide through the effect of cytochrome P450 2E1 (CYP2E1) [23] are two metabolic pathways that can be activated. Unlike the normal conditions, NNMT is induced under the increase in the dietary NAM intake, which accordingly catalyzes the NAM hypermethylation pathway where different underlying metabolites are produced [24]. These include N-methyl-2-pyridone-5-carboxamide (2-PY) and N-methyl-4-pyridone-5-carboxamide (4-PY), via the action of aldehyde oxidase (AOX) [17], and homocysteine (HCY), by the activity of the adenosylhomocysteinase (AHCY) [17, 25].

The reported toxicity of NAM following the synthesis of metNAM can be attributed to the disruption of methionine methylation cycle. The universal methyl donor S-adenosylmethionine (SAMe) level is expected to be consumed by NAM to produce metNAM and S-adenosylhomocysteine (SAH), which is converted to HCY by the activity of AHCY, also known as SAH hydrolase [15, 17, 26]. Hyperhomocysteinemia (HHCY), an elevated level of HCY, is a cytotoxic condition involved in cardiovascular disorders, Alzheimer, Parkinson's, inflammations, and heart diseases [27, 28].

Also, HHCY is associated with reduced fertility, risk of recurrent miscarriage and placental infarction, pregnancy loss at early stages, and premature birth with high incidence of congenital defects [27, 29]. Additionally, elevated levels of follicular HCY were associated with the poor qualities of oocytes and embryos in polycystic ovary syndrome patients undergoing assisted reproduction [30]. The mechanism of the HCY-induced damage is most likely accredited to the direct formation of high ROS levels, inhibition of the antioxidant defense system, and induction of proinflammatory responses, mitochondrial dysfunction, methylation related disorders, and epigenetic defects [15, 28, 31].

Despite the enormous studies on the antioxidant activity of melatonin, no data are available on the potential interplay between NAM and such hormone in the context of oocyte maturation and embryo development. In the current study, we sought to explore the effects and the underlying mechanisms of high NAM concentration on bovine oocytes in the presence and absence of melatonin. To achieve this, NAM and melatonin were administered during IVM, while oocyte maturation, actin-based cytoskeletal complex formation, developmental competence of embryos, ROS levels, mitochondrial distribution, apoptosis, autophagy, and DNA damage were inspected. Additionally, NAM methylation signaling pathway was also scrutinized in oocytes.

2. Materials and Methods

2.1. Ethical Approval and Chemicals. The experiments were performed according to the guidelines of Gyeongsang National University and under the regulations of the Institutional Animal Care and Use Committee (Approval ID: GAR-110502-X0017). All chemicals were purchased from Sigma-Aldrich (St. Louis, MO, USA) unless otherwise described.

2.2. Oocyte Aspiration and In Vitro Maturation (IVM). The ovaries of the Hanwoo cows were collected at a local slaughterhouse, transported in thermal bottles to the laboratory within 2 h from slaughtering, and washed in sterile physiological saline. Using 18-gauge needles, cumulus-oocyte complexes (COCs) were collected in 50 mL tube containing TL-HEPES (10 mM HEPES, 2 mM sodium bicarbonate, 114 mM sodium chloride, 0.34 mM sodium biphosphate, 10 mM sodium lactate, 0.5 mM magnesium chloride, 2.0 mM calcium chloride, 3.2 mM potassium chloride, 1 μL/mL phenol red, 100 IU/mL penicillin, and 0.1 mg/mL streptomycin). After washing in TL-HEPES, COCs with at least three layers of cumulus cells were picked up under stereomicroscope (Olympus SZ51, Tokyo, Japan) and washed four times in IVM medium (TCM-199 supplemented with 10% (v/v) fetal bovine serum (FBS), 1 μg/mL estradiol-17β, 10 ng/mL epidermal growth factor (EGF), 10 μg/mL follicle-stimulating hormone (FSH), 0.2 mM sodium pyruvate, 0.1 mg/mL streptomycin, 0.6 mM cysteine, and 100 IU/mL penicillin). The COCs were distributed into four-well plates containing 700 μL IVM at density of 50 COCs per well in the presence or absence of melatonin and NAM and incubated at 38.5°C and 5% CO_2 for 22 h. All experiments comprised three groups corresponding to 20 mM NAM,

combination of 10^{-7} M melatonin and 20 mM NAM, and the untreated control.

2.3. In Vitro Fertilization (IVF).

For fertilization of oocytes, the liquid nitrogen-frozen spermatozoa were thawed and diluted in prewarmed Dulbecco's phosphate-buffered saline (DPBS), then centrifuged at 1800 rpm for 5 min at room temperature. Sperm pellets were resuspended in 500 μL of 20 μg/mL prewarmed heparin supplemented with IVF medium (Tyrode's lactate solution with 22 mg/mL sodium pyruvate, 6 mg/mL bovine serum albumin (BSA), 0.1 mg/mL streptomycin, and 100 IU/mL penicillin) and incubated at 38.5°C and 5% CO_2 for 15 min. Concentrated sperm was then diluted in IVF medium to a density of $1 - 2 \times 10^6$ spermatozoa/mL. Each well of COCs was loaded with 700 μL of prepared sperm followed by incubation at 38.5°C and 5% CO_2 for 18-20 h.

2.4. In Vitro Culture (IVC) and Embryo Development.

Following fertilization, cumulus cells were detached by successive pipetting; then, presumed zygotes were maintained in 700 μL complete SOF medium [32] and incubated at 38.5°C and 5% CO_2. After three days (day 4 postfertilization), total cleavage and the number of 8-16 cell-stage embryos were recorded while the SOF medium was refreshed before incubating the plates for another four days. At day 8 postfertilization, blastocyst development rates were recorded while blastocysts were collected in 4% paraformaldehyde (PFA) and stored at 4°C until use.

2.5. Assessment of Oocyte Maturation.

Twenty-two hours from the onset of maturation, denuded oocytes, collected after repeated pipetting of COCs, were washed in PBS and the first polar body extrusion was directly visualized under microscope. To determine the stage of maturation, oocytes, incubated with 0.5% Triton X-100 for 20 min, were stained with 4',6-diamidino-2-phenylindole (DAPI: 1 μg/mL; Thermo Fisher Scientific, Waltham, MA, USA) for 15 min followed by visualization under confocal laser-scanning microscope (Olympus Fluoview FV1000, Tokyo, Japan). Based on the morphology of the nuclear material, the maturation stage of oocyte was classified as follows: germinal vesicle (GV), metaphase of the first meiosis (metaphase I: MI), and metaphase of the second meiosis (MII: mature).

2.6. Visualization of Cytoskeleton.

The filamentous actin (F-actin) was investigated using Alexa Fluor 488-conjugated phalloidin staining (Thermo Fisher Scientific). In brief, denuded oocytes (n = 10-15: triplicate) were fixed in 4% PFA, washed in PBS, and permeabilized with 0.5% Triton X-100 for 15 min. After washing in PBS, oocytes were incubated with Alexa Fluor 488-conjugated phalloidin for 40 min then washed and stained with DAPI for 15 min at room temperature. Oocytes were visualized under confocal laser-scanning microscope where the fluorescence intensities, in cytoplasm and zona pellucida/oolemma, were estimated using the ImageJ software (National Institutes of Health, Bethesda, MD, USA; https://imagej.nih.gov/ij/).

2.7. Measurement of Reactive Oxygen Species (ROS) Levels.

Denuded oocytes (n = 10-15: triplicate) were incubated with the ROS indicator 2,7-dichlorodihydrofluorescein diacetate (H_2DCFDA: 5 μM) for 20 min at 38.5°C followed by three-times washing in PBS and imaging under epifluorescence microscope (Olympus IX71, Tokyo, Japan). Fluorescence intensities of ROS were estimated using the ImageJ software.

2.8. Assessment of Mitochondrial Distribution Pattern.

To investigate the distribution pattern of mitochondria, denuded oocytes (n = 10-15: triplicate) were incubated with 100 nM MitoTracker deep Red stain (Invitrogen/Molecular Probes, Eugene, OR, USA) at 38.5°C for 40 min before fixation in 4% PFA. Oocytes were inspected under epifluorescence microscope where mitochondrial distribution pattern was classified either as aberrant (dispersed peripherally or semiperipherally in the cytoplasm) or homogeneous (uniformly distributed throughout the cytoplasm).

2.9. RNA Extraction and cDNA Synthesis.

Total RNA was extracted from oocytes (n = 50: triplicate) using Arcturus PicoPure RNA isolation kit (Arcturus, Foster, CA, USA) according to the manufacturer's guidelines. Fixed amounts of RNA (100 ng) were subjected to cDNA synthesis using iScript cDNA synthesis kit (Bio-Rad Laboratories, Hercules, CA, USA) as follows: RNA (15 μL) was mixed with 5x iScript reaction mixture (4 μL) and iScript reverse transcriptase (1 μL) then incubated at 25°C for 5 min, 42°C for 30 min, and 85°C for 5 min.

2.10. Quantitative Reverse Transcription PCR (RT-qPCR).

The RT-qPCR was carried out using iQ-SYBR Green Supermix (Bio-Rad Laboratories) according to the manufacturer's instructions. Briefly, 2 μL of forward and reverse primers mix (Table 1), 5 μL of SYBR Green mix, and 1 μL of nuclease-free water were mixed and distributed into hardshell 96-well skirted PCR plates (Bio-Rad Laboratories) before adding 2 μL of diluted cDNA (150 ng/μL). Using CFX96 instrument (Bio-Rad Laboratories), the qPCR was performed under the following conditions: 95°C for 3 min, 44 cycles of 95°C for 15 s, 58°C for 20 s, and 72°C for 30 s. Each cDNA sample was applied in duplicate (three biological replicates). The mRNA abundance of genes was estimated using GAPDH as a reference gene where the transcription level of each gene in the untreated control was set as 1.

2.11. Immunofluorescence.

Following IVM, oocytes (n = 10-15: triplicate) were fixed in 4% PFA, washed thrice in PBS, and permeabilized with 0.5% Triton X-100 for 20 min. After blocking in 10% FBS and 3% BSA, prepared in PBS, for 2 h, oocytes were incubated overnight at 4°C with the primary antibodies raised against Caspase-3, Caspase-9, Beclin-1, microtubule-associated protein 1 light chain 3 beta (LC3B), cyclooxygenase 2 (COX2), and 8-oxoguanine (8-OxoG) (Supplementary table 1). Samples were washed in PBS before adding the Alexa Fluor-conjugated secondary antibodies (Supplementary table 1). After 90 min incubation at room temperature, DAPI was added for 15 min then oocytes were spotted on glass sides and investigated under

TABLE 1: The primers used in RT-qPCR analysis.

Gene name	Gene sequence	Accession number	Product size
Apoptosis-related genes			
Caspase-3	F: CCCAAGTGTGACCACTGAAC R: CCATTAGGCCACACTCACTG	NM_001077840.1	169
BCL2	F: TGGATGACCGAGTACCTGAA R: CAGCCAGGAGAAATCAAACA	NM_001166486.1	120
BAX	F: CACCAAGAAGCTGAGCGAGTGT R: TCGGAAAAAGACCTCTCGGGGA	XM_027515208.1	118
Autophagy-related genes			
Beclin-1	F: AGTTGAGAAAGGCGAGACAC R: GATGGAATAGGAACCACCAC	NM_001033627.2	100
MAP1LC3A (LC3A)	F: CATGAGCGAGTTGGTCAAAA R: GGGAGGCGTAGACCATGTAG	XM_027558753.1	170
MAP1LC3B (LC3B)	F: TTATCCGAGAGCAGCATCC R: AGGCTTGATTAGCATTGAGC	NM_001001169.1	170
ATG7	F: ATGGCCTTTGAGGAACCTTT R: ATGCCTCCCTTCTGGTTCTT	XM_010817935.3	210
LAMP1	F: GTGAAGAATGGCAACGGAC R: GCATCAGCTGGACCTCGTAA	XM_027558031.1	250
LAMP2	F: AAGAGCAGACCGTTTCCGTG R: CGAACACTCTTGGGCAGTAG	XM_027535042.1	110
Cell cycle and DNA damage-related genes			
P21	F: GCAAATATGGGTCTGGGAGA R: AAATAGTCCAGGCCAGGATG	NM_001098958.2	112
P27	F: TGTCAAACGTGCGAGTGTCTA R: CTCTGCAGTGCTTCTCCAAGT	XM_019961532.1	150
P53	F: CTATGAGATGTTCCGAGAGC R: CTCTCTCTTGAGCATTGGTT	NM_174201.2	153
NAM methylation-related genes			
NNMT	F: CCCAGGTGCTCAAGTGTGAT R: CAGCCTCAAGACACAGGGAG	XM_015474625.2	99
AHCY	F: GCAACTGCTCACTCAGTCCT R: AGGCCTGGATGGTAAAGTGC	NM_001034315.1	81
AOX1	F: AATGTGACCCGGAAACTCCC R: ATGTGGCCCCCTAAAGAAGC	XM_024999354.1	116
Reference gene			
GADPH	F: CCCAGAATATCATCCCTGCT R: CTGCTTCACCACCTTCTTGA	NM_001034034.2	185

confocal laser scanning microscope. The fluorescence intensities were estimated using the ImageJ software.

2.12. Differential Staining of ICM and TE Cells. Day 8 blastocysts, fixed in PFA, were permeabilized with 0.25% Triton X-100 for 20 min, washed three times in washing buffer (0.1% Tween 20 and 0.1% BSA prepared in PBS), and incubated in blocking buffer (5% BSA prepared in PBS) for 1 h at room temperature. Samples were incubated overnight with anti-CDX2 (caudal-related homeobox 2) antibody (BioGenex, Hague, Netherlands) before washing and incubation with Alexa Fluor-568 donkey anti-mouse IgG at room temperature for 1 h. The CDX2 exclusively localizes in the trophectoderm (TE) and is thereby used to distinguish the TE from the inner cell mass (ICM). The nuclei were stained with DAPI for 15 min then the blastocysts were washed and mounted on glass slides and examined under confocal laser-scanning microscope where the total number of cells (DAPI positive), TE (CDX2 positive), and ICM (CDX2 negative) per each blastocyst were recorded.

2.13. Terminal Deoxynucleotidyl Transferase dUTP Nick-End Labeling (TUNEL) Assay. The TUNEL assay for detection of DNA fragmentation was performed using In Situ Cell Death Detection kit according to the manufacturer's instructions (Roche Diagnostics, Indianapolis, USA). In brief, PFA-fixed day 8 blastocysts were washed three times in 0.3% polyvinyl-pyrrolidone (PVP) prepared in PBS and incubated with 0.5% Triton X-100 and 0.1% sodium citrate for 30 min. Samples were treated with fluorescent-conjugated TUNEL solution at 38.5°C for 1 h; then, the nuclei were stained with DAPI for 15 min. Blastocysts were mounted on glass slides and

visualized under epifluorescence microscope where the numbers of bright red spots and DAPI-stained nuclei, indicators for DNA fragmentation, and total number of cells, respectively, were counted in each blastocyst.

2.14. Statistical Analysis. The statistical analyses were carried out using GraphPad Prism version 6 (San Diego, CA, USA). The comparison between NAM-treated group versus NAM-melatonin cotreated or the untreated group was performed using Student's *t*-test. Results are presented as the mean values ± the standard error of the mean (SEM). The degree of significance was presented as *, **, ***, and **** when the *P* values were below 0.05, 0.01, 0.001, and 0.0001, respectively. All experiments were repeated at least three times.

3. Results

3.1. Melatonin Reduces NAM-Associated Impairment of Oocyte Maturation and Actin Stabilization. We have previously reported that high NAM concentrations can negatively affect the process of embryo development [13]. To investigate whether melatonin can alleviate this effect, bovine oocytes were treated with 20 mM NAM for 22 h in the presence and absence of 10^{-7} M melatonin. The concentration of melatonin was selected based on previous studies on the protective role of melatonin during the IVM of bovine [33, 34], porcine [35], and goat [36] oocytes. Initial inspection of oocyte maturation revealed that NAM at 20 mM concentration significantly reduced polar body extrusion ($43.33 \pm 1.67\%$) compared to the untreated control ($66.67 \pm 1.67\%$), whereas melatonin supplementation succeeded to restore the normal maturation ($60.00 \pm 5.00\%$) (Figures 1(a) and 1(b)). For confirmation, the stage of nuclear maturation was inspected at the end of IVM through DAPI staining of the nuclear material. As shown in Figures 1(c) and 1(d), oocyte maturation was significantly reduced after NAM treatment ($44.16 \pm 3.70\%$), compared to the higher levels of melatonin-NAM cotreatment ($58.33 \pm 3.40\%$) and control ($72.92 \pm 3.99\%$). Representative images for the different stages of oocyte maturation are presented in Figure 1(c).

On the other hand, the effect of NAM and melatonin treatment on the filamentous actin (F-actin) integrity in oocyte's zona pellucida/oolemma and cytoplasm was investigated using phalloidin-based staining. As seen in Figures 1(e)–1(g), the fluorescence intensity of F-actin in oocytes decreased after NAM treatment compared to the untreated control, while significantly increased upon addition of melatonin.

3.2. Melatonin Diminishes Oxidative Stress and Mitochondrial Dysfunction in NAM-Treated Oocytes. To evaluate the potential of melatonin to scavenge the ROS during NAM treatment, in vitro matured oocytes were coincubated with the ROS-specific stain H_2DCFDA before visualization under microscope. Remarkably, melatonin supplementation was associated with a significant decrease in the ROS levels compared to the obvious increase under NAM sole treatment (Figures 2(a) and 2(b)). Furthermore, checking the distribution patterns of mitochondria revealed that melatonin can maintain the homogenous mitochondrial distri-

bution, whereas the aberrant distribution was dominant in NAM-treated oocytes compared to melatonin-NAM and control (Figure 2(c)). The morphological appearance of the different mitochondrial distribution patterns is shown in Figure 2(d).

3.3. Melatonin Protects Oocytes from NAM-Induced Apoptosis and Autophagy. Moving forward, the effect of NAM and melatonin on the expression level of different apoptosis and autophagy markers was investigated at transcriptional and/or translation levels. As shown in Figure 3(a), upregulation of Caspase-3 and BAX and downregulation of BCL2 were observed in NAM-treated oocytes as compared to control. Contrarily, the addition of melatonin was accompanied with downregulation of Caspase-3 and BAX. Despite the increase in BCL2 level under melatonin-NAM treatment, this effect did not reach the statistical significance ($P > 0.05$). For confirmation, inspecting the protein levels of Caspase-3 and Caspase-9 in oocytes using immunofluorescence showed a significant increase in the levels of these two proteins in NAM-treated oocytes compared to melatonin-NAM cotreatment and control ones (Figures 3(b)–3(e)). Similarly, the transcription patterns of the autophagy-related genes Beclin-1, LC3A, LC3B, ATG7, LAMP1, and LAMP2 and the translation patterns of Beclin-1 and LC3B were investigated in oocytes treated with NAM and melatonin-NAM. As shown in Figures 3(f)–3(j), an induction in these autophagy markers was observed in NAM-treated group compared to melatonin-NAM cotreatment and control.

3.4. Melatonin Attenuates DNA Damage and Cell Cycle Arrest in NAM-Treated Oocytes. To explore whether NAM accumulation can induce a disturbance in cell cycle and DNA repair mechanisms in oocytes, the abundance of the specific markers P21, P27, P53, COX2, and 8-OxoG was investigated using RT-qPCR and immunofluorescence. As seen in Figure 4(a), NAM treatment was associated with upregulation of the mRNA of P21, P27, and P53 compared to melatonin-NAM cotreatment or the untreated control. Protein expression showed an obvious overexpression of COX2 and 8-OxoG under NAM sole treatment whereas the opposite pattern was observed following melatonin administration (Figures 4(b)–4(e)).

3.5. Melatonin Restores the Developmental Competence of Embryos Post-NAM Treatment. We went further to check the developmental competence of embryos after NAM treatment in the presence and absence of melatonin. As shown in Figures 5(a) and 5(b), the total cleavage and the number of 8-16 embryos, recorded at day 4 postfertilization, displayed a significant decline under NAM sole treatment ($45.83 \pm 3.29\%$ for total cleavage and $30.63 \pm 3.60\%$ for 8-16 cell stage embryos) compared to the untreated control ($77.50 \pm 2.54\%$ for total cleavage and $63.07 \pm 3.20\%$ for 8-16 cell stage embryos). Interestingly, administration of melatonin succeeded to restore the normal development rates ($67.67 \pm 2.77\%$ for total cleavage and $52.10 \pm 3.25\%$ for 8-16 cell stage embryos). Similarly, day 8 blastocyst development showed the lowest rate in the group of

(a)

(b)

(c)

(d)

(e)

(f)

(g)
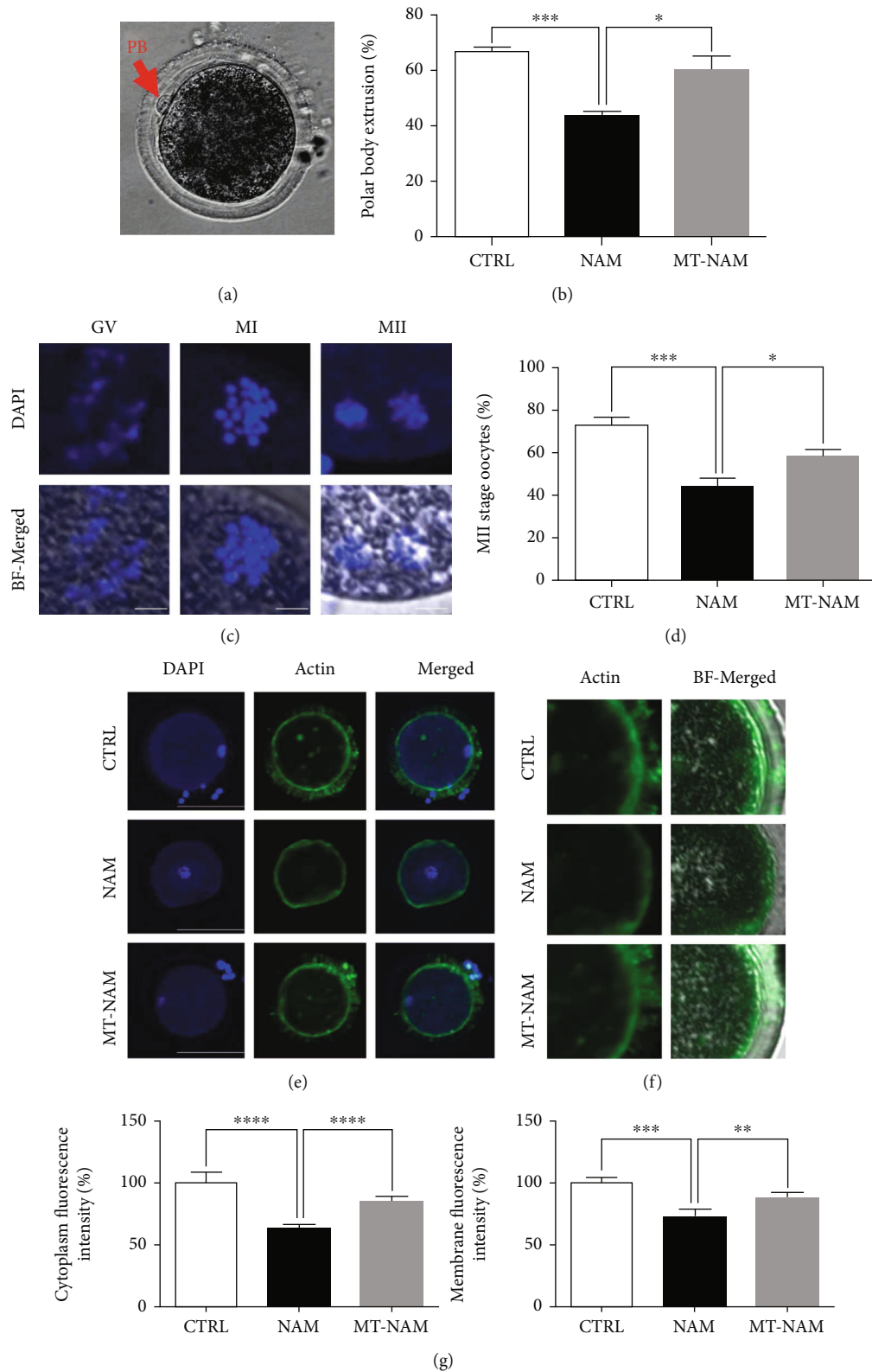
FIGURE 1: Effect of NAM administration on oocyte maturation in presence and absence of melatonin. (a) Light microscopy for the polar body (red arrow) of in vitro matured oocytes. (b) Percentages of oocytes with extruded polar bodies. (c) Microscopy of nuclear maturation using DAPI staining showing the different stages of maturation. (d) Proportion of oocytes that reached the MII stage. (e, f) Filamentous actin distribution in oocytes using Alexa Fluor 488 phalloidin staining. (g) Fluorescence intensity after phalloidin-based staining in oocyte's cytoplasm and zona pellucida/oolemma. Scale bar $= 100 \, \mu$m. The error bars represent the SEM of measurements of three replicates. PB: polar body; GV: germinal vesicle; MI: metaphase I; MII: metaphase II. BF: bright field; NAM: nicotinamide; MT: melatonin.

(a)

(b)

(c)

(d)

FIGURE 2: Effect of melatonin and NAM on ROS levels and mitochondrial distribution. (a) Representative images of oocytes stained wi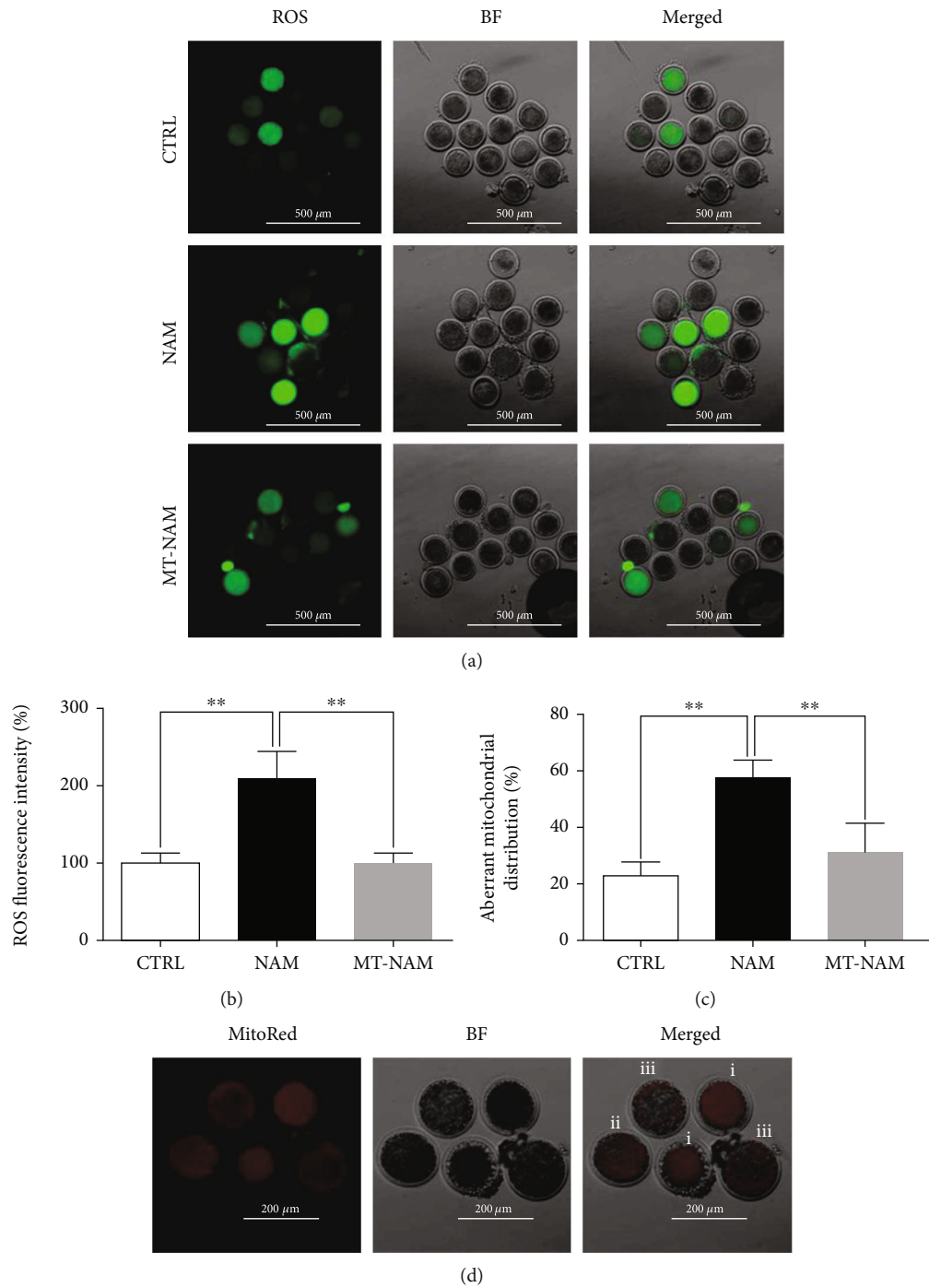th 2,7-dichlorodihydrofluorescein diacetate (H2DCFDA). Scale bar = 500 μm. (b) The ROS signals in oocytes. (c) Percentage of oocytes with aberrant (semiperipheral and peripheral) mitochondrial distribution after staining with MitoTracker Red. (d) Representative images of the different mitochondrial distribution patterns showing (i) homogenous, (ii) semiperipheral, and (iii) peripheral distribution. Scale bar = 200 μm. The error bars represent the SEM of measurements of three replicates. ROS: reactive oxygen species; MitoRed: MitoTracker Red; BF: bright field; NAM: nicotinamide; MT: melatonin.

NAM treatment compared to the melatonin-NAM dual-treated and the control groups (17.43 ± 1.72%, 23.57 ± 1.49%, and 30.43 ± 2.13% corresponding to NAM, melatonin-NAM, and control, respectively, Figure 5(c)).

We proceed to investigate the effect of NAM and melatonin treatment on the quality of embryos using differential staining. As shown in Figures 5(d) and 5(e), the total number of cells per blastocyst was significantly lower in NAM-treated

(a)

(b)

(c)

(d)

(e)
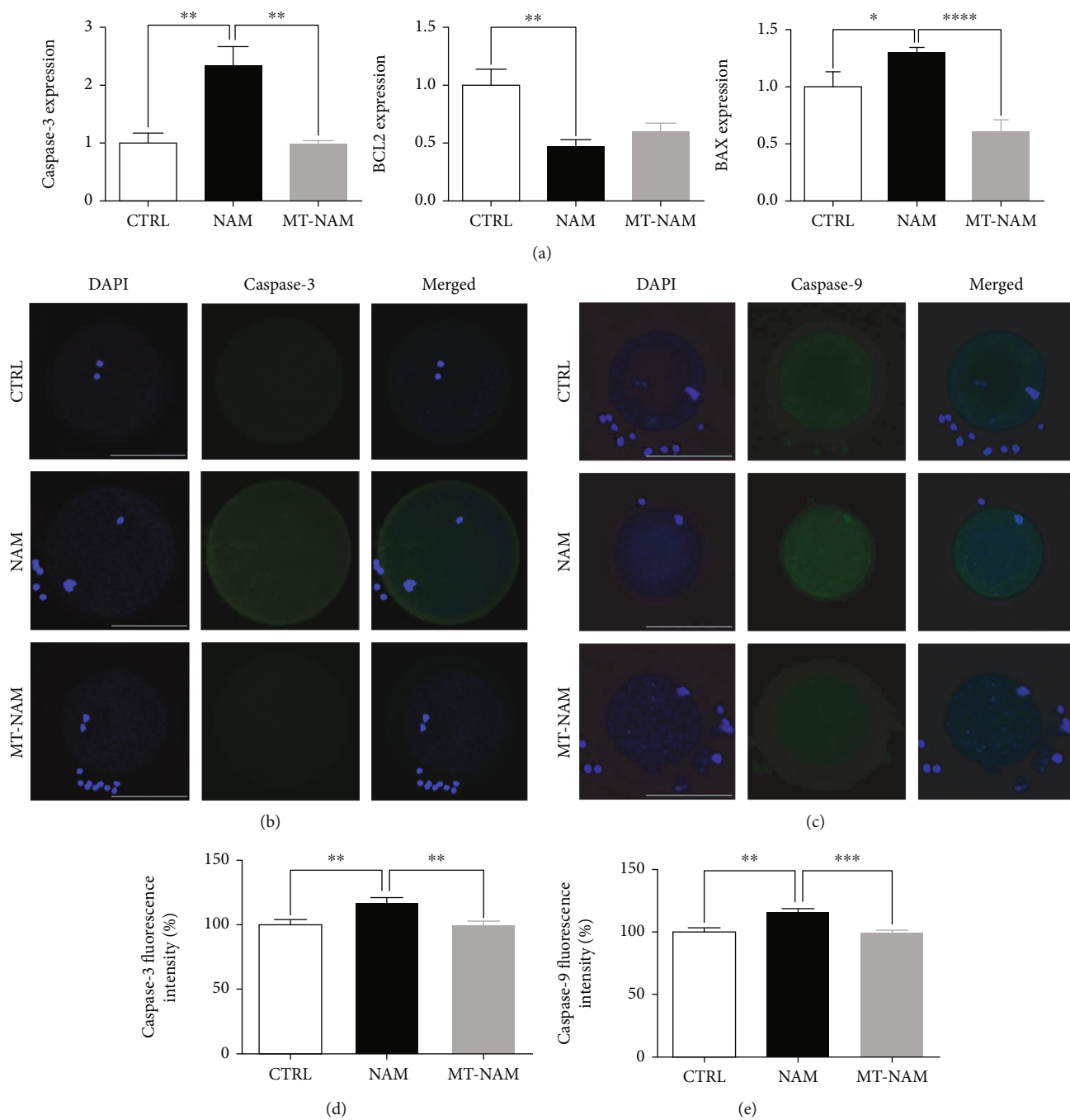
Figure 3: Continued.
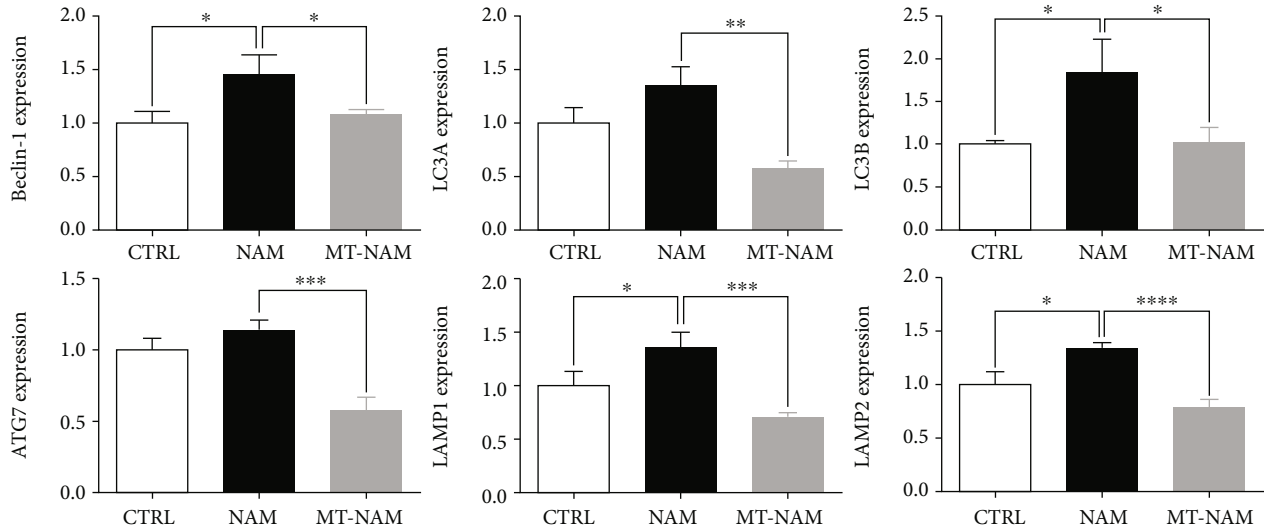
(f)
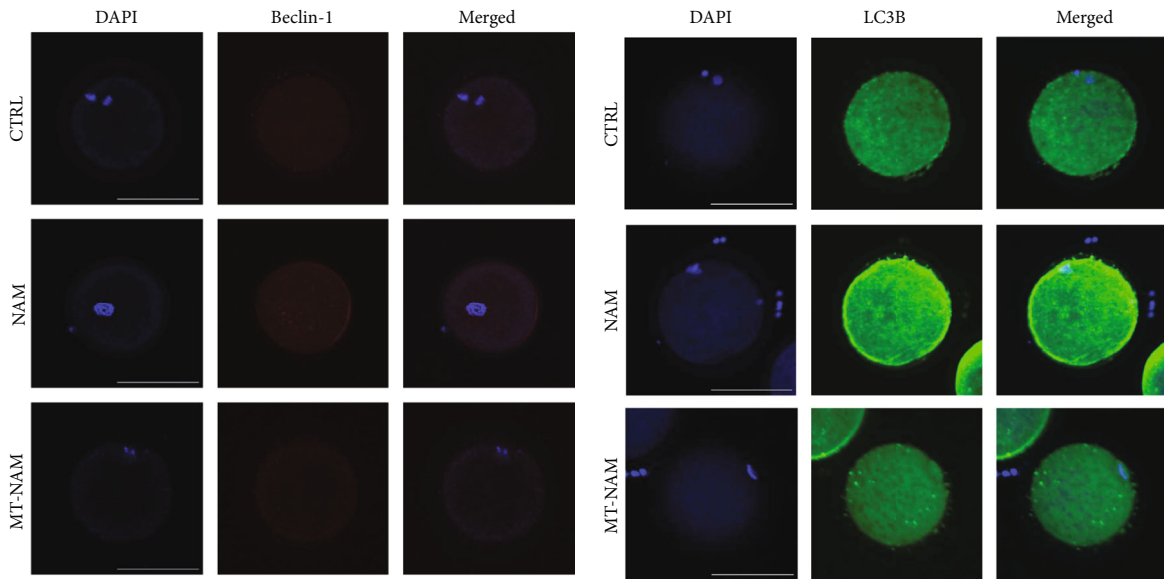
(g)

(h)
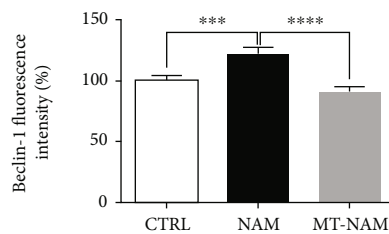
(i)
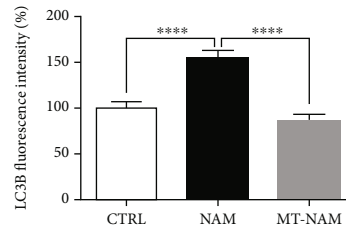
(j)

Figure 3: Effect of melatonin/NAM supplementation on apoptosis and autophagy in oocytes. (a) The transcription levels of apoptosis-related genes in matured oocytes. (b, c) Representative images of Caspase-3 and Caspase-9 immunofluorescence. (d, e) Fluorescence intensity of Caspase-3 and Caspase-9 in oocytes. (f) Transcriptional pattern of the different autophagy-related markers in oocytes. (g, h) Representative images of Beclin-1 and LC3B staining. (i, j) Fluorescence intensity of Beclin-1 and LC3B in oocytes. Scale bar = 100 μm. The error bars represent the SEM of measurements of three replicates. BCL2: B-cell lymphoma 2; BAX: Bcl-2-associated X apoptosis regulator; Beclin-1: autophagy-related gene 6; LC3A (MAP1LC3A): microtubule-associated protein 1 light chain 3 alpha; LC3B (MAP1LC3B): microtubule-associated protein 1 light chain 3 beta; ATG7: autophagy-related gene 6; LAMP1: lysosomal-associated membrane protein 1; LAMP2: lysosomal-associated membrane protein 2; NAM: nicotinamide; MT: melatonin.

(a)

(b)

(c)

(d)

(e)
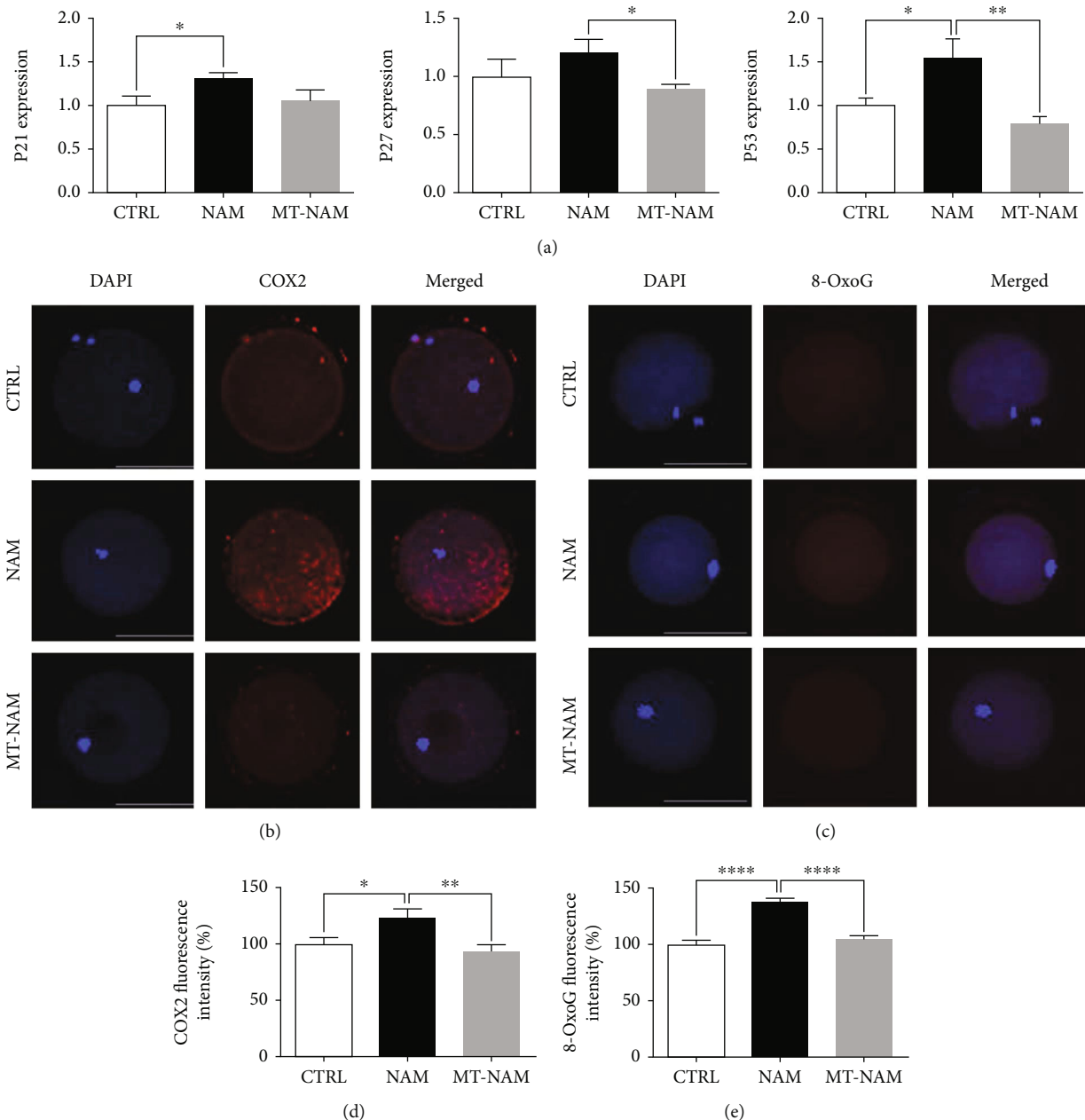
FIGURE 4: Effect of melatonin and NAM administration on cell cycle regulation and DNA damage in oocytes. (a) Relative expression of markers involved in cell cycle arrest and DNA damage. (b, c) Immunofluorescence of matured oocytes showing COX2 and 8-OxoG expression. (d, e) The fluorescence intensity of COX2 and 8-OxoG. The error bars represent the SEM of measurements of three replicates. Scale bar = 100 μm. P21: cyclin-dependent kinase inhibitor 1A; P27: cyclin-dependent kinase inhibitor 1B; COX2: cyclooxygenase 2; 8-OxoG: 8-oxoguanine; NAM: nicotinamide; MT: melatonin.

group compared to melatonin-NAM derived and the control embryos (92.32 ± 5%, 123.1 ± 6%, and 164.5 ± 6% for NAM, melatonin-NAM, and control, respectively). Since the ICM : TE ratio can be used for evaluating the quality of embryos [37], we used the TE-specific CDX2 transcription factor immunofluorescence to assess the differential staining of blastocysts. Obviously, NAM-treated group exhibited the lowest score of ICM (CDX2-negative) cells and accordingly the ICM : TE ratio compared to control, whereas melatonin succeeded to partially normalize these parameters (Figures 5(d) and 5(e)).

The potential protective role of melatonin on NAM developed embryos was also inspected through checking the DNA fragmentation using TUNEL assay. The results showed that NAM administration significantly increased, whereas melatonin supplementation succeeded to decrease the number of apoptotic cells in day 8 blastocysts (7.41 ± 1.25%, 4.41 ± 0.59%, and 3.94 ± 0.63% for NAM, melatonin-NAM, and control blastocysts, respectively, Figures 6(a) and 6(b)).

3.6. Melatonin Interacts with NAM Methylation Signaling Pathway. To clarify the underlying mechanisms behind the

Figure 5: Impact of melatonin and NAM on the developmental competence and quality of embryos. (a) Total cleavage, (b) 8-16 cell embryos, and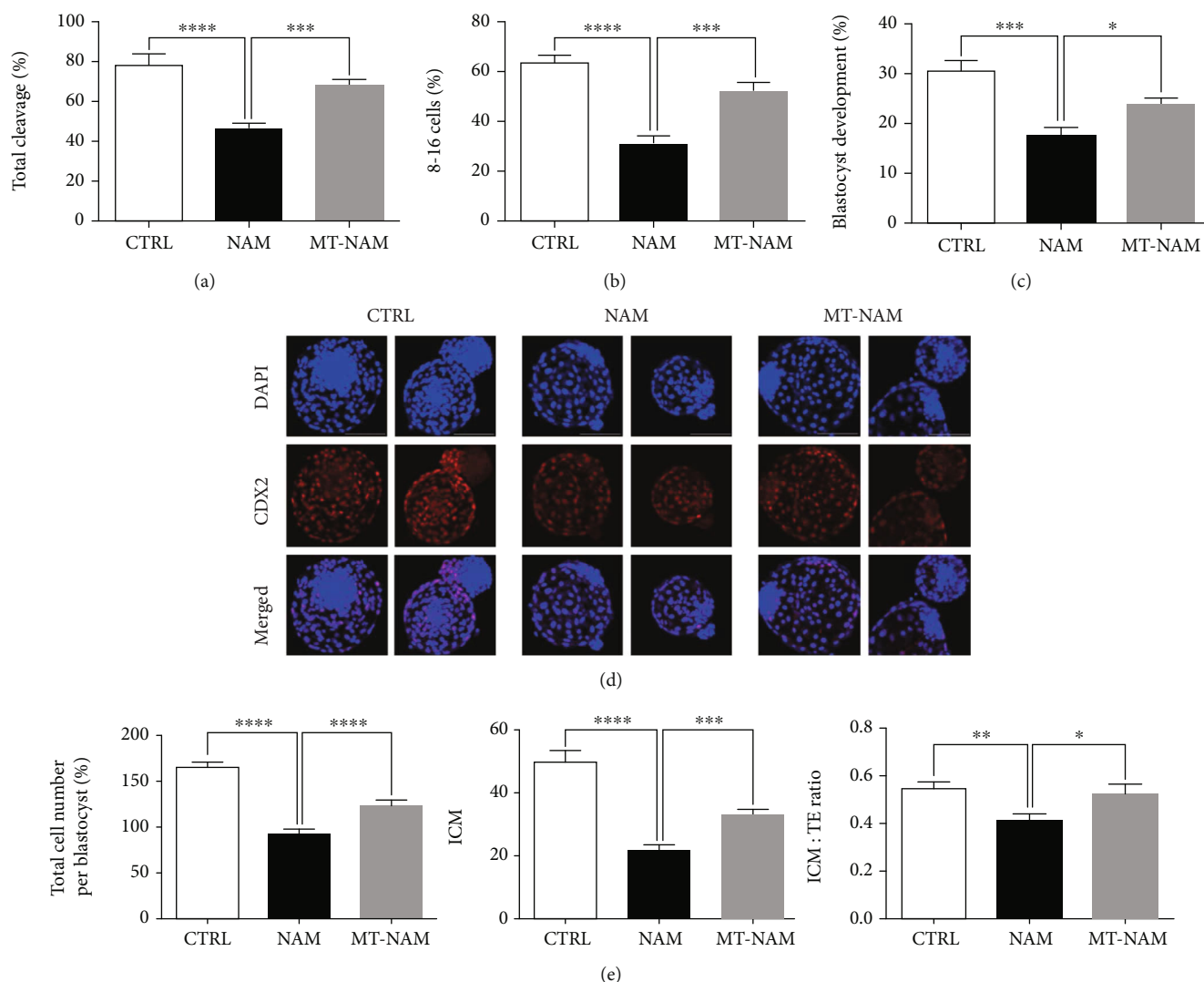 (c) blastocyst development rates after melatonin/NAM treatment. (d) Representative images of the differential staining using the TE-specific marker CDX2. (e) The total number of cells, ICM cells, and the ICM : TE ratio per blastocyst. Scale bar = $100 \, \mu$m. The error bars represent the SEM of measurements of at least three replicates. CDX2: caudal-related homeobox 2; TE: trophectoderm; ICM: inner cell mass; NAM: nicotinamide; MT: melatonin.

protective role of melatonin against NAM toxicity in oocytes, the transcription patterns of the key genes of NAM methylation signaling pathway were investigated using RT-qPCR. These genes included nicotinamide-N-methyltransferase (NNMT, for production of metNAM), adenosylhomocysteinase (AHCY, for homocysteine (HCY)), and aldehyde oxidase (AOX1, for 2-PY and 4-PY metabolites). As shown in Figure 7, upregulation of the tested genes, except AOX1, was observed in oocytes of NAM sole treatment compared to the untreated control. In addition, the administration of melatonin remarkably downregulated the transcription levels of the three tested genes (Figure 7).

4. Discussion

The antioxidant activity of melatonin during the process of embryonic development has been comprehensively studied,

whereas the impact of high NAM concentrations on such developmental process has been fewly reported [6, 7, 13, 18, 38]. To date, the potential linkage between melatonin and NAM in the context of embryo development has not yet been clarified. Using the in vitro bovine oocyte model, we sought to elucidate the interplay between these two biomolecules through studying the effect of NAM administration on the different steps of embryo development, in the presence and absence of melatonin.

Oocyte maturation, the progression from GV stage to MII, is an essential step for successful fertilization and embryo development [39]. The distribution of actin was reported to influence oocyte maturation [40, 41]. In the current study, microscopic examination of oocytes showed that NAM at 20 mM was associated with a significant decline in the number of oocytes with obviously extruded polar body and those reached the MII stage, the mature oocytes. It also

(a)

(b)
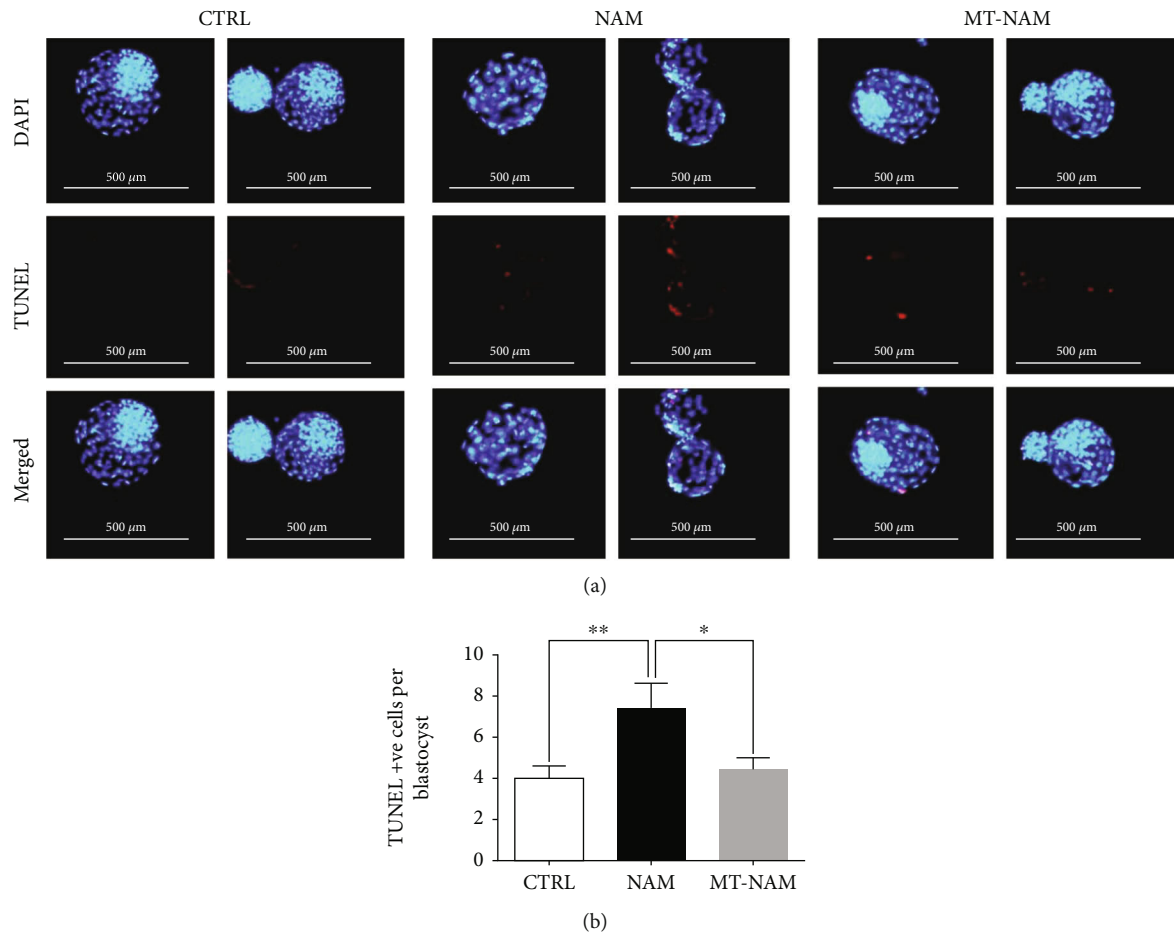
FIGURE 6: DNA fragmentation analysis after NAM treatment in the presence and absence of melatonin. (a) Representative images for DAPI and TUNEL of day 8 blastocysts. (b) The number of TUNEL positive cells per each blastocyst. Scale bar = 500 μm. The error bars represent the SEM of measurements of three replicates. DAPI: 4$'$,6-diamidino-2-phenylindole; TUNEL: terminal deoxynucleotidyl transferase dUTP nick-end labeling; NAM: nicotinamide; MT: melatonin.
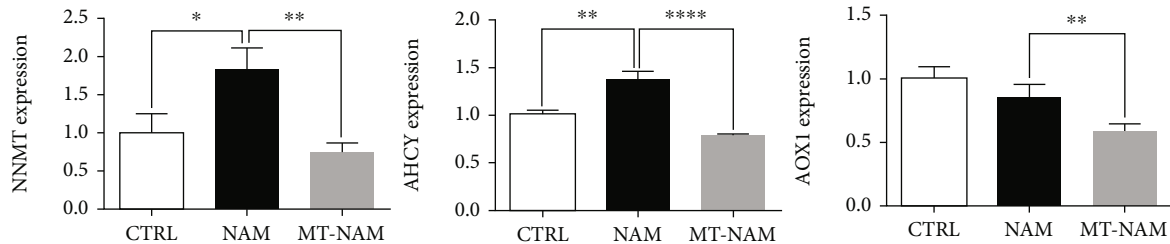
FIGURE 7: Effect of NAM and melatonin on the transcription patterns of genes involved in NAM methylation signaling in oocytes. The error bars represent the SEM of measurements of three replicates. NNMT: nicotinamide-N-methyltransferase; AHCY: adenosylhomocysteinase; AOX1: aldehyde oxidase. NAM: nicotinamide; MT: melatonin.

affected the distribution of filamentous actin in oocytes. Nonetheless, melatonin supplementation under the stress of NAM significantly restored the normal maturation and the actin formation. In line with this, Zhang et al. reported a delay of oocyte maturation and actin distribution in porcine oocytes following exposure to 5 mM NAM [18]. In addition, the ability of melatonin to protect oocytes against the deleterious effects of antidevelopmental compounds including aflatoxin B1, paraquat, and rotenone has been reported [2, 5, 34, 42]. This confirms our observation and reflects the beneficial role of such pineal hormone on oocyte maturation even under the stress of high NAM concentrations.

We have recently reported that exposing oocytes to high dosages of NAM activates the successive release of reactive oxygen species (ROS), which can considerably limit the processes of oocyte maturation and embryo development [13].

In the current study, we moved forward to investigate the potential ROS-scavenging activity of melatonin under the stress of NAM. Interestingly, oocytes matured following melatonin-NAM cotreatment displayed lower ROS levels compared to NAM sole treatment, assuring the, previously reported, protective role of melatonin against different toxic compounds [2, 5, 34, 42].

Overproduction of ROS can induce damage of mitochondria, the cellular organelles responsible for energy production, via ROS-induced ROS release mechanism [43]. Mitochondrial dysfunction has been observed in obesity, diabetes, tumors, and cardiovascular and cerebrovascular diseases [28, 31, 44]. In the current study, higher incidence of aberrant mitochondrial distribution pattern was observed in NAM-treated oocytes. Notably, the majority of oocytes matured under melatonin-NAM supplementation displayed homogenous distribution, an indicator for the quality and developmental competence of oocyte [45]. Consistent with these observations, melatonin enhanced mitochondrial biogenesis that protected the early porcine embryos against mitochondrial damage following rotenone treatment [42]. Altogether, this supports the aforementioned results of maturation and ROS of oocytes matured under melatonin/NAM treatment.

It has been shown that induction of apoptosis and autophagy during IVM negatively affects oocyte maturation and subsequent embryo development [46, 47]. We have previously found an association between high NAM concentrations and the induction of apoptosis and autophagy in oocytes [13]. Considering this, we herein investigated whether melatonin can protect oocyte from apoptosis and autophagy during NAM treatment. Testing the mRNA and/or protein levels of the apoptosis (Caspase-3, Caspase-9, BCL2, and BAX) and autophagy (Beclin-1, LC3A, LC3B, ATG7, LAMP1, and LAMP2) markers showed downregulation of BCL2 and upregulation of the other genes, in oocytes treated with NAM, whereas their levels were normalized by melatonin. The linkage between DNA damage and ROS production, apoptosis, mitochondrial dysfunction, reduced oocyte maturation, cell cycle arrest, and, in some cases, fertility loss has been reported [48, 49]. In the present study, upregulation of DNA damage and cell cycle arrest-related markers P21, P27, P53, COX2, and 8-oxoG was observed in oocytes exposed to NAM, but melatonin significantly restored their normal levels. This corroborates the previous studies that showed higher incidence of ROS production and DNA damage in developing rats after excessive NAM supplementation [15], as well as in oocytes treated with fipronil, an insecticide [48], and confirms the protective role of melatonin against NAM-induced oxidative stress in oocytes.

We went further to investigate whether melatonin administration during IVM can confer a long-term protection in developing embryos. In spite of the toxicity of sole NAM treatment, melatonin succeeded to restore the normal cleavage, 8-16 cell stage embryos, and blastocyst development rates. In addition, higher incidence of DNA fragmentation, lower number of cells per blastocyst, and lower index of ICM : TE were observed in embryos developed from NAM-treated oocytes compared to melatonin-NAM cotreatment
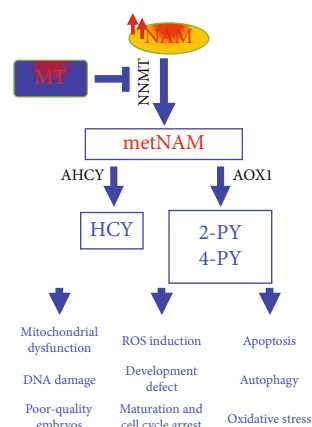

FIGURE 8: Schematic representation for the protective role of melatonin against NAM-induced toxicity in oocytes. NNMT: nicotinamide-N-methyltransferase; metNAM: N-methyl-nicotinamide; AHCY: adenosylhomocysteinase; AOX1: aldehyde oxidase; HCY: homocysteine; 2-PY: N-methyl-2-pyridone-5-carboxamide; 4-PY: N-methyl-4-pyridone-5-carboxamide; ROS: reactive oxygen species; NAM: nicotinamide; MT: melatonin.

or the untreated control. Since the DNA fragmentation and the CDX2-based differential staining are generally used, together with cleavage and blastocyst development rates assessment, for evaluating the quality of preimplantation embryos [50], our observations evidently revealed a protective role of melatonin on developing embryos by improving their quality.

Likewise, we sought to decipher the potential mechanisms behind melatonin and NAM interplay in oocyte. The NAM methylation, mediated by NAM-N-methyltransferase (NNMT), is a principal pathway for NAM metabolism in mammals. The first product of NAM methylation is the N-methyl-nicotinamide (metNAM) which can be further processed to the toxic metabolites 2-PY and 4-PY via the activity of aldehyde oxidase (AOX) [22–24]. In the current study, checking the expression pattern of the key genes involved in NAM methylation showed a dramatic increase in the transcription level of NNMT under the stress of NAM, the effect that was strongly abrogated by melatonin. Although the AOX1 level in oocytes treated with NAM did not show a significant difference compared to control, it was significantly downregulated upon melatonin supplementation. In line with our results, Kang-Lee et al. reported that NAM administration in rats was associated with an increase in metNAM and not 2-PY and 4-PY levels [24].

To clarify the possible involvement of other alternative metabolic pathways for metNAM rather than the AOX1 upregulation, the transcription pattern of the adenosylhomocysteinase (AHCY), the enzyme that converts S-adenosylhomocysteine (SAH) to homocysteine (HCY) within the S-adenosylmethionine (SAMe) methylation cycle, was investigated. The NNMT utilizes SAMe to produce metNAM and SAH, converted to HCY by AHCY [17]. Interestingly, a dramatic increase in the expression level of AHCY was observed in NAM-treated oocytes whereas a strong downregulation was witnessed after addition of melatonin.

In line with our findings, the involvement of HCY in the induction of mitochondrial dysfunction in rat ischemic brain [31] and reproduction disorders including reduced fertility, suppressed fertilization, and the developmental competence of oocytes and embryos, increased risk of recurrent miscarriage, placental infarction, and congenital defects was reported [27, 29, 30]. In addition, the protective role of melatonin against HCY-induced oxidative injury, through decreasing the levels of Caspase-3 and BAX and increasing BCL2, has been observed in human umbilical vein endothelial cells (HUVECs) and hippocampus of rats [51, 52]. Moreover, the high HCY levels observed in pinealectomized mouse highlights a potential linkage between the pineal hormone melatonin and the maintenance of the HCY levels [53].

In conclusion, to the best of our knowledge, this is the first study reporting that administration of melatonin during IVM can protect bovine oocytes against high NAM concentration-induced ROS accumulation, apoptosis, DNA damage, mitochondrial dysfunction, and reduced developmental competence of embryos. This can be attributed to a potential involvement of melatonin in regulating NAM hypermethylation signaling and hence alleviating the NNMT- and HCY-induced oxidative stress and mitochondrial dysfunction (Figure 8).

Data Availability

The data that support the findings of this study are available from the corresponding author upon reasonable request.

Conflicts of Interest

The authors declare no conflict of interest.

Authors' Contributions

ME-S and AAM conceived and designed the experiments. ME-S performed the experiments. ME-S and AAM analyzed the data. ME-S wrote the first draft of the manuscript. AAM made the intellectual critical revision and the reasonable corrections on the manuscript. S-HS and KJ helped in reagents preparation. I-KK supervised the study. All authors have read and agreed to the published version of the manuscript. ME-S and AAM contributed equally to this work.

Acknowledgments

Supplementary Materials

Supplementary Table 1: antibodies used in immunofluorescence. (Supplementary Materials)

References

[1] M. H. Cruz, C. L. V. Leal, J. F. . Cruz, D. X. Tan, and R. J. Reiter, "Role of melatonin on production and preservation of gametes and embryos: a brief review," Animal Reproduction Science, vol. 145, no. 3-4, pp. 150–160, 2014.

[2] L. Cheng, Y. Qin, X. Hu et al., "Melatonin protects in vitro matured porcine oocytes from toxicity of Aflatoxin B1," Journal of Pineal Research, vol. 66, no. 4, article e12543, 2019.

[3] M. H. Asghari, M. Abdollahi, M. R. de Oliveira, and S. M. Nabavi, "A review of the protective role of melatonin during phosphine-induced cardiotoxicity: focus on mitochondrial dysfunction, oxidative stress and apoptosis," The Journal of Pharmacy and Pharmacology, vol. 69, no. 3, pp. 236–243, 2017.

[4] Y. Li, Z. Z. Zhang, C. J. He et al., "Melatonin protects porcine oocyte in vitro maturation from heat stress," Journal of Pineal Research, vol. 59, no. 3, pp. 365–375, 2015.

[5] M. El Sheikh, A. Mesalam, A. A. Mesalam, M. Idrees, K. L. Lee, and I. K. Kong, "Melatonin abrogates the anti-developmental effect of the AKT inhibitor SH6 in bovine oocytes and embryos," International Journal of Molecular Sciences, vol. 20, no. 12, p. 2956, 2019.

[6] F. Wang, X. Z. Tian, Y. H. Zhou et al., "Melatonin improves the quality of in vitro produced (IVP) bovine embryos: implications for blastocyst development, cryotolerance, and modifications of relevant gene expression," PLoS One, vol. 9, no. 4, article e93641, 2014.

[7] H. J. Park, J. Y. Park, J. W. Kim et al., "Melatonin improves the meiotic maturation of porcine oocytes by reducing endoplasmic reticulum stress during in vitro maturation," Journal of Pineal Research, vol. 64, no. 2, p. e12458, 2018.

[8] B. Pan, H. Yang, Z. Wu et al., "Melatonin improves parthenogenetic development of vitrified(-)warmed mouse oocytes potentially by promoting G1/S cell cycle progression," International Journal of Molecular Sciences, vol. 19, no. 12, p. 4029, 2018.

[9] J. Nie, P. Xiao, X. Wang et al., "Melatonin prevents deterioration in quality by preserving epigenetic modifications of porcine oocytes after prolonged culture," Aging (Albany NY), vol. 10, no. 12, pp. 3897–3909, 2018.

[10] T. Lin, J. E. Lee, J. W. Kang et al., "Melatonin supplementation during prolonged in vitro maturation improves the quality and development of poor-quality porcine oocytes via antioxidative and anti-apoptotic effects," Molecular Reproduction and Development, vol. 85, no. 8-9, pp. 665–681, 2018.

[11] K. Papis, O. Poleszczuk, E. Wenta-Muchalska, and J. A. Modlinski, "Melatonin effect on bovine embryo development in vitro in relation to oxygen concentration," Journal of Pineal Research, vol. 43, no. 4, pp. 321–326, 2007.

[12] E. S. Hwang and S. B. Song, "Nicotinamide is an inhibitor of SIRT1 in vitro, but can be a stimulator in cells," Cellular and Molecular Life Sciences, vol. 74, no. 18, pp. 3347–3362, 2017.

[13] M. El Sheikh, A. A. Mesalam, M. Idrees et al., "Nicotinamide supplementation during the in vitro maturation of oocytes improves the developmental competence of preimplantation embryos: potential link to SIRT1/AKT signaling," Cells, vol. 9, no. 6, p. 1550, 2020.

[14] M. R. Horsman, M. Høyer, D. J. Honess, I. F. Dennis, and J. Overgaard, "Nicotinamide pharmacokinetics in humans and mice: a comparative assessment and the implications for radiotherapy," *Radiotherapy and Oncology*, vol. 27, no. 2, pp. 131–139, 1993.

[15] D. Li, Y. J. Tian, J. Guo et al., "Nicotinamide supplementation induces detrimental metabolic and epigenetic changes in developing rats," *The British Journal of Nutrition*, vol. 110, no. 12, pp. 2156–2164, 2013.

[16] Cosmetic Ingredient Review Expert Panel, "Final report of the safety assessment of niacinamide and niacin," *International Journal of Toxicology*, vol. 24, no. 5, pp. 1–31, 2005.

[17] E. S. Hwang and S. B. Song, "Possible adverse effects of high-dose nicotinamide: mechanisms and safety assessment," *Biomolecules*, vol. 10, no. 5, p. 687, 2020.

[18] L. Zhang, R. Ma, J. Hu, X. Ding, and Y. Xu, "Sirtuin inhibition adversely affects porcine oocyte meiosis," *PLoS One*, vol. 10, no. 7, article e0132941, 2015.

[19] T. Zhang, Y. Zhou, L. Li et al., "SIRT1, 2, 3 protect mouse oocytes from postovulatory aging," *Aging (Albany NY)*, vol. 8, no. 4, pp. 685–694, 2016.

[20] S. Imai, "Nicotinamide phosphoribosyltransferase (Nampt): a link between NAD biology, metabolism, and diseases," *Current Pharmaceutical Design*, vol. 15, no. 1, pp. 20–28, 2009.

[21] M. S. Bonkowski and D. A. Sinclair, "Slowing ageing by design: the rise of NAD(+) and sirtuin-activating compounds," *Nature Reviews. Molecular Cell Biology*, vol. 17, no. 11, pp. 679–690, 2016.

[22] P. Pissios, "Nicotinamide N-ethyltransferase: more than a vitamin B3 clearance enzyme," *Trends in Endocrinology and Metabolism*, vol. 28, no. 5, pp. 340–353, 2017.

[23] A. M. Real, S. Hong, and P. Pissios, "Nicotinamide N-oxidation by CYP2E1 in human liver microsomes," *Drug Metabolism and Disposition*, vol. 41, no. 3, pp. 550–553, 2013.

[24] Y. A. Kang-Lee, R. W. McKee, S. M. Wright, M. E. Swendseid, D. J. Jenden, and R. S. Jope, "Metabolic effects of nicotinamide administration in rats," *The Journal of Nutrition*, vol. 113, no. 2, pp. 215–221, 1983.

[25] J. M. Mato, M. L. Martinez-Chantar, and S. C. Lu, "Methionine metabolism and liver disease," *Annual Review of Nutrition*, vol. 28, no. 1, pp. 273–293, 2008.

[26] P. Handler, "The effect of excessive nicotinamide feeding on rabbits and guinea pigs," *Journal of Biological Chemistry*, vol. 154, no. 1, pp. 203–206, 1944.

[27] A. Rizzo and R. L. Sciorsci, "Role of homocysteine metabolism in animal reproduction: a review," *Research in Veterinary Science*, vol. 122, pp. 29–35, 2019.

[28] P. Kaplan, Z. Tatarkova, M. K. Sivonova, P. Racay, and J. Lehotsky, "Homocysteine and mitochondria in cardiovascular and cerebrovascular systems," *International Journal of Molecular Sciences*, vol. 21, no. 20, p. 7698, 2020.

[29] T. K. Eskes, "Homocysteine and human reproduction," *Clinical and Experimental Obstetrics & Gynecology*, vol. 27, no. 3-4, pp. 157–167, 2000.

[30] B. Berker, C. Kaya, R. Aytac, and H. Satiroglu, "Homocysteine concentrations in follicular fluid are associated with poor oocyte and embryo qualities in polycystic ovary syndrome patients undergoing assisted reproduction," *Human Reproduction*, vol. 24, no. 9, pp. 2293–2302, 2009.

[31] S. Chen, Z. Dong, Y. Zhao et al., "Homocysteine induces mitochondrial dysfunction involving the crosstalk between oxidative stress and mitochondrial pSTAT3 in rat ischemic brain," *Scientific Reports*, vol. 7, no. 1, p. 6932, 2017.

[32] A. Mesalam, K. L. Lee, I. Khan et al., "A combination of bovine serum albumin with insulin-transferrin-sodium selenite and/or epidermal growth factor as alternatives to fetal bovine serum in culture medium improves bovine embryo quality and trophoblast invasion by induction of matrix metalloproteinases," *Reproduction, Fertility, and Development*, vol. 31, no. 2, pp. 333–346, 2019.

[33] S. Yaacobi-Artzi, C. Shimoni, D. Kalo, P. J. Hansen, and Z. Roth, "Melatonin slightly alleviates the effect of heat shock on bovine oocytes and resulting blastocysts," *Theriogenology*, vol. 158, pp. 477–489, 2020.

[34] Y. W. Pang, X. L. Jiang, Y. C. Wang et al., "Melatonin protects against paraquat-induced damage during in vitro maturation of bovine oocytes," *Journal of Pineal Research*, vol. 66, no. 1, article e12532, 2019.

[35] Y. Li, J. Wang, Z. Zhang et al., "Resveratrol compares with melatonin in improving in vitro porcine oocyte maturation under heat stress," *Journal of Animal Science and Biotechnology*, vol. 7, no. 1, p. 33, 2016.

[36] S. Soto-Heras, M. G. Catalá, M. Roura et al., "Effects of melatonin on oocyte developmental competence and the role of melatonin receptor 1 in juvenile goats," *Reproduction in Domestic Animals*, vol. 54, no. 2, pp. 381–390, 2019.

[37] E. Wydooghe, L. Vandaele, J. Beek et al., "Differential apoptotic staining of mammalian blastocysts based on double immunofluorescent CDX2 and active caspase-3 staining," *Analytical Biochemistry*, vol. 416, no. 2, pp. 228–230, 2011.

[38] S. S. Kwak, S. A. Cheong, J. D. Yoon, Y. Jeon, and S. H. Hyun, "Expression patterns of sirtuin genes in porcine preimplantation embryos and effects of sirtuin inhibitors on in vitro embryonic development after parthenogenetic activation and in vitro fertilization," *Theriogenology*, vol. 78, no. 7, pp. 1597–1610, 2012.

[39] H. A. Tukur, R. S. Aljumaah, A. A. A. Swelum, A. N. Alowaimer, and I. M. Saadeldin, "The making of a competent oocyte–a review of oocyte development and its regulation," *Journal of Animal Reproduction and Biotechnology*, vol. 35, no. 1, pp. 2–11, 2020.

[40] C. Yin, J. Liu, Z. Chang, B. He, Y. Yang, and R. Zhao, "Heat exposure impairs porcine oocyte quality with suppressed actin expression in cumulus cells and disrupted F-actin formation in transzonal projections," *Journal of Animal Science and Biotechnology*, vol. 11, no. 1, p. 71, 2020.

[41] G. Coticchio, M. C. Guglielmo, D. F. Albertini et al., "Contributions of the actin cytoskeleton to the emergence of polarity during maturation in human oocytes," *Molecular Human Reproduction*, vol. 20, no. 3, pp. 200–207, 2014.

[42] Y. J. Niu, W. Zhou, Z. W. Nie, K. T. Shin, and X. S. Cui, "Melatonin enhances mitochondrial biogenesis and protects against rotenone-induced mitochondrial deficiency in early porcine embryos," *Journal of Pineal Research*, vol. 68, no. 2, article e12627, 2020.

[43] D. B. Zorov, M. Juhaszova, and S. J. Sollott, "Mitochondrial reactive oxygen species (ROS) and ROS-induced ROS release," *Physiological Reviews*, vol. 94, no. 3, pp. 909–950, 2014.

[44] A. Diaz-Vegas, P. Sanchez-Aguilera, J. R. Krycer et al., "Is mitochondrial dysfunction a common root of noncommunicable chronic diseases?," *Endocrine Reviews*, vol. 41, no. 3, pp. 491–517, 2020.

[45] K. L. Reader, J. L. Stanton, and J. L. Juengel, "The role of oocyte organelles in determining developmental competence," *Biology*, vol. 6, no. 4, p. 35, 2017.

[46] X. Duan, X. X. Dai, T. Wang, H. L. Liu, and S. C. Sun, "Melamine negatively affects oocyte architecture, oocyte development and fertility in mice," *Human Reproduction*, vol. 30, no. 7, pp. 1643–1652, 2015.

[47] J. W. Zhang, D. Q. Xu, and X. Z. Feng, "The toxic effects and possible mechanisms of glyphosate on mouse oocytes," *Chemosphere*, vol. 237, p. 124435, 2019.

[48] W. Zhou, Y. J. Niu, Z. W. Nie et al., "Fipronil induces apoptosis and cell cycle arrest in porcine oocytes during in vitro maturation," *Apoptosis*, vol. 24, no. 9-10, pp. 718–729, 2019.

[49] J. B. Kerr, K. J. Hutt, E. M. Michalak et al., "DNA damage-induced primordial follicle oocyte apoptosis and loss of fertility require TAp63-mediated induction of Puma and Noxa," *Molecular Cell*, vol. 48, no. 3, pp. 343–352, 2012.

[50] A. A. Fouladi-Nashta, R. Alberio, M. Kafi, B. Nicholas, K. H. S. Campbell, and R. Webb, "Differential staining combined with TUNEL labelling to detect apoptosis in preimplantation bovine embryos," *Reproductive Biomedicine Online*, vol. 10, no. 4, pp. 497–502, 2005.

[51] G. Baydas, R. J. Reiter, M. Akbulut, M. Tuzcu, and S. Tamer, "Melatonin inhibits neural apoptosis induced by homocysteine in hippocampus of rats via inhibition of cytochrome c translocation and caspase-3 activation and by regulating pro- and anti-apoptotic protein levels," *Neuroscience*, vol. 135, no. 3, pp. 879–886, 2005.

[52] G. Aykutoglu, M. Tartik, E. Darendelioglu, A. Ayna, and G. Baydas, "Melatonin and vitamin E alleviate homocysteine-induced oxidative injury and apoptosis in endothelial cells," *Molecular Biology Reports*, vol. 47, no. 7, pp. 5285–5293, 2020.

[53] G. Baydas, M. F. Gursu, G. Cikim, and H. Canatan, "Homocysteine levels are increased due to lack of melatonin in pinealectomized rats: is there a link between melatonin and homocysteine?," *Journal of Pineal Research*, vol. 32, no. 1, pp. 63-64, 2002.

Research Article

Bu Shen Yi Sui Capsule Alleviates Neuroinflammation and Demyelination by Promoting Microglia toward M2 Polarization, Which Correlates with Changes in miR-124 and miR-155 in Experimental Autoimmune Encephalomyelitis

Zheng Zha [ID],[1] **Yan-Fang Gao** [ID],[1] **Jing Ji** [ID],[1] **Ya-Qin Sun** [ID],[1] **Jun-Ling Li** [ID],[1] **Fang Qi** [ID],[1] **Nan Zhang,**[1] **Liang-Yun Jin,**[2] **Bing Xue,**[2] **Tao Yang** [ID],[3] **Yong-Ping Fan** [ID],[3] **Hui Zhao,**[1] **and Lei Wang** [ID][1]

[1]*School of Traditional Chinese Medicine, Beijing Key Lab of TCM Collateral Disease Theory Research, Capital Medical University, Beijing 100069, China*
[2]*Core Facility Center, Capital Medical University, Beijing 100069, China*
[3]*Beijing Tian Tan Hospital, Capital Medical University, Beijing 100070, China*

Correspondence should be addressed to Lei Wang; tmwangl@ccmu.edu.cn

Background. Bu Shen Yi Sui capsule (BSYS) is a traditional Chinese medicine prescription that has shown antineuroinflammatory and neuroprotective effects in treating multiple sclerosis (MS) and its animal model of experimental autoimmune encephalomyelitis (EAE). Microglia play an important role in neuroinflammation. The M1 phenotype of microglia is involved in the proinflammatory process of the disease, while the M2 phenotype plays an anti-inflammatory role. Promoting the polarization of microglia to M2 in MS/EAE is a promising therapeutic strategy. This study is aimed at exploring the effects of BSYS on microglial polarization in mice with EAE. *Methods.* The EAE model was established by the intraperitoneal injection of pertussis toxin and subcutaneous injection of myelin oligodendrocyte glycoprotein $(MOG)_{35-55}$ in C57BL/6J mice. The mice were treated with BSYS (3.02 g/kg), FTY720 (0.3 mg/kg), or distilled water by intragastric administration. H&E and LFB staining, transmission electron microscopy, qRT-PCR, immunofluorescence, ELISA, fluorescence in situ hybridization, and western blotting were used to detect the histological changes in myelin, microglial M1/M2 polarization markers, and the expression of key genes involved in EAE. *Results and Conclusions.* BSYS treatment of EAE mice increased the body weight, decreased the clinical score, and reduced demyelination induced by inflammatory infiltration. BSYS also inhibited the mRNA expression of M1 microglial markers while increasing the mRNA level of M2 markers. Additionally, BSYS led to a marked decrease in the ratio of M1 microglia $(iNOS^+/Iba1^+)$ and an obvious increase in the number of M2 microglia $(Arg1^+/Iba1^+)$. In the EAE mouse model, miR-124 expression was decreased, and miR-155 expression was increased, while BSYS treatment significantly reversed this effect and modulated the levels of C/EBP α, PU.1, and SOCS1 (target genes of miR-124 and miR-155). Therefore, the neuroprotective effect of BSYS against MS/EAE was related to promoting microglia toward M2 polarization, which may be correlated with changes in miR-124 and miR-155 in vivo.

1. Introduction

Multiple sclerosis (MS) is a chronic inflammatory disease of the central nervous system (CNS) characterized by demyelination [1], neurodegeneration, and sensitivity to oxidative stress [2, 3]. The disease usually occurs in young adults, and its main clinical manifestations include limb weakness, sensory abnormality, visual impairment, and ataxia [4]. Approximately 2.5 million people have MS worldwide [5]. The neuroimmune inflammatory response plays a crucial

role in the pathogenesis of MS. Therefore, anti-inflammatory strategies have attracted much attention in MS treatment.

Microglia are macrophages that reside in the brain and spinal cord and participate in the inflammatory process of the CNS [6]. Under inflammatory conditions in the brain, such as Parkinson's disease, multiple system atrophy, and MS, microglia may be rapidly activated and are polarized into M1 and M2 phenotypes [7]. M1 type microglia play a strong phagocytic role and release proinflammatory factors such as tumor necrosis factor- (TNF-) α, interleukin- (IL-) 1β, and IL-6, which aggravate the inflammatory reaction, resulting in nerve injury [8]. M2 microglia not only release anti-inflammatory factors, including IL-10, to reduce the level of inflammation but also secrete transforming growth factor- (TGF-) β to promote tissue repair and myelin regeneration [9]. Microglia polarize to the proinflammatory M1 type during MS onset, leading to an imbalance in M1/M2 in vivo, forming a proinflammatory microenvironment in the CNS and causing damage to the myelin sheath. Therefore, developing new drugs that promote M2 polarization may provide an effective treatment strategy in neurodegenerative diseases [10].

As crucial modulators of gene expression, microRNAs (miRs) have been widely studied in recent years; they are involved in posttranscriptional regulation and play an important role in modifying microglial polarization. Many studies have suggested that the biological processes of microglial polarization modulated by miRs are correlated with the immune inflammatory response of MS/EAE. miR-124 expression in the CNS of EAE was decreased, while that of miR-155 was increased [11, 12]. However, miR-124 upregulation [13] or miR-155 downregulation [14, 15] in vivo significantly alleviates the severity of EAE. Additionally, miR-124 and miR-155 are considered important regulators to balance the ratio of M1/M2 [16, 17], and a previous study demonstrated that miR-124 alleviates EAE not only by promoting microglial quiescence but also by skewing microglial polarization from the M1 phenotype to the M2 phenotype via targeting C/EBPα-PU.1 [18]. Furthermore, miR-155 is important for microglial polarization; it targets suppressor of cytokine signaling 1 (SOCS1) to promote macrophage/microglia polarization toward the M1 phenotype [19], while miR-155 deficiency leads to a shift from M1 to M2 [20]. Consequently, elevating the expression of miR-124 and decreasing the expression of miR-155 might be a promising therapeutic approach for EAE treatment by promoting microglial phenotypic transformation toward M2.

Growing evidence has confirmed that herbs in traditional Chinese medicine (TCM) are effective in treating neurodegenerative diseases of the CNS, including Alzheimer's disease (AD) [21, 22], amyotrophic lateral sclerosis (ALS) [23], and MS. Previous studies have shown that numerous prescriptions and herbal extracts of TCM have protective effects against diseases by modulating various miRs [24–27]. Thus, it is reasonable to explore new therapeutic strategies based on TCM to treat MS. Bu Shen Yi Sui capsule (BSYS) was modified from the Liu Wei Di Huang pill, a well-known traditional Chinese formula, which has been used for 10 years in MS clinical treatment at Tiantan Hospital (Beijing, China).

Our previous studies found that BSYS could ameliorate demyelination and axon injury by regulating Th17/Treg cells [28] and promoting oligodendrocyte progenitor cell (OPC) maturation [29, 30]. This study is aimed at evaluating the neuroprotective effects of BSYS on EAE mice and potential mechanisms of microglial polarization regulated by BSYS.

2. Materials and Methods

2.1. Drug Preparations. BSYS comprised the following Chinese herbs: Dihuang (Rehmanniae Radix), Shu dihuang (Rehmanniae Radix Praeparata), Heshouwu (Polygoni Multiflori Radix), Dahuang, (Rhei Radix et Rhizoma), Yimucao (Leonuri Herba), Zhebeimu (Fritillariae Thunbergii Bulbus), Shuizhi (Hirudo), Quanxie (Scorpio), Tianma (Gastrodiae Rhizoma), and Lianqiao (Forsythiae Fructus). BSYS was produced by Asia-East Biopharmaceutical Co., Ltd. (Beijing, China). A detailed description of the BSYS preparation and quality control procedures has been published elsewhere [31] [32]. Fingolimod (FTY720) was used as a positive control drug and was purchased from Novartis (Basel, Switzerland).

2.2. Animals. Healthy female C57BL/6J mice at 6–8 weeks of age (weighing between 15 and 17 g) were purchased from Vital River (Beijing, China) and were housed under specific pathogen-free (SPF) conditions in a 12/12 h light/dark cycle room with controlled temperature ($22 \pm 3°C$) and humidity (40–50%) at the Experimental Animal Center of Capital Medical University. All the mouse experiments were performed under the approval of the Animal Experiments and Experimental Animal Welfare Committee of Capital Medical University (permit number: AEEI-2018-137).

2.3. Model Establishment and Experimental Treatment. Five milligrams of myelin oligodendrocyte glycoprotein (MOG)$_{35-55}$ peptide, dissolved in normal saline (10 ml), was emulsified 1:1 in complete Freund's adjuvant supplemented with 0.3 mg of *Mycobacterium tuberculosis* H37Ra (BD Biosciences, San Diego, USA). Next, 0.2 ml of emulsion containing 50 μg of MOG$_{35-55}$ was administered subcutaneously into 4 different locations on the backs of female C57BL/6J mice. On Day 0 and Day 2 postimmunization (dpi), C57BL/6 mice were injected intraperitoneally with 500 ng of pertussis toxin (Sigma-Aldrich, St. Louis, USA).

The mice were randomly divided into four groups: (1) normal control group (NC, $n = 10$), (2) EAE model group (EAE, $n = 10$), (3) 0.3 mg/kg FTY720 treatment group [33, 34] (FTY720, $n = 10$), and 3.02 g/kg BSYS treatment group (BSYS, $n = 10$). Additionally, the clinical equivalent daily dose of BSYS in mice was 3.02 g/kg, which was the optimal dosage against EAE in our previous study [35]. The therapeutic group was administered the corresponding dose of BSYS or FTY720 daily by gavage, while the same volume of distilled water was used for the NC and EAE groups.

After the animal model was established, the clinical signs of EAE in mice were observed daily for 40 days based on the following grades. The score for tail deficiency was as follows: 0, normal; 1, partially paralyzed; and 2, completely paralyzed. Each hindlimb or forelimb was evaluated as follows [36, 37]:
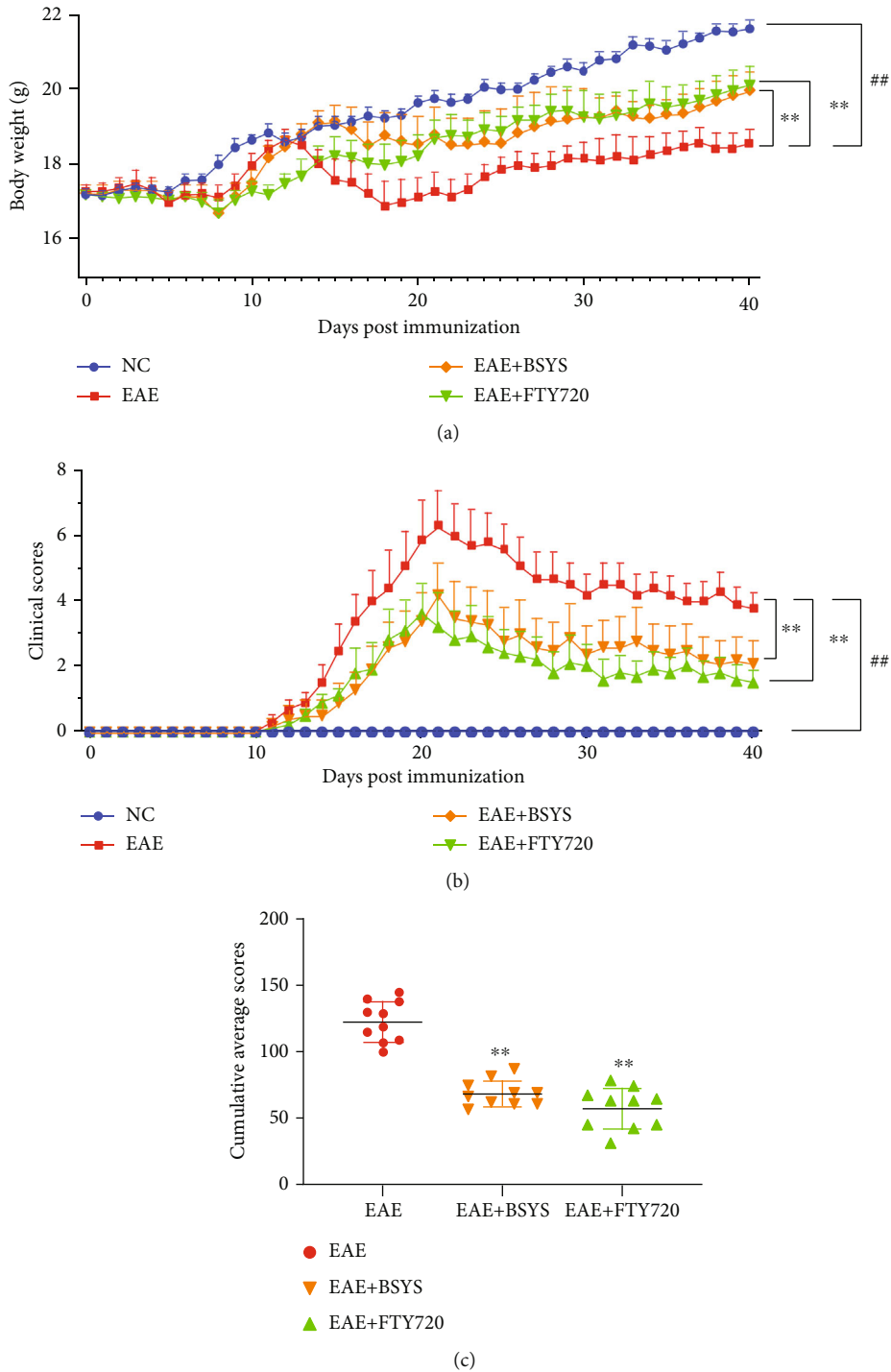
FIGURE 1: BSYS improved the body weight and ameliorated clinical symptoms of EAE mice: (a) changes in body weight of mice in each group ($n = 10$); (b) changes in the time of mean clinical score of mice in each group ($n = 10$); (c) cumulative clinical scores of different groups. The data are expressed as mean ± SEM, compared with the NC group, [##]$P < 0.01$; compared with the EAE group, [**]$P < 0.01$.

0, normal; 1, weak or altered gait; 2, paresis; and 3, completely paralyzed limb. Therefore, according to this scoring system, a mouse with complete quadriplegia will receive 14 points, while death will be scored as 15 points.

2.4. CNS Histopathological Staining. At 40 dpi, the mice were deeply anesthetized, sacrificed, and perfused with phosphate-buffered saline (PBS) and 4% paraformaldehyde (PFA). Brain and spinal cord sections from the subventricular zone (SVZ), corpus callosum (CC), and lumbar enlargement (LE) in the mice of the four groups were immersed in 4% PFA for 24 h and then embedded in paraffin. Tissue sections (5 μm) were subjected to hematoxylin and eosin (H&E) staining and Luxol Fast Blue (LFB) staining to assess the degree of
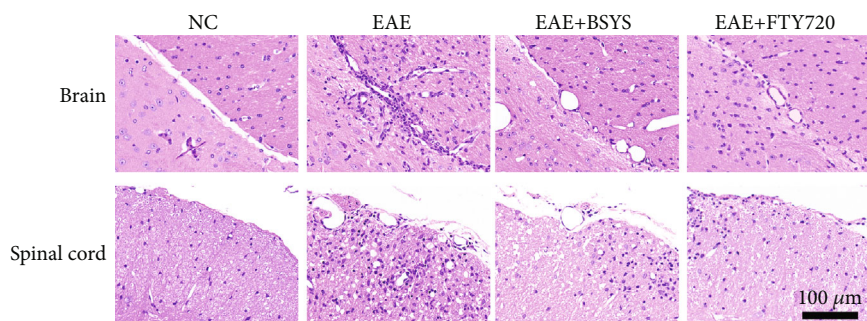
(a)
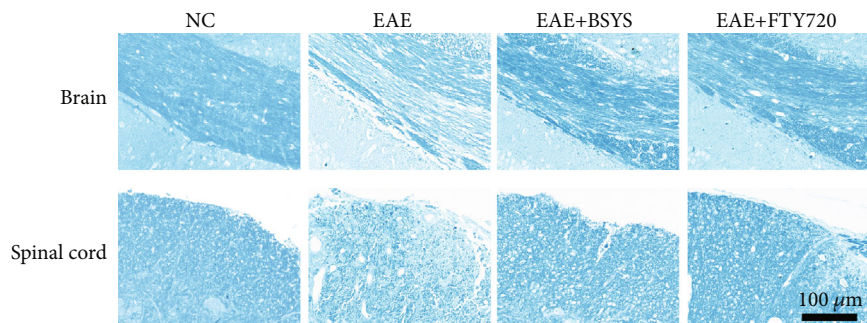
(b)
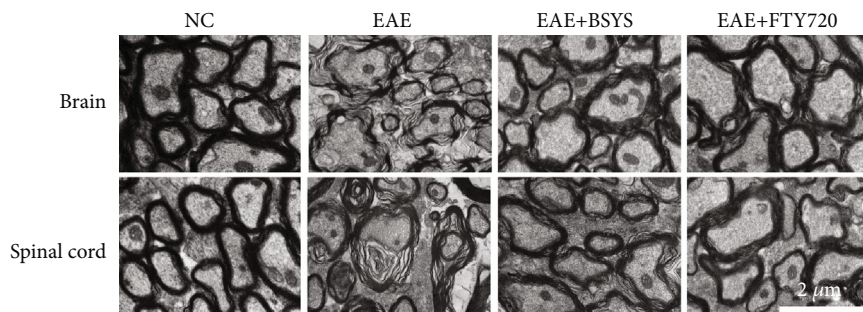
(c)
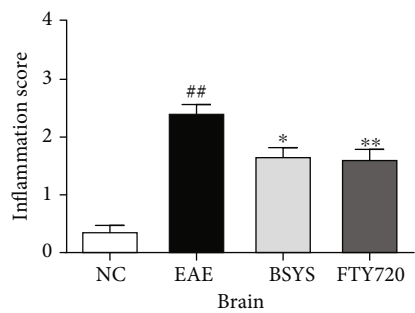
(d)
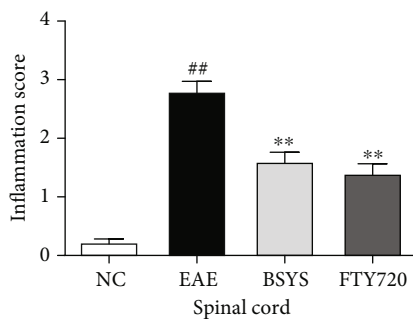
(e)
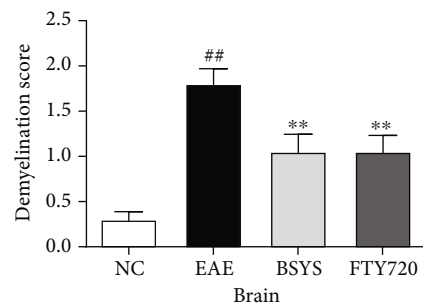
(f)

Figure 2: Continued.

(g)

(h)

(i)
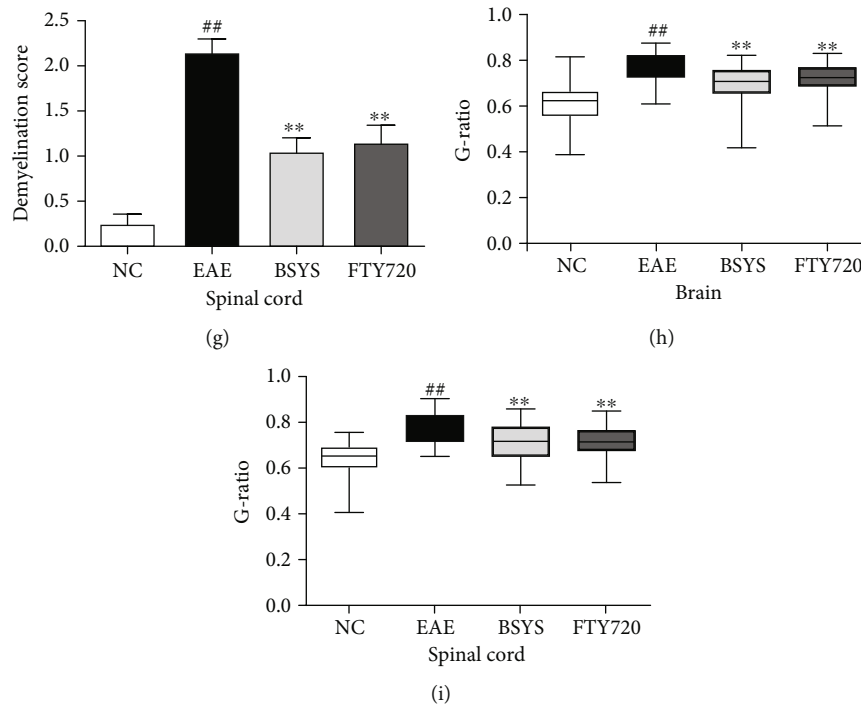
FIGURE 2: BSYS suppressed inflammatory cell infiltration and promoted myelination in EAE mice. (a) Inflammatory infiltrates of the SVZ and LE of mice in each group were observed by H&E staining. Scale bars: 100 μm. (b) Demyelination of the SVZ and LE of mice in each group was observed by LFB staining. Scale bars: 100 μm. (c) Myelin ultrastructure of the SVZ and LE of mice in each group was observed by TEM. Scale bars: 2 μm. (d, e) Histological quantification of H&E-stained sections in each group. (f, g) Histological quantification of LFB-stained sections in each group. (h, i) G-ratio of axons in spinal cords from mice in each group at day 40. Data are presented as means ± SD; compared with the NC group, $^{\#\#}P < 0.01$; compared with the EAE group, $^{*}P < 0.05$, $^{**}P < 0.01$.

inflammatory infiltration and demyelination. The inflammation level was assessed based on the following criteria [38]: 0, no inflammation; 1, the cells only infiltrated around the blood vessels and meninges rarely; 2, 1-10 cells infiltrated per area (mild cellular infiltration); 3, 11-100 cells infiltrated per area (moderate cellular infiltration); and 4, >100 cells infiltrated per area (serious cellular infiltration). As mentioned previously, the demyelination degree was calculated based on a 3-point scale as follows [39]: 0 = no demyelination area; 1 = a few foci of demyelination; 2 = a few areas of demyelination; and 3 = large areas of demyelination.

2.5. Transmission Electron Microscopy (TEM).

To evaluate the degree of demyelination, tissues were cut into approximately $1 \times 1 \times 3\,mm^3$ pieces, placed in 2.5% glutaraldehyde for 2 h, and then rinsed with 0.1 M PB buffer three times. Next, the tissues were fixed with 1% osmium acid, dehydrated with alcohol, soaked for 20 min, embedded with embedding agent, and baked and soaked in pure embedding agent. The embedded samples were sliced using an ultrathin microtome and then stained and coated. The sections were then viewed under TEM (H-7700; Hitachi, Japan) at a magnification of ×5000. The G-ratio was defined as the ratio of the diameter of a given axon and myelinated fiber diameter [40], which were measured 50 times for each group using ImageJ (NIH, Bethesda, USA).

2.6. Immunofluorescence Staining.

Brain and spinal cord sections from the SVZ and LE in the mice of the four groups were deparaffinized, boiled with citrate buffer at 95°C for 20 min, cooled to 30°C, and blocked with 1% bovine serum albumin (BSA) at 37°C for 1 h. The sections were then incubated overnight at 4°C with primary antibodies against Olig2 (1 : 400; AF2418; R&D Systems, Minneapolis, USA), CC-1 (1 : 200; OP80; Merck Chemicals, Darmstadt, Germany), iNOS (1 : 200; ab210823; Abcam, Cambridge, UK), Arginase 1 (Arg1; 1 : 200; ab91279; Abcam, Cambridge, UK), Iba1 (1 : 200; ab48004; Abcam, Cambridge, UK), followed by 1 h of incubation with FITC- (1 : 400-) and TRITC- (1 : 200-) conjugated secondary antibodies (Southern Biotech, Birmingham, USA) at 37°C. Nuclei were counterstained with DAPI (Southern Biotech, Birmingham, USA). We used a fluorescence microscope to capture the images and then analyzed them using ImageJ.

2.7. Enzyme-Linked Immunosorbent Assay (ELISA).

The brain and spinal cord samples were homogenized using a high-speed homogenizer and centrifuged at 5000 × g at 4°C for 10 min, and then, the supernatants were collected. The total protein concentration in the supernatants of each sample was calculated using a BCA protein assay kit (Applygen, Beijing, China). The expression levels of TNF-α, IL-1β, IL-6, and IL-10 were measured using ELISA kits (Neobioscience, Shenzhen, China) according to the manufacturer's protocol.

(a)

(b)

(c)

FIGURE 3: Continued.

(d)

(e)

(f)

(g)
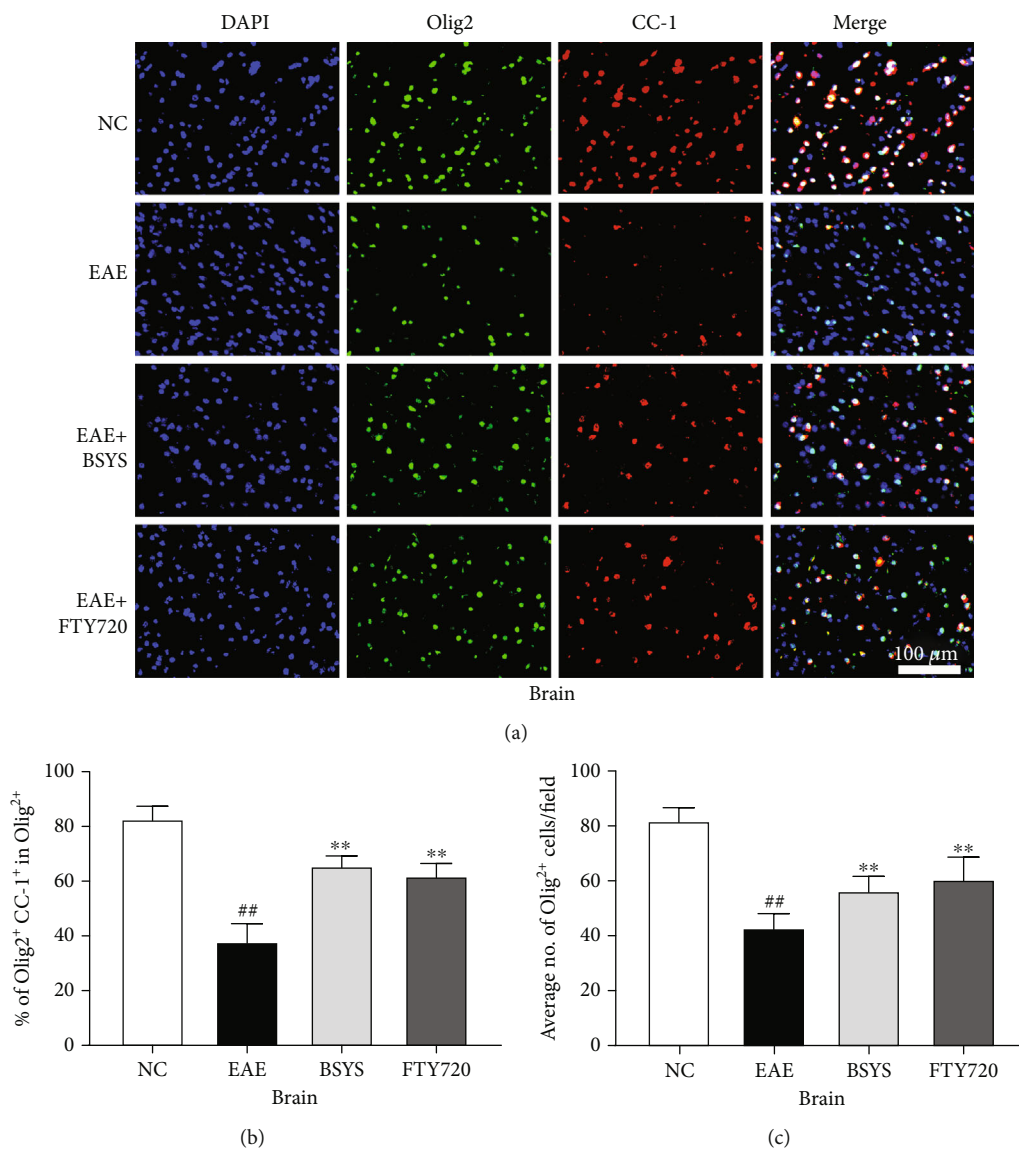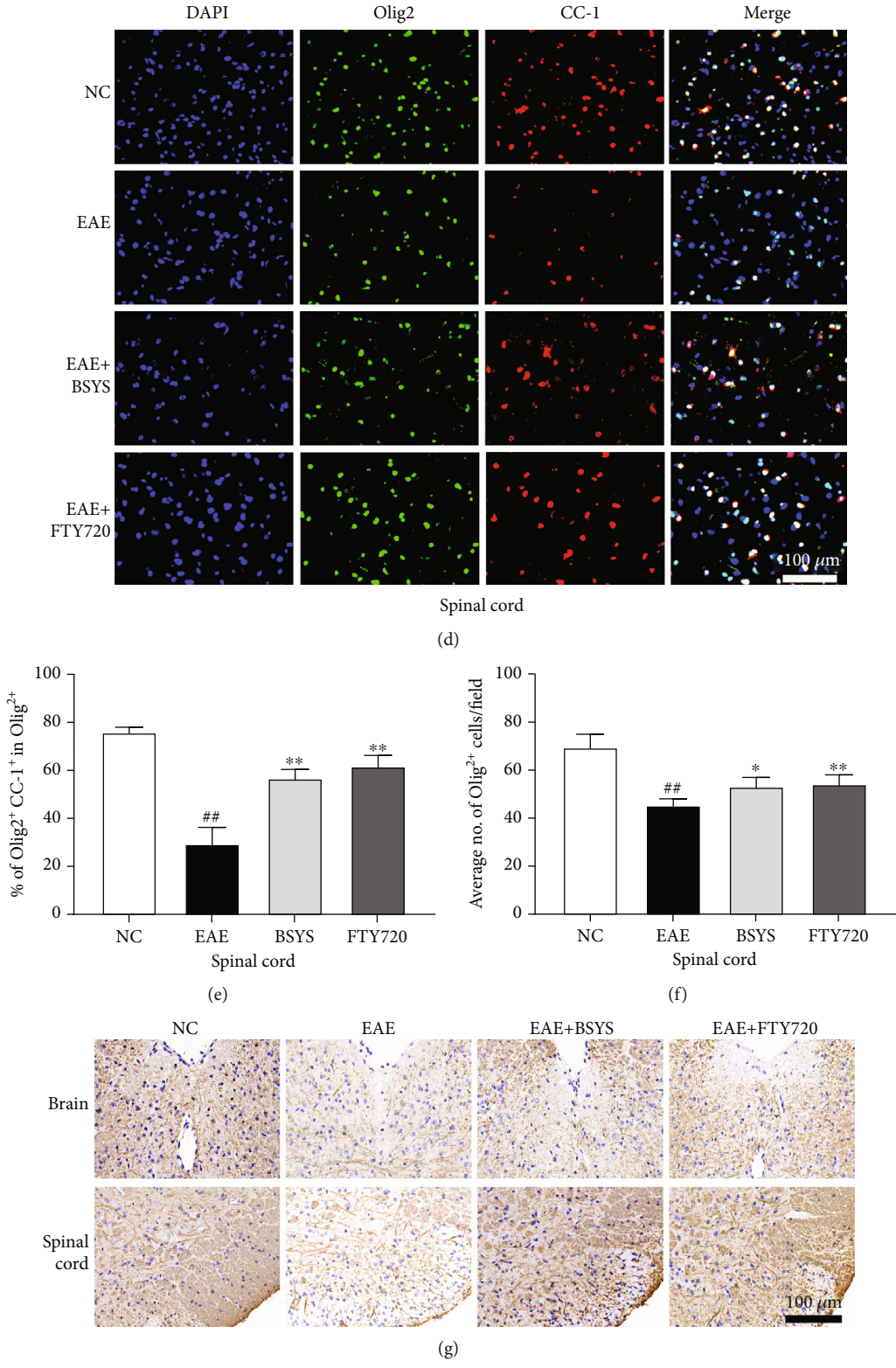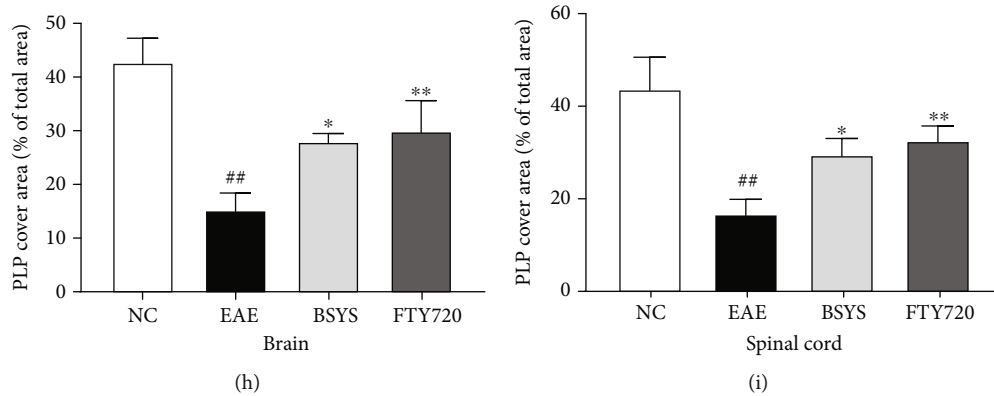
FIGURE 3: Continued.

(h)

(i)

Figure 3: BSYS promoted the maturation of oligodendrocytes in EAE mice. (a) Immunofluorescence of SVZ from mice in each group using antibodies against Olig2 (green) and CC-1 (red). Scale bars: 100 μm. (b) Quantification of Olig2+ cells density in SVZ. (c) Quantification of the percentage of CC-1+/Olig2+ cells in LE. (d) Immunofluorescence of LE using antibodies against Olig2 and CC-1. Scale bars: 100 μm. (e) Quantification of Olig2+ cells density in LE. (f) Quantification of the percentage of CC-1+/Olig2+ cells in LE. (g) The expression of PLP in SVZ and LE was detected by immunohistochemistry. Scale bars: 100 μm. (h, i) Percentage of MBP covered area in the SVZ and LE. Data are presented as means ± SD; compared with the NC group, $^{##}P < 0.01$; compared with the EAE group, $^{*}P < 0.05$, $^{**}P < 0.01$.

2.8. Quantitative Real-Time PCR (qRT-PCR) Analysis.

For mRNA expression detection, qRT-PCR analysis was performed using the One-Step qPCR kit (Toyobo Life Science, Osaka, Japan) and the SYBR Green method in the CFX Connect Real-Time PCR Detection System (Bio-Rad, Hercules, USA). The primers for gene amplification were as follows:

major histocompatibility complex-II (MHC-II, FWD-GATGTGGAAGACCTGCG, REV-TGCATCTTCTGAGGGGTTTC), inducible nitric oxide synthase (iNOS, FWD-CTGTGAGACCTTTGATGTCCGAAG, REV-CTGGATGAGCCTATATTGCTGTGG), cluster of differentiation marker 86 (CD86, FWD-GCCACCCACAGGATCAATTATCCT, REV-AAAGAGAGAGGCTGTTGGAGATAC), Trem2 (FWD-TGGAACCGTCACCATCACTC, REV-TGGTCATCTAGAGGGTCCTCC), Arg1 (FWD-CTTGGCTTGCTTCGGAACTC, REV-GGAGAAGGCGTTTGCTTAGTTC), CD206 (FWD-AGTGATGGTTCTCCTGTTTCC, REV-GGTGTAGGCTCGGGTAGTAGT), C/EBPα (FWD-AGCTTACAACAGGCCAGGTTTC, REV-CGGCTGGCGACATACAGTAC), PU.1 (FWD-CCCGGATGTGCTTCCCTTAT, REV-TCCAAGCCATCAGCTTCTCC), SOCS1 (FWD-CACCTTCTTGGTGCGCG, REV-AAGCCATCTTCACGCTGAGC), and β-actin (FWD-ATATCGCTGCGCTGGTCGTC, REV-AGGATGGCGTGAGGGAGAGC).

Real-time PCR was performed using the CFX Connect Real-Time System and the following reaction conditions: incubation at 95°C for 60 s, followed by 40 cycles of 95°C for 15 s (denaturation), 60°C for 15 s (annealing), and 72°C for 45 s (extension). The mRNA expression data were normalized to β-actin expression, while the level of miR-124/miR-155 was normalized to the U6 level. The data were analyzed using the relative quantification ($2^{-\Delta\Delta Ct}$) method.

2.9. hFluorescence In Situ Hybridization.

Fluorescence in situ hybridization (FISH) was performed on PFA-fixed, paraffin-embedded sections to detect miR-124 and miR-155 in brain and spinal cord tissue. The staining was performed according to established protocols. Briefly, 4% PFA-fixed paraffin-embedded sections were preheated for 2 h at 62°C. Xylene was used to remove paraffin from the tissue. The sections were incubated in decreasing concentrations of ethanol and then incubated with Proteinase K solution for 20-30 min at 37°C. After dehydration, biotin-labeled miR probes were added to the hybridization solution and incubated at 37°C overnight. The sections were counterstained with DAPI at room temperature (RT) for 8 min (in the dark). Finally, we used a fluorescence microscope to observe the slices.

2.10. Isolation and Identification of Exosomes from Mouse Serum.

Exosomes were isolated from the serum of mice using an exoRNeasy Serum Mid Kit (Qiagen, Hilden, Germany) following the manufacturer's protocol. Measurements of the average diameter and size distribution of serum exosomes were performed using nanoparticle tracking analysis (NTA), and morphological assessment was performed using TEM as described in our previous study. Biomarkers of exosomes, such as CD63, HSP70, and TSG101, were examined in exosome-depleted media and exosomes isolated from serum using western blot analysis.

2.11. Western Blot Analysis.

Tissues were lysed in RIPA buffer containing a protease inhibitor cocktail (Beyotime Institute of Biotechnology, Haimen, China). Total protein isolated from the myocardium was separated by SDS-PAGE and transferred to polyvinylidene difluoride (PVDF) membranes. The membranes were blocked in Tris-buffered saline with 0.1% Tween (TBST) containing 5% nonfat dry milk for 1 h at RT and then incubated in universal antibody diluent (New Cell & Molecular Biotech, Suzhou, China) using the appropriate primary antibody overnight at 4°C. The primary antibodies used in this experiment were specific to the following antigens: iNOS (1 : 1000; ab210823; Abcam, Cambridge, UK), Arg1 (1 : 1000; ab91279; Abcam, Cambridge, UK), C/EBPα (1 : 1000; 18311-1-AP; Proteintech, Chicago, USA), PU.1 (1 : 2000; ab88082; Abcam, Cambridge, UK), SOCS1 (1 : 1000; YT4362; Immunoway, Newark, USA),
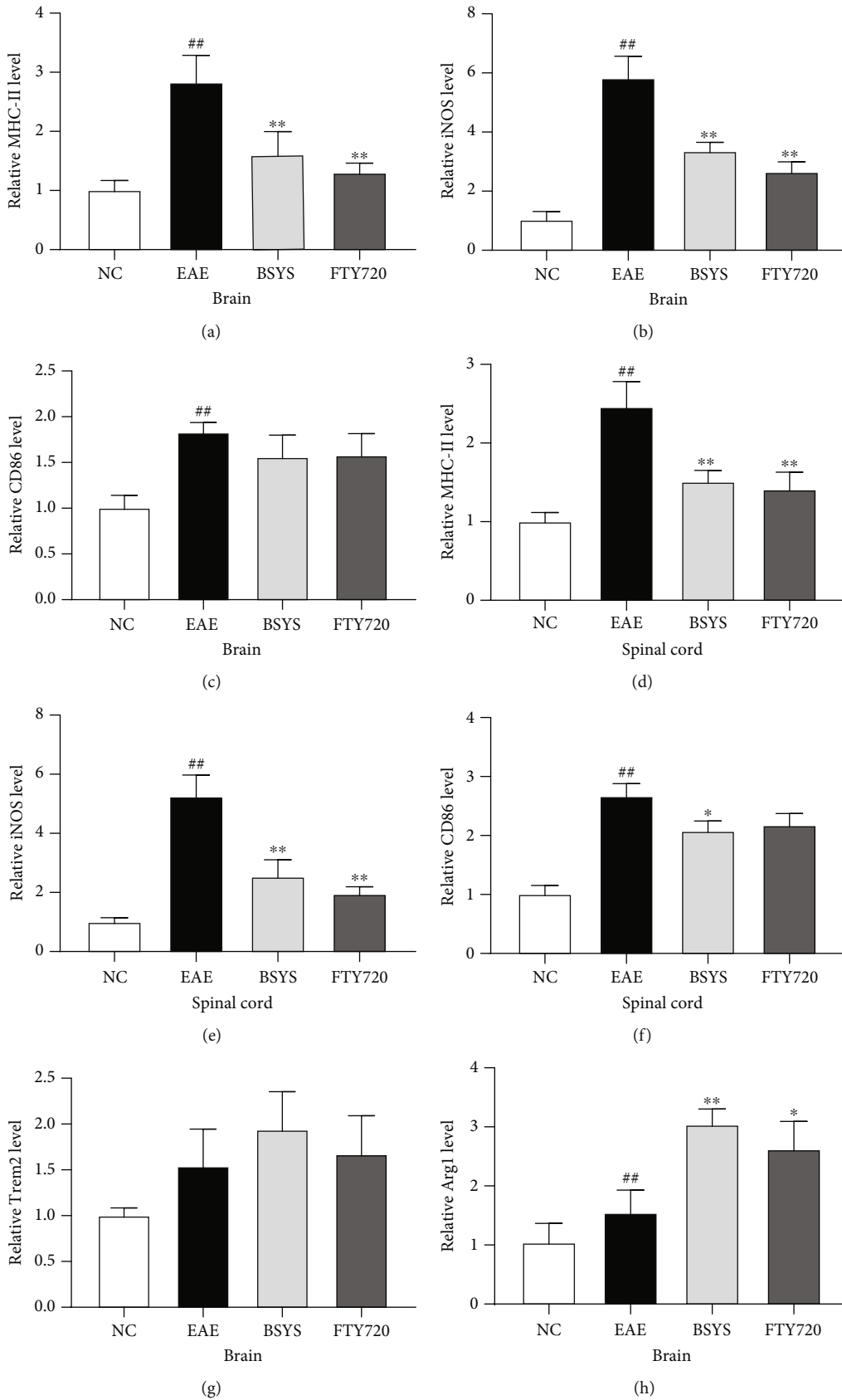
FIGURE 4: Continued.
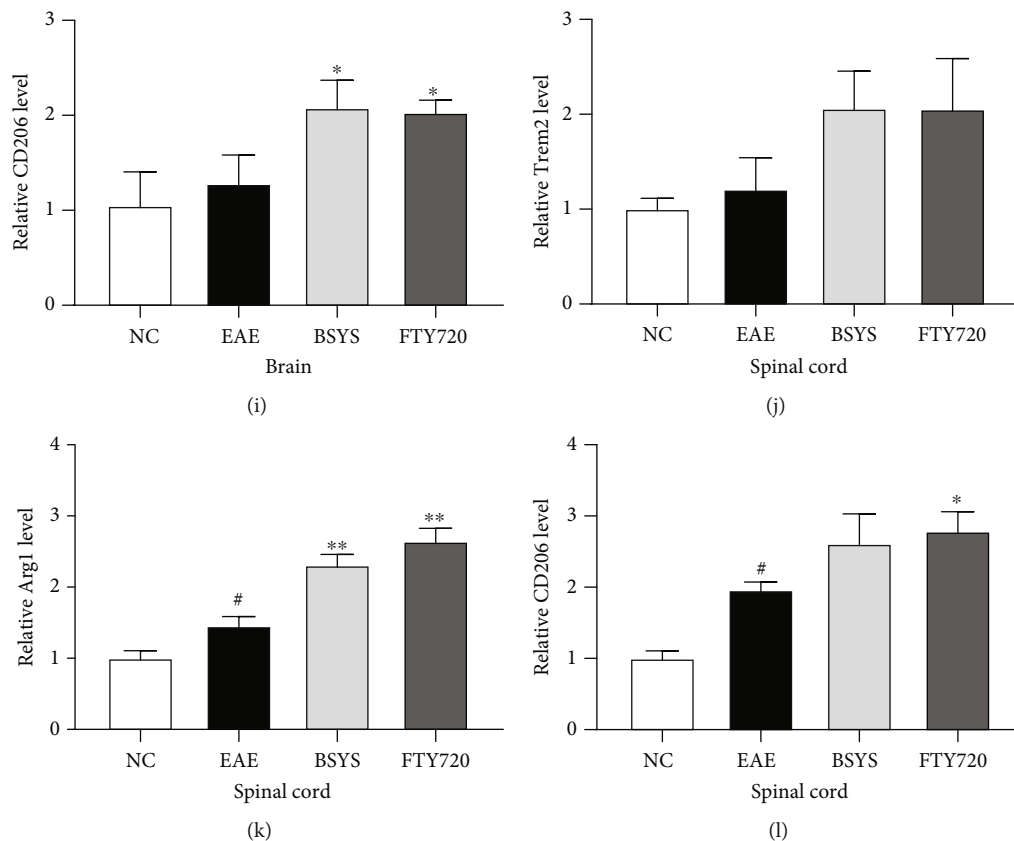
(i)

(j)

(k)

(l)

FIGURE 4: Effect of BSYS on microglial polarization markers. (a–f) M1 phenotype markers (MHC-II, iNOS, CD86) in brain and spinal cord were detected by qRT-PCR. (g–l) M2 phenotype markers (Trem2, Arg1, CD206) in brain and spinal cord were detected by qRT-PCR. Data are presented as means ± SD; compared with the NC group, $^#P < 0.05$, $^{##}P < 0.01$; compared with the EAE group, $^*P < 0.05$, $^{**}P < 0.01$.

CD63 (1 : 1000; ab213090; Abcam, Cambridge, UK), HSP70 (1 : 1000; ab2787; Abcam, Cambridge, UK), and TSG101 (1 : 1000; ab125011; Abcam, Cambridge, UK). The membranes were incubated with HRP-conjugated secondary antibodies after washing in 5% TBST. Finally, the protein bands were detected using a gel chemiluminescence imaging analysis system and the Immobilon Western Chemiluminescent HRP Substrate reagent (Millipore, Billerica, USA) and then were analyzed using ImageJ.

2.12. Statistical Analysis. Statistical analyses were performed using GraphPad Prism (version 8.01; San Diego, USA). H&E and LFB score statistics were analyzed using the Kruskal-Wallis test followed by Dunn's test. The EAE clinical scores and body weight were analyzed using two-way ANOVA with the Bonferroni posttest. Other analyses of three or more groups were performed using one-way ANOVA and the Bonferroni posttest. Values of $P < 0.05$ were considered statistically significant.

3. Results

3.1. BSYS Alleviates the Clinical Severity of EAE Mice. To evaluate the therapeutic effect of BSYS on EAE mice, the body weight and clinical score were tested daily for 40 days. The body weights of EAE mice were markedly decreased

from 13 to 40 dpi compared with those of NC mice; however, this tendency was alleviated in the FTY720 and BSYS groups (Figure 1(a)). No neurological symptoms were observed in the NC group during the entire 40 days. Compared with the NC group, the EAE group began to show neurological deficit symptoms at 11 dpi, and the clinical score of EAE mice increased rapidly, peaking at 21 dpi. From 11 dpi to 40 dpi, the increase in the clinical score in the FTY720 and BSYS groups was markedly lower than that in the EAE group (Figure 1(b)). The cumulative average scores of mice in the FTY720 and BSYS groups were also markedly decreased compared with those of the EAE group (Figure 1(c)).

3.2. BSYS Suppresses Inflammatory Cell Infiltration and Attenuated Demyelination. To further study the protective effect of BSYS on the degree of inflammation and demyelination, tissues in the brain (SVZ, CC) and spinal cord (LE) were observed by H&E and LFB staining. The EAE group showed a larger amount of inflammatory cell infiltration than the NC group (Figure 2(a)). Treatment with either BSYS or FTY720 alleviated the pathological severity. Additionally, large demyelination plaques were observed in the LE and CC of untreated EAE mice, while FTY720 and BSYS reduced the demyelination area in EAE mice (Figure 2(b)). Additionally, we observed the ultrastructure of the myelin sheath by TEM. The myelin sheath of the NC group was closely
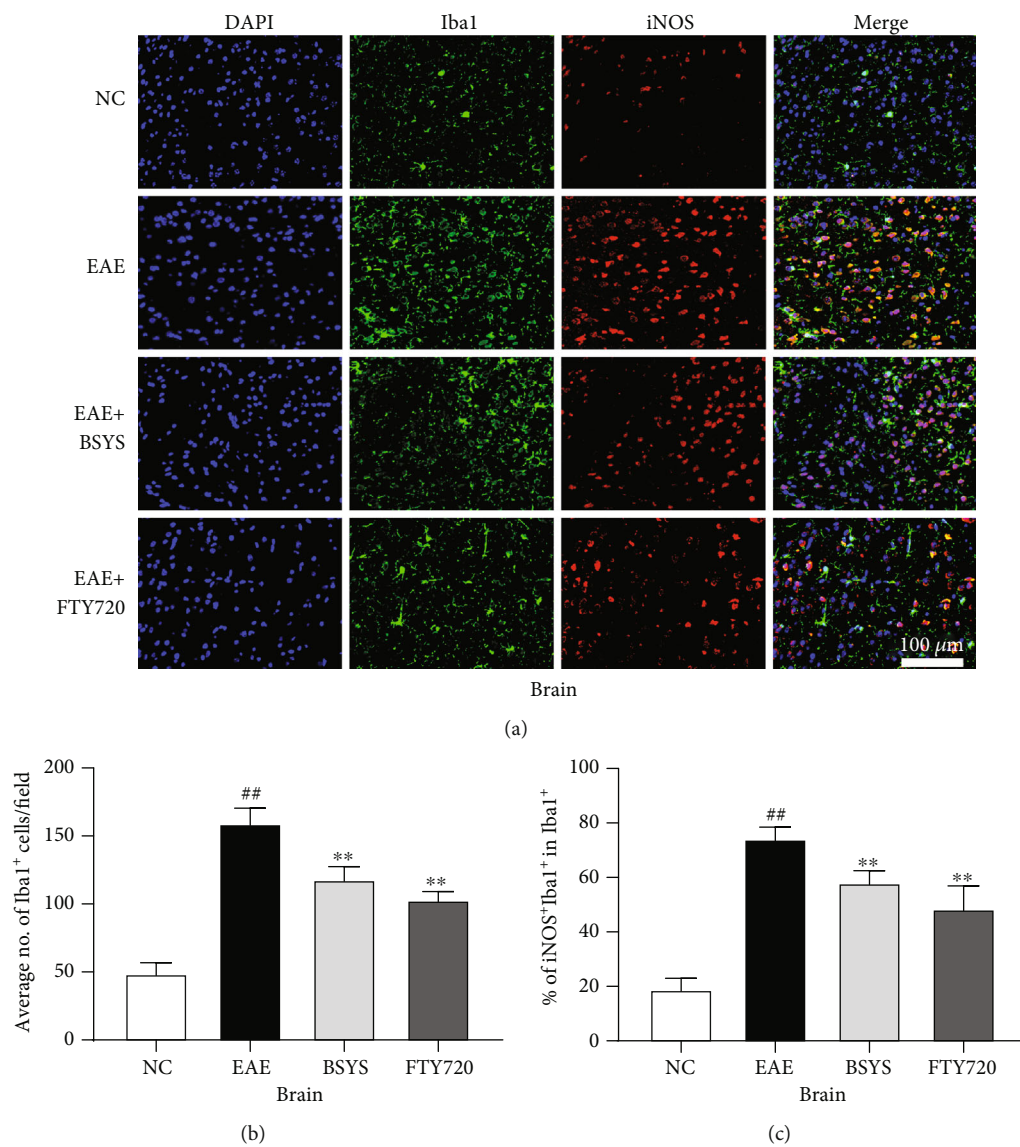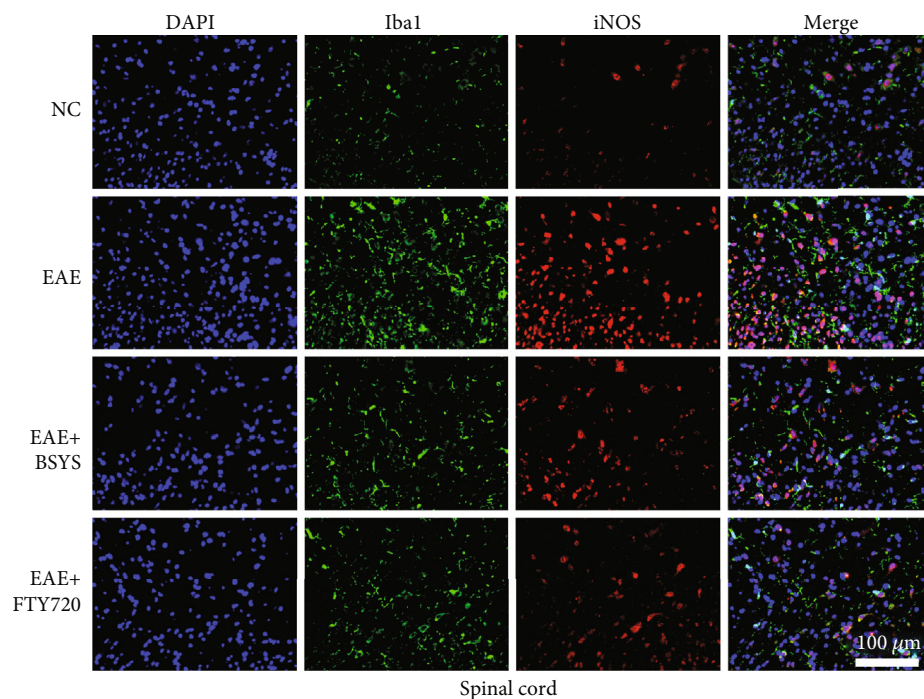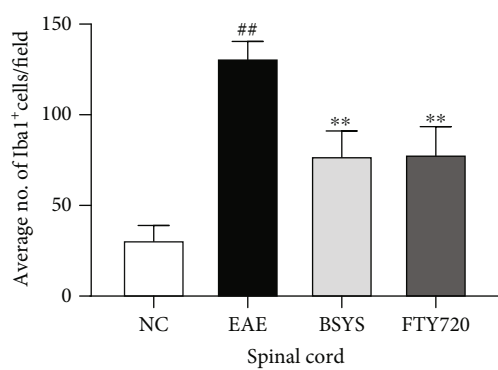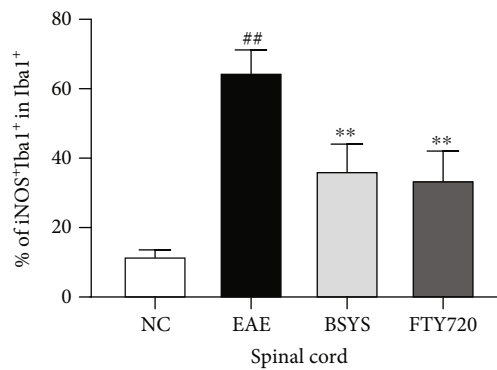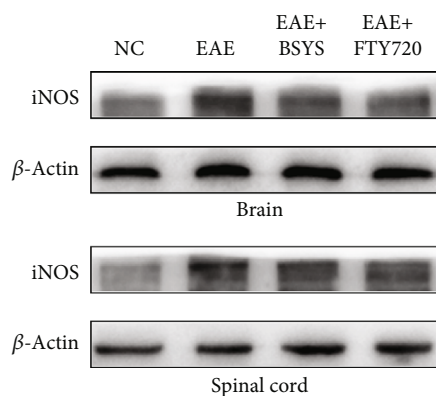
(a)

(b)

(c)

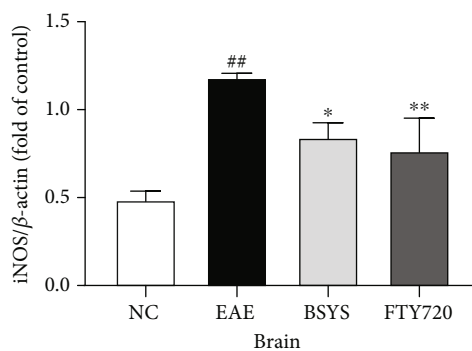FIGURE 5: Continued.

(d)

(e)

(f)
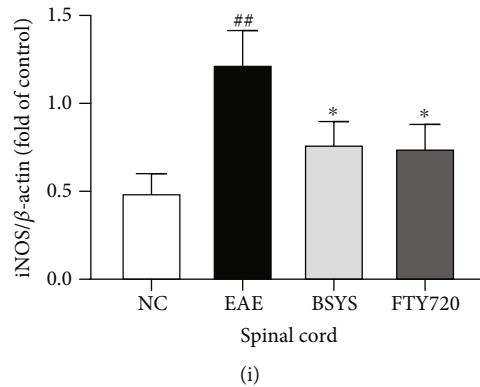

(g)

(h)

FIGURE 5: Continued.

FIGURE 5: BSYS inhibited the polarization of microglia to M1 phenotype in EAE mice. (a, d) Immunofluorescence of SVZ and LE from mice in each group using antibodies against Iba1 (green) and iNOS (red). Scale bars: 100 μm. (b, e) Quantification of the percentage of iNOS+/Iba1+ cells in SVZ and LE. (c, f) Quantification of Iba + cells density in SVZ and LE. (g) Representative western blot images of iNOS in brain and spinal cord tissues. (h, i) Quantitative data for iNOS expression in brain and spinal cord tissues. Data are presented as means ± SD; compared with the NC group, $^{\#\#}P < 0.01$; compared with the EAE group, $^{*}P < 0.05$, $^{**}P < 0.01$.

arranged, the structure was intact, and the morphology of mitochondria was normal. By contrast, untreated EAE mice showed a loose lamellar myelin structure, axonal edema, and nerve fiber disintegration. The ratio of the axon diameter to myelinated axon diameter (G-ratio) was used to quantify the degree of demyelination. Compared with that of the untreated group, the G-ratio of EAE mice treated with BSYS and FTY720 markedly decreased, and the integrity of the myelin sheath was protected (Figure 2(c)).

3.3. BSYS Promotes the Maturation of Oligodendrocytes in EAE Mice. Considering the significant improvement in neurological results, we aimed to explore whether BSYS affects the maturation of oligodendrocytes and remyelination process, which exerts a crucial effect on the recovery of EAE. CC-1 is a mature oligodendrocyte marker [41]. Immunofluorescence showed that, in both the brain and spinal cord, the CC-1^{+}/Olig2^{+} cell ratio in the BSYS-treated group was clearly higher than that in the EAE group (Figures 3(a)–3(f)).

Myelin proteolipid protein (PLP) is another marker of mature oligodendrocytes and one of the main membrane proteins that make up myelin [42]. We quantified PLP in the brain and spinal cord by IHC staining, revealing that the level of PLP in EAE mice was significantly reduced at 40 dpi. However, the PLP expression was increased in the FTY720- and BSYS-treated groups compared with that in the EAE group (Figures 3(g)–3(i)).

3.4. BSYS Treatment Promotes M2 Microglial Polarization in the Brain and Spinal Cord of EAE Mice. To explore the role of BSYS in microglial polarization, the mRNA expression levels of M1 markers (MHC-II, iNOS, CD86) and M2 markers (Trem2, Arg1, CD206) were measured at 40 dpi in the mouse brain and spinal cord. Compared with those in the NC group, the mRNA levels of M1 phenotype markers were elevated in the EAE group (Figures 4(a)–4(f)). However, BSYS and FTY720 treatment reduced the expression levels of M1-related markers; in particular, MHC-II and iNOS were significantly downregulated. By contrast, the levels of M2

polarization markers were increased in the BSYS-treated group compared with that in the EAE group, but only Arg1 upregulation was statistically significant in both the brain and spinal cord (Figures 4(g)–4(l)). These outcomes suggested that the antidemyelination effect of BSYS may be partly realized by suppressing M1 microglial polarization and reversing microglial polarization toward the M2 phenotype.

Next, microglial polarization was further investigated in the CNS by immunofluorescence. Brain and spinal cord sections were double-stained for Iba1 (microglial marker)/iNOS (M1 marker) or Iba1/Arg1 (M2 marker). EAE induced marked upregulation in the ratio of M1 microglia. However, BSYS and FTY720 treatment decreased the numbers of activated microglia (Iba1^{+} cells) (Figures 5(a), 5(b), 5(d), and 5(e)) and M1 microglia (Iba1^{+}/iNOS^{+} cells) (Figures 5(a), 5(c), 5(d), and 5(f)) and increased the proportion of M2 microglia in the treatment groups compared with that in the EAE group (Figures 6(a)–6(d)). Next, western blot analysis showed that the iNOS expression was significantly increased in the EAE group compared with that in the NC group. However, BSYS and FTY720 reversed the upregulation of iNOS (Figures 5(g)–5(i)) and downregulation of Arg1 induced by EAE (Figures 6(e)–6(g)). These outcomes were consistent with the results of immunofluorescence staining.

M1 and M2 microglia secrete pro- and anti-inflammatory cytokines, respectively, and ELISA was used to further evaluate the efficacy of BSYS in modulating microglial polarization. ELISA showed that the expression levels of the inflammatory cytokines IL-1β, IL-6, and TNF-α in the EAE group were higher than those in the NC group. The administration of FTY720 and BSYS suppressed the increase in proinflammatory cytokines in the CNS induced by EAE (Figures 7(a)–7(f)). However, compared with the EAE group, only the IL-6 reduction was statistically significant in both the brain and spinal cord in the BSYS treatment group. Moreover, the levels of IL-10 (Figures 7(g)–7(h)) secreted by M2 phenotype microglia were markedly increased in the BSYS group compared with those in the EAE group.
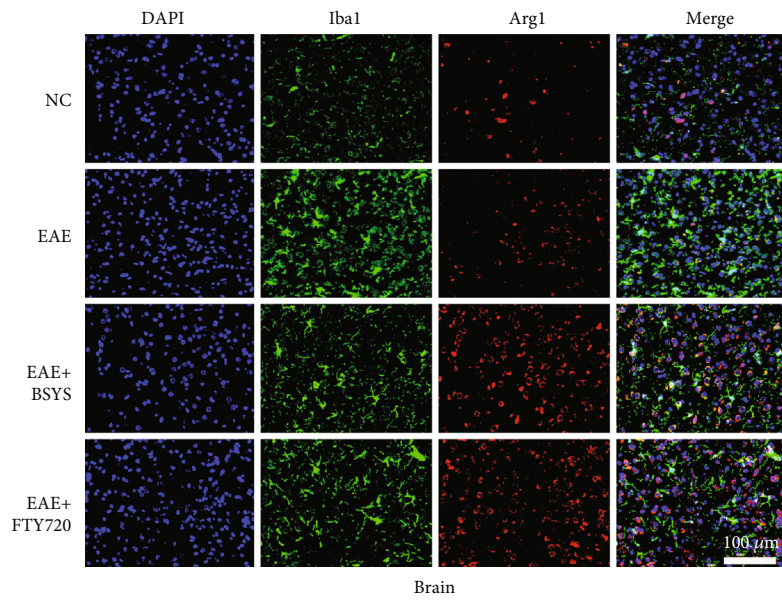
(a)
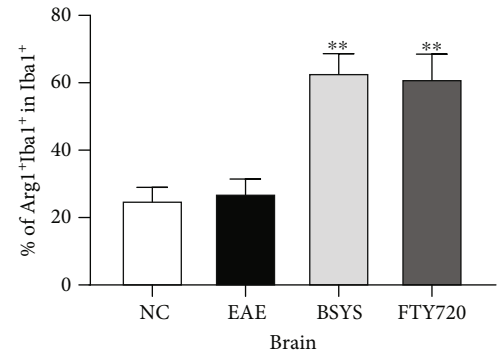
(b)
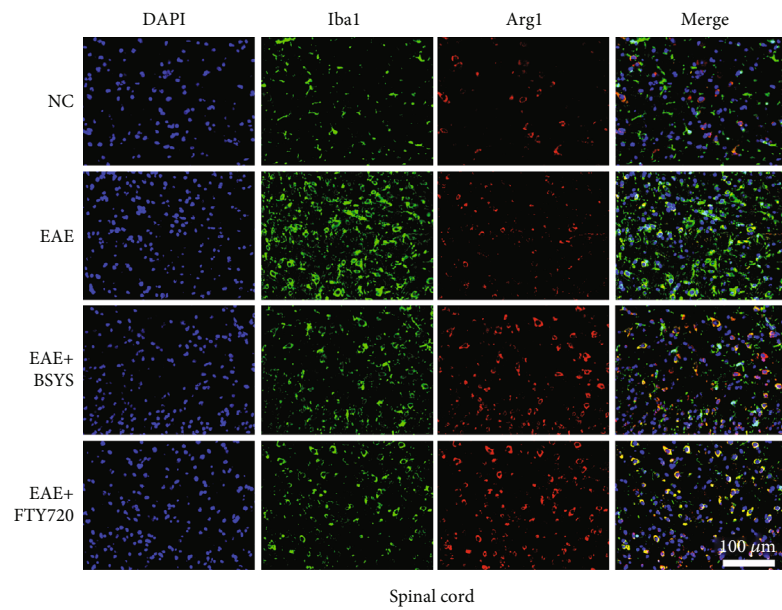
(c)
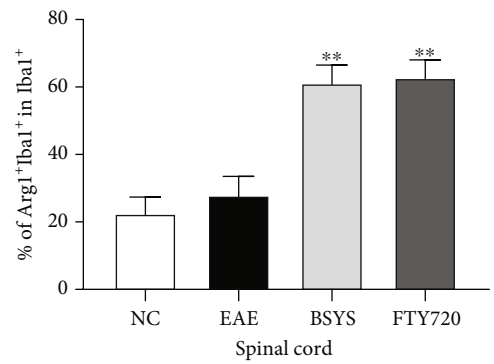
(d)

Figure 6: Continued.

(e)

(f)

(g)
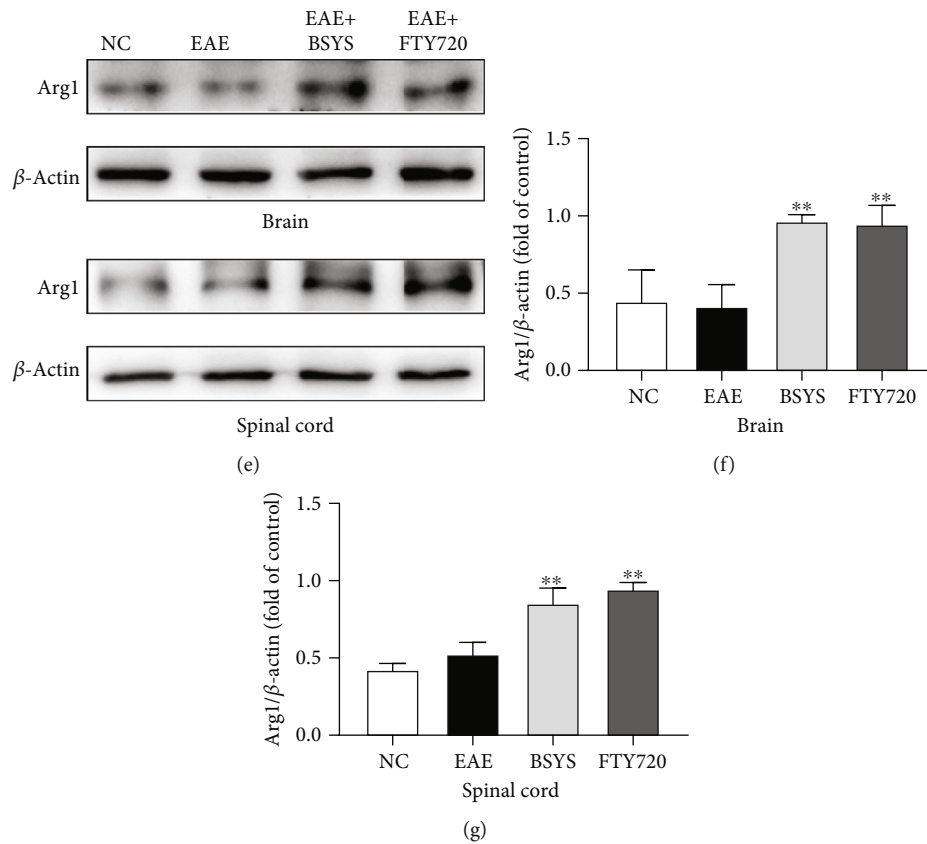
FIGURE 6: BSYS promoted the polarization of microglia to M2 phenotype in EAE mice. (a, c) Immunofluorescence of SVZ and LE from mice in each group using antibodies against Iba1 (green) and Arg1 (red). Scale bars: 100 μm. (b, d) Quantification of the percentage of Arg1+/Iba1+ cells in SVZ and LE. (e) Representative western blot images of Arg1 in brain and spinal cord tissues. (f, g) Quantitative data for Arg1 expression in brain and spinal cord tissues. Data are presented as means ± SD; compared with the EAE group, $^{**}P < 0.01$.

3.5. BSYS Regulates miR-124 and miR-155 in CNS. Many studies have shown that miR-124 and miR-155 play anti-inflammatory and proinflammatory effects in neuroinflammation and are the key regulatory genes of microglial polarization. Upregulation of miR-124 and downregulation of miR-155 promote M2 polarization, thus reducing nerve injury and protecting neural function. qRT-PCR showed that the EAE model significantly increased the miR-155 expression in the brain and spinal cord compared with that in the NC group (Figures 8(c) and 8(f)), while the miR-124 level was downregulated (Figures 9(c) and 9(f)). Treatment of EAE mice with either BSYS or FTY720 led to a significant decrease in the relative miR-155 expression in the brain and spinal cord. Additionally, BSYS increased the miR-124 expression. We also detected miRs in the SVZ and LE by fluorescence in situ hybridization, and the results were consistent with those of qRT-PCR (Figures 8(a), 8(b), 8(d), and 8(e); Figures 9(a), 9(b), 9(d), and 9(e)), indicating that BSYS regulates miR-124 and miR-155 in the CNS to play a potential role in promoting M2 polarization of microglia.

3.6. BSYS Increases miR-124 and Suppresses miR-155 in Peripheral Serum Exosomes. In recent years, exosomes in peripheral circulation were demonstrated to likely serve as neuroinflammatory mediators [43], and the expression of some miRs in plasma exosomes is abnormal in the progression of MS/EAE disease [44, 45]. Therefore, at 40 dpi, we used an exoEasy Kit to collect serum exosomes from mice from each group and identified the morphology and size of exosomes by TEM and NTA. The collected vesicles showed typical cup-shaped morphology, and the diameter of the particles was 80~200 nm (Figures 10(a) and 10(c)). Exosomal markers, such as CD63, HSP70, and TSG101, were detected by western blotting and were enriched in isolated exosomes from serum (Figure 10(b)). Furthermore, we isolated exosomal RNA and analyzed the miR-124 and miR-155 expression in the serum exosomes of mice in each group by qRT-PCR. Compared with the serum exosomal miR-155 level in NC mice, that in EAE mice markedly increased, while the content of miR-124 decreased. BSYS treatment increased the miR-124 level and reduced the miR-155 level in the serum exosomes of EAE mice (Figures 10(d) and 10(e)). The results are consistent with the changes in the CNS tissues.

3.7. Target Genes of miR-124 and miR-155 Related to M2 Microglial Polarization Are Modulated by BSYS. C/EBPα and PU.1 are downstream target genes of miR-124, and SOCS1 is a target gene of miR-155. Many studies have shown that changes in these genes can regulate microglial polarization and affect the progression of MS/EAE. Therefore, we

(a)

(b)

(c)

(d)

(e)

(f)

(g)

(h)
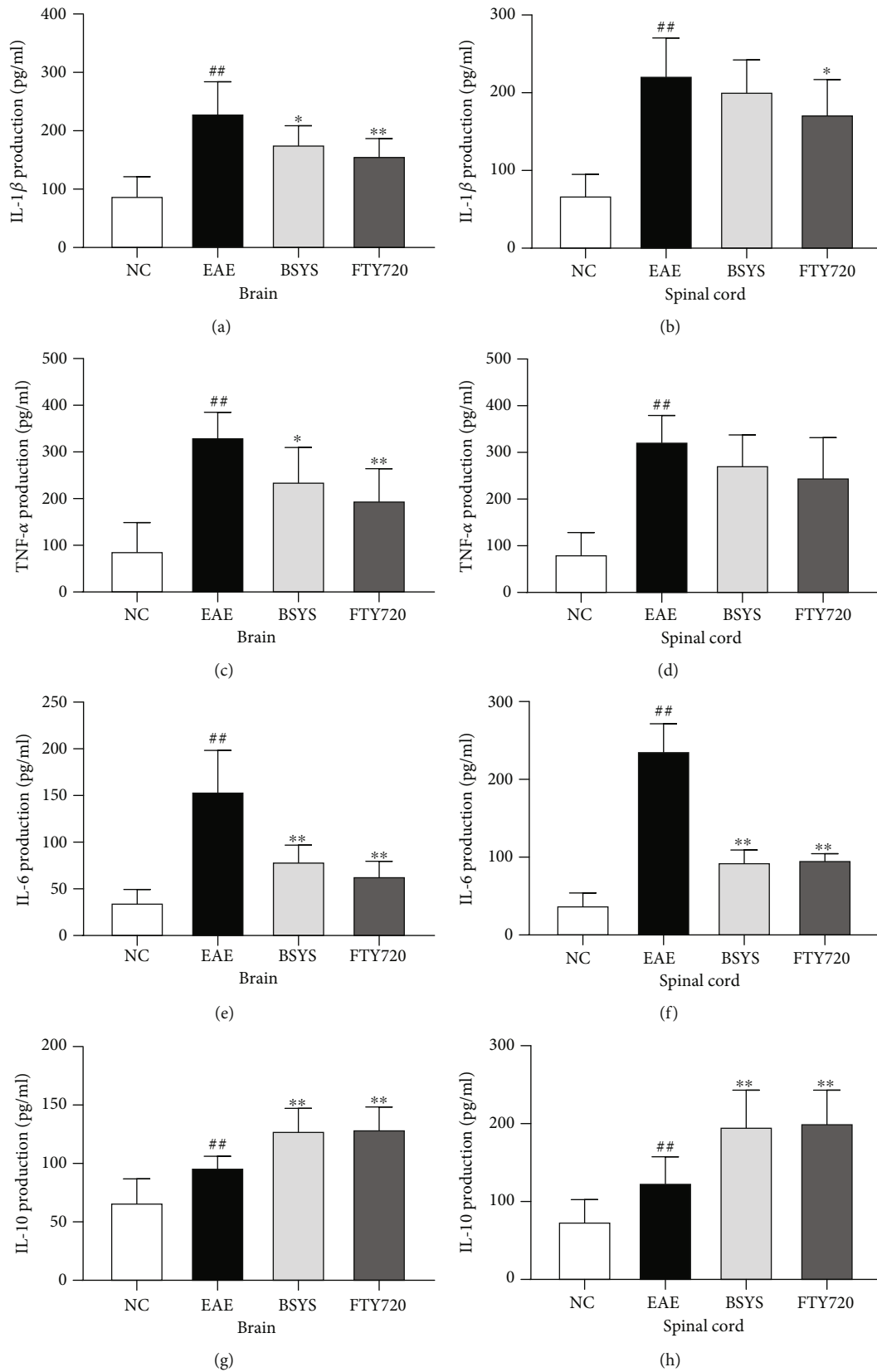
FIGURE 7: Effect of BSYS on cytokine levels of CNS in EAE mice. (a–f) The levels of proinflammatory cytokines (IL-1β, TNF-α, IL-6) in brain and spinal cord were detected by ELISA. (g–h) The levels of anti-inflammatory cytokine (Trem2, Arg1, CD206) in brain and spinal cord were detected by ELISA. Data are presented as means ± SD; compared with the NC group, [##]$P < 0.01$; compared with the EAE group, [*]$P < 0.05$, [**]$P < 0.01$.

(a)

(b)

(c)

(d)
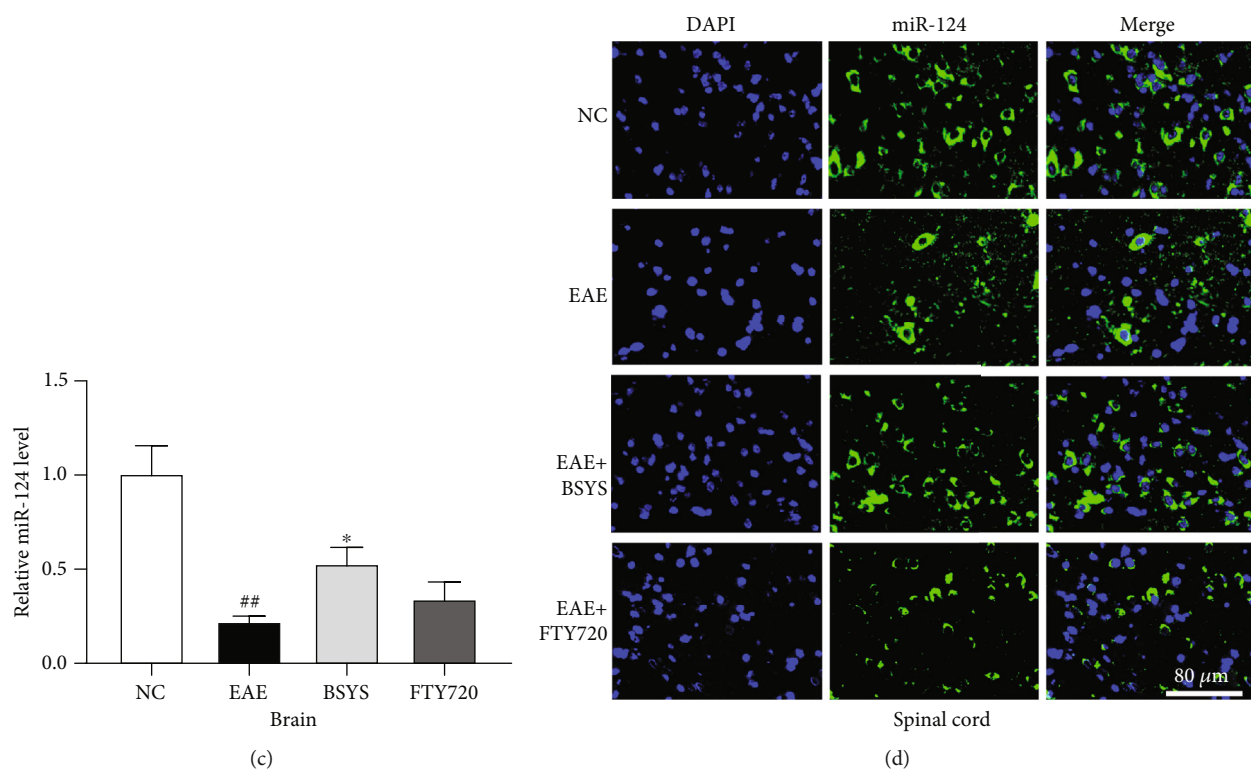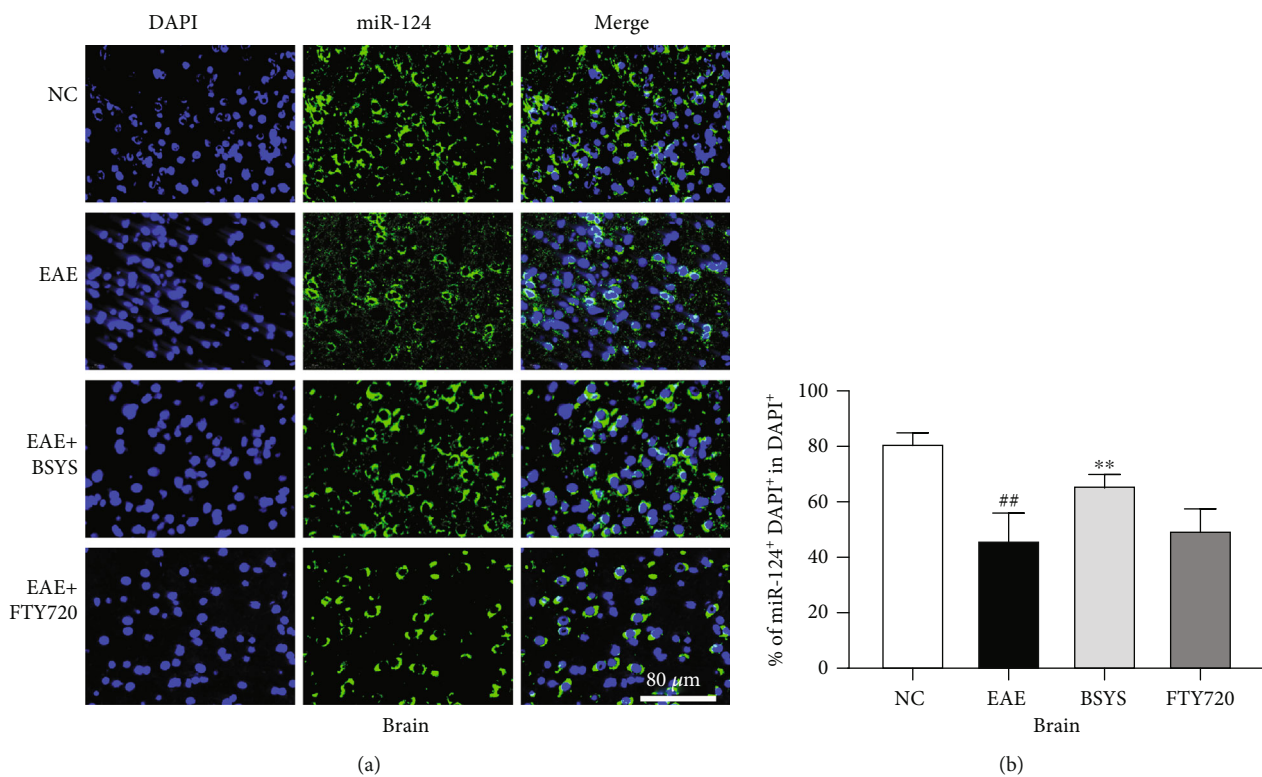
FIGURE 8: Continued.

(e)   (f)
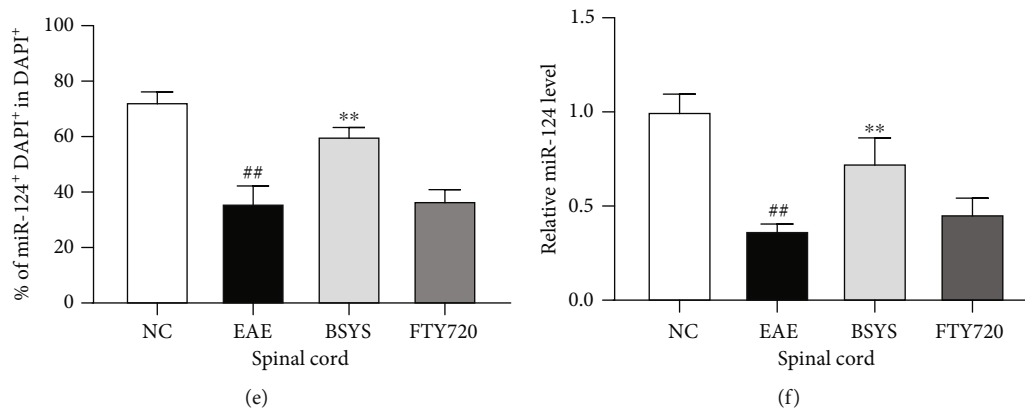
FIGURE 8: BSYS upregulated the expression of miR-124 in EAE mice. (a, d) miR-124 was labeled in SVZ and LE by fluorescence in situ hybridization. Scale bars: 80 μm. (b, e) Quantification of miR-124 + density in SVZ and LE. (c, f) The expression levels of miR-124 in brain and spinal cord from mice of each group were detected by qRT-PCR. Data are presented as means ± SD; compared with the NC group, [##]$P < 0.01$; compared with the EAE group, [*]$P < 0.05$, [**]$P < 0.01$.

examined these target genes by qRT-PCR and western blot analysis. The expression levels of C/EBPα and PU.1 were upregulated in the brain and spinal cord in the EAE group compared with those in the NC group at 40 dpi. However, compared with their levels in the EAE group, these proteins were markedly downregulated after BSYS treatment. By contrast, the expression level of SOCS1 was decreased in the EAE group compared with that in the NC group, and treatment with FTY720 and BSYS induced its expression compared with that in the EAE group at 40 dpi (Figures 11(a)–11(n)).

4. Discussion

MS is an autoimmune disease of the CNS characterized by inflammatory cell infiltration and demyelination with more than two million cases worldwide [46]. Currently, immunosuppressants (e.g., glucocorticoid) and immunomodulators (e.g., FTY720) are the main drugs for MS treatment; however, they have significant risks in terms of safety and side effects [47, 48]. Many studies have focused on developing new drugs that inhibit demyelination to assist functional and pathological recovery in EAE. In our study, we assessed a TCM called BSYS, a formula that has shown therapeutic efficacy in MS/EAE and determined the potential mechanism of its neuroprotective effects. The body weight and clinical scores showed that BSYS treatment significantly improved neurologic recovery in EAE. Moreover, H&E and LFB staining showed that BSYS prevented inflammatory infiltration and demyelination in the brain and spinal cord. Additionally, the structure of the myelin sheath was protected in the lesion site after BSYS treatment. Furthermore, the number of cells that were CC-1^{+}/Olig2^{+}, markers of mature oligodendrocytes, was increased by BSYS treatment. PLP is the most abundant protein in the myelin sheath of the CNS. The PLP content is a quantitative indicator of myelin membrane integrity, and myelin also depends on its specific lipid content. Therefore, we speculated that BSYS affects PLP formation to reduce damage to the myelin sheath, which is supported by the expression levels of PLP observed in the brain and spinal cord. These results indicate that BSYS

improves neurologic recovery in EAE mice by promoting oligodendrocyte maturation.

Previous studies clearly demonstrated that microglia regulate the microenvironment of the CNS and affect the process of remyelination [49]. In MS, microglia are activated and express signaling molecules and cytokines, leading to secondary nerve injury. Thus, inhibiting the overactivation of microglia and reducing the secretion of neurotoxic cytokines represent a new approach for MS treatment. Accumulating evidence has shown that microglial M1/M2 polarization plays a crucial role in neuroinflammation during EAE progression [50]. M1 microglia prevent oligodendrocyte maturation [51], while M2 microglia drive the differentiation of oligodendrocytes in neurodegenerative diseases [52]. Specifically, M1 microglia produce high levels of oxide metabolites, leading to CNS dysfunction. During neuroinflammation, many related receptors and enzymes in the M1 phenotype are upregulated to increase crosstalk and regulation of the CNS immune microenvironment, and MHC-II, iNOS, and CD86 are considered crucial markers [53]. The mRNA levels of these M1 phenotype markers (MHC-II, iNOS, CD86) increased in EAE mice. However, their expression was decreased in the BSYS group compared with that in the EAE group. However, the M2 phenotype secretes cytokines and expresses receptors related to anti-inflammation to induce tissue repair of the CNS, as demonstrated by the expression of triggering receptor expressed on myeloid cells 2 (Trem2), Arg1, and CD206 [54]. In our study, the mRNA expression of these genes was increased after BSYS treatment. Arg1 and iNOS share the same substrate; thus, only one of them is preferentially synthesized in microglia, making iNOS/Arg1 a suitable marker for microglial polarization. Indeed, consistent with our study, qRT-PCR showed that the most significant differences in M1 and M2 polarization markers between the EAE and treatment groups were in iNOS and Arg1, respectively. Thus, we used iNOS and Arg1 as markers to identify M1- and M2-polarized microglia in the CNS by immunofluorescence. Additionally, Iba1 is a microglia/macrophage-specific calcium-binding protein with actin-bundling activity that is widely used to identify activated microglia. FTY720 and BSYS treatment led to markedly
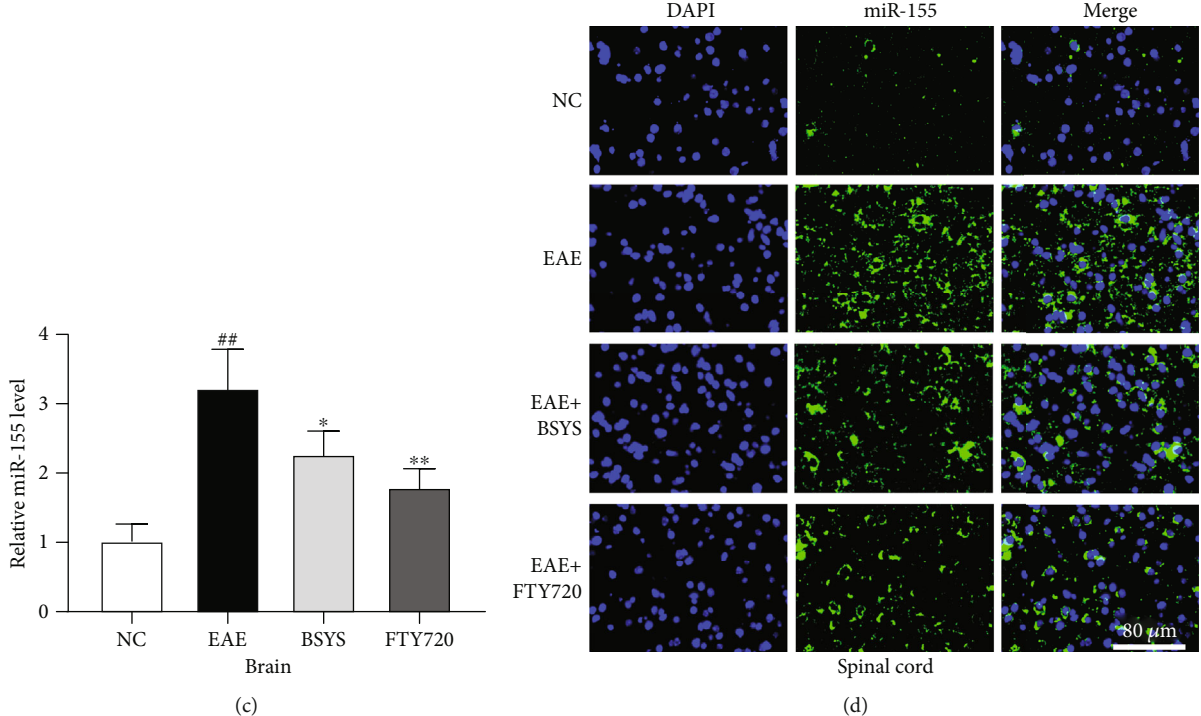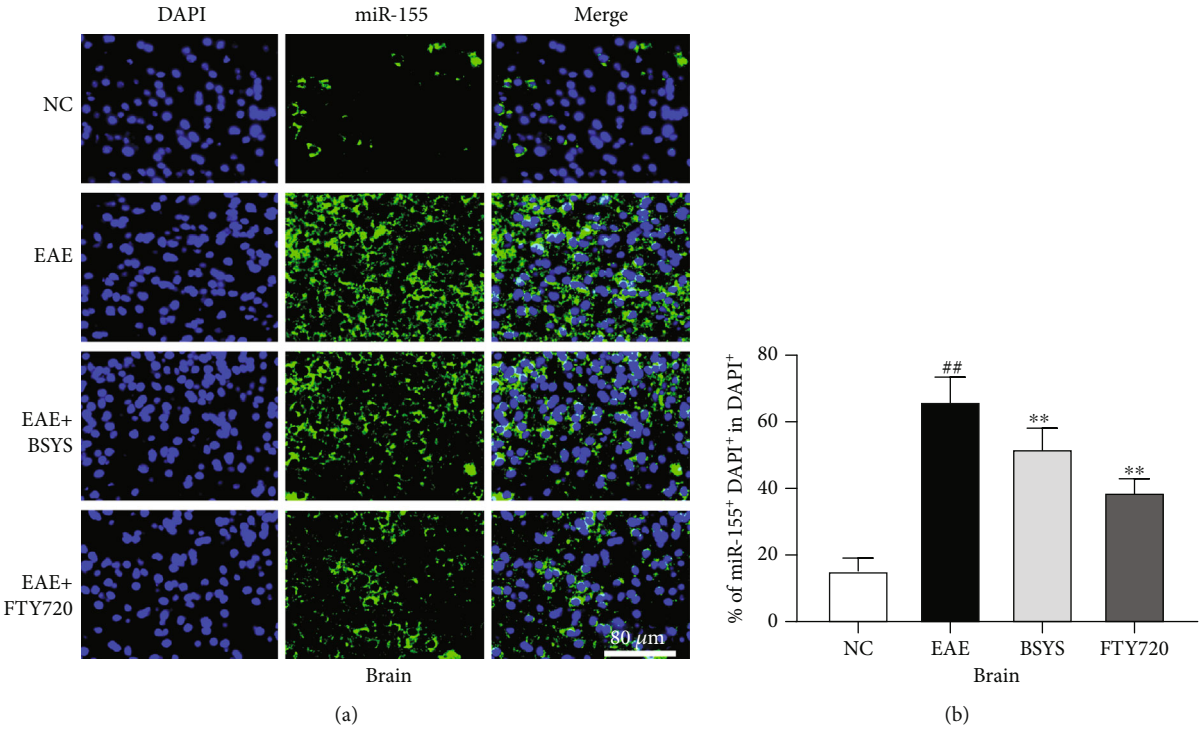
(a)

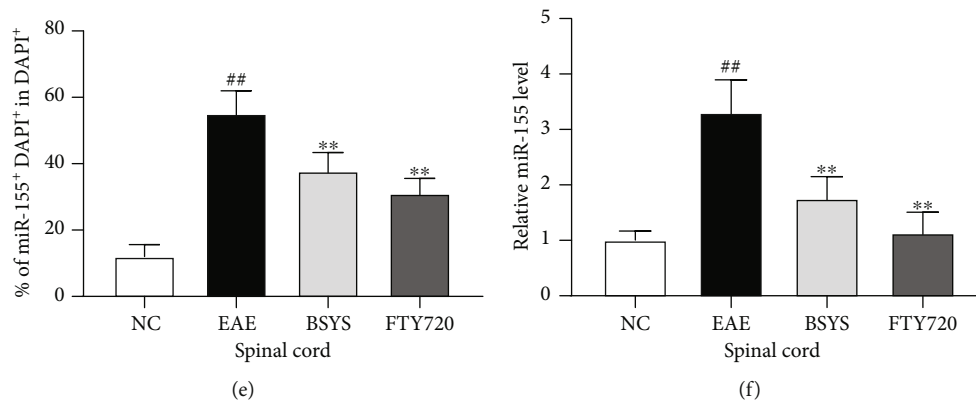(b)

(c)

(d)

FIGURE 9: Continued.

(e)

(f)

FIGURE 9: BSYS downregulated the expression of miR-155 in EAE mice. (a, d) miR-155 was labeled in SVZ and LE by fluorescence in situ hybridization. Scale bars: 80 μm. (b, e) Quantification of miR-155 + density in SVZ and LE. (c, f) The expression levels of miR-155 in brain and spinal cord from mice of each group were detected by qRT-PCR. Data are presented as means ± SD; compared with the NC group, [##]$P < 0.01$; compared with the EAE group, [*]$P < 0.05$, [**]$P < 0.01$.

increased expression of Arg1 (M2 marker) in Iba1^{+} cells, while iNOS (M1 marker) expression was decreased dramatically in EAE mice. Furthermore, M1 microglia secrete proinflammatory cytokines, while M2 microglia secrete cytokines that decrease inflammation [55]. Microglia activated in the EAE group were switched to the M1 phenotype and produced more proinflammatory cytokines to prevent remyelination. However, treatment with BSYS reduced the expression of IL-1β, IL-6, and TNF-α and increased the expression of IL-10, highlighting the neuroprotective effects of BSYS.

miRs are small non-protein-coding RNA molecules with a length of 18-25 nucleotides that play an important role in modulating gene expression and regulating diverse biological events [56]. In the past few years, miRs have been deemed potential regulators of microglial polarization during MS/EAE progression [18, 57]. Many studies have indicated that miRs alter the direction of microglial polarization, while the miRs expression level is different between the M1 and M2 phenotypes. In particular, miR-155 and miR-124 are representatives of the pro- and anti-inflammatory miRs, respectively, which are considered crucial to balance the polarization of M1 and M2 microglia [58].

Initially, miR-124 was assumed to be an anti-inflammatory miR [59] that contributes to suppressing microglial activation because the highest levels of miR-124 were detected in deactivated resident microglia, while the miR-124 levels were significantly decreased after stimulation with IFN-γ and LPS, which is known to potentiate the M1 phenotype. However, studies of miR-124-transfected microglia revealed that miR-124 decreased the expression of proteins associated with the M1 phenotype while increasing the expression of M2-associated markers. This result suggests that miR-124 not only deactivates microglia but also skews their polarization from the M1 phenotype toward the M2 phenotype [18]. Furthermore, during the acute phase of EAE, the increased levels of M1 markers in microglia occurred at the same time as the decrease in miR-124 expression in the CNS. By contrast, high expression of miR-124 and low expression of M1 markers were simultaneously observed in the CNS of normal mice or mice in the recovery phase of EAE [13, 60].

C/EBPα and PU.1 are downstream targets of miR-124, and C/EBPα is one of the C/EBP transcription factor family members that is widely expressed and regulates various cellular and physiological processes, including energy metabolism, immunity, and inflammation [61]. PU.1 serves as a critical regulator in the immune system. It exerts an important effect on regulating genes relevant to specialized functions of microglia [62, 63]. miR-124 controls multiple markers of microglial polarization by directly inhibiting C/EBP-α and its downstream transcription factor PU.1 [64]. miR-155, broadly considered a proinflammatory miR, contributes to microglia-mediated neurotoxicity, which is largely related to the M1 phenotype [65]. miR-155 was shown to be increased significantly in the MS/EAE brain and spinal cord [66]. It targets anti-inflammatory proteins in microglia, such as SOCS1, resulting in elevated expression levels of iNOS, IL-6, and TNF-α. Furthermore, SOCS1 induces differentiation from the M1 to M2 state and increased SOCS1 in the M2 phenotype, which plays an important role in sustaining the anti-inflammatory function [67]. Moreover, miR-155 can target M2-associated genes, and inhibition of miR-155 promotes the expression of M2 markers [68], such as Arg1, Ym1, and Fizz1. The above evidence suggests that the regulation of miR-124 and miR-155 in EAE has an important effect on the polarization of microglia, and the polarization of M1/M2 may also be accompanied by the changes of miR-124 and miR-155. In our study, the expression of miR-155 in the brain and spinal cord of EAE mice increased significantly because of autoimmune inflammation injury, while the expression of miR-124 decreased significantly compared with that in NC mice. However, after BSYS treatment, fluorescence in situ hybridization and qRT-PCR showed that the levels of miR-124 and miR-155 were reversed. These results indicate that microglial polarization to M2 caused by BSYS is related to changes in the miR expression.

Exosomes are secreted by various cells and carry cargos, including proteins, lipids, and noncoding RNAs [69]. After release, exosomes are transferred to specific target cells to exert multiple effects [70]. A recent study showed that peripheral circulating exosomes contribute to neuroinflammation under systemic inflammation conditions [43].
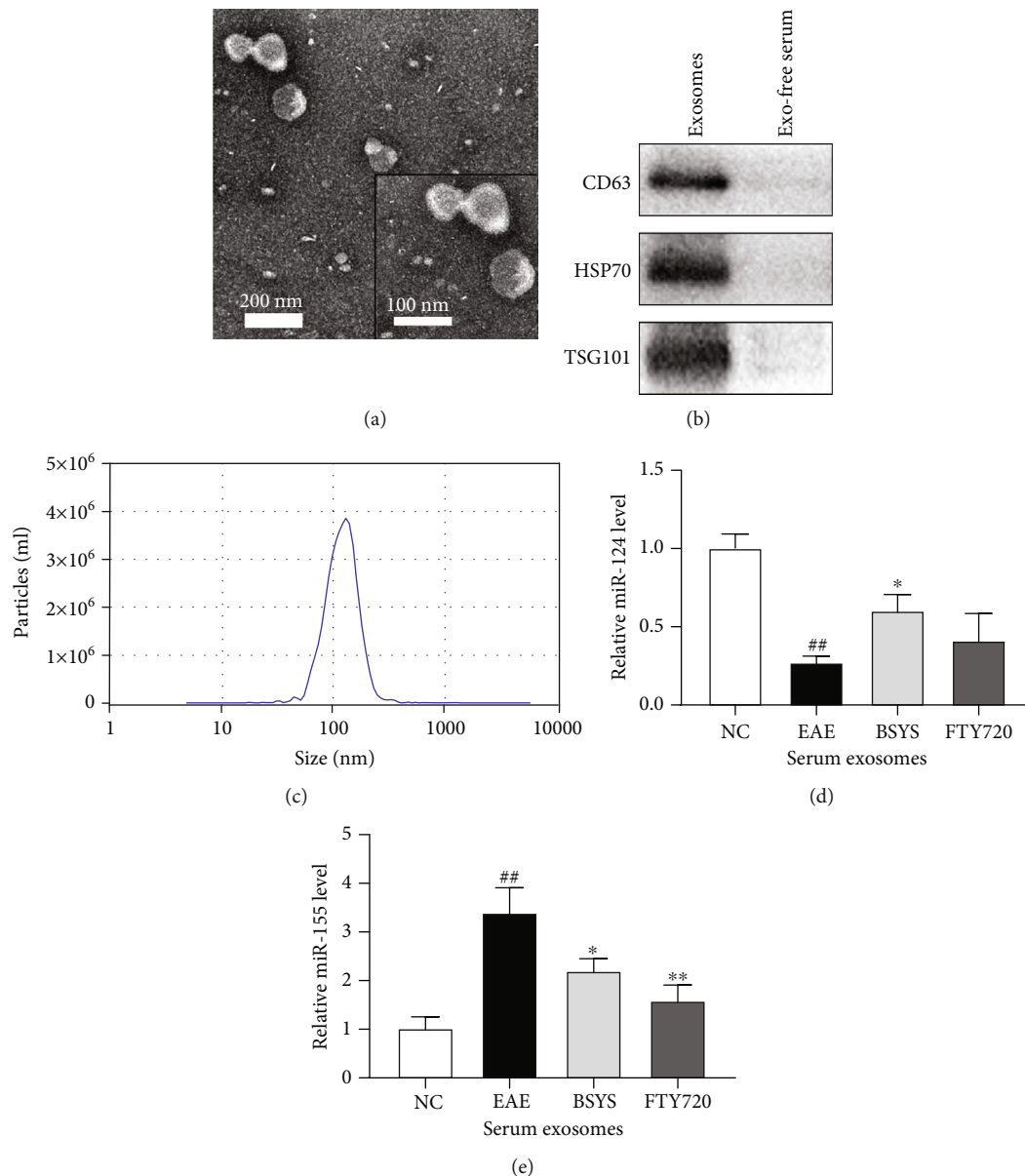
FIGURE 10: BSYS regulated the expression of serum exosomal miR-124 and miR-155 in EAE mice. (a) Exosomes derived from mice serum were observed by transmission electron microscopy. (b) Exosome markers (CD63, HSP70, and TGS101) were detected by western blot. (c) Particle sizes of serum exosomes were measured by NTA. (d, e) The expression levels of miR-124 and miR-155 in serum exosomes from mice of each group were detected by qRT-PCR. Data are presented as means ± SD; compared with the NC group, $^{##}P < 0.01$; compared with the EAE group, $^{*}P < 0.05$, $^{**}P < 0.01$.

Increased expression of inflammatory miRs in serum-derived exosomes may play a role in regulating the CNS immune response. Furthermore, the expression of miRs in serum exosomes was dysregulated at the onset and peak of MS/EAE [71]. Thus, circulating exosomal miRs represent promising candidate biomarkers for MS/EAE and could reflect the status and therapeutic efficacy of the disease [44]. Our study found that the expression of serum exosomal miR-124 and miR-155 in EAE mice was similar to that in brain and spinal cord tissues; the former was downregulated, and the latter was upregulated. Furthermore, BSYS treatment reversed this trend, which was also consistent with the differences in the

CNS tissues of mice in each group. Therefore, we confirmed the role of BSYS in regulating miRs at both the CNS and peripheral levels. Additionally, we analyzed the downstream target genes C/EBP α, PU.1, and SOCS1 of miR-124 and miR-155 in the CNS by western blotting and qRT-PCR. After BSYS treatment, the M1 phenotype-related SOCS1 was significantly suppressed, while the transcription factors C/EBPα and PU.1, which promote M2 polarization, were activated. These findings further suggest that the potential mechanism of BSYS is via promoting M2 polarization in the CNS of EAE mice, which may be related to the changes of miR-124 and miR-155 in vivo. However, all of our results were derived
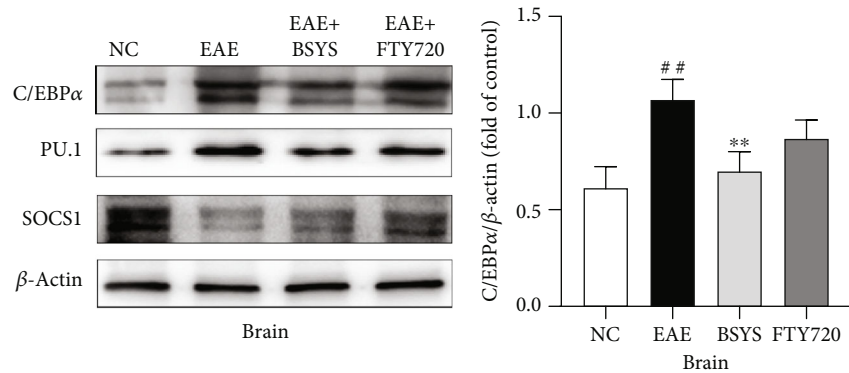
(a)

(b)
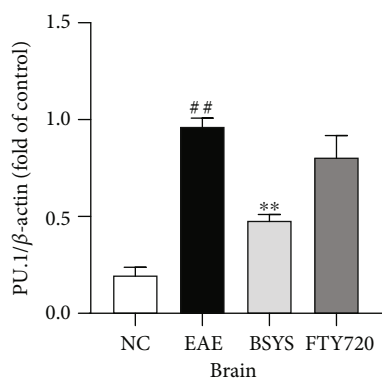
(c)
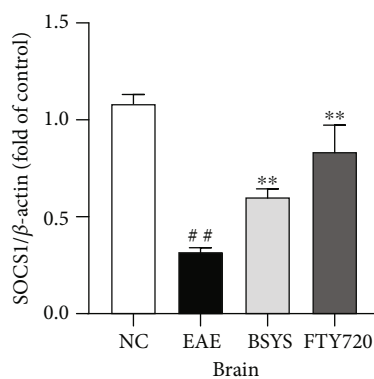
(d)
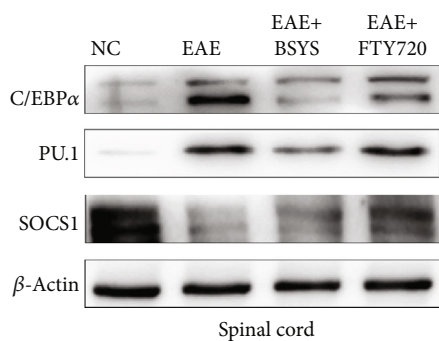
(e)
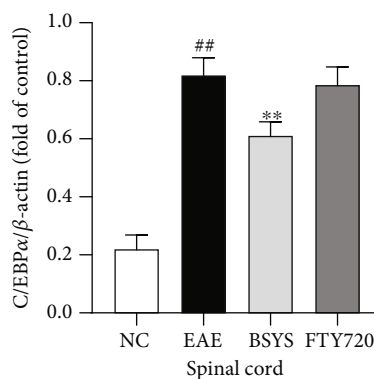
(f)
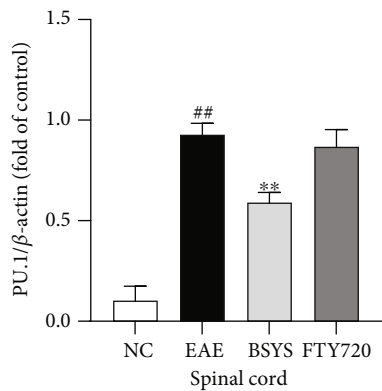
(g)
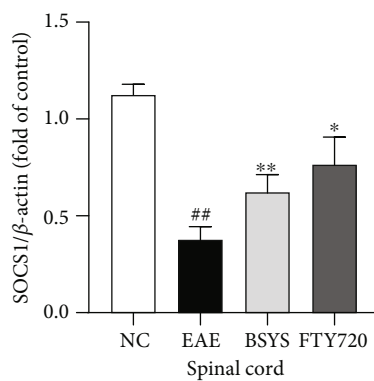
(h)

Figure 11: Continued.

(i)

(j)

(k)

(l)

(m)

(n)
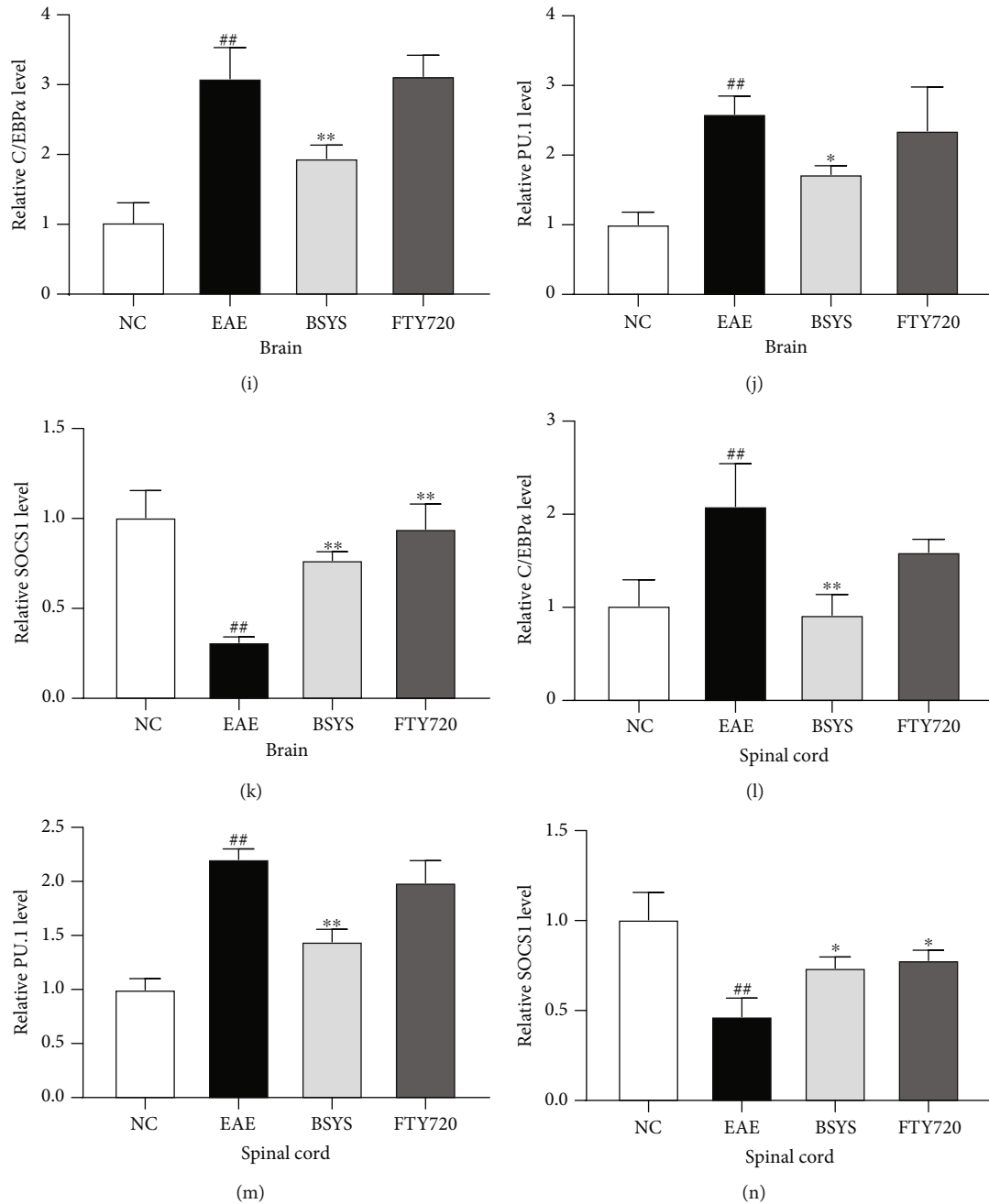
FIGURE 11: BSYS regulated the protein expressions of CEBP/α, PU.1, and SOCS1. (a, e) Representative images of western blot of CEBP/α, PU.1, and SOCS1 in the brain and spinal cord in EAE mice. (b–d, f–h) Quantitative analysis of CEBP/α, PU.1, SOCS1, and β-actin was used as the internal standard. (i–n) mRNA levels of CEBP/α, PU.1, and SOCS1 in the brain and spinal cord were detected by qRT-PCR. Data are presented as means ± SD; compared with the NC group, $^{##}P < 0.01$; compared with the EAE group, $^{*}P < 0.05$, $^{**}P < 0.01$.

from in vivo studies. The role of miR-124 and miR-155 in BSYS-mediated microglia M2 polarization has not been fully elucidated, warranting further exploration. In future studies, we will inhibit and overexpress miR-124 and miR-155 in EAE mice to further study the mechanism of BSYS-mediated neuroprotection. Additionally, the specific mechanism of M2 polarization regulated by BSYS must also be proven in cell experiments, we will further verify these conclusions in vitro.

In summary, our study suggests that BSYS alleviates the inflammatory response, which suppresses demyelination by promoting M2 polarization of microglia to regulate the secretion of pro/anti-inflammatory factors and ameliorate neurological function. The effect of BSYS on skewing M2 polarization may correlate with the changes of miR-124 and miR-155 in vivo. Therefore, BSYS is a promising therapeutic agent to suppress neuroinflammation and improve remyelination.

Data Availability

The data that support the findings of this study are available from the corresponding author upon reasonable request.

Conflicts of Interest

The authors declare that they have no conflicts of interest.

Acknowledgments

References

[1] J. Correale, M. I. Gaitan, M. C. Ysrraelit, and M. P. Fiol, "Progressive multiple sclerosis: from pathogenic mechanisms to treatment," *Brain*, vol. 140, no. 3, pp. 527–546, 2017.

[2] I. Y. Choi, P. Lee, P. Adany et al., "In vivo evidence of oxidative stress in brains of patients with progressive multiple sclerosis," *Multiple Sclerosis*, vol. 24, no. 8, pp. 1029–1038, 2018.

[3] V. Pegoretti, K. A. Swanson, J. R. Bethea, L. Probert, U. Eisel, and R. Fischer, "Inflammation and oxidative stress in multiple sclerosis: consequences for therapy development," *Oxidative Medicine and Cellular Longevity*, vol. 2020, Article ID 7191080, 19 pages, 2020.

[4] W. J. Brownlee, T. A. Hardy, F. Fazekas, and D. H. Miller, "Diagnosis of multiple sclerosis: progress and challenges," *Lancet*, vol. 389, no. 10076, pp. 1336–1346, 2017.

[5] Global, regional, and national burden of neurological disorders, 1990-2016, "A systematic analysis for the global burden of disease study," *the Lancet Neurology*, vol. 18, no. 5, pp. 459–480, 2019.

[6] M. Cowan and W. J. Petri, "Microglia: immune regulators of neurodevelopment," *Frontiers in Immunology*, vol. 9, p. 2576, 2018.

[7] D. Bruck, G. K. Wenning, N. Stefanova, and L. Fellner, "Glia and alpha-synuclein in neurodegeneration: a complex interaction," *Neurobiology of Disease*, vol. 85, pp. 262–274, 2016.

[8] L. Liu, Y. Xu, H. Dai, S. Tan, X. Mao, and Z. Chen, "Dynorphin activation of kappa opioid receptor promotes microglial polarization toward M2 phenotype via TLR4/NF-κB pathway," *Cell & Bioscience*, vol. 10, no. 1, p. 42, 2020.

[9] Y. Tang and W. Le, "Differential roles of M1 and M2 microglia in neurodegenerative diseases," *Molecular Neurobiology*, vol. 53, no. 2, pp. 1181–1194, 2016.

[10] T. Guan and J. Kong, "Functional regeneration of the brain: white matter matters," *Neural Regeneration Research*, vol. 10, no. 3, pp. 355-356, 2015.

[11] H. Soreq and Y. Wolf, "NeurimmiRs: microRNAs in the neuroimmune interface," *Trends in Molecular Medicine*, vol. 17, no. 10, pp. 548–555, 2011.

[12] C. A. Juźwik, S. Drake, Y. Zhang et al., "microRNA dysregulation in neurodegenerative diseases: a systematic review," *Progress in Neurobiology*, vol. 182, article 101664, 2019.

[13] K. Gandy, J. Zhang, P. Nagarkatti, and M. Nagarkatti, "Resveratrol (3, 5, 4'-Trihydroxy-trans-Stilbene) attenuates a mouse model of multiple sclerosis by altering the miR-124/sphingosine kinase 1 axis in encephalitogenic T cells in the brain," *Journal of Neuroimmune Pharmacology*, vol. 14, no. 3, article 9842, pp. 462–477, 2019.

[14] M. P. Mycko, M. Cichalewska, H. Cwiklinska, and K. W. Selmaj, "miR-155-3p drives the development of autoimmune demyelination by regulation of heat shock protein 40," *The Journal of Neuroscience*, vol. 35, no. 50, pp. 16504–16515, 2015.

[15] R. M. O'Connell, D. Kahn, W. S. Gibson et al., "MicroRNA-155 promotes autoimmune inflammation by enhancing inflammatory T cell development," *Immunity*, vol. 33, no. 4, pp. 607–619, 2010.

[16] C. Cunha, C. Gomes, A. R. Vaz, and D. Brites, "Exploring new inflammatory biomarkers and pathways during LPS-induced M1 polarization," *Mediators of Inflammation*, vol. 2016, Article ID 6986175, 17 pages, 2016.

[17] K. Essandoh, Y. Li, J. Huo, and G. C. Fan, "MiRNA-mediated macrophage polarization and its potential role in the regulation of inflammatory response," *Shock*, vol. 46, no. 2, pp. 122–131, 2016.

[18] E. D. Ponomarev, T. Veremeyko, N. Bartenova, A. M. Krichevsky, and H. L. Weiner, "MicroRNA-124 promotes microglia quiescence and suppresses EAE by deactivating macrophages via the C/EBP-α-PU.1 pathway," *Nature Medicine*, vol. 17, no. 1, pp. 64–70, 2011.

[19] L. L. Dickey, T. M. Hanley, T. B. Huffaker, A. G. Ramstead, R. M. O'Connell, and T. E. Lane, "MicroRNA 155 and viral-induced neuroinflammation," *Journal of Neuroimmunology*, vol. 308, pp. 17–24, 2017.

[20] K. A. Jablonski, A. D. Gaudet, S. A. Amici, P. G. Popovich, and M. Guerau-de-Arellano, "Control of the inflammatory macrophage transcriptional signature by miR-155," *PLoS One*, vol. 11, no. 7, article e159724, 2016.

[21] A. Peng, Y. Gao, X. Zhuang et al., "Bazhu decoction, a traditional Chinese medical formula, ameliorates cognitive deficits in the 5xFAD mouse model of Alzheimer's disease," *Frontiers in Pharmacology*, vol. 10, p. 1391, 2019.

[22] H. Pei, L. Ma, Y. Cao et al., "Traditional Chinese medicine for Alzheimer's disease and other cognitive impairment: a review," *The American Journal of Chinese Medicine*, vol. 48, no. 3, pp. 487–511, 2020.

[23] J. Zhu, L. Shen, X. Lin, Y. Hong, and Y. Feng, "Clinical research on traditional Chinese medicine compounds and their preparations for amyotrophic lateral sclerosis," *Biomedicine & Pharmacotherapy*, vol. 96, pp. 854–864, 2017.

[24] X. Zhao, X. Tang, Q. Yan et al., "Triptolide ameliorates lupus via the induction of miR-125a-5p mediating Treg upregulation," *International Immunopharmacology*, vol. 71, pp. 14–21, 2019.

[25] X. Liu, J. Ju, Q. Liu, Z. Zhu, and C. Liu, "The Chinese medicine, Shezhi Huangling decoction, inhibits the growth and metastasis of glioma cells via the regulation of miR-1298-5p/TGIF1 axis," *Cancer Management and Research*, vol. 12, pp. 5677–5687, 2020.

[26] J. Yang, X. Zhu, H. Hu, and X. Lin, "The inhibitory effect of Gualou Guizhi decoction on post-ischemic neuroinflammation via miR-155 in MCAO rats," *Annals of Palliative Medicine*, vol. 10, pp. 1370–1379, 2021.

[27] L. Mei, M. He, C. Zhang et al., "Paeonol attenuates inflammation by targeting HMGB1 through upregulating miR-339-5p," *Scientific Reports*, vol. 9, no. 1, article 19370, 2019.

[28] Q. Zheng, T. Yang, L. Fang et al., "Effects of Bu Shen Yi Sui Capsule on Th17/Treg cytokines in C57BL/6 mice with

experimental autoimmune encephalomyelitis," *BMC Complementary and Alternative Medicine*, vol. 15, no. 1, 2015.

[29] P. Y. Zhao, Y. Q. Wang, X. H. Liu et al., "Bu Shen Yi Sui capsule promotes remyelination correlating with Sema3A/NRP-1, LIF/LIFR and Nkx6.2 in mice with experimental autoimmune encephalomyelitis," *Journal of Ethnopharmacology*, vol. 217, pp. 36–48, 2018.

[30] P. Y. Zhao, J. Ji, X. H. Liu et al., "Bu-Shen-Yi-Sui capsule, an herbal medicine formula, promotes remyelination by modulating the molecular signals via exosomes in mice with experimental autoimmune encephalomyelitis," *Oxidative medicine and cellular longevity*, vol. 2020, Article ID 7895293, 19 pages, 2020.

[31] L. Fang, Q. Zheng, T. Yang et al., "Bushen Yisui Capsule ameliorates axonal injury in experimental autoimmune encephalomyelitis," *Neural Regeneration Research*, vol. 8, no. 35, pp. 3306–3315, 2013.

[32] Q. Zheng, L. Liu, H. Liu et al., "The Bu Shen Yi Sui formula promotes axonal regeneration via regulating the neurotrophic factor BDNF/TrkB and the downstream PI3K/Akt signaling pathway," *Frontiers in Pharmacology*, vol. 10, p. 796, 2019.

[33] H. Kataoka, K. Sugahara, K. Shimano et al., "FTY720, sphingosine 1-phosphate receptor modulator, ameliorates experimental autoimmune encephalomyelitis by inhibition of T cell infiltration," *Cellular & Molecular Immunology*, vol. 2, no. 6, pp. 439–448, 2005.

[34] J. Zhang, Z. G. Zhang, Y. Li et al., "Fingolimod treatment promotes proliferation and differentiation of oligodendrocyte progenitor cells in mice with experimental autoimmune encephalomyelitis," *Neurobiology of Disease*, vol. 76, pp. 57–66, 2015.

[35] T. Yang, Q. Zheng, H. Zhao et al., "Effect of Bushen Yisui Capsule () on oligodendrocyte lineage genes 1 and 2 in mice with experimental autoimmune encephalomyelitis," *Chinese Journal of Integrative Medicine*, vol. 22, no. 12, pp. 932–940, 2016.

[36] F. Giuliani, L. M. Metz, T. Wilson, Y. Fan, A. Bar-Or, and V. Wee Yong, "Additive effect of the combination of glatiramer acetate and minocycline in a model of MS," *Journal of Neuroimmunology*, vol. 158, no. 1-2, pp. 213–221, 2005.

[37] A. Weaver, A. G. da Silva, R. K. Nuttall et al., "An elevated matrix metalloproteinase (MMP) in an animal model of multiple sclerosis is protective by affecting Th1/Th2 polarization," *The FASEB Journal*, vol. 19, no. 12, pp. 1668–1670, 2005.

[38] F. Zhang, J. Yang, H. Jiang, and S. Han, "An $\alpha v \beta 3$ integrin-binding peptide ameliorates symptoms of chronic progressive experimental autoimmune encephalomyelitis by alleviating neuroinflammatory responses in mice," *Journal of Neuroimmune Pharmacology*, vol. 9, no. 3, pp. 399–412, 2014.

[39] G. X. Zhang, B. Gran, S. Yu et al., "Induction of experimental autoimmune encephalomyelitis in IL-12 receptor-beta 2-deficient mice: IL-12 responsiveness is not required in the pathogenesis of inflammatory demyelination in the central nervous system," *Journal of Immunology*, vol. 170, no. 4, pp. 2153–2160, 2003.

[40] R. Y. Kim, D. Mangu, A. S. Hoffman et al., "Oestrogen receptor β ligand acts on CD11c$^+$ cells to mediate protection in experimental autoimmune encephalomyelitis," *Brain*, vol. 141, no. 1, pp. 132–147, 2018.

[41] M. Kitada and D. H. Rowitch, "Transcription factor co-expression patterns indicate heterogeneity of oligodendroglial subpopulations in adult spinal cord," *Glia*, vol. 54, no. 1, pp. 35–46, 2006.

[42] D. L. Sherman and P. J. Brophy, "Mechanisms of axon ensheathment and myelin growth," *Nature Reviews. Neuroscience*, vol. 6, no. 9, pp. 683–690, 2005.

[43] J. J. Li, B. Wang, M. C. Kodali et al., "In vivo evidence for the contribution of peripheral circulating inflammatory exosomes to neuroinflammation," *Journal of Neuroinflammation*, vol. 15, no. 1, p. 8, 2018.

[44] S. Ebrahimkhani, F. Vafaee, P. E. Young et al., "Exosomal microRNA signatures in multiple sclerosis reflect disease status," *Scientific Reports*, vol. 7, no. 1, article 14301, 2017.

[45] M. P. Mycko and S. E. Baranzini, "microRNA and exosome profiling in multiple sclerosis," *Multiple Sclerosis*, vol. 26, no. 5, pp. 599–604, 2020.

[46] S. Hisahara, H. Okano, and M. Miura, "Caspase-mediated oligodendrocyte cell death in the pathogenesis of autoimmune demyelination," *Neuroscience Research*, vol. 46, no. 4, pp. 387–397, 2003.

[47] D. M. Harrison, "In the clinic. Multiple sclerosis," *Annals of Internal Medicine*, vol. 160, no. 7, pp. ITC4–ITC1, 2014.

[48] M. Filippi, A. Bar-Or, F. Piehl et al., "Multiple sclerosis," *Nature Reviews. Disease Primers*, vol. 4, no. 1, p. 43, 2018.

[49] A. F. Lloyd and V. E. Miron, "The pro-remyelination properties of microglia in the central nervous system," *Nature Reviews. Neurology*, vol. 15, no. 8, pp. 447–458, 2019.

[50] L. Cao and C. He, "Polarization of macrophages and microglia in inflammatory demyelination," *Neuroscience Bulletin*, vol. 29, no. 2, pp. 189–198, 2013.

[51] V. E. Miron and R. J. Franklin, "Macrophages and CNS remyelination," *Journal of Neurochemistry*, vol. 130, no. 2, pp. 165–171, 2014.

[52] V. E. Miron, A. Boyd, J. W. Zhao et al., "M2 microglia and macrophages drive oligodendrocyte differentiation during CNS remyelination," *Nature Neuroscience*, vol. 16, no. 9, pp. 1211–1218, 2013.

[53] V. Chhor, T. Le Charpentier, S. Lebon et al., "Characterization of phenotype markers and neuronotoxic potential of polarised primary microglia *in vitro*," *Brain, Behavior, and Immunity*, vol. 32, pp. 70–85, 2013.

[54] R. Franco and D. Fernandez-Suarez, "Alternatively activated microglia and macrophages in the central nervous system," *Progress in Neurobiology*, vol. 131, pp. 65–86, 2015.

[55] L. Du, Y. Zhang, Y. Chen, J. Zhu, Y. Yang, and H. L. Zhang, "Role of microglia in neurological disorders and their potentials as a therapeutic target," *Molecular Neurobiology*, vol. 54, no. 10, pp. 7567–7584, 2017.

[56] R. Schickel, B. Boyerinas, S. M. Park, and M. E. Peter, "MicroRNAs: key players in the immune system, differentiation, tumorigenesis and cell death," *Oncogene*, vol. 27, no. 45, pp. 5959–5974, 2008.

[57] C. E. McCoy, "miR-155 dysregulation and therapeutic intervention in multiple sclerosis," *Advances in Experimental Medicine and Biology*, vol. 1024, pp. 111–131, 2017.

[58] J. Guedes, A. L. Cardoso, and M. C. Pedroso de Lima, "Involvement of microRNA in microglia-mediated immune response," *Clinical & Developmental Immunology*, vol. 2013, article 186872, pp. 1–11, 2013.

[59] J. A. Slota and S. A. Booth, "MicroRNAs in neuroinflammation: implications in disease pathogenesis, biomarker discovery and therapeutic applications," *Noncoding RNA*, vol. 5, no. 2, p. 35, 2019.

[60] T. Veremeyko, A. Yung, M. Dukhinova et al., "Cyclic AMP pathway suppress autoimmune neuroinflammation by inhibiting functions of encephalitogenic CD4 T cells and enhancing M2 macrophage polarization at the site of inflammation," *Frontiers in Immunology*, vol. 9, p. 50, 2018.

[61] A. Yu, T. Zhang, H. Duan et al., "MiR-124 contributes to M2 polarization of microglia and confers brain inflammatory protection via the C/EBP-α pathway in intracerebral hemorrhage," *Immunology Letters*, vol. 182, pp. 1–11, 2017.

[62] C. Jiao, F. Gao, L. Ou et al., "Tetrahydroxystilbene glycoside antagonizes β-amyloid-induced inflammatory injury in microglia cells by regulating PU.1 expression," *Neuroreport*, vol. 29, no. 10, pp. 787–793, 2018.

[63] J. Satoh, N. Asahina, S. Kitano, and Y. Kino, "A comprehensive profile of ChIP-Seq-based PU.1/Spi1 target genes in microglia," *Gene regulation and systems biology*, vol. 8, pp. 127–139, 2014.

[64] X. Liu, Z. Feng, L. Du et al., "The potential role of MicroRNA-124 in cerebral ischemia injury," *International Journal of Molecular Sciences*, vol. 21, no. 1, p. 120, 2019.

[65] R. W. Freilich, M. E. Woodbury, and T. Ikezu, "Integrated expression profiles of mRNA and miRNA in polarized primary murine microglia," *PLoS One*, vol. 8, no. 11, article e79416, 2013.

[66] S. H. Venkatesha, S. Dudics, Y. Song, A. Mahurkar, and K. D. Moudgil, "The miRNA expression profile of experimental autoimmune encephalomyelitis reveals novel potential disease biomarkers," *International Journal of Molecular Sciences*, vol. 19, no. 12, p. 3990, 2018.

[67] C. S. Whyte, E. T. Bishop, D. Ruckerl et al., "Suppressor of cytokine signaling (SOCS)1 is a key determinant of differential macrophage activation and function," *Journal of Leukocyte Biology*, vol. 90, no. 5, pp. 845–854, 2011.

[68] Y. Zhang, Q. Chen, Y. Nai, and C. Cao, "Suppression of miR-155 attenuates neuropathic pain by inducing an M1 to M2 switch in microglia," *Folia Neuropathologica*, vol. 58, no. 1, pp. 70–82, 2020.

[69] R. Kalluri and V. S. LeBleu, "The biology, function, and biomedical applications of exosomes," *Science*, vol. 367, no. 6478, 2020.

[70] H. Valadi, K. Ekstrom, A. Bossios, M. Sjostrand, J. J. Lee, and J. O. Lotvall, "Exosome-mediated transfer of mRNAs and microRNAs is a novel mechanism of genetic exchange between cells," *Nature Cell Biology*, vol. 9, no. 6, pp. 654–659, 2007.

[71] B. Martinez and P. V. Peplow, "MicroRNAs as disease progression biomarkers and therapeutic targets in experimental autoimmune encephalomyelitis model of multiple sclerosis," *Neural Regeneration Research*, vol. 15, no. 10, pp. 1831–1837, 2020.

Research Article

Inhibition of Calcium Oxalate Formation and Antioxidant Activity of Carboxymethylated *Poria cocos* Polysaccharides

Chuang-Ye Li,[1] Li Liu,[1] Yao-Wang Zhao [ID],[1] Jia-Yun Chen,[2] Xin-Yuan Sun,[2] and Jian-Ming Ouyang [ID][2]

[1]*Department of Urology, Hunan Children's Hospital, Changsha 410007, China*
[2]*Institute of Biomineralization and Lithiasis Research, Jinan University, Guangzhou 510632, China*

Correspondence should be addressed to Yao-Wang Zhao; yw508@sina.com and Jian-Ming Ouyang; toyjm@jnu.edu.cn

Three carboxymethylated *Poria cocos* polysaccharides (PCP-C1, PCP-C2, and PCP-C3) with -COOH contents of 6.13%, 10.24%, and 16.22%, respectively, were obtained by carboxymethylation of the original polysaccharide (PCP-C0), which has a molecular weight of 4 kDa and a carboxyl (-COOH) content of 2.54%. The structure of the PCP-Cs was characterized by FT-IR, ^{1}H NMR, and ^{13}C NMR spectra. The four PCP-Cs exhibited antioxidant activity, and their ability to scavenge radicals (hydroxyl and DPPH) and chelate ferrous ions was positively correlated with the degree of carboxymethylation. As the content of -COOH groups in the PCP-Cs increases, their ability to regulate the growth of calcium oxalate (CaOx) crystals was enhanced, thus inhibiting the growth of calcium oxalate monohydrate (COM) crystals and inducing the formation of more calcium oxalate dihydrate (COD) crystals. The formed CaOx crystal was more round and blunt, the absolute value of the Zeta potential on the crystal surface increased, and the aggregation between crystals was inhibited. Thermogravimetric analysis curves showed that the proportions of PCP-C0, PCP-C1, PCP-C2, and PCP-C3 incorporated into the crystal were 20.52%, 15.60%, 10.65%, and 9.78%, respectively, in the presence of 0.4 g/L PCP-Cs. PCP-C protection resisted oxidative damages of human kidney proximal tubular epithelial cells (HK-2) caused by oxalate, resulting in increased cell viability and superoxide dismutase activity and decreased reactive oxygen species levels, malondialdehyde content, and 8-hydroxy-deoxyguanosine expression. Hence, PCP-Cs, especially PCP-C3, can inhibit the formation of CaOx crystals and may have the potential to be an alternative antistone drug.

1. Introduction

Kidney stones are a very common disease and are believed to be the result of the interaction between the genetic and environmental factors. About 80% of kidney stones are calcium oxalate (CaOx) stones, and the two main forms are calcium oxalate monohydrate (COM) and calcium oxalate dihydrate (COD) [1]. COM is more likely to damage renal epithelial cells [2]; the cell damage will promote the nucleation, growth, aggregation, and adhesion of crystals on its surface [3], thereby increasing the formation risk of kidney stones.

Polysaccharides are widely found in plants, animals, and microorganisms. Natural polysaccharides possess antioxidant, antidiabetic, antitumor, and other biological activities. The biological activity of polysaccharides is usually related

to their molecular weight and chain structure, especially the number of active groups [4, 5].

Biomacromolecules (such as polysaccharides) rich in acidic polyanionic groups can be used as effective inhibitors of CaOx calculus formation. Zhang et al. [6] found that 0.5 g/L *Sargassum* polysaccharide can inhibit the growth and aggregation of COM crystals and induce the formation of spherical COD crystals; the inhibition rates of crystal nucleation and aggregation are 69.2% and 76.8%, respectively.

The biological activity of polysaccharides is closely related to the content of acidic groups [7–10]. Xu et al. [9] extracted two polysaccharides from *E. acuminatum*; the neutral polysaccharide EAP-1N has a uronic acid content of 0.32%, and the acid polysaccharide EAP-2A has a uronic acid content of 9.46%. EAP-2A has a stronger ability to scavenge

free radicals, enhance the activity of antioxidant enzymes (including superoxide dismutase (SOD), catalase (CAT), and glutathione peroxidase (GSH-Px)), and inhibit lipid peroxidation. Huang et al. [10] compared the effects of five plant polysaccharides (PPSs) with -COOH contents of 6.3%, 8.9%, 9.1%, 13.6%, and 16.1%, respectively, on the growth of CaOx crystals; the ability of PPSs to inhibit CaOx growth and aggregation and induce COD formation was positively correlated with the percentage of -COOH groups in the polysaccharide.

Chemically modified polysaccharides show stronger biological activity than natural polysaccharides [11–15]. Wang et al. [11] modified *Poria cocos* polysaccharide by carboxymethylation and reported that the polysaccharide with the highest carboxymethylation degree had the highest chelating ability to ferrous ions and the highest scavenging ability to hydroxyl radicals. Wang et al. [13] prepared carboxymethylated polysaccharide (CATP) from *Tremella* polysaccharide (ATP) and found that CATP had significantly higher antioxidant activity and improved water solubility than ATP. Li et al. [15] treated hypercholesterolemic rats with a high dose of *Morchella angusticeps* Peck polysaccharide (PMEP) and its carboxymethylated polysaccharide (CPMEP) and reported that the serum total cholesterol levels of rats were 1.54 and 1.29 mmol/L, respectively; hence, CPMEP has stronger cholesterol-lowering activity and can upregulate the protein expression of CYP7A1 and LDL-R in rat livers, downregulate the expression of HMG-CoA, and improve its cholesterol-lowering ability.

P. cocos polysaccharide (PCP) is one of the main components of *P. cocos* [16] and can be used to treat chronic gastritis, nephropathy, dizziness, and vomiting [17]. PCP is mainly composed of four monosaccharides, namely, D-glucose, D-mannose, D-fucose, and D-xylose [18, 19]. Wang et al. [20] found that PCP extracted by an ultrasonic wave has the ability to reduce power and scavenge hydroxyl and DPPH radicals. Wu et al. [21] showed that PCP can inhibit acetaminophen-induced liver injury in mice and reduce the levels of the serological liver enzyme (ALT), lactate dehydrogenase (LD), and inflammatory cytokines (TNF-α, IL-6).

In this study, three carboxymethylated polysaccharides (PCP-C1, PCP-C2, and PCP-C3) with -COOH contents of 6.13%, 10.24%, and 16.22%, respectively, were obtained by carboxymethylation of *Poria* polysaccharide (PCP-C0) with initial -COOH content of 2.54%. Inhibitory effects on the formation of calcium oxalate crystals were studied in vitro to obtain potential anticalculus polysaccharide drugs.

2. Experimental Methods

2.1. Materials and Apparatus

2.1.1. Materials. *Poria cocos* polysaccharide (PCP-C0) was produced by Shaanxi Ciyuan Biological Company, with polysaccharide content ≥ 95%; the protein present in polysaccharide was removed by the Sevag method; after treating the polysaccharide with the chloroform-n-butanol mixed solution, the free protein is denatured into insoluble substances and the purpose of separation is achieved [22]. Phosphate-buffered solution (PBS), phenazine, 1,1-diphenyl-2-picrylhydrazyl (DPPH), phenanthroline, and other conventional reagents were of analytical grade and were purchased from Guangzhou Chemical Reagent Company (Guangzhou, China). The Cell Counting Kit-8 (CCK-8) was purchased from Dojindo Laboratory (Kumamoto, Japan). $2',7'$-Dichlorodihydrofluorescein diacetate (DCFH-DA) was purchased from Shanghai Beyotime Bio-Tech Co., Ltd. (Shanghai, China). The malonaldehyde (MDA) kit and superoxide dismutase (SOD) kit were purchased from Jiancheng Institute of Biotechnology (Nanjing, China). The Human 8-hydroxy-deoxyguanosine (8-OHdG) ELISA Kit was purchased by Boshen Biotechnology (Nanjing, China). The experimental water is double-distilled water.

2.1.2. Apparatus. The apparatus used in the study included the following: Fourier transform infrared spectrometer (FT-IR, Nicolet, USA); nuclear magnetic resonance (Varian Bruker-500 MHz, Bruker, Germany); ultrasonic apparatus (aligned with JP-100S); Ubbelohde capillary viscometer (0.4–0.5, Qihang Glass Instrument Factory, Shanghai, China); thermogravimetric analyzer (TGA/DSC 3+, Mettler Toledo, USA); D/max 2400-X-ray powder diffractometer (Rigaku, Japan); field emission scanning electron microscope (ULTRA55, Zeiss, Germany); OPTIMA-2000DV inductively coupled plasma (ICP) (ICP-AES, Optima 2000DV, PerkinElmer, CT, USA); Zetasizer 300HS nanoparticle size-Zeta potential analyzer (Malvern, UK); and Enzyme Mark Instrument (Safire^2, Tecan, Switzerland).

2.2. Carboxymethylation and Characterization of Poria cocos Polysaccharides (PCP-C0)

2.2.1. Carboxymethylation of PCP-C0 [23–25]. 300 mg PCP-C0 was suspended in 15 mL of isopropanol, stirred at room temperature for 15 min, slowly added 10 mL of 30% NaOH solution, stirred at 50°C water bath for 1 h, then added 2.63 g of monochloroacetic acid, and then heated at 60°C for 2 h. After cooling to room temperature, adjust to neutrality with 0.5 mol/L HCl, dialyze with distilled water (Mw retention 3000 Da) for 3 days, and concentrate and freeze-dry to obtain carboxymethylated polysaccharides (PCP-Cs) with different degrees of substitution.

2.2.2. Determination of -COOH Content in PCP-Cs [26]. -COOH content of PCP-Cs was determined by the method of conductometric titration. The conductivity titration curve was plotted using the conductivity value as the Y-axis and the used NaOH volume as the X-axis. From the conductivity titration curve, the volume of NaOH consumed by polysaccharide-COOH is obtained, and the percentage of -COOH is calculated. Each experiment was repeated three times.

2.2.3. FT-IR Characterization of PCP-Cs. FT-IR spectra of polysaccharides were determined using films prepared by

2.0 mg of the dry PCP-C sample and 200 mg KBr in the wavenumber range of 4000-400 cm^{-1}.

2.2.4. ^{1}H and ^{13}C NMR Characterization of PCP-Cs.

Approximately 20 mg of the dry PCP-C sample was dissolved in 0.5 mL of deuterated water (D$_2$O) in an NMR tube. After being completely dissolved, the polysaccharide sample is put into a magnetic field of a nuclear magnetic resonance spectrometer for detection.

2.3. Antioxidant Activity Detection of PCP-Cs

2.3.1. Hydroxyl Radical (˙OH) Scavenging Capacity.

The ˙OH scavenging ability of polysaccharides in vitro was detected by the H$_2$O$_2$/Fe system method [27]. Add 1 mL 2.5 mmol/L FeSO$_4$ solution and 1 mL 2.5 mmol/L phenanthroline solution to the test tube, then add PBS (20 mmol/L, 1 mL, pH = 7.4) and 1 mL 20 mmol/L H$_2$O$_2$ in sequence, and finally take 1 mL of different concentrations of polysaccharide samples (0.15, 0.5, 0.8, 1.0, 2.0, and 3.0 g/L) into test tubes. After mixing well, incubate at 37°C for 90 min and use a UV spectrophotometer to measure the absorbance at 536 nm; the average absorbance is A_3. Each experiment was repeated three times. The absorbance when hydrogen peroxide (H$_2$O$_2$) and polysaccharide solution were replaced with distilled water was A_2. The absorbance when polysaccharide solution was replaced with distilled water was A_1. The ascorbic acid (VC) was used as the positive control group. The ability to scavenge hydroxyl radicals was calculated using the following equation:

$$\text{Scavenging effect (\%)} = \frac{(A_3 - A_1)}{(A_2 - A_1)} \times 100\%. \quad (1)$$

2.3.2. DPPH Radical Scavenging Capacity [28, 29].

0.4 mmol/L DPPH was prepared by anhydrous ethanol, and 3 mL PCP-C (0.15-3 g/L) polysaccharide was mixed with DPPH (0.4 mmol/L, 1 mL). The mixture was incubated in the dark at 25°C for 30 min. The absorbance is detected at 517 nm to reflect the DPPH radical scavenging ability of polysaccharides. Each experiment was repeated three times.

$$\text{Scavenging effect (\%)} = \left[1 - \frac{(A_2 - A_1)}{A_0}\right] \times 100\%. \quad (2)$$

where A_2 was the absorbance of 3 mL sample solution+1 mL DPPH reagent, A_1 was the absorbance of 3 mL sample solution+1 mL anhydrous ethanol, and A_0 was the absorbance of 1 mL DPPH solution+3 mL water.

2.3.3. Ferrous Ion Chelating Capacity [30].

1 mL of PCP-Cs (0.15-3.0 g/L) was mixed with 2.25 mL distilled water and 0.05 mL 2.0 mmol/L ferrous chloride solution, respectively, and the reaction lasts for 30 s. Next, the solutions were mixed with 0.2 mL 5.0 mmol/L phenazine and reacted at room temperature for 10 min, and the absorbance of the mixture was measured at 562 nm. The experiment used water instead of polysaccharide solution and ferrous chloride solution as the blank group and control group.

EDTA-2Na was used as the positive control group. Lower absorbance indicated a stronger chelating capacity for ferrous ions. Each experiment was repeated three times.

$$\text{Polysaccharide chelating ability (\%)} = \frac{[A_0 - (A_1 - A_2)]}{A_0} \times 100. \quad (3)$$

where A_0 is the absorbance of the blank group, A_1 is the absorbance of the sample group, and A_2 is the absorbance of the control group.

2.4. Regulation of CaOx Crystal Growth by PCP-Cs [31]

2.4.1. CaOx Crystal Synthesis.

CaOx metastable solution was carried out in a 50 mL volumetric flask by adding 3.0 mL of 10 mmol/L CaCl$_2$ and 1 mL of 0.50 mol/L NaCl; then, add a certain amount of PCP-C solution to make the final concentrations of polysaccharide: 0.05, 0.1, 0.2, 0.4, and 0.8 g/L, add distilled water to about 45 mL, then add 3.0 mL of 10 mmol/L Na$_2$Ox, and finally dilute volume to scale with distilled water. The solution thus obtained is $c(\text{Ca}^{2+}) = c(\text{Ox}^{2-}) = 0.60$ mmol/L and $c(\text{NaCl}) = 10$ mmol/L. The crystal was filtered by a 0.22 μm microporous membrane. The above CaOx solution was poured into a 50 mL beaker for crystallization, and a clean glass slide was placed at the bottom of the beaker. In order to prevent supersaturation of the system due to volatilization of solvent water from driving crystal formation, crystal growth was carried out at static conditions. After the crystal grows for 3 d, the substrate was taken out and dried in a dryer. The concentration of soluble Ca^{2+} ions in the supernatant was measured through inductively coupled plasma (ICP) emission spectrometry.

The above synthesized CaOx crystals were characterized by Fourier infrared (FT-IR), field emission scanning electron microscope (SEM), X-ray diffraction (XRD), and Zeta potentiometer.

2.4.2. Characterization of SEM.

The samples were treated with gold spray and observed under a field emission scanning electron microscope for morphology analysis.

2.4.3. Characterization of FT-IR.

The dried CaOx sample (2.0 mg) was mixed with KBr (200 mg), followed by grinding with agate mortar, tableting, and scanning with an infrared spectrometer in the wavenumber range of 4000-400 cm^{-1}.

2.4.4. Characterization of XRD.

The synthesized crystals were analyzed in an X-ray diffractometer under the test conditions of CuKα ray, graphite monochromator, 30 kV, 25 mA, scanning range of 5-60°, scanning speed of 8°/min, and step width of 0.02°/s for qualitative and quantitative analyses.

The relative percentage contents of COM and COD in the CaOx precipitates were calculated through the K value method [31] and the relative percentage contents of COD:

$$\text{COD\%} = \frac{I_{\text{COD}}}{I_{\text{COD}} + I_{\text{COM}}}, \quad (4)$$

where I_{COM} and I_{COD} are the intensities of the spacing ($\bar{1}$01) of COM and (200) of COD crystals.

2.4.5. Zeta Potential Determination of the Crystal Surface. CaOx crystals (1 mg) were dispersed in 3.0 mL of double-distilled water. After ultrasonication for 10 min, the Zeta potential was detected with a Zetasizer Nano ZS90 apparatus at 25°C.

2.4.6. TGA for Determinating Polysaccharide Content in Crystals. According to Reference [26], the thermogravimetric analysis curves of CaOx crystals formed in the presence or absence of polysaccharides were measured by a Mettler Toledo thermal analyzer under a nitrogen atmosphere from 25°C to 900°C at a heating rate of 10°C/min. The polysaccharide content in the crystals was calculated from the thermal curves.

2.5. Cell Experiments

2.5.1. Cell Culture and Cytotoxicity Detection of PCP-Cs. HK-2 cells were cultured in DMEM-F12 containing 10% fetal bovine serum [32]. Cell suspension (density: 1×10^5 cells/mL) was inoculated into 96-well plates to make cells assemble into a monolayer; then, PCP-C0, PCP-C1, PCP-C2, and PCP-C3 with final concentrations of 20, 40, 60, 80, and 100 μg/mL were added to cells, respectively. After 24 h culture, the cell viability was measured by CCK-8. Absorbance (A) was measured at 450 nm by an enzyme reader according to the kit measurement method, and the cell viability rate was calculated. Each experiment was repeated in five parallel wells.

2.5.2. Cell Viability Detection [32]. After cells were confluent into the monolayer, the experiment was divided into 3 groups: (1) normal control group: only the serum-free culture medium was added; (2) damaged group: 2.8 mM of sodium oxalate was added, and cells were damaged for 3.5 h; and (3) protection group: PCP-C0, PCP-C1, PCP-C2, and PCP-C3 with final concentrations of 20, 40, 60, 80, and 100 μg/mL were added to preprotect cells for 12 h, followed by 2.8 mM oxalate injury for 3.5 h. After incubating the above groups for 12 h, add 10 μL of the CCK-8 reagent to each well and incubate at 37°C for 1.5 h. Absorbance (A) was measured by using the enzyme mark instrument at 450 nm. Each experiment was repeated in five parallel wells. Cell viability was determined using the equation below.

2.5.3. Reactive Oxygen Species (ROS) Level Detection [32]. Cells were inoculated into 12-well culture plates at concentrations of 1.0×10^5 cells/mL and 1 mL/well. The experimental model and grouping were the same as the CCK-8 experiment, and 100 μg/mL of PCP-Cs was used to protect the cells. The cells were stained with $2',7'$-dichlorodihydrofluorescein diacetate (DCFH-DA) at 37°C for 30 min. The cells were washed with PBS three times to remove DCFH-DA that did not enter the cells. The fluorescence intensity was observed under a fluorescence microscope and also detected by a microplate reader. Each experiment was repeated in three parallel wells.

2.5.4. Superoxide Dismutase (SOD) Activity Detection. SOD activity was assessed using a commercially available kit based on the autooxidation of hydroxylamine. The experimental model and grouping were the same as the CCK-8 experiment, and 100 μg/mL of PCP-Cs was used to protect the cells. At the indicated time points, the treated cells were homogenized in 100 mmol/L Tris-HCl buffer and centrifuged at 10,000 rpm for 20 min, and then the SOD activity was determined using assay kits. The absorbance of the supernatant was then measured directly by a microplate reader at 560 nm with a reference wavelength of 600 nm.

2.5.5. Malondialdehyde (MDA) Detection. For lipid peroxidation assay, we used a commercial kit to quantify the generation of MDA according to the manufacturer's protocol. The experimental model and grouping were the same as the CCK-8 experiment, and 100 μg/mL of PCP-Cs was used to protect the cells. The cells were harvested by trypsinization, and cellular extracts were prepared by sonication in ice-cold buffer (50 mM Tris-HCl, pH = 7.5, 5 mM EDTA, and 1 mM DTT). After sonication, lysed cells were centrifuged at 10,000 rpm for 20 min to remove debris. The supernatant was subjected to the measurement of MDA levels by detecting the absorbance at 532 nm.

2.5.6. 8-Hydroxy-Deoxyguanosine (8-OHdG) Detection. 8-OHdG is a commonly used marker of oxidative DNA damage. The experimental model and grouping were the same as the CCK-8 experiment, and 100 μg/mL of PCP-Cs was used to protect the cells. The concentration of 8-OHdG was measured using a commercial ELISA kit according to the manufacturer's instructions. The color change is measured spectrophotometrically at a wavelength of 450 nm.

2.6. Statistical Analysis. The normal distribution of experimental results was analyzed by the Shapiro–Wilk test. Data were assessed using a one-way ANOVA test, followed by Tukey's multiple comparison test for those following normal distribution. Experimental data were expressed by mean ± standard deviation($\bar{x} \pm$ SD). The data were presented as individual values and assessed using the Kruskal–Wallis test, followed by Dunn's multiple comparison test when following a nonnormal distribution. If $P < 0.05$, there was a significant difference; if $P < 0.01$, the difference was extremely significant; if $P > 0.05$, there was no significant difference.

3. Results

3.1. Carboxymethylation and Characterization of P. cocos Polysaccharide (PCP-C0)

3.1.1. Polysaccharide Carboxymethylation. The carboxymethylation reaction belongs to bimolecular nucleophilic substitution (SN2) reactions [33]. First, the hydroxyl group of PCP-C0 was reacted with NaOH to form an alkoxide, and the carboxymethyl group was reacted with the alkoxide to form a carboxymethylated polysaccharide (PCP-C) (Figure 1).
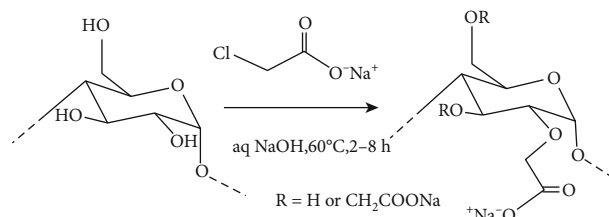
Figure 1: Carboxymethylation reaction of *Poria cocos* polysaccharide.

3.1.2. Detection of -COOH Content in PCP-Cs.

The -COOH content in each carboxymethylated polysaccharide (PCP-C) was determined by conductometric titration. The titration curves are shown in Figure 2(a). The -COOH contents of PCP-C0, PCP-C1, PCP-C2, and PCP-C3 were 2.54%, 6.13%, 10.24%, and 16.22%, respectively. After carboxymethylation modification, the molecular weight of the polysaccharide increased, but no obvious change in the molecular weight of the polysaccharide was detected [34].

3.1.3. FT-IR Characterization of PCP-Cs.

Figure 2(b) shows the FT-IR spectra of PCP-Cs with different degrees of carboxymethylation. The strong absorption band at $3428.1 \, cm^{-1}$ corresponds to the absorption peak of the stretching vibration of –OH in the polysaccharides. The absorption band at $2930.2 \, cm^{-1}$ corresponds to the stretching vibration of C-H. The peak at $1600 \, cm^{-1}$ corresponds to the stretching vibration of C-H-O and C-O bonds. The peak at $1428.6 \, cm^{-1}$ is the stretching vibration of the carboxyl group. Absorptions in the region of $1500\text{-}1000 \, cm^{-1}$ are attributed to epoxy vibration, (COH) side group stretching vibration, and C-O-C glycosidic bond vibration [35]. The peak at $1032.4 \, cm^{-1}$ corresponds to the stretching vibration of the pyranose ring of glucose residues [19].

After carboxymethylation of PCP-C0, a new absorption peak appeared at $1326.5 \, cm^{-1}$, which belongs to the absorption peak of carboxymethyl ($\text{-CH}_2\text{COOH}$). According to the carboxymethylation reaction (Figure 1), the substitution of $\text{-CH}_2\text{COOH}$ occurred on the -OH group of polysaccharides and manifested as a new absorption peak near $1326.5 \, cm^{-1}$, thereby confirming the successful carboxymethylation [36].

3.1.4. ^1H NMR Characterization of PCP-Cs.

In the ^1H NMR spectrum of PCP-C0 (Figure 2(c)), $\delta 5.14, 3.98, 3.67, 3.58, 3.81,$ and $3.66 \, ppm$ belong to the signal peaks of H-1 to H-6 of α-D-Gal; $\delta 4.95, 3.59, 3.98, 3.89, 4.08,$ and $1.14 \, ppm$ belong to the signal peaks of H-1 to H-6 of α-(1-6)-L-Fuc (Table 1); $\delta 4.95, 3.88, 3.75, 3.89, 4.08,$ and $1.14 \, ppm$ belong to the signal peaks of H-1 to H-6 of α-(1-3)-L-Fuc; $\delta 4.71 \, ppm$ corresponds to the signal peak of H-1 of β-(1-3)-D-Glc; and $\delta 4.59 \, ppm$ corresponds to the signal peak of H-1 of β-(1-3)-D-Gal [37, 38]. Compared with that of PCP-C0, the ^1H NMR of the carboxymethylated polysaccharide PCP-C1 showed no new strong signal peaks (Figure 2(d)).

3.1.5. ^{13}C NMR Characterization of PCP-Cs.

In the ^{13}C NMR spectrum of PCP-C0 (Figure 2(e)), the strong signals at $\delta 102.53, 74.12, 95.89, 69.58, 75.74,$ and $60.75 \, ppm$ belong to the C-1 to C-6 signal peaks of β-(1-3)-D-Glc (Table 2); $\delta 103.7, 73.5, 86.9, 69.1, 77.0,$ and $61.6 \, ppm$ belong to the C-1 to C-6 signal peaks of β-(1-3)-D-Gal; $\delta 73.6, 67.0, 70.5,$ and $61.3 \, ppm$ belong to the C-3 to C-6 signal peaks of α-D-Gal; $\delta 98.2, 67.7, 70.5, 71.6, 67.3,$ and $15.8 \, ppm$ belong to the C-1 to C-6 signal peaks of α-(1-6)-L-Fuc; and $\delta 98.2, 67.0, 69.7, 71.6, 67.3,$ and $15.8 \, ppm$ belong to the C-1 to C-6 signal peaks of α-(1-3)-L-Fuc [19, 37].

The main signals in the ^{13}C NMR spectrum of PCP-C1 were 102.8 (C-1), 79.2 (C-3), 74.8 (C-5), 73.1 (C-2), 69.6 (C-4), 60.9 (C-6), and $177.8 \, ppm$ (C-7) (Figure 2(f)). The signals at 71.2 and $73.1 \, ppm$ are assigned to the methylene carbon atom by the carboxymethyl substituent. The signal increased at $70.6 \, ppm$ and decreased at $60.7 \, ppm$, indicating the occurrence of carboxymethyl substitution at the C-6 position [36, 37]. For the ^{13}C NMR of the carboxymethylated polysaccharide PCP-C1, a new signal peak appeared at $177.8 \, ppm$, which belongs to the C=O bond of the carboxymethyl group ($\text{-CH}_2\text{COOH}$); this finding can be used as evidence of the carboxymethylation reaction, consistent with previous reports [23, 36].

3.2. Antioxidant Capacity of PCP-Cs

3.2.1. Scavenging Capacity of ˙OH Radicals.

˙OH radicals can cause tissue damage and cell death and lead to many diseases [39]. Therefore, scavenging OH radicals is one of the important characteristics of the antioxidant defense mechanism. As shown in Figure 3(a), as the concentration of PCP-Cs increased, the ability to remove ˙OH increased. At the same concentration, the higher the carboxymethylation degree is, the stronger the polysaccharide will be.

3.2.2. DPPH Radical Scavenging Capacity.

The DPPH radical has a characteristic absorption peak at 517 nm. When DPPH is reduced to the nonfree radical form DPPH-H by an antioxidant, the purple color of the DPPH radical fades, resulting in a decrease in absorbance [40]. The DPPH radical scavenging ability of PCP-Cs also has a concentration-dependent effect (Figure 3(b)), and PCP-C3 with the highest degree of carboxymethylation has the strongest scavenging ability.

3.2.3. Chelating Effect on Ferrous Ions.

Transition metal ions, such as Fe^{2+} and Cu^{2+}, can catalyze the chain reaction and generate free radicals, leading to cell oxidative damage [30]. Chelating off metal ions can interrupt chain reaction and prevent oxidative damage. Given that Fe^{2+} has high activity, the ability to chelate this ion is often used to evaluate the antioxidant ability of polysaccharides. As shown in Figure 3(c), when the concentration is 3 g/L, the chelating ability levels of PCP-C0, PCP-C1, PCP-C2, and PCP-C3 to Fe^{2+} are 46.9%, 51.5%, 61.9%, and 63.7%, respectively, and PCP-C3 has the strongest chelating ability.

The three experimental results mentioned above indicate that the carboxymethylation modification of the original PCP-C0 enhances the antioxidant capacity of the polysaccharide.

(a)

(b)

(c)

(d)

(e)

(f)
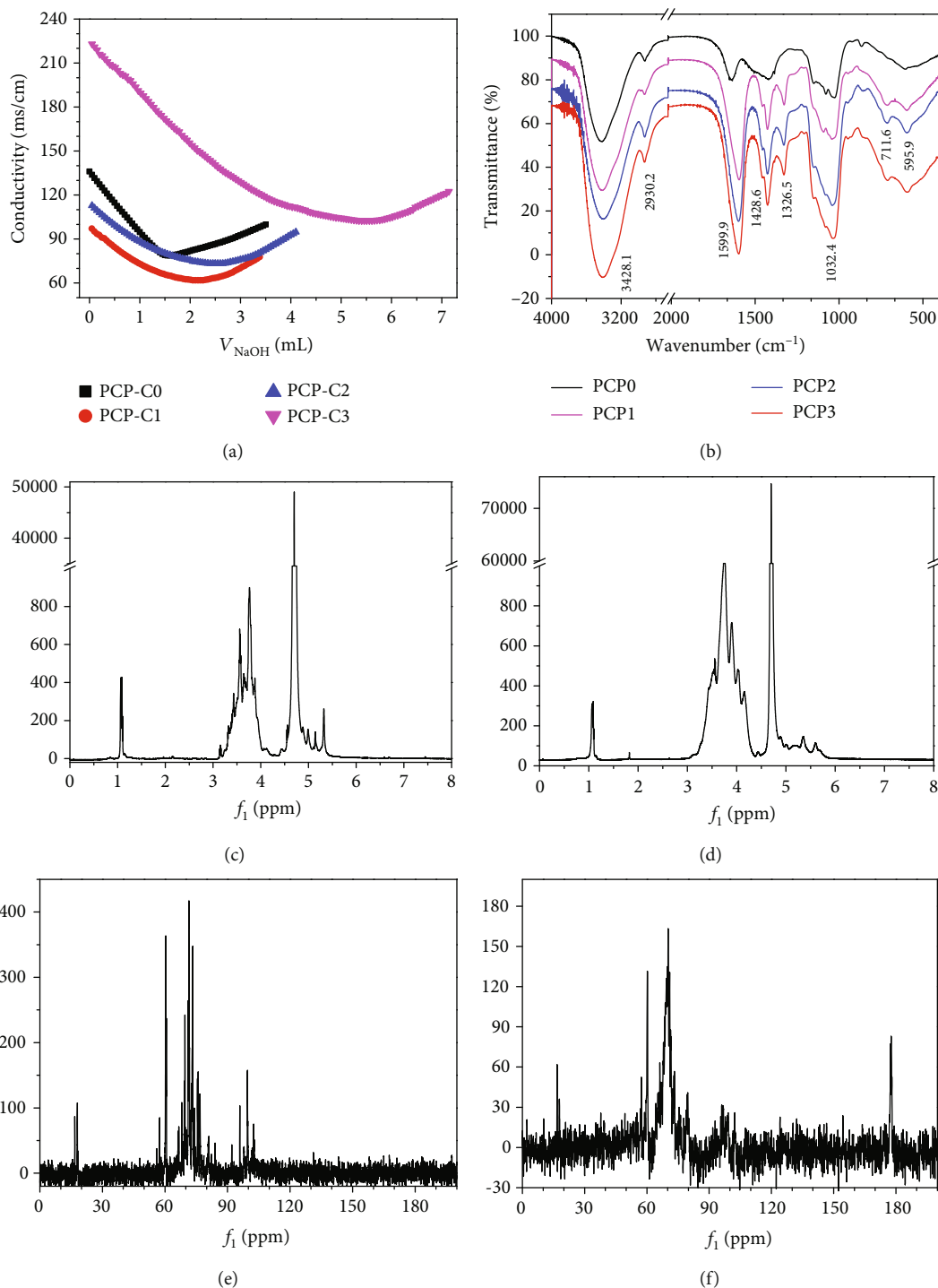
Figure 2: Characterization of PCP-Cs. (a) Titration curves for detecting -COOH content in four polysaccharides, c(PCP-Cs) = 0.10 g/L and c(NaOH) = 5.24 mmol/L. (b) FT-IR spectra of four polysaccharides. (c, d) ^{1}H NMR spectra of PCP-C0 and PCP-C1. (e, f) ^{13}C NMR spectra of PCP-C0 and PCP-C1.

3.3. Characterization of the CaOx Crystal Structure Induced by PCP-Cs

3.3.1. XRD Characterization. The effects of four kinds of PCP-Cs with different -COOH contents on the formation

of CaOx crystals were studied. Figure 4(a) shows the XRD patterns of CaOx crystals formed in the presence of 0.4 g/L PCP-Cs. The diffraction peaks at crystal plane spacing $d = 0.593, 0.364, 0.296$, and 0.235 nm belong to the $(\bar{1}01)$, (020), $(\bar{2}02)$, and (130) crystal planes of calcium oxalate

TABLE 1: Chemical shifts corresponding to the ^{1}H NMR spectrum of carboxymethylated polysaccharide PCP-C0.

Polysaccharide type	Sugar residue	^{1}H chemical shift (ppm)					
		H-1	H-2	H-3	H-4	H-5	H-6
PCP-C0	β-(1-3)-D-Glc	4.71	—	—	—	—	—
	β-(1-3)-D-Gal	4.59	—	—	—	—	—
	α-D-Gal	5.14	3.98	3.67	3.58	3.81	3.66
	α-(1-6)-L-Fuc	4.95	3.59	3.98	3.89	4.08	1.14
	α-(1-3)-L-Fuc	4.95	3.88	3.75	3.89	4.08	1.14

monohydrate (COM), respectively. The peaks at $d = 0.617$, 0.441, 0.277, and 0.224 nm belong to the diffraction peaks of (200), (211), (411), and (213) crystal planes of calcium oxalate dihydrate (COD), respectively [41].

Quantitative calculations according to the K value method [12, 26] indicated that as the -COOH content of PCP-Cs increases, the percentage of COD in the crystals induced by PCP-Cs gradually increases (Figure 4(b)). The percentages of COD induced by 0.4 g/L PCP-C0, PCP-C1, PCP-C2, and PCP-C3 were 45.7%, 76.4%, 82.7%, and 100%, respectively.

With PCP-C1 as a representative, the regulatory effect of polysaccharide concentration on CaOx crystal formation was studied (Figure 5(a)). In the absence of the polysaccharide, only the diffraction peaks of COM appeared. The addition of polysaccharides induced the formation of COD. With increasing PCP-C1 concentration, the intensity of the diffraction peak attributed to COD in the crystal increased continuously, indicating that the percentage of COD induced by the polysaccharide increased. Quantitative calculation also showed that in the presence of 0.05, 0.1, 0.2, 0.4, and 0.8 g/L PCP-C1, the contents of COD in the formed CaOx crystals were 15.4%, 37.4%, 48.4%, 74.7%, and 100%, respectively (Figure 5(b)).

3.3.2. FT-IR Characterization.

FT-IR detection further supported the regulatory effect of PCP-Cs on CaOx crystal formation (Figure 6(a)). In the absence of the polysaccharide, the following peaks were obtained: carbonyl asymmetric stretching vibration $\nu_{as}(COO^-)$ in the CaOx crystal at 1620 cm^{-1}, symmetric stretching vibration $\nu_s(COO^-)$ at 1316 cm^{-1}, and stretching vibration peaks at 3492-3062 cm^{-1}, which belong to the O-H bond of the crystal water. This finding indicated that the calcium oxalate formed is the pure COM crystal [42].

After PCP-Cs were added, $\nu_{as}(COO^-)$ and $\nu_s(COO^-)$ in the spectrogram undergo a blue shift in different degrees with increasing -COOH content in PCP-Cs (Figure 6(b)). In particular, $\nu_{as}(COO^-)$ gradually shifts from 1624 cm^{-1} to 1644 cm^{-1} and $\nu_s(COO^-)$ gradually shifts from 1320 cm^{-1} to 1329 cm^{-1}, indicating that the COM percentage in the CaOx crystal continuously decreases, while the COD percentage gradually increases. Given that the $\nu_{as}(COO^-)$ and $\nu_s(CO$

O$^-$) of COD are 1644 and 1329 cm^{-1} [41, 43], respectively, the blue shift values of $\nu_{as}(COO^-)$ and $\nu_s(COO^-)$ depend on the percentage of COD in the mixture.

In the fingerprint region, the absorption bands of COD crystals were found at 922 and 622 cm^{-1}, which differ from those of COM (959, 887, and 667 cm^{-1}), of which 887 and 667 cm^{-1} belong to COM C-C stretching vibration and O-C-O in-plane bending vibration, respectively [43].

Figure 7(a) shows the FT-IR spectra of CaOx crystals formed in the presence of PCP-C1 at different concentrations. As the PCP-C1 concentration increased from 0.05 g/L to 0.8 g/L, $\nu_{as}(COO^-)$ and $\nu_s(COO^-)$ are continuously blue-shifted (Figure 7(b)), where $\nu_{as}(COO^-)$ increased from 1619 cm^{-1} to 1644 cm^{-1} and $\nu_s(COO^-)$ increased from 1316 cm^{-1} to 1329.5 cm^{-1}. The higher the concentration of PCP-C1 is, the higher the percentage of COD in the induced CaOx crystals will be.

3.4. Regulation of PCP-Cs on CaOx Morphology.

Figure 8(a) shows the SEM images of CaOx crystals formed in the presence of different PCP-Cs. In the absence of the polysaccharide, most of the crystals formed were COM crystals (Figure 4(a)), which have sharp edges and high aggregation degrees. After adding 0.4 g/L PCP-Cs, COD crystals were formed. With increasing carboxymethylation degrees in PCP-Cs, not only the content of COD increased but also the shape of COD gradually changed from the usual tetragonal bipyramid shape to a round and blunt straw hat shape; meanwhile, the COD induced by PCP-C3 is disc-shaped.

The morphology of CaOx crystals formed by adjusting PCP-C1 concentration is shown in Figure 8(b). With the concentration of PCP-C1 increasing from 0.05 g/L to 0.8 g/L, the proportion of COD in the crystals gradually increased, and the crystal became rounder and blunter, the crystal surface became smoother, and the crystal dispersivity was improved.

3.5. Effect of PCP-Cs on the Zeta Potential of Crystals.

The particle surface with a high charge density has a large absolute value of the Zeta potential and electrostatic repulsion force between particles, it cannot easily aggregate, and it is stable in solution [43]. The Zeta potentials of CaOx crystals generated by different PCP-Cs are shown in Figure 9(a). With the -COOH content in PCP-Cs increasing from 2.54% to 6.13%, 10.24%, and 16.22%, the Zeta potential decreased from -4.66 mV to -5.82 mV, -8.35 mV, and -12.7 mV; i.e., the higher the -COOH content of polysaccharides is, the larger the absolute value of the Zeta potential on the surface of the CaOx crystal induced. This finding indicated that the more negatively charged PCP-C molecular weight was adsorbed on the crystal surface. For the same polysaccharide PCP-C1, the absolute value of the Zeta potential increased with increasing concentration (Figure 9(b)).

3.6. PCP-C Increases Soluble Ca^{2+} Concentration and Decreases CaOx Precipitation.

As shown in Figure 10(a), the molar amount of CaOx precipitates ($n(CaOx) = 9.8$-17.7 μmol) generated in the presence of different PCP-Cs is lower than that of the blank group

TABLE 2: Chemical shifts corresponding to ^{13}C NMR spectra of carboxymethylated polysaccharides (PCP-Cs).

Polysaccharide type	Sugar residue	^{13}C chemical shift (ppm)							
		C-1	C-2	C-3	C-4	C-5	C-6	-CH$_3$	C-7
	β-(1-3)-D-Glc	102.53	74.12	95.89	69.58	75.74	60.75	—	—
	β-(1-3)-D-Gal	103.7	73.5	86.9	69.1	77.0	61.6	—	—
PCP-C0	α-D-Gal	—	—	73.6	67.0	70.5	61.3	—	—
	α-(1-6)-L-Fuc	98.2	67.7	70.5	71.6	67.3	—	15.8	—
	α-(1-3)-L-Fuc	98.2	67.0	69.7	71.6	67.3	—	15.8	—
PCP-C1		102.8	73.1	79.2	69.6	74.8	60.9	—	177.8

(a)

(b)

(c)
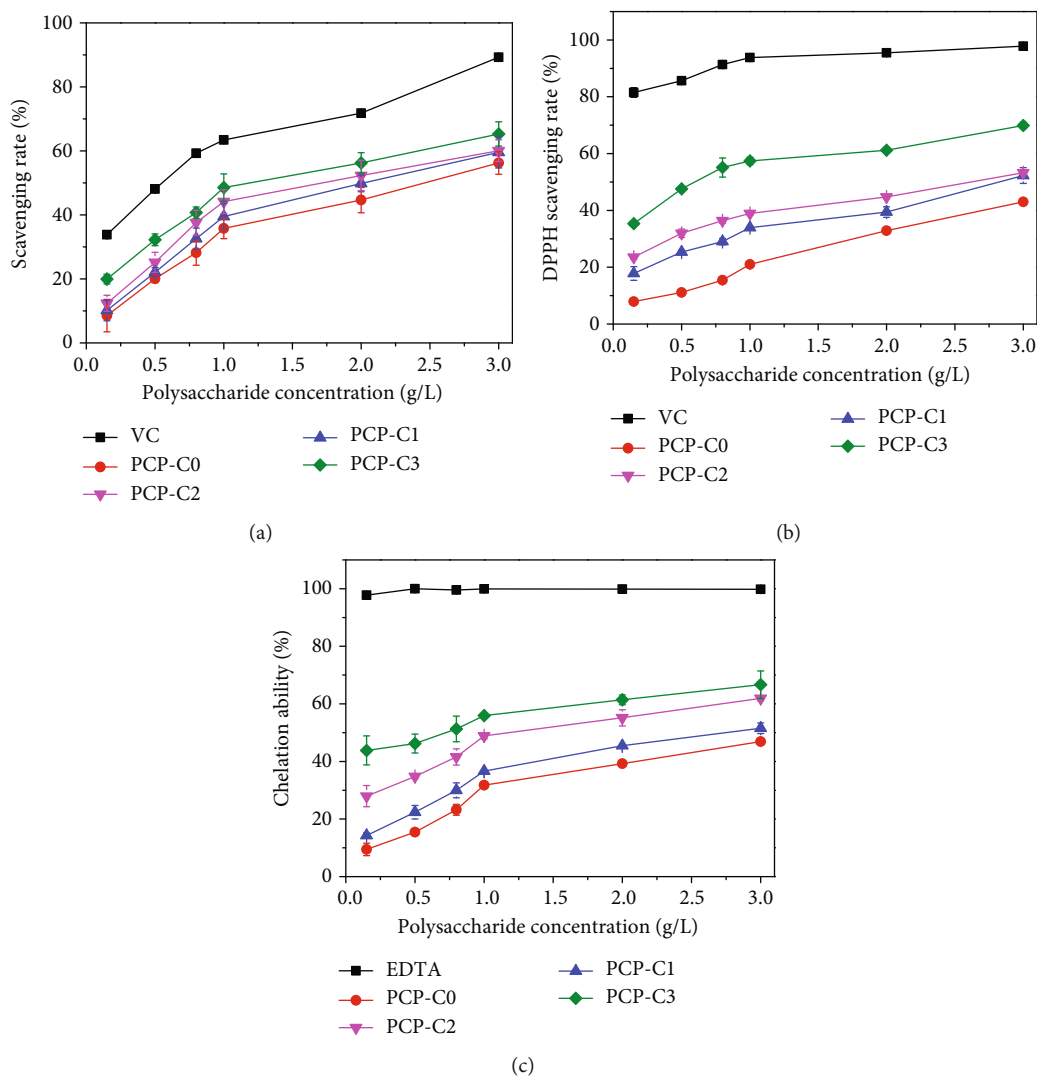
FIGURE 3: Antioxidant activity of different carboxymethylated *Poria cocos* polysaccharides (PCP-Cs). (a) PCP-C scavenging ability of OH radicals. (b) PCP-C scavenging ability of DPPH. (c) PCP-C chelating ability of Fe^{2+}.

(22.5 μmol), and m(CaOx) in the presence of PCP-C3 is the least (9.8 μmol). In the presence of different PCP-Cs, the concentration of soluble Ca^{2+} ions (c(Ca^{2+}) = 26.5 ~ 43.1 μmol/L) in the supernatant is greater than that in the blank group (16.5 μmol/L) (Figure 10(b)). The higher the content of -COOH in the polysaccharide is, the greater the c(Ca^{2+}) in the supernatant will be.

To verify the reliability of the results in Figure 10, we calculated the sum of the molar amount of soluble Ca^{2+} in the supernatant (n(Ca^{2+})) and the molar amount of Ca^{2+} in CaOx precipitates (n(Ca^{2+})) (Table 3). The obtained total molar amount of Ca^{2+} ions in each group is 30.7~33.1 μmol, which is consistent with the total molar amount of calcium in the reactant (30.0 μmol).

(a)

(b)
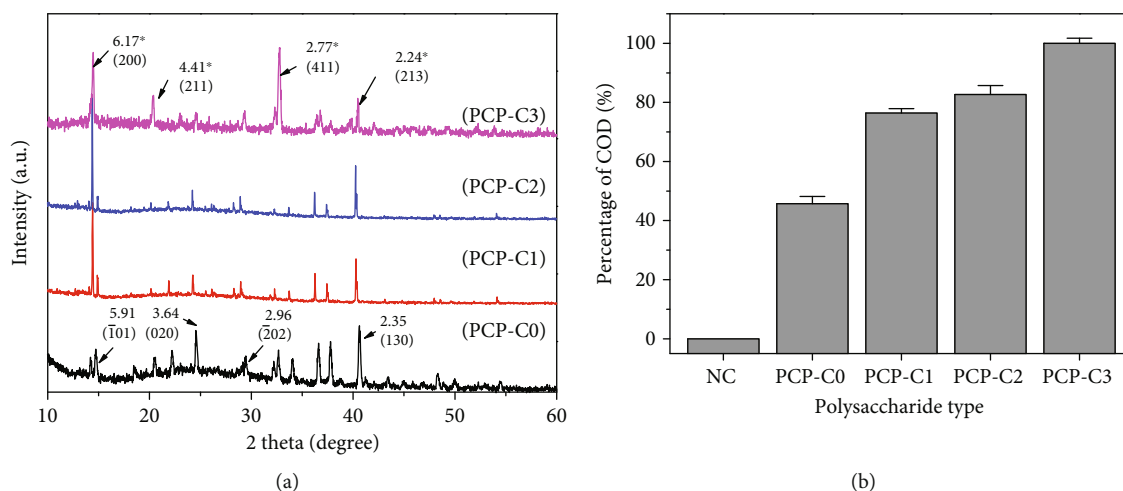
FIGURE 4: XRD spectrum (a) and COD percentage content (b) of the CaOx crystal formed by PCP-Cs with different COOH contents. (A) PCP-C0. (B) PCP-C1. (C) PCP-C2. (D) PCP-C3. Polysaccharide concentration: 0.4 g/L.

(a)

(b)
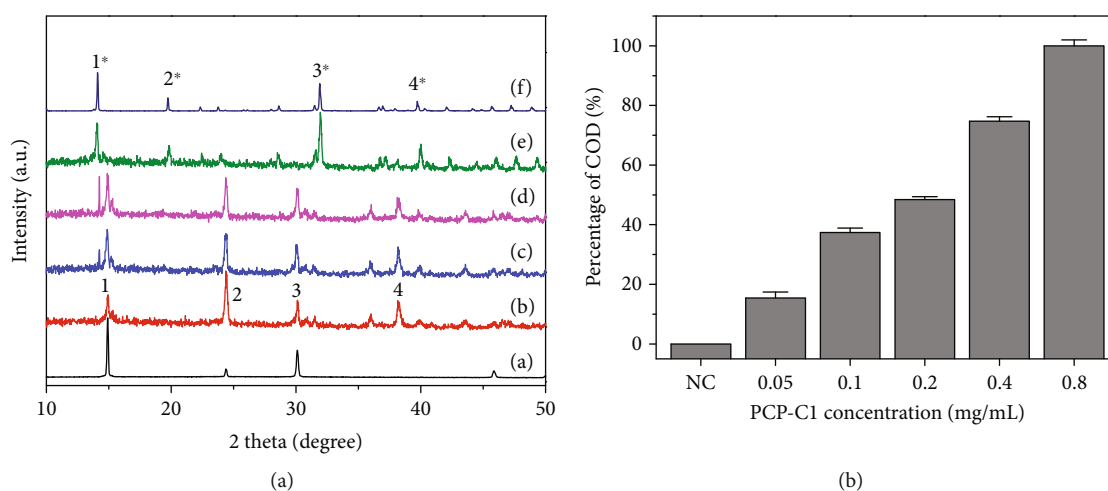
FIGURE 5: XRD spectrum (a) and COD percentage content (b) of the CaOx crystal formed in the presence of PCP-C1 with different concentrations. (A) 0, (B) 0.05, (C) 0.1, (D) 0.2, (E) 0.4, and (F) 0.8 g/L. The peaks of 1, 2, 3, and 4 belong to ($\bar{1}$01), (020), ($\bar{2}$02), and (130) crystal planes of COM crystals at $d = 0.593, 0.364, 0.296$, and 0.235 nm, respectively. The peaks of 1^*, 2^*, 3^*, and 4^* belong to (200), (211), (411), and (213) crystal faces of COD crystals at $d = 0.618, 0.442, 0.278$, and 0.224 nm, respectively.

3.7. Thermogravimetric Analysis of CaOx Crystals. As shown in Figure 11, the decomposition of CaOx crystals obtained in the blank group without the polysaccharide is divided into three steps, and the weight loss percentages were 12.18% (stage A), 8.33% (stage C), and 28.99% (stage D), consistent with the theoretical weight loss values of 12.33%, 19.17%, and 30.12% of COM ($CaC_2O_4 \cdot H_2O$) decomposed into CaC_2O_4, $CaCO_3$, and CaO [44].

However, the TGA curve of the CaOx crystal formed after adding 0.4 g/L PCP-C1 differed from that of the blank group due to the formation of COD crystals induced by PCP-C1 and the incorporation of PCP-C1 by the crystal. The CaOx crystals induced by the polysaccharides lose free water and crystalline water at 25°C~128°C (section A). When the temperature continues to rise to 200°C~400°C (section B), the polysaccharide molecules adsorbed on the crystals will

undergo thermal decomposition [45]. When the temperature reaches 741°C (section E), the CaOx sample was basically decomposed, and the weight percentages of the final residue of CaOx crystals regulated by PCP-C0, PCP-C1, PCP-C2, and PCP-C3 were 28.72%, 29.60%, 30.95%, and 31.16%, respectively.

The crystals obtained in the blank group without polysaccharides showed no thermogravimetric loss at 200°C~400°C (stage B), while the crystals induced by PCP-Cs underwent thermal decomposition; as such, the weight loss at this stage can be considered to be polysaccharide loss [45], that is, the weight of the polysaccharide incorporated into the crystal. Based on stage B in Figure 11, the proportions of PCP-C0, PCP-C1, PCP-C2, and PCP-C3 incorporated into the crystal were 20.52%, 15.60%, 10.65%, and 9.78%, respectively, and the decomposition temperatures were 205.10°C, 212.00°C,

(a)   (b)
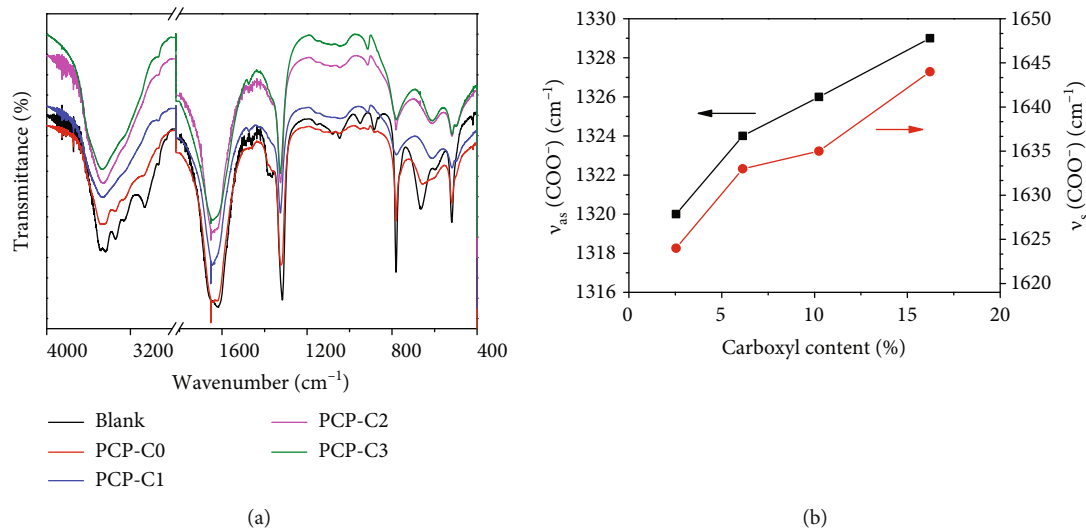
FIGURE 6: FT-IR spectrum (a) and change of the main absorption peak wavenumber (b) of CaOx crystals generated by regulation in the presence of PCP-Cs with different -COOH contents. c(CaOx) = 0.6 mmol/L.

(a)   (b)
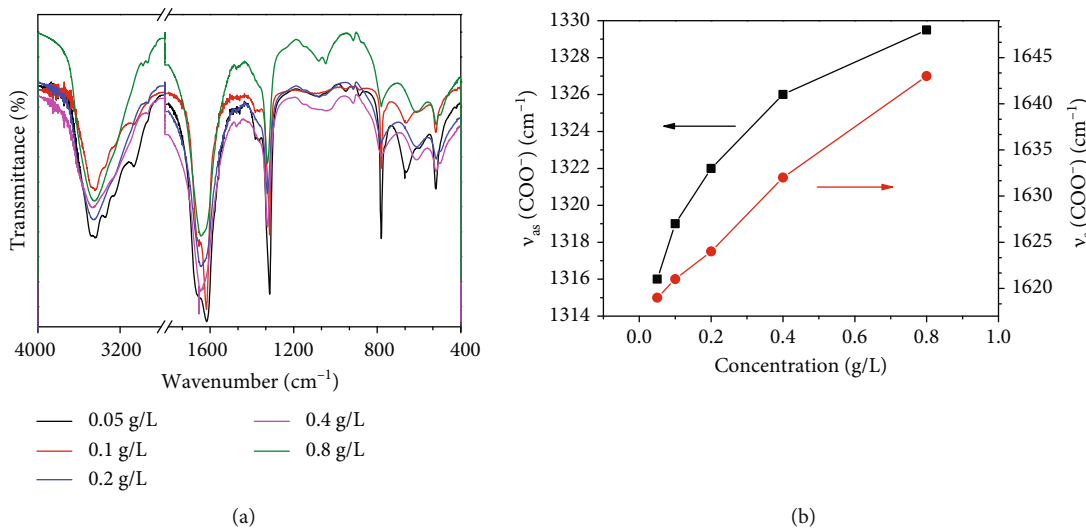
FIGURE 7: FT-IR spectrum (a) and change of the main absorption peak wavenumber (b) of CaOx crystals generated by regulation in the presence of PCP-C1 with different concentrations. c(CaOx) = 0.6 mmol/L.

212.67°C, and 212.05°C, respectively. PCP-C3, which has the highest degree of carboxymethylation, has the lowest proportion of incorporation into the crystals and has a higher decomposition temperature than the original PCP, indicating that PCP-C3 has a stronger specific interaction with the crystals and stronger binding. Given that the incorporation of PCP-Cs makes the decomposition temperature of the "PCP-C crystal" sample higher than that of the pure COM sample, the stability of the "PCP-C crystal" during heating is higher than that of pure crystals without the polysaccharide.

3.8. Toxicity Assessment of PCP-Cs on HK-2 Cells. The CCK-8 method was used to detect the toxicity of PCP-Cs with different -COOH contents on HK-2 cells (Figure 12(a)). After HK-2 interacted with PCP-Cs for 24 h, the cell viability was above 100%. Hence, PCP-Cs caused no cytotoxicity on HK-2 cells and promoted cell growth.

3.9. PCP-C Protects HK-2 Cells from Damage. Figure 12(b) shows the changes in HK-2 cell viability before and after preprotection with different carboxymethylated PCP-Cs. After 2.8 mM oxalate oxidation injury, the cell activity decreased from 100% of the control group to 56.6%. However, with different concentrations of PCP-C preprotection, the cell viability of the injured group was significantly higher than that of the injured group.

For the same polysaccharide with concentration < 100 μ g/L, the preprotection of PCP-Cs shows a concentration effect; i.e., the higher the concentration of PCP-Cs is, the better the protection effect will be.

At the same concentration, the cell viability of different polysaccharide protection groups followed the order of PCP-C0<PCP-C1<PCP-C2<PCP-C3; i.e., PCP-C3 with the highest -COOH content had the best protection effect. At 100 μg/L, the cell activity under PCP-C3 protection reached 90.3%.
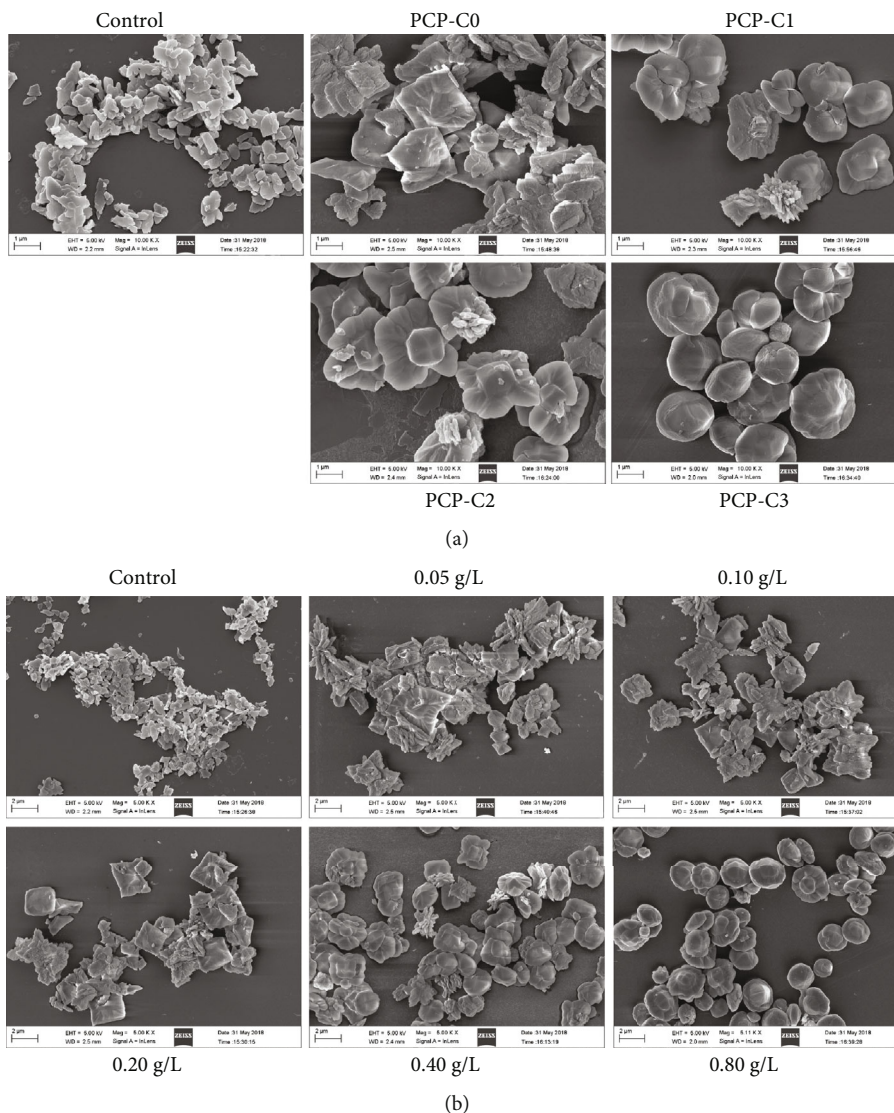
FIGURE 8: SEM image of the CaOx crystal formed by regulation of PCP-Cs. (a) Effects of -COOH content in PCP-Cs on CaOx morphology. (b) Effects of PCP-C1 concentration on CaOx morphology. (a) (A) PCP-C0, (B) PCP-C1, (C) PCP-C2, and (D) PCP-C3. Polysaccharide concentration: 0.4 g/L. (b) (A) 0, (B) 0.05, (C) 0.1, (D) 0.2, (E) 0.4, and (F) 0.8 g/L.
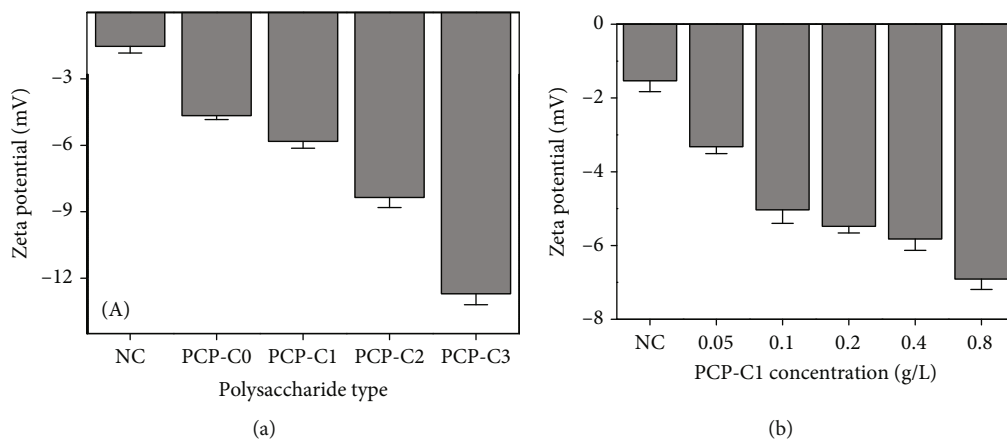
FIGURE 9: Zeta potential of the formed CaOx crystal regulated by PCP-Cs. (a) Effect of -COOH content of PCP-Cs on the Zeta potential. (b) Effect of PCP-C1 concentration on the Zeta potential.

(a)

(b)
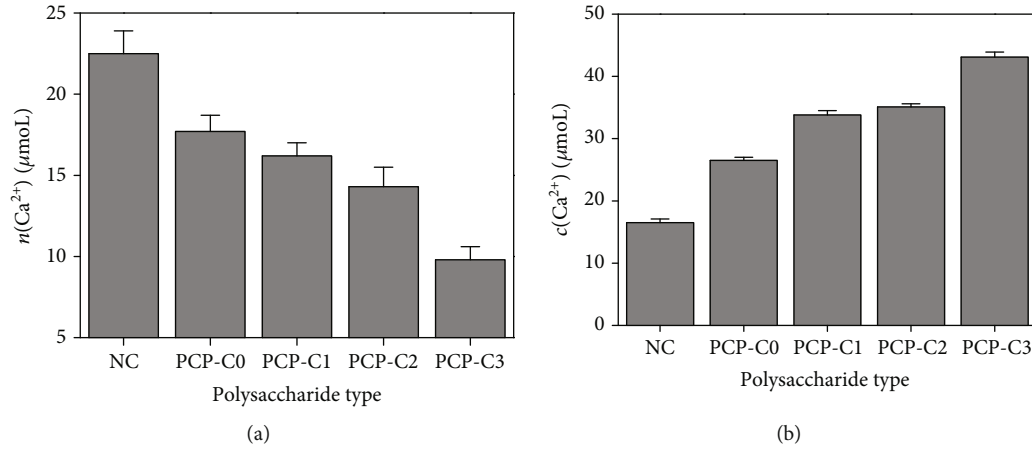
Figure 10: Effect of -COOH content of polysaccharides on the molar amount of CaOx precipitation and concentration of soluble Ca^{2+} in the supernatant. (a) Molar amount of CaOx precipitation. (b) Soluble calcium ion concentration. $c(PCP-Cs) = 0.4\,g/L$.

Table 3: Effect of PCP-Cs on the CaOx crystal phase, soluble Ca^{2+} ion concentration in solution, and CaOx precipitation mass.

Polysaccharide	Carboxyl content (%)	COD percentage (%)	$c(Ca^{2+})$ ($\mu mol/L$)	$n(Ca^{2+})$ (μmol)	Mass of CaOx (g)	$m(CaOx)^*$ (μmol)	Total Ca^{2+} (μmol)
Blank	—	0	16.5	8.2	0.00328	22.5	30.7
PCP-C0	2.54	45.7	26.5	13.3	0.00274	17.7	30.9
PCP-C1	6.13	76.4	33.8	16.9	0.00256	16.2	33.1
PCP-C2	10.24	82.7	35.1	17.5	0.00226	14.3	31.9
PCP-C3	16.22	100	43.1	21.6	0.00160	9.8	31.4

*When calculating the precipitation mass of CaOx $m(CaOx)$, the crystal waters in COM and COD should be considered; that is, the molar mass of COM and COD is 146 and 164 g/mol, respectively.
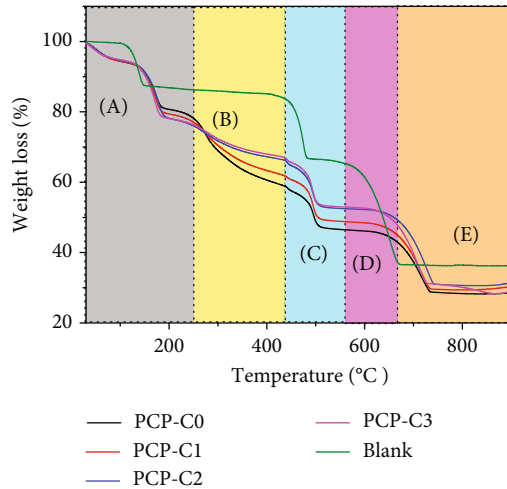
Figure 11: Thermogravimetric analysis curves of CaOx crystals formed in the presence of 0.4 g/L PCP-Cs, respectively.

3.10. PCP-C Protection Reduces Reactive Oxygen Species (ROS) Production Caused by Oxalate.

Figure 13(a) shows the ROS level changes in HK-2 cells before and after PCP-C preprotection. In the normal group, the cells grew tightly, with the lowest ROS fluorescence intensity, that is, less ROS. The intensity of ROS fluorescence in cells damaged by oxalate was significantly enhanced. After 100 μg/mL of four

PCP-Cs was preprotected, the fluorescence intensity of ROS in cells became weak, which was between the normal group and the protection group (Figure 13(b)), indicating that PCP-Cs can resist oxidative damage from oxalate after protection.

At the same time, the preprotection effect of PCP-C1 with different concentrations on HK-2 cells was also detected by a microplate reader (Figure 13(c)). With the increase of PCP-C1 concentration, the ROS level of cells gradually decreased, indicating that PCP-C1 has a concentration effect when protecting cells.

3.11. PCP-C Protection Increases Antioxidant Ability and Reduces Oxidative Damage.

The reduction of SOD activity in the organism implies decreased ability to resist free radical-induced damage in the organism. The SOD activity in the oxalate-damaged group was decreased to $28.78 \pm 4.02\%$ of the control value. After the protection by PCP-C0, PCP-C1, PCP-C2, and PCP-C3, the SOD activity increased to 49.22%, 64.78%, 74.57%, and 84.18%, respectively (Figure 14(a)).

The change of MDA content usually reveals the level of lipid peroxidation in vivo and indirectly reflects the degree of cell injury. After oxalate was used to damage the cells, the MDA content increased to 222.84% of the control group. The MDA content was obviously reduced in the PCP-C-protected groups; the released content was reduced to

(a)

(b)
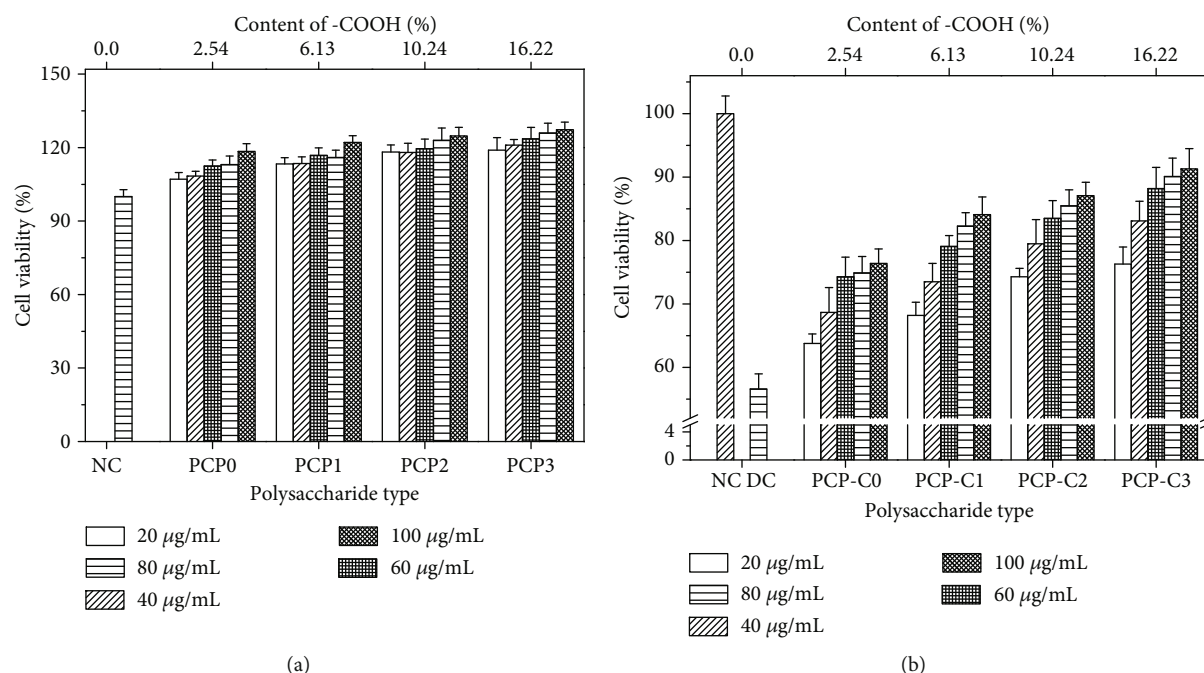
FIGURE 12: CCK-8 method to detect HK-2 cell viability. (a) Cytotoxicity of PCP-Cs with different concentrations. (b) The viability of HK-2 cells damaged by oxalate with or without PCP-C protection. NC: normal control group; DC: injury control group. Oxalate concentration: 2.8 mM. Injury time: 3.5 h. Protection time: 12 h. Compared with the injury group: $^{*}P < 0.05$; $^{**}P < 0.01$.

197.97% (PCP-C0), 164.84% (PCP-C1), 132.68% (PCP-C2), and 117.65% (PCP-C3) of the control group (Figure 14(b)). PCP-C3 with the highest -COOH contents has the strongest ability to inhibit MDA release.

The concentration of 8-OHdG is considered a marker of oxidative DNA damage. The 8-OHdG expression was low in the normal control cells (80.65 pg/mL). In the oxalate-damaged group, the 8-OHdG expression obviously increased to 223.61 pg/mL. The expression level of 8-OHdG in the PCP-C-protected groups obviously decreased compared to the oxalate-damaged group. The 8-OHdG concentration decreased to 195.31–130.25 pg/mL (Figure 14(c)). PCP-C3 with the highest -COOH contents presented the optimum DNA protection ability.

4. Discussion

4.1. Carboxymethylation Modification of P. cocos Polysaccharide

4.1.1. Influence of Reaction Conditions.
Carboxymethylation of PCP-C0 includes two steps. Firstly, NaOH reacts with -OH of polysaccharide molecules to generate alkoxide groups on the PCP-C0; then, the carboxymethyl group was formed in polysaccharide alkoxide and monochloroacetic acid (ClCH$_2$COOH) by SN2 reaction [14, 15]. The factors that affect the degree of substitution of polysaccharide carboxymethylation include reactant concentration, temperature, and reaction time (Table 4). In this experiment, three carboxymethylated polysaccharides PCP-C1, PCP-C2, and PCP-C3 were obtained at 60°C by changing the reaction time and reactant concentration. The contents of -COOH were

6.13%, 10.24%, and 16.22%, respectively, which were greater than 2.54% of the initial polysaccharide PCP-C0. Duan et al. [33] carboxymethylated the natural polysaccharide RNP extracted from *blackcurrant* fruits. As the temperature increased from 50°C to 70°C, the substitution degree increased from 0.57 to 1.10, which may be due to the increased temperature enhancing the solubility of polysaccharide alkoxide, resulting in better contact between polysaccharide alkoxide and ClCH$_2$COOH. When the temperature increased further, the substitution degree decreased, which is attributed to the fact that too high a temperature is conducive to the occurrence of side reactions. Liu et al. [46] modified *Sarcandra glabra* polysaccharide by carboxymethylation and found that with the extension of reaction time, the degree of carboxymethylation first increased and then decreased. Prolonging the reaction time helps polysaccharides to expand and promote ClCH$_2$COOH to enter the polysaccharide molecules. However, too long reaction time at higher temperatures is conducive to the formation of side reaction products, such as glycolate.

4.1.2. Structural Identification of Carboxymethylated Polysaccharides.
From ^{1}H NMR and ^{13}C NMR spectra (Figure 2), PCP-C0 was composed of glucose, galactose, and fucose, and the main polysaccharide residues were α-D-Gal, α-(1-6)-L-Fuc, α-(1-3)-L-Fuc, β-(1-3)-D-Glc, and β-(1-3)-D-Gal, which was basically consistent with the structure reported by Meikuang et al. [47] and Wang et al. [19]. After carboxymethylation, the ^{13}C NMR of PCP-C1 showed a new absorption peak at 177.8 ppm, which showed the characteristic absorption peak of the carboxymethyl group (-CH$_2$COOH) [23, 48].

(a)

(b)

(c)
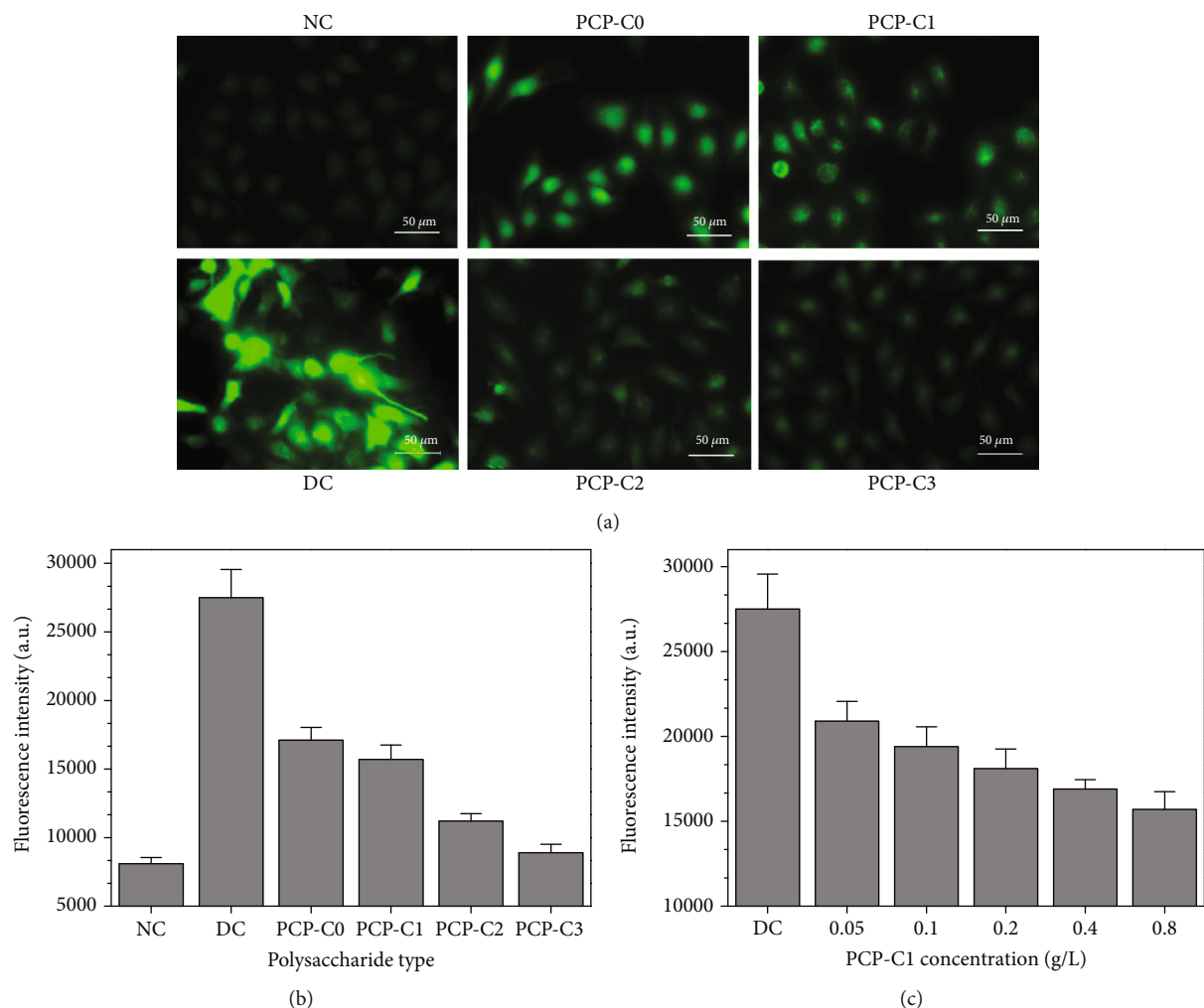
Figure 13: Effects of PCP-Cs before and after protection on ROS expression in HK-2 cells. (a, b) Effects of COOH content in PCP-Cs. Polysaccharide concentration: 100 μg/mL. (c) Effect of PCP-C1 concentration. NC: normal control group; DC: injury control group. Oxalate concentration: 2.8 mM. Injury time: 3.5 h. Protection time: 12 h.

FT-IR spectra show that the main chain structures of the four carboxymethylated polysaccharides are similar, but the carboxymethylated polysaccharides have a new characteristic absorption peak at 1326.5 cm^{-1}, which is attributed to -CH$_2$COOH groups. The experimental results are consistent with the ^{13}C NMR results.

4.1.3. Enhancement of Antioxidant Activity of Polysaccharides after Carboxymethylation. Carboxymethylation modification can enhance the antioxidant activity of polysaccharide, which is related to the following factors:

(1) The introduction of the substituent group -CH$_2$COOH changes the configuration of polysaccharide, which weakens the dissociation energy of hydrogen bonds in polysaccharide molecules [49] and improves the hydrogen supply capacity of polysaccharide

(2) The biological activity of polysaccharides is positively correlated with their water solubility. Carboxymethy-

lation modification can increase the water solubility of polysaccharides [50], so the degree of freedom of polysaccharides is increased, and the ability to exert activity is stronger

(3) Polysaccharides have two mechanisms for antioxidant activity. One is that polysaccharides inhibit the generation of free radicals by chelating transition metal ions (such as Fe^{2+} and Cu^{2+} ions) [51, 52]. The other is that polysaccharides can provide single electrons or hydrogen atoms for free radicals, thus terminating free radical chain reaction and achieving the purpose of scavenging free radicals. As the content of -COOH in carboxymethylated polysaccharide increases significantly, its ability to chelate transition metal ions and provide single electron or hydrogen atoms all increases, thereby increasing the antioxidant activity

Shi et al. [34] extracted the original crude *Enteromorpha prolifera* polysaccharide (PE) with a molecular weight of

(a)

(b)

(c)
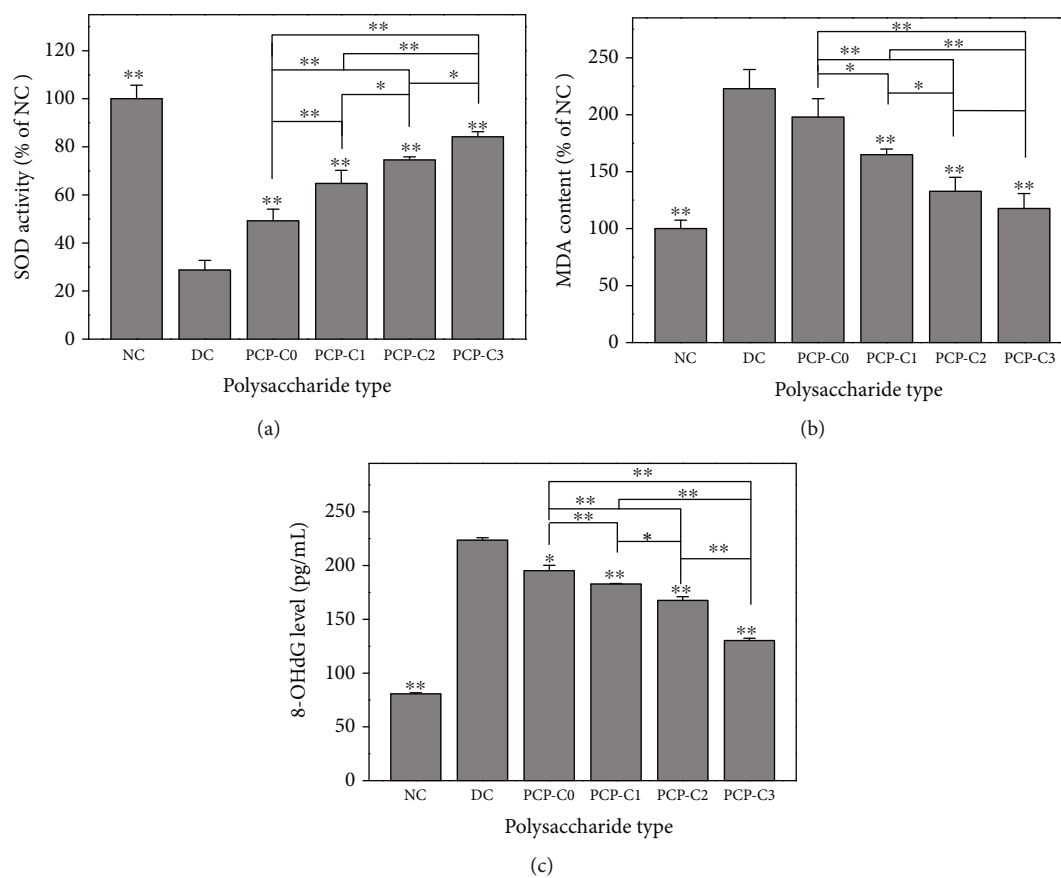
FIGURE 14: Effects of PCP-Cs before and after protection on SOD activity (a), MDA content (b), and 8-OHdG expression (c) in HK-2 cells. NC: normal control group; DC: injury control group. Oxalate concentration: 2.8 mM. Injury time: 3.5 h. Protection time: 12 h. Compared with the injury group: $^{*}P < 0.05$; $^{**}P < 0.01$.

TABLE 4: Carboxymethylation conditions of PCP-Cs and carboxyl content of polysaccharides.

Polysaccharide type	Isopropanol volume (mL)	NaOH volume (mL)	Chloroacetic acid amount (g)	Reaction time (h)	Temperature	COOH content (%)
PCP-C0	—	—	—	—		2.54
PCP-C1	15	10	2.63	2	60	6.13
PCP-C2	15	10	2.63	8	60	10.24
PCP-C3	10	15	6.00	4	60	16.22

1400 kDa, degraded it to obtain a low molecular weight polysaccharide DPE with a molecular weight of 44 kDa, and carboxymethylated the DPE to obtain CDPE. The DPPH scavenging ability, hydroxyl radical scavenging ability, and reducing ability of the three polysaccharides are CDPE>DPE>PE. Li et al. [53] also showed that the radical scavenging ability and total antioxidant ability of the carboxymethylated degraded *Sargassum fusiforme* polysaccharide (CDPSSF) are significantly higher than those of the degraded polysaccharide (DPSF); the antioxidant activity of DPSF is higher than that of the nondegraded polysaccharide (PSF).

4.2. Carboxymethylated Polysaccharides Have Stronger Ability to Regulate CaOx Crystal Growth. Carboxymethylated polysaccharides can significantly inhibit COM crystal

growth, induce COD crystal formation, and inhibit crystal aggregation (Figure 15).

First, after carboxymethylation, the content of -COOH in polysaccharides increases, which can complex a large number of Ca^{2+} ions in the system to inhibit the combination of Ca^{2+} and Ox^{2-} to form CaOx precipitates. The higher the degree of carboxymethylation is, the stronger the inhibitory ability will be.

Second, Ca^{2+} ions on the polysaccharide surface are highly enriched, forming a high energy interface because the carboxymethylated polysaccharide has enhanced ability to complex Ca^{2+} ions [54]. After Ca^{2+} ions are adsorbed, their degree of freedom decreases and the energy state of calcium increases, which are conducive to promoting the formation of COD [26].
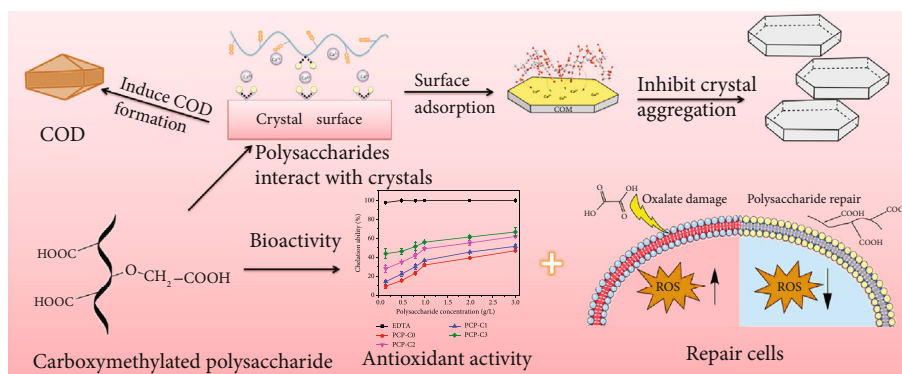
FIGURE 15: Model diagram of biological activity of carboxymethylated polysaccharides (PCP-Cs) and their regulatory effect on CaOx crystals.

TABLE 5: TGA curve analysis of CaOx crystals formed in the presence of 0.4 g/L PCP-Cs and the blank group, respectively.

PCP-Cs	A		B		C		D		Residual weight (%)
	Decomp. T (°C)[*1]	Weight loss (%)	Decomp. T (°C)	Weight loss (%)[*2]	Decomp. T (°C)	Weight loss (%)	Decomp. T (°C)	Weight loss (%)	
Blank	95.73	12.08	—	—	409.14	18.33	552.94	28.99	36.55
PCP-C0	110.33	13.49	205.10	20.52	427.84	12.61	602.29	17.36	28.72
PCP-C1	106.94	14.89	212.00	15.60	427.14	13.17	598.17	18.85	29.60
PCP-C2	107.68	16.62	212.67	10.65	426.54	13.93	605.64	21.23	30.95
PCP-C3	102.97	16.87	212.05	9.78	424.50	14.24	589.75	21.57	31.16

[*1]Decomp. T: decomposition temperature. [*2]The weight loss in stage B is the content of polysaccharides.

Third, the results of thermogravimetric analysis (Figure 11) showed that during the process of PCP-Cs regulating the growth of CaOx, PCP-Cs were adsorbed or incorporated into the CaOx crystals (Table 5). The adsorption of PCP-Cs resulted in the accumulation of high-density negative charges on the surface of the CaOx crystals, causing the absolute value of the Zeta potential to increase (Figure 9), thereby inhibiting the aggregation of CaOx crystals. Zhang et al. [6] showed that *Sargassum* polysaccharide (SGP) can significantly inhibit the aggregation of COM crystals; the inhibition rate of SGP at a concentration of 0.5 g/L on the aggregation of COM crystals is as high as 76.8%.

Fourth, the Ca^{2+} ions at the tip and edge of the crystal are easy to coordinate with -COOH of polysaccharides in solution due to the dissociation-precipitation equilibrium between a large number of -COOH groups in carboxymethylated polysaccharide and the formed CaOx crystals. The continuous dissociation-precipitation finally makes the CaOx crystal blunt (Figure 8). Given that the damage degree of the sharp-edged COM crystal to renal epithelial cells is higher than that of the blunt COD crystal and the affinity between the COM with the positively charged surface and the damaged renal epithelial cells with the negatively charged surface is higher than that of the COD crystal [53, 54], COD is easier to be excreted out of the body with urine. PCP-Cs induce the formation of more or even all COD crystals, thereby reducing the risk of CaOx kidney stone formation.

As shown in Figure 8, the crystal size of the control group is significantly smaller due to the maximum supersaturation of CaOx in the control system without the polysaccharide and the maximum nucleation rate of the crystal. Under the condition of fixing the total amount of CaOx, rapid nucleation reduced the average size of each crystal. This finding also explains why PCP-C3 has the strongest complexing ability with CaOx, but the crystal size induced by PCP-C3 does not decrease; i.e., the number of formed crystals is small, but the size is still large.

4.3. Carboxymethylated Polysaccharide Has Stronger Ability to Protect Renal Epithelial Cells from Oxalate Toxicity. High-level ROS can react with intracellular macromolecules rapidly, impairing the function of normal cells and even leading to cell death [51]. The increase of SOD activity in the organism implies an elevated ability to resist free radical-induced damage in the organism. The change of MDA content reveals the level of lipid peroxidation and indirectly reflects the degree of cell injury. The concentration of 8-OHdG is considered a marker of oxidative DNA damage. After protecting HK-2 cells with different degrees of carboxymethylated PCP-Cs, oxidative damage from oxalate can be alleviated, thereby increasing cell viability (Figure 12(b)) and superoxide dismutase activity (Figure 14(a)) and decreasing ROS level (Figure 13), MDA content (Figure 14(b)), and 8-OHdG expression (Figure 14(c)). Thus, PCP-Cs can protect

HK-2 cells from oxidative damage by oxalate and improve cellular antioxidant ability. PCP-C with a higher carboxymethylation degree has a stronger protection ability.

Zhang et al. [55] used thrombin to induce inflammation of rat endothelial progenitor cells (EPC) and found that *Astragalus* polysaccharide (APS) has a protective effect on injured endothelial progenitor cells. APS can block the nuclear factor kappa B (NF-κB) signaling in EPC, upregulate the expression of the vascular endothelial growth factor (VEGF) and its receptor, and inhibit the expression of intercellular adhesion molecule-1 (ICAM-1) induced by thrombin, thereby protecting cells from damage. Li et al. [56] found that Chinese chive polysaccharide (CCP) can inhibit the oxidative damage to the kidney of mice with chronic renal failure (CRF). Sulfated polysaccharides from *Codium fragile* polysaccharide (CFCE-PS) have protective effects on H_2O_2-induced oxidative stress-damaged cells [57]. After being protected by CFCE-PS, the cell vitality is enhanced, the intracellular ROS level is reduced, and the cell apoptosis is inhibited.

Our results indicated that carboxymethylated PCP-Cs have the ability to inhibit calcium oxalate formation and resist the oxidative damage of oxalate in vitro. However, more in-depth molecular mechanisms and verification in vivo need to be further studied in the future.

5. Conclusions

Carboxymethylation of PCP-C0 with -COOH content of 2.54% was carried out, and three carboxymethylated polysaccharides with -COOH contents of 6.13%, 10.24%, and 16.22% were obtained. Compared with PCP-C0, the carboxymethylated polysaccharides (PCP-Cs) can significantly enhance its antioxidant capacity, protect renal epithelial cells from oxidative damage, inhibit COM growth, induce COD formation, inhibit crystal aggregation, and increase the concentration of soluble Ca^{2+} ions in the system, all of which are beneficial to inhibit the formation of CaOx kidney stones. With increasing carboxymethylation degrees in PCP-Cs, its biological activity gradually increases. This study suggests that carboxymethylation of polysaccharides is an effective method to enhance biological activity and anticalculus ability. The higher the degree of carboxymethylation is, the stronger the activity of polysaccharides will be.

Data Availability

All the data supporting the results were shown in the paper and can be available from the corresponding authors.

Conflicts of Interest

The authors declare that they have no competing interests.

Acknowledgments

References

[1] C.-Y. Li, L. Liu, Y. W. Zhao et al., "Repair of tea polysaccharide promotes the endocytosis of nanocalcium oxalate monohydrate by damaged HK-2 cells," *Oxidative Medicine and Cellular Longevity*, vol. 2020, Article ID 2198976, 12 pages, 2020.

[2] B. Akın, M. Öner, Y. Bayram, and K. D. Demadis, "Effects of carboxylate-modified, "green" inulin biopolymers on the crystal growth of calcium oxalate," *Crystal Growth & Design*, vol. 8, no. 6, pp. 1997–2005, 2008.

[3] H. Liu, L.-H. Huang, X.-Y. Sun, and J.-M. Ouyang, "High-phosphorus environment promotes calcification of A7R5 cells induced by hydroxyapatite nanoparticles," *Materials Science and Engineering: C*, vol. 107, p. 110228, 2020.

[4] I. Wijesekara, R. Pangestuti, and S.-K. Kim, "Biological activities and potential health benefits of sulfated polysaccharides derived from marine algae," *Carbohydrate Polymers*, vol. 84, no. 1, pp. 14–21, 2011.

[5] Y. Yu, M. Shen, Q. Song, and J. Xie, "Biological activities and pharmaceutical applications of polysaccharide from natural resources: a review," *Carbohydrate Polymers*, vol. 183, pp. 91–101, 2018.

[6] C. Y. Zhang, W. H. Wu, J. Wang, and M. B. Lan, "Antioxidant properties of polysaccharide from the brown seaweed *Sargassum graminifolium* (Turn.), and its effects on calcium oxalate crystallization," *Marine Drugs*, vol. 10, no. 12, pp. 119–130, 2012.

[7] X. T. Ma, X. Y. Sun, K. Yu, B. S. Gui, Q. Gui, and J. M. Ouyang, "Effect of content of sulfate groups in seaweed polysaccharides on antioxidant activity and repair effect of subcellular organelles in injured HK-2 cells," *Oxidative Medicine and Cellular Longevity*, vol. 2017, Article ID 2542950, 13 pages, 2017.

[8] K. Teodosio Melo, R. Gomes Camara, M. Queiroz et al., "Evaluation of sulfated polysaccharides from the brown seaweed Dictyopteris justii as antioxidant agents and as inhibitors of the formation of calcium oxalate crystals," *Molecules*, vol. 18, no. 12, pp. 14543–14563, 2013.

[9] Z. Xu, S. Feng, S. Shen et al., "The antioxidant activities effect of neutral and acidic polysaccharides from *Epimedium acuminatum* Franch. on *Caenorhabditis elegans*," *Carbohydrate Polymers*, vol. 144, pp. 122–130, 2016.

[10] L. S. Huang, X. Y. Sun, Q. Gui, and J. M. Ouyang, "Effects of plant polysaccharides with different carboxyl group contents on calcium oxalate crystal growth," *CrystEngComm*, vol. 19, no. 32, pp. 4838–4847, 2017.

[11] Y. Wang, Q. Mo, Z. Li et al., "Effects of degree of carboxymethylation on physicochemical and biological properties of pachyman," *International Journal of Biological Macromolecules*, vol. 51, no. 5, pp. 1052–1056, 2012.

[12] F. Huang, X. Y. Sun, and J. M. Ouyang, "Preparation and characterization of selenized *Astragalus* polysaccharide and its inhibitory effect on kidney stones," *Materials Science and Engineering: C*, vol. 110, article 110732, 2020.

[13] X. Wang, Z. Zhang, and M. Zhao, "Carboxymethylation of polysaccharides from *Tremella fuciformis* for antioxidant and moisture-preserving activities," *International Journal of Biological Macromolecules*, vol. 72, pp. 526–530, 2015.

[14] Z. Duan, W. Duan, F. Li, Y. Li, P. Luo, and H. Liu, "Effect of carboxymethylation on properties of fucoidan from *Laminaria japonica*: Antioxidant activity and preservative effect on strawberry during cold storage," *Postharvest Biology and Technology*, vol. 151, pp. 127–133, 2019.

[15] Y. Li, Y. Yuan, L. Lei et al., "Carboxymethylation of polysaccharide from *Morchella angusticeps* Peck enhances its cholesterol-lowering activity in rats," *Carbohydrate Polymers*, vol. 172, pp. 85–92, 2017.

[16] K. H. Lai, M. C. Lu, Y. C. du et al., "Cytotoxic lanostanoids from Poria cocos," *Journal of Natural Products*, vol. 79, no. 11, pp. 2805–2813, 2016.

[17] Y. Sun, "Biological activities and potential health benefits of polysaccharides from *Poria cocos* and their derivatives," *International Journal of Biological Macromolecules*, vol. 68, pp. 131–134, 2014.

[18] X. Jia, L. Ma, P. Li, M. Chen, and C. He, "Prospects of *Poria cocos* polysaccharides: Isolation process, structural features and bioactivities," *Trends in Food Science & Technology*, vol. 54, pp. 52–62, 2016.

[19] Y. Wang, M. Zhang, D. Ruan et al., "Chemical components and molecular mass of six polysaccharides isolated from the sclerotium of *Poria cocos*," *Carbohydrate Research*, vol. 339, no. 2, pp. 327–334, 2004.

[20] N. Wang, Y. Zhang, X. Wang et al., "Antioxidant property of water-soluble polysaccharides from *Poria cocos* Wolf using different extraction methods," *International Journal of Biological Macromolecules*, vol. 83, pp. 103–110, 2016.

[21] K. Wu, J. Fan, X. Huang, X. Wu, and C. Guo, "Hepatoprotective effects exerted by *Poria Cocos* polysaccharides against acetaminophen-induced liver injury in mice," *International Journal of Biological Macromolecules*, vol. 114, pp. 137–142, 2018.

[22] H. Zhang, J.-Q. Wang, S.-P. Nie, Y.-X. Wang, S. W. Cui, and M.-Y. Xie, "Sulfated modification, characterization and property of a water-insoluble polysaccharide from Ganoderma atrum," *International Journal of Biological Macromolecules*, vol. 79, pp. 248–255, 2015.

[23] X. Sun, X. Jin, W. Pan, and J. Wang, "Syntheses of new rare earth complexes with carboxymethylated polysaccharides and evaluation of their in vitro antifungal activities," *Carbohydrate Polymers*, vol. 113, pp. 194–199, 2014.

[24] S. Li, Q. Xiong, X. Lai et al., "Molecular modification of polysaccharides and resulting bioactivities," *Compr Rev Food Sci Food Saf*, vol. 15, no. 2, pp. 237–250, 2016.

[25] Y. Y. Ren, P. P. Sun, Y. P. Ji, X. T. Wang, S. H. Dai, and Z. Y. Zhu, "Carboxymethylation and acetylation of the polysaccharide from Cordyceps militaris and their α-glucosidase inhibitory activities," *Natural Product Research*, vol. 34, no. 3, pp. 369–377, 2020.

[26] J.-Y. Chen, X. Y. Sun, and J. M. Ouyang, "Modulation of calcium oxalate crystal growth and protection from oxidatively damaged renal epithelial cells of corn silk polysaccharides with different molecular weights," *Oxidative Medicine and Cellular Longevity*, vol. 2020, Article ID 6982948, 19 pages, 2020.

[27] W. Tang, L. Lin, J. Xie et al., "Effect of ultrasonic treatment on the physicochemical properties and antioxidant activities of polysaccharide from *Cyclocarya paliurus*," *Carbohydr Polym*, vol. 151, pp. 305–312, 2016.

[28] X. Pan, S. Wu, Y. Yan et al., "Rice bran polysaccharide-metal complexes showed safe antioxidant activity *in vitro*," *International Journal of Biological Macromolecules*, vol. 126, pp. 934–940, 2019.

[29] L. Chen and G. Huang, "Antioxidant activities of sulfated pumpkin polysaccharides," *International Journal of Biological Macromolecules*, vol. 126, pp. 743–746, 2019.

[30] G. Y. Xu, A. M. Liao, J. H. Huang, J. G. Zhang, K. Thakur, and Z. J. Wei, "Evaluation of structural, functional, and antioxidant potential of differentially extracted polysaccharides from potatoes peels," *International Journal of Biological Macromolecules*, vol. 129, pp. 778–785, 2019.

[31] J. Chung, I. Granja, M. G. Taylor, G. Mpourmpakis, J. R. Asplin, and J. D. Rimer, "Molecular modifiers reveal a mechanism of pathological crystal growth inhibition," *Nature*, vol. 536, no. 7617, pp. 446–450, 2016.

[32] X.-Y. Sun, H. Zhang, J. Liu, and J.-M. Ouyang, "Repair activity and crystal adhesion inhibition of polysaccharides with different molecular weights from red algae Porphyra yezoensis against oxalate-induced oxidative damage in renal epithelial cells," *Food & Function*, vol. 10, no. 7, pp. 3851–3867, 2019.

[33] S. Duan, M. Zhao, B. Wu et al., "Preparation, characteristics, and antioxidant activities of carboxymethylated polysaccharides from blackcurrant fruits," *International Journal of Biological Macromolecules*, vol. 155, pp. 1114–1122, 2020.

[34] M. Shi, X. Wei, J. Xu et al., "Carboxymethylated degraded polysaccharides from *Enteromorpha prolifera*: Preparation and *in vitro* antioxidant activity," *Food Chemistry*, vol. 215, pp. 76–83, 2017.

[35] J. Tang, J. Nie, D. Li et al., "Characterization and antioxidant activities of degraded polysaccharides from *Poria cocos* sclerotium," *Carbohydrate polymers.*, vol. 105, pp. 121–126, 2014.

[36] Y. Chen, H. Zhang, Y. Wang, S. Nie, C. Li, and M. Xie, "Acetylation and carboxymethylation of the polysaccharide from *Ganoderma atrum* and their antioxidant and immunomodulating activities," *Food Chemistry*, vol. 156, pp. 279–288, 2014.

[37] X. Chen, L. Zhang, and P. C. K. Cheung, "Immunopotentiation and anti-tumor activity of carboxymethylated-sulfated β-(1→3)-D-glucan from Poria cocos," *International Immunopharmacology*, vol. 10, no. 4, pp. 398–405, 2010.

[38] X. Li, Y. He, P. Zeng et al., "Molecular basis for Poria cocos mushroom polysaccharide used as an antitumour drug in China," *Journal of Cellular and Molecular Medicine*, vol. 23, no. 1, pp. 4–20, 2019.

[39] Z. Wang, J. Xie, M. Shen, S. Nie, and M. Xie, "Sulfated modification of polysaccharides: synthesis, characterization and bioactivities," *Trends in Food Science & Technology*, vol. 74, pp. 147–157, 2018.

[40] Y. Yuan and D. Macquarrie, "Microwave assisted extraction of sulfated polysaccharides (fucoidan) from *Ascophyllum nodosum* and its antioxidant activity," *Carbohydr Polym*, vol. 129, pp. 101–107, 2015.

[41] H. Liu, X. Y. Sun, F. X. Wang, and J. M. Ouyang, "Regulation on calcium oxalate crystallization and protection on HK-2 cells of tea polysaccharides with different molecular weights," *Oxidative Medicine and Cellular Longevity*, vol. 2020, Article ID 5057123, 14 pages, 2020.

[42] X.-Y. Sun, C.-Y. Zhang, P. Bhadja, and J.-M. Ouyang, "Preparation, properties, formation mechanisms, and cytotoxicity of calcium oxalate monohydrate with various morphologies," *CrystEngComm*, vol. 20, no. 1, pp. 75–87, 2018.

[43] A. Stanković, B. Njegić Džakula, J. Kontrec, D. Kovačević, B. Marković, and D. Kralj, "Preparation and characterization of calcium oxalate dihydrate seeds suitable for crystal growth kinetic analyses," *Journal of Crystal Growth*, vol. 500, pp. 91–97, 2018.

[44] V. S. Joshi, B. B. Parekh, M. J. Joshi, and A. B. Vaidya, "Herbal extracts of *Tribulus terrestris* and *Bergenia ligulata* inhibit

growth of calcium oxalate monohydrate crystals in vitro," *Journal of Crystal Growth*, vol. 275, no. 1-2, pp. e1403–e1408, 2005.

[45] W. Fang, H. Zhang, J. Yin et al., "Hydroxyapatite crystal formation in the presence of polysaccharide," *Crystal Growth & Design*, vol. 16, no. 3, pp. 1247–1255, 2016.

[46] W. Liu, C. Hu, Y. Liu et al., "Preparation, characterization, and α-glycosidase inhibition activity of a carboxymethylated polysaccharide from the residue of *Sarcandra glabra* (Thunb.) Nakai," *International Journal of Biological Macromolecules*, vol. 99, pp. 454–464, 2017.

[47] M. K. Lu, J. J. Cheng, C. Y. Lin, and C. C. Chang, "Purification, structural elucidation, and anti-inflammatory effect of a water-soluble 1,6-branched 1,3-α-d-galactan from cultured mycelia of *Poria cocos*," *Food Chemistry*, vol. 118, no. 2, pp. 349–356, 2010.

[48] Y. Liu and G. Huang, "The antioxidant activities of carboxymethylated cushaw polysaccharide," *International Journal of Biological Macromolecules*, vol. 121, pp. 666–670, 2019.

[49] L. Yang, T. Zhao, H. Wei et al., "Carboxymethylation of polysaccharides from *Auricularia auricula* and their antioxidant activities *in vitro*," *International Journal of Biological Macromolecules*, vol. 49, no. 5, pp. 1124–1130, 2011.

[50] J. Xu, W. Liu, W. Yao, X. Pang, D. Yin, and X. Gao, "Carboxymethylation of a polysaccharide extracted from *Ganoderma lucidum* enhances its antioxidant activities *in vitro*," *Carbohydrate Polymers*, vol. 78, no. 2, pp. 227–234, 2009.

[51] J. Wang, S. Hu, S. Nie, Q. Yu, and M. Xie, "Reviews on mechanisms of in vitro antioxidant activity of polysaccharides," *Oxidative Medicine and Cellular Longevity*, vol. 2016, Article ID 5692852, 13 pages, 2016.

[52] F. Y. Kagimura, M. A. A. da Cunha, T. V. Theis et al., "Carboxymethylation of (1→6)-β-glucan (lasiodiplodan): Preparation, characterization and antioxidant evaluation," *Carbohydrate Polymers*, vol. 127, pp. 390–399, 2015.

[53] Y. T. Li, B. J. Chen, W. D. Wu et al., "Antioxidant and antimicrobial evaluation of carboxymethylated and hydroxamated degraded polysaccharides from *Sargassum fusiforme*," *International Journal of Biological Macromolecules*, vol. 118, Part B, pp. 1550–1557, 2018.

[54] B. Grohe, K. A. Rogers, H. A. Goldberg, and G. K. Hunter, "Crystallization kinetics of calcium oxalate hydrates studied by scanning confocal interference microscopy," *Journal of Crystal Growth*, vol. 295, no. 2, pp. 148–157, 2006.

[55] X. Zhang, K. Yao, L. Ren, T. Chen, and D. Yao, "Protective effect of *Astragalus* polysaccharide on endothelial progenitor cells injured by thrombin," *International Journal of Biological Macromolecules*, vol. 82, pp. 711–718, 2016.

[56] Q. M. Li, H. R. Chena, X. Q. Zha, C. Q. Lu, L. H. Pan, and J. P. Luo, "Renoprotective effect of Chinese chive polysaccharides in adenine-induced chronic renal failure," *International Journal of Biological Macromolecules*, vol. 106, pp. 988–993, 2018.

[57] L. Wang, J. Y. Oh, J. G. Je et al., "Protective effects of sulfated polysaccharides isolated from the enzymatic digest of *Codium fragile* against hydrogen peroxide-induced oxidative stress in *in vitro* and *in vivo* models," *Algal Research*, vol. 48, article 101891, 2020.

Research Article

Preclinical Evaluation of Safety, Pharmacokinetics, Efficacy, and Mechanism of Radioprotective Agent HL-003

Yahong Liu ⓘ**, Longfei Miao** ⓘ**, Yuying Guo** ⓘ**, and Hongqi Tian** ⓘ

Tianjin Key Laboratory of Radiation Medicine and Molecular Nuclear Medicine, Institute of Radiation Medicine, Peking Union Medical College and Chinese Academy of Medical Science, Tianjin 300192, China

Correspondence should be addressed to Hongqi Tian; tianhongqi@irm-cams.ac.cn

Amifostine is a radioprotector with high efficacy but poor safety, short half-life, no oral formulation, and poor compliance, which limits its application. With the increasing risk of exposure to radiation, the development of new radioprotective agents is critical. We previously synthesized a new amifostine derivative, the small molecule compound HL-003. In this study, we focused on evaluating the radioprotective properties of HL-003. Using the *in vitro* 2,2-diphenyl-1-picrylhydrazyl assay, we initially confirmed HL-003 as a strong antioxidant and demonstrated that its free radical scavenging activity was stronger than that of amifostine. Then, we performed an acute toxicity test, a 28-day toxicity test, a 30-day survival rate test, and a pharmacokinetic study, all of which provided aggregate evidence that HL-003 functioned as a small molecule radioprotector with high efficacy, a favorable safety profile, a long half-life, and oral administration. The intestinal radioprotective mechanism of HL-003 was explored in male C57 mice after abdominal irradiation by analyzing intestinal tissue samples with hematoxylin-eosin staining, immunohistochemistry, TUNEL staining, and immunofluorescence detection. The results showed that HL-003 protected intestinal DNA from radiation damage and suppressed the expression of phosphorylated histone H2AX, phosphorylated p53, and the apoptosis-related proteins caspase-8 and caspase-9, which contributed to maintaining the normal morphology of the small intestine and provided insights into the mechanism of radioprotection. Thus, HL-003 is a small molecule radioprotector with a potential application in radiation medicine.

1. Introduction

The civilian population is at an increased risk of radiation exposure due to the increased possibility of nuclear weapon explosion, destruction of nuclear facilities, exposure to radioactive materials, terrorist attacks, and nuclear accidents, all of which can have a catastrophic impact on public health [1]. Acute radiation syndrome (ARS) occurs when the intensity of the whole-body or partial-body irradiation is greater than 1 Gy. The main clinical manifestations are hematopoiesis (2–6 Gy), along with the gastrointestinal (6–8 Gy) and cerebrovascular syndrome (>8 Gy) [2–4]. In the past 60 years, despite significant scientific and technological advances in the development of safe, nontoxic, and effective radiation strategies for ARS, the U.S. Food and Drug Administration has not approved any drugs [5]. At present, radiation countermeasures can be divided into three categories: radiopro-

tective agents administered before exposure to prevent damage, radiation mitigators applied shortly after radiation exposure but before the appearance of radiation symptoms to accelerate recovery or repair, and radiation therapeutics or treatments given after the onset of symptoms to stimulate repair or regeneration [6]. Our research was aimed at radioprotective agents.

Previous reports indicated that the mechanism of radiation injury is closely associated with the production of reactive oxygen species (ROS), causing oxidative damage to proteins, lipids, and DNA, and activates activating signal transduction pathways [7–9]. Thus, using antioxidants for radioprotection is a critical medical countermeasure. Amifostine is the most active small molecule radioprotector that was developed by Walter Reed Army Institute of Research in 1959 to protect soldiers against the damage caused by nuclear radiation [5, 10, 11]. However, its application is

severely limited due to its short half-life, its administration by injection, the lack of an oral formulation, poor compliance, and serious side effects, including nausea, vomiting, and hypotension [12, 13].

To obtain radioprotectors with fewer side effects than amifostine, a variety of amino mercaptan analogs were designed and synthesized, including β-aminoethyl isothiourea (AET), N-acetyl-L-cysteine (NAC), N-2-mercaptopropionylglycine (MPG), diethyldithiocarbamate (DDC), 2,2-dimethylthiazolidine, and PrC-210 [14–16]. However, the radioprotective effect of these compounds still needs to be improved, except for PrC-210 [17]. Furthermore, although well-known natural antioxidants, such as curcumin, resveratrol, vitamin C, and red ginseng, have low toxicity and high tolerability, their radioprotection is less effective than that of amifostine [18–21]. Hence, there is an urgent need to develop oral small molecule radioprotectors with high efficiency and low toxicity.

We previously developed a new small molecule, HL-003, with 100% intellectual property rights [22]. In the current study, we initially used a cell-free system to investigate the antioxidant activity of HL-003 and its protective effect against oxidative damage of DNA. We then systematically evaluated the safety, efficacy, and pharmacokinetic (PK) characteristics of HL-003, including its ability to cross the blood-brain barrier (BBB). Finally, we studied the radioprotection mechanism of HL-003 in radiation-induced small intestinal injury. Our analysis indicated that the small molecule antioxidant HL-003 has a potential clinical value as a radioprotectant against ARS.

2. Materials and Methods

2.1. Animals. Male C57BL/6 mice (21–22 g), male ICR mice (21–22 g), and male SD rats (200–300 g) were purchased from SPF HFK Bioscience Co., Ltd. (Beijing, China), JOINN Laboratories (Beijing, China), and Charles River Laboratories (Beijing, China), respectively. All experimental animals were maintained in an accredited animal facility according to the guidelines of the National Animal Welfare Law of China and the NIH Guide for the Care and Use of Laboratory Animals. All animal procedures were approved by the Institutional Animal Care and Use Committee of the Institute of Radiation Medicine, Chinese Academy of Medical Science (permit number: 2017053).

2.2. 2,2-Diphenyl-1-picrylhydrazyl (DPPH) Free Radical Scavenging Test. DPPH (CAS No. 1898-664) was precisely weighed (6.4 mg) and fully dissolved in 32 mL anhydrous ethanol to prepare a stock solution for storage at 4°C. Before the experiment, the stock solution was diluted to 50 μg/mL. HL-003 (10 mg) was dissolved with 1 mL ddH$_2$O and twofold serially diluted to obtain working solutions of 10, 5, 2.5, 1.25, 0.625, 0.3125, 0.15625, 0.078125, and 0.0390625 mg/mL. Aliquots of 180 μL DPPH ethanol solution were dispensed on a 96-well plate (No. 14319035; Corning Inc., Corning, NY, USA) and mixed with 20 μL aliquots of HL-003 at different concentrations. Control samples contained 180 μL ethanol solution mixed with 20 μL HL-003 solution at different concentrations. Each sample was prepared and processed in trip-

licate. The test was performed by incubating the samples in the dark for 30 min at room temperature. The samples were analyzed by measuring the absorbance at 515 nm using a microplate reader (SM600, Shanghai Utrao Medical Instrument Co., Ltd.).

2.3. Acute Toxicity Test. A total of 88 male C57BL/6 mice were randomly assigned to the acute toxicity test groups. Sixty mice were divided into six HL-003 groups (10 mice per group). Each group received a different HL-003 dose (1200, 1600, 1800, 2000, 2400, and 3200 mg/kg) by oral gavage. Eighteen mice were treated with amifostine (No. 112901-68-5; Jiangsu Aikon Biopharmaceutical R&D Co., Ltd.). The mice were divided into three groups (6 mice per group), each of which received a different amifostine dose (600, 700, and 800 mg/kg) by oral gavage. In the control group (10 mice), oral gavage was performed to administer the HL-003 vehicle containing 85% of a 20% hydroxypropyl-β-cyclodextrin solution (HP-β-CD, No. 20190414; Zhiyuan Biotechnology) and 15% Solutol HS-15 (HF08982; Shenzhen hiboled Century Biotechnology Co., Ltd.). The toxicity of the treatments and the death of mice were monitored and recorded for 14 days postadministration. All surviving mice were euthanized at the end of the experiment.

2.4. Long-Term Toxicity Test. A total of 50 male C57BL/6 mice were randomly assigned to the long-term toxicity test groups. Forty mice were divided into four HL-003 groups (10 mice per group). For 28 days, each treatment group received a different HL-003 dose (800, 1000, 1200, and 1600 mg/kg) by oral gavage. The control group (10 mice) received the HL-003 vehicle solution for 28 days by oral gavage. The toxicity of the treatments and the death of mice were observed and recorded for 28 days. All surviving mice were euthanized at the end of the experiment.

2.5. Radioprotective Efficacy of Orally Administered HL-003 and Amifostine. Fifty-two male C57BL/6 mice were randomly divided into seven groups: the control group ($n = 7$), IR 8 Gy group ($n = 7$), HL-003 800 mg/kg ($n = 7$), HL-003 1200 mg/kg ($n = 7$), HL-003 1600 mg/kg ($n = 7$), amifostine 200 mg/kg ($n = 7$), and amifostine 500 mg/kg ($n = 10$). HL-003 was orally administered 1 h before the 8 Gy whole-body irradiation (WBI) in all HL-003 groups. In the amifostine groups, a dose of 200 or 500 mg/kg amifostine was orally administered 0.5 or 1 h before the 8 Gy WBI, respectively. In the IR 8 Gy group, the HL-003 vehicle solution was orally administered 1 h before the 8 Gy WBI. In the control group, the HL-003 vehicle solution was orally administered without radiation exposure. A ^{137}Cs source enclosed in an Exposure Instrument Gammacell-40 (Atomic Energy of Canada Limited, Chalk River, ON, Canada) was used as the radiation source. The mice were continuously monitored for 30 days after irradiation. The death of mice was recorded, and the survival curve was generated using GraphPad Prism 6.0 software.

2.6. Screening for the Optimal Time to Perform Oral HL-003 Administration. Sixty male C57BL/6 mice were randomly divided into six groups (10 mice per group): the control

group, IR 8 Gy group, HL-003 0.5 h group, HL-003 1 h group, HL-003 2 h group, and HL-003 4 h group. HL-003 (1600 mg/kg) was orally administered 0.5, 1, 2, or 4 h before the 8 Gy WBI. In the IR 8 Gy group, the HL-003 vehicle solution was orally administered 1 h before the 8 Gy WBI. In the control group, the HL-003 vehicle solution was orally administered without irradiation. The mice were continuously monitored for 30 days after irradiation. The death of mice was recorded, and the survival curve was generated using GraphPad Prism 6.0 software.

2.7. Radioprotective Efficacy of HL-003 at 10 Gy. Fifty male C57BL/6 mice were randomly divided into five groups (10 mice per group): the control group, IR 10 Gy group, HL-003 3 h group, HL-003 4 h group, and HL-003 6 h group. HL-003 (1600 mg/kg) was orally administered 3, 4, and 6 h before the 10 Gy WBI. In the IR 10 Gy group, the HL-003 vehicle solution was orally administered 4 h before the 10 Gy WBI. In the control group, the HL-003 vehicle solution was orally administered without irradiation. The mice were continuously monitored for 30 days after irradiation. The death of mice was recorded, and the survival curve was generated using GraphPad Prism 6.0 software.

2.8. PK Study of HL-003. Six male SD rats were randomly divided into two groups (3 rats per group), receiving a dose of either 100 mg/kg HL-003 by intravenous (i.v.) injection or 400 mg/kg HL-003 per os (p.o.). Blood samples were collected at 0.08, 0.25, 0.5, 1, 2, 4, 8, and 24 h after HL-003 administration (i.v. or p.o.). Aliquots of $50 \mu L$ plasma were derived from each blood sample. The plasma aliquots were loaded on a 96-well plate and mixed with $250 \mu L$ acetonitrile (WXBC4001V; Sigma-Aldrich, St. Louis, MO, USA). The plate was swirled and centrifuged at 400 rpm for 20 min. Each supernatant $(150 \mu L)$ was mixed with $150 \mu L$ of 0.1% formic acid (C1728048; Aladdin) and swirled for 10 min. Aliquots of $10.0 \mu L$ per sample were injected and analyzed by liquid chromatography-tandem mass spectrometry (LC/MS/MS, TQU335, Thermo Scientific, Wilmington, MA, USA).

2.9. BBB Permeability Evaluation of HL-003. At 0.25, 0.5, 1, 2, 3, 4, 6, and 8 h after male ICR mice received an oral dose of 400 mg/kg HL-003, whole blood aliquots of approximately $200 \mu L$ were collected in blood collection vessels containing EDTA, and brain tissue samples were recovered by necropsy. The collected blood was placed on ice and centrifuged at 4000 rpm for 20 min. The plasma was separated into 1.5 mL EP tubes. After the mice were euthanized, the brains were quickly removed. The residual blood on the brain tissue was cleaned with ice water, and the residual water on the brain tissue was dried with dry medical gauze. After weighing, the brain and plasma samples were stored at -80°C for testing. Samples were analyzed by LC/MS/MS (TQU335, Thermo Scientific).

2.10. Analysis of the Protective Mechanism of HL-003 against Intestinal Irradiation. Nine male SD rats were randomly divided into three groups (3 rats per group): the control group, IR group, and HL-003+IR group. The rats in the IR group received 15 Gy abdominal irradiation (ABI). In the

HL-003+IR group, a dose of 1600 mg/kg HL-003 was orally administered 4 h before the 15 Gy ABI. Five days after the IR, all rats were sacrificed to collect small intestinal tissue for mechanism analysis.

2.11. Hematoxylin and Eosin (He) Staining. Tissue samples of the small intestine were fixed in 4% paraformaldehyde, embedded in paraffin, and cut into $4 \mu m$ sections. The sections were dewaxed with xylene, stained with HE, and analyzed with a microscope (Olympus America, Melville, NY, USA).

2.12. Immunohistochemistry Analysis. Tissue samples of the small intestine were fixed in 4% paraformaldehyde, embedded in paraffin, cut into $4 \mu m$ sections, and dewaxed with xylene. The sections were evenly covered with goat serum and sealed for 30 min at room temperature. After discarding the sealing fluid, the slices were incubated overnight at 4°C with a primary antibody at an appropriate dilution, including anti-Lgr5 antibody (1:300, bs-20747R; Bioss), anti-lysozyme antibody (1:100, ab108508; Abcam), and anti-Ki67 antibody (1:300, ab15580; Abcam), followed by incubation with secondary antibodies conjugated to peroxidase for 50 min at room temperature. Subsequently, the sections were stained with $3,3'$-diaminobenzidine (DAB) and hematoxylin for microscopic analysis (OLYMPUS DP26). Hematoxylin stained the nuclei blue, and DAB produced a brown stain for positive expression of the targeted proteins.

2.13. TUNEL Assay. Tissue samples of the small intestine were fixed in 4% paraformaldehyde, embedded in paraffin, cut into $4 \mu m$ sections, and dewaxed with xylene. The sections were processed with a TUNEL kit (*In Situ* Cell Death Detection Kit, 11684817910; Roche), and the images were analyzed with a fluorescence microscope (OLYMPUS BX51).

2.14. Immunofluorescence Analysis. Tissue samples of the small intestine were fixed in 4% paraformaldehyde, embedded in paraffin, cut into $4 \mu m$ sections, and dewaxed with xylene. The sections were evenly covered with goat serum and sealed for 30 min at room temperature. After discarding the sealing fluid, the slices were incubated overnight at 4°C with a primary antibody at an appropriate dilution, including anti-γ-H2AX antibody (1:100, bs-3185R; Bioss), anti-p53 antibody (1:100, ab26; Abcam), anti-caspase-8 antibody (1:50, ab25901; Abcam), or anti-caspase-9 antibody (1:100, ab52298; Abcam), followed by incubation with secondary antibodies for 50 min at room temperature. Subsequently, the nuclei were restained using DAPI and analyzed under a microscope (OLYMPUS BX51). Hematoxylin stained the nuclei blue, and DAB produced a brown stain for positive expression of the targeted proteins. DAPI-stained nuclei were blue under UV excitation, and the positive expression of targeted proteins was detected as a red or green light signal, depending on the fluorescein label.

2.15. Statistical Analysis. All data were expressed as mean ± SD (standard deviation). The survival rates were analyzed by applying the Kaplan-Meier method, and mean comparisons were performed using the unpaired *t*-test. Statistical

analysis was performed using GraphPad Prism 6.0, and the ImageJ 1.42q software was used for quantitative analysis of immunofluorescence images. Statistical significance was set at $p < 0.05$.

3. Results

3.1. HL-003 Is a Strong Free Radical Scavenger In Vitro. Because HL-003 was designed as an amino mercaptan antioxidant, we initially evaluated its antioxidant capacity *in vitro* using the DPPH assay. The results showed that HL-003 efficiently scavenged DPPH within 30 min in a concentration-dependent manner (Figure 1), which proved that HL-003 is a powerful free radical scavenger with strong antioxidant activity.

3.2. HL-003 Has a Better Safety Profile than Amifostine. Since HL-003 was designed and developed as an oral ARS-protective agent, we evaluated its oral safety by an acute toxicity test and a 28-day long-term toxicity test (Tables 1 and 2). The acute toxicity test showed that the maximum tolerated doses (MTDs) of HL-003 and amifostine were 1800 and 600 mg/kg in mice, indicating that HL-003 was better tolerated than amifostine. In the long-term toxicity test, HL-003 had a 28-day MTD of 1000 mg/kg, which indicated that the compound had a strong safety profile. The mortality rate in the acute and long-term toxicity test control groups was 0% (data not shown).

3.3. Oral Administration of Different Doses of HL-003 Significantly Improved Survival in Irradiated Mice. To evaluate the potential of HL-003 as an oral ARS-protective agent, we assessed the radioprotective efficacy of different doses of oral HL-003 in male C57BL/6 mice (Figure 2 and Table S2). Thirty days after receiving 8 Gy WBI, the mice in the IR group had a survival rate of 0%. The survival rates in mice exposed to oral amifostine for 30 days were 28.6% and 30% in the amifostine 200 mg/kg and 500 mg/kg groups, respectively. The survival in the amifostine groups did not significantly differ from that in the IR group. Interestingly, oral administration of different HL-003 doses significantly increased the survival of irradiated mice, which had survival rates of 57% ($p < 0.05$), 57% ($p < 0.05$), and 85.71% ($p < 0.01$) in the HL-003 800, 1200, and 1600 mg/kg groups, respectively.

3.4. Optimal Time for Oral HL-003 Administration Was 4 h before Irradiation. We used the best dose of 1600 mg/kg to determine the optimal time for HL-003 administration in male C57BL/6 mice. In the IR group, the mice began to die 9 days after receiving 8 Gy WBI. The last mouse in this group died 13 days postirradiation, and the 30-day survival rate was 0%. Administration of HL-003 at 0.5, 1, and 2 h before irradiation delayed the death time of the first animal from 9 days postirradiation to 12, 14, and 14 days, respectively, and the 30-day survival rate was 10%, 60%, and 60%, respectively. The survival curves of the HL-003 treatment groups differed significantly from that of the IR group ($p < 0.0001$). More importantly, no mouse died when HL-003 was administered 4 h prior to irradiation, and the survival increased to 100% in
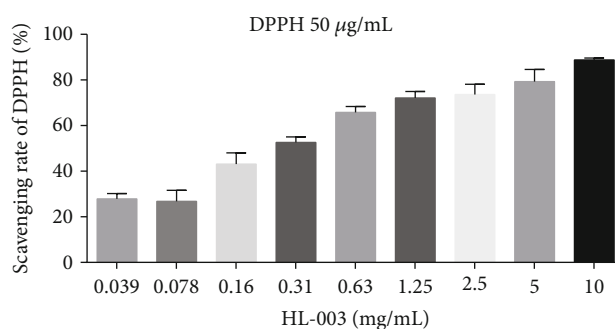
FIGURE 1: The strong free radical scavenging capability of HL-003 was concentration dependent. Quantitative histogram analysis of free radical scavenging by HL-003 in a cell-free system.

irradiated mice. Thus, the optimal HL-003 administration time was 4 h before 8 Gy WBI (Figure 3, Table S3).

3.5. Oral Administration of HL-003 Increased the Radiation Tolerance Dose in Mice. In this experiment, we tested whether HL-003 could improve the survival rate in mice under high-dose irradiation. The results showed that administering a dose of 1600 mg/kg HL-003 at 3, 4, and 6 h prior to irradiation significantly improved the survival rate in mice exposed to 10 Gy WBI ($p < 0.05$, Figure 4) Although the survival rate of mice irradiated from 8 Gy to 10 Gy decreased from 100% to 40% under the same administration conditions of HL-003 (1600 mg/kg, 4 h before irradiation), it was improved to some extent under the irradiation dose of 10 Gy. The specific values are shown in Supporting Information Table S4.

3.6. Evaluation of PK Parameters of HL-003. We assessed the oral efficacy of HL-003 and evaluated its PK parameters and oral bioavailability in male SD rats (Table 3). The plasma half-life ($T_{1/2}$) values for HL-003 after i.v. injection and p.o. administration were 0.67 ± 0.28 and 6.65 ± 2.49 h, respectively. After p.o. administration of 400 mg/kg HL-003, the maximum drug concentration (C_{max}) in plasma was 21580.4 ± 8971.2 ng/mL, and the time to reach the peak value (T_{max}) was 0.28 ± 0.21 h. Moreover, the bioavailability of HL-003 was up to $42.29 \pm 6.68\%$.

In addition, the BBB was evaluated by ICR mice. The parameters obtained in the experiment were calculated using the Winnonlin 7.0 noncompartment model (Figure 5 and Table S5). The AUC in plasma was 24627 ± 2418 hr*ng/mL, and the AUC in brain tissue was 4536 ± 780 hr*ng/g. The calculated B/P ratio was $18.40 \pm 2.23\%$, indicating that HL-003 could cross into the brain tissue through the BBB.

3.7. HL-003 Alleviated Radiation-Induced Morphological Injury of Small Intestine. We evaluated the protective effect of HL-003 on radiation-induced intestinal injury in male C57BL/6 mice to explore the mechanism of radioprotection. We evaluated the effect of HL-003 on the intestinal morphology in mice 3 days after ABI with 15 Gy by HE staining of tissue samples (Figure 6). In contrast to the normal morphology of the nonirradiated intestinal tissue, the small intestinal villi

TABLE 1: Acute toxicity test of HL-003 and amifostine in C57BL/6 mice.

mg/kg	Survival rate								
	600	700	800	1200	1600	1800	2000	2400	3200
Amifostine	100% (6/6)	83.33% (5/6)	66.67% (4/6)	NA	NA	NA	NA	NA	NA
HL-003	NA	NA	NA	100% (10/10)	100% (10/10)	100% (10/10)	50% (5/10)	40% (4/10)	0% (0/10)

NA: not available. NA indicates that no acute toxicity test was conducted at this dose. (n_1/n_2): n_1 represents the number of surviving mice 14 days postadministration and n_2 represents the number of mice in each group preadministration.

TABLE 2: 28-day long-term toxicity test of HL-003 in C57BL/6 mice.

mg/kg	Survival rate			
	800	1000	1200	1600
HL-003	100% (10/10)	100% (10/10)	80% (8/10)	50% (5/10)

(n_1/n_2): n_1 represents the number of surviving mice 14 days postadministration and n_2 represents the number of mice in each group preadministration.
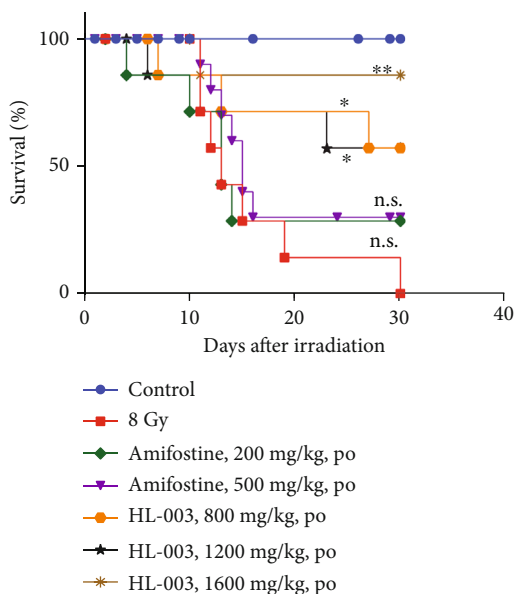
FIGURE 2: Oral administration of different HL-003 doses improved the survival rate in irradiated mice, whereas oral amifostine had no beneficial effect. Male C57BL/6 mice received oral HL-003 or amifostine 1 or 0.5 h before WAI. Kaplan-Meier survival analysis of mice exposed to 8.0 Gy ($^*p < 0.05$, $^{**}p < 0.01$; group size, $n = 7$ or $n = 10$).

of the irradiated mice were broken, and the crypt was damaged. Oral administration of HL-003 significantly improved the morphological changes in the small intestine of irradiated mice, which resembled that of nonirradiated mice.

3.8. HL-003 Promotes Proliferation, Differentiation, and Regeneration of Crypt Cells in Irradiated Male C57BL/6 Mice.
The intestinal epithelium can continuously renew itself to maintain homeostasis and rapidly regenerate after injury [23, 24]. In this study, immunohistochemical staining was performed to assess the effect of HL-003 on proliferation and differentiation of crypt cells and its effect on maintaining intestinal cell regeneration. Lgr5$^+$ intestinal stem cells (ISCs),
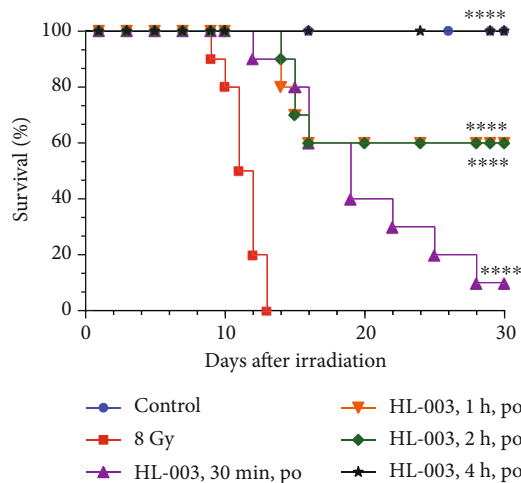
FIGURE 3: The optimal administration time of oral HL-003 was 4 h before irradiation. The 30-day survival rate of each group was evaluated after oral administration of 1600 mg/kg HL-003 at 0.5, 1, 2, and 4 h before irradiation. Kaplan-Meier survival analysis of mice exposed to 8.0 Gy ($^{****}p < 0.0001$; group size, $n = 10$).

lysozyme$^+$ Paneth cells, and Ki67$^+$ transient amplifying cells (TACs) were evaluated at 3 days after 15 Gy ABI (Figure 7). Compared with the status in the control group, irradiation severely reduced the numbers of Lgr5$^+$ ISCs, Ki67$^+$ TACs, and lysozyme$^+$ Paneth cells in the IR group, whereas these cell types were significantly increased in the small intestinal tissue of irradiated mice treated with HL-003, indicating that HL-003 increased the proliferation, differentiation, and regeneration capability of intestinal crypt cells in these mice.

3.9. HL-003 Reduced Apoptosis in Small Intestine Tissue of Irradiated Male C57BL/6 Mice.
The effect of HL-003 on apoptosis of small intestine tissue cells in irradiated mice was evaluated by TUNEL analysis (Figure 8). We found that the IR group had more apoptotic small intestinal cells than the control group, but administration of HL-003 significantly reduced the apoptosis of small intestinal cells in irradiated mice, and the difference was statistically significant ($p = 0.020$).

3.10. HL-003 Protects DNA Double Strands against Radiation Damage.
To investigate whether HL-003 protected DNA from radiation damage, the expression of the DNA damage marker γ-H2AX was analyzed in irradiated male C57BL/6 mice [25]. The results are shown in Figure 9. Compared with the γ-H2AX expression status in the control group, the expression of γ-H2AX was stimulated in small intestinal cells

FIGURE 4: HL-003 increased the survival rate in high-dose irradiated mice. The 30-day survival rate of each group was evaluated after oral administration of 1600 mg/kg HL-003 at 3, 4, and 6 h before irradiation. Kaplan-Meier survival analysis of mice exposed to 10.0 Gy ($^*p < 0.05$, $^{**}p < 0.01$; group size, $n = 10$).

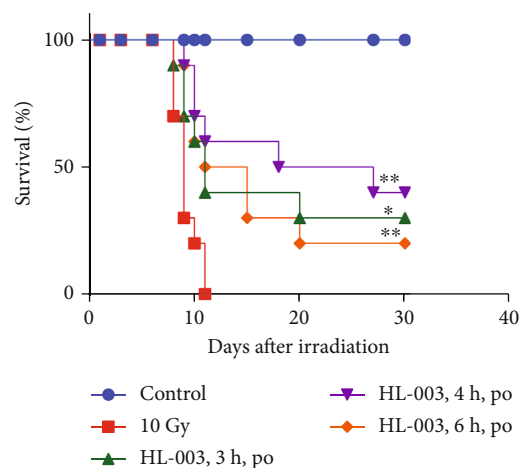TABLE 3: PK parameters of HL-003 in SD rats. SD rats (group size, $n = 3$) received an HL-003 dose of 100 mg/kg i.v. or 400 mg/kg p.o., and blood samples were collected from 0 to 24 h for PK parameter analysis.

PK parameter	Mean	Standard deviation
PK parameters of HL-003 in male SD rats after a dose of 100 mg/kg i.v.		
HL_Lambda_z ($T_{1/2}$, h)	0.67	0.28
C_{max} (ng/mL)	77510.6	2202.1
AUC$_{last}$ (h*ng/mL)	30589.1	1199.2
AUCINF_pred (h*ng/mL)	30606.8	1198.3
MRTlast (h)	0.32	0.05
Vz_pred (L/kg)	3.15	1.26
Cl_pred (L/h/kg)	3.27	0.13
Λz calculation time range (h)	NA	NA
PK parameters of HL-003 in male SD rats after a dose of 400 mg/kg p.o.		
HL_Lambda_z ($T_{1/2}$, h)	6.65	2.49
T_{max} (h)	0.28	0.21
C_{max} (ng/mL)	21580.4	8971.2
AUC$_{last}$ (h*ng/mL)	51744.1	8389.0
AUCINF_pred (h*ng/mL)	55842.4	6086.6
MRTlast (h)	5.71	0.70
Vz_F_pred (L/kg)	70.55	32.64
Cl_F_pred (L/hr/kg)	7.22	0.82
λz calculation time range (h)	NA	NA
F (%)	42.29	6.86

NA: not available. NA means that the data has not been calculated.

of irradiated mice, whereas administration of HL-003 suppressed the γ-H2AX expression in small intestinal cells of irradiated mice, and the difference was significant
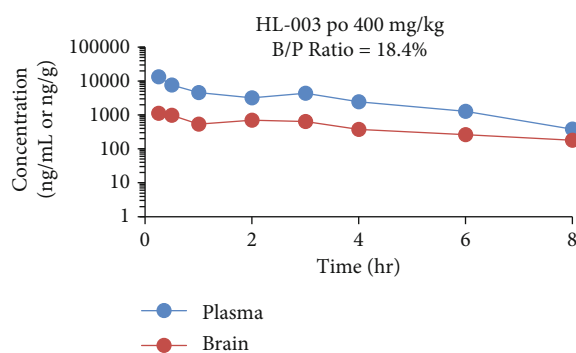
FIGURE 5: HL-003 concentration in plasma (ng/mL) and brain tissue (ng/g) of ICR mice.
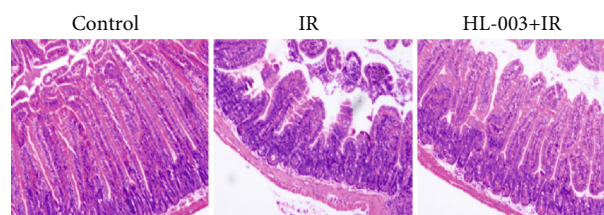
FIGURE 6: HL-003 improves the morphological changes of small intestine tissue in irradiated mice. Microphotographs show the cross-sectional structure of the small intestine (HE staining).

($p = 0.014$). These results suggested that HL-003 alleviated the irradiation-induced DNA damage.

3.11. HL-003 Inhibited Intestinal Cell Apoptosis in Irradiated Mice by Suppressing Apoptosis-Related Pathway Proteins. To further study the mechanism of the protective effect of HL-003 on radiation-induced intestinal injury, the expression levels of apoptosis-related pathway proteins p53 and caspase-8/9 were assessed by immunofluorescence (Figure 10). The small intestine of the IR group had higher expression levels of p53 and the caspase-8 and caspase-9 proteins than that of the control group. However, HL-003 treatment of irradiated mice significantly suppressed the expression levels of p53 ($p = 0.0009$), caspase-8 ($p = 0.003$), and caspase-9 ($p < 0.0001$), compared with those levels in irradiated male C57BL/6 mice without further treatment. These results suggested that HL-003 exerted a protective effect on radiation-induced intestinal injury via the p53 pathway and the mitochondrial apoptosis pathway.

4. Discussion

To date, the potential radiation hazard has become a serious public health challenge due to the rapid development and wide application of the nuclear industry [26]. Especially radioprotectors should be safe, effective, and easy-to-administer because they should be given to military personnel and first responders prior to entering a known radiation area [27]. During the Cold War, the Walter Reed Army Institute of Research in the United States developed a powerful, highly radioprotective antioxidant containing sulfhydryl

(a)

(b)

(c)

(d)
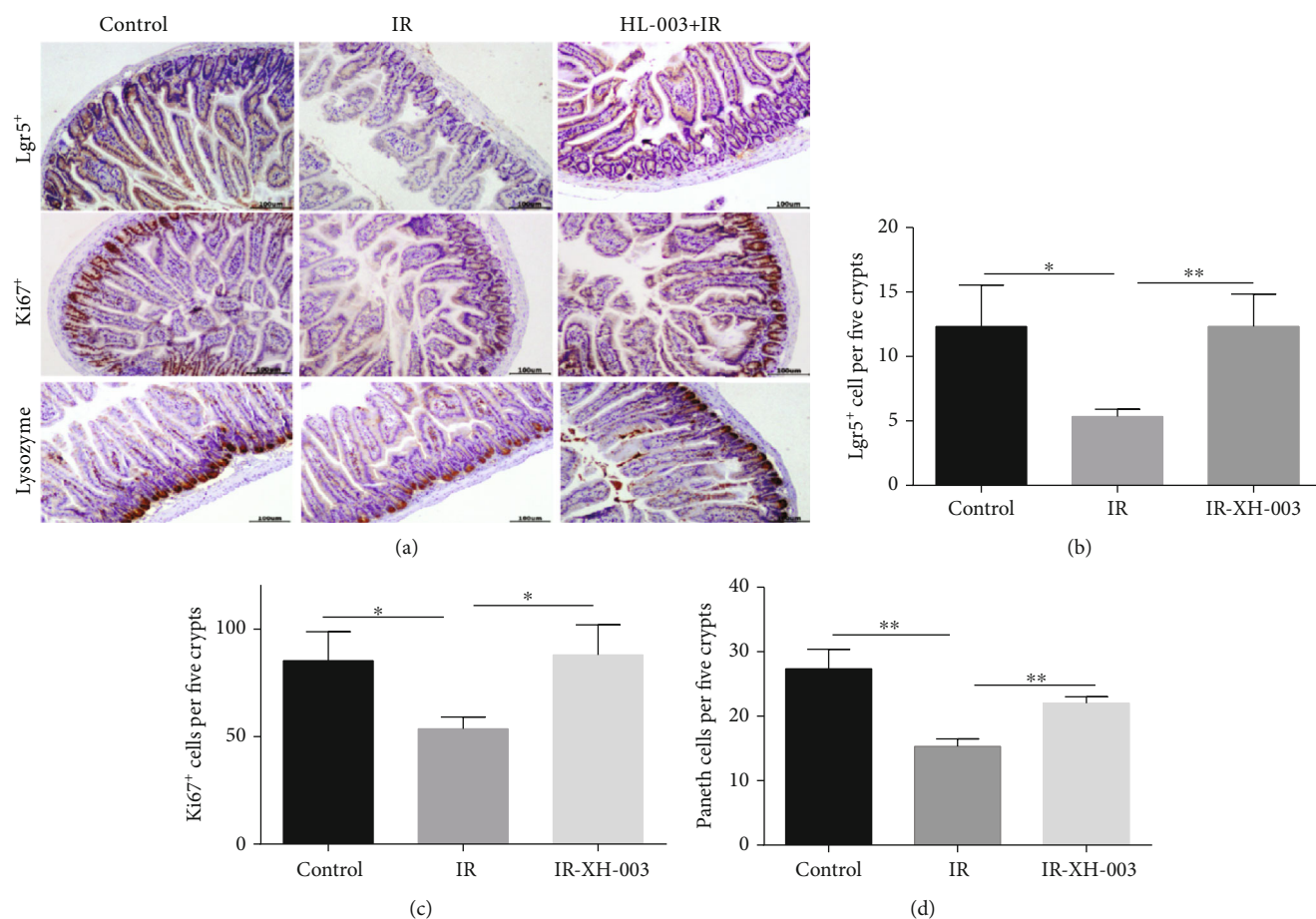
Figure 7: HL-003 promoted the proliferation, differentiation, and regeneration of crypt cells after ABI. (a) Microphotographs of Lgr5$^+$, Ki67$^+$, and lysozyme$^+$ immunohistochemical staining. (b) Quantitative histogram analysis of Lgr5$^+$ cells. (c) Quantitative histogram analysis of Ki67$^+$ cells. (d) Quantitative histogram analysis of lysozyme$^+$ cells. $^*p < 0.05$, $^{**}p < 0.01$, $^{***}p < 0.001$, and $^{****}p < 0.0001$.

groups, named amifostine (or WR2721). However, its application is limited because of its serious side effects, short half-life, nonoral nature, and other disadvantages [28, 29]. The search for a radioprotective agent with a long half-life, oral administration, and no obvious side effects on the human body has always been an important issue in the field of radiation medicine [30, 31].

We previously used the structure of amifostine to design and synthesize a small molecule compound containing a sulfhydryl group, HL-003, for which we have 100% independent intellectual property rights. In the current study, we initially evaluated the antioxidant capacity of HL-003 in a cell-free system *in vitro*. We found that the strong free radical scavenging activity of HL-003 was concentration dependent. The acute toxicity test showed that the safety profile of HL-003 (MTD = 1800 mg/kg) was better than that of amifostine (MTD = 600 mg/kg), and the MDT in the 28-day long-term toxicity test of oral HL-003 for 28 days was 1000 mg/kg, indicating that this compound was a highly safe antioxidant.

By evaluating the effects of different HL-003 doses on the 30-day survival rate in irradiated mice, we observed that oral HL-003 administration improved survival among irradiated mice, whereas oral amifostine did not provide an effective

radioprotection. Furthermore, we found that the right time for oral HL-003 administration was 4 h prior to an irradiation dose of 8 Gy. HL-003 still shows a certain radiation protective effect, although the effect under the irradiation dose of 10 Gy is weaker than that of 8 Gy. Therefore, HL-003 is a small molecule radioprotector with a good safety profile, high efficacy, and oral administration.

We further analyzed the PK characteristics of HL-003 *in vivo*. The plasma half-life of HL-003 administered intravenously ($T_{1/2} = 40.2 \pm 16.8$ min) and orally ($T_{1/2} = 6.65 \pm 2.49$ h) was longer than that of amifostine ($T_{1/2} = 10$ min). Its oral bioavailability was as high as 42.29%. Interestingly, HL-003 can cross the BBB and has a potential radioprotective effect on brain radiation damage. These results show that HL-003 is a radioprotective agent with a favorable safety profile, high efficacy, oral administration, and a long half-life. Specifically, in our preclinical studies, HL-003 had higher radioprotective efficacy than amifostine.

To further analyze the radioprotective properties of HL-003 in our study, its mechanism of protection against radiation-induced intestinal injury was assessed. The small intestine is very susceptible to irradiation, and radiotherapy patients are often affected by severe intestinal reactions, such

(a)

(b)
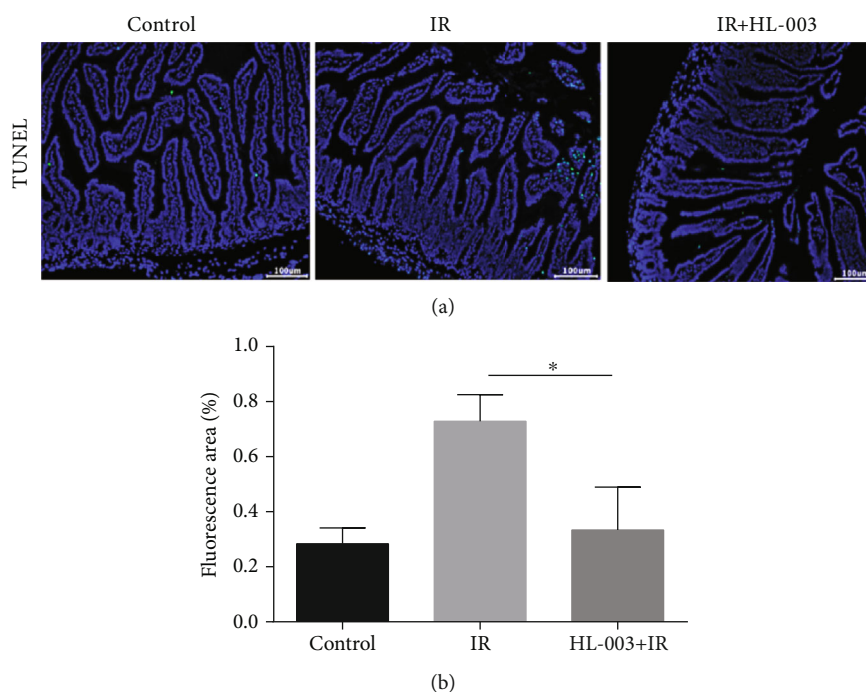
FIGURE 8: HL-008 reduced the apoptosis of small intestinal cells in irradiated mice. (a) Representative immunofluorescence images assessing apoptosis in tissue samples of the small intestine (green, apoptotic cells). (b) Quantitative histogram analysis of apoptosis ($^*p < 0.05$, $^{**}p < 0.01$, $^{***}p < 0.001$, and $^{****}p < 0.0001$).

(a)

(b)
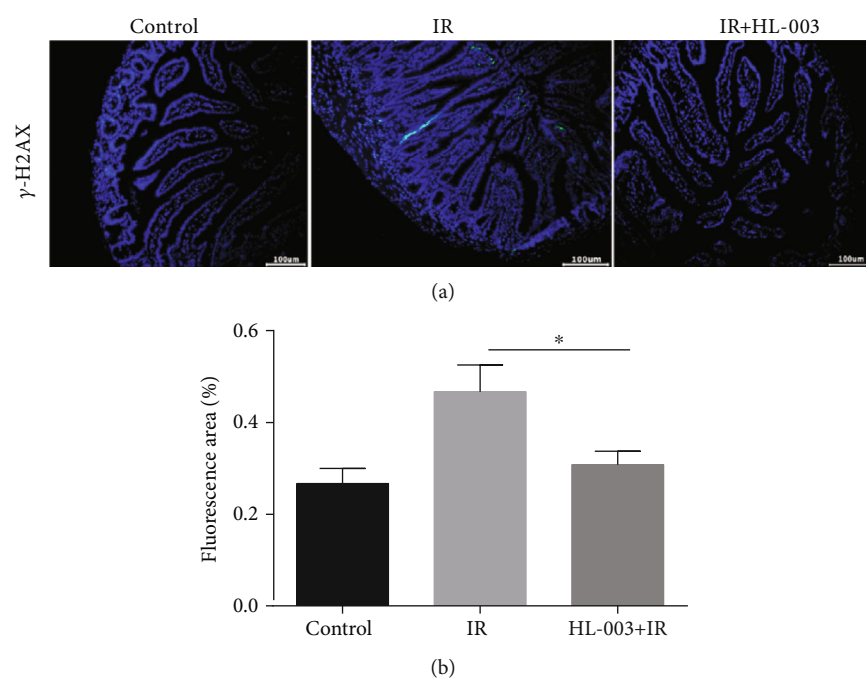
FIGURE 9: HL-003 suppressed the expression of DNA damage marker protein γ-H2AX in small intestinal cells of irradiated mice. (a) Representative immunofluorescence images for the expression of γ-H2AX in tissue samples of the small intestine (green, γ-H2AX). (b) Quantitative histogram analysis of the γ-H2AX positive signal ($^*p < 0.05$, $^{**}p < 0.01$, $^{***}p < 0.001$, and $^{****}p < 0.0001$).

as nausea, vomiting, and diarrhea, which seriously diminish the quality of life in those patients [32]. Unfortunately, there is no specific drug for radiation-induced intestinal injury in

clinical use [33]. Hence, the development of effective radio-protectors is a critical goal. Staining of intestinal tissue samples with HE revealed that HL-003 significantly improved

(a)

(b)

(c)   (d)
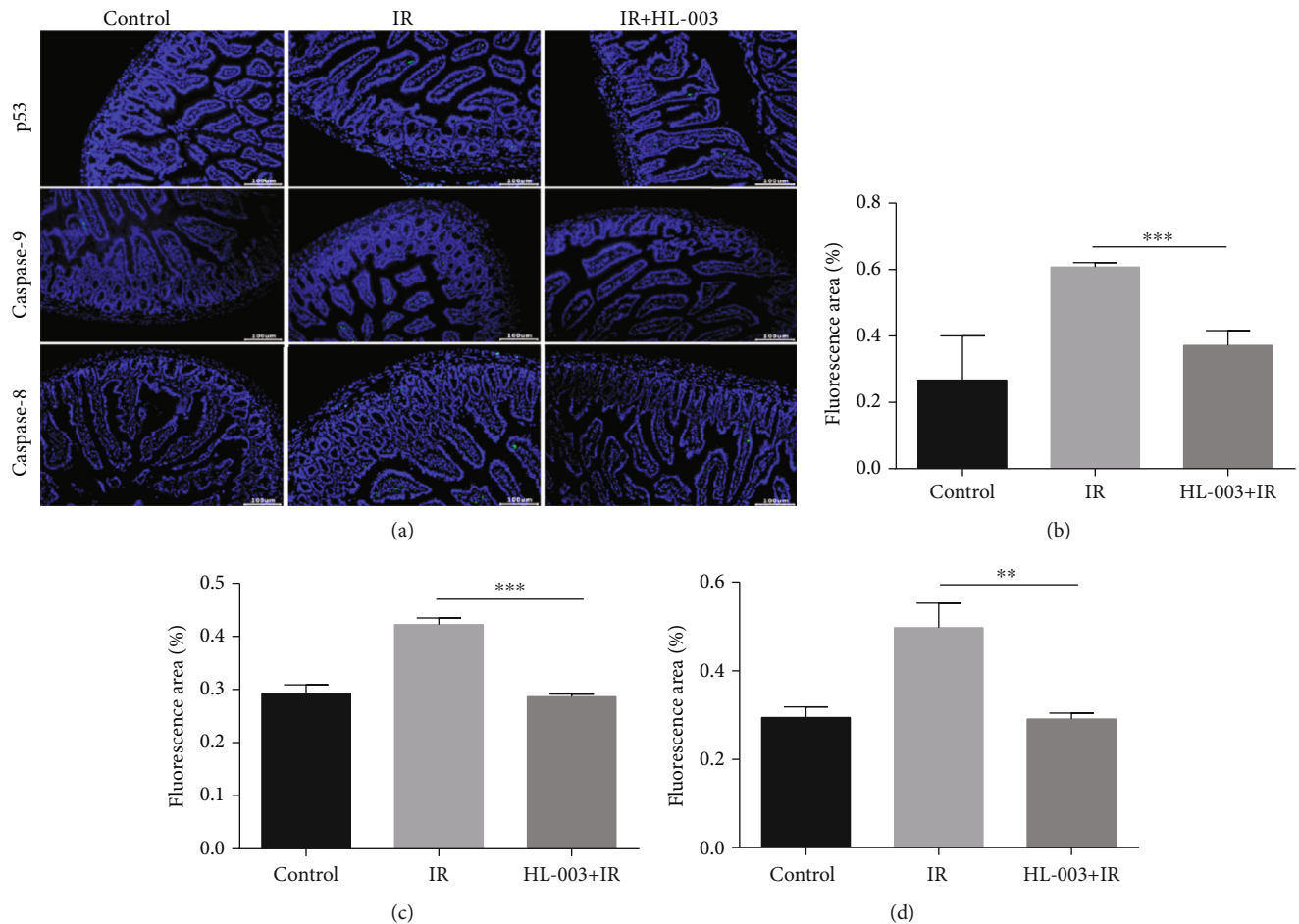
Figure 10: HL-003 suppressed the expression of apoptosis-related proteins p53, caspase-8, and caspase-9 in the small intestine of irradiated mice. (a) Representative immunofluorescence images for the expression of p53, caspase-8, and caspase-9 in tissue samples of the small intestine (green: p53, caspase-9, and -8). (b) Quantitative histogram analysis of p53 positive signal. (c) Quantitative histogram analysis of caspase-9 positive signal. (d) Quantitative histogram analysis of caspase-8 positive signal. ($^*p < 0.05$, $^{**}p < 0.01$, $^{***}p < 0.001$, $^{****}p < 0.0001$).

the intestinal morphological changes in irradiated mice, indicating that it was effective against radiation-induced intestinal injury.

The intestinal epithelium is the fastest self-renewing tissue in mammals that depends on self-renewal by intestinal epithelial stem cells located in the crypts to maintain the dynamic balance with the environment and to regenerate quickly after damage [34, 35]. ISCs renew themselves by expressing Lgr5, which is an intestinal stem cell marker. The Lg5^{+} ISCs are a known key factor in intestinal regeneration after radiation injury [36, 37]. In addition, Paneth cells, which are located at the bottom of crypt cells, maintain homeostasis of the intestinal environment by secreting lysosomes and other antibacterial proteins [38]. Interestingly, there is a positive correlation between the number of Paneth cells and the number of Lgr5^{+} stem cells [39]. The hyperplastic cells of the small intestinal epithelium can be identified due to the expression of the proliferation marker protein Ki67 [40]. We found that HL-003 significantly prevented the irradiation-induced decrease in Lgr5^{+}

ISCs, Ki67^{+} TACs, and lysozyme^{+} Paneth cells, and it promoted the regeneration, differentiation, and proliferation of intestinal epithelial cells and maintained homeostasis of the intestinal epithelium.

In this study, TUNEL staining analysis showed that HL-003 significantly reduced the apoptosis in the small intestine of irradiated mice. Immunofluorescence analysis was performed to explore the pathway related to apoptosis. It is known that radiation can directly induce DNA damage through ROS production, which mediates the activation of apoptosis-related pathways that can result in the loss of tissue and organ function [41]. Phosphorylated histone H2AX is an important marker of DNA double-strand breaks [42], which can promote the phosphorylation of p53, a proapoptotic factor [43]. Specifically, activated p53 can regulate DNA damage repair and cell cycle checkpoints. Moreover, it can promote the release of cytochrome c from the mitochondria, activate the caspase cascade, and induce cell apoptosis [44]. HL-003 treatment significantly lowered the levels of phosphorylated histone H2AX, phosphorylated p53, and activated caspase-

8 and caspase-9 in the intestine of mice after irradiation, indicating that HL-003 significantly reduced radiation-induced DNA damage, inhibited the activation of p53, blocked the caspase cascade reaction, and protected the small intestine from radiation injury.

5. Conclusion

In this study, we built on our earlier work on the small molecule antioxidant agent HL-003 by comprehensively evaluating the compound's safety, pharmacokinetics, and efficacy. We proved that HL-003 is an ideal radioprotective agent with a promising safety profile, high efficacy, oral administration, and a long half-life. We further investigated the mechanism of radioprotection by HL-003 against radiation-induced intestinal injury. We found that HL-003 provided radioprotection by promoting the proliferation, differentiation, and regeneration of the intestinal epithelium, protecting DNA from radiation damage, and inhibiting the activation of apoptosis-related pathways. Thus, HL-003 is a potential small molecule radioprotector.

Data Availability

The data used to support the findings of this study are available from the corresponding author upon request.

Conflicts of Interest

The authors confirm that there are no conflicts of interest.

Authors' Contributions

Hong-Qi Tian conceived and designed the experiments. Ya-Hong Liu and Longfei Miao performed the experiments. Ya-Hong Liu analyzed and interpreted the results and prepared the manuscript. Yuying Guo also contributed to manuscript preparation and data analysis. Yahong Liu and Longfei Miao are the co-first authors of this research paper.

Acknowledgments

Supplementary Materials

There are five tables included in the supplementary materials: The data for average percentage of DPPH scavenged by HL-003 at different concentrations is shown in Table S1; the data for radioprotective efficiency of HL-003 and amifostine orally administrated after 8 Gy irradiation is shown in Table S2; the data for radioprotective effect of HL-003 at different administration time points after 8 Gy irradiation is shown in Table S3; the data for radioprotective effect of HL-003 at different administration time points after 10 Gy irradiation is shown in Table S4; and

the PK parameters of HL-003 in ICR mice were shown in Table S5. (Supplementary materials)

References

[1] V. K. Singh, P. L. P. Romaine, and T. M. Seed, "Medical countermeasures for radiation exposure and related injuries," Health Physics, vol. 108, no. 6, pp. 607–630, 2015.

[2] E. J. Hall and A. J. Giaccia, "Radiobiology for the Radiobiologist" 6th edition, Lippincott Williams and Wilkins, Philadelphia, PA, 2006.

[3] N. Dainiak, "Medical management of acute radiation syndrome and associated infections in a high-casualty incident," Journal of Radiation Research, vol. 59, suppl_2, pp. ii54–ii64, 2018.

[4] J. P. Williams and W. H. McBride, "After the bomb drops: a new look at radiation-induced multiple organ dysfunction syndrome (MODS)," International Journal of Radiation Biology, vol. 87, no. 8, pp. 851–868, 2011.

[5] V. K. Singh, V. L. Newman, P. L. P. Romaine, S. Y. Wise, and T. M. Seed, "Radiation countermeasure agents: an update (2011 – 2014)," Expert Opinion on Therapeutic Patents, vol. 24, no. 11, pp. 1229–1255, 2014.

[6] H. B. Stone, J. E. Moulder, C. N. Coleman et al., "Models for evaluating agents intended for the prophylaxis, mitigation and treatment of radiation injuries Report of an NCI Workshop, December 3–4, 2003," Radiation Research, vol. 162, no. 6, pp. 711–728, 2004.

[7] J. L. Wei, B. Wang, H. H. Wang et al., "Radiation-induced normal tissue damage: oxidative stress and epigenetic mechanisms," Oxidative Medicine and Cellular Longevity, vol. 2019, Article ID 3010342, 11 pages, 2019.

[8] E. Vorotnikova, R. A. Rosenthal, M. Tries, S. R. Doctrow, and S. J. Braunhut, "Novel synthetic SOD/catalase mimetics can mitigate capillary endothelial cell apoptosis caused by ionizing radiation," Radiation Research, vol. 173, no. 6, pp. 748–759, 2010.

[9] P. Dent, A. Yacoub, P. B. Fisher, M. P. Hagan, and S. Grant, "MAPK pathways in radiation responses," Oncogene, vol. 22, no. 37, pp. 5885–5896, 2003.

[10] R. M. Johnke, J. A. Sattler, and R. R. Allison, "Radioprotective agents for radiation therapy: future trends," Future Oncology, vol. 10, no. 15, pp. 2345–2357, 2014.

[11] M. Z. Kamran, A. Ranjan, N. Kaur, S. Sur, and V. Tandon, "Radioprotective agents: strategies and translational advances," Medicinal Research Reviews, vol. 36, no. 3, pp. 461–493, 2016.

[12] V. K. Singh and T. M. Seed, "The efficacy and safety of amifostine for the acute radiation syndrome," Expert Opinion on Drug Safety, vol. 18, no. 11, pp. 1077–1090, 2019.

[13] M. King, S. Joseph, A. Albert et al., "Use of amifostine for cytoprotection during radiation therapy: a review," Oncology, vol. 98, no. 2, pp. 61–80, 2020.

[14] M. E. Crowe, C. J. Lieven, A. F. Thompson, N. Sheibani, and L. A. Levin, "Borane-protected phosphines are redox-active radioprotective agents for endothelial cells," Redox Biology, vol. 6, pp. 73–79, 2015.

[15] M. V. Vasin, I. B. Ushakov, and V. V. Antipov, "Potential role of catecholamine response to acute hypoxia in the modification of the effects of radioprotectors," Bulletin of Experimental Biology and Medicine, vol. 159, no. 5, pp. 597–600, 2015.

[16] M. V. Vasin, I. B. Ushakov, V. Y. Kovtun et al., "Pharmacological analysis of the therapeutic effect of radioprotectors cystamine and indralin in the capacity of radiomitigators," *Bulletin of Experimental Biology and Medicine*, vol. 162, no. 4, pp. 466–469, 2017.

[17] X. J. Li and H. Q. Tian, "Research progress in radioprotectors from the family of aminothiols," *China Medical Herald*, vol. 16, pp. 42–45, 2019.

[18] G. C. Jagetia, "Radioprotection and radiosensitization by curcumin," *Advances in Experimental Medicine and Biology*, vol. 595, pp. 301–320, 2007.

[19] H. Zhang, H. Yan, X. L. Zhou et al., "The protective effects of resveratrol against radiation-induced intestinal injury," *BMC Complementary and Alternative Medicine*, vol. 17, no. 1, article 1915, p. 410, 2017.

[20] H. Mozdarani and E. Nazari, "Frequency of micronuclei in 4–8 cell mouse embryos generated after maternal gamma-irradiation in the presence and in the absence of vitamin C," *Radiation and Environmental Biophysics*, vol. 46, no. 4, pp. 417–422, 2007.

[21] Y. J. Lee, J. Y. Han, C. G. Lee et al., "Korean Red Ginseng saponin fraction modulates radiation effects on lipopolysaccharide-stimulated nitric oxide production in RAW264.7 macrophage cells," *Journal of Ginseng Research*, vol. 38, no. 3, pp. 208–214, 2014.

[22] Y. H. Liu, K. Li, and H. Q. Tian, "Renoprotective effects of a new free radical scavenger, XH-003, against cisplatin-induced nephrotoxicity," *Oxidative Medicine and Cellular Longevity*, vol. 2020, 12 pages, 2020.

[23] C. Metcalfe, N. M. Kljavin, R. Ybarra, and F. J. de Sauvage, "_Lgr5_ $^+$ Stem Cells Are Indispensable for Radiation-Induced Intestinal Regeneration," *Cell Stem Cell*, vol. 14, no. 2, pp. 149–159, 2014.

[24] A. Negroni, S. Cucchiara, and L. Stronati, "Apoptosis, necrosis, and necroptosis in the gut and intestinal homeostasis," *Mediators of Inflammation*, vol. 2015, 10 pages, 2015.

[25] M. R. Pan, G. Peng, W. C. Hung, and S. Y. Lin, "Monoubiquitination of H2AX Protein Regulates DNA Damage Response Signaling," *The Journal of Biological Chemistry*, vol. 286, no. 32, pp. 28599–28607, 2011.

[26] X. N. Lin, L. F. Miao, X. X. Wang, and H. Q. Tian, "Design and evaluation of pH-responsive hydrogel for oral delivery of amifostine and study on its radioprotective effects," *Colloids and Surfaces. B, Biointerfaces*, vol. 195, p. 111200, 2020.

[27] A. C. Miller, R. Rivas, R. McMahon et al., "Radiation protection and mitigation potential of phenylbutyrate: delivered via oral administration," *International Journal of Radiation Biology*, vol. 93, no. 9, pp. 907–919, 2017.

[28] J. R. Kouvaris, V. E. Kouloulias, and L. J. Vlahos, "Amifostine: the first selective-target and broad-spectrum radioprotector," *The Oncologist*, vol. 12, no. 6, pp. 738–747, 2007.

[29] D. M. Brizel, T. H. Wasserman, M. Henke et al., "Phase III randomized trial of amifostine as a radioprotector in head and neck cancer," *Journal of Clinical Oncology*, vol. 18, no. 19, pp. 3339–3345, 2000.

[30] X. Yang, Y. P. Ding, T. J. Ji et al., "Improvement of the _in vitro_ safety profile and cytoprotective efficacy of amifostine against chemotherapy by PEGylation strategy," *Biochemical Pharmacology*, vol. 108, pp. 11–21, 2016.

[31] R. R. Patyar and S. Patyar, "Role of drugs in the prevention and amelioration of radiation induced toxic effects," *European Journal of Pharmacology*, vol. 819, pp. 207–216, 2018.

[32] P. Monti, J. Wysocki, A. van der Meeren, and N. M. Griffiths, "The contribution of radiation-induced injury to the gastrointestinal tract in the development of multi-organ dysfunction syndrome or failure," *The British Journal of Radiology*, vol. Supplement_27, no. 1, pp. 89–94, 2005.

[33] Y. Cheng, Y. P. Dong, Q. L. Hou et al., "The protective effects of XH-105 against radiation-induced intestinal injury," *Journal of Cellular and Molecular Medicine*, vol. 23, no. 3, pp. 2238–2247, 2019.

[34] B. J. Leibowitz, L. Wei, L. Zhang et al., "Ionizing irradiation induces acute haematopoietic syndrome and gastrointestinal syndrome independently in mice," *Nature Communications*, vol. 5, no. 1, p. 3494, 2014.

[35] F. Hugenholtz and W. M. de Vos, "Mouse models for human intestinal microbiota research: a critical evaluation," *Cellular and Molecular Life Sciences*, vol. 75, no. 1, pp. 149–160, 2018.

[36] W. Liu, Q. Chen, S. Wu et al., "Radioprotector WR-2721 and mitigating peptidoglycan synergistically promote mouse survival through the amelioration of intestinal and bone marrow damage," *Journal of Radiation Research*, vol. 56, no. 2, pp. 278–286, 2015.

[37] N. Barker, J. H. van Es, J. Kuipers et al., "Identification of stem cells in small intestine and colon by marker gene _Lgr5_," *Nature*, vol. 449, no. 7165, pp. 1003–1007, 2007.

[38] L. Lu, M. Jiang, C. Zhu, J. He, and S. Fan, "Amelioration of whole abdominal irradiation-induced intestinal injury in mice with 3,3'-Diindolylmethane (DIM)," *Free Radical Biology & Medicine*, vol. 130, pp. 244–255, 2019.

[39] T. Sato and H. Clevers, "Growing self-organizing mini-guts from a single intestinal stem cell: mechanism and applications," *Science*, vol. 340, no. 6137, pp. 1190–1194, 2013.

[40] Q. Hou, L. Liu, Y. Dong et al., "Effects of thymoquinone on radiation enteritis in mice," *Scientific Reports*, vol. 8, no. 1, article 15122, 2018.

[41] X. Sun, Q. Wang, Y. Wang, L. Du, C. Xu, and Q. Liu, "Brusatol enhances the radiosensitivity of A549 cells by promoting ROS production and enhancing DNA damage," *International Journal of Molecular Sciences*, vol. 17, no. 7, p. 997, 2016.

[42] E. P. Rogakou, D. R. Pilch, A. H. Orr, V. S. Ivanova, and W. M. Bonner, "DNA double-stranded breaks induce histone H2AX phosphorylation on serine 139," *The Journal of Biological Chemistry*, vol. 273, no. 10, pp. 5858–5868, 1998.

[43] S. S. Foster, S. de, L. K. Johnson, J. H. Petrini, and T. H. Stracker, "Cell cycle- and DNA repair pathway-specific effects of apoptosis on tumor suppression," *Proceedings National Academy of Sciences United States of America*, vol. 109, no. 25, pp. 9953–9958, 2012.

[44] J. R. Jeffers, E. Parganas, Y. Lee et al., "Puma is an essential mediator of p53-dependent and -independent apoptotic pathways," *Cancer Cell*, vol. 4, no. 4, pp. 321–328, 2003.

Research Article

Ascorbic Acid: A New Player of Epigenetic Regulation in LPS-*gingivalis* Treated Human Periodontal Ligament Stem Cells

Guya D. Marconi,[1] Luigia Fonticoli,[2] Simone Guarnieri,[3] Marcos F. X. B. Cavalcanti,[4] Sara Franchi,[5] Valentina Gatta,[5] Oriana Trubiani ⓘ,[2] Jacopo Pizzicannella,[6] and Francesca Diomede[2]

[1]*Department of Medical, Oral and Biotechnological Sciences, University "G. d'Annunzio" of Chieti-Pescara, 66100 Chieti, Italy*
[2]*Department of Innovative Technologies in Medicine & Dentistry, University "G. d'Annunzio" of Chieti-Pescara, 66100 Chieti, Italy*
[3]*Department of Neuroscience, Imaging and clinical Sciences-Center for Advanced Studies and Technology (CAST), University "G. d'Annunzio" of Chieti-Pescara, 66100 Chieti, Italy*
[4]*Nove de Julho University, 01506-000 São Paulo, Brazil*
[5]*Department of Psychological, Health and Territorial Sciences, School of Medicine and Health Sciences, "G. d'Annunzio" University, 66100 Chieti, Italy*
[6]*"Ss. Annunziata" Hospital, ASL 02 Lanciano-Vasto-Chieti, 66100 Chieti, Italy*

Correspondence should be addressed to Oriana Trubiani; trubiani@unich.it

Periodontitis is usually sustained from microorganism of oral cavity, like *Porphyromonas gingivalis* (*P. gingivalis*). Periodontal disease is an infectious disease that afflicts a large number of people. Researches are investigating on the mesenchymal stem cells (MSCs) response to inflammatory events in combination with antioxidant substances. In particular, ascorbic acid (AA) increased cell proliferation, upregulated the cells pluripotency marker expression, provide a protection from inflammation, and induced the regeneration of periodontal ligament tissue. The purpose of the present research was to investigate the effects of AA in primary culture of human periodontal ligament stem cells (hPDLSCs) exposed to *P. gingivalis* lipopolysaccharide (LPS-G). The effect of AA on hPDLSCs exposed to LPS-G was determined through the cell proliferation assay. The molecules involved in the inflammatory pathway and epigenetic regulation have been identified using immunofluorescence and Western blot analyses. miR-210 level was quantified by qRT-PCR, and the ROS generation was finally studied. Cells co-treated with LPS-G and AA showed a restoration in terms of cell proliferation. The expression of NFκB, MyD88, and p300 was upregulated in LPS-G exposed cells, while the expression was attenuated in the co-treatment with AA. DNMT1 expression is attenuated in the cells exposed to the inflammatory stimulus. The level of miR-210 was reduced in stimulated cells, while the expression was evident in the hPDLSCs co-treated with LPS-G and AA. In conclusion, the AA could enhance a protective effect in *in vitro* periodontitis model, downregulating the inflammatory pathway and ROS generation and modulating the miR-210 level.

1. Introduction

In the last few years, regenerative medicine based its success on the role of human mesenchymal stem cells (hMSCs). Human MSCs are characterized from two properties: self-renewal ability and multipotent differentiation potential [1]. Furthermore, hMSCs can differentiate and expand into mature cells as osteoblast, adipocytes, and chondroblasts and maintain the stem cell population [2]. They express specific surface markers, such as CD105, CD90, and CD73 and lack the expression for HLA-DR, CD45, CD34, and other hematopoietic markers [3]. These multipotent cells are located in different sites of the body. The bone marrow represents the gold standard tissue to isolate the hMSCs, but they can be also detected in the adipose and dental tissues, peripheral blood, umbilical cord blood, and amniotic

membrane [4]. Several studies have been focused on alternative tissue sources for adult mesenchymal stem cells, like the dental pulp, dental follicle, apical papilla, periodontal ligament, and palatine tonsil [5]. In particular, hMSCs, derived from oral tissues, as dental pulp and periodontal ligament, are able to regulate tooth homeostasis and help tissue repair [6]. In particular, stem cells derived from human periodontal ligament (hPDLSCs) showed the ability to differentiate into mesengic lineages. One of the most important features of hPDLSCs is the capacity to protect against infectious diseases related to their immunomodulatory properties [7, 8]. Periodontal disease is an infectious disease that leads to the progressive destruction of the periodontal ligament tissue and to the bone and tooth loss. Traditional clinical approaches for periodontal diseases are still insufficient to induce the full tissue regeneration of periodontium [9]. The hPDLSCs are not tumorigenic, maintain their classic phenotype and karyotype features in long-term passage cultures and are characterized by immunoregulatory properties [10, 11]. All hMSCs play an active role in the immune response; they interact with natural killer cells, dendritic cells, B lymphocytes, and T lymphocytes. Therefore, hMSCs avoid improper activation of T lymphocytes and limit the immune response during healing [12–14]. Nowadays, a great number of researches are investigating on the MSC response to inflammatory events in combination with antioxidant substances. Gram-negative bacteria showed on the outer of the cell membrane a component called lipopolysaccharide (LPS), and it is considered to be a major link for virulence in periodontitis [15]. Periodontitis is usually sustained from several microorganisms placed in the oral cavity, like *Porphyromonas gingivalis* (*P. gingivalis*, G), that afflicts a large number of people [16, 17]. Ascorbic acid (AA), known as vitamin C or ascorbate, consumed as a dietary supplement is a water-soluble vitamin that helps many enzyme activities [18]. AA is deeply involved in the reduction of reactive oxygen species (ROS) and showed a key role as an antisenescence agent [19]. When added to the cell culture, AA increased cell proliferation, upregulated the cell pluripotency marker expression [20], promoted MSCs regeneration of the periodontal ligament tissue, and protect inflammatory conditions induced by 2-hydroxyethyl methacrylate (HEMA) treatment reducing the intracellular inflammatory pathway [21].

Studies have shown that there exist a correlation between the periodontal diseases and some biomarkers, like microRNAs (miRNAs). miRNAs, noncoding small molecule RNAs, have influenced the development of periodontitis, as miR-146a, miR-128, and miR-200b [22–24]. miR-210 is related in the protection of the periodontitis; other than this, it has been identified in the triggering of several pathologies like cancers and immunological diseases [25]. Recent studies reported that miR-210 can be considered a key factor in the critical promotion of the osteogenic and angiogenic processes other than in cell survival [26, 27].

The purpose of the present study was to analyze the response of hPDLSCs to LPS-G, as a periodontitis *in vitro* model, alone or in presence of AA, in order to establish the potential protective role of AA on the inflammatory process triggered by LPS-G and in the preservation of the hPDLSCs reservoir.

2. Materials and Methods

2.1. Ethic Statement. Ethical Committee at the Medical School, "G. d'Annunzio" University, Chieti, Italy (number 266/April 17, 2014) approved the present study protocol. Informed consent form was filled and signed by all patients enrolled in the present research. All the procedures are in compliance with the 1964 Helsinki declaration and its later revisions, other than following the ethical standards of the institutional and/or national research committee.

2.2. Cell Culture Establishment. To collect hPDLSCs, we have enrolled six patients in good general health and without oral cavity diseases. They were to undergo surgical procedures to start the orthodontic treatment. After the collection, the periodontal ligament fragments were washed five times with phosphate-buffered saline solution (PBS, Lonza, Basel, Switzerland) [28]. The washed tissue fragments were placed in a culture dish in an incubator at 37°C in a humidified atmosphere of 5% CO_2 in air. The mesenchymal stem cell growth medium-chemically defined (MSCGM-CD, Lonza) was used as a medium and changed every two days. Isolated cells were migrated spontaneously from the tissue fragments after two weeks of culture [29, 30].

2.3. Human PDLSC Characterization by FACS Analysis. Human PDLSCs were washed in PBS and then analyzed for CD14, CD34, CD45, CD73, CD90, and CD105 expressions [31]. Briefly, cells were stained for CD45, CD73, and CD90 with fluorescein isothiocyanate-conjugated antihuman antibodies and for CD14, CD34, and CD105 with phycoerythrin-conjugated antibodies. After staining procedures, FACStar-plus flow-cytometry system running CellQuest software (Becton-Dickinson, Mountain View, CA, USA) was used. All reagents used for flow cytometry were purchased from Becton Dickinson [32].

2.4. In Vitro hPDLSC Multilineage Differentiation. The capacity of hPDLSCs to differentiate into mesengic lineages, as adipogenic and osteogenic differentiation, was evaluated by means of colorimetric detection and reverse transcription polymerase chain reaction (RT-PCR). In particular, hPDLSCs were placed in a 24 multiwell with a density of 2×10^4 cells/well. To induce adipogenic differentiation, cells were maintained in MSCBM-CD supplemented with 10 mmol/L dexamethasone, 10 nmol/L 3-isobutyl-1-methylxanthine, 5 mg/mL insulin, and 60 mmol/L indomethacin for 28 days. The medium was refreshed every 3 days. Oil Red O solution (Sigma-Aldrich, Milan, Italy) was used to evaluate the adipogenic phenotype, staining the lipid droplet at cytoplasmic level. To induce the osteogenic commitment, the hPDLSCs were placed in a 24-multiwell with a density of 2×10^4 cells/well. Cells were cultured with MSCBM-CD supplemented with 10 nmol/L dexamethasone, 10 nmol/L beta glycerophosphate (Sigma–Aldrich), and 50 mmol/L ascorbic acid for 21 days. Alizarin red S (Sigma-Aldrich) solution was used to stain the calcium depositions. Differentiated

(a)

(b)

(c)

MSC markers		
CD73	CD90	CD105
95.3% ± 2.8	98.5% ± 3.1	94.1% ± 2.4
Haematopoietic markers		
CD14	CD34	CD45
nd	nd	nd

(d)

(e)

(f)
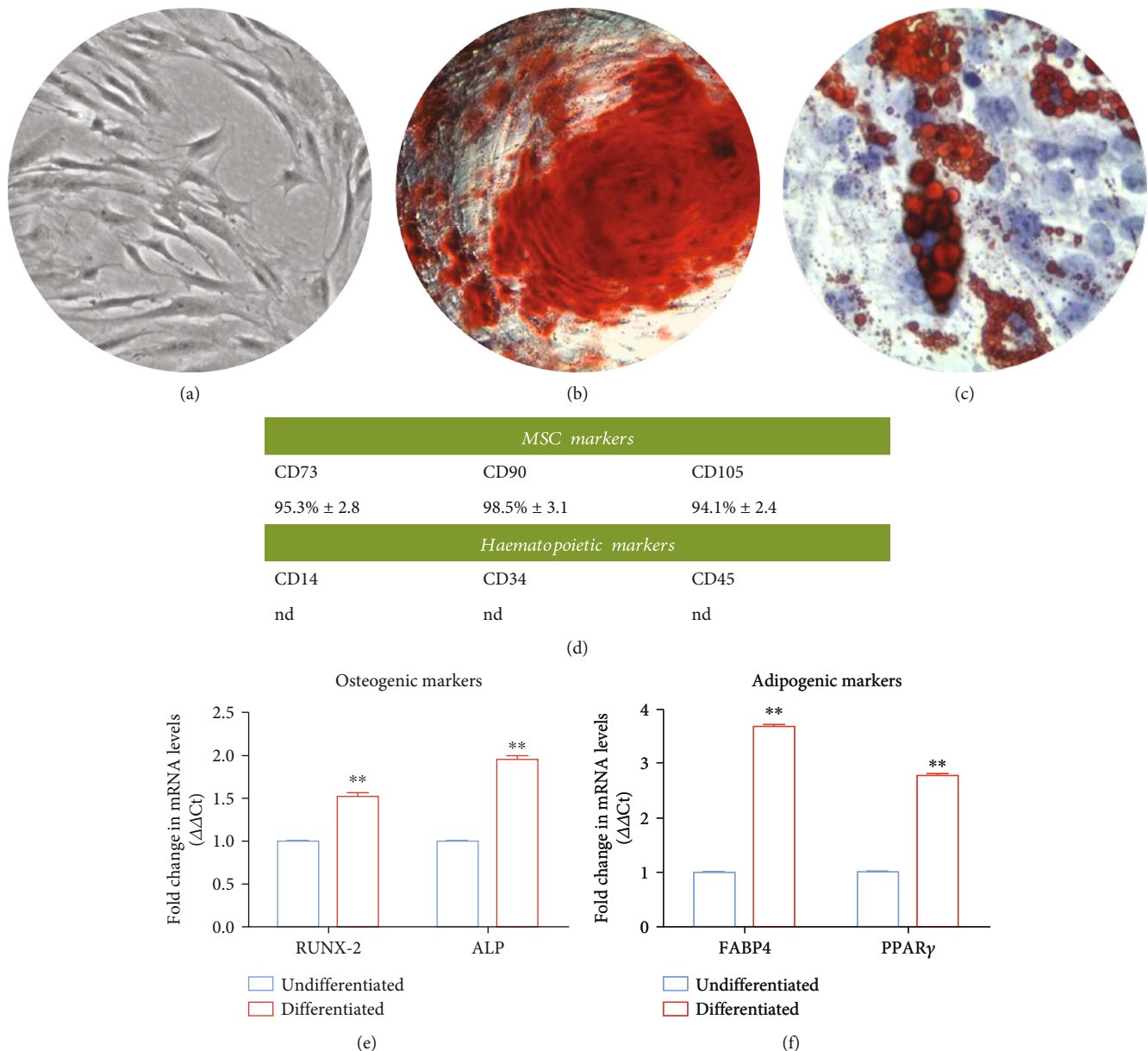
FIGURE 1: Phenotypic and functional characterization of hPDLSCs. (a) Representative images showing the morphology of hPDLSCs observed under light microscopy. (b) hPDLSC adipogenic differentiation: intracellular red lipid droplet stained with Oil Red O solution. (c) Human PDLSCs osteogenic differentiation: alizarin red staining of calcium deposition. (d) Cytofluorimetric analysis showed the positive expression for CD73, CD90 and CD105 and a negative expression for CD14, CD34, and CD45. (e) RT-PCR of RUNX-2 and ALP to detect the osteogenic differentiation. (f) RT-PCR of adipogenic markers. $P < 0.001$ was considered statistically significant ($**$). Scale bar: $10 \, \mu m$.

hPDLSCs were visualized to the inverted light microscopy Leica DMIL (Leica Microsystem, Milan, Italy). Furthermore, to evaluate the specific gene expression for adipogenic and osteogenic differentiation, RT-PCR has been performed. FABP4 and PPARγ were evaluated for adipogenesis commitment, and RUNX-2 and ALP were analyzed for osteogenesis [33].

2.5. Study Design. All experiments were performed in triplicate with hPDLSCs at passage 2.

The study design is reported as follows:

(i) Untreated hPDLSCs, used as negative control (CTRL)

(ii) hPDLSCs treated for 24 h with $50 \, \mu g \, mL^{-1}$ with ascorbic acid (AA)

(iii) hPDLSCs treated for 24 h with ultrapure lipopolysaccharide from *P. gingivalis* (tlrl-ppglps, InvivoGen, San Diego, CA, USA) $5 \, \mu g \, mL^{-1}$ (LPS-G)

(iv) hPDLSCs co-treated for 24 h with $50 \, \mu g \, mL^{-1}$ with ascorbic acid (AA) and LPS-G $5 \, \mu g \, mL^{-1}$ (LPS-G+AA)

2.6. MTT Assay. Cell viability of all experimental groups was determined using MTT colorimetric assay. Human PDLSCs

were cultured in a 96-well at a density of 2×10^3 cells/well. To evaluate the cell metabolic activity at 24, 48, and 72 h of culture, $20\,\mu L$ of MTT solution (CellTiter 96 AQueous One Solution reagent, Promega, Milan, Italy) was added to each well. Samples were maintained in the incubator, and after 3 h, the plates were read at 490 nm wavelength by means of a microplate reader (Synergy HT, BioTek Instruments, Winooski, VT, USA) [34].

2.7. Immunofluorescence and Confocal Laser Scanning Microscope (CLSM) Analyses. Sample fixation was performed with a solution of 4% of paraformaldehyde in 0.1 M of PBS (Lonza) [35, 36]. The following steps were performed: cells were permeabilized with 0.5% Triton X-100 in PBS for 10 min; samples blocking with 5% skimmed milk in PBS for 30 min [37]; primary antibodies (anti-NFκB, 1 : 200, Santa Cruz Biotechnology; anti-MyD800, Thermo Fisher Scientific; anti-DNMT1, 1 : 200, EpiGentek; and anti-p300, 1 : 200, Ori-Gene) incubation for 2 h at room temperature; and finally, secondary antibody (Alexa Fluor 568 red fluorescence-conjugated goat anti-rabbit antibody, 1 : 200, Molecular Probes, Invitrogen, Eugene, OR, USA) incubation for 1 h at 37°C. Cells were stained for 1 h with Alexa Fluor 488 phalloidin green fluorescent conjugate (1 : 400, Molecular Probes) and for 1 h with TOPRO (1 : 200, Molecular Probes) to mark the cytoskeleton actin and nuclei, respectively [38, 39]. The Zeiss LSM800 confocal system (Zeiss, Jena, Germany) has been used to acquire microphotographs.

2.8. Western Blot Analysis. Proteins ($50\,\mu g$) from all sample groups were processed as previously described [40]. Sheets were incubated 12 h at 4°C in with primary antibodies to NFκB (1 : 500, Santa Cruz Biotechnology), MyD88 (1 : 1000, Thermo-Fisher Scientific), p300 (1 : 750, EpiGentek), DNMT1 (1 : 750, OriGene), and β-actin (1 : 1000, Santa Cruz Biotechnology) [41, 42]. Then, sheets were maintained at room temperature for 30 min with peroxidase-conjugated secondary antibody diluted 1 : 1000 in 1x TBS, 5% milk, and 0.05% Tween-20 [43]. The ECL method was used for band visualization, and the protein level were measured by means of the Bio-Rad Protein Assay (Bio-Rad Laboratories, Hercules, CA, USA) [44].

2.9. ROS Analysis. Human PDLSCs were seeded in 35 mm imaging dish (μ-Dish, ibidi GmbH, Gräfelfing, D). Cells were treated for 24 hours in culture medium containing $5\,\mu g\,mL^{-1}$ LPS-G; (hPDLSCs+LPS-G) or $5\,\mu g\,mL^{-1}$ LPS-G plus $50\,\mu g/mL$ ascorbic acid (hPDLSCs+LPS-G+AA) or $50\,\mu g/mL$ ascorbic acid (AA) or culture medium alone (control, hPDLSCs). At the selected time, the cells were washed with normal external solution (NES) containing (in mM): 125 NaCl, 5 KCl, 1 MgSO4, 1 KH_2PO_4, 5.5 glucose, 1 $CaCl_2$, 20 HEPES, and pH 7.4 and incubated with $10\,\mu M$ of $2',7'$-dichlorodihydrofluorescein diacetate (H2DCFDA, Thermo Fisher Scientific) at 37°C in a humidified incubator (for 30 min) maintaining for all procedures the respective culture media treatments. At the end of dye incubation, the cells were washed with NES and observed in NES alone (hPDLSCs) or maintaining in NES plus hPDLSCs+LPS-G or AA alone. For each condition, confocal images were randomly acquired
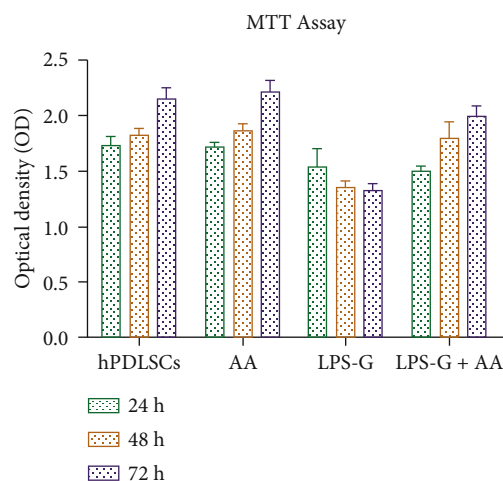
FIGURE 2: Cell viability analysis on hPDLSCs. Bar graph showed the cell viability of hPDLSCs treated with AA ($50\,\mu g\,mL^{-1}$) and LPS-G ($5\,\mu g\,mL^{-1}$) alone or in co-treatment with AA for 24, 48, and 72 h. The results are the mean (±S.E.M.) of three different experiments. $^{**}P < 0.001$.

using a Zeiss LSM800 microscope (Carl Zeiss), equipped with an inverted microscope Axio-obserber.D1 and an objective W-Plan-Apo 40X/1.3 DIC. Excitation was fixed at 488 nm and emission was collected, setting the filter set over 505–530 nm. The acquisition settings were maintained constant between specimens. Fiji distribution of ImageJ software was used to analyze the captured images.

2.10. MicroRNA Quantization. MicroRNAs were extracted using the PureLink RNA mini kit (Life Technologies), treated with the RNase-Free DNase Set (Qiagen, Venlo, Netherlands) according to the manufacturer's instructions and quantified by means Nanodrop2000 (Thermo Scientific, Waltham, MA, USA). Gene sequences were from NCBI (http://www.ncbi .nlm.nih.gov), and RNA sequences for miR-210 were used into the Universal ProbeLibrary (UPL) Assay Design Center software (https://www.rocheappliedscience.com) to identify primers and UPL probe. Total RNA (50–200 ng) was retro-transcribed with High-Capacity cDNA Reverse-Transcription Kit (Life Technologies, Milan, Italy). MicroRNA quantization was performed using stem-loop RT primers designed with a modification to include the UPL #21 sequence-binding site [45]. The target amount, normalized to endogenous reference 18S/RNU44 and relative to a calibrator, was given by $2^{-\Delta\Delta Ct}$ and/or $2^{-\Delta\Delta Ct}$ methods (Life Technologies).

2.11. Statistical Analysis. Statistical evaluation has been performed using GraphPad 4.0 software using t-test and ordinary one-way ANOVA followed by post hoc Bonferroni's multiple comparisons tests. Values of $P < 0.05$ were considered statistically significant.

3. Results

3.1. Characterization of hPDLSCs Culture. Human hPDLSCs show a typical fibroblastoid morphology, and they are able to adhere to plastic surfaces (Figure 1(a)). The minimal

(a)

(b)

(c)

(d)

FIGURE 3: Immunofluorescence analyses of the expression of NFκB. (a) Untreated hPDLSCs (CTRL). (b) Cells treated with AA (AA). (c) Cells treated with LPS-G (LPS-G). (d) Cells co-treated with LPS-G and AA (LPS-G+AA). NFκB was stained in red fluorescence (Alexa Fluor 568 for secondary antibody). Cytoskeleton actin was stained in green fluorescence (Alexa-phalloidin 488). Cell nuclei were stained in blue fluorescence (TO-PRO). Merged image showed the overlap of all abovementioned channels. Scale bar: 10 μm.

criteria defined by the International Society for Cellular Therapy were used to characterize hPDLSCs. Human PDLSCs are able to differentiate into adipogenic and osteogenic phenotypes as demonstrated in Figure 1. Alizarin Red solution demonstrated with a red staining the calcium deposition (Figure 1(b)), and Oil Red O solution stained the intracellular lipid vacuoles (Figure 1(c)). Graph bars of RT-PCR validated the qualitative data, showing an upregulation of FABP4, PPARγ, RUNX-2, and ALP in differentiated cells (Figures 1(e) and 1(f)). Flow cytometry

results showed the positive expression for CD73, CD90, and CD105 and the negative expression for CD14, CD34, and CD45 (Figure 1(d)).

3.2. MTT Cell Viability Assay. To evaluate the effects of AA, LPS-G, and AA in coadministration with LPS-G on hPDLSCs viable cells, the MTT assay was executed. During experiment, the hPDLSCs treated with AA showed a similar rate to the CTRL group, while hPDLSCs treated with LPS-G ($5 \, \mu g \, mL^{-1}$) evidenced a significant reduction of viable cells

(a)

(b)

(c)

(d)

Figure 4: Immunofluorescence analyses of the expression of MyD88. (a) Untreated hPDLSCs (CTRL). (b) Cells treated with AA (AA). (c) Cells treated with LPS-G (LPS-G). (d) Cells co-treated with LPS-G and AA (LPS-G+AA). MyD88 was stained in red fluorescence (Alexa Fluor 568 for secondary antibody). Cytoskeleton actin was stained in green fluorescence (Alexa-phalloidin 488). Cell nuclei were stained in blue fluorescence (TO-PRO). Merged image showed the overlap of all abovementioned channels. Scale bar: 10 μm.

with respect to the other samples. After 24 h, the presence of AA reverts the effects of LPS-G showing a similar cell viability rate to the samples. A similar trend was reported after 48 and 72 hours of treatment with AA, LPS-G, and LPS-G+AA. The AA treatment showed beneficial effects, in terms of proliferation rate, after 24, 48, and 72 hours of treatment on both cell cultures (Figure 2).

3.3. Signaling Pathway NFκB, MyD88, p300, and DNMT1 Analyses. Microphotographs captured by means of CLSM

showed the intracellular expression of NFκB, MyD88, p300, and DNMT1 (Figures 3–6). The hPDLSCs treated with LPS-G showed cell morphological changes compared to the untreated cells. The cells cotreated with LPS-G and AA evidenced a protective effect, hence the hPDLSCs a morphology reasonably comparable to the untreated hPDLSCs (CTRL). Furthermore, to confirm signaling network stimulated by LPS-G administration in hPDLSCs, the expression of NFκB, MyD88, p300, and DNMT1 was examined after 24 h of culture. Immunofluorescence experiments to detect NFκB,
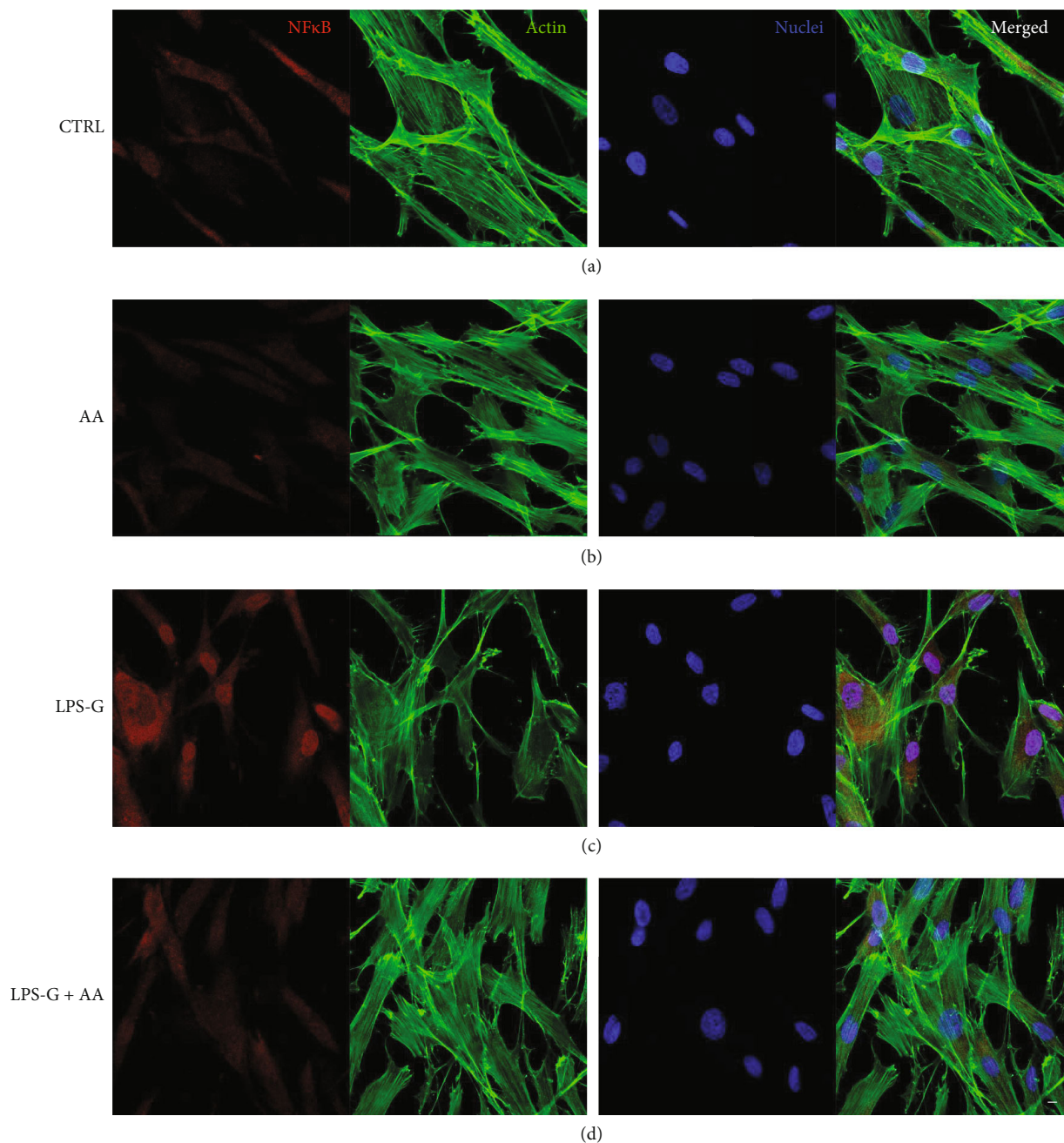
(a)

(b)

(c)

(d)
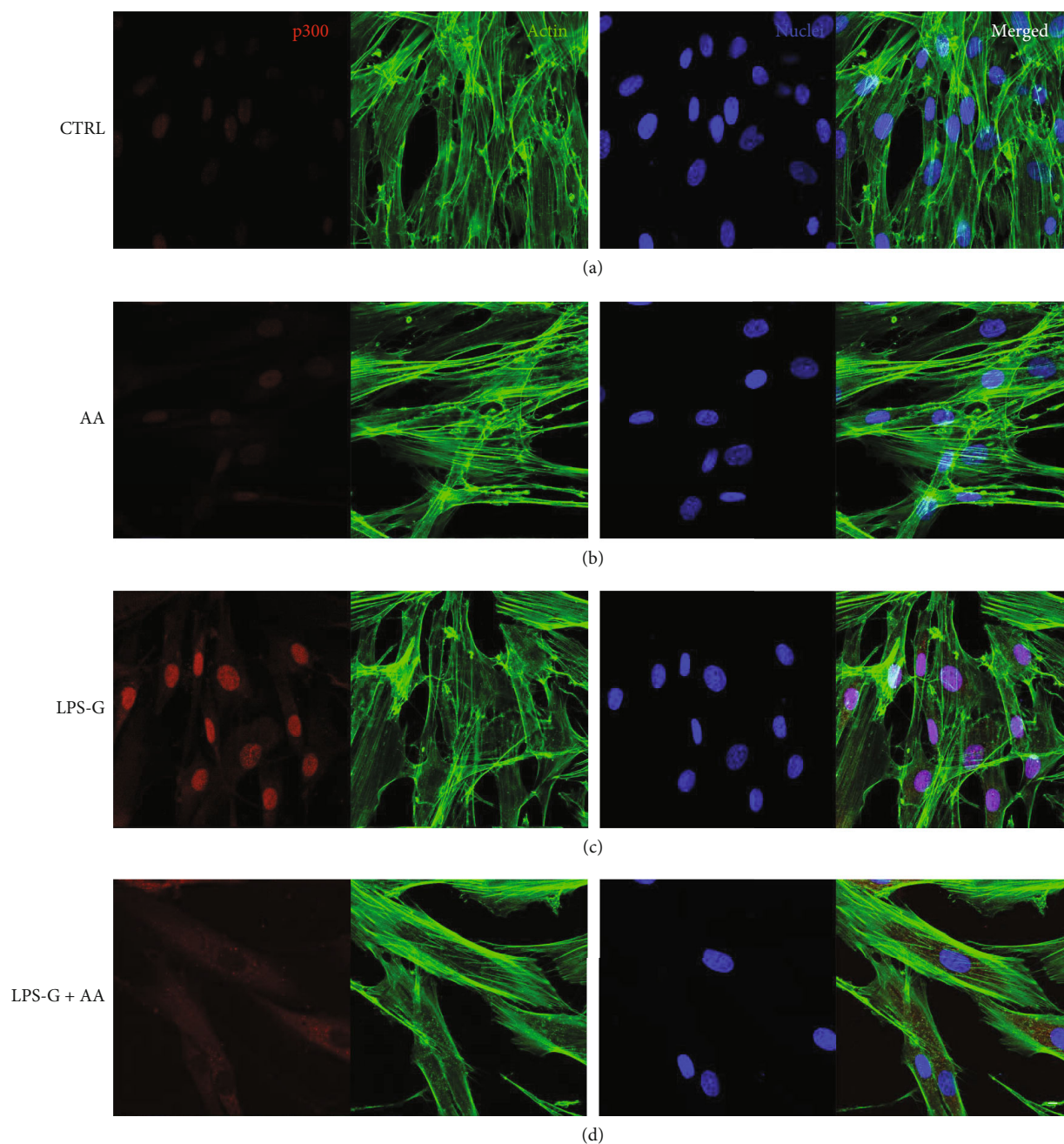
FIGURE 5: Immunofluorescence analyses of the expression of p300. (a) Untreated hPDLSCs (CTRL). (b) Cells treated with AA (AA). (c) Cells treated with LPS-G (LPS-G). (d) Cells co-treated with LPS-G and AA (LPS-G+AA). p300 was stained in red fluorescence (Alexa Fluor 568 for secondary antibody). Cytoskeleton actin was stained in green fluorescence (Alexa-phalloidin 488). Cell nuclei were stained in blue fluorescence (TO-PRO). Merged image showed the overlap of all abovementioned channels. Scale bar: 10 μm.

MyD88, p300, and DNMT1 localization were executed in hPDLSCs tested in all conditions stated above. Images in Figures 3–5 showed an increased fluorescence signal derived from NFκB, MyD88, and p300 immunostaining in hPDLSCs treated with LPS-G compared to the hPDLSCs under other experimental conditions, in particular to the cells treated with AA. Immunofluorescence detection for DNMT1 showed a decrease in LPS-G-treated cells, meanwhile the expression level increases in cells cotreated with LPS-G and AA, similar to the CTRL and AA samples (Figure 6). LPS-

G operates on the receptor and initiates a molecular cascade upregulating MyD88 and causing NFκB to translocate at the nuclear level (Figures 4 and 5).

3.4. NFκB, MyD88, p300, and DNMT1 Protein Expressions. Western blotting assay was evaluated to assess NFκB, MyD88, p300, and DMNT1 protein expressions. In Figure 7, bands of NFκB, MyD88, and p300 were augmented in LPS-G administered in hPDLSCs, while in cells treated with LPS-G+AA, a downregulation of NFκB, MyD88, and
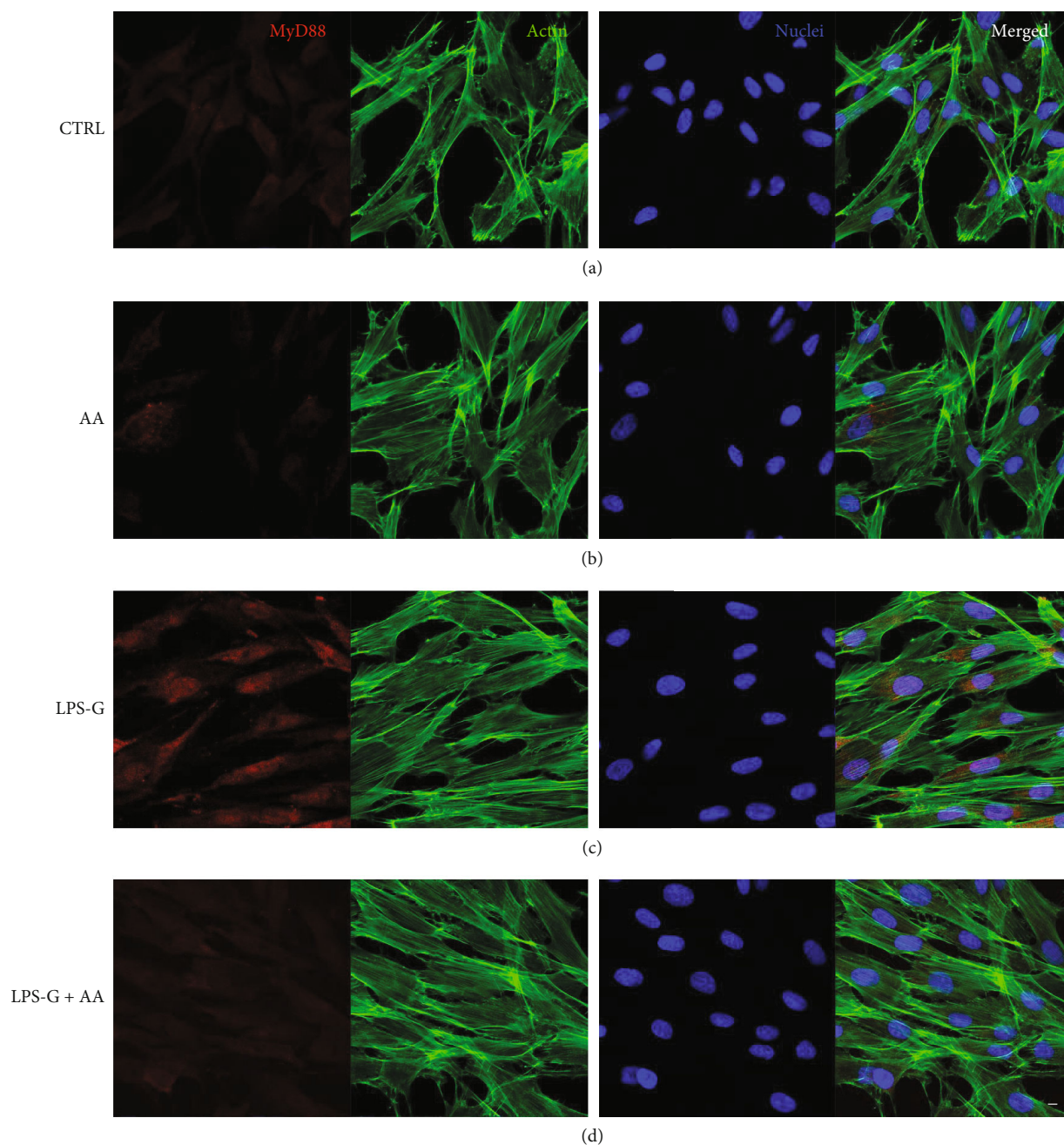
(a)

(b)

(c)

(d)
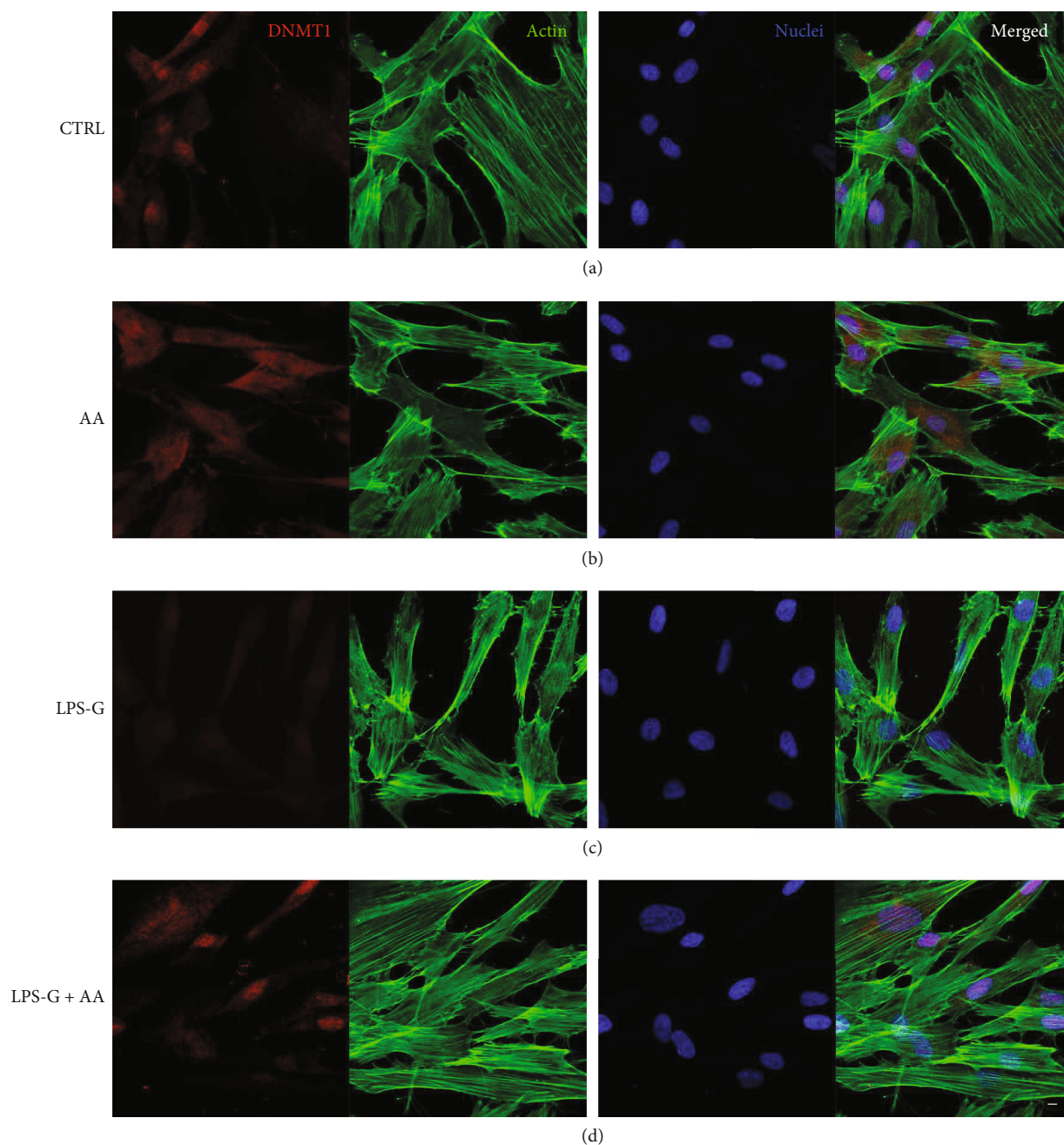
Figure 6: Immunofluorescence analyses of the expression of DNMT1. (a) Untreated hPDLSCs (CTRL). (b) Cells treated with AA (AA). (c) Cells treated with LPS-G (LPS-G). (d) Cells co-treated with LPS-G and AA (LPS-G+AA). DNMT1 was stained in red fluorescence (Alexa Fluor 568 for secondary antibody). Cytoskeleton actin was stained in green fluorescence (Alexa-phalloidin 488). Cell nuclei were stained in blue fluorescence (TO-PRO). Merged image showed the overlap of all abovementioned channels. Scale bar: 10 μm.

p300 was existent. DNMT1 protein is expressed in hPDLSCs and in cells treated with AA and cotreated with LPS-G+AA.

3.5. ROS Production. To verify the ROS production stimulated by LPS-G, hPDLSCs were loaded with the cell-permeant H2DCFDA a probe, used as an indicator for ROS. Figures were taken in live cells by means of confocal microscopy, and the single cell fluorescence recorded was finally offline investigated. In Figure 8(a), typical images

acquired in our experimental circumstances are shown. Comparing the images taken, in the LPS-G-treated cells, there is an evident increase in emitted fluorescence with respect to the others, while the cotreatment of LPS-G in presence of AA appeared quite similar to that obtained in hPDLSC or AA alone. Quantitative results (Figure 8(b)) showed a growth in ROS production in $5 \mu g \, mL^{-1}$ LPS-G-treated hPDLSCs vs. hPDLSCs (means ± S.E.M.: LPS-G 0.1 ± 0.02 vs. hPDLSCs 0.04 ± 0.005). The co-presence of

(a)

(b)
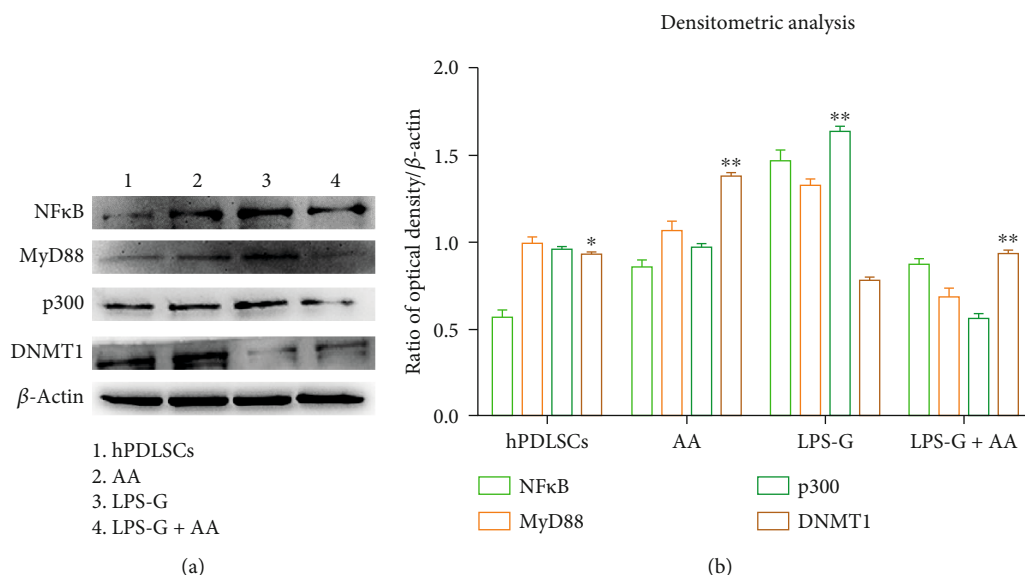
FIGURE 7: Protein expression. (a) Western blotting analysis of NFκB, MyD88, p300, and DNMT1 expressions in hPDLSCs treated with LPS-G alone or in co-treatment of AA. (b) Densitometric analysis of protein bands expressed as a ratio of protein quantification normalized with β-actin. The error bars on these graphs evidence standard deviation ($\pm$ SD). Graph bars showed the densitometric analysis. β-Actin was used as a housekeeping protein. The experiments were performed in triplicate. $^{**}P < 0.001$, $^{*}P < 0.01$.

(a)

(b)
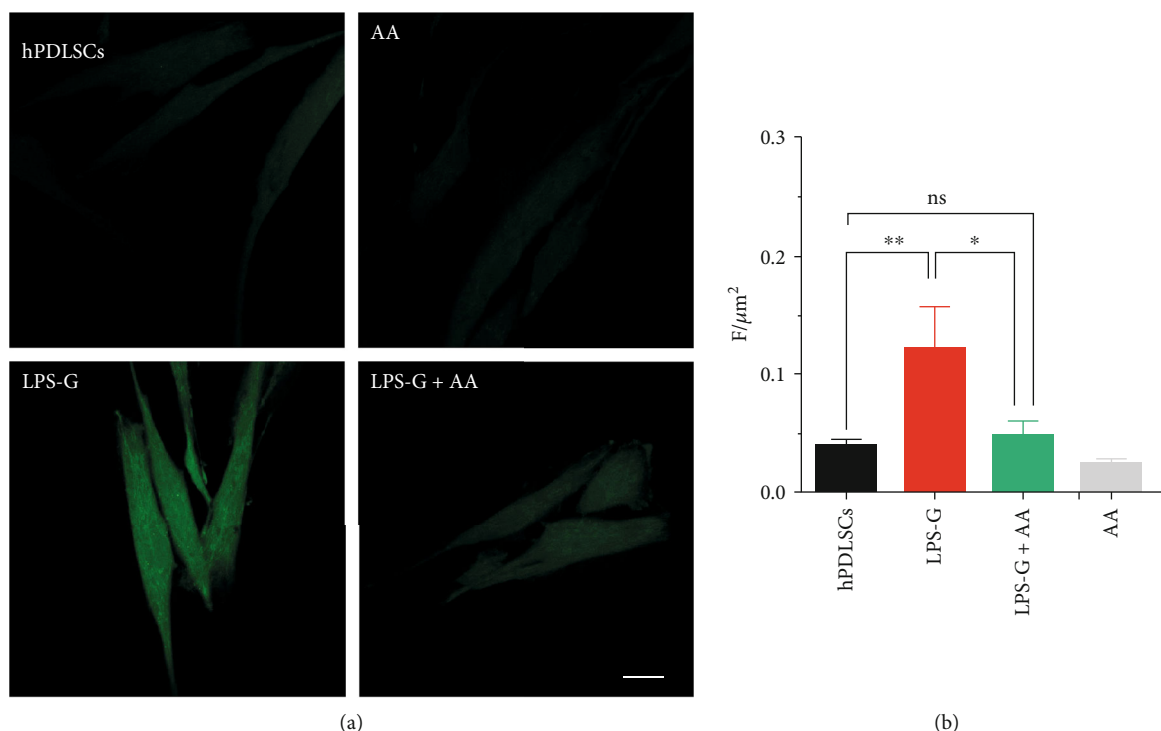
FIGURE 8: Single-cell ROS measurements. (a) Images of live cells loaded with H2DCFDA and acquired by confocal microscopy: hPDLSCs (control sample), LPS-G (LPS-G-treated cells), LPS-G+AA (LPS-G plus ascorbic acid-treated cells), and AA (ascorbic acid alone-treated cells). (b) Quantitative analysis of ROS production represented as arbitrary unit of fluorescence per cell surface unit (F/μm^2). Data are expressed as mean $\pm$ S.E.M (hPDLSCs $n = 26$, LPS-G $n = 21$, LPS-G+AA $n = 16$, AA $n = 23$; $N = 3$; $^{**}P < 0.001$, $^{*}P < 0.01$). Statistical analysis was performed by one-way ANOVA and post hoc Bonferroni). Scale bar = 20 μm.

ascorbic acid successfully appeared to be able to block the ROS production induced by LPS-G (LPS-G+AA 0.05 $\pm$ 0.001), while the AA alone did not modify the ROS basal levels acquired in hPDLSC samples (AA 0.040 $\pm$ 0.003).

3.6. miR-210 Expression. miR-210 expression was downregulated in hPDLSCs administered with LPS-G, while in cells treated with AA and cotreated with LPS-G+AA, the miRNA-210 level is comparable to the CTRL group (Figure 9).
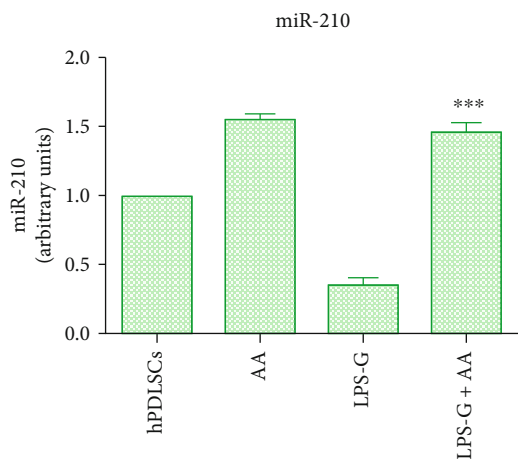
miR-210

FIGURE 9: MicroRNA-210 expression. Graph bar showed the expression of miR-210 in all conditions. miR-210 was downregulated in cells treated with LPS-G, while in cells cotreated with LPS-G and AA was overexpressed. $^{**}P < 0.001$.

4. Discussion

Periodontitis is a chronic inflammatory illness, worldwide distributed and often correlated to many other chronic diseases such as cardiovascular disease, inflammatory bowel disease, rheumatoid arthritis, respiratory tract infection, and Alzheimer's disease, exhibiting a given attention in the relationship between oral and systemic health [3–5]. Periodontitis is sustained by a definite oral microorganism that is localized in the gum plaque, as *Porphyromonas gingivalis*, *Treponema denticola*, *Tannerella forsythia*, and *Aggregatibacter actinomycetemcomitans*. The periodontal disease worsening brings to the loss of periodontal ligament, alveolar bone, and consequently the tooth leakage [9].

The maintenance of the periodontal health becomes a real challenge to ameliorate the quality life of a wide part of population [10]. The human oral microbiome can be considered essential in the pathogenesis and in the development of the periodontal disease.

Periodontal tissue damage is a result of an aberrant host response to the bacterial infection and immune response activated from the polymorphonuclear leukocytes (PMNs) that are critically implicated versus the periodonto pathogens. This antimicrobial response at the infection site triggers numerous intracellular signaling pathways, including reactive oxygen species release (ROS), that can be considered the principal cause for the periodontal tissue injury in periodontal illness [46, 47].

The inflammation, involved in the stimulation and maintenance of the periodontitis, induced the epigenetic modifications in the periodontal ligament niche. Epigenetic modifications are a complex molecular mechanism with chemical modifications of DNA and their related proteins that lead to the activation or inactivation of some gene transcription [48].

In the present study, hPDLSCs were administered with LPS-G to mimic in vitro the periodontitis model.

The in vivo periodontitis scenario is very complex and involves the interaction of several cell bacteria and factors. The use of ultrapure preparation of LPS-G in a human cellular model could understand the mechanisms of the inflammatory response in periodontitis and the development of future clinical treatments. As previously reported, to study the periodontitis model, it is important to consider two key factors: (i) the LPS-G preparation, "standard" or "ultrapure" [49] and (ii) the in vitro model, mouse or human, to better reflect the in vivo situation. The use of mouse models could underestimate the role of LPS-G in the triggering and sustaining of human pathology [50].

LPS-G treatment activated the MyD88 and p300 signal transduction and induced NFκB nuclear translocation. Meanwhile, the immunofluorescence and protein analyses showed a suppression in the expression of DNMT1 [51, 52]. As previously reported, DNMT1 expression is downregulated in oral epithelial cell and hPDLSCs treated with *P. gingivalis* (whole bacteria) or LPS-G [53].

AA supplemented with the diet exerts an antioxidant outcome, downregulating the free radical production and operating as a cofactor in cell functions [54, 55]. AA is also considered vital in the maintenance of periodontal health for its role in the downregulation of ROS production [56]. As earlier described, the role of AA in periodontal disease is in the avoiding and reducing the progression of the destruction process, stimulating the differentiation of periodontal ligament progenitor cells [57]. In the present study, the effects of AA in the periodontal disease in vitro model has been assessed in terms of cell viability, inflammatory pathways, gene expression, ROS production, and miRNA 210 expression. The treatment with AA increased the viability of hPDLSCs, while the LPS-G treatment showed a decrease in cell viability; moreover, the co-treatment of AA and LPS-G restore the conditions obtained in CTRL samples.

LPS-G treatment induces the inflammatory intracellular signaling cascades, as NFκB, MyD88, and p300 pathways. NFκB is a family of transcription factors implicated in the activation of inflammatory genes and in periodontal disease progression. NFκB showed a redox-sensitive potential for ROS in different tissues, as endothelial and vascular smooth muscle; other than that, it has been extensively studied as a proinflammatory nuclear transcription factor in a rat model related to the hypertension [58]. As reported in the literature, in an experimental rat model, the treatment with AA lead to a downexpression of NFκB and a reduction of the excessive ROS production, responsible of blood vessel inflammation, as beneficial effects [59, 60]. p300 is a general transcriptional factor that can change the chromatin structure from heterochromatin to euchromatin, in order to enhance the binding of transcriptional factors to promoters [61]. p300 is necessary for the transcriptional activity of NFκB, a crucial mediator of inflammatory responses [62, 63].

In our periodontitis in vitro model, LPS-G augmented the expression of NFκB, MyD88, and p300. Moreover, our results reported a decrease expression of DNMT1 in LPS-G-treated samples. Meanwhile, the co-treatment of LPS-G and AA showed a downregulation of NFκB, MyD88, and

p300 and conversely an upregulation of DNMT1 in a similar way to the untreated cells.

Latest study has demonstrated that the NFκB pathway can be initiated to promote proinflammatory cytokine expression in periodontitis [64]; in particular, NFκB can be activated in hPDLSCs treated with LPS-G [65]. NFκB signaling pathway is inhibited by miR-210, as reported by Zhang et al., leading to a reduction of the inflammatory cascade in osteoarthritis [66]. Our results suggest that the cells treated with LPS-G showed an activation of NFκB signaling and a reduction in the expression of miR210, as also reported by Jia et al. [67]. miR-210 is decreased in patients with periodontitis in comparison to the healthy individuals. When cells were co-treated with LPS-G and AA, it showed an overexpression of miR210 that could inhibit the NFκB pathway induced by AA treatment. LPS administration stimulated both p38 MAPK and NFκB signaling pathways [67], while miR-210 overexpression repressed the p38MAPK/NFκB pathway in LPS-stimulated PDLCs; similar results was obtained by Chen and Li [68].

5. Conclusions

In conclusion, the present work reported that miR-210 level was downregulated and the inflammatory signaling pathways are activated in an *in vitro* periodontitis model, while the co-treatment with AA could attenuate the inflammatory response. However, the results in our study should be further investigated by future *in vivo* models.

Data Availability

The data used to support the findings of the present study are available from the corresponding authors upon request.

Conflicts of Interest

The authors declare that there is no conflict of interest regarding the publication of this paper.

Authors' Contributions

GDM, LF, and SG contributed to data collection and analysis, data interpretation, preparation of figures, drafting of manuscript, editing and revising manuscript, and approving final version of manuscript. MFXBC, SF, and VG contributed to data analysis, data interpretation, preparation of figures, revising manuscript, and approving final version of manuscript. OT, JP, and FD conceived the study and contributed to study design, experiments, data analysis, data interpretation, preparation of figures, editing and revising manuscript, and approving final version of manuscript. Guya D. Marconi and Luigia Fonticoli contribute equally to the work. Jacopo Pizzicannella and Francesca Diomede contribute equally to the work as senior author.

Acknowledgments

References

[1] Q. Z. Zhang, A. L. Nguyen, W. H. Yu, and A. D. Le, "Human oral mucosa and Gingiva," *Journal of dental research*, vol. 91, no. 11, pp. 1011–1018, 2012.

[2] A. R. Sanz, F. S. Carrion, and A. P. Chaparro, "Mesenchymal stem cells from the oral cavity and their potential value in tissue engineering," *Periodontology 2000*, vol. 67, no. 1, pp. 251–267, 2015.

[3] M. Tatullo, B. Codispoti, A. Pacifici et al., "Potential use of human periapical cyst-mesenchymal stem cells (hPCy-MSCs) as a novel stem cell source for regenerative medicine applications," *Frontiers in cell and developmental biology*, vol. 5, 2017.

[4] M. Tatullo, M. Marrelli, and F. Paduano, "The regenerative medicine in oral and maxillofacial surgery: the most important innovations in the clinical application of mesenchymal stem cells," *International journal of medical sciences*, vol. 12, no. 1, pp. 72–77, 2015.

[5] Y. Chen, X. Wang, J. Fang et al., "Mesenchymal stem cells participate in oral mucosa carcinogenesis by regulating T cell proliferation," *Clinical immunology*, vol. 198, pp. 46–53, 2019.

[6] P. T. Sharpe, "Dental mesenchymal stem cells," *Development*, vol. 143, no. 13, pp. 2273–2280, 2016.

[7] O. Andrukhov, C. Behm, A. Blufstein, and X. Rausch-Fan, "Immunomodulatory properties of dental tissue-derived mesenchymal stem cells: Implication in disease and tissue regeneration," *World journal of stem cells*, vol. 11, no. 9, pp. 604–617, 2019.

[8] L. L. Zhou, W. Liu, Y. M. Wu, W. L. Sun, C. E. Dorfer, and K. M. Fawzy El-Sayed, "Oral mesenchymal stem/progenitor cells: the immunomodulatory masters," *Stem cells international*, vol. 2020, Article ID 1327405, 2020.

[9] B. L. Pihlstrom, B. S. Michalowicz, and N. W. Johnson, "Periodontal diseases," *Lancet*, vol. 366, no. 9499, pp. 1809–1820, 2005.

[10] H. Yang, L. N. Gao, Y. An et al., "Comparison of mesenchymal stem cells derived from gingival tissue and periodontal ligament in different incubation conditions," *Biomaterials*, vol. 34, no. 29, pp. 7033–7047, 2013.

[11] O. Trubiani, J. Pizzicannella, S. Caputi et al., "Periodontal ligament stem cells: current knowledge and future perspectives," *Stem cells and development*, vol. 28, no. 15, pp. 995–1003, 2019.

[12] M. E. Castro-Manrreza and J. J. Montesinos, "Immunoregulation by mesenchymal stem cells: biological aspects and clinical applications," *Journal of immunology research*, vol. 2015, Article ID 394917, 20 pages, 2015.

[13] O. Trubiani, G. D. Marconi, S. D. Pierdomenico, A. Piattelli, F. Diomede, and J. Pizzicannella, "Human oral stem cells, biomaterials and extracellular vesicles: a promising tool in bone tissue repair," *International Journal of Molecular Sciences*, vol. 20, no. 20, p. 4987, 2019.

[14] T. S. Rajan, S. Giacoppo, O. Trubiani et al., "Conditioned medium of periodontal ligament mesenchymal stem cells exert anti- inflammatory effects in lipopolysaccharide-activated mouse motoneurons," *Experimental cell research*, vol. 349, no. 1, pp. 152–161, 2016.

[15] C. Li, B. Li, Z. Dong et al., "Lipopolysaccharide differentially affects the osteogenic differentiation of periodontal ligament stem cells and bone marrow mesenchymal stem cells through Toll-like receptor 4 mediated nuclear factor κB pathway," *Stem cell research & therapy*, vol. 5, no. 3, p. 67, 2014.

[16] G. Hajishengallis, "Periodontitis: from microbial immune subversion to systemic inflammation," *Nature reviews Immunology*, vol. 15, no. 1, pp. 30–44, 2015.

[17] P. N. Papapanou and C. Susin, "Periodontitis epidemiology: is periodontitis under-recognized, over-diagnosed, or both?," *Periodontology 2000*, vol. 75, no. 1, pp. 45–51, 2017.

[18] F. Diomede, G. D. Marconi, S. Guarnieri et al., "A novel role of ascorbic acid in anti-inflammatory pathway and ROS generation in HEMA treated dental pulp stem cells," *Materials*, vol. 13, no. 1, p. 130, 2020.

[19] B. Frei, L. England, and B. N. Ames, "Ascorbate is an outstanding antioxidant in human blood plasma," *Proceedings of the National Academy of Sciences*, vol. 86, no. 16, pp. 6377–6381, 1989.

[20] P. D. Potdar and S. B. D'Souza, "Ascorbic acid induces in vitro proliferation of human subcutaneous adipose tissue derived mesenchymal stem cells with upregulation of embryonic stem cell pluripotency markers Oct 4 and SOX 2," *Human cell*, vol. 23, no. 4, pp. 152–155, 2010.

[21] F. L. Wei, C. Y. Qu, T. L. Song et al., "Vitamin C treatment promotes mesenchymal stem cell sheet formation and tissue regeneration by elevating telomerase activity," *Journal of Cellular Physiology*, vol. 227, no. 9, pp. 3216–3224, 2012.

[22] S. Y. Jiang, D. Xue, Y. F. Xie et al., "The negative feedback regulation of microRNA-146a in human periodontal ligament cells after Porphyromonas gingivalis lipopolysaccharide stimulation," *Inflammation Research*, vol. 64, no. 6, pp. 441–451, 2015.

[23] H. S. Na, M. H. Park, Y. R. Song et al., "Elevated microRNA-128 in periodontitis mitigates tumor necrosis Factor-α response via p38 signaling pathway in macrophages," *Journal of Periodontology*, vol. 87, no. 9, pp. E173–E182, 2016.

[24] A. Z. Kalea, R. Hoteit, J. Suvan et al., "Upregulation of gingival tissue miR-200b in obese periodontitis subjects," *Journal of Dental Research*, vol. 94, 3_supplement, pp. 59s–69s, 2015.

[25] K. Dang and K. A. Myers, "The role of hypoxia-induced miR-210 in cancer progression," *International Journal of Molecular Sciences*, vol. 16, no. 12, pp. 6353–6372, 2015.

[26] J. Pizzicannella, F. Diomede, A. Gugliandolo et al., "3D printing PLA/gingival stem cells/ EVs upregulate miR-2861 and -210 during osteoangiogenesis commitment," *International Journal of Molecular Sciences*, vol. 20, no. 13, p. 3256, 2019.

[27] J. Pizzicannella, M. Cavalcanti, O. Trubiani, and F. Diomede, "MicroRNA 210 mediates VEGF upregulation in human periodontal ligament stem cells cultured on 3DHydroxyapatite ceramic scaffold," *International Journal of Molecular Sciences*, vol. 19, no. 12, p. 3916, 2018.

[28] A. Gugliandolo, F. Diomede, P. Cardelli et al., "Transcriptomic analysis of gingival mesenchymal stem cells cultured on 3D bioprinted scaffold: a promising strategy for neuroregeneration," *Journal of biomedical materials research Part A*, vol. 106, no. 1, pp. 126–137, 2018.

[29] F. Diomede, N. Zini, J. Pizzicannella et al., "5-Aza exposure improves reprogramming process through embryoid body formation in human gingival stem cells," *Frontiers in genetics*, vol. 9, 2018.

[30] O. Trubiani, E. Toniato, D. Di Iorio et al., "Morphological analysis and interleukin release in human gingival fibroblasts seeded on different denture base acrylic resins," *International journal of immunopathology and pharmacology*, vol. 25, no. 3, pp. 637–643, 2012.

[31] M. Dominici, K. Le Blanc, I. Mueller et al., "Minimal criteria for defining multipotent mesenchymal stromal cells. The International Society for Cellular Therapy position statement," *Cytotherapy*, vol. 8, no. 4, pp. 315–317, 2006.

[32] P. Ballerini, F. Diomede, N. Petragnani et al., "Conditioned medium from relapsing-remitting multiple sclerosis patients reduces the expression and release of inflammatory cytokines induced by LPS- gingivalis in THP-1 and MO3.13 cell lines," *Cytokine*, vol. 96, pp. 261–272, 2017.

[33] B. Sinjari, J. Pizzicannella, M. D'Aurora et al., "Curcumin/liposome nanotechnology as delivery platform for anti-inflammatory activities via NFkB/ERK/pERK pathway in human dental pulp treated with 2-hydroxyethyl methacrylate (HEMA)," *Frontiers in physiology*, vol. 10, 2019.

[34] M. F. X. B. Cavalcanti, D. A. Maria, N. de Isla et al., "Evaluation of the proliferative effects induced by low-level laser therapy in bone marrow stem cell culture," *Photomedicine and laser surgery*, vol. 33, no. 12, pp. 610–616, 2015.

[35] F. Diomede, M. D'Aurora, A. Gugliandolo et al., "A novel role in skeletal segment regeneration of extracellular vesicles released from periodontal-ligament stem cells," *International journal of nanomedicine*, vol. Volume 13, pp. 3805–3825, 2018.

[36] A. Mazzatenta, G. D. Marconi, V. Macchi et al., "Coexpression of galanin and nestin in the chemoreceptor cells of the human carotid body," *Respirology*, vol. 885, pp. 77–82, 2015.

[37] J. Pizzicannella, R. Rabozzi, O. Trubiani, and G. Di Giammarco, "HTK solution helps to preserve endothelial integrity of saphenous vein: an immunohistochemical and ultrastructural analysis," *Journal of biological regulators and homeostatic agents*, vol. 25, no. 1, pp. 93–99, 2011.

[38] C. Di Giulio, G. D. Marconi, S. Zara et al., "Selective expression of galanin in neuronal-like cells of the human carotid body," *Advances in experimental medicine and biology*, vol. 860, pp. 315–323, 2015.

[39] O. Trubiani, S. Guarnieri, F. Diomede et al., "Nuclear translocation of PKCα isoenzyme is involved in neurogenic commitment of human neural crest-derived periodontal ligament stem cells," *Cellular signalling*, vol. 28, no. 11, pp. 1631–1641, 2016.

[40] S. Giacoppo, S. R. Thangavelu, F. Diomede et al., "Anti-inflammatory effects of hypoxia-preconditioned human periodontal ligament cell secretome in an experimental model of multiple sclerosis: a key role of IL-37," *The FASEB Journal*, vol. 31, no. 12, pp. 5592–5608, 2017.

[41] S. Mammana, A. Gugliandolo, E. Cavalli et al., "Human gingival mesenchymal stem cells pretreated with vesicular moringin nanostructures as a new therapeutic approach in a mouse model of spinal cord injury," *Journal of tissue engineering and regenerative medicine*, vol. 13, pp. 1109–1121, 2019.

[42] F. Diomede, M. D'Aurora, A. Gugliandolo et al., "Biofunctionalized scaffold in bone tissue repair," *International Journal of Molecular Sciences*, vol. 19, no. 4, p. 1022, 2018.

[43] F. Diomede, N. Zini, V. Gatta et al., "Human periodontal ligament stem cells cultured onto cortico-cancellous scaffold drive bone regenerative process," *European cells & materials*, vol. 32, pp. 181–201, 2016.

[44] A. Mazzatenta, G. D. Marconi, S. Zara, A. Cataldi, A. Porzionato, and C. Di Giulio, "In the carotid body, galanin

is a signal for neurogenesis in young, and for neurodegeneration in the old and in drug-addicted subjects," *Frontiers in Physiology*, vol. 5, 2014.

[45] F. Diomede, I. Merciaro, S. Martinotti et al., "miR-2861 is involved in osteogenic commitment of human periodontal ligament stem cells grown onto 3D scaffold," *J Biol Regul Homeost Agents*, vol. 30, no. 4, pp. 1009–1018, 2016.

[46] D. R. Miller, I. B. Lamster, and A. I. Chasens, "Role of the polymorphonuclear leukocyte in periodontal health and disease," *Journal of clinical periodontology*, vol. 11, no. 1, pp. 1–15, 1984.

[47] T. E. Van Dyke and G. A. Hoop, "Neutrophil function and oral disease," *Critical Reviews in Oral Biology & Medicine*, vol. 1, pp. 117–133, 2016.

[48] F. Diomede, S. R. Thangavelu, I. Merciaro et al., "Porphyromonas gingivalis lipopolysaccharide stimulation in human periodontal ligament stem cells: role of epigenetic modifications to the inflammation," *European Journal of Histochemistry*, vol. 61, 2017.

[49] C. Behm, A. Blufstein, S. Y. Abhari et al., "Response of human mesenchymal stromal cells from periodontal tissue to LPS depends on the purity but not on the LPS source," *Mediators of Inflammation*, vol. 2020, Article ID 8704896, 17 pages, 2020.

[50] B. Nativel, D. Couret, P. Giraud et al., "_Porphromonas gingivalis_ lipopolysaccharides act exclusively through TLR4 with a resilience between mouse and human," *Scientific Reports*, vol. 7, no. 1, 2017.

[51] F. Diomede, M. Zingariello, M. Cavalcanti et al., "MyD88/ERK/NFkB pathways and pro-inflammatory cytokines release in periodontal ligament stem cells stimulated by Porphyromonas gingivalis," *European Journal of Histochemistry*, vol. 61, no. 2, 2017.

[52] J. Pizzicannella, F. Diomede, I. Merciaro et al., "Endothelial committed oral stem cells as modelling in the relationship between periodontal and cardiovascular disease," *Journal of Cellular Physiology*, vol. 233, no. 10, pp. 6734–6747, 2018.

[53] L. Yin and W. O. Chung, "Epigenetic regulation of human β-defensin 2 and CC chemokine ligand 20 expression in gingival epithelial cells in response to oral bacteria," *Mucosal immunology*, vol. 4, no. 4, pp. 409–419, 2011.

[54] A. C. Carr and B. Frei, "Toward a new recommended dietary allowance for vitamin C based on antioxidant and health effects in humans," *The American journal of clinical nutrition*, vol. 69, no. 6, pp. 1086–1107, 1999.

[55] S. J. Padayatty, A. Katz, Y. Wang et al., "Vitamin C as an antioxidant: evaluation of its role in disease prevention," *Journal of the American College of Nutrition*, vol. 22, no. 1, pp. 18–35, 2003.

[56] I. L. Chapple and J. B. Matthews, "The role of reactive oxygen and antioxidant species in periodontal tissue destruction," *Periodontology 2000*, vol. 43, no. 1, pp. 160–232, 2007.

[57] Y. Yan, W. Zeng, S. Song et al., "Vitamin C induces periodontal ligament progenitor cell differentiation via activation of ERK pathway mediated by PELP1," *Protein & cell*, vol. 4, no. 8, pp. 620–627, 2013.

[58] F. C. Luft, "Angiotensin, inflammation, hypertension, and cardiovascular disease," *Current hypertension reports*, vol. 3, no. 1, pp. 61–67, 2001.

[59] V. R. Baichwal and P. A. Baeuerle, "Apoptosis: Activate NF-κB or die?," *Current Biology*, vol. 7, no. 2, pp. R94–R96, 1997.

[60] T. O. Ajibade, A. A. Oyagbemi, T. O. Omobowale, E. R. Asenuga, and K. O. Adigun, "Quercetin and vitamin C mitigate cobalt chloride-induced hypertension through reduction in oxidative stress and nuclear factor kappa beta (NF-Kb) expression in experimental rat model," *Biological Trace Element Research*, vol. 175, no. 2, pp. 347–359, 2017.

[61] D. J. Steger and J. L. Workman, "Remodeling chromatin structures for transcription: what happens to the histones?," *BioEssays*, vol. 18, no. 11, pp. 875–884, 1996.

[62] W. Vanden Berghe, K. De Bosscher, E. Boone, S. Plaisance, and G. Haegeman, "The nuclear Factor-κB engages CBP/p300 and histone acetyltransferase activity for transcriptional activation of the interleukin-6 gene promoter," *The Journal of biological chemistry*, vol. 274, no. 45, pp. 32091–32098, 1999.

[63] J. Zhao, A. Y. Gong, R. Zhou, J. Liu, A. N. Eischeid, and X. M. Chen, "Downregulation of PCAF by miR-181a/b provides feedback regulation to TNF-α–Induced transcription of proinflammatory genes in liver epithelial cells," *The Journal of Immunology*, vol. 188, no. 3, pp. 1266–1274, 2012.

[64] L. Golz, S. Memmert, B. Rath-Deschner et al., "Hypoxia and P. gingivalis Synergistically Induce HIF-1 and NF-κB Activation in PDL Cells and Periodontal Diseases," *Mediators of Inflammation*, vol. 2015, Article ID 438085, 12 pages, 2015.

[65] W. X. Huang, Y. L. Zhan, Y. F. Zheng, Y. Han, W. J. Hu, and J. X. Hou, "Up-regulated ferritin in periodontitis promotes inflammatory cytokine expression in human periodontal ligament cells through transferrin receptor via ERK/P38 MAPK pathways," *Clinical Science*, vol. 133, no. 1, pp. 135–148, 2019.

[66] D. W. Zhang, X. R. Cao, J. Li, and G. Y. Zhao, "MiR-210 inhibits NF-kappa B signaling pathway by targeting DR6 in osteoarthritis," *Scientific Reports*, vol. 5, 2015.

[67] S. H. Jin, J. G. Zhou, X. Y. Guan, J. H. Bai, J. G. Liu, and L. W. Chen, "Development of an miRNA-Array-Based Diagnostic Signature for Periodontitis," *Frontiers in Genetics*, vol. 11, 2020.

[68] Y. Chen and H. Li, "Alkannin protects human renal proximal tubular epithelial cells from LPS- induced inflammatory injury by regulation of microRNA-210," *Biomedicine & Pharmacotherapy*, vol. 108, pp. 1679–1685, 2018.

Research Article

Phloroglucinol Strengthens the Antioxidant Barrier and Reduces Oxidative/Nitrosative Stress in Nonalcoholic Fatty Liver Disease (NAFLD)

Krzysztof Drygalski [iD],[1,2] **Katarzyna Siewko** [iD],[2] **Andrzej Chomentowski,**[3] **Cezary Odrzygóźdź,**[4] **Anna Zalewska** [iD],[5] **Adam Krętowski** [iD],[1,2] **and Mateusz Maciejczyk** [iD][6]

[1]*Clinical Research Center, Medical University of Bialystok, Poland*
[2]*Department of Endocrinology, Diabetology and Internal Medicine, Medical University of Bialystok, Poland*
[3]*Department of Biophysics, Medical University of Bialystok, Poland*
[4]*Department of Molecular and Systems Biology, Institute of Bioorganic Chemistry, Polish Academy of Sciences, Poznań, Poland*
[5]*Experimental Dentistry Laboratory, Medical University of Bialystok, Poland*
[6]*Department of Hygiene, Epidemiology and Ergonomics, Medical University of Bialystok, Poland*

Correspondence should be addressed to Mateusz Maciejczyk; mat.maciejczyk@gmail.com

Nonalcoholic fatty liver disease (NAFLD) is one of the most commonly occurring diseases within western dietary patterns. Usually untreated, it may lead to type 2 diabetes mellitus (T2DM), steatohepatitis (NASH), and hepatocellular carcinoma (HCC). Besides its severe aftermath, up to now, there is no known therapeutic approach to this disease in everyday clinical practice. Most NAFLD patients are encouraged to do physical activities or diet change and remain without pharmacological treatment. In this study, we present phloroglucinol (PHG) as a novel and promising compound in NAFLD treatment. PHG significantly increased the level of enzymatic and nonenzymatic antioxidants both in palmitate and hydrogen peroxide-induced oxidative stress models. Strengthened antioxidative defense reduced the oxidative/nitrosative damage to cell proteins, lipids, and carbohydrates. Furthermore, PHG treatment reduced hepatic steatosis; lowered inflammatory markers, such as NF-κB or HIF-1α; and inhibited cell apoptosis. Moreover, PHG had a more comprehensive effect than other commonly used antioxidants: N-acetylcysteine (NAC) and α-lipoic acid (ALA), suggesting its clinical usability. Therefore, our paper supports the benefits of natural compounds as a therapeutical approach to NAFLD.

1. Introduction

Nonalcoholic fatty liver disease (NAFLD) is a chronic medical condition associated with the excessive accumulation of free fatty acids, diglycerides, and triglycerides in the liver [1]. NAFLD's leading cause has been attributed to excessive high fat intake referred to as "western dietary pattern." It is estimated that around 25% of the world's population might be affected, whereas, in western countries, prevalence is higher [2]. The lipid overload state present in NAFLD results in a dysregulation of hepatocytes' metabolic activity, leading to inflammatory response and liver tissue injury [3]. The most common aftermath of liver steatosis in NAFLD is insulin resistance, leading to type 2 diabetes mellitus (T2DM) [4–6]. Additionally, patients affected by NAFLD are also more likely to develop systemic hypertension, while frequent vascular complications increase the rate of cardiac incidents [7–9]. What is more, long-lasting steatosis induces oxidative stress and inflammation which results in the development of nonalcoholic steatohepatitis (NASH). It remains the leading cause of hepatocellular carcinoma (HCC) in western countries [1–3].

Oxidative stress plays a critical role in the progression of NAFLD [10, 11]. Generally, oxidative stress refers to the

imbalance between the formation of oxygen/nitrogen free radicals and the efficiency of mechanisms responsible for their elimination. Under physiological conditions, reactive oxygen species (ROS) formed in metabolic processes are effectively scavenged by enzymatic and nonenzymatic antioxidants. However, under pathology, redox imbalance occurs in favor of oxidation reactions, and as a consequence, overproduction of ROS causes oxidative damage to biomolecules and cell structures [12]. The oxidative damage may manifest as both protein and lipid oxidation and the creation of advanced glycation end products (AGEs). Increased production of ROS in NAFLD relates to blockage of β-oxidation, which triggers an impairment of the mitochondrial electron transport chain [13]. What is more, the incomplete oxidation of acyl-carnitine causes aggregation of lipotoxic intermediates, which can be an indirect source of ROS [14]. Additionally, recent studies showed the possible role of cytochrome CYP2E1 as a source of ROS in the liver tissue [15]. Since there is no approved medication for NAFLD, whereas mild to moderate lifestyle changes do not bring significant benefits to NAFLD patients, it is crucial to investigate potentially effective drug treatment [16]. Current therapeutic approaches focus their efforts on the reduction of oxidative stress. As for now, silymarin, vitamins E and D, polyunsaturated fatty acids of the omega-3 series, coenzyme Q10, berberine, and curcumin are considered to exert moderate effects after prolonged use [17]. Out of the presented substances, the effects of vitamin E seem to be best documented. However, there are some concerns about the safety of vitamin E supplementation. It has been reported that oral vitamin E supplementation among healthy men increases prostate cancer risk and risk for hemorrhagic stroke in the general population and heart failure in patients with left ventricular dysfunction [18–20]. Based on the above information, we chose phloroglucinol (PHG), a phenolic compound of natural origin, mainly known for its nonspecific antispasmodic properties in gastric tract disorders. Phloroglucinol is safe to use and constitutes an active ingredient in various antispasmodic compositions [21]. Indeed, it has been proven that PHG may have anti-inflammatory and antioxidant capabilities in different medical conditions [22, 23]. Some studies even report its anticancer potential [24, 25]. Nevertheless, it has never been assessed as a potential drug counteracting NAFLD and preventing its progress towards NASH.

In our study, we developed a HepG2 cell line to assess their response to the changes in oxidative balance caused by NAFLD and the feasibility of alleviating these effects using PHG. Furthermore, we compared the effectiveness of PHG with two other compounds of renowned antioxidative properties: N-acetylcysteine (NAC) and α-lipoic acid (ALA). The oxidative stress was generated in two models: hydrogen peroxide or palmitic acid-induced steatosis.

2. Results

2.1. Cell Viability.
PHG showed a dose-dependent decrease of cell viability which was statistically significant in concentrations above $100\,\mu$M ($200\,\mu$M: -33.6% $p < 0.05$; $400\,\mu$M: -47.3% $p < 0.01$; $1000\,\mu$M: -82.7% $p < 0.001$). H_2O_2 also

decreased cell viability in a dose-dependent manner, which was significant in concentrations above $1\,$mM ($2\,$mM: -20.4% $p < 0.01$; $5\,$mM: -35.8% $p < 0.0001$; $10\,$mM: -59.7% $p < 0.0001$). With the addition of PHG to $10\,$mM H_2O_2, the medium did not affect cell viability in concentrations below $200\,\mu$M of PHG. Basing on the cell viability, we choose the PHG concentration of $100\,\mu$M and $10\,$mM concentration of H_2O_2 for further experiments (Figure 1).

2.2. Antioxidant Defense.
Antioxidants are substances that, in low concentrations, protect against oxidation or delay the oxidation of cell components. In our study, we used both enzymatic (catalase, CAT; glutathione peroxidase, GSH-Px; glutathione reductase, GR; superoxide dismutase, SOD) and nonenzymatic (reduced glutathione, GSH) antioxidants to assess the antioxidant barrier.

2.2.1. NAFLD Model.
PHG lowered cellular total glutathione content (PHG: -25.1% $p < 0.05$) and GSH concentration (PHG: -45.4%; NAFLD: -65.7% $p < 0.0001$; NAFLD+PHG: -18.8%, NAFLD+NAC: +0.9%, NAFLD+ALA: +10.3%). All the analyzed antioxidants decreased PA-induced GSSG (NAFLD:+38.8% $p < 0.01$; NAFLD+PHG: -3.9% $p < 0.01$; NAFLD+NAC: -14% $p < 0.001$; NAFLD+ALA: -19.9% $p < 0.0001$), and some of them normalised the GSH/GSSG ratio (NAFLD+NAC: -23.6% $p < 0.05$; NAFLD+ALA: -59.3% $p < 0.001$). Moreover, the activity of GSH-Px was markedly elevated in the NAFLD+PHG-treated group while being significantly lower in the group treated with NAFLD alone (PHG:-10.3%; NAFLD: -57.2% $p < 0.0001$; NAFLD+PHG: +33.5% $p < 0.001$; NAFLD+NAC: -5.8%; NAFLD+ALA: +15.5%). The activity of CAT was increased in all but one (PHG) of the experimental groups (PHG: +35.1%; NAFLD: +171.7% $p < 0.01$; NAFLD+PHG: +364% $p < 0.0001$; NAFLD+NAC: +244.7% $p < 0.0001$; NAFLD+ALA: +246.4% $p < 0.0001$) when compared to the control and significantly higher in NAFLD+PHG when compared to other groups. Additionally, PHG together with NAFLD elevated GR activity compared to all groups except NAFLD+ALA (PHG: +6.9%; NAFLD: -19.9%; NAFLD+PHG: +57.1% $p < 0.0001$; NAFLD+NAC: +13.7%, NAFLD+ALA: +26.3%). PHG had no substantial impact on SOD activity (PHG: -12%; NAFLD: -64.5% $p < 0.0001$; NAFLD+PHG: +15.2%, NAFLD+NAC: -18.2%, NAFLD+ALA:-7.2%) (Figure 2).

2.2.2. H_2O_2 Model.
Total glutathione was slightly decreased in the H_2O_2+PHG group (-27.8% $p < 0.05$). Both PHG and H_2O_2 alone depleted GSH with no significant differences to control in other groups (PHG: -45.3% $p < 0.01$; H_2O_2: -70% $p < 0.0001$) However, NAC and ALA normalised H_2O_2-induced GSH drop (H_2O_2+NAC: -5.5%; H_2O_2+ALA: -3.3% $p < 0.0001$). In contrast, H_2O_2 decreased GSH-Px activity with nonsignificant elevation in the group treated with H_2O_2+PHG (PHG: -10.3%; H_2O_2: -55.8% $p < 0.001$; H_2O_2+PHG: +30.7%; H_2O_2+NAC: +2.6%; H_2O_2+ALA: +15.4%). H_2O_2 significantly increased the GSSG concentration which was normalised by all analyzed antioxidants (H_2O_2: +52.8% $p < 0.001$; H_2O_2+PHG: -18.7%; H_2O_2+NAC: -37.9%; H_2O_2+ALA: -13.5% $p < 0.0001$). GSH/GSSG ratio was decreased

(a)

(b)

(c)

(d)

(e)
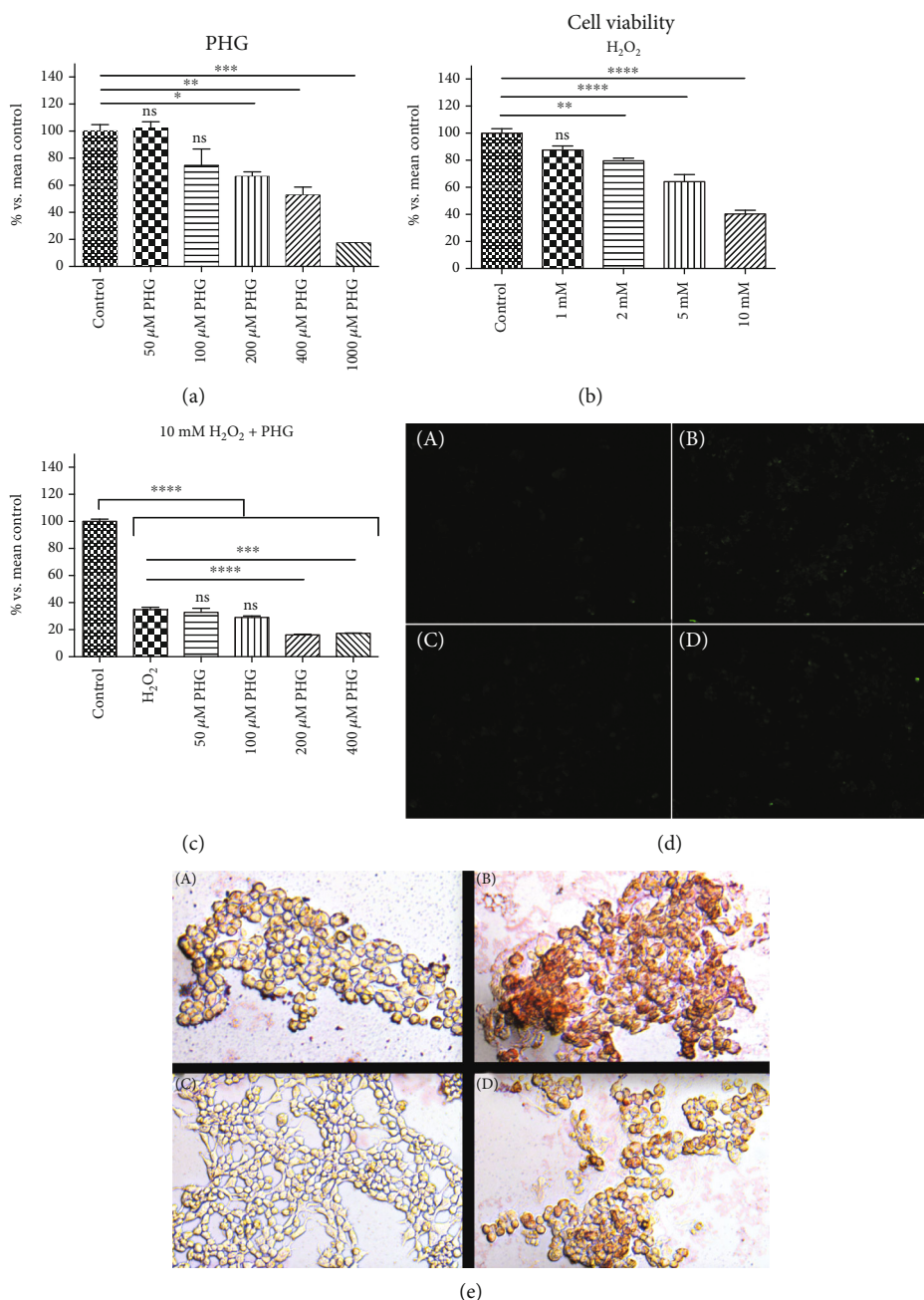
FIGURE 1: The effect of PHG on cell viability and steatosis. (a, c) PHG was nontoxic, both referring to the control and H_2O_2 in concentrations below 200 μM and dose-dependently lowered cell viability in concentrations above 200 μM. (b) H_2O_2 showed a dose-dependent effect on cell viability with GI_{50} around 10 mM. (d) Immunofluorescence staining of active Caspase 3 (A: control group; B: NAFLD; C: PHG; D: NAFLD +PHG). (e) Oil Red O staining of HepG2 cells (A: control group; B: NAFLD; C: PHG; D: NAFLD+PHG).

by H_2O_2 and normalised by NAC and ALA (H_2O_2: -94.1% $p < 0.05$; H_2O_2+NAC: +58.3% $p < 0.0001$; H_2O_2+ALA: +6% $p < 0.01$). The H_2O_2+PHG group generated a rise of GR activity, in opposition to the group with H_2O_2 only, in which we noted low activity of GR (PHG:+6.9%; H_2O_2: -43.1% $p < 0.05$; H_2O_2+PHG: +61.7% $p < 0.01$; H_2O_2+NAC: +2.1%; H_2O_2+ALA: +38.7%). CAT activity was significantly increased only by incubation with H_2O_2 (PHG: +35.1%; H_2O_2: +61% $p < 0.05$; H_2O_2+PHG: +30.6%; H_2O_2+NAC: +54.5%; H_2O_2+ALA: +49.3%). PHG, NAC, and ALA together with H_2O_2 decreased the SOD level (PHG: -12%;

H_2O_2: -2%; H_2O_2: +PHG: -31.4% $p < 0.01$; H_2O_2+NAC: -38% $p < 0.0001$; H_2O_2+ALA: -46.1% $p < 0.0001$) (Figure 3).

2.3. ROS Production and Nitrosative Stress. For the evaluation of ROS production rate, we determined the NADPH oxidase activity (NOX), which is the main prooxidative enzyme responsible for the formation of free radicals in the cell. For the assessment of nitrosative stress, we used both nitric oxide (NO) and peroxynitrite (the most reactive form of RNS (reactive nitrogen species)).

FIGURE 2: Antioxidant defense in the NAFLD model. The activity of the enzymatic and nonenzymatic antioxidants in HepG2 cell cultures incubated with phloroglucinol (PHG), palmitate (NAFLD), both PHG and NAFLD, and palmitate with other known antioxidants: N-acetylcysteine (NAFLD+NAC) and alpha-lipoic acid (NAFLD+ALA). (a) Phloroglucinol alone decreased the concentration of total glutathione; however, no effect was observed in the group incubated with palmitate and PHG together. (b–d) PHG similarly to other antioxidants normalised the level of reduced and oxidized glutathione but not the GSH/GSSG ratio. (e) The intensity of glutathione peroxidase activity (GSH-Px) was markedly elevated in the NAFLD+PHG group. (f) The activity of catalase (CAT) was significantly higher in the NAFLD+PHG group compared to other groups. (g) PHG increased the activity of glutathione reductase (GR) in lipid overload state (NAFLD+PHG). (h) PHG exerted no effect on superoxide dismutase compared with the control; however, the difference was significant between the NAFLD, PHG, and NAFLD+PHG groups.

2.3.1. NAFLD Model. Both NOX and peroxynitrite were markedly elevated in the NAFLD group (PHG: -26.2%; NAFLD: +103.6% $p < 0.0001$; NAFLD+PHG: +13.8%; NAFLD+NAC: -5.4%; NAFLD+ALA: -3.1%) (PHG: +22%; NAFLD: +98.3% $p < 0.0001$; NAFLD+PHG: +39.4%; NAFLD+NAC: +14.2%; NAFLD+ALA: +17.4%) as compared to the control. NO level was significantly lower in the NAFLD and NAFLD+PHG groups (PHG: -4.3%; NAFLD:
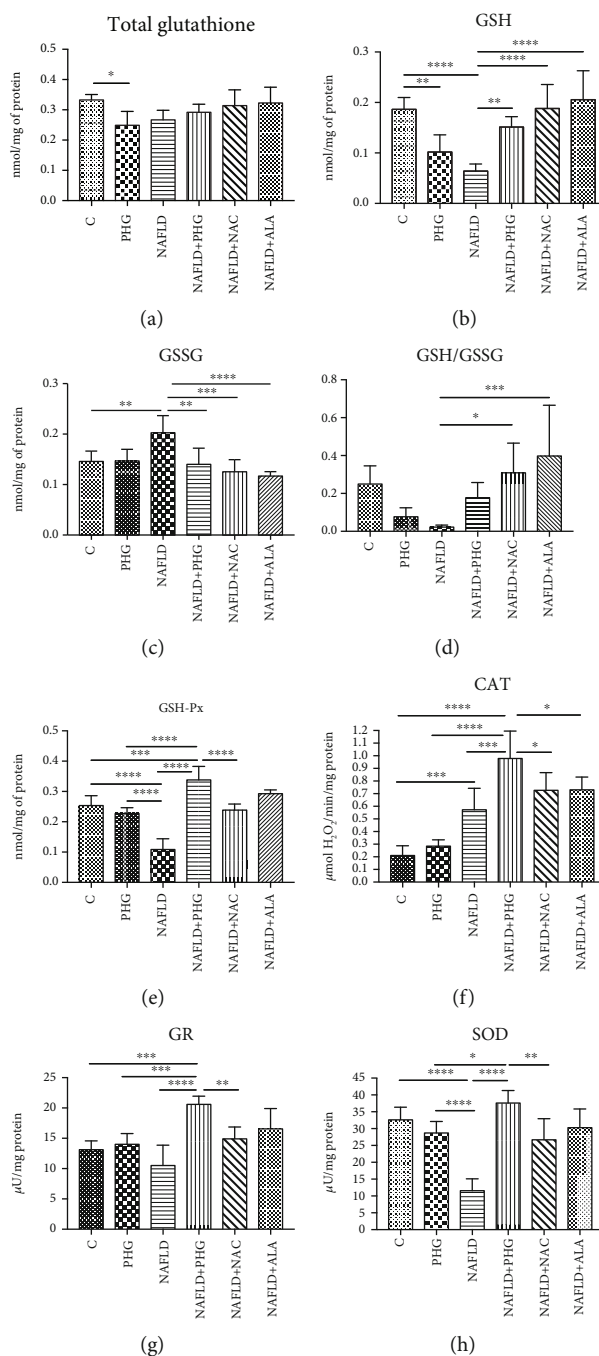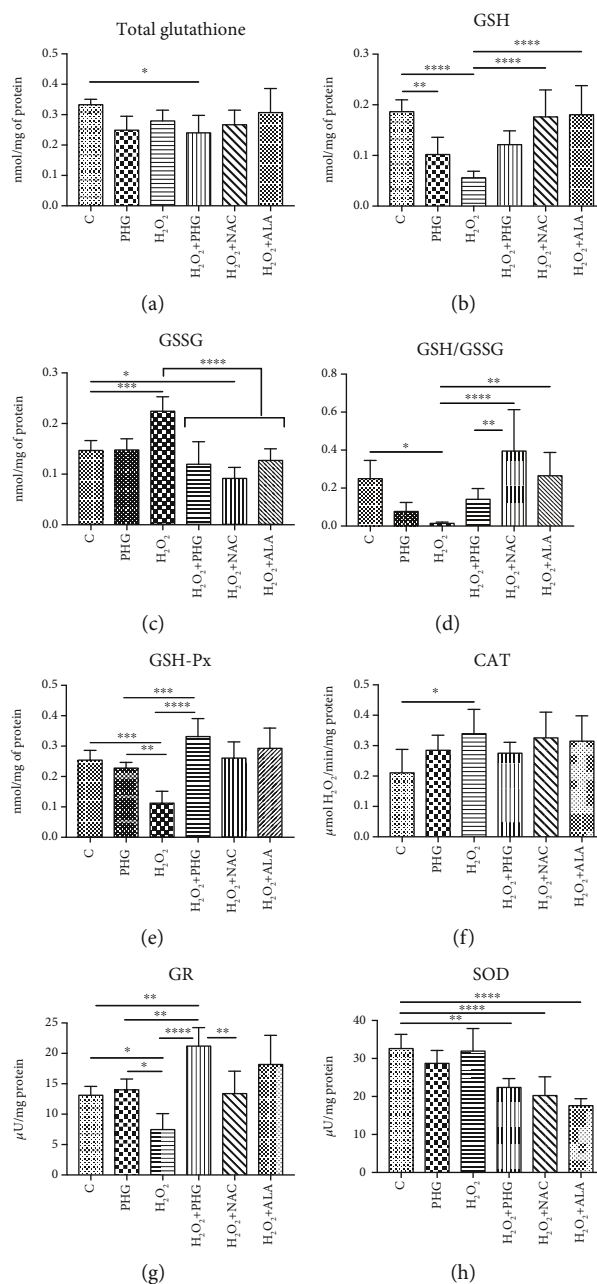
Figure 3: Antioxidant defense in the H_2O_2 model. The activity of the enzymatic and nonenzymatic antioxidants in HepG2 cell cultures incubated with phloroglucinol (PHG), hydrogen peroxide (H_2O_2), both PHG and H_2O_2, and hydrogen peroxide with other known antioxidants: N-acetylcysteine (H_2O_2+NAC) alpha-lipoic acid (H_2O_2+ALA). (a) The concentration of total glutathione (GSH) was slightly lowered only in the H_2O_2+PHG group. (b–d) PHG similar to other antioxidants normalised the level of reduced and oxidized glutathione but not the GSH/GSSG ratio. (e, f) Phloroglucinol significantly increased the activity of glutathione peroxidase (GSH-Px) decreased by H_2O_2. The exposure to H_2O_2 stimulated the activity of catalase (CAT). (g) The activity of glutathione reductase (GR) was intensified by phloroglucinol in the NAFLD+PHG group. (h) Phloroglucinol and other antioxidants decreased the activity of superoxide dismutase in NAFLD conditions.

-46.7% $p < 0.0001$; NAFLD+PHG: -37.5% $p < 0.001$) (Figure 4).

2.3.2. H_2O_2 Model. Incubation with H_2O_2 resulted in substantially increased creation of peroxynitrite (PHG: -26.2%; H_2O_2: +161.2% $p < 0.0001$; H_2O_2+PHG: +40.7% $p < 0.01$; H_2O_2+NAC: +27%; H_2O_2+ALA: +10.5%) as well as elevated activity of NOX (PHG: +22%; H_2O_2: +150.6% $p < 0.0001$;

H_2O_2+PHG: +67.8%; H_2O_2+NAC: +48.8%; H_2O_2+ALA: +36.7%). Concentration of NO was lowered in groups incubated with H_2O_2, H_2O_2+PHG, and H_2O_2+NAC (PHG: -4.3%; H_2O_2: -28.3% $p < 0.05$; H_2O_2+PHG: -30.8% $p < 0.01$; H_2O_2+NAC -36.8% $p < 0.001$) (Figure 4).

2.4. Protein Glycooxidative Damage. For the evaluation of protein glycooxidation products, we used oxidative modified

(a)

(b)

(c)

(d)

(e)

(f)

Figure 4: Concentration of the nitrosative stress products in HepG2. Cell cultures incubated with (first row) phloroglucinol (PHG), palmitate (NAFLD), both PHG and NAFLD, or palmitate with other known antioxidants: N-acetylcysteine (NAFLD+NAC) and alpha-lipoic acid (NA-FLD+ALA); (second row) phloroglucinol (PHG), hydrogen peroxide (H_2O_2), both PHG and H_2O_2, and hydrogen peroxide with other known antioxidants: N-acetylcysteine (H_2O_2+NAC) alpha-lipoic acid (H_2O_2+ALA). (a, c, d, f) The concentration of NADPH oxidase (NOX) and peroxynitrite was elevated significantly in NAFLD and H_2O_2 groups, respectively. (b, e) The concentration of nitric oxide was lower in the NAFLD and H_2O_2 groups.

amino acids (dityrosine, kynurenine, N-formylkynurenine, and tryptophan) and advanced oxidation protein products (AOPP), as well as beta-amyloid formation.

2.4.1. NAFLD Model. Incubation with PA resulted in significantly higher dityrosine (PHG: +12.2%; NAFLD: +126.5% $p < 0.0001$; NAFLD+PHG: +47.8% $p < 0.01$, NAFLD+NAC: +9%; NAFLD+ALA: +17.1%), kyneurenine (PHG: -25.3%; NAFLD: +29.8% $p < 0.05$; NAFLD+PHG: +10.5%, NAFLD+NAC: -7.6%; NAFLD+ALA: -40.9% $p < 0.001$), N-formylkynurenine (PHG: -34.2% $p < 0.01$; NAFLD: +60.8% $p < 0.0001$; NAFLD+PHG: +27.8% $p < 0.05$; NAFLD+NAC:

+17.1%, NAFLD+ALA: +46.3% $p < 0.001$), AOPP (PHG: -13.7%; NAFLD: +58.6% $p < 0.0001$; NAFLD+PHG: +9.5%; NAFLD+NAC: +2.8%, NAFLD+ALA: +5.7%), and amyloid cross structure formation (PHG: -4.3%; NAFLD: +65.8% $p < 0.0001$; NAFLD+PHG: +279.5%; NAFLD+NAC: +28.6%, NAFLD+ALA: +42.5% $p < 0.01$). Additionally, formation of dityrosine and AOPP was significantly higher in the NAFLD group than in other groups. Tryptophan levels were found to be lower in the NAFLD-treated group (PHG: +7%; NAFLD: -29.4% $p < 0.05$; NAFLD+PHG: -12.2%; NAFLD+NAC: -8.8%, NAFLD+ALA: -1%) (Figure 5).

2.4.2. H_2O_2 Model.
Levels of dityrosine (PHG: +12.2%; H_2O_2: +133.2% $p < 0.0001$; H_2O_2+PHG: +42.4%; H_2O_2+NAC: +4.7%; H_2O_2+ALA: +27.1%) and AOPP (PHG: -13.7%; H_2O_2: +95.4% $p < 0.0001$; H_2O_2+PHG: +45.8% $p < 0.01$; H_2O_2+NAC: +37% $p < 0.05$; H_2O_2+ALA: +43.6% $p < 0.01$) were substantially elevated in the group exposed to H_2O_2. By comparison, concentration of tryptophan in the same group was moderately but significantly lower compared to that in the control (PHG: +7%; H_2O_2: -31.4% $p < 0.05$; H_2O_2+PHG: -10.5%; H_2O_2+NAC: -11.6%; H_2O_2+ALA: -15.2%). N-formylkynurenine level was decreased in the PHG group and significantly elevated in other examined groups (PHG: -34.2% $p < 0.01$; H_2O_2: +70.4% $p < 0.0001$; H_2O_2+PHG: +50.4% $p < 0.0001$; H_2O_2+NAC: +37.9% $p < 0.01$; H_2O_2+ALA: +45.5% $p < 0.001$). There was no effect on the amyloid cross structure observed (PHG: -4.3%; H_2O_2: +11.8%; H_2O_2+PHG: +16.1%; H_2O_2+NAC: -15.2%; H_2O_2+ALA: -4.7%) (Figure 6).

2.5. Lipid and Carbonyl Damage.
We assessed the oxidative damage to lipids by evaluating the concentration of malondialdehyde (MDA) and lipid hydroperoxides (LOOH). To assess carbonyl stress, we used advanced glycation end products (AGE).

2.5.1. NAFLD Model.
It was revealed that LOOH and MDA levels were substantially increased in the group exposed to PA (PHG: -17.6%; NAFLD: +66.8% $p < 0.0001$; NAFLD+PHG: -6.7%, NAFLD+NAC: -11.3%, NAFLD+ALA: -3.8%) (PHG: +6.5%; NAFLD: +64.7% $p < 0.0001$; NAFLD+PHG: +15.7%, NAFLD+NAC: +5.7%, NAFLD+ALA:+1.7%) whereas AGE levels rose in NAFLD, NAFLD+PHG, NAFLD+NAC, and NAFLD+ALA groups (PHG: -1.2%; NAFLD: +144.8% $p < 0.0001$; NAFLD+PHG: +71.7% $p < 0.0001$; NAFLD+NAC: +55.3% $p < 0.01$; NAFLD+ALA: +67.2% $p < 0.001$) as compared to the control (Figure 7).

2.5.2. H_2O_2 Model.
In comparison to the control, LOOH and MDA levels were increased significantly in the group treated with H_2O_2, H_2O_2+PHG, H_2O_2+NAC, and H_2O_2+ALA (PHG: -17.6%; H_2O_2: +123.2% $p < 0.0001$; H_2O_2+PHG: +51.4% $p < 0.01$; H_2O_2+NAC: +39.7% $p < 0.05$; H_2O_2+ALA: +56.2% $p < 0.01$) (PHG: +6.5%; H_2O_2: +122.8% $p < 0.0001$; H_2O_2+PHG: +71% $p < 0.0001$; H_2O_2+NAC: +72.5% $p < 0.0001$; H_2O_2+ALA: +69.9% $p < 0.001$) while significant growth in AGE levels was registered in H_2O_2, H_2O_2+NAC, and H_2O_2+ALA sets (PHG: -1.2%; H_2O_2: +199.1% $p < 0.0001$; H_2O_2+PHG: +39.8%; H_2O_2+NAC: +71.7% $p < 0.05$; H_2O_2+ALA: +79.5% $p < 0.01$) (Figure 7).

2.6. Inflammation, Hypoxia, and Apoptosis.
The expression of proteins involved in the inflammatory and apoptotic pathways was assessed only in the main experimental and NAFLD model. PHG, both alone and combined with PA, decreased significantly the HIF-1α level compared to the control (PHG: -57.8%, PA+PHG: -28.3%; $p < 0.05$). What is more, we found that PA incubation increased NF-κB expression (PA: +80%; $p < 0.05$), which was normalised when PHG was added to the steatotic medium (PA+PHG: -100.4%; p

< 0.01). PHG also selectively inhibited COX-1 (PHG: -66.8%; $p < 0.01$) but did not significantly affect COX-2 (Figure 8). Furthermore, both PHG and PA increased TNFα levels in the incubation media (PA: +9.4%; PHG: +12.8%, PA +PHG: +24.2%; $p < 0.05$). PHG significantly lowered PA induced elevation of Il-1β (PA: +32.4%, $p < 0.0001$; PA +PHG: +10.3%, $p < 0.001$) and Il-6 (PA: +23.2%, $p < 0.01$; PA+PHG: +5.2%, $p < 0.05$) (Figure 9). It was revealed that PA activated Caspase 9 (PA: +59.4%; $p < 0.01$) and Caspase 3 (PA: +83.7%; $p < 0.0001$), which was normalised when PHG was added to the incubation media (PA+PHG: -25.5%; $p < 0.05$) (Figure 8).

3. Discussion

This is the first study to assess the effect of PHG on redox homeostasis and oxidative/nitrosative damage in HepG2 cells treated with palmitic acid and hydrogen peroxide. We have shown that PHG strengthens the enzymatic and nonenzymatic antioxidant barrier and prevents oxidative/nitrosative stress comparable to other commonly used antioxidants. Additionally, PHG reduces inflammation and apoptosis in the NAFLD model (Figure 10).

NAFLD is one of the most underestimated diseases in the XXI century. Despite its severe aftermaths, such as T2DM, obesity, liver cirrhosis, and HCC, commonly occurring in the developed countries, it still does not have an acknowledged and efficient treatment method [26, 27]. What is more, NAFLD, as a root cause of liver cirrhosis and HCC, became one of the main reasons for liver transplantation in countries with western dietary pattern [28]. NAFLD's clinical significance in creating its long-term effects may be explained by the "two-hit" theory [29]. Following this theory, the first hit is related to excessive lipid accumulation in the liver, mostly due to an unbalanced diet and overnutrition, resulting in hepatocyte steatosis. The second hit is represented by the lipotoxicity of accumulated lipids, leading to increased oxidative stress, impaired metabolic function, inflammatory process, and NASH development [30]. Indeed, the critical role of redox imbalance in the pathogenesis of fibrosis and steatosis in NAFLD patients has recently been highlighted [31]. Interestingly, there is a significant overproduction of hepatic hydrogen peroxide and progressive depletion of glutathione reserves in NAFLD patients, leading to enhanced protein and lipid oxidative injury. That is why finding new approaches to fight NAFLD and introducing them into clinical practice seems to be crucial to prevent the development of liver steatosis aftermath. So far, numerous compounds, such as resveratrol, quercetin, enterolactone, vitamin E, ALA, or NAC, have been tested for that purpose [27, 32–36]. However, despite promising results *in vitro*, most of the polyphenols have very poor bioavailability in humans, and some have numerous side effects that limit their clinical usability. Thus, in our study, we focused on PHG, a phenolic antioxidant characterized by excellent pharmacokinetics, which may be found in seaweeds such as *Ecklonia cava* or *Cystoseira discors* [22, 37, 38]. PHG was discovered in 1855, yet it was not used in applications other than as an antispasmodic drug. It has a similar structure to resveratrol, and as we
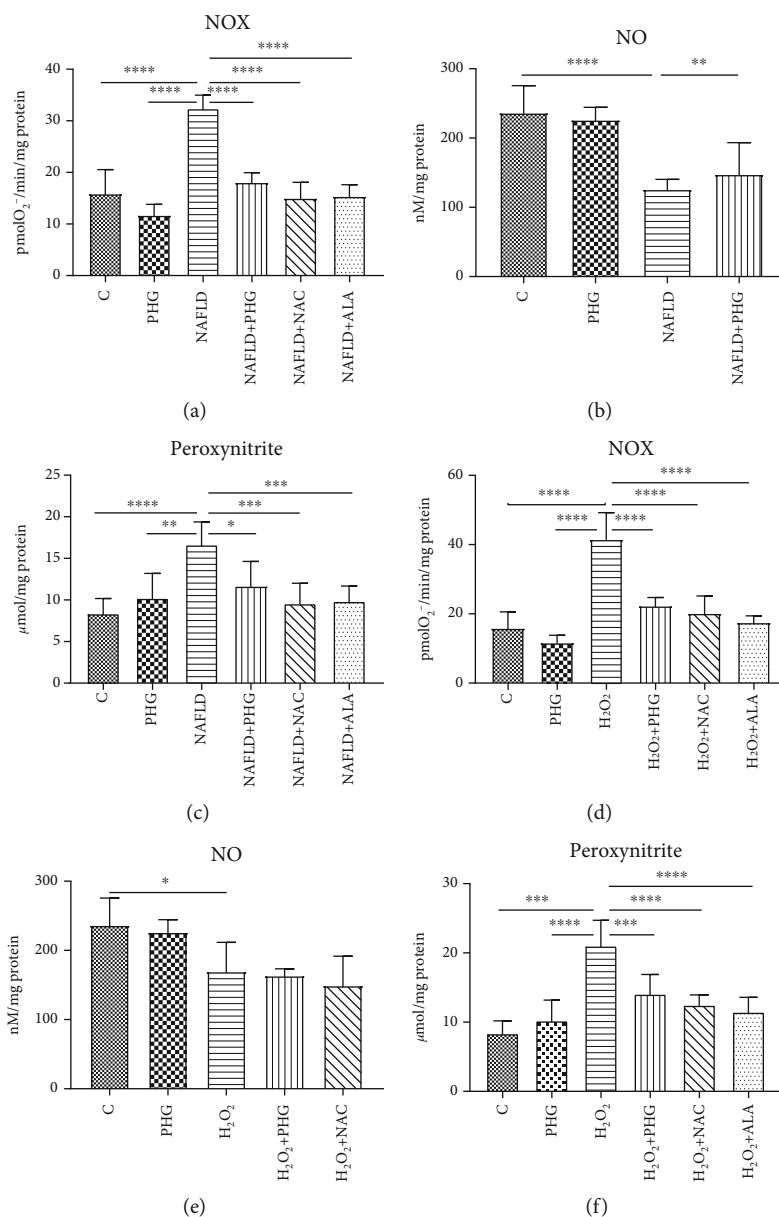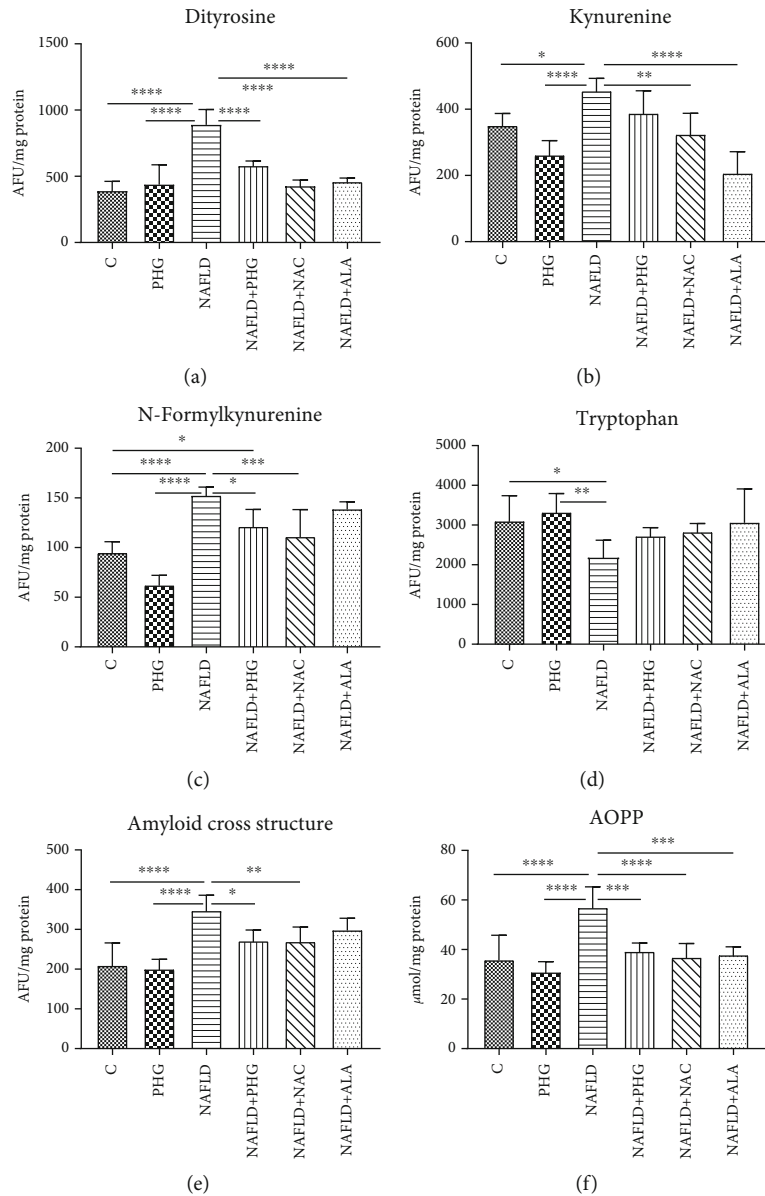
FIGURE 5: Protein glycooxidation damage in the NAFLD model. The concentration of the protein damage products in HepG2 cell cultures incubated with phloroglucinol (PHG), palmitate (NAFLD), both PHG and NAFLD, and palmitate with other known antioxidants: N-acetylcysteine (NAFLD+NAC) and alpha-lipoic acid (NAFLD+ALA). (a, b, e, f) The content of dityrosine, kynurenine, advanced oxidation protein products (AOPP), and the amyloid cross structure was increased significantly only in the NAFLD group. (c) The concentration of N-formylkynurenine was significantly elevated in the NAFLD group with a slight increase in the NAFLD+PHG group compared to the control (d). Concentration of tryptophan was decreased after incubation in NAFLD conditions compared with those of the control and PHG groups.

show herewith, similar to it, PHG decreases liver steatosis, strengthens antioxidative barriers, and reduces inflammation. In the following study, we assessed properties of PHG both in NAFLD and in hydrogen peroxide model and compared its effects with routinely used antioxidants—NAC and ALA.

In NAFLD, the excesses of saturated fatty acids, especially palmitic acid, accumulated in the liver inducing oxidative stress due to impaired mitochondrial β-oxidation and the generation of lipotoxic intermediates such as ceramides, diacylglycerols, and lysophosphatidylcholine [30]. A signifi-

cant source of oxidative stress at NAFLD is the overproduction of hydrogen peroxide, so we decided on a second experimental model in our study. 50% growth inhibition (GI_{50}) of H_2O_2 equal to around 10 mM was obtained in the MTT test. PHG was nontoxic to HepG2 cells in concentrations below $200\,\mu M$. It reduced visible lipid accumulation and decreased the active form of Caspase 3 in the palmate-induced steatosis model (Figure 1). Since overproduction of ROS and reduced antioxidant defense are among the effects of excessive lipid accumulation in the liver, we analyzed the cellular content of enzymatic and nonenzymatic antioxidants
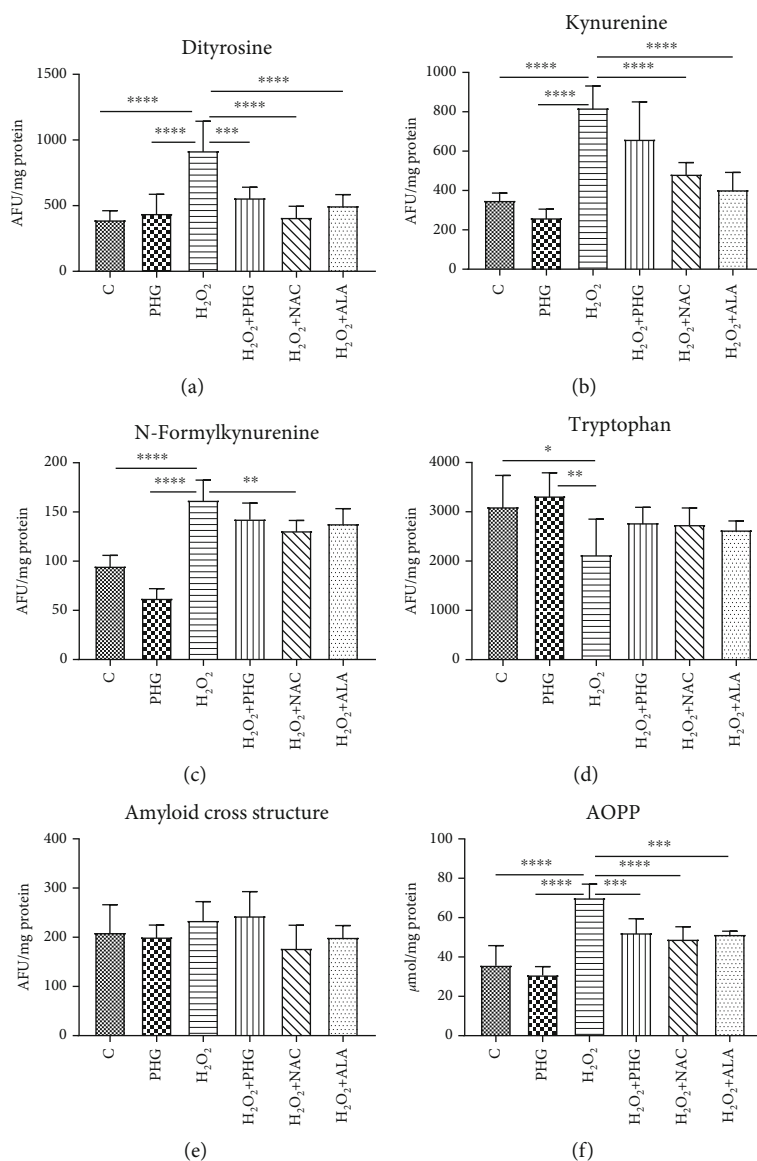
FIGURE 6: Protein glycooxidation damage in the H_2O_2 model. The concentration of the protein damage products in HepG2 cell cultures incubated with phloroglucinol (PHG), hydrogen peroxide (H_2O_2), both PHG and H_2O_2, and hydrogen peroxide with other known antioxidants: N-acetylcysteine (H_2O_2+NAC) alpha-lipoic acid (H_2O_2+ALA). (a–c, f) The content of dityrosine, kynurenine, N-formylkynurenine, and advanced oxidation protein products (AOPP) was raised in the H_2O_2 group only. (d) The content of tryptophan was significantly lower in the H_2O_2 group compared to the control and PHG. (e) No differences in the concentration of amyloid cross structure between groups were observed.

[13, 14]. The exposure to both palmitate and H_2O_2 resulted in a decreased level of reduced glutathione (GSH), which is the major nonenzymatic antioxidant in the liver [14, 39]. The addition of antioxidants is accompanied by an increase of enzymes involved in the restoration of a reduced form of glutathione (GR, GSH-Px) and other enzymatic antioxidants such as SOD and CAT. These effects were observed in both experimental models with a slight predominance of the NAFLD model. Interestingly, within all analyzed compounds (NAC, ALA, and PHG), PHG had the most decisive influence on the enzymatic antioxidant barrier (Figures 2 and 3). Only the increase in GSH level and redox ratio was significantly lower compared to NAC and ALA. However, this should not come as a surprise because the latter are direct

precursors to glutathione biosynthesis. This is particularly important because NAC and ALA have a proven therapeutic effect in NAFLD therapy. However, their limited use is due to the need to administer very high doses (up to 0.5 g per kg of body weight), causing numerous side effects [35, 40]. Although it is difficult to predict the side effects of PHG without human studies, we do not know any of the harmful actions of this compound. As far as enzymatic and nonenzymatic antioxidants are concerned, our observations are consistent with Quéguineur et al., who analyzed the dose-dependent effects of PHG on tert-butyl hydroperoxide-induced oxidative stress [41]. Despite the differences in used concentrations and experimental models, this seems to confirm the beneficial role of PHG in strengthening the liver
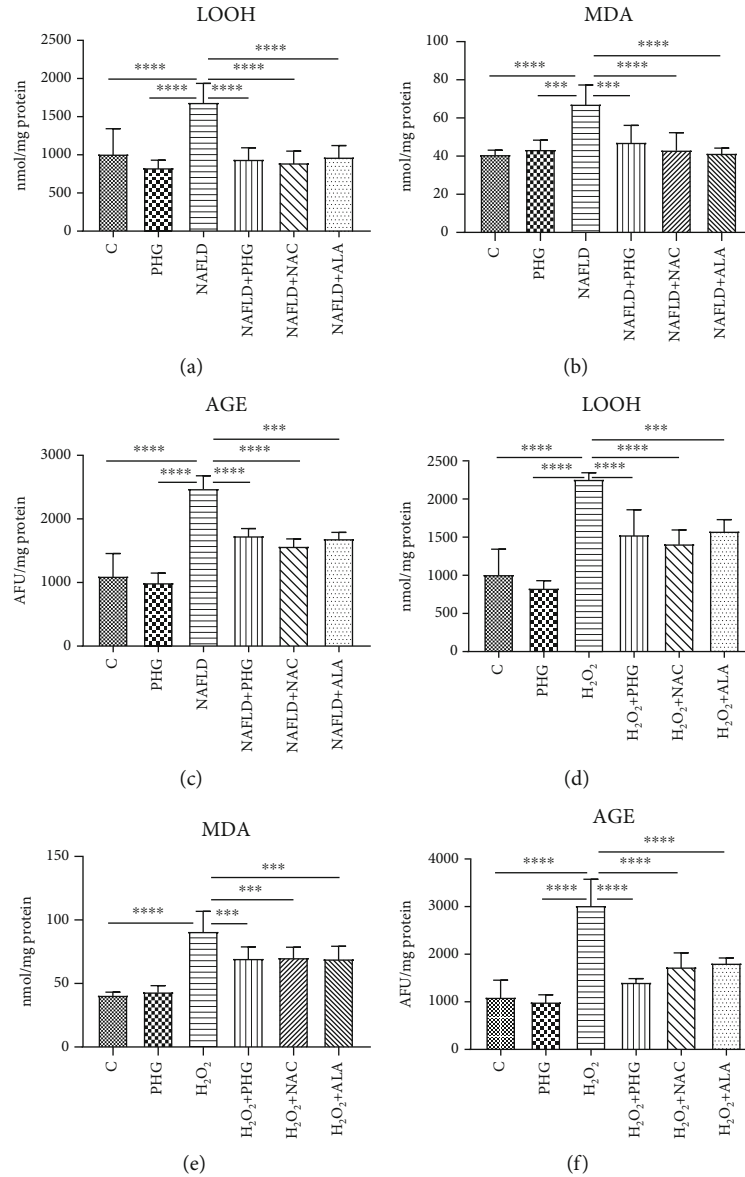
Figure 7: Lipid and carbonyl damage. The concentration of the lipid and carbonyl damage products in HepG2 cell cultures incubated with (first row) phloroglucinol (PHG), palmitate (NAFLD), both PHG and NAFLD, and palmitate with other known antioxidants: N-acetylcysteine (NAFLD+NAC) and alpha-lipoic acid (NAFLD+ALA); (second row) phloroglucinol (PHG), hydrogen peroxide (H_2O_2), both PHG and H_2O_2, and hydrogen peroxide with other known antioxidants: N-acetylcysteine (H_2O_2+NAC) alpha-lipoic acid (H_2O_2+ALA). (a–f) Concentration of total hydroperoxides (LOOH), malondialdehyde (MDA), and advanced glycation end products (AGE) was markedly elevated only in groups incubated in NAFLD and H_2O_2 conditions alone.

antioxidant defense. On the other hand, PHG, in contrast to myricetin and pyrogallol, failed to increase antioxidant defense in yeast *Saccharomyces cerevisiae* what might suggest an animal-specific effect of PHG [42]. Although we did not assess the rate of hydrogen peroxide production, probably, the observed increase in GSH-Px and CAT activity does not result from the adaptive reaction to the increased formation of H_2O_2 by phloroglucinol. Previous studies showed that PHG elevates CAT activity and its protein expression, while CAT inhibitor abolished the protective effect of PHG from H_2O_2-induced cellular damage [43].

In animals, the primary source of ROS generation in physiological conditions is β-oxidation. However, in NAFLD, lipotoxic intermediates created by the incomplete oxidation of acyl-carnitine may also constitute an additional source of ROS [14]. Liver steatosis and exposure to H_2O_2 may also activate membrane NADPH oxidase (NOX), which catalase the process of superoxide anion formation [44]. Under these conditions, NO is also synthesized by inducible NO synthase (iNOS). iNOS is present in the liver and may be upregulated due to steatosis, cirrhosis, and liver cholestasis [45, 46]. Interestingly, the interaction of superoxide anions with NO results in highly reactive peroxynitrite, which might explain lowered NO concentration in experimental models. Indeed, peroxynitrite is one of the strongest prooxidizing factors in living organisms [47, 48]. Peroxynitrite and its
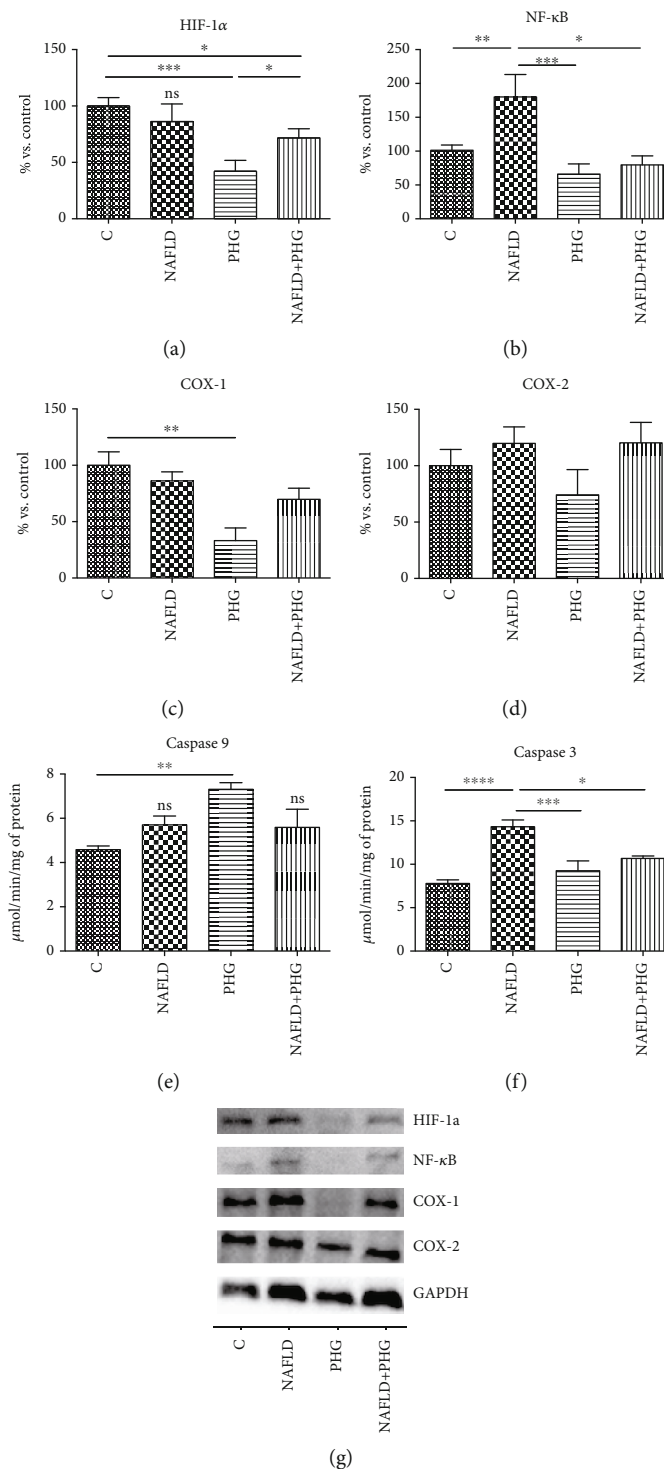
FIGURE 8: Inflammation, hypoxia, and apoptosis. PHG significantly reduced HIF-1α level (a) and PA induced NF-κB activation (b) in HepG2 cells. Furthermore, it selectively inhibited COX-1 (c) with no effect on COX-2 (d). PHG stimulated Caspase 9 (e) and inhibited steatosis-induced activation of Caspase 3, showing its antiapoptotic properties (f). The expression of proteins involved in the inflammatory process assessed in Western blot (g). The band intensity was calculated as a % of control.

derivatives react both with amino acids (including tyrosine, cysteine, and tryptophan), lipids, and several antioxidants. Peroxynitrite causes the formation of carbonyl groups, dimerization, nitration, and nitrosylation of amino acids

and thiol compounds [48–50]. It was shown that nitrosative stress plays a critical role in various pathological conditions such as cardiovascular diseases, liver cirrhosis, diabetes, or cancer [22, 51]. In our experiment, we observed that all

(a)

(b)

(c)
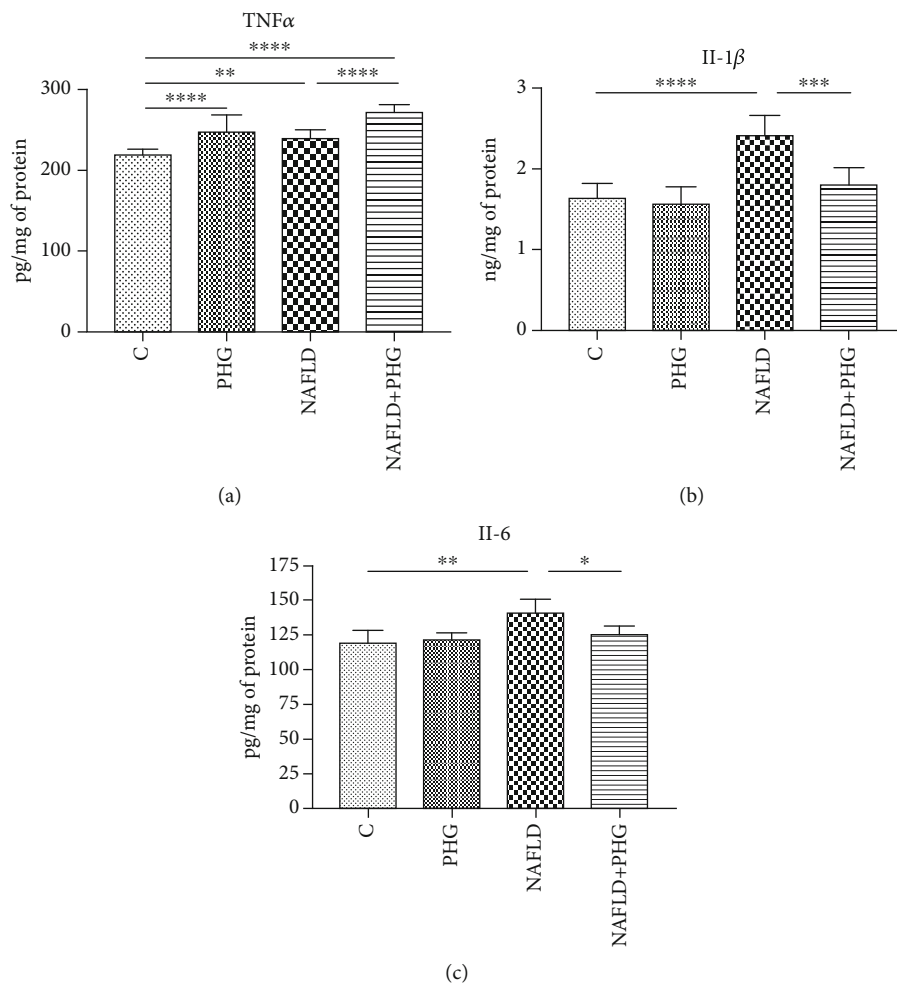
FIGURE 9: Proinflammatory cytokines. The TNFα concentration in the incubation media was slightly elevated in all the experimental groups when comparing to the control (a). Cell steatosis significantly increased the media level of main proinflammatory interleukins: Il-1β and Il-6 which were normalised when PHG was added (b, c).

analyzed antioxidants presented a similar ability to diminish nitrosative stress both in the NAFLD and H_2O_2 models (Figure 4).

Once we established the antioxidant status and the level of the primary oxidative stress sources, we wanted to verify if PHG could prevent the formation of oxidative damage products. One of the most commonly used markers of overall protein damage is AOPP, which is created in interaction with chlorinated oxidants [52]. AOPP, similarly to MDA, CAT, and serum lipids, have been used recently to create a multi-marker test aimed at improving the early identification of NAFLD and prediabetic patients [53]. As depicted in Figures 5 and 6, all analyzed compounds were efficient in decreasing AOPP. The increase of AOPP in experimental models can correspond with the lowered cellular GSH level (Figures 2 and 3) which suggests that protein oxidation in the liver is a result of a diminished antioxidant barrier [54]. Other commonly used markers of ROS generated protein damage are oxidized forms of tryptophan: N-formylkynurenine and kynurenine. N-formylkynurenine results from posttranslational oxidation of tryptophan, which may be further converted into kynurenine [55]. ALA was the

most potent among tested antioxidants in diminishing kynurenine, while PHG and NAC were more efficient in lowering the level of N-formylkynurenine (Figures 5 and 6). Furthermore, we evaluated the level of dityrosine; a ROS-modified amino acid responsible for amyloid cross-linking, and the generation of Aβ plaques [56]. Both exposures to palmitate and H_2O_2 resulted in a significant increase of dityrosine, which was normalised in the presence of antioxidants. Interestingly, elevated amyloid cross structure content was observed only in the NAFLD model and partly decreased due to PHG and NAC action (Figures 5 and 6). Finally, we assessed the lipid and carbonyl damage products. Similar to proteins, both NAFLD and H_2O_2 caused a steep increase of oxidized forms of lipids such as MDA or LOOH and the elevation of glycation end products that were efficiently lowered when PHG, NAC, or ALA were added to the incubation media (Figure 7). Reducing the oxidation/nitrosylation of liver proteins and lipids may slow down the progression of NAFLD. It is well known that the increase in protein and lipid glycation is responsible for the development of ischemia and hepatic fibrosis, and thus, the progression of NAFL to NASH [14–57]. The accumulation of AGE and AOPP in
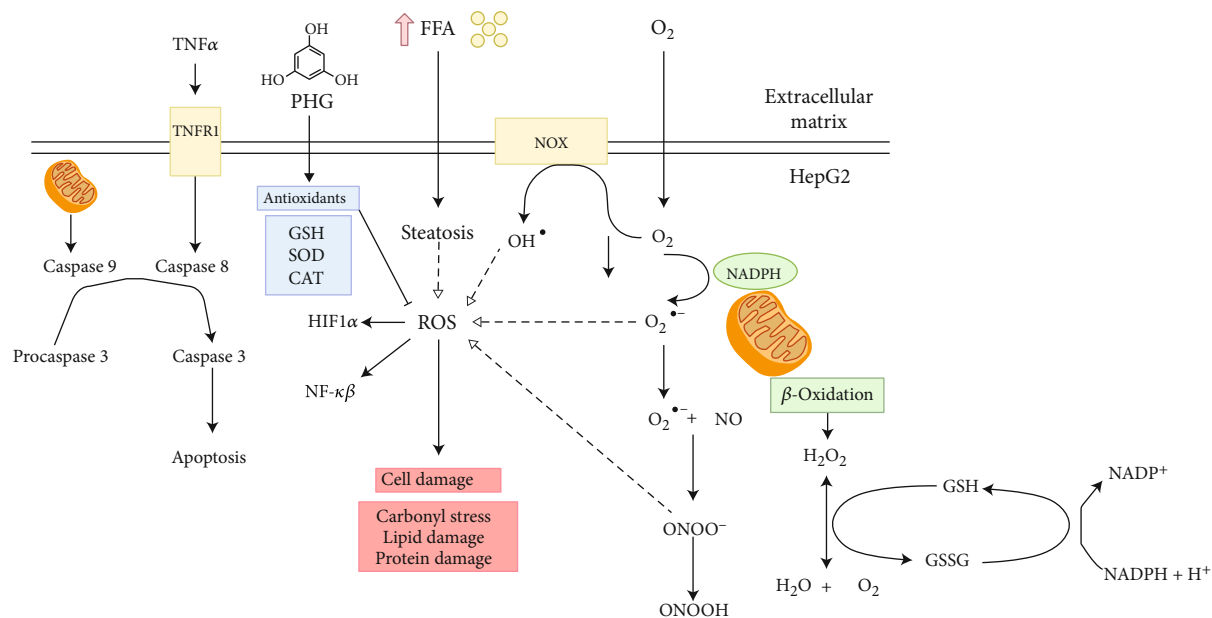
FIGURE 10: The potential mechanism underlying oxidative/nitrosative stress in nonalcoholic fatty liver disease (NAFLD).

the liver not only will increase the production of ROS (through NOX induction in the positive feedback mechanism) but also increases the expression of Fas ligand (protein from tumor necrosis factor (TNF) family) and activates the NF-κB transcription factor (nuclear factor kappa-light-chain-enhancer of activated B cells), which stimulates neutrophil chemotaxis in the hepatocytes [31, 58] In our study, PHG, by strengthening the antioxidant barrier, not only reduces ROS production and oxidative/glycooxidation damage to proteins and lipids but also prevents excessive nitrosylation of the cell.

To assess the influence of PHG on inflammation and cell survival, we analyzed the expression of key proteins involved in apoptosis. As depicted in Figures 1 and 8, PHG revealed antiapoptotic properties by inhibiting the caspase cascade in the steatotic liver. The drop in Caspase 3 activity corresponded to lowered HIF-1α which might explain increased HepG2 survival. HIF-1α upregulates FOXO3, which is responsible for promoting Bax over Bcl-2 signaling [59]. In contrast to antiapoptotic Bcl-2, Bax opens voltage-dependent anion channels and creates pores in the mitochondrial outer membrane that initiate apoptosis [60]. Another interesting observation was a PHG-induced down-regulation of NF-κB, a key regulator of proinflammatory signaling (Figure 8). As a result of its activation, NF-κB raises the TNFα level and stimulates iNOS, and COX-2 leads to proinflammatory prostaglandins and NO [61]. Despite the lack of statistically significant changes in COX-2, PHG inhibited COX-1 which may suggest its selectivity towards this isozyme (Figure 8). Nevertheless, the increased NO synthesis and inflammation results in oxidative/nitrosative stress and the creation of ROS and RNS, which weakens the antioxidative defense, and results in elevated protein accumulation, lipid, and carbonyl damage products. Finally, NF-κB may also induce HIF-1α expression as a downstream effect of the PI3K-Akt-NF-κB signaling pathway [62].

Our study confirms previous reports on the antioxidant properties of PHG. Indeed, it was shown that PHG protected human HaCaT keratinocytes against ultraviolet B- (UVB-) induced oxidative stress by scavenging intracellular ROS production [63]. PHG also decreased serum glucose level and formation of AGE in streptozotocin-induced diabetic rats [64]. Reduced oxidative stress under the influence of PHG was also noted in endothelial, neuronal, retinal, and neoplastic cells, which indicates the possibility of PHG as a promising therapeutic agent in several diseases [65–68]. A good pharmacokinetic profile and few PHG side effects are the additional advantages of this compound. However, as the mechanism of the antioxidant/antiglycation effect of PHG is not yet exactly known, further research is needed.

Nevertheless, our manuscript also has some limitations. We have evaluated the effect of PHG only on HepG2 cells, so further studies on other cell lines are necessary. Furthermore, we have only assessed selected oxidative/nitrosative stress biomarkers, so we cannot fully characterize the effect of PHG on NAFLD redox homeostasis. The next step is also to evaluate the therapeutic effect of PHG on the animal model and choose the dose characterizing the maximum therapeutic effect.

4. Conclusions

To sum up, our study showed that NAFLD and hydrogen peroxide models are comparable and suitable for assessing the oxidative/nitrosative stress in the liver. Although our study does not fully explain the PHG action's mechanism, this compound may be considered a new nutraceutical in counteracting NAFLD and preventing its severe molecular and clinical aftermath. Its effectiveness is comparable with other renowned antioxidants α-lipoic acid and N-acetylcysteine, which brings a promising perspective for the therapeutical application of phloroglucinol. The potential mechanism

underlying oxidative/nitrosative stress in NAFLD are depicted on Figure 10.

5. Materials and Methods

5.1. Cell Culture. The study was conducted on HepG2 cells obtained from ATCC (American Type Culture Collection). The cells were incubated in DMEM (Dulbecco's modified Eagle's medium) enriched with 10% fetal bovine serum (FBS) and 1% penicillin/streptomycin for five days at 37°C in a humidified atmosphere containing 5% of CO_2 until they will reach a confluence of 70%. The media were changed every 48 h preceded by rinsing in PBS. Subsequently, cells were transferred to 6-well plates and cultured in the growth medium until they achieved 90% of confluence. Then experimental incubations were conducted. Subsequently, cells were scrubbed in ice-cold RIPA buffer containing protease and phosphatase inhibitors (Roche Diagnostics GmbH, Germany) and ultrasonicated (Hielscher UP50H, Germany).

5.2. Experimental Models. To induce steatosis, cells were serum-starved for five h in a medium deprived of glucose and then incubated for 16 h in media containing either 0.75 mM palmitate alone or both PA and experimental compounds: 100 μM PHG or 100 μM ALA or 10 μM NAC. Sodium palmitate was dissolved in absolute ethanol and heated to 70°C before conjugation with 10% fatty acid-free bovine serum albumin (BSA). Subsequently, the palmitic acid solution was added to serum-free DMEM supplemented with 10 mM Hepes, similarly to previously described methods [26, 27, 69]. The H_2O_2 model was prepared simply by adding an appropriate amount of hydrogen peroxide to the standard growth medium. Sigma-Aldrich, Poland, provided all the compounds.

5.3. Redox Homeostasis. The performed analyses included determination of antioxidant enzymes [catalase (CAT), glutathione peroxidase (GSH-Px), glutathione reductase (GR), and superoxide dismutase (SOD)] and nonenzymatic antioxidants [GSH], determination of prooxidant enzymes (NADPH oxidase, NOX), determination of oxidative damage to proteins [advanced glycation end products (AGE) and advanced oxidation protein products (AOPP)] and lipids [malondialdehyde (MDA) and total lipid hydroperoxides (LOOH)], and determination of protein glycooxidative products [dityrosine, kynurenine, N-formylkynurenine, and tryptophan], as well as the determination of nitrosative stress products [nitric oxide (NO) and peroxynitrite]. The absorbance/fluorescence was analyzed using the Infinite M200 PRO Microplate Reader (Tecan, Männedorf, Switzerland). All results were standardized to mg of the total protein. In the analysis of redox homeostasis and oxidative damage products, we followed the methods of Maciejczyk et al. [70].

5.4. Enzymatic and Nonenzymatic Antioxidants. The activity of catalase (CAT, EC 1.11.1.6) was estimated using the colorimetric method by measuring hydrogen peroxide (H_2O_2) decomposition at 240 nm [71, 72]. One unit of CAT activity was defined as the quantity of the enzyme catalyzing decomposition of 1 mmol H_2O_2 per 1 min. The activity of glutathi-

one peroxidase (GSH-Px, EC 1.11.1.9) was analyzed colorimetrically by measuring the NADPH oxidation at 340 nm [73]. One unit of GPx activity was defined as the quantity of enzyme catalyzing the oxidation of 1 mmol NADPH per 1 min. The activity of glutathione reductase (GR, EC 1.8.1.7) was analyzed colorimetrically by measuring the decrease in NADPH absorbance at 340 nm [74]. One unit of GR activity was defined as the amount of enzyme catalyzing the oxidation of 1 μmol NADPH per 1 min. The activity of superoxide dismutase (SOD, EC 1.15.1.1) was determined colorimetrically by measuring the inhibition of adrenaline oxidation at 480 nm [71]. One unit of SOD activity was defined as the quantity of enzyme inhibiting adrenaline oxidation by 50%.

The level of total glutathione was measured based on an enzymatic reaction with 5,5′-dithiobis-(2-nitrobenzoic acid) (DTNB), NADPH, and GR [75]. Oxidized glutathione (disulfide glutathione, GSSG) was determined similarly to the assay performed for total glutathione. However, prior to the determination, the samples had been thawed and neutralized to pH 6–7 using 1 M chlorhydrol triethanolamine. Then, samples were incubated with 2-vinylpyridine. The level of reduced glutathione (GSH) was calculated from the difference between the level of total glutathione and disulfide glutathione [75]. Redox ratio was calculated using the formula $[GSH]^2/[GSSG]$ [76].

5.5. ROS Production and Nitrosative Stress. NADPH oxidase activity (NOX, EC 1.6.3.1) was analyzed by the luminescence method using lucigenin as an electron acceptor [77, 78]. One unit of NOX activity was defined as the quantity of enzyme required to release 1 nmol of the superoxide anion per 1 min. The cells used for ROS production measurements were cultured in pyruvate and antibiotic-free media.

The concentration of nitric oxide (NO) was determined using the Griess method based on the reaction of nitrates with sulfanilamide and N-(1-naphthyl)-ethylenediamine dihydrochloride [79, 80]. The absorbance was measured at 490 nm. The concentration of peroxynitrite was estimated colorimetrically based on peroxynitrite-mediated nitration of phenol to nitrophenol [81]. The absorbance was measured at 320 nm.

5.6. Protein Glycooxidation Products. The content of protein glycooxidation products (dityrosine, kynurenine, N-formylkynurenine, and tryptophan) was estimated fluorimetrically by measuring fluorescence at 330/415 nm (dityrosine), 365/480 nm (kynurenine), 325/434 nm (N-formylkynurenine), and 95/340 nm (tryptophan). Immediately before the assay, cells were diluted in 0.1 M H_2SO_4 (1 : 10, v/v). The results were normalised to fluorescence of 0.1 mg/mL quinine sulfate in 0.1 M H2SO4 [54]. The concentration of advanced oxidation protein products (AOPP) was estimated colorimetrically by measuring the sample's iodide ion oxidizing capacity at 340 nm [10].

5.7. Lipid and Carbonyl Damage. The concentration of total hydroperoxides (LOOH) was determined colorimetrically based on the reaction of Fe^{3+} (resulting from Fe^{2+} after its

oxidation by LOOH) with xylenol orange [82]. The absorbance of the resulting complex was measured at 560 nm. Immediately before the assay, cells were diluted in 0.02 M PBS, pH 7.4 (1 : 5, $v : v$) [71]. The concentration of malondialdehyde (MDA) was determined colorimetrically using the thiobarbituric acid reactive substances (TBARS) method. The absorbance was measured at 535 nm, and 1,3,3,3-tetraethoxypropane was used as a standard [83]. The concentration of advanced glycation end products (AGE) was detected fluorimetrically by measuring AGE-specific fluorescence at 350/440 nm [84]. Immediately before the assay, cells were diluted in 0.02 M phosphate-buffered saline (PBS) pH 7.4 (1 : 5, $v : v$) [83].

5.8. In Situ Immunofluorescence. Approximately 10^6 cells were seeded on a 12-well plate and grown overnight. The next day, cells were treated in the same manner as cells from the main part of the experiment. At the end of 16 h, experimental incubation cells were rinsed with PBS and fixed in 3.7% paraformaldehyde for 15 min, permeabilized with 0.1% Triton X-100 for 20 min, and blocked with 2% FBS 1% BSA in PBS for 30 min at room temperature. Subsequently, cells were incubated with the primary monoclonal anticleaved Caspase 3 antibody (1 : 200, Abcam, UK) and then with the secondary goat-anti-rabbit antibody conjugated with Alexa Fluor 488 (1 : 1000, Abcam, UK) both for 1 h at room temperature. Finally, cell nuclei were counterstained with DAPI (1 : 5000, Sigma-Aldrich). The images were obtained with a fluorescent microscope (Leica DMi8, Germany).

5.9. Oil Red O Staining. Approximately 10^6 cells were seeded on a 12-well plate and grown overnight. The next day, cells were treated in the same manner as cells from the main part of the experiment. After experimental treatment, cells were fixed in 3.7% paraformaldehyde for 15 min and then stained with 0.5% Oil Red O solution. The images were obtained with a fluorescent microscope (Leica DMi8, Germany).

5.10. Western Blotting. Proteins of interest expression were analyzed using the standard Western blot technique. To standardize samples, total protein concentration was assessed using the bicinchoninic acid method (BCA) with BSA as a standard. Cell lysates were separated by 10% sodium dodecyl sulfate-polyacrylamide gel electrophoresis (SDS-PAGE) and transferred to nitrocellulose membranes. Subsequently, they were blocked with 5% nonfat dry milk and immunoblotted with primary antibodies of interest and incubated with secondary antibodies labeled with horseradish peroxidase (HRP). The protein bands were quantified densitometrically using the ChemiDoc visualisation system (Bio-Rad, Poland). Equal protein loading was controlled by Ponceau S staining. All the proteins' expression was standardized to the GAPDH (Santa Cruz Biotechnology, USA) expression, and the control was set as 100%.

5.11. ELISA. TNFα, IL-1, and IL-6 concentrations were analyzed using a standard ELISA kit purchased from Abcam, UK (TNFα) and EIAab, China (IL-1 and IL-6). All the procedures were made on cell culture media samples standardized to protein concentration following the manufacturer's instructions. The assay was done in triplicate, and the results were averaged.

5.12. Statistical Analysis. The results were expressed as mean ± SD based on six independent repetitions. Statistical significance was tested with one-way analyses of variance (ANOVA) and Tukey HSD post hoc test using GraphPad Prism 7 (GraphPad Software Inc., La Jolla, CA, USA). Multiplicity adjusted p value was also calculated. Results were considered statistically significant at $p \leq 0.05$.

Data Availability

The data used to support the findings of this study are available from the corresponding author upon request.

Conflicts of Interest

The authors declare no conflict of interest.

Authors' Contributions

K. D. and K. S. contributed equally to this work.

Acknowledgments

References

[1] M. E. Rinella, "Nonalcoholic fatty liver disease: a systematic review," *JAMA*, vol. 313, no. 22, pp. 2263–2273, 2015.

[2] Z. M. Younossi, G. Marchesini, H. Pinto-Cortez, and S. Petta, "Epidemiology of nonalcoholic fatty liver disease and nonalcoholic steatohepatitis: implications for liver transplantation," *Transplantation*, vol. 103, no. 1, pp. 22–27, 2019.

[3] B. Gao and H. Tsukamoto, "Inflammation in alcoholic and nonalcoholic fatty liver disease: friend or foe?," *Gastroenterology*, vol. 150, no. 8, pp. 1704–1709, 2016.

[4] T. Jelenik, K. Kaul, G. Séquaris et al., "Mechanisms of insulin resistance in primary and secondary nonalcoholic fatty liver," *Diabetes*, vol. 66, no. 8, pp. 2241–2253, 2017.

[5] B. Fruci, S. Giuliano, A. Mazza, R. Malaguarnera, and A. Belfiore, "Nonalcoholic fatty liver: a possible new target for type 2 diabetes prevention and treatment," *International Journal of Molecular Sciences*, vol. 14, no. 11, pp. 22933–22966, 2013.

[6] L. A. Adams, O. R. Waters, M. W. Knuiman, R. R. Elliott, and J. K. Olynyk, "NAFLD as a risk factor for the development of diabetes and the metabolic syndrome: an eleven-year follow-

up study," *The American Journal of Gastroenterology*, vol. 104, no. 4, pp. 861–867, 2009.

[7] S. Wu, F. Wu, Y. Ding, J. Hou, J. Bi, and Z. Zhang, "Association of non-alcoholic fatty liver disease with major adverse cardiovascular events: a systematic review and meta-analysis," *Scientific Reports*, vol. 6, no. 1, article 33386, p. 1, 2016.

[8] C. Söderberg, P. Stål, J. Askling et al., "Decreased survival of subjects with elevated liver function tests during a 28-year follow-up," *Hepatology*, vol. 51, no. 2, pp. 595–602, 2010.

[9] C. R. Wong and J. K. Lim, "The association between nonalcoholic fatty liver disease and cardiovascular disease outcomes," *Clinics in Liver Disease*, vol. 12, no. 2, pp. 39–44, 2018.

[10] S. Spahis, E. Delvin, J. M. Borys, and E. Levy, "Oxidative stress as a critical factor in nonalcoholic fatty liver disease pathogenesis," *Antioxidants and Redox Signaling*, vol. 26, no. 10, pp. 519–541, 2017.

[11] F. Ucar, S. Sezer, S. Erdogan, S. Akyol, F. Armutcu, and O. Akyol, "The relationship between oxidative stress and nonalcoholic fatty liver disease: Its effects on the development of nonalcoholic steatohepatitis," *Redox Report*, vol. 18, no. 4, pp. 127–133, 2013.

[12] M. Maciejczyk, A. Skutnik-Radziszewska, I. Zieniewska et al., "Antioxidant defense, oxidative modification, and salivary gland function in an early phase of cerulein pancreatitis," *Oxidative Medicine and Cellular Longevity*, vol. 2019, Article ID 8403578, 14 pages, 2019.

[13] I. Grattagliano, O. de Bari, T. C. Bernardo, P. J. Oliveira, D. Q. H. Wang, and P. Portincasa, "Role of mitochondria in nonalcoholic fatty liver disease-from origin to propagation," *Clinical Biochemistry*, vol. 45, no. 9, pp. 610–618, 2012.

[14] M. Masarone, V. Rosato, M. Dallio et al., "Role of oxidative stress in pathophysiology of nonalcoholic fatty liver disease," *Oxidative Medicine and Cellular Longevity*, vol. 2018, Article ID 9547613, 14 pages, 2018.

[15] E. Kathirvel, P. Chen, K. Morgan, S. W. French, and T. R. Morgan, "Oxidative stress and regulation of anti-oxidant enzymes in cytochrome P4502E1 transgenic mouse model of nonalcoholic fatty liver," *Journal of Gastroenterology and Hepatology*, vol. 25, no. 6, pp. 1136–1143, 2010.

[16] K. Tsunoda, Y. Kai, N. Kitano, K. Uchida, T. Kuchiki, and T. Nagamatsu, "Impact of physical activity on nonalcoholic steatohepatitis in people with nonalcoholic simple fatty liver: a prospective cohort study," *Preventive Medicine*, vol. 88, pp. 237–240, 2016.

[17] A. Cicero, A. Colletti, and S. Bellentani, "Nutraceutical approach to non-alcoholic fatty liver disease (NAFLD): the available clinical evidence," *Nutrients*, vol. 10, no. 9, article 1153, 2018.

[18] E. A. Klein, I. M. Thompson, C. M. Tangen et al., "Vitamin E and the risk of prostate cancer: the Selenium and Vitamin E Cancer Prevention Trial (SELECT)," December 2020, http://www.jama.com.

[19] M. Schürks, R. J. Glynn, P. M. Rist, C. Tzourio, and T. Kurth, "Effects of vitamin E on stroke subtypes: meta-analysis of randomised controlled trials," *BMJ*, vol. 341, no. 7781, article 1033, 2010.

[20] R. Marchioli, G. Levantesi, A. Macchia et al., "Vitamin E increases the risk of developing heart failure after myocardial infarction: results from the GISSI-Prevenzione trial," *Journal of Cardiovascular Medicine*, vol. 7, no. 5, pp. 347–350, 2006.

[21] A. Annaházi, R. Róka, A. Rosztóczy, and T. Wittmann, "Role of antispasmodics in the treatment of irritable bowel syndrome," *World Journal of Gastroenterology*, vol. 20, no. 20, pp. 6031–6043, 2014.

[22] M. J. So and E. J. Cho, "Phloroglucinol attenuates free radical-induced oxidative stress," *Preventive Nutrition and Food Science*, vol. 19, no. 3, pp. 129–135, 2014.

[23] Y. Q. He, W. T. Zhang, C. H. Shi, F. M. Wang, X. J. Tian, and L. L. Ma, "Phloroglucinol protects the urinary bladder via inhibition of oxidative stress and inflammation in a rat model of cyclophosphamide-induced interstitial cystitis," *Chinese Medical Journal*, vol. 128, no. 7, pp. 956–962, 2015.

[24] R.-K. Kim, Y. Suh, K.-. C. Yoo et al., "Phloroglucinol suppresses metastatic ability of breast cancer cells by inhibition of epithelial-mesenchymal cell transition," *Cancer Science*, vol. 106, no. 1, pp. 94–101, 2015.

[25] M. H. Kang, I. H. Kim, and T. J. Nam, "Phloroglucinol induces apoptosis via apoptotic signaling pathways in HT-29 colon cancer cells," *Oncology Reports*, vol. 32, no. 4, pp. 1341–1346, 2014.

[26] M. V. Machado and H. Cortez-Pinto, "Non-alcoholic fatty liver disease: what the clinician needs to know," *World Journal of Gastroenterology*, vol. 20, no. 36, pp. 12956–12980, 2014.

[27] T. Yan, N. Yan, P. Wang et al., "Herbal drug discovery for the treatment of nonalcoholic fatty liver disease," *Acta Pharmaceutica Sinica B*, vol. 10, no. 1, pp. 3–18, 2020.

[28] P. Angulo, "Nonalcoholic fatty liver disease and liver transplantation," *Liver Transplantation*, vol. 12, no. 4, pp. 523–534, 2006.

[29] C. P. Day and O. F. W. James, "Hepatic steatosis: innocent bystander or guilty party?," *Hepatology*, vol. 27, no. 6, pp. 1463–1466, 1998.

[30] W. Peverill, L. Powell, and R. Skoien, "Evolving concepts in the pathogenesis of NASH: beyond steatosis and inflammation," *International Journal of Molecular Sciences*, vol. 15, no. 5, pp. 8591–8638, 2014.

[31] M. Świderska, M. Maciejczyk, A. Zalewska, J. Pogorzelska, R. Flisiak, and A. Chabowski, "Oxidative stress biomarkers in the serum and plasma of patients with non-alcoholic fatty liver disease (NAFLD). Can plasma AGE be a marker of NAFLD? Oxidative stress biomarkers in NAFLD patients," *Free Radical Research*, vol. 53, no. 8, pp. 841–850, 2019.

[32] K. Drygalski, K. Berk, T. Charytoniuk et al., "Does the enterolactone (ENL) affect fatty acid transporters and lipid metabolism in liver?," *Nutrition & Metabolism*, vol. 14, no. 1, p. 69, 2017.

[33] K. Berk, K. Drygalski, E. Harasim-Symbor et al., "The effect of enterolactone on liver lipid precursors of inflammation," *Life Sciences*, vol. 221, pp. 341–347, 2019.

[34] M. N. Stanković, D. Mladenović, M. Ninković et al., "The effects of α-lipoic acid on liver oxidative stress and free fatty acid composition in methionine-choline deficient diet-induced NAFLD," *Journal of Medicinal Food*, vol. 17, no. 2, pp. 254–261, 2014.

[35] M. Khoshbaten, A. Aliasgarzadeh, K. Masnadi et al., "N-acetylcysteine improves liver function in patients with non-alcoholic fatty liver disease," *Hepatitis Monthly*, vol. 10, no. 1, pp. 12–16, 2010.

[36] T. Charytoniuk, E. Harasim-Symbor, A. Polak et al., "Influence of resveratrol on sphingolipid metabolism in hepatocellular carcinoma cells in lipid overload state," *Anti-Cancer Agents in Medicinal Chemistry*, vol. 19, no. 1, pp. 121–129, 2019.

[37] G. Dollo, F. Chevanne, P. Le Corre, C. Chemtob, and R. Le Verge, "Biodisponibilite du phloroglucinol chez l'homme," *Journal de pharmacie de Belgique*, vol. 54, no. 3, pp. 75–82, 1999.

[38] K. Fujie and H. Ito, "Distribution and excretion of 1,3,5-trihydroxybenzene," *Arzneimittelforschung*, vol. 22, no. 4, pp. 777–780, 1972.

[39] M. Żebrowska-Gamdzyk, M. Maciejczyk, A. Zalewska, K. Guzińska-Ustymowicz, A. Tokajuk, and H. Car, "Whey protein concentrate WPC-80 intensifies glycoconjugate catabolism and induces oxidative stress in the liver of rats," *Nutrients*, vol. 10, no. 9, article 1178, 2018.

[40] A. M. Gusdon, K. X. Song, and S. Qu, "Nonalcoholic fatty liver disease: pathogenesis and therapeutics from a mitochondria-centric perspective," *Oxidative Medicine and Cellular Longevity*, vol. 2014, Article ID 637027, 20 pages, 2014.

[41] B. Quéguineur, L. Goya, S. Ramos, M. A. Martín, R. Mateos, and L. Bravo, "Phloroglucinol: antioxidant properties and effects on cellular oxidative markers in human HepG2 cell line," *Food and Chemical Toxicology*, vol. 50, no. 8, pp. 2886–2893, 2012.

[42] V. Mendes, R. Vilaça, V. De Freitas, P. M. Ferreira, N. Mateus, and V. Costa, "Effect of myricetin, pyrogallol, and phloroglucinol on yeast resistance to oxidative stress," *Oxidative Medicine and Cellular Longevity*, vol. 2015, Article ID 782504, 10 pages, 2015.

[43] K. A. Kang, K. H. Lee, S. Chae et al., "Cytoprotective effect of phloroglucinol on oxidative stress induced cell damage via catalase activation," *Journal of Cellular Biochemistry*, vol. 97, no. 3, pp. 609–620, 2006.

[44] S. Sahoo, D. N. Meijles, and P. J. Pagano, "NADPH oxidases: key modulators in aging and age-related cardiovascular diseases?," *Clinical Science*, vol. 130, no. 5, pp. 317–335, 2016.

[45] I. Grattagliano, G. Calamita, T. Cocco, D. Q. Wang, and P. Portincasa, "Pathogenic role of oxidative and nitrosative stress in primary biliary cirrhosis," *World Journal of Gastroenterology*, vol. 20, no. 19, pp. 5746–5759, 2014.

[46] A. Panic, J. Stanimirovic, M. Obradovic et al., "Estradiol-mediated regulation of hepatic iNOS in obese rats: impact of Src, ERK1/2, AMPKα, and miR-221," *Biotechnology and Applied Biochemistry*, vol. 65, no. 6, pp. 797–806, 2018.

[47] M. Maciejczyk, J. Szulimowska, K. Taranta-Janusz, A. Wasilewska, and A. Zalewska, "Salivary gland dysfunction, protein glycooxidation and nitrosative stress in children with chronic kidney disease," *Journal of Clinical Medicine*, vol. 9, no. 5, article 1285, 2020.

[48] C. Gersch, S. P. Palii, W. Imaram et al., "Reactions of peroxynitrite with uric acid: formation of reactive intermediates, alkylated products and triuret, and in vivo production of triuret under conditions of oxidative stress," *Nucleosides, Nucleotides and Nucleic Acids*, vol. 28, no. 2, pp. 118–149, 2009.

[49] J. Toczewska, T. Konopka, A. Zalewska, and M. Maciejczyk, "Nitrosative stress biomarkers in the non-stimulated and stimulated saliva, as well as gingival crevicular fluid of patients with periodontitis: review and clinical study," *Antioxidants*, vol. 9, no. 3, p. 259, 2020.

[50] P. Pacher, J. S. Beckman, and L. Liaudet, "Nitric oxide and peroxynitrite in health and disease," *Physiological Reviews*, vol. 87, no. 1, pp. 315–424, 2007.

[51] K. Dhama, S. K. Latheef, M. Dadar et al., "Biomarkers in stress related diseases/disorders: diagnostic, prognostic, and thera-

[52] B. K. Tiwari, K. B. Pandey, A. B. Abidi, and S. I. Rizvi, "Markers of oxidative stress during diabetes mellitus," *Journal of Biomarkers*, vol. 2013, Article ID 378790, 8 pages, 2013.

[53] A. Klisic, A. Isakovic, G. Kocic et al., "Relationship between oxidative stress, inflammation and dyslipidemia with fatty liver index in patients with type 2 diabetes mellitus," *Experimental and Clinical Endocrinology & Diabetes*, vol. 126, no. 6, pp. 371–378, 2018.

[54] J. Borys, M. Maciejczyk, B. Antonowicz et al., "Glutathione metabolism, mitochondria activity, and nitrosative stress in patients treated for mandible fractures," *Journal of Clinical Medicine*, vol. 8, no. 1, p. 127, 2019.

[55] T. M. Dreaden Kasson, S. Rexroth, and B. A. Barry, "Light-induced oxidative stress, N-formylkynurenine, and oxygenic photosynthesis," *PLoS One*, vol. 7, no. 7, article e42220, 2012.

[56] Y. K. Al-Hilaly, T. L. Williams, M. Stewart-Parker et al., "A central role for dityrosine crosslinking of amyloid-β in Alzheimer's disease," *Acta Neuropathologica Communications*, vol. 2, no. 1, 2014.

[57] Z. Chen, R. Tian, Z. She, J. Cai, and H. Li, "Role of oxidative stress in the pathogenesis of nonalcoholic fatty liver disease," *Free Radical Biology and Medicine*, vol. 152, pp. 116–141, 2020.

[58] D. D. Xiong, M. Zhang, N. Li, J. F. Gai, L. Mao, and M. Li, "Mediation of inflammation, obesity and fatty liver disease by advanced glycation endoproducts," *European Review for Medical and Pharmacological Sciences*, vol. 21, no. 22, pp. 5172–5178, 2017.

[59] J. M. Kim, I.-H. Hwang, I.-S. Jang et al., "*Houttuynia cordata* Thunb promotes activation of HIF-1A-FOXO3 and MEF2A pathways to induce apoptosis in human HepG2 hepatocellular carcinoma cells," *Integrative Cancer Therapies*, vol. 16, no. 3, pp. 360–372, 2017.

[60] K. McArthur, L. W. Whitehead, J. M. Heddleston et al., "BAK/BAX macropores facilitate mitochondrial herniation and mtDNA efflux during apoptosis," *Science*, vol. 359, no. 6378, article eaao6047, 2018.

[61] Y. Y. Huang, A. C. H. Chen, J. D. Carroll, and M. R. Hamblin, "Biphasic dose response in low level lighttherapy," *Dose-Response*, vol. 7, no. 4, pp. 358–383, 2009.

[62] Y. G. Figueroa, A. K. Chan, R. Ibrahim et al., "NF-κB plays a key role in hypoxia-inducible factor-1-regulated erythropoietin gene expression," *Experimental Hematology*, vol. 30, no. 12, pp. 1419–1427, 2002.

[63] M. J. Piao, M. J. Ahn, K. A. Kang et al., "Phloroglucinol inhibits ultraviolet B radiation-induced oxidative stress in the mouse skin," *International Journal of Radiation Biology*, vol. 90, no. 10, pp. 928–935, 2014.

[64] S. K. Goswami, S. K. Gangadarappa, M. Vishwanath et al., "Antioxidant potential and ability of phloroglucinol to decrease formation of advanced glycation end products increase efficacy of sildenafil in diabetes-induced sexual dysfunction of rats," *Sexual Medicine*, vol. 4, no. 2, pp. e106–e114, 2016.

[65] E. Moine, P. Brabet, L. Guillou, T. Durand, J. Vercauteren, and C. Crauste, "New lipophenol antioxidants reduce oxidative damage in retina pigment epithelial cells," *Antioxidants*, vol. 7, no. 12, p. 197, 2018.

[66] J. Mária and Ž. Ingrid, "Effects of bioactive compounds on senescence and components of senescence associated secretory

phenotypes in vitro," *Food and Function*, vol. 8, no. 7, pp. 2394–2418, 2017.

[67] E. J. Yang, S. Ahn, J. Ryu et al., "Phloroglucinol attenuates the cognitive deficits of the 5XFAD mouse model of Alzheimer's disease," *PLoS One*, vol. 10, no. 8, article e0135686, 2015.

[68] K. Broadley, L. Larsen, P. M. Herst, R. A. J. Smith, M. V. Berridge, and M. J. McConnell, "The novel phloroglucinol PMT7 kills glycolytic cancer cells by blocking autophagy and sensitizing to nutrient stress," *Journal of Cellular Biochemistry*, vol. 112, no. 7, pp. 1869–1879, 2011.

[69] T. Charytoniuk, N. Iłowska, K. Berk, K. Drygalski, A. Chabowski, and K. Konstantynowicz-Nowicka, "The effect of enterolactone on sphingolipid pathway and hepatic insulin resistance development in HepG2 cells," *Life Sciences*, vol. 217, pp. 1–7, 2019.

[70] M. Maciejczyk, K. Taranta-Janusz, A. Wasilewska, A. Kossakowska, and A. Zalewska, "A case-control study of salivary redox homeostasis in hypertensive children. Can salivary uric acid be a marker of hypertension?," *Journal of Clinical Medicine*, vol. 9, no. 3, p. 837, 2020.

[71] H. P. Misra and I. Fridovich, "The role of superoxide anion in the autoxidation of epinephrine and a simple assay for superoxide dismutase," *Journal of Biological Chemistry*, vol. 247, no. 10, pp. 3170–3175, 1972.

[72] "Oxygen radicals in biological systems, volume 105 - 1st edition," December 2020, https://www.elsevier.com/books/oxygen-radicals-in-biological-systems/kaplan/978-0-12-182005-3.

[73] D. E. Paglia and W. N. Valentine, "Studies on the quantitative and qualitative characterization of erythrocyte glutathione peroxidase," *The Journal of Laboratory and Clinical Medicine*, vol. 70, no. 1, pp. 158–169, 1967.

[74] C. E. Mize and R. G. Langdon, "Hepatic glutathione reductase. I. Purification and general kinetic properties," *The Journal of Biological Chemistry*, vol. 237, pp. 1589–1595, 1962.

[75] O. W. Griffith, "Determination of glutathione and glutathione disulfide using glutathione reductase and 2-vinylpyridine," *Analytical Biochemistry*, vol. 106, no. 1, pp. 207–212, 1980.

[76] B. Choromańska, P. Myśliwiec, M. Łuba et al., "A longitudinal study of the antioxidant barrier and oxidative stress in morbidly obese patients after bariatric surgery. Does the metabolic syndrome affect the redox homeostasis of obese people?," *Journal of Clinical Medicine*, vol. 9, no. 4, p. 976, 2020.

[77] K. K. Griendling, C. A. Minieri, J. D. Ollerenshaw, and R. W. Alexander, "Angiotensin II stimulates NADH and NADPH oxidase activity in cultured vascular smooth muscle cells," *Circulation Research*, vol. 74, no. 6, pp. 1141–1148, 1994.

[78] J. Borys, M. Maciejczyk, B. Antonowicz, J. Sidun, M. Świderska, and A. Zalewska, "Free radical production, inflammation and apoptosis in patients treated with titanium mandibular fixations — an observational study," *Frontiers in Immunology*, vol. 10, 2019.

[79] N. Prajda and G. Weber, "Malignant transformation-linked imbalance: decreased xanthine oxidase activity in hepatomas," *FEBS Letters*, vol. 59, no. 2, pp. 245–249, 1975.

[80] M. B. Grisham, G. G. Johnson, and J. R. Lancaster, "Quantitation of nitrate and nitrite in extracellular fluids," *Methods in Enzymology*, vol. 268, pp. 237–246, 1996.

[81] J. S. Beckman, H. Ischiropoulos, L. Zhu et al., "Kinetics of superoxide dismutase- and iron-catalyzed nitration of phenolics by peroxynitrite," *Archives of Biochemistry and Biophysics*, vol. 298, no. 2, pp. 438–445, 1992.

[82] K. Grintzalis, D. Zisimopoulos, T. Grune, D. Weber, and C. D. Georgiou, "Method for the simultaneous determination of free/protein malondialdehyde and lipid/protein hydroperoxides," *Free Radical Biology and Medicine*, vol. 59, pp. 27–35, 2013.

[83] J. A. Buege and S. D. Aust, "Microsomal lipid peroxidation," *Methods in Enzymology*, vol. 52, no. C, pp. 302–310, 1978.

[84] M. Kalousová, T. Zima, V. Tesař, and J. Lachmanová, "Advanced glycation end products and advanced oxidation protein products in hemodialyzed patients," *Blood Purification*, vol. 20, no. 6, pp. 531–536, 2002.

Research Article

Metabolomic Analysis of the Ameliorative Effect of Enhanced Proline Metabolism on Hypoxia-Induced Injury in Cardiomyocytes

Jiacheng Wang,[1,2] **Zhimin Xue,**[1,2] **Chunting Hua,**[3] **Jun Lin,**[1,2] **Zhida Shen,**[1,2] **Yinjing Song,**[3] **Hangying Ying,**[1,2] **Qingbo Lv,**[1,2] **Meihui Wang,**[1,2] **and Binquan Zhou** [1,2]

[1]*Department of Cardiology, Sir Run Run Shaw Hospital, Zhejiang University School of Medicine, Hangzhou, China*
[2]*Key Laboratory of Cardiovascular Intervention and Regenerative Medicine of Zhejiang Province, Hangzhou, China*
[3]*Department of Dermatology, Sir Run Run Shaw Hospital School of Medicine Zhejiang University, Hangzhou, China*

Correspondence should be addressed to Binquan Zhou; zhoubinquan@zju.edu.cn

Background. Coronary heart disease is currently the leading cause of death in humans. Its poor prognosis and high mortality are associated with myocardial ischemia, which leads to metabolic disorder-related cardiomyocyte apoptosis and reactive oxygen species (ROS) production. Previous cardiovascular metabolomics studies in humans and mice have shown that proline metabolism is severely altered after cardiomyocyte hypoxia. Proline dehydrogenase (PRODH) is located on the inner mitochondrial membrane and is an enzyme that catalyzes the first step of proline catabolism, which plays an important role in improving the cellular redox state. In vitro oxygen-glucose deprivation can mimic in vivo myocardial ischemic injury. This study is aimed at investigating whether enhancing proline metabolism by overexpressing PRODH can ameliorate hypoxia-induced injury in cardiomyocytes and to reveal the related altered metabolites and mechanistic pathway via untargeted metabolomics analysis. *Methods and Results*. First, through public database analysis and RT-qPCR and western blot analyses in a cardiomyocyte hypoxia model, we found that the expression of the proline-degrading enzyme PRODH was downregulated after myocardial infarction and hypoxia exposure. Second, LDH assays, terminal deoxynucleotidyl transferase dUTP nick end labeling (TUNEL), DHE staining, flow cytometric apoptosis analysis with DCFH and Annexin V-FITC/PI, and western blot analysis were used to assess the injury level in cardiomyocytes. Enhanced proline metabolism induced by PRODH overexpression reduced the levels of reactive oxidative stress and apoptosis, whereas PRODH knockdown had the opposite effects. Third, untargeted metabolomics analysis revealed that the protective effect was associated with significant changes in metabolism linked to sphingolipid signaling pathways, unsaturated fatty acid biosynthesis, phosphocreatine, glutathione disulfide, aminoacyl-tRNA biosynthesis, and ABC transporters. *Conclusions*. Our study demonstrated a protective effect of enhanced proline metabolism in cardiomyocytes under hypoxia, providing a novel strategy for exploring new treatments for coronary heart disease.

1. Introduction

According to the most recently updated American Heart Association (AHA) statistics, the overall prevalence of cardiovascular disease (CVD) in the United States among adults is 48.0%, and coronary heart disease (CHD)—a group of diseases including stable angina, unstable angina, myocardial infarction (MI), and sudden cardiac death—is the leading cause (43.2%) of death from CVD [1]. Myocardial ischemia, characterized by the interruption of blood and oxygen flow to the myocardium, can trigger excessive reactive oxygen species (ROS) production and a significant increase in cardiomyocyte apoptosis [2]. Although many treatments for CHD are available, such as early revascularization, β-blockers,

statins, and angiotensin-converting enzyme inhibitors, these treatments provide limited symptomatic relief, and the discovery of new therapeutic strategies for myocardial ischemia is urgently needed.

Metabolic disorders, termed "metabolic remodeling," caused by cardiomyocyte hypoxia during CHD are the causes of cardiomyocyte apoptosis and ROS production [3]. Transcriptomics and proteomics can predict future events, but metabolomics can reveal past events in an organism. This approach, which allows comprehensive profiling of small molecular substances in biological systems, is increasingly being applied to investigate CVD mechanisms and potential new treatment targets [4]. Previous cardiovascular metabolomics studies in humans and mice have shown that proline metabolism is severely altered after hypoxia in cardiomyocytes [5, 6]. Proline and its metabolism impact cell survival and death outcomes by influencing the cellular redox state and maintaining cellular energy under oxidative and nutrient stress conditions, contributing to the tricarboxylic acid cycle and glutathione (GSH) biosynthesis [7].

Proline dehydrogenase (PRODH) is located on the inner mitochondrial membrane and is an enzyme that catalyzes the first step of proline catabolism [8]. Under the catalysis of PRODH, two electrons are transferred from proline to the flavin cofactor to generate 1-pyrroline-5-carboxylic acid (P5C) and reduced flavin. Simultaneously, flavin adenine dinucleotide (FAD) is reduced to FADH2, which can be used in oxidative phosphorylation to generate ATP [9]. After P5C is spontaneously converted to gamma-glutamate semialdehyde (GSA), using nicotinamide adenine dinucleotide as the electron acceptor, P5C dehydrogenase (P5CDH) oxidizes GSA to L-glutamic acid [10]. The glutamic acid produced by the oxidation of proline enters the tricarboxylic acid cycle after being converted into α-ketoglutarate. Oxidation of a proline molecule can produce approximately 30 equivalents of ATP, which provide vital energy for cells [7].

In addition, previous studies have shown that PRODH involves in mitochondrial redox regulations and plays an important role in protecting cancer cells against hydrogen peroxide-mediated oxidative stress damage [8]. However, the changes in intracellular metabolism under hypoxia after enhancement of proline metabolism by PRODH overexpression have not been reported. Therefore, whether enhancing proline metabolism by overexpressing PRODH can improve the redox state of cardiomyocytes with hypoxic damage is an urgent question to be answered. In this study, we used untargeted metabolomic analysis to reveal related altered metabolites and pathways after enhancement of proline metabolism in cardiomyocytes under hypoxia.

2. Materials and Methods

2.1. Cell Culture and Hypoxia Model Establishment.
The rat cardiomyocyte cell line H9c2 was purchased from the American Type Culture Collection (ATCC), and cells at passage 3-8 were used. H9c2 cells were maintained in DMEM supplemented with 10% FBS at 37°C in a humidified atmosphere of 5% CO_2. Cells were subjected to experimental procedures at 80%-90% confluence. To mimic ischemic injury in vitro,

the OGD model was employed. In brief, H9c2 cells were incubated in glucose-free/serum-free DMEM and exposed to a hypoxic environment containing 94% N_2, 5% CO_2, and 1% O_2 for 16 h.

2.2. Adenoviral Infection Experiments.
A recombinant adenoviral vector overexpressing rat PRODH (Gene ID: 680409) and an adenovirus expressing a small hairpin RNA (shRNA) sequence (Ad-shPRODH) targeting rat PRODH were successfully constructed by Shanghai GenePharma Biomedical Technology (Shanghai, China). We also constructed a control adenoviral vector encoding green fluorescent protein that did not include the PRODH coding sequence, and this construct was used as a negative control (Ad-NC). Similarly, a scrambled shRNA construct was designed and synthesized and was used as a negative control (Ad-shNC). The sequence of the shRNA against rat PRODH was 5′-GGACTATGGTG TGGAGGAA-3′, and the sequence of the negative control (Ad-shNC) sequence was 5′-GTTCTCCGAACGTGTC ACGT-3′, which had no significant homology to known genes. H9c2 cells at 50% confluence were infected with Ad-PRODH, Ad-NC, Ad-shPRODH, or Ad-shNC (MOI = 100) for 12 h and were then used for further experiments.

2.3. Analysis of LDH Leakage.
Cell injury was assessed by the biomarker LDH. At the end of incubation, LDH release into the culture supernatant was measured at 490 nm with a commercial LDH kit (CK12, Dojindo, Japan) according to the manufacturer's instructions.

2.4. Apoptosis Assay.
Apoptosis was detected with an Annexin V-FITC/PI Apoptosis Detection Kit (KGA108, KeyGen, China) and TUNEL using an In Situ Cell Death Detection Kit (Roche, USA) according to the manufacturer's instructions as we described previously [11].

2.5. Measurement of Intracellular ROS.
ROS levels in H9c2 cells were measured by flow cytometry with the fluorescent probe DCFH-DA (10 μM) (Sigma, USA, D6883) as we described previously [11]. The fluorescence probe DHE was used to measure intracellular superoxide anion levels. Cultured H9c2 cells were incubated with 10 μM DHE (Yeason, China, 50102ES02) and 1X Hoechst 33342 (Beyotime Biotechnology, China, C1029) for 30 min. Then, the cells were washed with serum-free DMEM 3 times to remove background fluorescence and were observed by fluorescence microscopy.

2.6. Dataset Analysis.
The RNA-seq dataset GSE46224 contains mRNA expression levels in the cardiac tissues of 8 nonfailing patients and 8 ischemic HF patients (https://www.ncbi .nlm.nih.gov/geo/query/acc.cgi?acc=GSE46224) [12]. We compared the RPKM values of the proline-degrading enzyme PRODH between the 8 nonfailing patients and 8 ischemic HF patients or 8 nonischemic HF patients. The RNA-seq dataset GSE114695 contains mRNA expression levels in LV tissues of mice in the 1-day, 1-week, and 8-week MI groups and the sham group (https://www.ncbi.nlm.nih.gov/geo/ query/acc.cgi?acc=GSE114695) [13]. We compared the

RPKM values of the proline-degrading enzyme PRODH between the sham and 1-day, 1-week, and 8-week MI groups.

2.7. Untargeted Metabolomic Analysis. Detailed methodology of LC-MS/MS analysis and data processing can be found in the previous study [14]. For statistical analysis of metabolomics results, after normalization to the total peak intensity, the processed data were uploaded into before being imported into SIMCA-P (version 14.1, Umetrics, Umea, Sweden) and MetaboAnalyst (https://www.metaboanalyst.ca/) [15], where they were subjected to multivariate data analysis, including Pareto-scaled PCA and OPLS-DA. Sevenfold cross-validation and response permutation testing were used to evaluate the robustness of the model. The VIP value of each variable in the OPLS-DA model was calculated to indicate its contribution to the classification. Metabolites with a VIP value of >1 were further subjected to Student's t-test at the univariate level to measure the significance of each metabolite, and p values of less than 0.05 were considered statistically significant. Based on multivariate analysis and the original MS spectra, the discriminating metabolites were identified by comparison with the human metabolome database (http://www.hmdb.ca). Pathway analyses were performed using MetaboAnalyst and KEGG (http://geneontology.org/). In the enrichment analysis of the KEGG pathway annotations of the target metabolite set, the KEGG pathway was taken as a unit, and all metabolites in each pathway were taken as the background, and the distribution of each KEGG pathway in the target metabolite set and the total metabolite set was accurately evaluated by Fisher's exact test to evaluate the significance level of the enrichment of a metabolite in a KEGG pathway. Metabolite cluster analysis (clustering) was performed as follows: first, the quantitative information of the target protein set was normalized (with an interval of (-1)). Second, Cluster3.0 software was used to simultaneously classify the two dimensions of sample and protein expression (distance algorithm: Euclid, connection mode: Average linkage). Finally, the hierarchical clustering heat map was generated in Java TreeView software.

2.8. RNA Isolation and Real-Time PCR. A detailed methodology can be found in our previous description [11]. The sequences of the primers were as follows: β-actin (forward, 5′-AAGTCCCTCACCCTCCCAAAAG-3′, reverse, 5′-AAGCAATGCTGTCACCTTCCC-3′) and PRODH (forward, 5′-GCCAGTGACGGTGGTTTTTC-3′, reverse, 5′-CATCTTGGCGATGCTCTCCT-3′).

2.9. Western Blot Analysis. A detailed methodology can be found in our previous description [11]. Primary antibodies against the following proteins were used in the present study: β-actin (#100118, GeneTex), PRODH (#22980-1-AP, Proteintech), and cleaved caspase 3 (#19677-1-AP, Proteintech).

2.10. Statistical Analysis. One-way ANOVA or Student's t-test was applied to determine the statistical significance of differences in GraphPad Prism 8.0. All results are expressed as the mean ± SD values. Differences with a p value of less than 0.05 were considered statistically significant. The num-

ber of independent experiments performed is indicated in the figure legends.

3. Results

3.1. The Expression of the Proline-Degrading Enzyme PRODH Is Downregulated after MI and Hypoxia. The RNA-seq dataset GEO46224 contains mRNA expression levels of cardiac tissues from 8 nonfailing patients and 8 ischemic heart failure (HF) patients (https://http://www.ncbi.nlm.nih.gov/geo/query/acc.cgi?acc=GSE46224) [12]. We compared the reads per kilobase million mapped reads (RPKM) values of the proline-degrading enzyme PRODH between the 8 nonfailing patients and 8 ischemic HF patients. The expression fold changes and statistical analysis results showed that the expression of the proline-degrading enzyme PRODH decreased significantly after ischemic HF (Figure 1(a)). The RNA-seq dataset GEO114695 contains mRNA expression levels from left ventricle (LV) tissues of MI or sham mice. We compared the RPKM values of the proline-degrading enzyme PRODH between the sham group and the 1-day, 1-week, and 8-week MI groups [13]. The expression fold changes and statistical analysis results showed that the expression of the proline-degrading enzyme PRODH decreased significantly after MI (Figure 1(b)).

To mimic ischemic injury in vitro, the oxygen-glucose deprivation (OGD) model was employed. OGD injury was induced by incubating H9c2 cells with glucose-free DMEM and exposing them to a hypoxic environment containing 94% N_2, 5% CO_2, and 1% O_2 for 16 h. The protein and mRNA expression levels of the proline-degrading enzyme PRODH were dramatically decreased in H9c2 cardiomyocytes after hypoxic injury (Figures 1(c) and 1(d)), indicating that the proline-degrading enzyme PRODH might be involved in mediating hypoxic injury in cardiomyocytes.

3.2. Enhanced Proline Metabolism Induced by Overexpression of PRODH Reduces Apoptosis Levels, whereas PRODH Knockdown Has the Opposite Effect. Cardiomyocyte apoptosis is an essential element associated with myocardial hypoxia-induced injury. Therefore, flow cytometric analysis was employed to evaluate H9c2 cardiomyocyte apoptosis. Quantitative analysis of flow cytometry data confirmed that compared to the proportion of apoptotic cells in the normoxia control group, the proportion of apoptotic cells was significantly increased after hypoxic injury, while PRODH overexpression in H9c2 cardiomyocytes markedly inhibited this increase. Conversely, knockdown of PRODH in H9c2 cardiomyocytes increased the proportion of apoptotic cells (Figure 2(a)). As lactate dehydrogenase (LDH) release is a recognized marker of cell injury, the release of LDH into the culture medium was also investigated. Compared to that in the control group, LDH release was significantly increased after hypoxic injury, while PRODH overexpression in H9c2 cardiomyocytes markedly inhibited the release of LDH. Conversely, knockdown of PRODH in H9c2 cardiomyocytes increased the release of LDH (Figure 2(b)). Similarly, compared to the number of TUNEL-positive cells in the normoxia control group, the number of TUNEL-positive cells
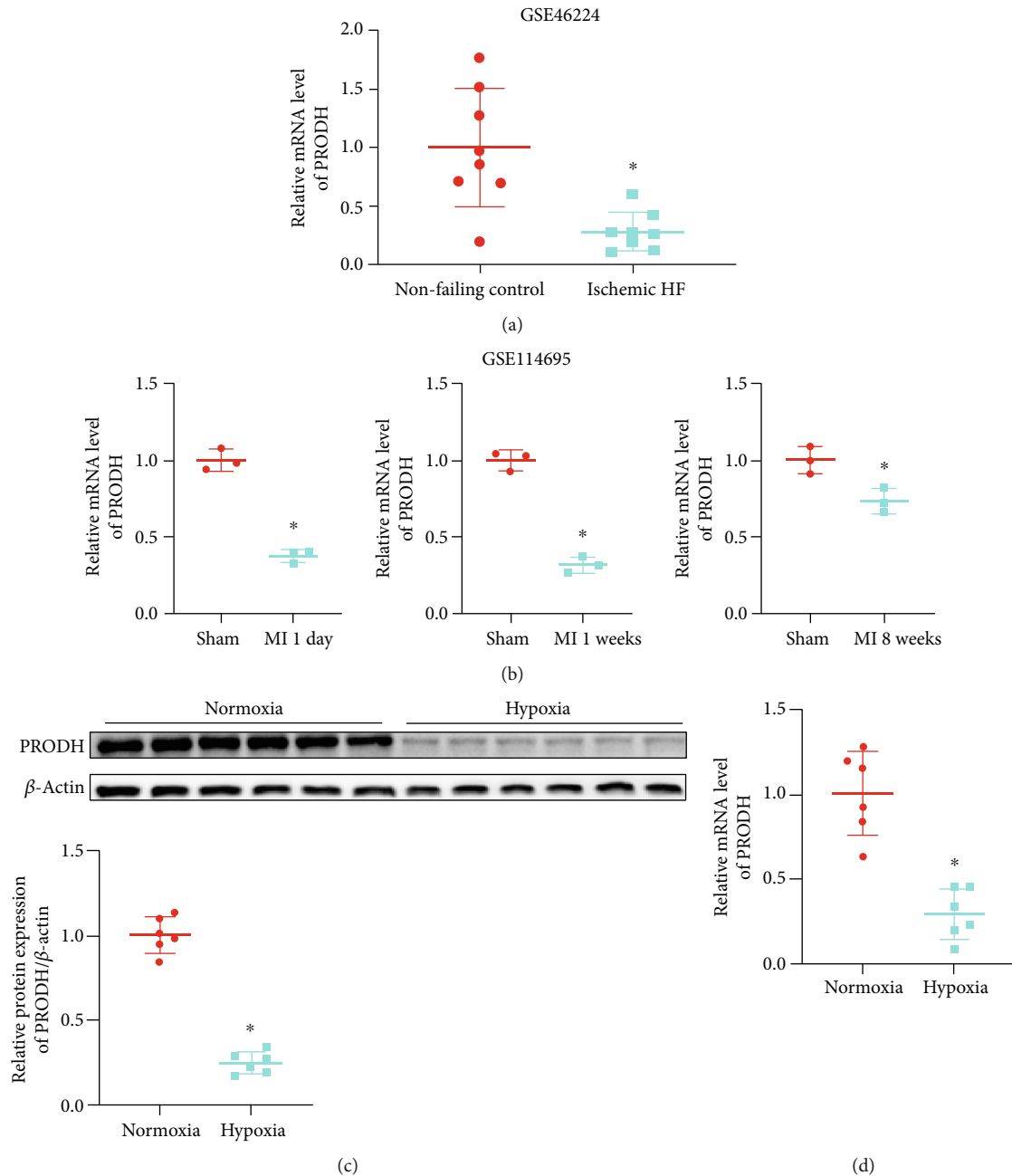
Figure 1: The expression of the proline-degrading enzyme PRODH is downregulated after MI and hypoxia. (a) Relative expression levels of the proline-degrading enzyme PRODH in 8 nonfailing patients and 8 ischemic HF patients from dataset GSE46224 ($n = 8$). (b) Relative expression levels of the proline-degrading enzyme PRODH between the sham and 1-day, 1-week, or 8-week MI groups from dataset GSE114695 ($n = 3$). (c) Western blot analysis and quantification of PRODH expression in the normoxia control group and the hypoxia group ($n = 6$). (d) Results of quantitative statistical analysis of PRODH expression as measured by RT-qPCR in the normoxia control group and the hypoxia group ($n = 6$). The data are presented as the mean ± SD values. $^*p < 0.05$ versus the normoxia control group.

was significantly increased after hypoxic injury, while PRODH overexpression in H9c2 cardiomyocytes markedly inhibited this increase. In contrast, knockdown of PRODH in H9c2 cardiomyocytes resulted in a marked increase in the number of TUNEL-positive cells (Figure 2(c)). Moreover, quantitative analysis confirmed that compared to normoxia control group, the protein expression of cleaved caspase-3, a marker of apoptosis, was significantly increased after hypoxic injury, while PRODH overexpression in H9c2 cardio-

myocytes markedly inhibited this increase. Conversely, knockdown of PRODH in H9c2 cardiomyocytes increased the protein expression of cleaved caspase-3 (Figure 2(d)).

3.3. Enhanced Proline Metabolism Induced by Overexpression of PRODH Decreases Reactive Oxidative Stress, whereas PRODH Knockdown Has the Opposite Effect. ROS are the key executors of oxidative stress, which induces cardiomyocyte apoptosis during ischemia and hypoxia. Thus, we
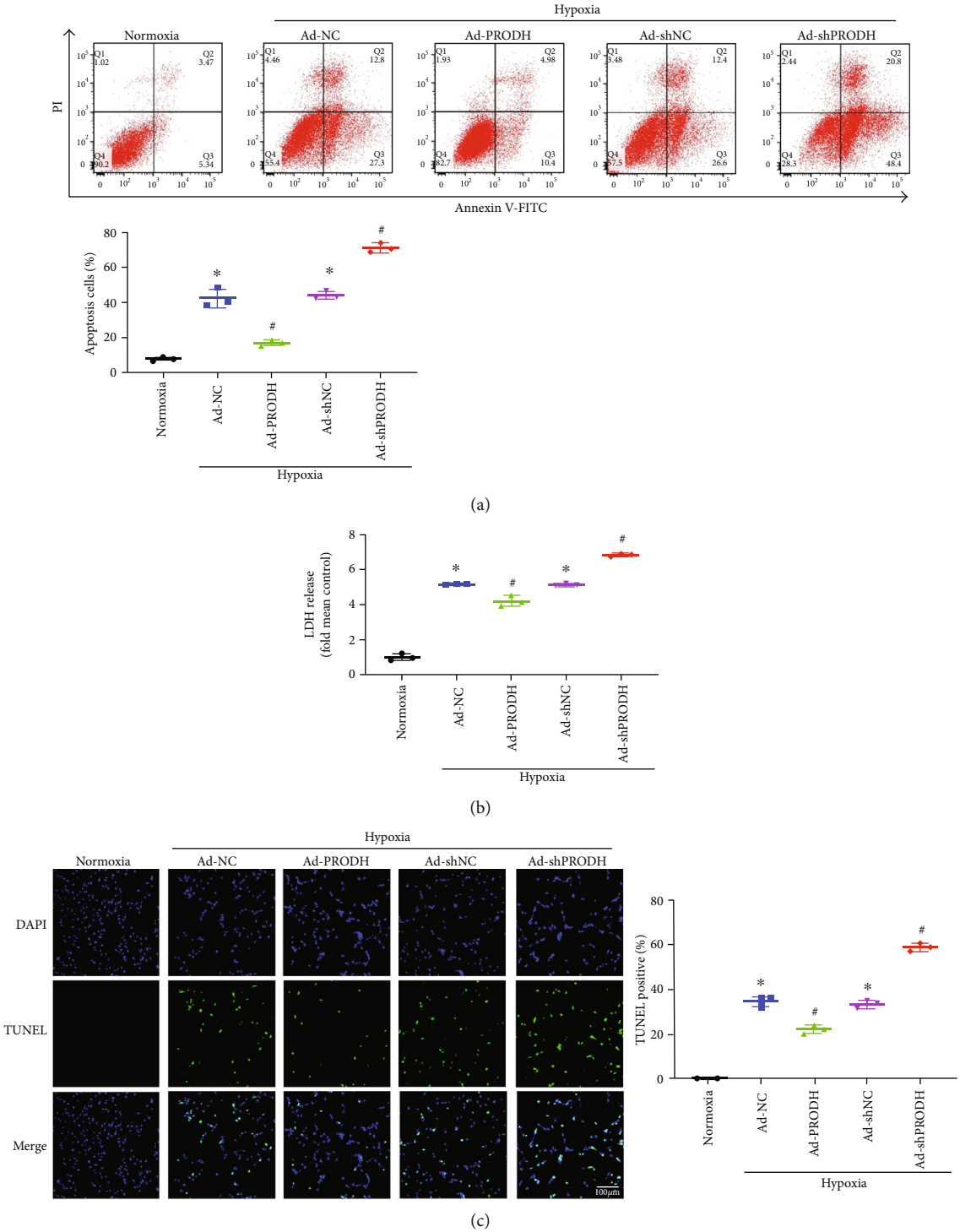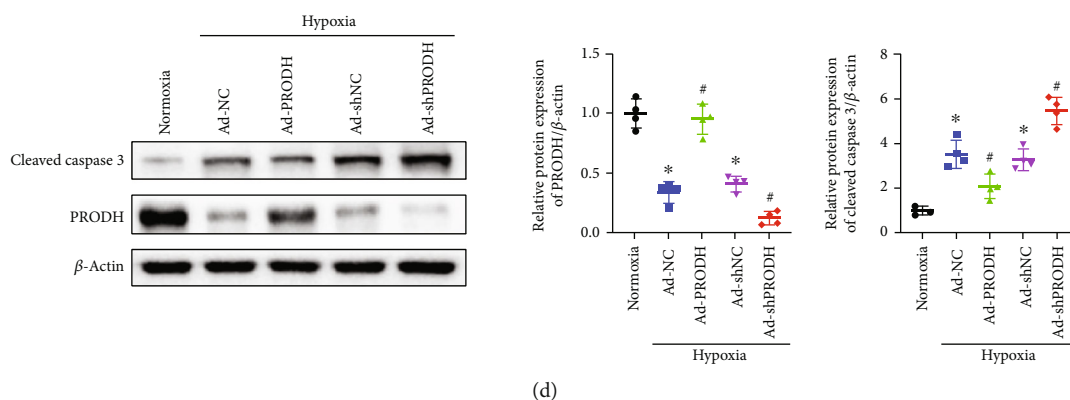
(a)

(b)

(c)

Figure 2: Continued.

(d)

FIGURE 2: Enhanced proline metabolism induced by the overexpression of PRODH reduces apoptosis levels, whereas PRODH knockdown has the opposite effect. (a) Representative images and analysis of FITC-Annexin V/PI-positive apoptotic H9c2 cells by flow cytometry ($n = 3$). (b) Relative LDH release ($n = 3$). (c) Cardiomyocyte apoptosis was evaluated by TUNEL, and the percentage of TUNEL-positive cells is shown. Scale bar, 100μm ($n = 3$). (d) Representative images and quantitative analysis of cleaved caspase-3 expression in H9c2 cells ($n = 4$). The data are presented as the mean ± SD values. $^*p < 0.05$ versus the normoxia control group; $^#p < 0.05$ versus the Ad-NC or Ad-shNC negative control group.

assessed ROS levels by $2',7'$-dichlorodihydrofluorescein diacetate (DCFH-DA) staining with flow cytometry and by dihydrogen ethidium (DHE) staining with fluorescence microscopy. Quantitative analysis showed that compared to those in the normoxia control group, the relative DCFH fluorescence intensity and the proportion of DHE-positive cells were increased after hypoxic injury, while PRODH overexpression in H9c2 cardiomyocytes markedly inhibited these increases (Figures 3(a) and 3(b)). Conversely, knockdown of PRODH in H9c2 cardiomyocytes markedly increased the relative DCFH fluorescence intensity and the proportion of DHE-positive cells (Figures 3(a) and 3(b)).

3.4. Overexpression of the Proline-Degrading Enzyme PRODH to Enhance Proline Metabolism Reprograms the Metabolism of Cardiomyocytes with Hypoxia-Induced Injury. Numerous studies have shown that cardiomyocyte hypoxia after MI leads to myocardial metabolic disorders [16], and altering the metabolism of certain substances after myocardial cell hypoxia can ameliorate this metabolic disorder and reduce cardiomyocyte injury [17, 18]. Therefore, we hypothesized that the enhancement of proline metabolism by overexpression of PRODH and the resulting reductions in cardiomyocyte apoptosis and ROS production may also be caused by improving specific aspects of cardiomyocyte metabolism. We used untargeted metabolomics analysis to reveal these potential mechanisms. In total, 10935 features in positive ion mode and 8069 in negative ion mode were identified in 10 samples from the Ad-NC group and the Ad-PRODH group.

The representative total ion current (both positive and negative) data obtained from the cell samples in the quality control (QC) group, Ad-NC group, and Ad-PRODH group are shown in Figure 4(a). The retention time of each major chromatographic peak in the different groups, with good overlap, demonstrated the excellent stability and reproducibility of the liquid chromatography-mass spectrometry (LC-MS) system throughout the sequence. All data were ana-

lyzed using SIMCA-P software for discrimination and selection of significant variables. The principal component analysis (PCA) score plot for the QC group, Ad-NC group, and Ad-PRODH group is shown in Figure 4(b). The plot shows a trend of intragroup aggregation and intergroup separation. The high degree of aggregation in the QC group demonstrated the high stability of the LC-MS system throughout the sequence.

We further used partial least squares discriminant analysis (PLS-DA) to screen the differentially expressed metabolites between the Ad-NC group and the Ad-PRODH group. The PLS-DA scores showed a clear separation between the Ad-NC group and the Ad-PRODH group (Figures 5(a) and 5(b)). In addition, we used orthogonal partial least square discriminant analysis (OPLS-DA) for supervised data analysis to elucidate the metabolic variations. An OPLS-DA model was constructed to distinguish metabolic patterns between the Ad-NC group and the Ad-PRODH group in both positive and negative ion modes. In theory, the R2Y and Q2 values should be close to 1, which indicates a high predictive ability. As illustrated in Figures 5(c)–5(f), the metabolic profiles of cardiomyocyte samples were distinctly different between the Ad-NC group and the Ad-PRODH group.

According to the criteria for multivariate and univariate statistical significance (variable importance in projection (VIP) > 1 and $p < 0.1$), 15 metabolites were differentially expressed between the Ad-NC group and the Ad-PRODH group in negative ion mode, and 32 differentially expressed metabolites were identified in positive ion mode. These metabolites are listed in Table 1. Obviously, proline metabolism was indeed enhanced by the overexpression of the proline-degrading enzyme PRODH, and we observed significant decreases in the levels of both L-proline and D-proline (Figure 6(a)). In addition, a hierarchical clustering heat map was generated to visualize the data more intuitively. The heat map indicated that the concentrations of metabolic biomarkers in the Ad-PRODH group differed from those in the Ad-NC group (Figure 6(b)). Then, pathway analysis
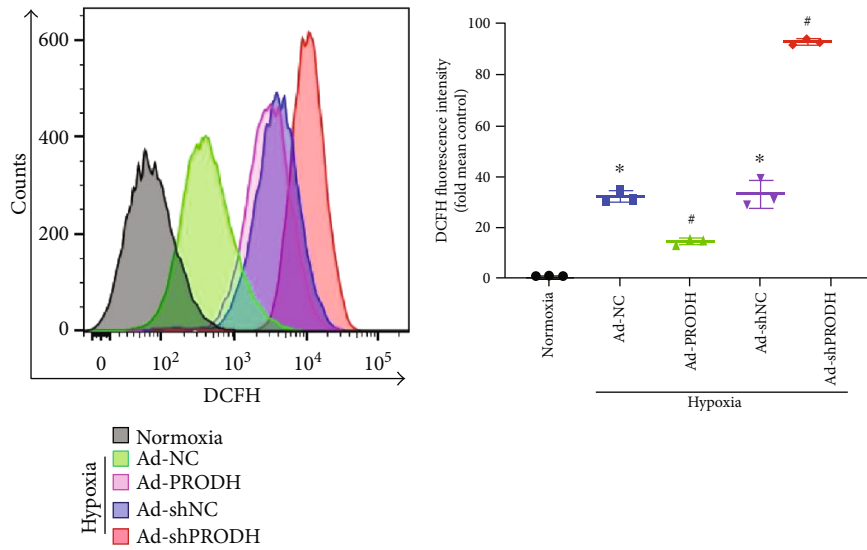
(a)
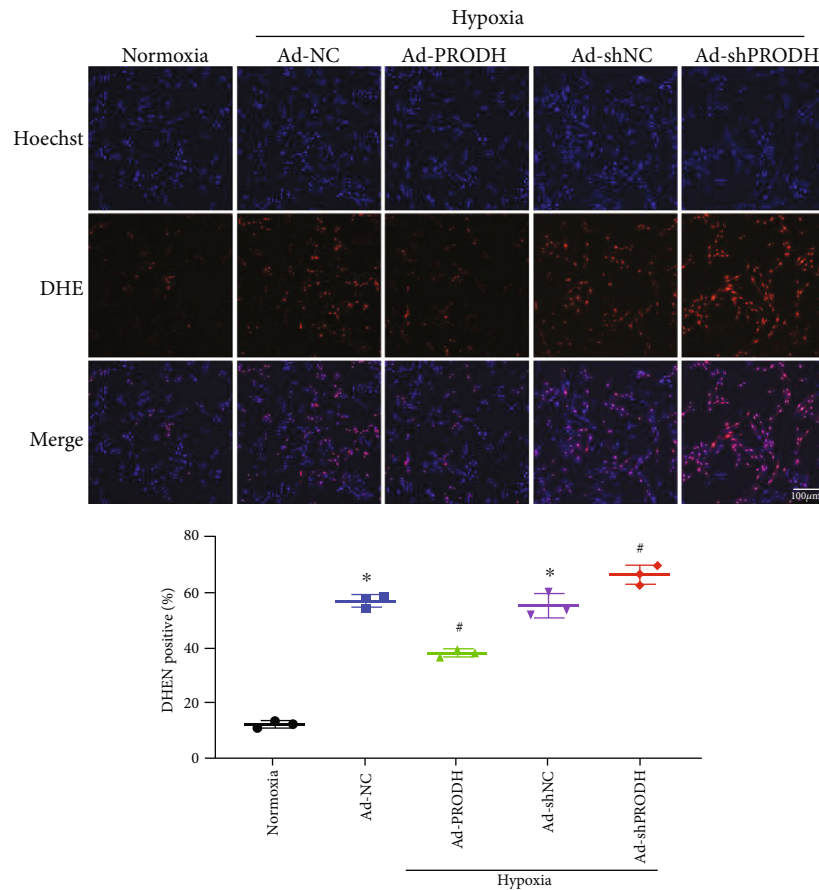
(b)

FIGURE 3: Enhanced proline metabolism induced by overexpression of PRODH decreases reactive oxidative stress, whereas PRODH knockdown has the opposite effect. (a) Representative images and quantitative analysis of reactive oxidative stress as assessed by flow cytometric analysis with DCFH fluorescent staining ($n = 3$). (b) Representative images and quantitative analysis of superoxide production as measured by DHE fluorescence. Scale bar, 100μm ($n = 3$). The data are presented as the mean ± SD values. $^*p < 0.05$ versus the normoxia control group; $^\#p < 0.05$ versus the Ad-NC or Ad-shNC negative control group.

(a)

(b)
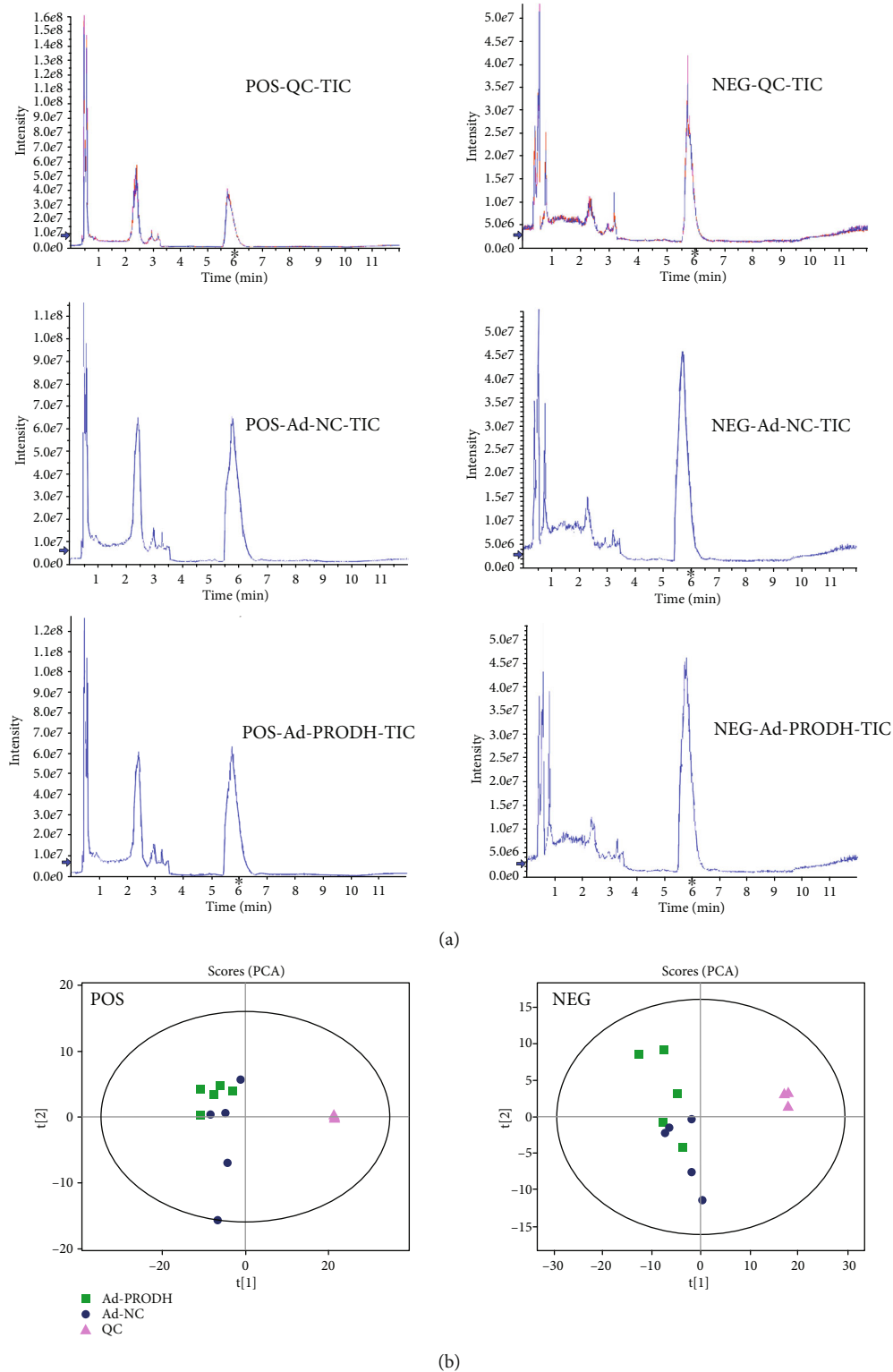
Figure 4: (a) Total ion chromatograms for the QC group, Ad-NC group, and Ad-PRODH group in positive and negative ion modes. (b) PCA score plot: (▲) QC group (■) Ad-PRODH group, and (●) Ad-NC group.

using the Kyoto Encyclopedia of Genes and Genomes (KEGG) database showed that the metabolites that were significantly altered between the Ad-NC group and the Ad-PRODH group were highly associated with ABC trans-porters, aminoacyl-tRNA biosynthesis, biosynthesis of unsat-urated fatty acids, arginine and proline metabolism, sphingolipid signaling pathways, fatty acid biosynthesis, and so on (Figure 7(a)). Furthermore, to reveal the metabolic
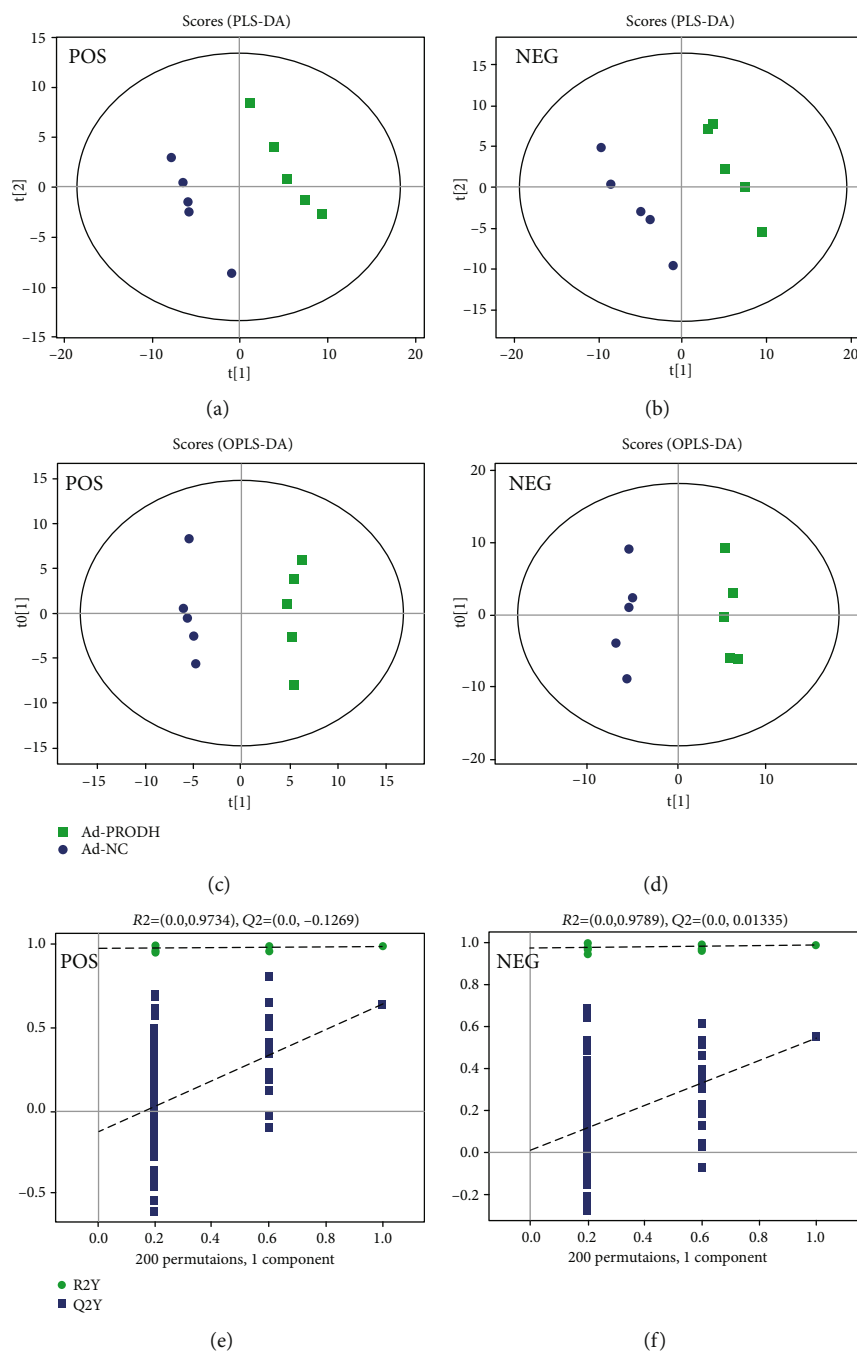
FIGURE 5: PLS-DA score plot and OPLS-DA for the model discriminating cell samples from the Ad-NC group and Ad-PRODH group. (a) POS-PLS-DA score plot. (b) NEG-PLS-DA score plot. (c, d) POS-OPLS-DA score plot. (e, f) NEG-OPLS-DA score plot: (■) Ad-PRODH group, and (●) Ad-NC group.

processes involving these metabolites, the significantly altered metabolites were entered into MetaboAnalyst 4.0 (https://www.metaboanalyst.ca/) for enrichment pathway analysis [15]. According to the fold enrichment values of the pathways, the major modulated pathways involved biosynthesis of unsaturated fatty acids, arginine and proline metabolism, aminoacyl-tRNA biosynthesis, sphingolipid metabolism, sphingolipid metabolism, and so on (Figure 7(b)).

4. Discussion

Despite advancements in percutaneous coronary intervention (PCI) and drug therapy over the past decades, CHD remains a leading cause of morbidity and mortality and, indeed, is a worldwide epidemic. Hypoxic injury is the primary cause of ROS production and apoptosis in cardiomyocytes [2]. Accumulating evidence suggests that metabolic remodeling resulting from myocardial ischemia is the

TABLE 1: Statistical analysis of 47 differential metabolites from the comparison of the Ad-NC group and the Ad-PRODH group under hypoxia in cardiomyocyte.

| Ion mode	Description	m/z	rt(s)	VIP	FC	p value
	1,2-dioleoyl-sn-glycero-3-phosphatidylcholine	786.60	143.49	7.05	0.90	6.59E-04
	1-Stearoyl-2-arachidonoyl-sn-glycerol	627.53	113.65	6.55	2.27	9.58E-03
	2-Methylbutyroylcarnitine	246.17	242.30	1.05	1.59	7.77E-03
	Acetylcarnitine	204.12	315.31	3.30	0.72	7.71E-04
	Cytidine 5′-diphosphocholine (CDP-choline)	489.11	449.49	1.19	0.66	1.33E-03
	D-Proline	116.07	323.98	2.54	0.77	4.70E-02
	Eicosapentaenoic acid	369.17	32.89	4.15	2.00	4.22E-02
	Glutathione disulfide	613.16	573.61	1.62	0.45	1.32E-02
	L-.alpha.-Amino-.gamma.-butyrolactone	102.05	89.49	4.18	5.89	4.38E-02
	L-Aspartate	134.04	421.99	1.48	1.72	3.27E-02
	L-Carnitine	162.11	387.09	1.70	0.66	2.55E-02
	L-Leucine	132.10	323.23	1.85	1.26	5.45E-04
	L-Phenylalanine	166.09	322.60	1.64	1.26	3.08E-04
	Lumichrome	243.09	62.21	1.01	0.88	2.51E-02
	N-Docosanoyl-4-sphingenyl-1-O-phosphorylcholine	809.65	118.37	2.21	2.91	9.87E-04
	Nicotinamide adenine dinucleotide (NAD)	664.12	491.16	1.82	0.37	6.03E-03
Positive	Pantothenate	220.12	278.37	3.10	0.52	6.44E-06
	PC (16:0/16:0)	756.55	144.77	1.37	0.94	3.98E-02
	Phosphocreatine	212.04	445.88	1.82	0.44	6.92E-05
	Phthalic acid mono-2-ethylhexyl ester	279.16	31.75	4.76	0.88	4.17E-03
	Sphinganine	302.30	125.24	1.37	1.42	1.46E-03
	Taurine	126.02	297.31	5.11	0.81	2.94E-03
	Thioetheramide-PC	758.57	144.77	5.66	0.91	7.10E-04
	Tyramine	120.08	322.71	2.08	1.25	2.95E-04
	1-Methylnicotinamide	137.07	256.68	2.60	0.76	8.53E-02
	1-Oleoyl-sn-glycero-3-phosphocholine	544.34	182.66	1.70	1.19	9.05E-02
	1-Stearoyl-2-oleoyl-sn-glycerol 3-phosphocholine (SOPC)	788.62	37.07	2.47	0.93	5.96E-02
	1-Stearoyl-sn-glycerol 3-phosphocholine	568.34	184.81	1.35	1.21	6.54E-02
	Creatine	132.08	348.95	1.64	0.61	5.78E-02
	Erucamide	338.34	33.13	4.86	0.86	9.98E-02
	Ile-Thr	233.15	52.99	1.02	0.60	8.87E-02
	Sphingomyelin (d18:1/18:0)	731.60	120.65	1.50	1.14	8.86E-02
	2E-Eicosenoic acid	309.28	47.05	2.95	1.31	4.19E-03
	2-Oxoadipic acid	141.02	228.32	6.48	0.47	4.34E-02
	(4Z,7Z,10Z,13Z,16Z,19Z)-4,7,10,13,16,19-Docosahexaenoic acid	327.23	35.15	5.34	1.64	8.52E-04
	Arachidonic acid (peroxide free)	303.23	47.62	9.91	1.66	2.94E-02
	Heptadecanoic acid	269.25	35.37	2.03	1.36	2.93E-04
	L-Proline	114.06	324.79	1.12	0.60	2.44E-02
	Myristic acid	227.20	35.15	2.95	1.19	3.11E-02
Negative	N-acetyl-D-lactosamine	442.15	370.14	1.06	0.70	1.06E-02
	Oleic acid	281.25	48.74	11.43	1.27	4.97E-02
	Pantothenate	218.10	279.08	3.31	0.38	1.25E-05
	Pentadecanoic acid	241.22	51.09	3.28	1.28	4.64E-03
	Taurine	124.01	297.53	4.03	0.75	1.23E-03
	1-Palmitoyl-2-oleoyl-phosphatidylglycerol	747.52	51.23	1.10	0.87	8.74E-02
	Cyanuric acid	128.01	59.06	1.72	0.59	5.57E-02
	Dodecanoic acid	199.17	6.28	2.18	1.78	9.90E-02

(a)

(b)
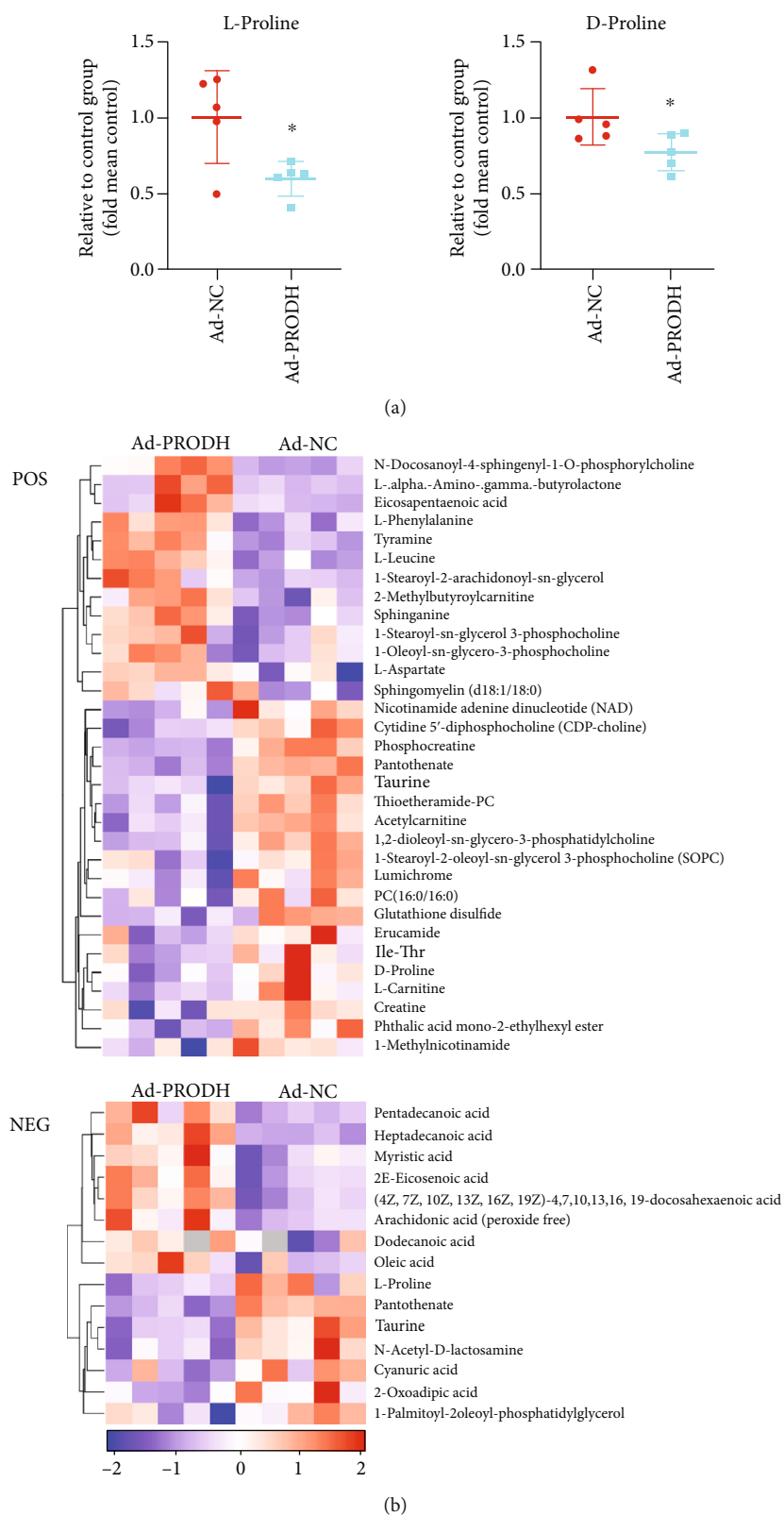
FIGURE 6: (a) Relative levels of L-proline and D-proline in the Ad-NC group and the Ad-PRODH group. (b) Heat map of the 47 differentially regulated endogenous metabolites between the Ad-NC group and the Ad-PRODH group in positive and negative ion modes. The data are presented as the mean ± SD values. $^*p < 0.05$ versus the normoxia control group.
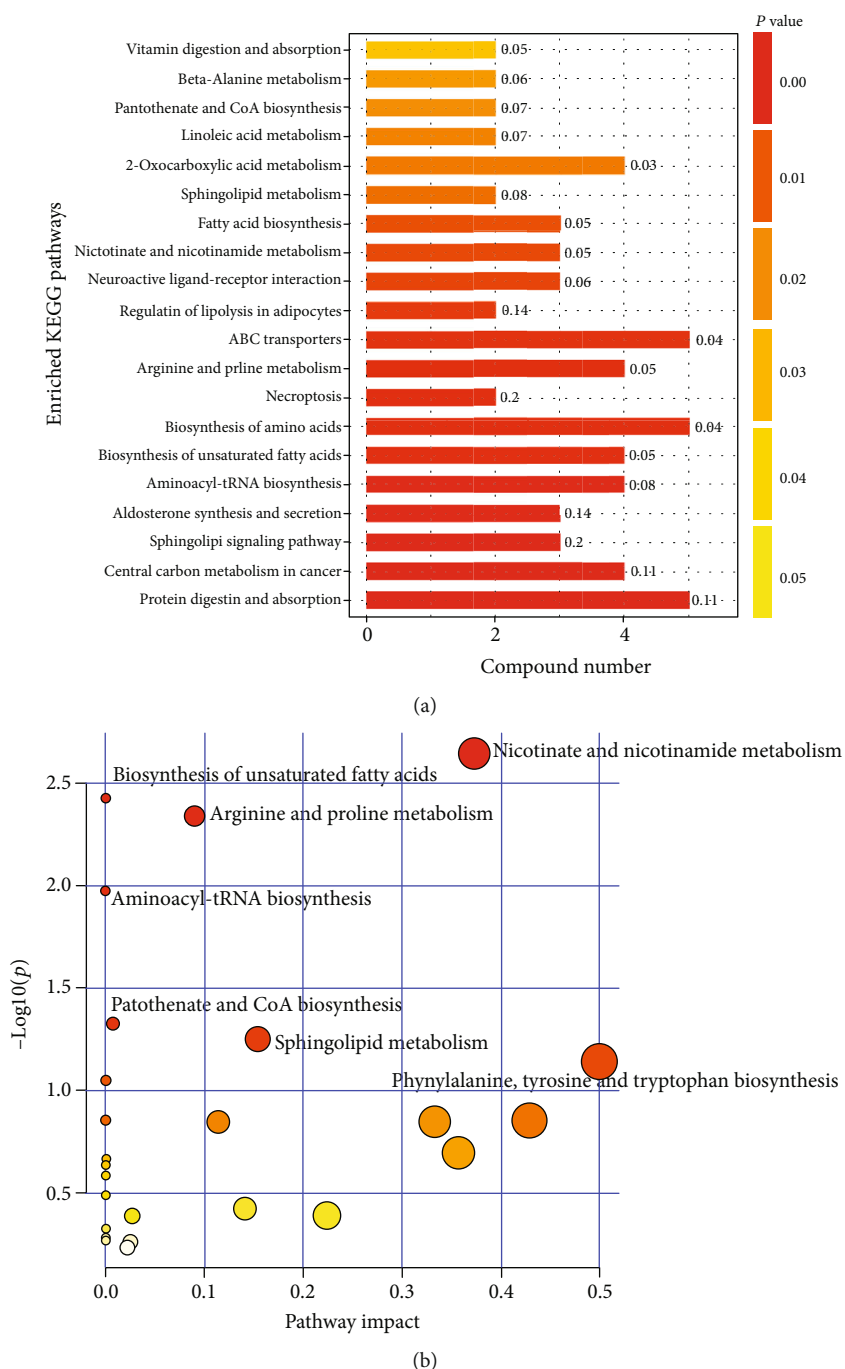
(a)

(b)

FIGURE 7: Altered metabolic pathways between the Ad-NC group and the Ad-PRODH group. (a) Metabolism-related pathways with significant changes as determined by KEGG pathway analysis. (b) Summary of pathway analysis results related to the differentially regulated metabolites generated by MetaboAnalyst.

primary reason for the poor prognosis of CHD, and advancing the understanding of metabolic alterations occurring in CHD patients is quite urgent to improve the prognosis of patients with CHD [19]. In this study, for the first time, liquid chromatography-tandem mass spectrometry- (LC-MS/MS-) based untargeted metabolomics analysis was performed to reveal the pathways associated with metabolic alterations after enhancement of proline metabolism in an H9c2 cardiomyocyte OGD model, which was utilized to mimic the ische-

mic injury observed in vivo. Via processing and statistical analysis of the metabolomics data, we discovered a variety of metabolites and metabolic pathways related to hypoxic injury in cardiomyocytes that were altered after enhancement of proline metabolism.

Sphingolipids are a class of lipids that are major components of eukaryotic cell membranes, which are biologically essential for maintaining cell structure and function, as well as cell growth, survival, and apoptosis [20]. Recent studies

have proven that sphingolipids are released during ischemia and hypoxia in the human myocardium [21] and that this release may promote the protection of myocardial cells against ischemic injury [22, 23]. In this study, we observed that sphinganine (VIP = 1.3672, FC = 1.4180, $p = 0.0015$) and other related products of phospholipid metabolism were altered significantly when proline metabolism was enhanced in cardiomyocytes under hypoxia, suggesting that enhanced proline metabolism may play a protective role through regulation of phospholipid metabolism.

In addition, cardiomyocytes with enhancement of proline metabolism under hypoxia exhibited increased synthesis of fatty acids, especially unsaturated fatty acids such as eicosapentaenoic acid (EPA) (VIP = 4.1471, FC = 1.9963, $p = 0.0422$). Changes in lipid metabolism during myocardial ischemia can cause changes in membrane fluidity, permeability, or signaling cascades and exert complex effects on the physiological functions of the heart. EPA, a very-long-chain n-3 fatty acid, is highly unsaturated and increases membrane fluidity. Through modulation of the physical properties of membranes, EPA provides a specific environment to support the function of membrane proteins, such as receptors, transporters, ion channels, and signaling enzymes [24]. To date, substantial evidence has accumulated from prospective and case–control studies indicating that a higher intake of EPA is associated with a lower risk of adverse CVD outcomes in populations [25, 26]. The conclusion that very-long-chain n-3 fatty acids have a role in reducing the risk of CVD, especially CHD, is fully supported by the American Heart Association [27].

Phosphocreatine (P-Cr) is a high-energy phosphoric acid compound found in muscles or other excitatory tissues (such as brain and nerves) and is a temporary storage form of high-energy phosphoric acid groups [28]. When phosphocreatine is hydrolyzed, 10.3 kcal of free energy is released per mole of compound, which is more than the amount of energy released by ATP (7.3 kcal per mole). Under pathological conditions where energy production is impeded, such as hypoxia, phosphocreatine rapidly transfers its phosphate group to ADP, thus reconstituting the ATP store that could not otherwise be replenished due to hypoxia [29]. Our study showed that the enhancement of proline metabolism after hypoxia significantly reduced the level of phosphocreatine (VIP = 1.8213, FC = 0.4369, $p = 0.00007$), indicating that the cardiomyocyte phosphocreatine/creatine system prevents or delays the exhaustion of the ATP store that would otherwise occur because of the lack of oxidative glycolysis consequent to hypoxia. In addition to the level of phosphocreatine, the level of glutathione disulfide (VIP = 1.6194, FC = 0.4546, $p = 0.0132$) was also decreased after enhancement of proline metabolism under hypoxia. Glutathione and its oxidized form is one of the most important redox buffer pairs in the cell [30]. On the one hand, it can directly eliminate ROS, and at the same time, it has an important regulatory effect on cellular ROS signal transduction during oxidative stress [7]. Different studies have shown that enhanced proline metabolism increases the level of reduced glutathione in cells and reduces that of glutathione disulfide. Our research also confirms this event, which is one of the mecha-

nisms by which intracellular ROS production decreases after enhancement of proline metabolism under hypoxia.

Aminoacyl-tRNA biosynthesis, which is key for delivering amino acids to the ribosome and ensuring the accuracy of translation, was significantly altered after enhancement of proline metabolism under hypoxia in cardiomyocytes [31]. The latest clinical evidence suggests that aminoacyl-tRNA biosynthesis plays a key role in maintaining left ventricular diastolic function, which opens new research perspectives for the treatment and early prevention of HF [32]. Our study also showed that the ABC transporter pathway was changed significantly after the enhancement of proline metabolism. ABC transporters are a family of ATP-dependent transporters that can transport a variety of endogenous compounds, including amino acids, ions, nucleotides, lipids, and peptides, across the cell membrane. Researchers have found that ABC transporters are altered after MI and are involved in cardiac homeostasis [33, 34], which constitute future research directions regarding the cardioprotective effect of proline metabolism.

The limitation of this study is that although the OGD hypoxic injury model was used to simulate the in vivo ischemic state, metabolism is a process of systemic changes in the organism. The future clinical therapeutic application of enhanced proline metabolism requires additional experiments to prove the effectiveness of this approach in vivo. Another limitation of this study was that only an untargeted semiquantitative MS approach was used to screen differential metabolites. Thus, further verification with a targeted quantitative method is required. Based on the discussion of the above-untargeted metabolomics results, we will conduct further verification and functional studies on the basis of these significantly changed metabolites and metabolic pathways to clarify the possible mechanism by which enhanced proline metabolism protects cardiomyocytes against hypoxic damage and to explore new treatments for ischemic heart disease.

5. Conclusions

In summary, our study demonstrated a protective effect of enhanced proline metabolism in cardiomyocytes under hypoxia. First, we found that the expression of the proline-degrading enzyme PRODH was downregulated after MI and hypoxia. Second, we demonstrated that enhanced proline metabolism induced by overexpression of PRODH reduced reactive oxidative stress and apoptosis levels, whereas PRODH knockdown had the opposite effects. Third, untargeted metabolomics analysis revealed that the protective effect was associated with significant changes in metabolism associated with sphingolipid signaling pathways, unsaturated fatty acid biosynthesis, phosphocreatine, glutathione disulfide, aminoacyl-tRNA biosynthesis, and ABC transporters. The changes discussed above provide insight into novel mechanisms by which enhanced proline metabolism protects cardiomyocytes against hypoxic injury and support the exploration of these mechanisms to design new therapeutic approaches for CHD.

Data Availability

The datasets used and analyzed during the current study are available from the corresponding author upon reasonable request.

Conflicts of Interest

All authors declare that they have no competing interests.

Authors' Contributions

Jiacheng Wang and Zhimin Xue are co-first authors of the article and contributed equally to this work.

Acknowledgments

References

[1] E. J. Benjamin, P. Muntner, A. Alonso et al., "Heart disease and stroke statistics—2019 update: a report from the American Heart Association," *Circulation*, vol. 139, pp. e56–e528, 2019.

[2] G. Olivetti, R. Abbi, F. Quaini et al., "Apoptosis in the failing human heart," *The New England Journal of Medicine*, vol. 336, no. 16, pp. 1131–1141, 1997.

[3] H. Taegtmeyer, M. E. Young, G. D. Lopaschuk et al., "Assessing cardiac Metabolism," *Circulation Research*, vol. 118, no. 10, pp. 1659–1701, 2016.

[4] R. W. McGarrah, S. B. Crown, G.-F. Zhang, S. H. Shah, and C. B. Newgard, "Cardiovascular metabolomics," *Circulation Research*, vol. 122, no. 9, pp. 1238–1258, 2018.

[5] Y. Fan, Y. Li, Y. Chen et al., "Comprehensive metabolomic characterization of coronary artery diseases," *Journal of the American College of Cardiology*, vol. 68, no. 12, pp. 1281–1293, 2016.

[6] B. E. Sansbury, A. M. DeMartino, Z. Xie et al., "Metabolomic analysis of pressure-overloaded and infarcted mouse hearts," *Circulation: Heart Failure*, vol. 7, no. 4, pp. 634–642, 2014.

[7] X. Liang, L. Zhang, S. K. Natarajan, and D. F. Becker, "Proline mechanisms of stress survival," *Antioxidants & Redox Signaling*, vol. 19, no. 9, pp. 998–1011, 2013.

[8] S. K. Natarajan, W. Zhu, X. Liang et al., "Proline dehydrogenase is essential for proline protection against hydrogen peroxide-induced cell death," *Free Radical Biology & Medicine*, vol. 53, no. 5, pp. 1181–1191, 2012.

[9] C. D'Aniello, E. J. Patriarca, J. M. Phang, and G. Minchiotti, "Proline metabolism in tumor growth and metastatic progression," *Frontiers in Oncology*, vol. 10, p. 776, 2020.

[10] Y. Fichman, S. Y. Gerdes, H. Kovács, L. Szabados, A. Zilberstein, and L. N. Csonka, "Evolution of proline biosynthesis: enzymology, bioinformatics, genetics, and transcriptional regulation," *Biological Reviews*, vol. 90, no. 4, pp. 1065–1099, 2015.

[11] J. Wang, Z. Xue, J. Lin et al., "Proline improves cardiac remodeling following myocardial infarction and attenuates cardio-myocyte apoptosis via redox regulation," *Biochemical Pharmacology*, vol. 178, article 114065, 2020.

[12] K.-C. Yang, K. A. Yamada, A. Y. Patel et al., "Deep RNA sequencing reveals dynamic regulation of myocardial noncoding RNAs in failing human heart and remodeling with mechanical circulatory support," *Circulation*, vol. 129, no. 9, pp. 1009–1021, 2014.

[13] J. O. Kim, J. H. Park, T. Kim et al., "A novel system-level approach using RNA-sequencing data identifies miR-30-5p and miR-142a-5p as key regulators of apoptosis in myocardial infarction," *Scientific Reports*, vol. 8, no. 1, article 14638, 2018.

[14] X. Yan, J. Jin, X. Su et al., "Intestinal flora modulates blood pressure by regulating the synthesis of intestinal-derived corticosterone in high salt-induced hypertension," *Circulation Research*, vol. 126, no. 7, pp. 839–853, 2020.

[15] J. Chong, O. Soufan, C. Li et al., "MetaboAnalyst 4.0: towards more transparent and integrative metabolomics analysis," *Nucleic Acids Research*, vol. 46, no. W1, pp. W486–W494, 2018.

[16] G. Heusch et al., "Cardiovascular remodelling in coronary artery disease and heart failure," *The Lancet*, vol. 383, no. 9932, pp. 1933–1943, 2014.

[17] W. Wang, F. Zhang, Y. Xia et al., "Defective branched chain amino acid catabolism contributes to cardiac dysfunction and remodeling following myocardial infarction," *American Journal of Physiology-Heart and Circulatory Physiology*, vol. 311, no. 5, pp. H1160–H1169, 2016.

[18] H. Sun, K. C. Olson, C. Gao et al., "Catabolic defect of branched-chain amino acids promotes heart failure," *Circulation*, vol. 133, no. 21, pp. 2038–2049, 2016.

[19] C. J. Zuurbier, L. Bertrand, C. R. Beauloye et al., "Cardiac metabolism as a driver and therapeutic target of myocardial infarction," *Journal of Cellular and Molecular Medicine*, vol. 24, no. 11, pp. 5937–5954, 2020.

[20] E. E. Egom, M. A. Mamas, and A. L. Clark, "The potential role of sphingolipid-mediated cell signaling in the interaction between hyperglycemia, acute myocardial infarction and heart failure," *Expert Opinion on Therapeutic Targets*, vol. 16, no. 8, pp. 791–800, 2012.

[21] E. E. Egom, M. A. Mamas, S. Chacko et al., "Serum sphingolipids level as a novel potential marker for early detection of human myocardial ischaemic injury," *Frontiers in Physiology*, vol. 4, 2013.

[22] E. E. A. Egom, T. M. A. Mohamed, M. A. Mamas et al., "Activation of Pak 1/Akt/eNOS signaling following sphingosine-1-phosphate release as part of a mechanism protecting cardiomyocytes against ischemic cell injury," *American Journal of Physiology-Heart and Circulatory Physiology*, vol. 301, no. 4, pp. H1487–H1495, 2011.

[23] Y. Hadas, A. S. Vincek, E. Youssef et al., "Altering sphingolipid metabolism attenuates cell death and inflammatory response after myocardial infarction," *Circulation*, vol. 141, no. 11, pp. 916–930, 2020.

[24] P. C. Calder, "Very long-chain n-3 fatty acids and human health: fact, fiction and the future," *The Proceedings of the Nutrition Society*, vol. 77, no. 1, pp. 52–72, 2018.

[25] C. Bilato, "n-3 fatty acids and cardiovascular disease: the story is not over yet," *Aging Clinical and Experimental Research*, vol. 25, no. 4, pp. 357–363, 2013.

[26] A. W. Qureshi, R. Altamimy, A. el Habhab et al., "Ageing enhances the shedding of splenocyte microvesicles with

endothelial pro-senescent effect that is prevented by a short-term intake of omega-3 PUFA EPA:DHA 6:1," *Biochemical Pharmacology*, vol. 173, article 113734, 2020.

[27] E. B. Rimm, L. J. Appel, S. E. Chiuve et al., "Seafood long-chain n-3 polyunsaturated fatty acids and cardiovascular disease: a science advisory from the American Heart Association," *Circulation*, vol. 138, no. 1, pp. e35–e47, 2018.

[28] P. A. Bottomley, K. C. Wu, G. Gerstenblith, S. P. Schulman, A. Steinberg, and R. G. Weiss, "Reduced myocardial creatine kinase flux in human myocardial Infarction," *Circulation*, vol. 119, no. 14, pp. 1918–1924, 2009.

[29] M. Balestrino, M. Sarocchi, E. Adriano, and P. Spallarossa, "Potential of creatine or phosphocreatine supplementation in cerebrovascular disease and in ischemic heart disease," *Amino Acids*, vol. 48, no. 8, pp. 1955–1967, 2016.

[30] N. Krishnan, M. B. Dickman, and D. F. Becker, "Proline modulates the intracellular redox environment and protects mammalian cells against oxidative stress," *Free Radical Biology & Medicine*, vol. 44, no. 4, pp. 671–681, 2008.

[31] E. R. S. Torres, R. Hall, G. Bobe et al., "Integrated metabolomics-DNA methylation analysis reveals significant long-term tissue-dependent directional alterations in aminoacyl-tRNA biosynthesis in the left ventricle of the heart and hippocampus following proton irradiation," *Frontiers in Molecular Biosciences*, vol. 6, p. 77, 2019.

[32] Z.-Y. Zhang, V. G. Marrachelli, W. Y. Yang et al., "Diastolic left ventricular function in relation to circulating metabolic biomarkers in a population study," *European Journal of Preventive Cardiology*, vol. 26, no. 1, pp. 22–32, 2018.

[33] E. A. Hausner, S. A. Elmore, and X. Yang, "Overview of the components of cardiac metabolism," *Drug Metabolism and Disposition*, vol. 47, no. 6, pp. 673–688, 2019.

[34] H. Bai, K. Sun, J. H. Wu et al., "Proteomic and metabolomic characterization of cardiac tissue in acute myocardial ischemia injury rats," *PLOS ONE*, vol. 15, no. 5, article e0231797, 2020.

Research Article

Gender Difference on the Effect of Omega-3 Polyunsaturated Fatty Acids on Acetaminophen-Induced Acute Liver Failure

Yunzhi Liu,[1,2] Yu Chen,[1,2] Xinghuan Xie,[2] Aiping Yin,[2] Yue Yin,[1,2] Yan Liu,[1,2] Lijun Dong,[1,2] Zhengyumeng Zhu,[2] Jia Zhou ⓘ,[2] Qingchun Zeng,[3] Xiao Lu,[2] Zhengliang Chen ⓘ,[2] Kun Wen ⓘ,[4,5] and Daming Zuo ⓘ[1,5]

[1]*Institute of Molecular Immunology, School of Laboratory Medicine and Biotechnology, Southern Medical University, Guangzhou, Guangdong 510515, China*
[2]*Guangdong Province Key Laboratory of Proteomics, Department of Immunology, School of Basic Medical Sciences, Southern Medical University, Guangzhou 510515, China*
[3]*Key Laboratory for Organ Failure Research, Department of Cardiology, Nanfang Hospital, Southern Medical University, Guangzhou, Guangdong 510515, China*
[4]*Division of Laboratory Medicine, Zhujiang Hospital, Southern Medical University, Guangzhou, Guangdong 510282, China*
[5]*Microbiome Medicine Center, Zhujiang Hospital, Southern Medical University, Guangzhou, Guangdong 510282, China*

Correspondence should be addressed to Zhengliang Chen; zhlchen@smu.edu.cn, Kun Wen; kunwen@gmail.com, and Daming Zuo; zdaming@smu.edu.cn

Acetaminophen (APAP) toxicity is the leading cause of drug-induced liver failure, which is closely related to mitochondrial dysfunction and oxidative damage. Studies in clinical trials and in animal models have shown that omega-3 polyunsaturated fatty acids (n-3 PUFAs) affect the progression of various types of liver damage. Interestingly, the sex-dependent effect of n-3 PUFAs on human health has also been well documented. However, it is unknown whether supplementation of n-3 PUFAs modulates the pathogenesis of APAP-induced liver failure with sex-specificity. Our results showed that both endogenous and exogenous n-3 PUFAs significantly aggravated the APAP-induced liver injury in male mice, whereas the opposite effects were observed in females. In vivo and in vitro studies demonstrated that estrogen contributes to the gender difference in the regulation of n-3 PUFAs on APAP overdose. We found that n-3 PUFA-mediated regulation of hepatic oxidative stress response and autophagy upon APAP challenge is distinct between male and female mice. Moreover, we provided evidence that β-catenin signaling activation is responsible for the sex-dependent regulation of APAP hepatotoxicity by n-3 PUFAs. Together, these findings indicated that supplementation with n-3 PUFAs displays sex-differential effect on APAP hepatotoxicity and could have profound significance in the clinical management for drug-induced liver injury.

1. Introduction

Acetaminophen (APAP) is currently one of the most widely used antipyretic and analgesic drugs. Although this drug has been considered safe for decades, an overdose can cause severe liver damage, which ultimately may cause acute liver failure [1]. APAP hepatotoxicity involves its conversion to N-acetyl-p-benzoquinone imine (NAPQI), which consumes glutathione (GSH) and leads to the generation of reactive

oxygen species (ROS). The accumulation of ROS contributes to sustained c-Jun N-terminal kinase (JNK) activation, which acts as determined signaling related to hepatocyte necrosis and apoptosis [2, 3]. It was reported that both inhibitors of ROS or JNK protected mice from APAP-induced liver injury [4, 5]. Autophagy is a cellular process that can degrade impaired mitochondria, thereby removing accumulated ROS [6]. It has been confirmed that increased autophagy protects mice against APAP-induced liver failure [7, 8].

During autophagy, cytosolic microtubule-associated protein 1 light chain 3 (LC3-I) is conjugated with phosphatidylethanolamine (PE). The PE-conjugated form of LC3 (LC3-II) is then recruited to the autophagosomal membrane, leading to the formation of autophagosome [9]. p62 (SQSTM1) is one of the selective autophagy receptors, which directly binds to LC3, transporting ubiquitination-related protein accumulates to the autophagosome [10].

n-3 polyunsaturated fatty acids (n-3 PUFAs), mainly including eicosapentaenoic acid (EPA) and docosahexaenoic acid (DHA), are essential to human health [11]. In particular, studies have documented that n-3 PUFAs affect the progression of various liver diseases [12–16]. Mechanically, several studies have reported that n-3 PUFAs modulated the hepatic oxidative stress response and autophagy activation during liver injury [14, 16]. Interestingly, the sex differences in the effects of n-3 PUFAs on health and disease have been widely studied [17–20]. Previous researches have demonstrated the sex-dependent differences in the metabolism of n-3 PUFAs in both humans and animals [21, 22]. Phang et al. reported that the differential regulation of hemostasis by n-3 PUFA supplementation in men and women is significantly associated with the levels of sex hormones [20]. It is of note to mention that sex hormones altered the synthesis of n-3 PUFAs in human primary hepatocytes [23], and the effect of n-3 PUFAs on nonalcohol fatty liver disease- (NAFLD-) related liver injury also exhibited gender difference [19].

The *fat-1* mice, which express the *Caenorhabditis elegans fat-1* gene, are capable of endogenous conversion of n-6 PUFAs to n-3 PUFAs, resulting in elevated amounts of n-3 PUFAs in their organs and tissues compared with the wild-type (WT) littermates [24]. In this study, we aimed to investigate the effect of n-3 PUFAs on APAP-induced liver damage in male and female *fat-1* mice. The result showed that male *fat-1* mice were susceptible to APAP-induced liver injury compared to WT mice, while the female *fat-1* mice were resistant to the APAP toxicity compared to the WT counterparts. Male *fat-1* mice had a lower activation of autophagy and higher generation of ROS than WT mice upon the APAP challenge. In female mice, the *fat-1* mice displayed promoted autophagy activation and limited ROS production compared to WT controls in response to APAP overdose. We have demonstrated that β-catenin signaling activation is involved in the differential regulation of APAP hepatotoxicity by n-3 PUFAs in male and female mice. Furthermore, we also provided evidence that exogenous n-3 PUFAs modulated the APAP hepatotoxicity in a sex-dependent manner.

2. Materials and Methods

2.1. Animals. WT C57BL/6 mice were obtained from the Laboratory Animal Center of Southern Medical University (Guangzhou, China). *Fat-1* mice were backcrossed with C57BL/6 mice, and the *fat-1* genotype of each mouse was identified by PCR assay using isolated genomic DNA from mouse tails as previously described [25]. All animal experiments were approved by the Welfare and Ethical Committee for Experimental Animal Care of Southern Medical University.

2.2. Reagents. DHA (D2534) and β-estradiol (E8875) were purchased from Sigma-Aldrich (St. Louis, MO, USA). The primary antibodies of β-catenin (66379-1-Ig), GSK3β (22104-1-AP), and GAPDH (10494-1-AP) were obtained from Proteintech (Chicago, IL, USA). Antibodies against phospho-β-catenin (DF2989) and phospho-JNK (AF3318) were from Affinity (Ancaster, ON, Canada). Antibodies for JNK (9252) and phospho-GSK3β (D3A4) were purchased from Cell Signaling Technology (Danvers, MA, USA).

2.3. Induction of Liver Injury. APAP (Santa Cruz Biotechnology, Santa Cruz, CA, USA) was dissolved in phosphate-buffered saline. Mice (8 weeks old) were fasted overnight and injected with APAP intraperitoneally at the dose of 400 mg/kg to induce hepatotoxicity and at the dose of 600 mg/kg to monitor survival rate. The serum was collected for alanine aminotransferase (ALT) and lactate dehydrogenase (LDH) assay. The tissue homogenates from the mouse liver were used to evaluate the levels of GSH with a commercial kit (Jiancheng Biotech, Nanjing, China). Liver damage was detected by hematoxylin and eosin (H&E) staining. Cell death was evaluated by TUNEL staining (Beyotime Biotechnology, Shanghai, China) according to the manufacturer's instruction. In some cases, male WT and *fat-1* mice were injected with 100 mg/kg β-estradiol (E2) intraperitoneally 1 week before APAP administration. To test the effect of exogenous n-3 PUFAs on APAP toxicity, male and female WT mice were fed with an n-3 PUFA-enriched diet 3 weeks before APAP injection.

2.4. Cell Culture and Treatment. HepaRG cells were obtained from Biopredic International (Rennes, France). The cells were cultured in William's E medium supplemented with 10% fetal bovine serum (FBS), 5 μg/mL insulin, and hydrocortisone. The cells were stimulated with 20 mM APAP. In some cases, cells were pretreated with 50 μM DHA, 2 μM XAV939, or 100 nM E2.

2.5. Isolation of Hepatocytes. Hepatocytes were isolated as previously described [26]. Briefly, livers from APAP-treated WT or *fat-1* mice were perfused with the calcium-free salt solution through the portal vein, followed by perfusion with type IV collagenase *in situ*. The livers were then filtered with polyamide mesh. After centrifugation at 50 × g for 3 minutes, the supernatants were removed. The cells were used for flow cytometric assay or immunoblotting assay. For the culture of primary hepatocytes, cells were plated in 6-well plates coated with mouse tail collagen in William's E medium containing 10% FBS. After 4 hours of incubation, the culture was washed with phosphate-buffered saline and replaced with serum-free RPMI 1640 medium. Cells were incubated overnight before further treatment.

2.6. Flow Cytometric Assay. Annexin V/PI apoptosis kit was obtained from MultiSciences (Hangzhou, China). To measure the intracellular level of ROS, hepatocytes from APAP-treated WT and *fat-1* mice or APAP-stimulated HepaRG cells were incubated with 10 μM DCFH-DA in the dark for 30 minutes at 37°C. The lipophilic cationic fluorescent dye JC-1 (KeyGEN, Nanjing, China) was used to detect changes in the

mitochondrial membrane potential. The cells were acquired and analyzed using the BD FACSDiva program in the flow cytometry FACS LSRFortessa (BD Biosciences, San Jose, CA, USA).

2.7. Immunoprecipitation and Immunoblotting.

Protein samples extracted from mouse liver or HepaRG cells were separated by SDS-PAGE and then transferred onto polyvinylidene fluoride (PVDF) membranes (Millipore, Billerica, MA, USA). The membranes were blocked by bovine serum albumin (BSA, 5%) for 1 hour at room temperature and incubated with indicated primary antibodies at 4°C overnight. Subsequently, the membranes were stained with horseradish peroxidase- (HRP-) conjugated corresponding secondary antibody. For immunoprecipitation, whole-cell lysates (WCLs) were incubated with antibodies (1 μg) and protein A/G agarose (Santa Cruz Biotechnology) at 4°C overnight. Eluted immunoprecipitates were resolved on SDS-PAGE and examined for an association of proteins of interest using specific antibodies. Finally, measurement of the target protein was conducted with enhanced chemiluminescence (Thermo Fisher, Carlsbad, CA, USA) according to the manufacturer's protocol.

2.8. Immunohistochemistry and Immunofluorescence.

After hydration, antigen retrieval was performed in citrate buffer (pH 6.0) at 100°C for 10 minutes, and endogenous peroxidase activity was blocked by incubation with 3% H_2O_2 for 15 minutes. After blocking with normal goat serum at 37°C for 1 hour, the sections were stained with the anti-β-catenin antibody at 4°C overnight followed by incubation with HRP-conjugated secondary antibody at 37°C for 1 hour. Visualization of the immunoreactivity was performed by enhanced diaminobenzidine kit (TransGen Biotech) and nuclear staining with hematoxylin.

For analysis of the colocalization of β-catenin with GSK3β, the HepaRG cells were fixed with 2% paraformaldehyde for 20 minutes and permeabilized with 0.1% Triton X-100 for another 5 minutes at room temperature. After blocking with 10% goat serum for 1 hour, cells were stained with primary antibodies overnight at 4°C followed by incubation with the corresponding fluorescent-labeled secondary antibodies for 1 hour at room temperature. The images were acquired with a ×63 oil immersion objective on an Olympus FV1000 confocal microscope (Shinjuku, Tokyo, Japan).

2.9. Statistical Analysis.

The experimental data were expressed as mean ± SEM. One-way ANOVA was used to analyze the significant differences among multiple groups. Differences between two groups in the experiments were evaluated by Student's t-test. Comparison of the survival curves was determined using the log-rank test. Differences were considered statistically significant at $p < 0.05$.

3. Results

3.1. Endogenous n-3 PUFAs Exhibit the Sex-Dependent Manner in the Regulation of APAP-Induced Liver Injury.

To determine the effect of n-3 PUFAs on APAP-induced liver injury, sex- and age-matched WT or *fat-1* mice were challenged with a lethal dose of APAP. Surprisingly, the male

fat-1 mice exhibited higher mortality than male WT mice in response to APAP administration. However, the endogenous n-3 PUFAs significantly enhanced the survival rate in APAP-treated female mice (Figure 1(a)). To further evaluate the effect of n-3 PUFAs on APAP-induced liver injury, mice received a low dose of APAP, followed by biochemical and histological analyses. Consistently, elevated sera activities of ALT and LDH were observed in APAP-treated male *fat-1* mice compared to male WT controls, while sera from APAP-treated female *fat-1* mice displayed significantly decreased activities of ALT and LDH compared with those from female WT control mice (Figures 1(b) and 1(c)). Histological analysis showed that liver tissues from male *fat-1* mice exhibited much more centrilobular hepatic necrosis than those from male WT mice after APAP challenge (Figure 1(d)). By contrast, the histological changes were significantly reduced in APAP-treated female *fat-1* mice compared to the female WT counterparts (Figure 1(d)). Additionally, the TUNEL-positive cells were significantly higher in the livers of male *fat-1* mice than in those of male WT mice upon APAP challenge, while the number of TUNEL-positive hepatocytes in APAP-treated *fat-1* females was less than that in female counterparts (Figure 1(e)). Together, these data implicate that endogenous n-3 PUFAs aggravate APAP-induced liver injury in male mice but ameliorate APAP-induced liver injury in female mice.

3.2. Estrogen Contributes to the Gender Difference in the Effect of n-3 PUFAs on APAP-Induced Hepatotoxicity.

We hypothesized that estrogen might play a critical role in determining the regulatory function of n-3 PUFAs on APAP-induced hepatotoxicity. Male WT and *fat-1* mice were injected with E2 one week prior to APAP administration. Interestingly, the hormone-treated *fat-1* mice exhibited milder liver damage than WT controls in response to APAP injection, as indicated by H&E staining (Figure 2(a)). Also, attenuated activities of ALT and LDH were found in sera obtained from E2-injected *fat-1* mice compared to those from WT counterparts after the APAP challenge (Figures 2(b) and 2(c)). Moreover, we evaluated the effect of estrogen on n-3 PUFA-mediated regulation of APAP toxicity in human HepaRG cells, a reliable model to study mechanisms of APAP hepatotoxicity in humans [27]. The result showed that DHA alone accelerated APAP-induced cell death, but DHA plus estrogen treatment strongly attenuated the APAP hepatotoxicity (Figure 2(d)). These results indicate that the hormonal factor is responsible for the sex difference in n-3 PUFA-modulated APAP hepatotoxicity.

3.3. n-3 PUFA-Mediated Regulation of Hepatic Oxidative Stress Response and Autophagy Is Distinct between Male and Female Mice.

The APAP hepatoxicity is mainly due to the formation of NAPQI, which is generally detoxified by GSH [28]. Surprisingly, we found comparable GSH levels in the liver tissue homogenate from both APAP-treated WT and *fat-1* mice without sex difference (Supplemental Fig. 1A). Also, the hepatic GSH levels in APAP-injected WT and *fat-1* mice were similar after estrogen treatment
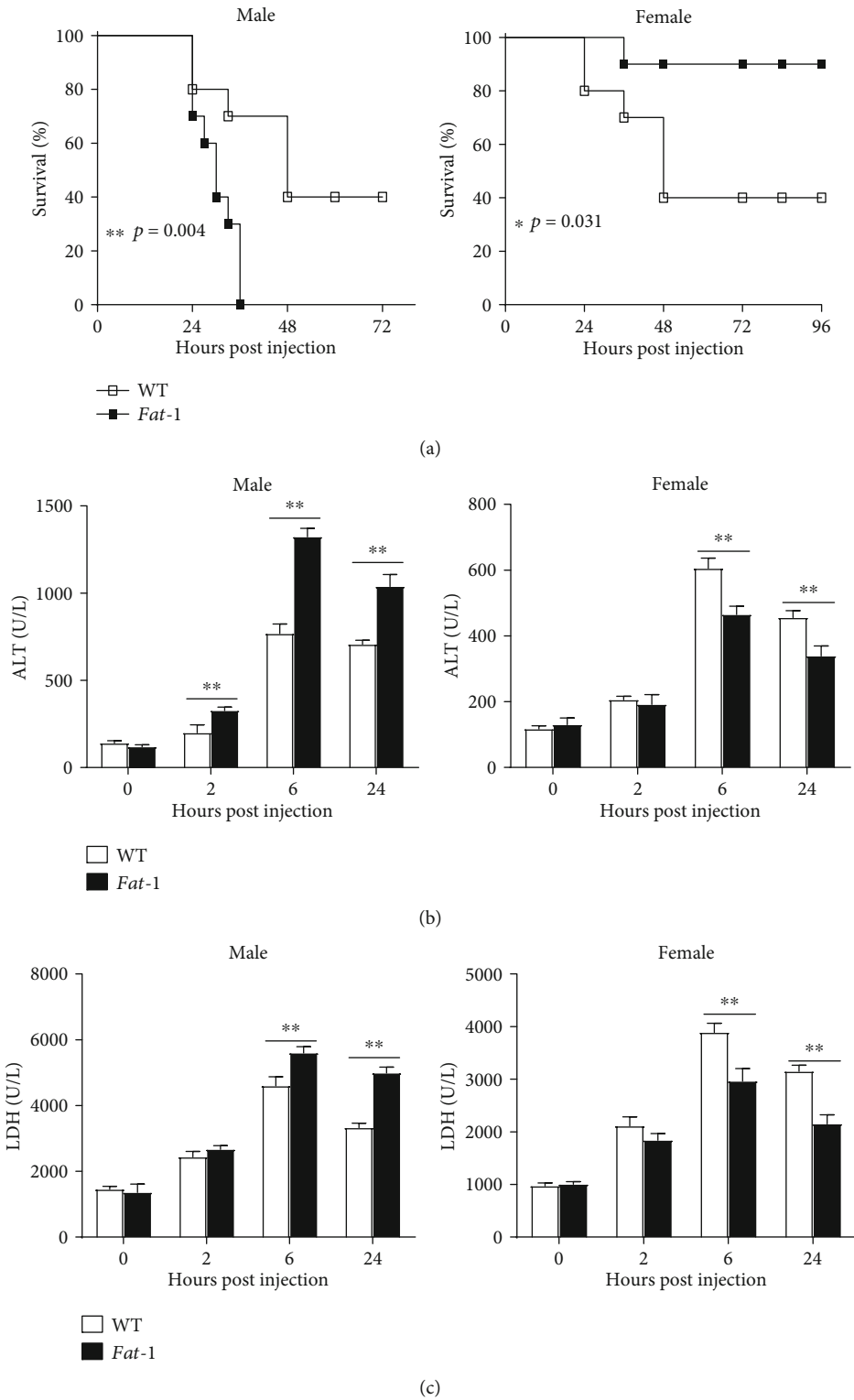
(a)

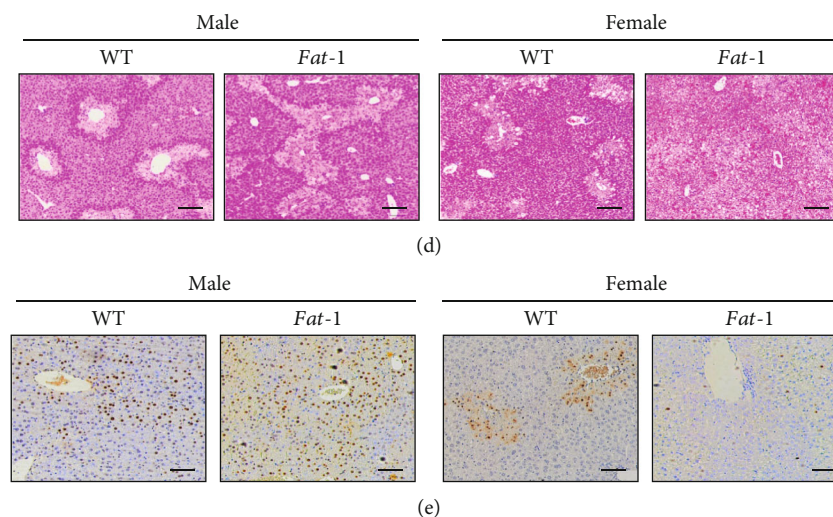
(b)

(c)

Figure 1: Continued.

(d)

(e)

FIGURE 1: Endogenous n-3 PUFAs exhibit sex-differential effects on APAP-induced liver damage. (a) Male or female WT and *fat-1* mice ($n = 10$) were challenged with APAP at the dose of 600 mg/kg, and the survival of mice was monitored. (b–e) APAP (400 mg/kg) was intraperitoneally injected into male or female WT and *fat-1* transgenic mice ($n = 5$). (b, c) Serum ALT and LDH levels at different time points after APAP injection were measured. (d) Histological analysis of mouse livers was performed at 24 hours post-APAP injection by H&E staining. Scale bars = 100 μm. (e) TUNEL staining was used to evaluate cell apoptosis in mouse livers. Scale bars = 50 μm. $^*p < 0.05$, $^{**}p < 0.01$. One of the three independent experiments is shown.

(Supplemental Fig. 1B). ROS are critical mediators of APAP-induced cell death [29, 30]. Our result showed that hepatocytes from male *fat-1* mice contained much more intracellular ROS levels than those from WT males upon APAP challenge, which indicated that n-3 PUFAs might promote the oxidative stress during APAP treatment in male mice (Figure 3(a)). In contrast, a reduced ROS level was observed in the hepatocytes in the APAP-injected female *fat-1* mice compared to the female WT counterparts (Figure 3(a)). Given that mitochondria are a primary source of ROS in animal cells, we used JC-1 dye to evaluate the mitochondrial membrane potential by flow cytometry. The results indicated more damaged mitochondria in the hepatocytes from male *fat-1* mice than male WT counterparts, while there were less injured mitochondria in the liver cells from female *fat-1* mice compared with female WT controls, after APAP challenge (Figure 3(b)).

In hepatocytes, JNK plays an essential role in stress response and is activated by a diverse array of stresses, including oxidative stress [30]. We, therefore, investigated activation of the JNK pathway during APAP-induced liver injury. The results showed that APAP induced a strongly higher level of JNK phosphorylation in livers from male *fat-1* mice than those from male WT counterparts (Figure 3(c)). On the contrary, decreased JNK phosphorylation was observed in female *fat-1* mice compared to WT mice after the APAP challenge (Figure 3(c)).

Autophagy is involved in the clearance of damaged mitochondria, thereby ameliorating intracellular oxidative stress response during APAP treatment [7]. Upon APAP challenge, reduced LC3 and p62 expressions were observed in the liver obtained from male *fat-1* mice compared to that from male WT mice (Figure 3(d)). By contrast, elevated LC3 and p62 levels were found in the liver tissues from female *fat-1* mice compared

with those from female WT controls after APAP injection (Figure 3(d)).

Next, we questioned whether estrogen modulates the n-3 PUFA-mediated regulation of APAP-induced oxidative stress and autophagy. DHA significantly enhanced the ROS production and JNK phosphorylation initiated by APAP stimulation in human hepatocytes. However, DHA downregulated APAP-triggered ROS production and JNK pathway activation in the presence of estrogen (Figures 3(e) and 3(f)). Consistently, DHA treatment reduced LC3 and p62 expressions in HepaRG cells upon APAP challenge, while increased LC3 and p62 levels were found in DHA-treated cells in combination with estrogen stimulation compared to the cells treated with estrogen alone (Figure 3(g)). Collectively, these data indicate that n-3 PUFA-modulated hepatic oxidative response and autophagy activation against APAP toxicity are sex-dependent.

3.4. Estrogen Mediates the Sex-Dependent Effect of n-3 PUFAs on APAP-Induced Hepatotoxicity via Regulation of β-Catenin Signaling. Given that the β-catenin pathway is a negative modulator of autophagy and repressor of both LC3 and p62 expressions [31], we next investigated whether β-catenin signaling is involved in the differential effect of n-3 PUFAs on APAP hepatotoxicity between male and female mice. As determined by immunoblotting analysis and immunohistochemical staining, an elevated level of β-catenin was found in liver tissues from male *fat-1* mice compared with those from WT controls while livers from female *fat-1* mice exhibited decreased β-catenin expression compared to female WT mice after APAP injection (Figures 4(a) and 4(b)). Consistently, DHA significantly boosted β-catenin expression in hepatocytes during APAP exposure, whereas DHA plus estrogen treatment suppressed the expression level of β-
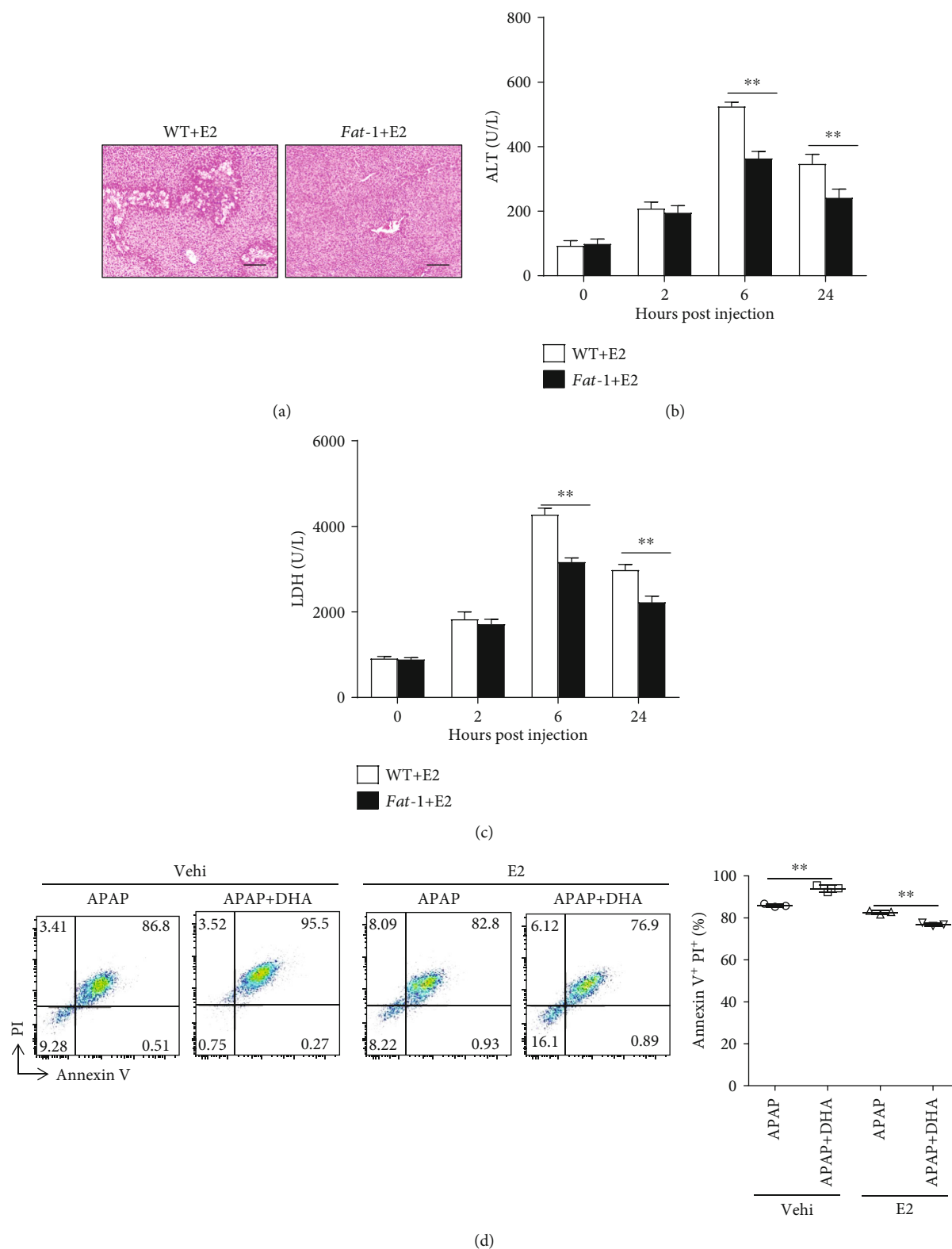
(a)

(b)

(c)

(d)

FIGURE 2: Estrogen is responsible for the sex-related function of n-3 PUFAs on APAP hepatotoxicity. (a–c) 100 mg/kg E2 was intraperitoneally injected into male WT or *fat-1* mice 7 days before 400 mg/kg APAP administration ($n = 5$). (a) 24 hours after APAP injection, histological analysis of livers was performed by H&E staining. Scale bars = 100 μm. (b, c) Serum ALT and LDH levels in various time points after APAP administration was evaluated. (d) HepaRG cells were pretreated with 50 μM DHA with or without 100 nM E2, followed by stimulation with 20 mM APAP for 24 hours. The cells were harvested and stained with Annexin V-FITC and PI for FACS analysis. $^{**}p < 0.01$. The data represent three independent experiments with similar results.
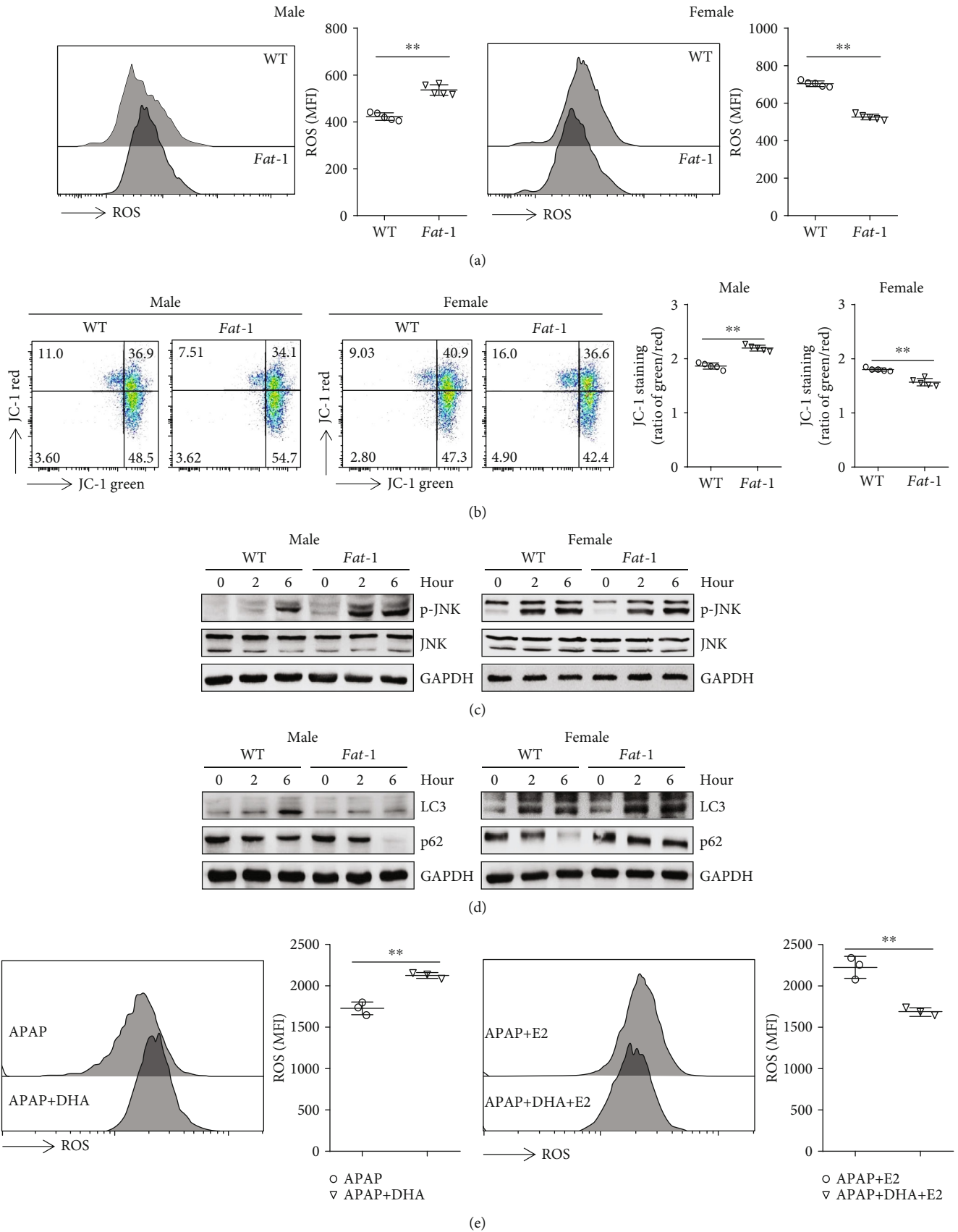
(a)

(b)

(c)
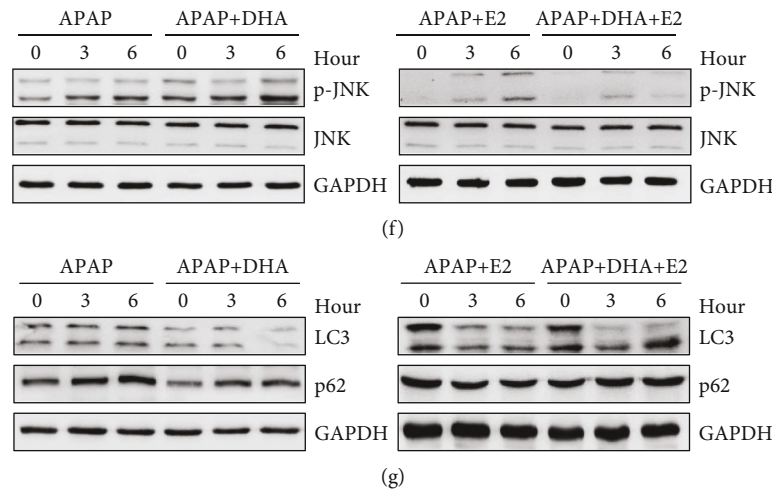

(d)

(e)

Figure 3: Continued.

(f)

(g)

FIGURE 3: n-3 PUFA-modulated hepatic oxidative response and autophagy activation against APAP toxicity is distinct between male and female mice. (a–d) Male or female WT and *fat-1* mice were injected with 400 mg/kg APAP, and livers were collected at 6 hours post-APAP injection ($n = 5$). (a) Flow cytometry analysis of the intercellular ROS level by the fluorescent probe DCFH-DA in hepatocytes was carried out. (b) The mitochondrial membrane potential in hepatocytes was measured by the JC-1 dye staining for flow cytometry analysis. (c) Phosphorylation of JNK was evaluated by immunoblotting analysis at the indicated time after APAP challenge. (d) The protein levels of LC3 and p62 were examined by immunoblotting analysis. (e–g) HepaRG cells were pretreated with $50\,\mu$M DHA with or without100 nM E2 prior to stimulation with 20 mM APAP. (e) The ROS level in the cells was analyzed by flow cytometry labeling with fluorescent probe DCFH-DA at 6 hours following APAP administration. (f) Phosphorylation of JNK expression in the APAP-treated cells was evaluated by immunoblotting analysis. (g) The hepatic levels of LC3 and p62 were determined by immunoblotting analysis. $^*p < 0.05$, $^{**}p < 0.01$. The data represent three independent experiments with similar results.

catenin in cells compared to the cells treated with estrogen alone in response to APAP stimulation (Figure 4(c)).

To further confirm the role of β-catenin in n-3 PUFA-mediated regulation of APAP hepatotoxicity, HepaRG cells were pretreated with XAV939, a β-catenin inhibitor [32], prior to APAP stimulation. Surprisingly, APAP-induced cell death was similar in DHA only or DHA plus estrogen-treated cells with XVA939 pretreatment (Figure 4(d)). Similarly, XVA939 pretreatment abrogated the estrogen-mediated downregulation of ROS production and JNK phosphorylation in hepatocytes against APAP stimulation (Figures 4(e) and 4(f)). Moreover, the levels of LC3 and p62 were comparable in cells treated with DHA alone or with DHA combined with estrogen in the presence of XVA939 (Figure 4(g)). Furthermore, the primary hepatocytes from WT and *fat-1* mice were isolated and stimulated with APAP. In the presence of the β-catenin inhibitor, APAP-triggered ROS production was similar in the hepatocytes treated with or without estrogen (Supplemental Fig. 2A). Besides, the activation of the JNK pathway and the expressions of LC3 and p62 were comparable between the APAP-treated hepatocytes stimulated with or without estrogen, in the presence of XVA939 (Supplemental Fig. 2B and C). These data suggest that β-catenin signaling is responsible for the differential regulation of APAP hepatotoxicity by n-3 PUFAs in male and female mice.

3.5. GSK3β Is Involved in the Regulation of β-Catenin Signaling in Response to n-3 PUFAs.
Suppression of GSK3-mediated β-catenin phosphorylation is considered to be a critical event in Wnt/β-catenin signaling [33, 34]. Herein, increased phosphorylation of GSK3β and decreased phosphor-

ylation of β-catenin were displayed in the livers from APAP-treated male *fat-1* mice compared with those from male WT controls (Figure 5(a)). On the contrary, the liver tissues from female *fat-1* mice exhibited much more reduced GSK3β phosphorylation and elevated β-catenin phosphorylation than those from female WT mice after APAP challenge (Figure 5(a)). An *in vitro* study demonstrated that DHA boosted GSK3β phosphorylation, thereby reducing the level of GSK3β and phosphorylated β-catenin in hepatocytes against APAP exposure (Figure 5(b)). However, DHA showed a reverse effect on the GSK3β phosphorylation and β-catenin signaling activation in APAP-stimulated cells in the presence of estrogen (Figure 5(b)). It has been reported that β-catenin is phosphorylated by GSK3β in a complex that consists of Axin, GSK3β, and β-catenin [34]. Immunoprecipitation assay showed that DHA treatment suppressed the interaction between β-catenin and GSK3β upon APAP challenge, while DHA promoted the binding of β-catenin with GSK3β in APAP-stimulated cells in the presence of estrogen (Figure 5(c)). Furthermore, immuno-fluorescence staining validated that DHA alone limited the interaction between β-catenin and GSK3β, while DHA plus estrogen enhanced the binding of β-catenin with GSK3β compared to estrogen alone in the APAP-stimulated cells (Figure 5(d)). These results suggest that GSK3β contributes to the sex hormone-dependent effect of DHA on β-catenin signaling activation.

3.6. Exogenous n-3 PUFAs Exhibit Similar Effect on APAP-Induced Liver Injury with Endogenous n-3 PUFAs.
To better characterize our findings, C57BL/6 mice were fed with n-3 PUFA-enriched diet for 3 weeks, before APAP injection.
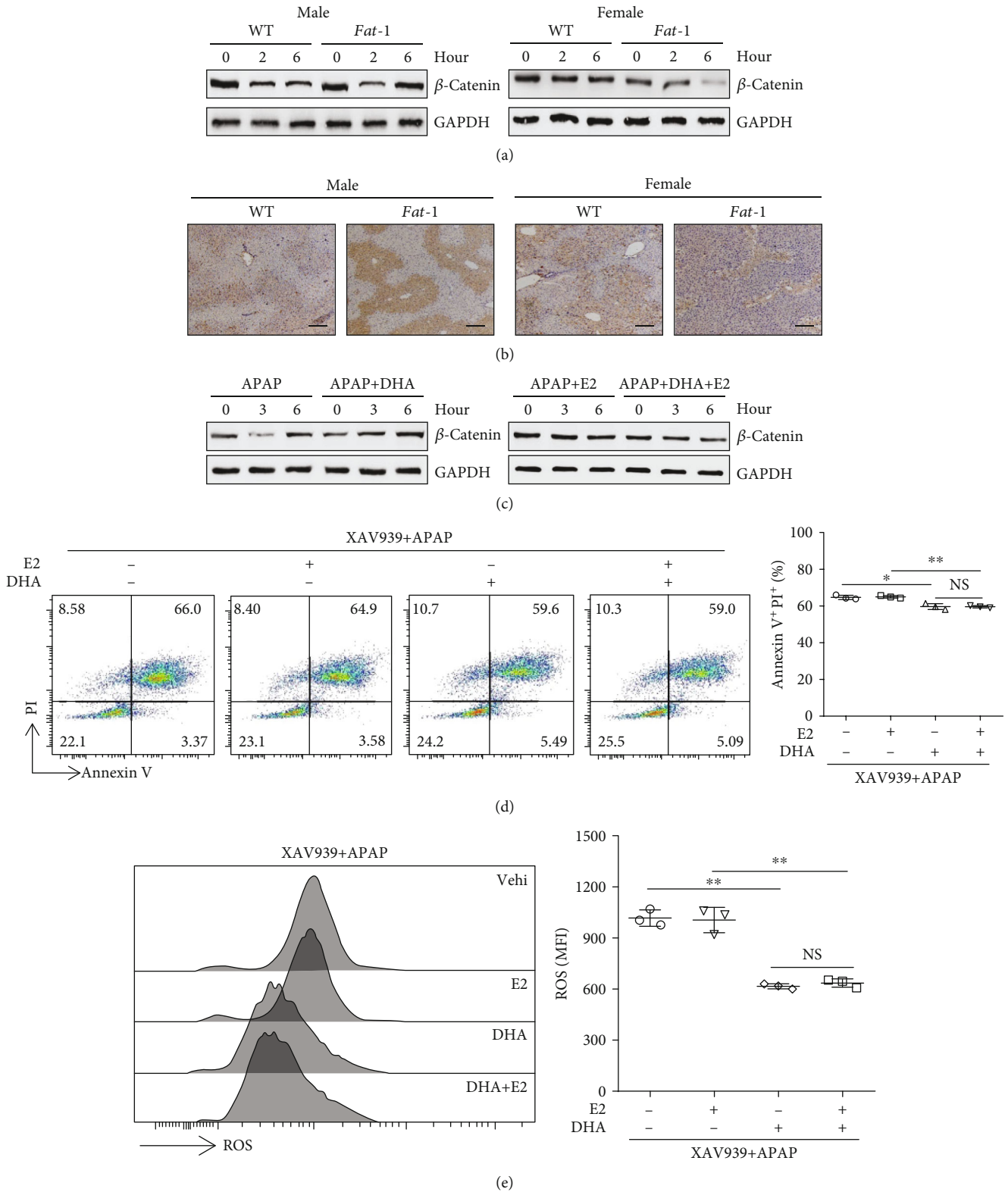
(a)

(b)

(c)

(d)

(e)

FIGURE 4: Continued.

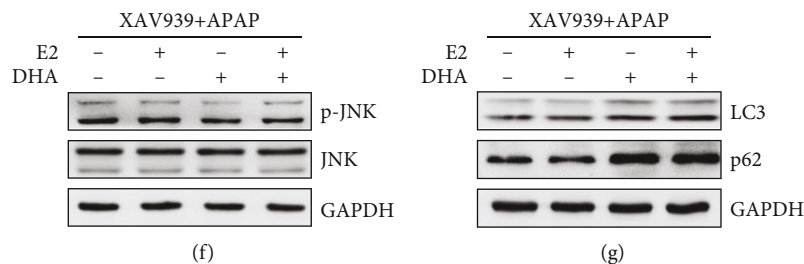(f)   (g)

FIGURE 4: β-Catenin signaling is involved in the differential effect of n-3 PUFAs on APAP hepatotoxicity between male and female mice. (a, b) APAP (400 mg/kg) was intraperitoneally injected to male or female WT and *fat-1* mice ($n = 5$). Subsequently, the liver tissues were collected at 6 hours post-APAP injection. (a) The protein level of β-catenin in the liver tissues was evaluated by western blotting. (b) Immunohistochemical staining for β-catenin was determined in the liver tissue. Scale bars = 100 μm. (c) HepaRG cells were pretreated with 50 μM DHA without 100 nM E2 before stimulation with 20 mM APAP. Western blot assay of β-catenin was performed at the indicated time point after APAP stimulation. (d–g) HepaRG cells were pretreated with 2 μM XAV939 for 2 hours combined with 100 nM E2 in the presence or absence of 50 μM DHA. Subsequently, the cells were stimulated with APAP for another 24 hours. (d) Apoptosis was measured by Annexin V-PI staining, followed by FACS analysis. (e) The ROS level in the cells was analyzed by flow cytometry labeling with fluorescent probe DCFH-DA at 6 hours following APAP administration. (f) Phosphorylation of JNK expression in the APAP-treated cells was evaluated at 6 hours following APAP administration by immunoblotting analysis. (g) The expression of LC3 and p62 was determined by immunoblotting analysis. $^*p < 0.05$, $^{**}p < 0.01$. NS: not significant. The data represent three independent experiments with similar results.

Similar to *fat-1* mice, n-3 PUFA-fed male mice performed severer liver injury than the control mice during APAP exposure, while female mice with dietary n-3 PUFAs showed attenuated hemorrhage area as implied by H&E staining (Figure 6(a)). Consistently, exogenous n-3 PUFAs elevated serum ALT and LDH activities in male APAP-challenged mice but decreased activities of ALT and LDH in female APAP-administrated mice (Figures 6(b) and 6(c)). Meanwhile, we observed comparable hepatic GSH levels between n-3 PUFA-fed mice and the control mice upon APAP injection (Supplemental Fig. 1C). Besides, upon APAP injection, attenuated expressions of LC3 and p62 were detected in liver tissues from male mice fed with n-3 PUFAs compared to those from the control mice. By contrast, increased hepatic levels of LC3 and p62 were found in female n-3 PUFA-fed mice (Figure 6(d)). Likewise, the livers obtained from n-3 PUFA-fed male mice exhibited aggravated JNK phosphorylation, but n-3 PUFA-treated female mice showed an attenuated hepatic level of phosphorylated JNK against APAP challenge (Figure 6(e)). Moreover, exogenous n-3 PUFA administration promoted GSK3β phosphorylation, thereby preventing β-catenin phosphorylation in male mice. As a result, the hepatic level of β-catenin was higher in n-3 PUFA-fed male mice than in the control mice after APAP injection (Figure 6(f)). By contrast, the expression of β-catenin was significantly reduced in liver tissues from n-3 PUFA-fed female mice compared with those from the control mice upon APAP exposure (Figure 6(f)). These data indicate that the exogenous n-3 PUFA supplement exhibits similar effects with endogenous n-3 PUFAs on APAP hepatotoxicity.

4. Discussion

n-3 PUFAs have been reported to exhibit a wide effect on liver injury in several animal models [12, 14, 16]. In our current study, we have demonstrated that n-3 PUFAs exert sex-specific control of APAP hepatotoxicity in mice. Our data

showed that n-3 PUFAs aggravated APAP-induced liver injury in male mice but ameliorated APAP hepatotoxicity in female mice through differential regulation of autophagy activation. Additionally, we revealed that the GSK3β-mediated activation of β-catenin signaling is related to the sex-dependent effect of n-3 PUFAs on APAP hepatotoxicity.

Sex differences in the pathogenesis of most chronic liver diseases are evident [35, 36]. Estrogens can reduce drug-induced liver injury in mice [37], while androgen excess drives progression to liver inflammation and increases the risk of NAFLD in women with polycystic ovary syndrome [38]. Zaima et al. observed that dietary intake of n-3 PUFAs increased the serum level of testosterone in mice, suggesting that n-3 PUFAs might modulate testosterone metabolism [39]. Our findings were in line with the previous study which reported that endogenous n-3 PUFAs protect against APAP-induced hepatotoxicity in female mice [40]. Intriguingly, we here observed that n-3 PUFAs aggravated the APAP-induced liver injury in male mice. Moreover, our study showed that estrogen treatment reversed the effect of n-3 PUFAs on the APAP hepatotoxicity in male *fat-1* mice, indicating that estrogen contributes to the sex differences in the regulation of APAP toxicity by n-3 PUFAs. APAP-induced hepatotoxicity is majorly characterized by overwhelmingly increased oxidative stress [41]. The lower susceptibility of female mice is achieved by the enhanced detoxification of ROS related to the accelerated recovery of mitochondrial GSH levels, which ameliorates the subsequent JNK activation and liver damage [42]. Our data also showed that n-3 PUFAs modulated the generation of intercellular ROS and JNK activation in APAP-challenged mice. The differential regulation of APAP hepatotoxicity by n-3 PUFAs in male and female mice was associated with the change of oxidative response.

Autophagy plays a vital role in liver physiology [14, 43] and has been considered as a possible therapeutic
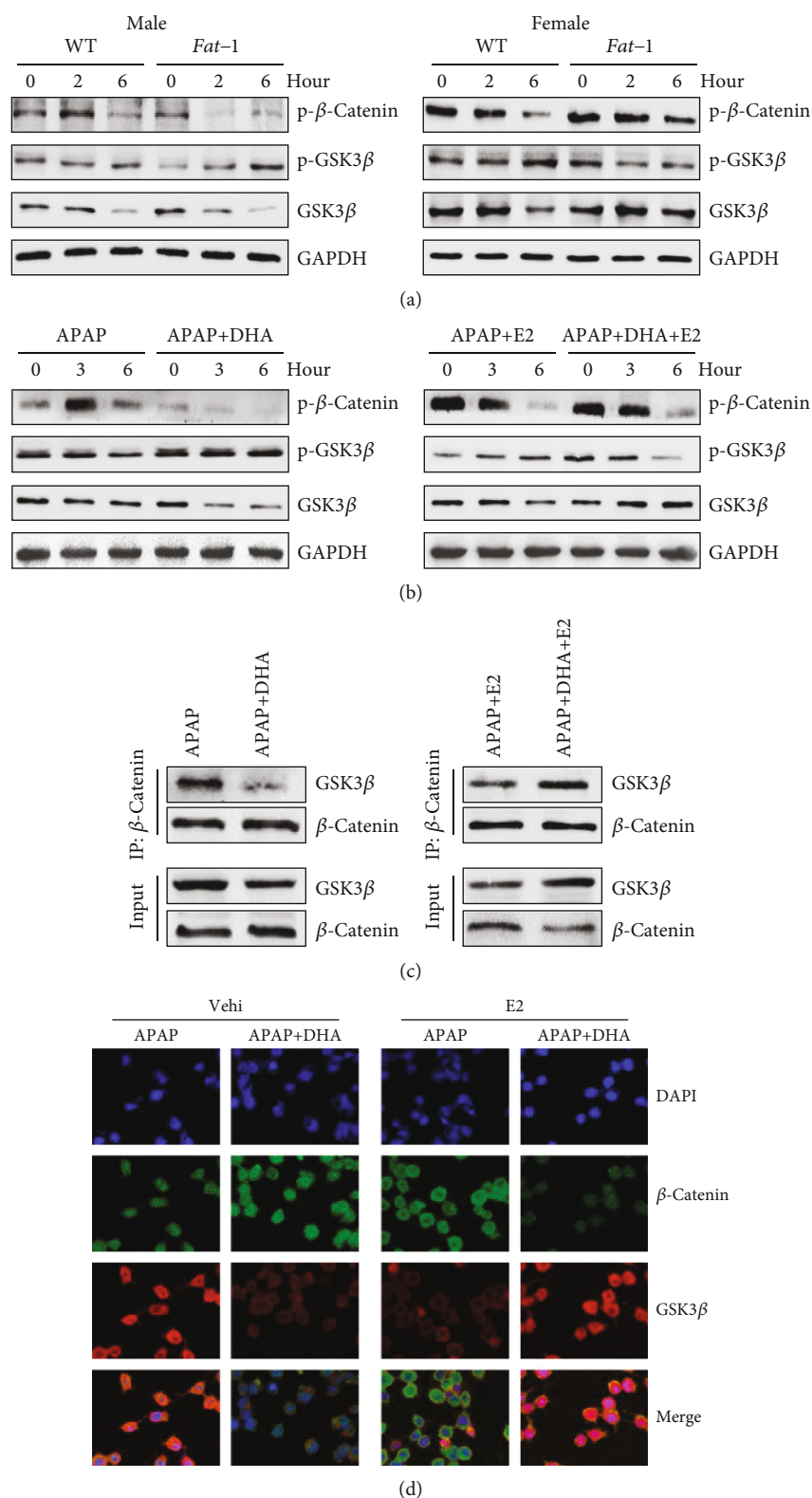
(a)

(b)

(c)

(d)

FIGURE 5: GSK3β contributes to the β-catenin signaling activation in response to n-3 PUFAs. (a) APAP (400 mg/kg) was intraperitoneally injected to male or female WT and fat-1 transgenic mice ($n = 5$). The phosphorylated levels of β-catenin and GSK3β were determined by immunoblotting assay. (b–d) HepaRG cells were pretreated with 50 μM DHA for 2 hours or 100 nM E2 for overnight before stimulated with 20 mM APAP. (b) The phosphorylation of β-catenin and GSK3β was determined by immunoblotting analysis at the indicated time point after APAP stimulation. (c, d) After being stimulated with APAP for 24 hours, the association of β-catenin with GSK3β in the cells was evaluated by immunoprecipitation (c) and immunofluorescence staining (d). The data represent three independent experiments with similar results.
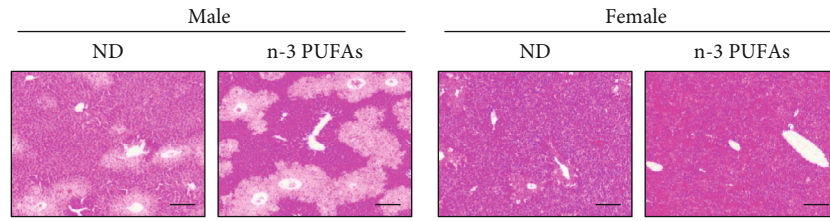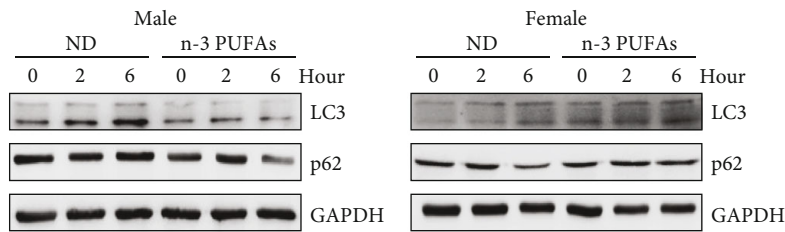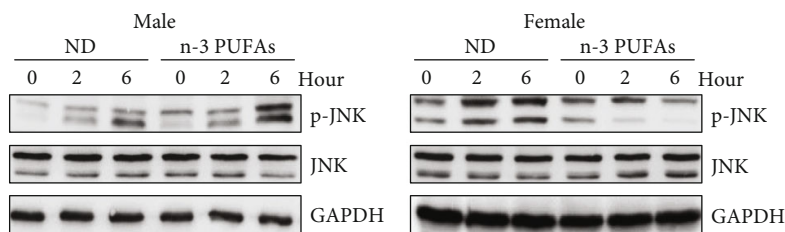
(a)
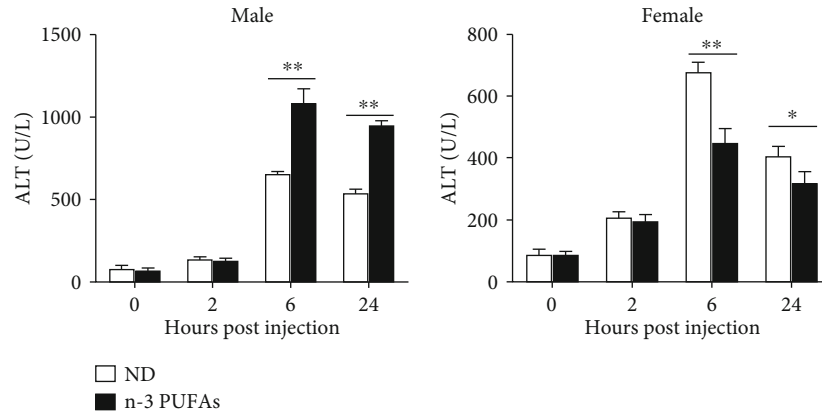
(b)
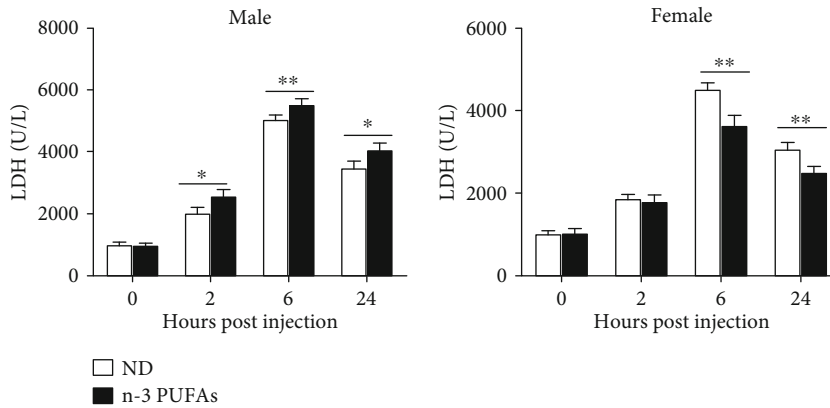
(c)
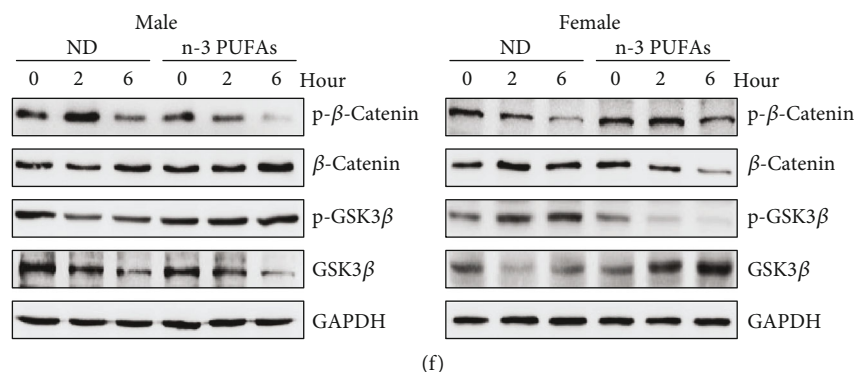

(d)

(e)

FIGURE 6: Continued.

(f)

FIGURE 6: Sex-specific effect of exogenous n-3 PUFAs on APAP-induced liver damage. APAP (400 mg/kg) was intraperitoneally injected into male or female WT mice fed with normal diet or n-3 PUFA-enriched diet ($n = 5$). (a) 24 hours after APAP injection, histological analysis of mouse livers was performed by H&E staining. Scale bars = 100 μm. (b, c) Serum ALT and LDH levels at different time points post-APAP injection were measured. (d) The protein levels of LC3 and p62 in liver tissues were determined by immunoblotting analysis. (e) Phosphorylation of JNK expression in livers was evaluated by immunoblotting analysis. (f) The phosphorylation of β-catenin and GSK3β was determined by immunoblotting analysis at the indicated time point after APAP administration. $^{**}p < 0.01$. The data represent three independent experiments with similar results.

target for APAP overdose [44]. Interestingly, it has been reported that ROS inhibited autophagy activation through TRPM2-CAMK2-BECN1P Ca^{2+} influx signaling during APAP hepatoxicity [45]. Our studies found inhibited autophagy activation and aggravated ROS production in male *fat-1* mice but promoted autophagy activation and limited ROS level in female *fat-1* mice. As previously reported, both upregulated LC3 and p62 expressions were observed in cisplatin-induced acute kidney injury, which involved the crosstalk between autophagy and signaling related to oxidative response [46]. We supposed that n-3 PUFAs suppressed autophagy activation, which led to accumulated injured mitochondria, thereby resulting in excessive ROS production during APAP exposure. The enhanced ROS production may in turn inhibit autophagy activation in the damaged hepatocytes. Moreover, estrogen might modulate the n-3 PUFA-mediated regulation of autophagy-oxidative stress interconnection during drug-induced liver injury.

β-Catenin plays an essential role in liver regeneration, and the role of β-catenin in acute liver injury has been steadily discovered [47]. Jiang et al. reported increased β-catenin-aggravated Con A-induced liver damage through regulation of the NF-κB pathway [48]. Loss of β-catenin in hepatocytes significantly ameliorated fulminant hepatitis via a similar mechanism [49]. Furthermore, β-catenin has been found to inhibit both LC3 and p62 expressions, which indicated impaired autophagosome formation [31]. We found higher levels of β-catenin in hepatocytes accompanied by severer liver damage during APAP exposure. Surprisingly, n-3 PUFAs exhibit a distinct effect on β-catenin signaling activation between male and female mice with APAP administration. Besides, estrogen did not affect the APAP hepatotoxicity by n-3 PUFA treatment when the Wnt/β-catenin signaling was blocked by XAV939, suggesting that the gender-dependent effect of n-3 PUFAs on APAP-induced liver injury relies on the regulation of the Wnt/β-catenin signaling pathway. Indeed, the crosstalk between Wnt/β-

catenin and estrogen receptor signaling has been reported in cell differentiation [50]. It is noteworthy that GSK3 plays a critical role in a diverse range of signaling pathways [33, 51]. GSK3β phosphorylation triggers β-catenin destabilization which is a key event in Wnt/β-catenin signaling [33]. Krishnankutty et al. found that GSK3β was principally in the active form with little Ser9 phosphorylation in mouse brains, and the phosphoisotypes of GSK3β change related to the regions of the brain, age, sex, and disease conditions [52]. In this study, we determined that GSK3β activity is differentially regulated by n-3 PUFAs in the liver depending on sex. Our data suggest that gender disruption in GSK3β-mediated Wnt/β-catenin pathway activation is linked to the differential regulation of autophagy and oxidative response in male and female n-3 PUFA-enriched mice upon APAP challenge.

In summary, our data revealed the significant differences in n-3 PUFA-regulated APAP hepatotoxicity in male and female mice. We demonstrated that β-catenin-mediated regulation of the autophagy process is the essential event for the n-3 PUFA-modulated APAP hepatotoxicity. This work would also provide a better understanding of the role of GSK3β/Wnt/β-catenin signaling in autophagy activation in relation to the sex-dependent manner of n-3 PUFAs in the regulation of APAP-induced liver injury.

Abbreviations

ALT: Alanine aminotransferase
APAP: Acetaminophen
BSA: Bovine serum albumin
DHA: Docosahexaenoic acid
E2:   17β-Estradiol
EPA: Eicosapentaenoic acid
FBS: Fetal bovine serum
GSH: Glutathione
H&E: Hematoxylin and eosin
HRP: Horseradish peroxidase

JNK: c-Jun N-terminal kinase
LC3-I: Cytosolic microtubule-associated protein 1
               light chain 3
LDH: Lactate dehydrogenase
n-3 PUFAs: Omega-3 polyunsaturated fatty acids
NAFLD: Nonalcohol fatty liver disease
NAPQI: N-Acetyl-p-benzoquinone imine
PE: Phosphatidylethanolamine
ROS: Reactive oxygen species
WCL: Whole-cell lysate
WT: Wild type.

Data Availability

The data used to support the findings of this study are available from the corresponding author upon request.

Conflicts of Interest

The authors declare that they have no known competing financial interests or personal relationships that could have appeared to influence the work reported in this paper.

Authors' Contributions

YL, ZC, KW, and DZ conceived the project. YL and DZ designed the experiments. YL, YC, AY, XX, ZZ, and YY performed the experiments. YL, JZ, DL, QZ, and XL carried out the data analysis. YL, KW, and DZ wrote the manuscript. All authors went through and approved the final manuscript.

Acknowledgments

Supplementary Materials

Supplemental Figure 1: sex-dependent effect of n-3 PUFAs on APAP-induced liver damage did not rely on NAPQI formation. (A) 400 mg/kg of APAP was intraperitoneally injected to male or female WT and fat-1 transgenic mice ($n = 5$). Hepatic GSH levels were measured at the indicated time point after APAP injection. (B) Male WT or fat-1 mice ($n = 5$) were intraperitoneally injected with 100 mg/kg of E2 7 days before APAP (400 mg/kg) administration. Hepatic GSH level was detected after APAP challenge. (C) 400 mg/kg of APAP was intraperitoneally injected into male or female WT mice fed with normal diet or n-3 PUFA-enriched diet ($n = 5$). Hepatic GSH level was determined at the indicated time point. NS: not significant. The data represent three independent experiments with similar results. Supplemental Figure 2: β-catenin inhibition abrogated the effect of estrogen on oxidative stress response and autophagy activation during APAP exposure. Primary hepatocytes from male WT or fat-1 mice were isolated and pretreated with 100 nM E2 overnight. Subsequently, the cells were incubated with 2 μM XAV939 for 2 hours and stimulated with APAP for another 6 hours. (A) The ROS level in the cells was detected by flow cytometry labeling with fluorescent probe DCFH-DA at 6 hours post-APAP administration. (B) Phosphorylation of JNK expression was measured by immunoblotting analysis. (C) The levels of LC3 and p62 were evaluated by immunoblotting analysis. $^{**}p < 0.01$; NS: not significant. The data represent three independent experiments with similar results. *(Supplementary Materials)*

References

[1] R. D. Goldman, "Acetaminophen in children an old drug with new warnings," *Canadian Family Physician*, vol. 59, no. 10, pp. 1065-1066, 2013.

[2] W. M. Lee, "Acetaminophen (APAP) hepatotoxicity–isn't it time for APAP to go away?," *Journal of Hepatology*, vol. 67, no. 6, pp. 1324–1331, 2017.

[3] B. K. Gunawan, Z. X. Liu, D. Han, N. Hanawa, W. A. Gaarde, and N. Kaplowitz, "c-Jun N-terminal kinase plays a major role in murine acetaminophen hepatotoxicity," *Gastroenterology*, vol. 131, no. 1, pp. 165–178, 2006.

[4] C. Latchoumycandane, C. W. Goh, M. M. K. Ong, and U. A. Boelsterli, "Mitochondrial protection by the JNK inhibitor leflunomide rescues mice from acetaminophen-induced liver injury," *Hepatology*, vol. 45, no. 2, pp. 412–421, 2007.

[5] C. Saito, C. Zwingmann, and H. Jaeschke, "Novel mechanisms of protection against acetaminophen hepatotoxicity in mice by glutathione and N-acetylcysteine," *Hepatology*, vol. 51, no. 1, pp. 246–254, 2010.

[6] G. Filomeni, D. De Zio, and F. Cecconi, "Oxidative stress and autophagy: the clash between damage and metabolic needs," *Cell Death and Differentiation*, vol. 22, no. 3, pp. 377–388, 2015.

[7] S. Shan, Z. Shen, and F. Song, "Autophagy and acetaminophen-induced hepatotoxicity," *Archives of Toxicology*, vol. 92, no. 7, pp. 2153–2161, 2018.

[8] H. M. Ni, A. Bockus, N. Boggess, H. Jaeschke, and W. X. Ding, "Activation of autophagy protects against acetaminophen-induced hepatotoxicity," *Hepatology*, vol. 55, no. 1, pp. 222–232, 2012.

[9] Y. Kabeya, N. Mizushima, T. Ueno et al., "LC3, a mammalian homologue of yeast Apg8p, is localized in autophagosome membranes after processing," *EMBO Journal*, vol. 19, no. 21, pp. 5720–5728, 2000.

[10] N. Mizushima, T. Yoshimori, and B. Levine, "Methods in mammalian autophagy research," *Cell*, vol. 140, no. 3, pp. 313–326, 2010.

[11] M. J. Zhang and M. Spite, "Resolvins: anti-inflammatory and proresolving mediators derived from omega-3 polyunsaturated fatty acids," *Annual Review of Nutrition*, vol. 32, no. 1, pp. 203–227, 2012.

[12] L. L. Huang, J. B. Wan, B. Wang et al., "Suppression of acute ethanol-induced hepatic steatosis by docosahexaenoic acid is associated with downregulation of stearoyl-CoA desaturase 1 and inflammatory cytokines," *Prostaglandins, Leukotrienes, and Essential Fatty Acids*, vol. 88, no. 5, pp. 347–353, 2013.

[13] C. Schmocker, K. H. Weylandt, L. Kahlke et al., "Omega-3 fatty acids alleviate chemically induced acute hepatitis by suppression of cytokines," *Hepatology*, vol. 45, no. 4, pp. 864–869, 2007.

[14] Y. Li, Y. Tang, S. Wang et al., "Endogenous n-3 polyunsaturated fatty acids attenuate T cell-mediated hepatitis via autophagy activation," *Frontiers in Immunology*, vol. 7, p. 350, 2016.

[15] E. Scorletti and C. D. Byrne, "Omega-3 fatty acids and nonalcoholic fatty liver disease: evidence of efficacy and mechanism of action," *Molecular Aspects of Medicine*, vol. 64, pp. 135–146, 2018.

[16] J. Yang, M. Fernández-Galilea, L. Martínez-Fernández et al., "Oxidative stress and non-alcoholic fatty liver disease: effects of omega-3 fatty acid supplementation," *Nutrients*, vol. 11, no. 4, p. 872, 2019.

[17] K. A. Abbott, M. Veysey, M. Lucock et al., "Sex-dependent association between erythrocyte *n*-3 PUFA and type 2 diabetes in older overweight people," *British Journal of Nutrition*, vol. 115, no. 8, pp. 1379–1386, 2016.

[18] S. P. Hoile, R. Clarke-Harris, R. C. Huang et al., "Supplementation with N-3 long-chain polyunsaturated fatty acids or olive oil in men and women with renal disease induces differential changes in the DNA methylation of FADS2 and ELOVL5 in peripheral blood mononuclear cells," *PLoS One*, vol. 9, no. 10, article e109896, 2014.

[19] J. Oya, T. Nakagami, S. Sasaki et al., "Intake of *n*-3 polyunsaturated fatty acids and non-alcoholic fatty liver disease: a cross-sectional study in Japanese men and women," *European Journal of Clinical Nutrition*, vol. 64, no. 10, pp. 1179–1185, 2010.

[20] M. Phang, F. E. Scorgie, M. Seldon, M. L. Garg, and L. F. Lincz, "Reduction of prothrombin and factor V levels following supplementation with omega-3 fatty acids is sex dependent: a randomised controlled study," *The Journal of Nutritional Biochemistry*, vol. 25, no. 10, pp. 997–1002, 2014.

[21] Y. H. Lin, J. A. Brown, C. DiMartino, I. Dahms, N. Salem, and J. R. Hibbeln, "Differences in long chain polyunsaturates composition and metabolism in male and female rats," *Prostaglandins Leukotrienes and Essential Fatty Acids*, vol. 113, pp. 19–27, 2016.

[22] C. E. Childs, M. Romeu-Nadal, G. C. Burdge, and P. C. Calder, "Gender differences in the *n*-3 fatty acid content of tissues," *Proceedings of the Nutrition Society*, vol. 67, no. 1, pp. 19–27, 2008.

[23] C. M. Sibbons, J. T. Brenna, P. Lawrence et al., "Effect of sex hormones on n-3 polyunsaturated fatty acid biosynthesis in HepG2 cells and in human primary hepatocytes," *Prostaglandins Leukotrienes and Essential Fatty Acids*, vol. 90, no. 2-3, pp. 47–54, 2014.

[24] J. X. Kang, J. Wang, L. Wu, and Z. B. Kang, "*Fat-1* mice convert *n*-6 to *n*-3 fatty acids," *Nature*, vol. 427, no. 6974, p. 504, 2004.

[25] Z. Chen, Y. Zhang, C. Jia et al., "mTORC1/2 targeted by n-3 polyunsaturated fatty acids in the prevention of mammary tumorigenesis and tumor progression," *Oncogene*, vol. 33, no. 37, pp. 4548–4557, 2014.

[26] Y. Osawa, H. Uchinami, J. Bielawski, R. F. Schwabe, Y. A. Hannun, and D. A. Brenner, "Roles for C_{16}-ceramide and sphingosine 1-phosphate in regulating hepatocyte apoptosis in response to tumor necrosis factor-α," *Journal of Biological Chemistry*, vol. 280, no. 30, pp. 27879–27887, 2005.

[27] H. Li, Y. Liu, J. Li et al., "Mannan-binding lectin attenuates acetaminophen-induced hepatotoxicity by regulating CYP2E1 expression via ROS-dependent JNK/SP1 pathway," *European Journal of Immunology*, vol. 49, no. 4, pp. 564–575, 2019.

[28] B. Bhushan and U. Apte, "Acetaminophen tests battery (ATB): a comprehensive method to study acetaminophen-induced acute liver injury," *Gene Expression*, 2020.

[29] H. Jaeschke and A. Ramachandran, "Oxidant stress and lipid peroxidation in acetaminophen hepatotoxicity," *Reactive Oxygen Species*, vol. 5, no. 15, pp. 145–158, 2018.

[30] M. J. Czaja, "Cell signaling in oxidative stress-induced liver injury," *Seminars in Liver Disease*, vol. 27, no. 4, pp. 378–389, 2007.

[31] K. J. Petherick, A. C. Williams, J. D. Lane et al., "Autolysosomal *β*-catenin degradation regulates Wnt-autophagy-p62 crosstalk," *EMBO Journal*, vol. 32, no. 13, pp. 1903–1916, 2013.

[32] D. Stakheev, P. Taborska, Z. Strizova, M. Podrazil, J. Bartunkova, and D. Smrz, "The WNT/*β*-catenin signaling inhibitor XAV939 enhances the elimination of LNCaP and PC-3 prostate cancer cells by prostate cancer patient lymphocytes *in vitro*," *Scientific Reports*, vol. 9, no. 1, p. 4761, 2019.

[33] D. Wu and W. Pan, "GSK3: a multifaceted kinase in Wnt signaling," *Trends in Biochemical Sciences*, vol. 35, no. 3, pp. 161–168, 2010.

[34] J. Qian, C. Trzepacz, C. Phiel, and J. Groden, "A dual-kinase mechanism controls APC phosphorylation and dissociation from microtubules during mitosis," *Faseb Journal*, vol. 23, 2009.

[35] E. Buzzetti, P. M. Parikh, A. Gerussi, and E. Tsochatzis, "Gender differences in liver disease and the drug-dose gender gap," *Pharmacological Research*, vol. 120, pp. 97–108, 2017.

[36] S. Sutti and F. Tacke, "Liver inflammation and regeneration in drug-induced liver injury: sex matters!," *Clinical Science*, vol. 132, no. 5, pp. 609–613, 2018.

[37] M. Chen, A. Suzuki, J. Borlak, R. J. Andrade, and M. I. Lucena, "Drug-induced liver injury: interactions between drug properties and host factors," *Journal of Hepatology*, vol. 63, no. 2, pp. 503–514, 2015.

[38] B. Kumarendran, M. W. O'Reilly, K. N. Manolopoulos et al., "Polycystic ovary syndrome, androgen excess, and the risk of nonalcoholic fatty liver disease in women: a longitudinal study based on a United Kingdom primary care database," *PLoS Medicine*, vol. 15, no. 3, article e1002542, 2018.

[39] N. Zaima, S. Kinoshita, N. Hieda et al., "Effect of dietary fish oil on mouse testosterone level and the distribution of eicosapentaenoic acid-containing phosphatidylcholine in testicular interstitium," *Biochemistry and Biophysics Reports*, vol. 7, pp. 259–265, 2016.

[40] R. Feng, Y. Wang, C. Liu et al., "Acetaminophen-induced liver injury is attenuated in transgenic *fat-1* mice endogenously synthesizing long-chain n-3 fatty acids," *Biochemical Pharmacology*, vol. 154, pp. 75–88, 2018.

[41] W. Liu, F. Innocenti, M. H. Wu et al., "A functional common polymorphism in a Sp1 recognition site of the epidermal growth factor receptor gene promoter," *Cancer Research*, vol. 65, no. 1, pp. 46–53, 2005.

[42] K. Du, C. D. Williams, M. R. McGill, and H. Jaeschke, "Lower susceptibility of female mice to acetaminophen hepatotoxicity: role of mitochondrial glutathione, oxidant stress and c-jun *N-*

terminal kinase," *Toxicology and Applied Pharmacology*, vol. 281, no. 1, pp. 58–66, 2014.

[43] M. J. Czaja, W. X. Ding, T. M. Donohue et al., "Functions of autophagy in normal and diseased liver," *Autophagy*, vol. 9, no. 8, pp. 1131–1158, 2014.

[44] Q.-Z. Sun, G. F. Lin, L. L. Li et al., "Discovery of potent and selective inhibitors of Cdc2-like kinase 1 (CLK1) as a new class of autophagy inducers," *Journal of Medicinal Chemistry*, vol. 60, no. 14, pp. 6337–6352, 2017.

[45] Q. Wang, W. Guo, B. Hao et al., "Mechanistic study of TRPM2-Ca^{2+}-CAMK2-BECN1 signaling in oxidative stress-induced autophagy inhibition," *Autophagy*, vol. 12, no. 8, pp. 1340–1354, 2016.

[46] W. Liao, Z. Wang, Z. Fu et al., "p62/SQSTM1 protects against cisplatin-induced oxidative stress in kidneys by mediating the cross talk between autophagy and the Keap1-Nrf2 signalling pathway," *Free Radical Research*, vol. 53, no. 7, pp. 800–814, 2019.

[47] H. Clevers and R. Nusse, "Wnt/β-catenin signaling and disease," *Cell*, vol. 149, no. 6, pp. 1192–1205, 2012.

[48] R. Jiang, D. Chen, J. Hou et al., "Survival and inflammation promotion effect of PTPRO in fulminant hepatitis is associated with NF-κB activation," *Journal of Immunology*, vol. 193, no. 10, pp. 5161–5170, 2014.

[49] S. S. Zou, W. Yang, H. X. Yan et al., "Role of β-catenin in regulating the balance between TNF-α- and Fas-induced acute liver injury," *Cancer Letters*, vol. 335, no. 1, pp. 160–167, 2013.

[50] Y. Gao, E. Huang, H. Zhang et al., "Crosstalk between Wnt/β-catenin and estrogen receptor signaling synergistically promotes osteogenic differentiation of mesenchymal progenitor cells," *PLoS One*, vol. 8, no. 12, article e82436, 2013.

[51] E. Beurel, S. F. Grieco, and R. S. Jope, "Glycogen synthase kinase-3 (GSK3): regulation, actions, and diseases," *Pharmacology & Therapeutics*, vol. 148, pp. 114–131, 2015.

[52] A. Krishnankutty, T. Kimura, T. Saito et al., "*In vivo* regulation of glycogen synthase kinase 3β activity in neurons and brains," *Scientific Reports*, vol. 7, no. 1, article 8602, 2017.